Upper Crustal and Lithosphere-Asthenosphere Boundary Seismic Structure of 0-75 Ma old Normal Oceanic Lithosphere in the Equatorial Atlantic Ocean

Pranav Audhkhasi

Université de Paris

Ecole doctorale 560 - Physique de l'Univers

l'INSTITUT DE PHYSIQUE DU GLOBE DE PARIS

Upper Crustal and Lithosphere-Asthenosphere Boundary Seismic Structure of 0-75 Ma old Normal Oceanic Lithosphere in the Equatorial Atlantic Ocean

Par: **Pranav Audhkhasi**

Thèse de doctorat de Sciences de la Terre et de l'environment

Dirigée par: Satish C. Singh

Présentée et soutenue publiquement le 14 septembre 2020

Devant un jury composé de :

Ingo Grevemeyer Professeur (GEOMAR - Germany)	Rapporteur
James B. Gaherty Professeur (Northern Arizona University – USA)	Rapporteur
Barbara Romanowicz Professeure (UC Berkeley – USA)	Membre
Claude Jaupart Professeur (IPG Paris – France)	Président
Alessia Maggi Professeure (IPG Strasbourg - France)	Membre
Anne Becel Chercheure (LDEO, Columbia University - USA)	Membre
Satish C. Singh Professeur (IPG Paris - France)	Directeur de thése

Upper Crustal and Lithosphere-Asthenosphere Boundary Seismic Structure of 0-75 Ma old Normal Oceanic Lithosphere in the Equatorial Atlantic Ocean

Pranav Audhkhasi

Supervisor: Satish C. Singh

14/09/2020

Résumé

Depuis que l'idée d'une lithosphère rigide flottante rigide sur une asthénosphère convective a été proposée il y a plus d'un siècle, beaucoup de scientifiques se sont intéressés à mieux comprendre la nature et l'évolution de la lithosphère océanique depuis sa formation niveau des rides océaniques jusqu'aux marges continentales. Sur l'axe de la ride, il l'épaisseur de croûte océanique est mince mais, en se refroidissant, celle-ci s'affaisse et s'épaissit avec l'âge en s'éloignant de l'axe de la ride. Bien que ce processus de vieillissement lithosphérique soit bien compris en général, la connaissance des détails de ce mécanisme reste trés peu compris. Dans cette thèse, je présenterai l'évolution de la croûte océanique supérieure et de la frontière lithosphère-asthénosphère de la dorsale médio-atlantique, dite lente, à de l'âge zéro à 75 Ma. Je détaillerai principalement une zone située au niveau de la région équatoriale Atlantique sur la plaque africaine. J'utiliserai des données de sismique réflexion à déport ultra-long acquises lors du projet d'imagerie transatlantique de la limite de la lithosphère-asthénosphère (LAB) (TransAtlantic-ILAB) en 2015, où 1400 km de données sismiques multitraces ont été acquises à l'aide d'un streamer isométrique de 12 km et d'une source de canons à air très puissant, cela afin d'imager la structure sismique jusqu'à 90 km de profondeur tout en permettant également de quantifier la nature de la croûte océanique supérieure.

Les deux premiers kilomètres de la croûte océanique, définissant la croûte supérieure, sont dynamiques et sont affectés par différents processus tels que le magmatisme, la tectonique, la subsidence, la circulation hydrothermale et la sédimentation. La croûte est subdivisée en une couche basaltique extrusive, la couche 2A, et la couche sous-jacente 2B. La plupart des études précédentes sur la croûte supérieure ont été basées sur la sismique grand angle qui a une mauvaise résolution pour la croûte océanique supérieure et les forages qui fournissent seulement des informations locales. Dans ce travail, je trouve que la limite de la couche 2A/2B, étant un événement grand angle, est observée dans les données sismiques multitraces tout le long du profil de 0 à 75 Ma. L'inversion tomographique pour les vitesses des ondes P de la croûte supérieure obtenues en utilisant les premières arrivées extraploées vers le bas à des âges distincts de 0 à 75 Ma montre que les vitesses des ondes P au sommet de la croûte ne dépassent jamais 4,5 km/s. De plus, les vitesses des ondes P au sommet de la croûte (i.e., couche 2A) et au sommet de la couche 2B deviennent statistiquement constantes au-delà de 4 Ma, suggérant que la majeure partie de l'évolution de la croûte supérieure est limitée aux 4 premiers Ma à partir de l'axe de la ride. Une sédimentation rapide à l'écart de l'axe de la ride est également observée dans les 4 premiers Ma, indiquant un lien possible entre la sédimentation et l'évolution de la couche 2A. Outre la sédimentation, l'apport de chaleur réduit loin de l'axe de la ride limite l'étendue de la circulation hydrothermale à haute température/active aux 4 premiers Ma, au-delà

de laquelle la circulation hydrothermale à basse température/passive affecte la couche 2A. L'épaisseur de la couche 2A passe de ∼900 m à l'axe de la crête à ∼600 m hors axe, la circulation hydrothermale étant responsable de la modification de la base de la couche 2A. Les estimations de la porosité à partir des vitesses des ondes P indiquent en outre que les résultats du forage sont bien expliqués par la couche 2A ayant des fissures trois fois plus minces par rapport à la couche 2B. La limite de la couche 2A/2B se trouve être la limite de lave/dyke au niveau de l'axe de la ride et une limite d'altération hydrothermale dans le flux de lave loin de l'axe de la ride. L'analyse des données de flux de chaleur conductrices en ce même lieu confirme l'hypothèse proposée de poursuite de la circulation hydrothermale loin de l'axe de la ride, car les valeurs de flux de chaleur observées sont inférieures aux valeurs de flux de chaleur prévues. La différence entre le flux de chaleur observé et celui prévu est attribuée à la circulation de l'eau de mer redistribuant la chaleur. De plus, les données de flux de chaleur colocalisées sont également utilisées pour estimer les perméabilités et des estimations de porosité-perméabilité sont déduites.

Le fond rugueux de la croûte océanique plus jeune rend l'imagerie de la limite lithosphère asthenosphere (appelée LAB) difficile, mais nous imageons un événement à 2 Ma situé ∼25 km en-dessous du fond marin plongeant vers une lithosphère océanique plus ancienne, suggérant une lithosphère épaisse près de la ride. La LAB est mal imagée entre 5 Ma et 27 Ma. Cependant, la LAB est bien imagée entre 27 et 75 Ma. Entre 27 et 47 Ma, on observe deux reflexions: la première plongeant vers un âge avancé et la seconde presque plate à 85 km de profondeur. La réflexion supérieure a une polarité négative, suggérant une diminution de la vitesse des ondes P tandis que la réflexion plus profonde a une polarité positive, indiquant un contraste de vitesse élevé ou une augmentation de la vitesse. La réflexion supérieure correspond à l'isotherme ∼1300°C, suggérant que cette réflexion pourrait être la base de la lithosphère, et la deuxième réflexion plus profonde pourrait être la base du canal LAB. La réflexion supérieure pourrait être la limite entre une zone liquide et le manteau encaissant, tandis que la réflexion inférieure pourrait représenter la base d'une zone de fusion près de l'axe de la ride, et la zone entre ces deux réflexions pourrait être un canal de fusion sous-lithosphérique. Cependant, pour une lithosphère plus âgée entre 49 et 75 Ma, nous n'observons qu'une seule réflexion avec une polarité négative, où la vitesse de l'onde P chute de ∼8.8%. Cette réflexion est moins profonde et est associée à l'isotherme 1130°C. Fait intéressant, nous observons également une élévation de 400 m du socle et une anomalie de bouguer négative, toutes deux indicatives d'une anomalie thermique dans le manteau. Dans l'ensemble, ces observations suggèrent que la faible profondeur de cette réflexion est associée à l'amincissement de la lithosphère en raison d'une anomalie thermique et au réchauffement de la lithosphère en raison de l'écoulement mantellique chaud du point chaud du Cameroun. L'absence de réflexion plus profonde pourrait être due au réchauffement de la base du canal de fusion, créant une frontière diffuse. Ces résultats indiquent que la LAB est plus hétérogène que précédemment supposé.

Abstract

Ever since the idea of a rigid floating lithosphere over a convective asthenosphere was proposed over a century ago, there has been great interest in understanding the nature and evolution of the oceanic lithosphere from its formation at ocean spreading centers to continental margins. On the ridge axis, it is thin but as it cools, it subsides and thickens with age away from the ridge axis. Although there is a broad understanding of this lithospheric aging process, the details remain poorly understood. In this thesis, I will present the evolution of the upper oceanic crust and the lithosphere-asthenosphere boundary from the Mid-Atlantic Ridge at zero age to 75 Ma in the equatorial Atlantic region on the African Plate for a lithosphere formed in a slow spreading environment. I will use ultra-long offset seismic reflection data acquired during the Trans-Atlantic Imaging of Lithosphere-Asthenosphere Boundary (LAB, TransAtlantic-ILAB) project in 2015 where 1400 km of multi-channel multi-component seismic data was acquired using a 12 km long Isometric streamer and a very large air-gun source in order to image seismic structure down to 90 km depth while also allowing to quantify the nature of upper oceanic crust.

The upper 2 km of the oceanic crust, i.e. the upper crust, is dynamic and is affected by different processes such as magmatism, faulting, subsidence, hydrothermal circulation and sedimentation, and has been previously sub-divided into an extrusive basaltic layer, layer 2A and the underlying 2B. Most of the previous studies of the upper crust have been based on wide-angle seismic which have poor resolution for upper oceanic crust and on boreholes which provide only local information. I find that the layer 2A/2B boundary, being a wide-angle event, is observed in the multi-channel seismic data all along the profile from 0-75 Ma. Tomographic inversion for upper crustal P-velocities using the downward continued first arrivals at distinct ages from 0-75 Ma shows that the P-velocities at top of the crust never exceed 4.5 km/s. Additionally, the P-velocities at top of the crust (layer 2A) and top of layer 2B become statistically constant beyond 4 Myr, suggesting that most of the evolution of the upper crust is limited to the first 4 Myr from the ridge-axis. Rapid sedimentation away from the ridge-axis is also observed within the first 4 Myr, indicating a possible link between sedimentation and evolution of the layer 2A. Apart from sedimentation, reduced heat supply away from the ridge-axis limits the extent of high-temperature/active hydrothermal circulation to the first 4 Myr, beyond which low-temperature/passive hydrothermal circulation affects the layer 2A. The thickness of the layer 2A decreases from ∼900 m at the ridge-axis to ∼600 m off-axis, with hydrothermal circulation responsible for altering the base of layer 2A. Porosity estimates from P-velocities further indicate that the borehole results are well explained by layer 2A having three times thinner cracks with respect to layer 2B. The layer 2A/2B boundary is

found to be the lava/dyke boundary at the ridge-axis and a hydrothermal alteration boundary within the lava flow away from the ridge-axis. Analysis of the co-located conductive heat-flow data confirms the proposed hypothesis of continuing hydrothermal circulation away from the ridge -axis as the observed heat-flow values are lower than the predicted heat-flow values. This difference between observed and predicted heat-flow is attributed to circulation of seawater redistributing the heat. Additionally, the co-located heat-flow data is also used to estimate permeabilities and porosity-bulk permeability estimates are deduced.

The rough seafloor for younger oceanic crust makes imaging of the LAB challenging, but we do image an event for 2 Ma at ∼25 km below the seafloor dipping towards older oceanic lithosphere, suggesting a thick lithosphere near the ridge. The LAB is poorly imaged from 5 Myr to 27 Myr. However, the LAB is well imaged from 27 to 75 Myr. Between 27 and 47 Myr, we observe two reflections, the first one dipping towards older age and the second one nearly flat at 85 km depth. The upper reflection has a negative polarity, suggesting a decrease in P-wave velocity while the deeper reflection has a positive polarity, indicating a high velocity contrast or increase in velocity. The upper reflection corresponds to ∼1300°C isotherm, suggesting that this reflection could be the base of the lithosphere, and the second deeper reflection could be the base of the LAB channel. The upper reflection could be the freezing boundary whereas the lower reflection could represent the base of the melting zone near the ridge-axis, and the zone between these two reflections could be a sub-lithospheric melt-channel. However, for older lithosphere aged between 49 and 75 Myr, we only observe a single reflection with a negative polarity, where the P-wave velocity drops by ∼8.8%. This reflection is shallower and is associated with 1130°C isotherm. Interestingly, we also observe a 400 m upliftment of the basement and a negative mantle bouguer anomaly, both indicative of a thermal anomaly in the mantle. Taken together, these observations suggest that the shallowing of this reflection is associated with the thinning of the lithosphere due to thermal anomaly and re-heating of the lithosphere due to hot mantle flow from the Cameroon hotspot. The absence of the deeper reflection could be due to the re-heating of the base of the melt-channel, creating a diffuse boundary. These results indicate that the LAB is more heterogeneous than previously realized.

Acknowledgements

The journey of my PhD has been far more difficult than what I had envisioned when I embarked upon it. The technical difficulties in imaging a reflection hundred kilometers in deep Earth heavily outweighed the scientific importance of the project. I persevered and got success quite late, extending a three year PhD into almost five years. I would like to thank a number of people below who have contributed to the culmination of this journey.

First I am grateful to my supervisor Satish C. Singh for shaping this thesis into its present form. His suggestion to divert my thesis to upper crustal analysis when I was struggling to get the LAB results was very crucial. The publications from this thesis are a result of many scientific discussions with him. I would also like to thank him for financially supporting my thesis throughout the five long years.

I am also grateful to the members of my annual thesis committee, Jean-Paul Montagner and especially Hélène Carton, for their encouraging reports on my often not so solid progress.

Fares provided important help during the initial part of my PhD, when I had no idea how to take this project ahead. Hanchao helped me a lot with the tomography code and motivated me to finish my thesis at a time when I was two years into my PhD and without any interesting results. Thanks also to Gabriel and Yanfang for solving the trivial issues I faced from time to time. Thanks also to some former members of the team: Shihao, Weiguang, Momoh and Oceane who have contributed to my experience here in some way.

My administrative life during the PhD has been very well taken care of by Marie-Dominique and Lydie Guillerot. Mihai Roharik has helped me countless times with the various technical issues I faced from time to time. To them, I am sincerely thankful.

A special thanks is also due to Milena, who mentored me during my master internship and also provided useful insights relevant to my thesis. I am quite lucky to have Emma as an office mate during the final stages of my PhD. I cannot forget some of the memorable day long cycling trips with Venkata and also thank him for introducing me to the Buddhist philosophy. I am also thankful to other members of our team including Alex, Aline, Aurelie, Benjamin, Hanjin, Jie, Lianjun, Zhikai, Manon, Matilde, Nirmit, Souradeep and Vaibhav and some others from the seismology group. Shipra and Venkatesh have been good friends throughout their PhD. Gaurav, Satish (the other one) and another Gaurav were like big brothers to me and helped me get used to the PhD life here at IPGP during my initial stages.

Thanks is also due to my friends outside work - Akash, Amey, Rohit, Sathya for making my life outside the lab interesting and with whom I have shared memorable trips across Europe. I am also thankful to my audiologist, Elisa, for solving the various problems I have faced with my hearing aids.

I am grateful to the jury members of the defence committee for accepting to review my thesis and for agreeing to participate in an online defence especially in these difficult times.

Lastly, I would like to thank my family for supporting me during the struggling stages in this journey.

Contents

Chapter 1

Introduction

Depuis les premières observations sismiques d'une lithosphère flottante rigide couvrant une asthénosphère à basse vitesse (*Gutenberg*, 1926, 1948, 1955, 1959) dans le manteau, la formation et l'évolution de la lithosphère océanique ont été encore plus largement étudiées par les géophysiciens. Cette thèse vise à améliorer la compréhension scientifique de la lithosphère océanique et les différents processus qui l'affectent. La lithosphére océanique elle-même peut être divisée en une croûte lithosphérique, qui constitue les premiers ∼6 km de la lithosphère et le manteau lithosphèrique sous-jacent. Les deux premiers kilometres de la croûte lithosphèrique est également classé comme une croûte océanique supérieure et est l'un des objectifs de cette thèse. Les divers processus affectant la croûte océanique supérieure comprennent l'affaissement de la croute lorsqu'elle s'éloigne de la ride, elle s'affaisse également; la sédimentation le dépôt de sédiments sur la croûte supérieure; la circulation hydrothermale - l'interaction de l'eau de mer avec les roches basaltiques de la croûte océanique supérieure. Le manteau lithosphérique plus profond et la frontière Lithosphère-Asthénosphère (également appelée G-discontinuité dans certaines études) est l'autre objectif de cette thèse. Les processus affectant le manteau lithosphérique et la limite lithosphère-asthénosphère (LAB) sont principalement des hétérogénéités dispersées et des anomalies thermiques dans le manteau. Les hétérogénéités sont principalement de la pyroxénite grenat et de l'éclogite (*Anderson*, 2006) formées en raison du recyclage de la couche de basalte sur la plaque entrant en subduction dans les zones de subduction et sont censées être uniformément réparties dans le manteau (*Kennett and Furumura*, 2015). Les anomalies thermiques dans le manteau sont principalement causées par des panaches de remontée mantellique dans des points chauds tels que Hawaii (*Li et al.*, 2000) et La Réunion (*Bonneville et al.*, 1997).

La compréhension de l'évolution et des divers processus affectant la croûte supérieure était limitée jusqu'à très récemment en raison du manque de données sur la croûte océanique mature (> 40 Ma). Une autre raison était que les données sismiques grand angle étaient utilisées pour déduire les proprietés de la croûte océanique supérieure (*Grevemeyer and Weigel*, 1996), mais que celle-ci ont une résolution très faible dans la croûte océanique supérieure. De nombreuses études ont montré que la croûte océanique supérieure est subdivisée en basaltes extrusifs (couche 2A) et en une couche sous-jacente (2B) (*Tivey et al.*, 1998). La composition de la couche 2B n'a pas été vérifiée car il y a conflit entre les données de forage (*Carlson*, 2011) et les études sismiques (*Vera et al.*, 1990; *Harding et al.*, 1993). Les études sismologiques telles que les fonctions récepteurs (*Kawakatsu et al.*, 2009; *Kumar and Kawakatsu*, 2011), la vitesse de cisaillement des ondes de surface (*Maggi et al.*, 2006; *Auer et al.*, 2014) et l'anisotropie (*Burgos et al.*, 2014) ainsi que les études magnétotelluriques (*Naif et al.*, 2013) ont réussi à imager la structure profonde de la lithosphère. Cependant, ces méthodes souffrent de l'inconvénient d'avoir une faible résolution verticale, de l'ordre de ∼10 km. En conséquence, la structure à échelle fine du manteau supérieur est lissée. Pour remédier à ces limites, le projet d'imagerie transatlantique de la limite lithosphère-asthénosphère (Lithosphere-Asthenosphere Boundary, LAB) a été conçu. Lors de la première expédition en 2015, des données sismiques multitraces (MCS) utilisant une flûte de 12 km ont été collectées au niveau d'une lithosphère océanique normale de 0 à 75 Ma dans l'océan Atlantique équatorial.

Le streamer utilisé était un streamer Isometrix avancé (*Vassallo et al.*, 2013) avec 3857 récepteurs espacés tous les 3,125 m. Le réseau de canons à air utilisé comme source était l'un des plus puissants de l'industrie avec une capacité de 10170 pouces cubes. Le profil a été acquis dans trois lignes différentes couvrant chacune 0-1,8 Ma, 1,8-46,7 Ma et 49,3-75,6 Ma que j'ai combinées ensemble pour obtenir une variation continue de 0-75 Ma. L'océan Atlantique équatorial sur la plaque africaine est délimité par la zone de fracture de la chaîne au nord et la zone de fracture de l'Ascension au sud. Un certain nombre de zones de fracture et de petites discontinuités dans la région d'étude sont attribués à un rift se propageant plus lentement vers le nord entre les plaques Afrique et Amérique du Sud, qui s'est initié à ∼110 Ma en raison du point chaud de Tristan (*Granot and Dyment*, 2015). Plus à l'est du profil se terminant à 75,6 Ma se trouvent les lignes volcaniques de Sainte-Hélène et du Cameroun. La deuxième expédition a eu lieu en 2017 et une bathymétrie haute résolution avec un swath de 11 km, un flux de chaleur conducteur, des données parason et des données sismiques grand angle ont été acquis sur le même profil que celui de 1,8 à 46,7 Ma de la première expédition. J'utilise principalement les données MCS de l'expédition 2015 pour atteindre les objectifs et prendre le support des données de flux de chaleur de l'expédition 2017 pour améliorer mon interprétation.

Cette thèse est scindée en deux pour aborder les deux objectifs de la compréhension de l'évolution de la croûte océanique supérieure et de la lithosphère (LAB). Le chapitre 1 décrit en détail les deux expéditions effectuées, les différents modèles expliquant les processus de subsidence et de refroidissement de la lithosphère, les observations existantes et les modèles concurrents de la croûte océanique supérieure et de la LAB et enfin, l'évolution générale de la région d'étude. Le chapitre 2 décrit les aspects théoriques des méthodologies et du traitement des données utilisés dans cette thèse. Le chapitre 3 se concentre sur la structure de la croûte océanique supérieure que j'étudie à la fois par imagerie sismique et par tomographie haute résolution. De plus, j'ai utilisé les données de flux de chaleur colocalisées pour mieux contraindre l'interprétation. Dans le chapitre 4, j'étudie les effets possibles des chaînes volcaniques de Sainte-Hélène et du Cameroun sur la lithosphère et la LAB la plus proche de ces chaînes. Dans le chapitre 5, la lithosphère éloignée de ces chaînes volcaniques est analysée pour fournir une image complète de la lithosphère océanique. Je conclus les résultats scientifiques de cette thèse dans le chapitre 6 et énumère quelques travaux en cours et publications prévues.

Ever since the first seismic observations of a rigid floating lithosphere overlying a low velocity asthenosphere (*Gutenberg*, 1926, 1948, 1955, 1959) in the mantle, the formation and evolution of the oceanic lithosphere has been even more extensively studied by the geophysicists. This thesis is an attempt to improve upon the scientific understanding of the oceanic lithosphere and the various processes affecting it. The oceanic lithosphere itself can be divided into a lithospheric crust, which is the top ∼6 km of the lithosphere and the underlying lithospheric mantle. The top ∼2 km of the lithospheric crust is further classified as upper oceanic crust and is one of the objectives of this thesis. The various processes affecting the upper oceanic crust include subsidence - as the crust is formed at the ridge-axis and moves away, it also subsides; sedimentation - deposition of sediments on the upper crust; hydrothermal circulation - the interaction of seawater with the basaltic rocks of the upper oceanic crust. The deeper lithospheric mantle and the Lithosphere-Asthenosphere boundary (also termed as the G-discontinuity in some studies) is the other objective of this thesis. The processes affecting the lithospheric mantle and the Lithosphere-Asthenosphere boundary (LAB) are mainly the scattered heterogeneties and thermal anomalies in the mantle. The heterogeneities are mainly garnet pyroxenite and eclogite (*Anderson*, 2006) formed due to the recycling of the subducting basaltic slab at subduction zones and are assumed to be uniformly distributed in the mantle (*Kennett and Furumura*, 2015). The thermal anomalies in the mantle are mainly caused due to upwelling plumes at hotspots such as Hawaii (*Li et al.*, 2000) and Reunion (*Bonneville et al.*, 1997).

The understanding of the evolution of the upper crust and various processes affecting it was limited until very recently due to lack of data for mature oceanic rust (>40 Ma). Another reason was that wide-angle seismic data was being used to constrain the properties of the upper oceanic crust (*Grevemeyer and Weigel*, 1996), which have very low resolution in the upper oceanic crust. Previous studies have shown that the upper oceanic crust is sub-divided into extrusive basalts (layer 2A) and the underlying layer 2B (*Tivey et al.*, 1998). The compositon of layer 2B has not been ascertained as there are conflicting borehole (*Carlson*, 2011) and seismic studies (*Vera et al.*, 1990; *Harding et al.*, 1993). Seismological studies such as receiver functions (*Kawakatsu et al.*, 2009; *Kumar and Kawakatsu*, 2011), surface wave shear-velocity (*Maggi et al.*, 2006; *Auer et al.*, 2014) and anisotropy (*Burgos et al.*, 2014) along with magnetotelluric studies (*Naif et al.*, 2013) have been successful in imaging the deeper lithospheric structure. However, they suffer from the drawback of having a low vertical resolution of the order of ∼10 km. As a result, the fine-scale structure of the upper mantle is smoothed out. To address these limitations of the upper oceanic crust and lithosphere, the Trans-Atlantic Imaging of the Lithosphere-Asthenosphere Boundary (iLAB) project was designed. In the first expedition in 2015, active-source multi-channel seismic (MCS) data using a 12 km long streamer was collected from 0-75 Ma old normal oceanic lithosphere in the Equatorial Atlantic ocean. The streamer used was an advanced Isometrix streamer (*Vassallo et al.*, 2013) with 3857 receivers spaced at every 3.125 m. The air-gun array used as a source was one of the largest in industry with a capacity of 10170 cubic inch. The profile was acquired in three different flow lines each spanning 0-1.8 Ma, 1.8-46.7 Ma and 49.3-75.6, Ma which I combined together to get a continuous variation of 0-75 Ma. The equatorial Atlantic ocean on the African plate is bounded by the Chain fracture zone in the north and the Ascension fracture zone in the South. A number of fracture zones and smaller order discontinuities in the study region is attributed to slower northward propagating rift between the African and South American plates which initiated at ∼110 Ma due to Tristan hotspot (*Granot and Dyment*, 2015). Further East to the profile ending at 75.6 Ma are the St. Helena and Cameroon volcanic lines. The second expedition was in 2017 and high-resolution bathymetry with a 11-km swath, conductive heatflow, parasound data and wide-angle seismic data was acquired on the same profile as that of 1.8-46.7 Ma of the first expedition. I primarily use the MCS data from the 2015 expedition to address the objectives and take the support of heatflow data from 2017 expedition to improve my interpretation.

This thesis is bifurcated into addressing the two-fold objectives of understanding the evolution of the upper oceanic crust and the lithosphere (LAB). Chapter 1 describes in detail the two expeditions carried out, the various models explaining the processes of subsidence and cooling of the lithosphere, the existing observations and the competing models of the upper oceanic crust and the LAB and lastly, the general evolution of the study region. Chapter 2 describes the theoretical aspects of the methodologies

and data processing used in this thesis. Chapter 3 focuses on the upper oceanic crustal structure which I investigate by means of both seismic imaging and high-resolution tomography. Additionally I used the co-located heatflow data to constrain the interpretation better. In chapter 4, I investigate the possible effects of the St. Helena and Cameroon volcanic chains on the lithosphere and the LAB closest to these chains. In chapter 5 the lithosphere away from these volcanic chains is analyzed to provide a complete picture of the oceanic lithosphere. I conclude the scientific outcomes of this thesis in chapter 6 and list some ongoing works and planned publications.

1.1 Earth's subsurface

The Earth is a fascinating planet that supports life. Geophysics is the branch of science which studies the otherwise inaccessible Earth's subsurface. The Earth's subsurface is divided into various layers according to two primary classifications: the mechanical (or rheological) and the chemical (or petrological). The mechanical classification is based on the differences in physical properties of the various layers of the sub-surface and was proposed by Prof. Reginald Daly of Harvard university (*Daly*, 1940). Though the concept of plate tectonics was put forward by Alfred Wegener in 1912 (*Wegener*, 1912), it did not gain support until further studies such as *Daly* (1940). With the development of sciences such as petrology, the chemical classification came into existence and characterized the various layers in the Earth's subsurface as per their elemental/mineral composition. According to the mechanical classification, the Earth is differentiated into lithosphere, asthenosphere, mesosphere and the core whereas according to the the chemical classification, is divided into crust, mantle, outer core and innner core. The two classifications and the various divisions are illustrated in figure 1.1 and further elaborated below.

Chemical Classification:

1. Crust: The crust is the uppermost layer of the Earth. Oceanic crust is ∼6 km thick on average with mainly mafic composition (basalt) whereas continental crust is 35-40 km thick with felsic composition (granite). The boundary at the base of the crust (crust-mantle boundary) is termed as the Mohrovičić discontinuity or the Moho in short and represents an increase in P-velocities from ∼6.8-7 km/s at base of crust to ∼8 km/s at top of mantle. The oceanic crust is sub-divided into extrusive basalts (layer 2A), sheeted dykes (layer 2B) and gabbros (layer 3). Some studies identify a layer 2C as the transition between layer 2B and 3.

2. Mantle: The mantle is the second most thickest layer in the Earth's subsurface after the core. It is divided into an upper mantle consisting of peridotites and serpentinites and a lower mantle. The upper mantle consists of a 410 km discontinuity due to a first order phase transition from α-olivine to β-spinel causing a 5-6% increase in P-velocity and density (*Kennett and Engdahl*, 1991; *Melbourne and Helmberger*, 1998). Another prominent discontinuity is the 670 km discontinuity which is considered to be the boundary between the mantle convection in the upper mantle and lower mantle (*Christensen*, 1995). It is represented by a phase change in the γ-olivine to perovskite and magnesiowustite and the transformation from garnet to perovskite (*Condie*, 2001). These phase changes result in an overall increase in P-velocity and density by 6-11%. A debatable discontinuity is considered to be at 520 km (*Vidale and Benz*, 1992; *Cummins et al.*, 1992; *Bock*, 1994) and represents a phase change of β-spinel to γ-spinel within the olivine component with a minor increase in P-velocity and density (*Shearer*, 1991; *Revenaugh and Jordan*, 1991; *Flanagan and Shearer*, 1998). The core-mantle boundary is at a depth of ∼2890 km below the Earth's surface.

3. Core: The core is the innermost and the most dense layer of the Earth with temperatures reaching 4000°C. It is composed of elements such as iron and nickel and is reponsible for Earth's magnetic field.

Mechanical Classification:

1. Lithosphere: The lithosphere is the more rigid, upper layer of the Earth's sub-surface which is deformed elastically and by brittle failures over long periods of time by the tectonic forces. The continental lithosphere easily extends to 200-250 km depth beneath cratons whereas the oceanic lithosphere is considered to be age-dependent and extends from 12-15 km beneath mid-ocean ridges to 100 km beneath older oceanic lithosphere. It has a lower strain rate and a higher shear strength as compared to the underlying asthenosphere.

2. Asthenosphere: The asthenosphere is the less viscous part of the mantle over which the lithosphere 'floats'. It accommodates strain by plastic deformation and is characterized by lower P- and S-

velocities as compared to the overlying lithosphere. The difference between the lithosphere and asthenosphere are further highlighted in section 1.5.

3. Mesosphere: Both Lithosphere and Asthenosphere form the upper mantle whereas the lower mantle is termed as the Mesosphere. The 670 km discontinuity represents the transition from upper to lower mantle, or equivalently the asthenosphere and mesosphere. The mesosphere occupies ∼56% of the total Earth's volume and represents the transition between asthenosphere and the core. As stated in the chemical classification, the lower mantle or the mesosphere is composed of bridgmanite and magnesiowustite (*Condie*, 2001) and is denser than the overlying asthenosphere. This mesosphere is not to be confused with the atmospheric mesosphere.

4. Core: The core refers to the same layer as in the chemical classification extending below the mesosphere from ∼2900 km depth to the centre of the Earth at a depth of ∼6371 km. In the mechanical classification, the core is sub-divided into a liquid outer core and a solid inner core.

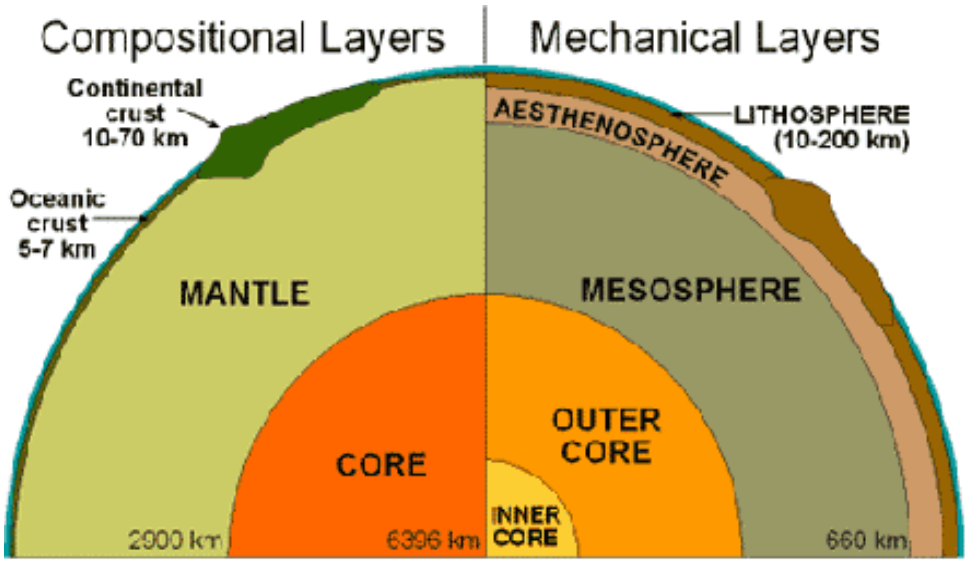

Figure 1.1: Mechanical (rheological) and Chemical (petrological) classification of the Earth's subsurface. Source: *Pearson Education*

Among the above various sub-divisions of the Earth, I will mainly focus on the oceanic lithosphere in this thesis. It is necessary to understand the oceanic lithosphere and the several processes affecting it which I briefly describe in the next section.

1.2 Oceanic Lithosphere and processes

The oceanic lithosphere is relatively rigid and floats over a ductile asthenosphere as defined above. The oceanic lithosphere is formed at oceanic spreading centers such as Mid-Atlantic ridge and is destructed at subduction zones such as Sumatra subduction zone as shown in figure 1.2. As the oceanic lithosphere forms at the spreading centre and moves away, its evolution is known to be affected by some phenomena as described below.

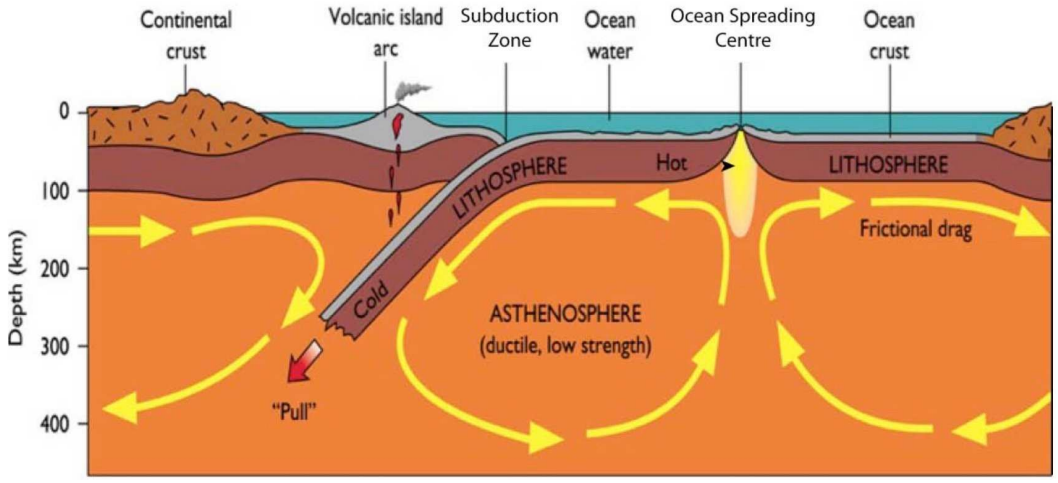

Figure 1.2: Schematic sketch of an oceanic lithosphere-asthenosphere system. The oceanic spreading center is the plate boundary where the oceanic lithosphere is formed and the subduction zone is the plate boundary where the oceanic lithosphere is destructed. Top ∼6 km of the oceanic lithosphere is the oceanic crust. Credit: *Satish Singh*

1.2.1 Subsidence

The oceanic lithospheric plate is formed by upwelling magmatic activity at the spreading center and as it moves away due to spreading by tectonic forces, it subsides. The decrease in the magmatic upwelling activity and temperature away from the ridge-axis leads to subsidence phenomena. There are two main models that describe the subsidence of the oceanic plate as it moves away from the ridge-axis - plate-cooling model and the half-space model. Whereas half-space model is a more theoretical model and assumes infinite half-space cooling of the plate, the plate-cooling model was developed to better fit the observations of a flatter base of the plate at older ages. Here I describe the two models with respect to subsidence below and also discuss a modification of the half-space cooling model (*Hasterok*, 2013) based on updated heatflow and bathymetry data.

1. Plate cooling subsidence: The plate cooling model describes the basement subsidence (d) as function of the distance from the ridge-axis (x) by *McKenzie* (1967):

$$d(x) = d_r + d_s \times [1 - 8/\pi^2 \sum_{j=1}^{\infty} j^{-2} e^{(-\beta_j x/a)}], \tag{1.1}$$

$$\text{where} \quad d_s = \frac{\alpha \rho_m (T_m - T_0) a}{2(\rho_m - \rho_w)}, \tag{1.2}$$

$$\text{and} \quad \beta_j = \sqrt{R^2 + j^2 \pi^2} - R, \tag{1.3}$$

$$\text{and} \quad R = \nu a/(2\kappa), \tag{1.4}$$

$$\tag{1.5}$$

where d_r is the ridge-axis depth, ν is the half-spreading rate of the plate, a is the asymptotic plate thickness, T_m and T_0 denote the mantle temperatures and temperature at top of the plate

respectively; ρ_m and ρ_w are the densities of the mantle and water respectively; α is the thermal expansion coefficient and κ is the thermal diffusivity. In deriving the above equations, the above boundary conditions have been assumed: $T(0,t) = T_0, T(\inf,t) = T_m$ and $T(z,0) = T_m$.

2. Half-space cooling subsidence: The half-space cooling model deduces a basement subidence (d) to have a linear relation with the square root of age (t) (*Turcotte and Schubert*, 2002). The 2D heat flow equation as described shortly is superimposed with the following boundary conditions: $T(0,t) = T_0, T(\inf,t) = T_m$ and $T(z,0) = T_m$ to get the following equation of half-space subsidence:

$$d(t) = d_r + constant \times \sqrt{(t)}, \tag{1.6}$$

$$\text{where} \quad constant = 2 * \sqrt{(\kappa t/\pi)} * (T_m - T_0) * \alpha * \rho_m/(\rho_m - \rho_w), \tag{1.7}$$

$$\tag{1.8}$$

where the parameters T_m, T_0, ρ_m, ρ_w, α, κ have same meaning as before in plate-cooling model. It is noted that half-space subsidence is independent of the spreading rate and plate thickness. Several studies have appropriated a value to the constant on the basis of the then available seafloor-age-depth and seafloor age-heat-flow observations. *Parsons and Sclater* (1977) determines the constant to be 350 $\text{mMa}^{-\frac{1}{2}}$, *Stein and Stein* (1992) proposes 360 $\text{mMa}^{-\frac{1}{2}}$, *Crosby and McKenzie* (2009) on the basis of analysis of residual topography and gravity determines a smaller value of 325 $\text{mMa}^{-\frac{1}{2}}$, *Korenaga and Korenaga* (2008) further reduces it 320 $\text{mMa}^{-\frac{1}{2}}$ and *Hasterok* (2013) proposes a much higher value of 414.5 $\text{mMa}^{-\frac{1}{2}}$. This is summarized in table 1.1.

Table 1.1: Values of the half-space constant in various studies

Study	Constant Value ($\text{mMa}^{-\frac{1}{2}}$)
Parsons and Sclater (1977)	350
Stein and Stein (1992)	360
Crosby and McKenzie (2009)	325
Korenaga and Korenaga (2008)	320
Hasterok (2013)	414.5 ($\leq$17.4 Ma)

An important distinction between these studies is the data set used to determine the values. The latter study of *Hasterok* (2013) uses a more recent and updated compilation of ~15000 heat flow observations (*Hasterok et al.*, 2011) and also allows for a more reasonable mantle temperature 1350°C. The sites for these heat flow measurements have been filtered to remove the effect of hydrothermal circulation by choosing sites having at least 400 m thick sediment cover and at least 60 km away from the nearest seamount. Furthermore, *Hasterok* (2013) finds a numerical error in the plate cooling model computation of *McKenzie et al.* (2005) and states that the thermal conductivity-temperature relation proposed (*Hofmeister*, 1999) is inaccurate and outdated (*Hofmeister*, 2005). Lastly, *Hasterok* (2013) does not neglect the 4 mWm^{-2} radiogenic heat flow from the lithosphere which cause a 30% difference between the observed and proposed models (*Staudigel*, 2003). These were the reasons I also took into account Hasterok's subsidence model (*Hasterok*, 2013) given by:

$$d(t) = d_r + 414.5\sqrt{t} \quad if \quad t \leq 17.4 \quad Myr \tag{1.9}$$

$$d(t) = d_r + 3109 - 2520e^{-0.034607t} \quad if \quad t > 17.4 \quad Myr \tag{1.10}$$

The subsidence models are extensively used in chapter 3 and chapter 4 to characterize the data set used in this thesis.

1.2.2 Hydrothermal circulation

Hydrothermal circulation is the phenomenon resulting due to interaction of the sea-water with the lithospheric plate. The sea-water is able to penetrate to various depths in the oceanic lithospheric plate due to presence of the fractures and voids in the plate. The site where seawater enters the lithospheric plate is called the recharge site and the site where the heated seawater (along with dissolved minerals of the sub-surface rocks) leaves the sub-surface is called the discharge site. Depending upon the available heat supply, the circulating sea-water can also chemically react with the surrounding minerals in a process called hydrothermal alteration. In case of high-temperature hydrothermal systems such as near the ridge-axis, greenschist facies are deposited by circulating sea-water and in case of low temperature hydrothermal systems, zeolite facies are deposited in the surrounding minerals (*Humphris*, 1977). Figure 1.3 shows the phenomena of hydrothermal circulation and the formation of smoker files due to interaction of hot hydrothermal fluids with cold sea-water. Depending on the chemical composition of the emerging hot hydrothermal fluids, smoker fields are either black (containing sulphides) or white (containing calcium, silicon etc.) when they interact with the colder sea-water. The phenomena of hydrothermal circulation is known to most affect the upper crust and further implications based on the observations from this data set are made in chapter 3.

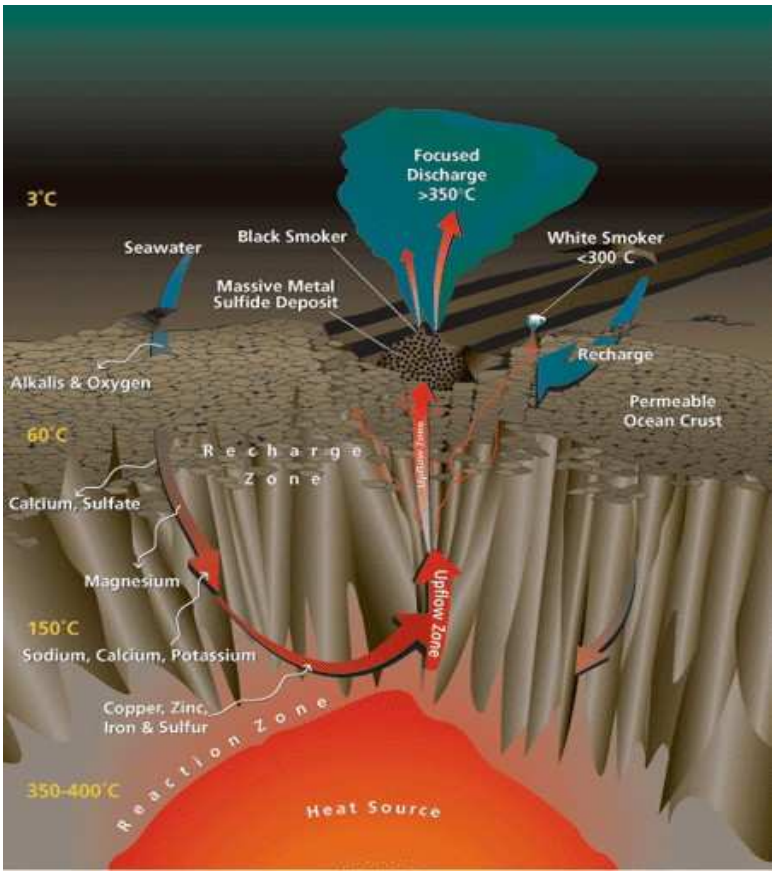

Figure 1.3: Schematic sketch showing a hydrothermal system: recharge and discharge zones of circulating seawater, black and white smokers along with their chemical composition and temperatures. Source: *Humphris et al.* (1998)

1.2.3 Sedimentation

Sedimentation implies the deposition of sediments on the top of oceanic lithospheric plate and hence sediments are also termed as Layer 1. The oceanic sediments can be classified as pelagic and hemipelagic sediments. The pelagic sediments mostly contain the remains of dead organic matter in the ocean which gradually settles to seafloor. The source of this dead matter is mostly phytoplanktons (algae) that are found above the thermohaline gradient a few hundred meters below the sea-surface (*Viličić et al.*, 2009).

The thermohaline gradient is the region characterizing a drop in water temperature and salinity in the sea-water column. The dead phytoplanktons often settle to seafloor in episodes of seawater downwelling in which warmer seawater at shallower depths in brought down while the colder seawater at greater depths moves up (*Cronan and Wakefield*, 1994). Large-scale seawater downwelling (and upwelling) is usually accompanied by processes such as change in glaciation (*Wagner*, 2000). Hemipelagic sediments, on the other hand, do not have a purely oceanic origin. They are usually found in continental shelves and delta fans of large rivers and are carried into deeper ocean. They are comprised of dead organic matter and dust but having a terrestrial origin. Sediments, whether pelagic or hemi-pelagic, once deposited on the seafloor, act as a barrier between the sea-water and top of the lithospheric plate (*Harris et al.*, 2004). The barrier is due to much lower permeabilities in the sediments, making it difficult for the sea-water to interact with the lithospheric plate (hydrothermal circulation). A number of previous studies take sedimentation into account for the evolution of the lithosphere (particularly the upper oceanic crust). The difference between the two types of sediments as well as the role of sediments in the upper crustal evolution is further examined in chapter 3.

1.2.4 Cooling/Thermal structure

As the lithospheric plate moves away from the ridge-axis, i.e. the zone of magmatic upwelling, there is decrease in temperature of the lithospheric plate. This is refered to as cooling of the lithospheric plate with age and is a phenomena also affecting the lithospheric plate subsidence. The thermal structure of the lithosphere or the cooling of lithospheric plate with age is described by plate cooling models and half-space models, similar to subsidence. These are elaborated briefly below.

1. Half-space cooling model: The half-space model assumes cooling of the lithospheric plate over an infinite half-space as it moves away from the ridge axis (*Davis and Lister*, 1974). The lithospheric plate is considered to be rigid, spreading at an uniform rate with an underlying hot, low-viscosity asthenosphere. The 2D heat equation representing the problem is:

$$\frac{\partial^2 T}{\partial x^2} + \frac{\partial^2 T}{\partial z^2} + A = \frac{\nu}{\kappa}\frac{\partial T}{\partial x}, \tag{1.11}$$

where T is the temperature, κ is the thermal diffusivity, A is the radiogenic heat production and ν is the spreading rate of the plate.

The left terms in above equation represent diffusion and the right term represent advection of heat by motion of the plate. At distances greater from the ridge axis ($x >> 0$), it can be shown that lateral diffusion is much smaller than the vertical heat diffusion and so can be neglected. Also, the radiogenic heat, A is very small as compared to the other terms and is also neglected. Replacing the spreading rate of the plate, ν with $\frac{\partial x}{\partial t}$, we get

$$\frac{\partial^2 T}{\partial z^2} = \frac{1}{\kappa}\frac{\partial T}{\partial t}, \tag{1.12}$$

which is the half-space cooling equation. The boundary conditions include $T(0,t) = T_0, T(\infty,t) = T_m, T(z,0) = T_m$ where T_0 is the lithospheric plate-surface temperature and T_m is the asthenospheric mantle temperature. The solution to the above equation is given by:

$$T(t,z) - T_0 = (T_m - T_0)\frac{1}{\sqrt{\pi}}\int_{-z/\sqrt{4\kappa t}}^{+z/\sqrt{4\kappa t}} e^{-t^2} dt \tag{1.13}$$

$$\tag{1.14}$$

Table 1.2: Estimation of plate cooling model parameters acording to different studies

Model/Parameter	PS77 (North Atlantic)	GDH1	CHABLIS	McKenzie (2005)	R1
a (km)	128±10	95±15	105	106	125±15
$T_m(^\circ C)$	1365±276	1450±250	1340±30	1315	1360
$\alpha(\times\ 10^{-5}\mathrm{K}^{-1})$	3.1±1.11	3.1±0.8	4.2	T-dependent	2.39
k ($\mathrm{Wm}^{-1}\mathrm{K}^{-1}$)	3.1	3.25	4.2	T-dependent	4.39

where the thermal diffusivity, κ, is taken to be 8.12×10^{-7} $\mathrm{m}^2\mathrm{s}^{-1}$ (*Parsons and Sclater*, 1977; *Stein and Stein*, 1992; *Katsura*, 1995) and the thermal conductivity, k, is taken to be 3.13 $\mathrm{Wm}^{-1}\mathrm{C}^{-1}$. The thermal diffusivity, κ, is related to the thermal conductivity, k, as $\kappa = \frac{k}{\rho_m C_p}$ with ρ_m being the mantle density and C_p being the specific heat in the mantle. Most of the studies based on plate models assume a mantle temperature, T_m around 1300°C but a very recent study on decompression melting found it to be 1410°C (*Sarafian et al.*, 2017).

2. Plate cooling model: Unlike the half-space model in which cooling of the lithospheric plate occurs throughout the semi-infinite domain, the plate cooling model assumes cooling can continue to a fixed depth. This model was originally proposed to primarily explain the apparent flattening of seafloor at mature ages (>50 Ma) by *McKenzie* (1967). The base of the lithosphere is considered to be at a constant temperature like the half-space model and continues to cool until the plate reaches its asymptotic thickness unlike the infinite half-space cooling model. If R is the Peclet number (thermal equivalent of Rayleigh number), T_0 is the temperature of the top of the lithospheric plate, T_m is the asthenospheric mantle temperature, a is the asymptotic plate thickness, the thermal model ($T(x,z)$) as a function of distance (x) and depth (z) is described by *McKenzie* (1967):

$$T(x,z) = (T_m - T_0) \times [z/a + \sum_{n=1}^{\infty} c_n e^{-\beta_n x/a} \sin(n\pi z/a)], \tag{1.15}$$

$$\text{where} \quad c_n = 2/(n\pi), \tag{1.16}$$

$$\text{and} \quad \beta_n = \sqrt{R^2 + n^2\pi^2} - R, \tag{1.17}$$

$$\text{and} \quad R = \nu a/(2\kappa). \tag{1.18}$$

$$\tag{1.19}$$

Different fits to observed heat-flow and bathymetry data have yielded different estimates of the parameters, a, T_m and α. In the table 1.2, I perform a small comparison among different studies: PS77 model (*Parsons and Sclater*, 1977); GDH1 (*Stein and Stein*, 1992); CHABLIS model which proposes a Constant Heat flux At the Base of LIthoSphere (*Doin and Fleitout*, 1996) in addition to a constant asymptotic temperature at base of lithosphere as used in previous studies; *McKenzie et al.* (2005) proposed a model which included variations of thermal conductivity and specific heat with temperature (*Hofmeister*, 1999); *Grose* (2012) also take into consideration the mineral physics of the mantle olivine in the calculation of thermal expansion and specific heat and propose their best-fit model R1. I do not discuss some other models (*Hillier and Watts*, 2005) as they are not global and/or do not consider the Atlantic ocean, which is the interest of my study.

The most recent model proposed by *Hasterok* (2013) proposes a variant of the plate model with a =90 km, T_m =1364°C, α =3.5×10^{-5} K^{-1}, k =3.5 $\mathrm{Wm}^{-1}\mathrm{K}^{-1}$ and a variant of CHABLIS model with a =119 km, T_m =1368°C, α =$4.9\times\ 10^{-5}$ K^{-1}, k =3.2 $\mathrm{Wm}^{-1}\mathrm{K}^{-1}$. The different plate cooling models described here will be used extensively in chapter 4 and chapter 5 to estimate the thermal boundaries associated with reflections deeper in the lithosphere.

1.2.5 Mantle heterogeneities/anomalies

Mantle heterogeneities are essentially anomalous material in the mantle having a different composition/temperature (thermal anomaly) than that of the surroundings. These heterogeneities are assumed to be uniformly ditributed in the lithospheric and asthenospheric mantle with varying compositions of 2-4% (*Kennett and Furumura*, 2015). The source of these mantle heterogeneities is usually the subducting lithospheric plate which gets recycled into minerals such as eclogite and garnet pyroxenite (*Anderson*, 2006). Although mantle anomalies uniformly distributed in the mantle with 2-4% composition are not very significant, their significance increases in the presence of features such as mantle plumes. In order to better understand mantle anomalies, it is necessary to understand mantle dynamics and mantle processes such as mantle convection. These are briefly elaborated in the next section (section 1.3).

1.3 Mantle convection and plumes

Mantle plumes refer to upwelling mantle material in narrow conduits that mostly create a linear chain of volcanic islands, known as hotspots (such as Reunion, Hawaii). Hotspots have been of great interest to geoscientists and have been studied thoroughly since several decades. Although recent advances in seismology have made deeper imaging possible (*Montelli et al.*, 2004; *Russell et al.*, 1998), the origin of the hotspots had been a matter of debate. There has been extensive gravity, bathymetry, magnetic, geochemical, heatflow and seismic studies over many of observed hotspots and several models of their origin have been proposed from the observations of these studies. One of the earliest models proposed by *Hofmann* (1997) considers the plume to originate at core-mantle boundary or the 670 km discontinuity or both as shown in figure 1.4. The mantle convection is proposed to explain the plate tectonic motion and origin of the plumes and is either considered to be a distinct two layer convection (between LAB and 670 km discontinuity and between 670 km discontinuity and core-mantle boundary) or a whole mantle convection.

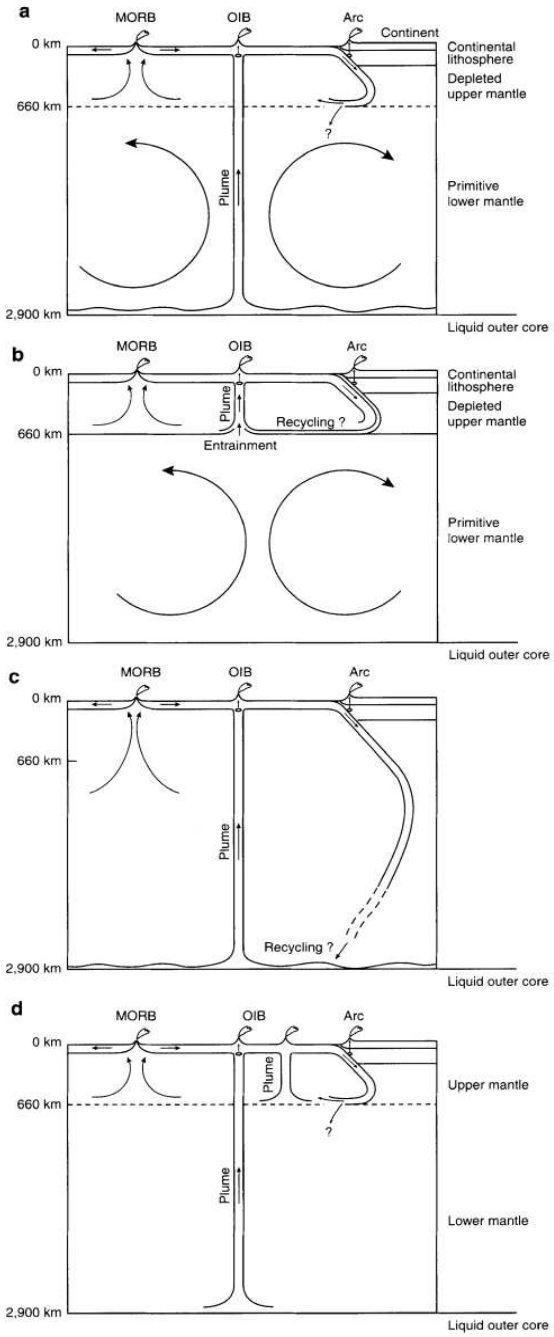

Figure 1.4: Models of mantle convection with plume origin within the geophysical community as elaborated by *Hofmann* (1997). MORB is the mid-ocean ridge basalts and denote spreading centres, OIB is the ocean island basalts like Hawaii etc.(a) Two-layer mantle convection in upper and lower mantle with the 660 km discontinuity decoupling the two. The top of the upper mantle convection is the LAB and the bottom of the lower mantle convection is the core-mantle boundary. The plume source is the core-mantle boundary. (b) A two layer mantle convection with plume arising from 660 km discontinuity and composed of material recycled at subduction zones. (c) A single layer-whole mantle convection with the subducting slab recycled to the core-mantle boundary where it feeds the plume source. (d) A hybrid model in which plume source arises from both the 660 km discontinuity and core-mantle boundary. Source: *Hofmann* (1997).

The first compilation for global hotspot tracks was made by *Crough* (1983) which was improved subsequently by *Davies* (1988); *Sleep* (1990); *Steinberger* (2000); *Courtillot et al.* (2003); *Anderson* (2005); *King and Adam* (2014). *Steinberger* (2000) made implications on global mantle flow on the basis of present day hotspot tracks from models varying in viscosity (constant/variable) and plume origin (core-mantle boundary/670 km discontinuity). On the basis of global models of isotropic shear waves velocity at core-mantle boundary, *Courtillot et al.* (2003) proposed three types of plumes exist: Primary or super-

plumes which have the origin at the core-mantle boundary (*Gung and Romanowicz*, 2002) and include Hawaii, Easter and Louisville in the Pacific hemisphere and Iceland, Afar, Reunion and Tristan in the Indo-Atlantic hemisphere. The secondary plumes originate from a superswell at the 670 km discontinuity such as Polynesia (*Cazenave et al.*, 1989) and tertiary plumes which arise from tensile stresses in lithosphere and decompression melting (*Anderson*, 2000). These have been illustrated in figure 1.5.

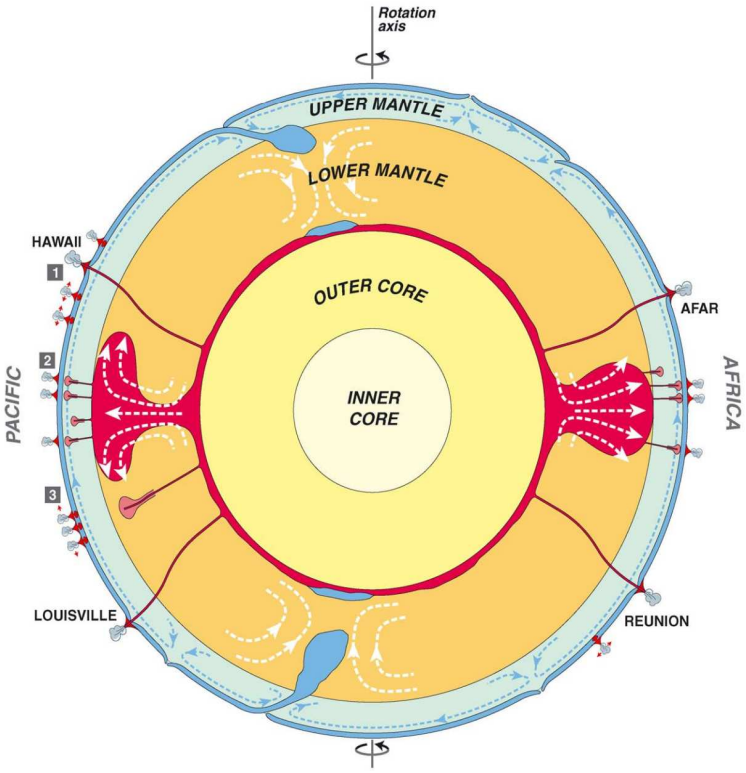

Figure 1.5: Recent models of plume origin as elaborated by *Courtillot et al.* (2003). Primary or superplumes arising from the core-mantle boundary such as Hawaii, Afar, Reunion. Secondary plumes as a by-product of superswells formed just below the 670 km discontinuity such as Polynesia. Tertiary plumes arising from tensile stresses in lithosphere and decompression melting.

There have been a number of studies on the interaction of mantle plumes with the oceanic lithosphere. Not only the oceanic lithosphere, but the embedded mantle heterogeneities are influenced differently by the mantle plumes. Mantle plume-lithosphere interaction is one of the subjects of this thesis and is further examined in detail in chapter 4. Having described the oceanic lithosphere and several processes affecting its evolution, I now look at some of the previous studies on the upper oceanic crust and the lithosphere.

1.4 Upper oceanic crust and processes

The upper ∼6 km of the oceanic lithosphere forms the oceanic crust. This is chemically (or petrologically) distinct from the underlying mantle as discussed in section 1.1. About 70% of the Earth's crust is formed at the mid-ocean ridges by a combination of magmatic and tectonic processes. The nature of oceanic crust depends on the spreading rate (*Purdy et al.*, 1992) and processes such as hydrothermal circulation. At fast and intermediate spreading centers, where the crust is dominantly formed by magmatic process, the oceanic crust could be divided into layer 2 and layer 3. The upper crust, layer 2, is mainly formed by extrusive lava flows and dikes whereas the lower crust, layer 3, is formed by the cooling and crystallization of magma, forming a gabbroic layer (*Morgan and Chen*, 1993; *Detrick et al.*, 1994). However, on slow and ultra-slow spreading ridges, tectonic processes like faulting could dominate, leading to complex crustal structures. Another factor that controls the nature of oceanic crust is hydrothermal circulation, where the sea water enters the crust, gets heated and cools the oceanic crust. The water also reacts with host rocks, dissolving minerals that can get precipitated on the way up to the seafloor, filling the pore spaces and hence changing the nature of the crust. Because of the high temperature near the ridge axis, the hydrothermal circulation is very robust near the ridge axis, and decreases as the crust cools and subsides away from the ridge axis. As the crust cools, it subsides with age, sediments are deposited, blanketing the oceanic crust from ocean water, hence affecting the hydrothermal circulation that in turn could change the nature of the oceanic crust. The layer 2 is usually further sub-divided into two layers: layers 2A and 2B. The oceanic magnetic anomalies are attributed to layer 2A, which mainly consists of pillow lavas (*Tivey et al.*, 1998). This overlies the higher P-velocity layer 2B. As the layer 2A is the uppermost layer of the crust, it gets most affected by the different processes namely subsidence, sedimentation and hydrothermal circulation, it is important to determine the variation of layer 2A with age to understand the evolution of the oceanic crust and lithosphere.

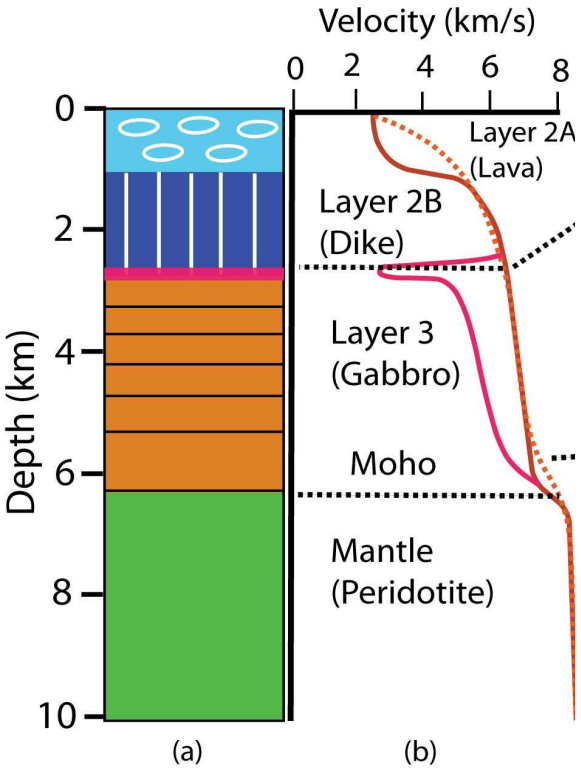

Figure 1.6: Sketch showing ocean crust comprising of layer 2A (lavas), layer 2B (dykes) and layer 3 (gabbros) and a typical 1-D velocity profile from *Singh and Nicolas (2014)*. In this thesis, I will mainly focus on the upper 2 km of the oceanic crust comprising of layer 2A and top of layer 2B.

1.4.1 Previous studies on upper oceanic crust

The earliest studies documenting the existence of the uppermost oceanic crust layer 2 (*Hill*, 1957; *Raitt*, 1963) using seismic refraction data indicated that both the velocity and thickness of this layer vary significantly. Highly porous lava flows (layer 2A) could have a low P-wave velocity (2.5 km/s), whereas the dikes (layer 2B) underneath can have high P-wave velocity (5-6 km/s) with a high velocity gradient at the transition of layer 2A and 2B, leading to a triplication in seismic travel time (*Harding et al.*, 1993; *Vera and Diebold*, 1994). The results from deep sea drilling at 37°N Mid-Atlantic Ridge (MAR) (*Hyndman and Drury*, 1976) indicated a much higher velocity of 5.04±0.69 km/s for the basaltic rocks than that observed at the ridge-axis from seismic studies (2.5 km/s), requiring the presence of fractures and voids to explain the much lower velocities observed in the upper oceanic crust by seismic studies.

Houtz and Ewing (1976) compiled a data set from sonobuoys in the Atlantic and Pacific Oceans and concluded that layer 2A shows a gradual increase in the P-wave velocity from 3.3 km/s at ridge crest to 4.5 km/s at 40 Ma, where it merges with the underlying layer 2B. No such age-dependency is observed in the underlying layers 2B and 3. *Whitmarsh* (1978) presented the results of a seismic refraction study at distinct ages ranging from 2-79 Ma and found the absence of a relatively low velocity layer in the top 200 m of the oceanic crust at 46 and 79 Ma. They also found that the velocity gradient in layer 2 (ranging from 0.85-1.35 /s) is similar for all the ages. On the other hand, *Schreiber and Fox* (1977) and *Lewis* (1978) found an increase in P-wave velocity with age, which they attributed to be due to the cementation of cracks. However, *Christensen and Salisbury* (1972) noted a decrease in seismic velocity with age of basalts from borehole data, which they explained to be due to increased alteration and low grade metamorphism with increasing age in agreement with the results of *Le Pichon et al.* (1965) and *Raitt* (1963). Some recent studies based on ocean bottom hydrophone (OBH) data (*Grevemeyer and Weigel*, 1996) suggest that most of the evolution of layer 2A takes within the first 10 My, after which no further evolution takes place. This compilation was expanded by *Carlson* (1998) who finds velocities in layer 2A <3 km/s for young crust aged <1 Myr which increase to 4.4 km/s within 7.5 Myr. He also finds that the velocities in layer 2A rarely reach those of 2B (∼5.2 km/s) and suggests layer 2A persists beyond 40 Ma as a low velocity layer capping the oceanic crust. Recently, *Kardell et al.* (2018) have analyzed the evolution of layer 2A with age in the South Atlantic. Their study shows South Atlantic upper crustal velocity increases to 4.2 km/s at 6 Ma and then gradually increases to 4.9 km/s at 71 Ma. The authors attribute continuous evolution of layer 2A to low temperature hydrothermal circulation and precipitation. They observed higher heterogeneity in layer 2A velocities and thickness at slow spreading crust as compared to intermediate spreading crust.

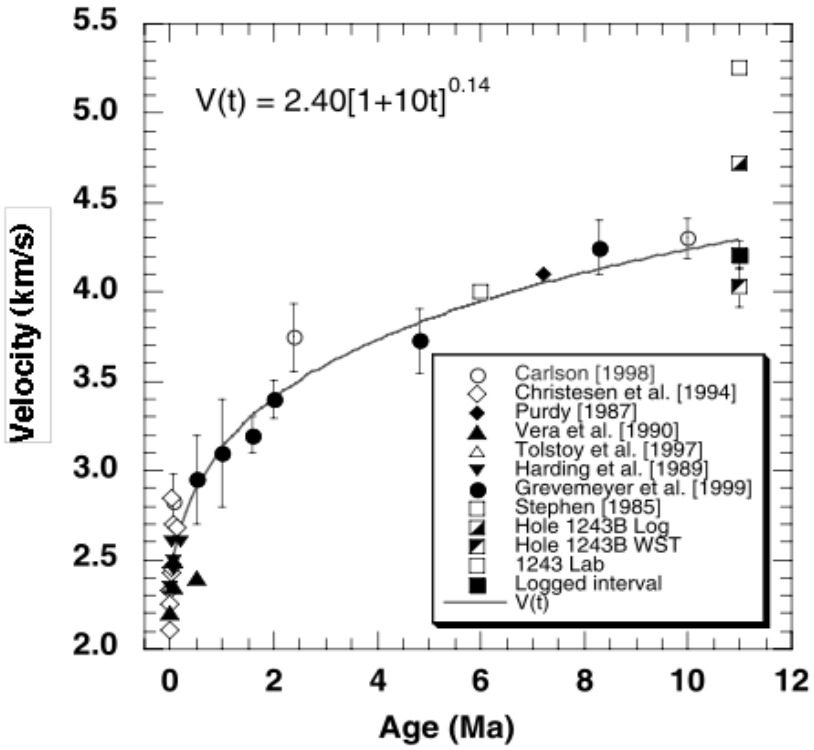

Figure 1.7: A compilation of previous studies based on wide-angle seismic and borehole studies on the evolution of P-velocities of layer 2A with respect to age (*Carlson*, 2004).

Several studies of layer 2A have been carried out at slow spreading centers, particularly at the Mid-Atlantic Ridge (MAR), that include the Reykajanes ridge segment (*Peirce et al.*, 2007; *Navin et al.*, 1998) the 35 N segment (*Hussenoeder et al.*, 2002a; *Barclay et al.*, 1998), the Lucky Strike segment (*Calvert*, 1995; *Singh et al.*, 2006; *Seher et al.*, 2010), and the Ascension Islands region (*Minshull et al.*, 2003; *Evangelidis et al.*, 2004). However, most of these studies have focused on the ridge axis and hence cannot be used to determine the evolution of layer 2A with age. The above results lack consistent observations and their interpretations of layer 2A. There could be two main reasons for these inconsistencies. As the receiver spacing for sonobuoy and OBH data is very large, these data do not have much resolution for layer 2A (*Arnulf et al.*, 2014). Secondly, until very recently, the streamer lengths for seismic reflection studies were not large enough to capture the triplication from the Layer 2A/2B boundary for older (and hence deeper) mature oceanic crust in order to provide a seismic image. The data set used in this thesis, discussed later in section 1.6, overcomes these limitations of previous studies.

A high velocity gradient at the transition of layer 2A to 2B gives rise to a triplication in seismic records, the cusp of which when stacked gives an image of layer 2A. This breakthrough in seismic imaging of layer 2A was made when *Harding et al.* (1993) proposed a method to stack the cusp of the triplication generated by the high velocity gradient at the base of layer 2A, allowing to continuously image layer 2A from seismic reflection data. This triplication arising from high velocity gradient between layers 2A and 2B is further examined in detail in the next chapter. Whereas the preceding paragraph described the upper crustal studies at slow spreading ridges, a number of studies have also been carried out at fast and intermediate spreading centers. At the fast spreading 9° N East Pacific Rise, a rapid increase in layer 2A thickness was found from 100-200 m to 250-600 m within 1-2 km of the rise axis which was attributed to be associated with the dike subsidence beyond the neo-volcanic zone (*Harding et al.*, 1993; *Vera and Diebold*, 1994). At the intermediate spreading centers, the thickness of layer 2A at zero-age is greater than that at the fast spreading centers but exhibits higher variability and has been found to be in the range of 250-350 m at Juan de Fuca ridge (*Canales et al.*, 2005) and 350-600 m at the Blanco Transform fault (*Christeson et al.*, 2010). A gradual off axis thickening of layer 2A ranging from <40% at the Galapagos spreading center (*Blacic et al.*, 2004) to 60-90% at Juan de Fuca ridge (*Canales et al.*, 2005) is observed. A good

review of the upper 2 kilometers of the oceanic crust at fast and intermediate spreading centers can be found in *Karson* (2002). At slow spreading centers such as the Mid-Atlantic Ridge (MAR), a 1-km thick layer 2A has been observed at the Lucky Strike segment (*Singh et al.*, 2006; *Seher et al.*, 2010; *Combier et al.*, 2015) and 0.8-1.3 km thick layer 2A at the Reykjanes segment (*Peirce et al.*, 2007; *Navin et al.*, 1998). A thicker layer 2A at slow spreading ridges is explained by a slower spreading rate and hence accumulation of the fresh basalts. Off-axis thinning of layer 2A at slow spreading centers to 350-600 m is observed (*Hussenoeder et al.*, 2002a) which is similar to off-axis thickness of layer 2A at other spreading centers. *Estep et al.* (2019) have observed layer 2A in the South Atlantic in crust aged 0-48 Ma with a mean thickness of 760±290 m.

The boundary between layer 2A and 2B has been debated to be a lava/dike transition (*Toomey et al.*, 1990; *Harding et al.*, 1993; *Christeson et al.*, 1996) or an alteration boundary within the lava unit (*Rohr et al.*, 1988; *Vera et al.*, 1990) or both (*Karson and Christeson*, 2003; *Christeson et al.*, 2010; *Carlson*, 2011). From regions where oceanic crust is exposed, the seismic layer 2A/2B boundary is suggested to be a hydrothermal alteration boundary that can occur at the lava/dike transition such as at Hess Deep or within the lava unit such as at Blanco Fracture zone *Christeson et al.* (2007). Borehole studies at Holes 504B and 1256D suggest that hydrothermal alteration at or near the base of lava/dike transition zone is associated with a high velocity gradient leading to the triplication seen in the seismic records (*Carlson*, 2011). The increase in seismic velocity from layer 2A to that of layer 2B has been attributed to a porosity change with depth (*Carlson*, 2010, 2011, 2014a) or a change in the aspect ratio of the cracks (*Wilkens et al.*, 1991). On the basis of borehole evidence and some seismic studies, *Carlson* (2018) suggests the dike section to be distinct from layer 2B and denoted by layer 2C as observed first by *Houtz and Ewing* (1976). These different studies lack a consistent interpretation of thee layer 2A/2B boundary and will also be examined in detail in chapter 3.

1.5 The Lithosphere-Asthenosphere Boundary (LAB)

The boundary between the lithosphere and the asthenosphere is known as the Lithosphere-Asthenosphere Boundary (LAB) and is one of the subjects of this thesis. There has been a great interest in the LAB in the geophysical community ever since the idea of a rigid lithosphere floating over a plastic asthenosphere was first proposed nearly a century ago by *Barrell* (1914). The first seismic observation of an asthenospheric low velocity channel was reported by Gutenberg (*Gutenberg*, 1926, 1948, 1955, 1959) and so the LAB is also called the G-discontinuity, although some recent studies make a distinction between them. In the following sections, I attempt to compile the various definitions, observations and models of the LAB known from previous studies with a main focus on the oceanic LAB.

1.5.1 Definitions of the LAB

- Mechanical or rheological LAB: As described in section 1.1, this definition considers the difference between the rigid lithosphere and viscous asthenosphere to explain mechanical decoupling for differential motion. The brittle lithosphere is deformed non-elastically in shallow depths and by ductile thermally activated dislocation creep around the LAB, in contrast to the asthenosphere which accommodates strain by plastic deformation. In other words, the shear strength drops at the LAB while the strain rate increases sharply (*Eaton et al.*, 2009).

- Thermal LAB: According to this definition, the LAB separates the thermally conductive lithosphere lid from the adiabatic convective asthenosphere. Several plate cooling models to explain the observed subsidence and thermal characteristic of lithosphere have been proposed. The 1300°C isotherm is denoted to be the LAB (*Artemieva*, 2006). This temperature is significantly higher than the limit of the elastic behavior which is considered to be at 650°C (*Anderson*, 1995), resulting in a discrepancy between the elastic (mechanical boundary layer) and thermal lithosphere.

- Seismological LAB: Seismological studies have associated the lithosphere with higher P- and S-velocities relative to the underlying asthenosphere (discussed in detail shortly). Mechanisms such as melt presence along LAB, hydration contrast or chemical and mineralogical changes are used to explain the LAB. Anisotropy is also used to differentiate the fossil shape-oriented lithosphere from the underlying present-day flow-oriented asthenosphere. The anisotropy in the lithosphere is more prominent along the spreading-parallel and perpendicular directions with the spreading-parallel direction having higher velocities due to the prefered orientation of the sheared melt lenses (*Debayle and Ricard*, 2013; *Beghein et al.*, 2014).

- Electrical LAB: Electrical conductivity (or resistivity) from deep Earth magnetotelluric experiments have identified a contrast in the electrical properties of the more resistive lithosphere and the more conductive asthenosphere (*Jones et al.*, 2001; *Evans et al.*, 2011; *Naif et al.*, 2013). The depth range at which this change takes place is represented as the electrical LAB. To explain the increase of conductivity/decrease of resistivity, the presence of two primary volatiles is considered: water and carbon in the form of carbon dioxide with the former being almost three times as effective as the latter to stabilize partial melts (*Hirschmann*, 2010).

Another less common definition used is on the basis of the chemical properties, for instance, to reconcile the thermal LAB with the chemical LAB, the thermal conductive lithosphere is split into two layers (*Lee et al.*, 2005): an upper chemically depleted, dry and strong layer and an underlying transitional convective sublayer of variable thickness. These various definitions to characterize the LAB are fundamentally related (*Eaton et al.*, 2009). For instance, the mechanical LAB is the depth at which most earthquakes occur as observed by seismological LAB; the temperature defining the thermal LAB relates to the shear modulus and velocity (mechanical LAB); an increase of shearing at the LAB (mechanical LAB) would increase the porosity and would store volatiles such as water and carbon dioxide (*Hirschmann et al.*, 2009) which would in turn increase it conductivity (electrical LAB).

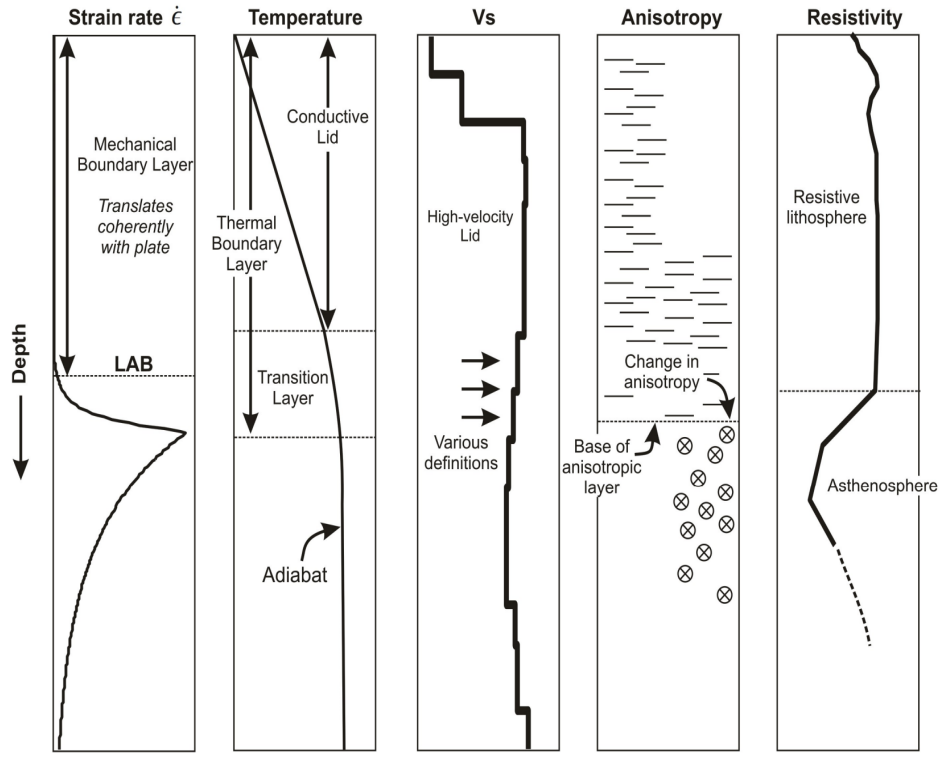

Figure 1.8: Several definitions of the Lithosphere-Asthenosphere boundary as proposed by *Eaton et al.* (2009). From left: The mechanical definition of the LAB corresponds to a sharp increase in the strain rate. The thermal definition of the LAB separates the conductive lithosphere from the adibatic convective asthenosphere. The seismological LAB is deduced from decrease in the observed P-and S-velocity and earthquake depths. The seismological studies have also differentiated an anisotropic lithosphere from the isotropic asthenosphere. The electrical LAB differentiates a resistive lithosphere from a conductive asthenosphere.

1.5.2 Observations of the LAB

Different geophysical experiments have been used to observe/image the LAB in the past few decades. These experiments are based on using the contrasting properties of the lithosphere and the underlying asthenosphere to image the LAB. Some of these properties include surface waves velocity, surface waves anisotropy, surface wave dispersion, P-velocity, density contrast and electrical resistivity. There are two types of body waves or waves which travel through the Earth's volume - P (primary) and S (secondary). The interaction of the body waves at the free surface of the Earth produces surface waves which have a vertical component (Rayleigh) and a horizontal component (Love). The surface waves travel through the surface of the Earth and are more easily distinguishable than body waves on seismograms. Surface wave velocity (particularly Rayleigh) have been used to image hundreds of kilometres below the ocean floor. Surface wave anisotropy refers to differential velocity between the Rayleigh and Love components with respect to azimuth and distance. Different frequency components of the surface waves have different phase velocities and as a result, dispersion occurs. Seismic reflection studies use the P-velocity and density contrast of the lithosphere and asthenosphere to obtain high-resolution images of the LAB interface. Magnetotelluric experiments obtain electrical resistivity structures hundreds of km below the sub-surface and distinguish the lithsophere and asthenosphere. The several properties described here have been used to obtain the following observations of the LAB.

1. Surface waves velocity: The vertical shear velocity component of the Rayleigh waves (V_{sv}), has been used to image structures of lateral resolution ∼250 km and vertical resolution ∼50 km upto depths of 300 km in the mantle. A decrease in the vertical shear velocities at age-dependent depths has been observed from the tomography results (*Zhang and Tanimoto*, 1991; *Priestley and MKenzie*, 2006; *Maggi et al.*, 2006; *Auer et al.*, 2014). V_{sv} is strongly sensitive to temperature (*Priestley*

and MKenzie, 2006; *Faul and Jackson*, 2005) and other factors such as composition (*Lee*, 2003), partial melt (*Hammond and Humphreys*, 2000), volatiles (*Karato and Jung*, 1998) and anelasticity also affect it. However, the vertical resolution of surface waves is of the order of tens of kilometres and hence cannot image reflections within tens of kilometres apart. Figure 1.9 shows a the shear velocity structure beneath the Pacific and Atlantic oceans from *Auer et al.* (2015).

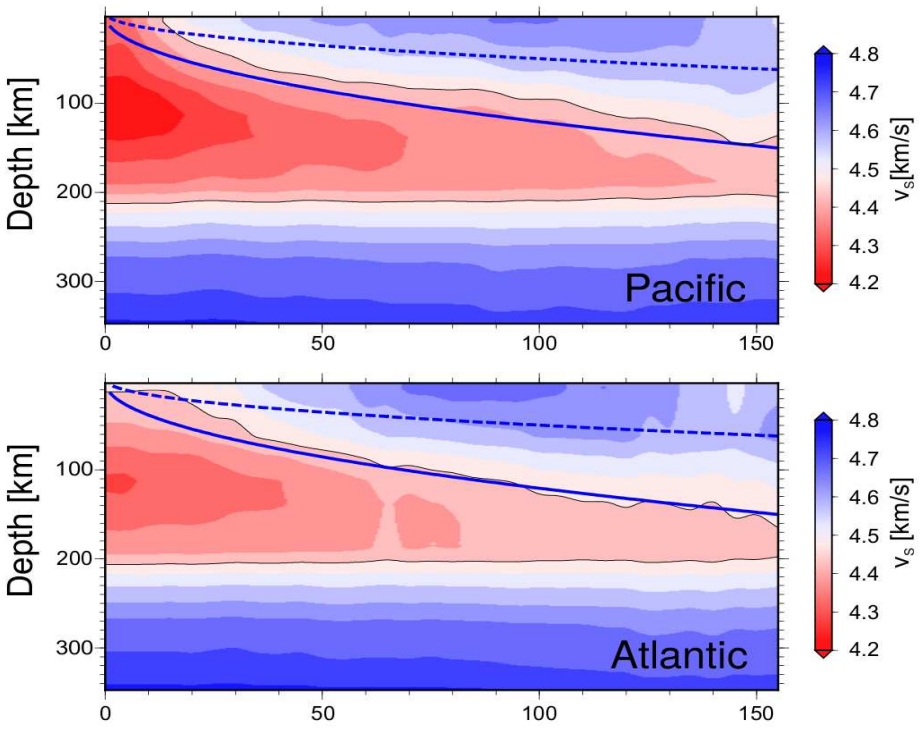

Figure 1.9: Isotropic shear wave velocity structure beneath the Pacific and Atlantic oceans obtained by surface wave tomography (*Auer et al.*, 2014). The horizontal axis represents the seafloor ages in Ma from *Müller et al.* (2008). The blue solid line corresponds to the half-space 1200°C isotherm, the blue dashed line corresponds to the 600°C isotherm and the solid black line is the 4.4 km/s S-wave velocity contour.

2. Surface waves anisotropy: Two forms of anisotropy are commonly considered: radial, which is related to the difference between the vertical and horizontal shear velocity components, and azimuthal, which is the dependence of vertical and horizontal shear velocity components on the direction of propogation. Azimuthal anisotropy has been observed in the oceanic lithosphere and uppermost asthenosphere (*Montagner and Tanimoto*, 1991; *Plomerova et al.*, 2002; *Maggi et al.*, 2006; *Ekström*, 2011; *Burgos et al.*, 2014). The fast axes is usually aligned with the plate-spreading direction and the magnitude of anisotropy depends on the spreading rate (*Debayle and Ricard*, 2013). Radial anisotropy in the upper mantle underneath the Central Pacific has been imaged by a number of studies *Ekström and Dziewonski* (1998); *French et al.* (2013); *Burgos et al.* (2014) which peaks at depths of 100-120 km. However, *Burgos et al.* (2014) notes different LAB depth estimates from radial anisotropy and shear wave vertical velocities as shown in figure 1.10.

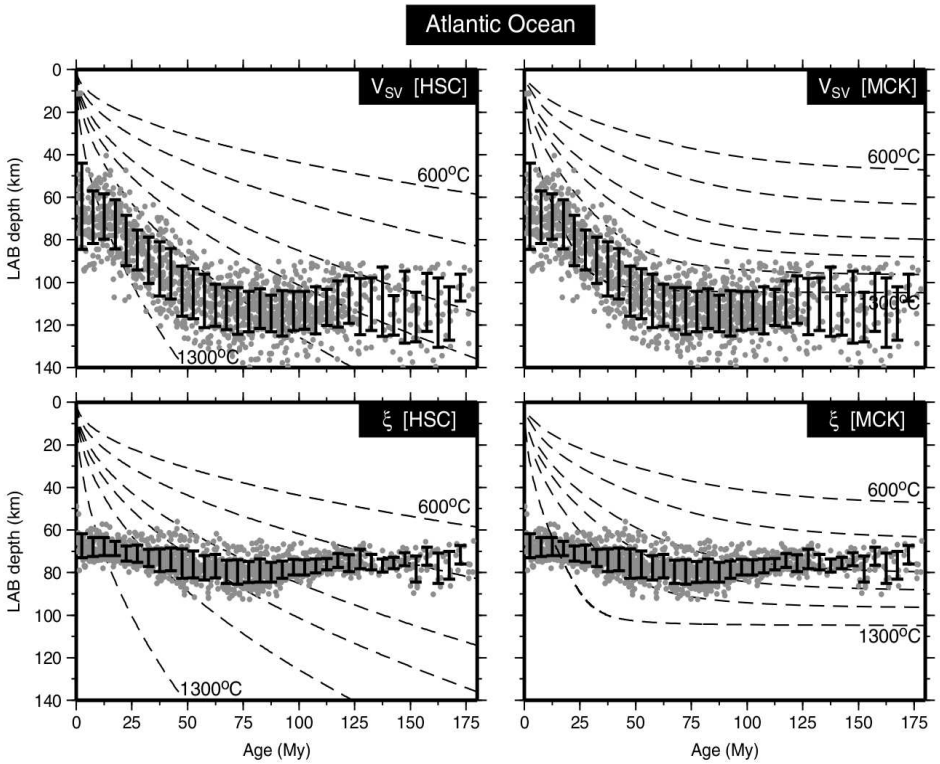

Figure 1.10: Different LAB depth estimated from shear wave velocities (top panel) and radial anisotropy (bottom panel) for the Atlantic ocean (*Burgos et al.*, 2014). Vertical shear wave velocities indicate an age dependent lab consistent with the 1300°C isotherm of plate cooling model (*McKenzie et al.*, 2005) whereas the radial anisotropy estimates an age independent LAB at 60-80 km depth. HSC refers to half-space cooling and MCK refers to plate-cooling.

3. Receiver function (RF) studies: The receiver function studies are essentially teleseismic waveforms used to map the LAB with higher resolution as compared to surface wave dispersion studies. S-to-P converted waves or the S-RF have been used to image the LAB in continents (*Kumar et al.*, 2005; *Rychert et al.*, 2005). These S-to-P conversions are relatively free from shallow layer crustal multiples and samples much larger region as compared to P-to-S conversions. In the oceanic regime, *Kawakatsu et al.* (2009) was able to image a sharp LAB at 60-80 km depth at the Japan-Pacific subduction and proposed a model melt-lubricated asthenosphere. From a more extensive dataset, *Kumar and Kawakatsu* (2011) have imaged LAB at distinct oceanic ages from 10-130 Ma (figure 1.11) and concur that the evolution of oceanic lithosphere is governed by the thermal cooling plate models. Some studies have also imaged LAB using short- and long-period SS precursor waveforms (*Rychert and Shearer*, 2011; *Schmerr*, 2012; *Rychert et al.*, 2012).

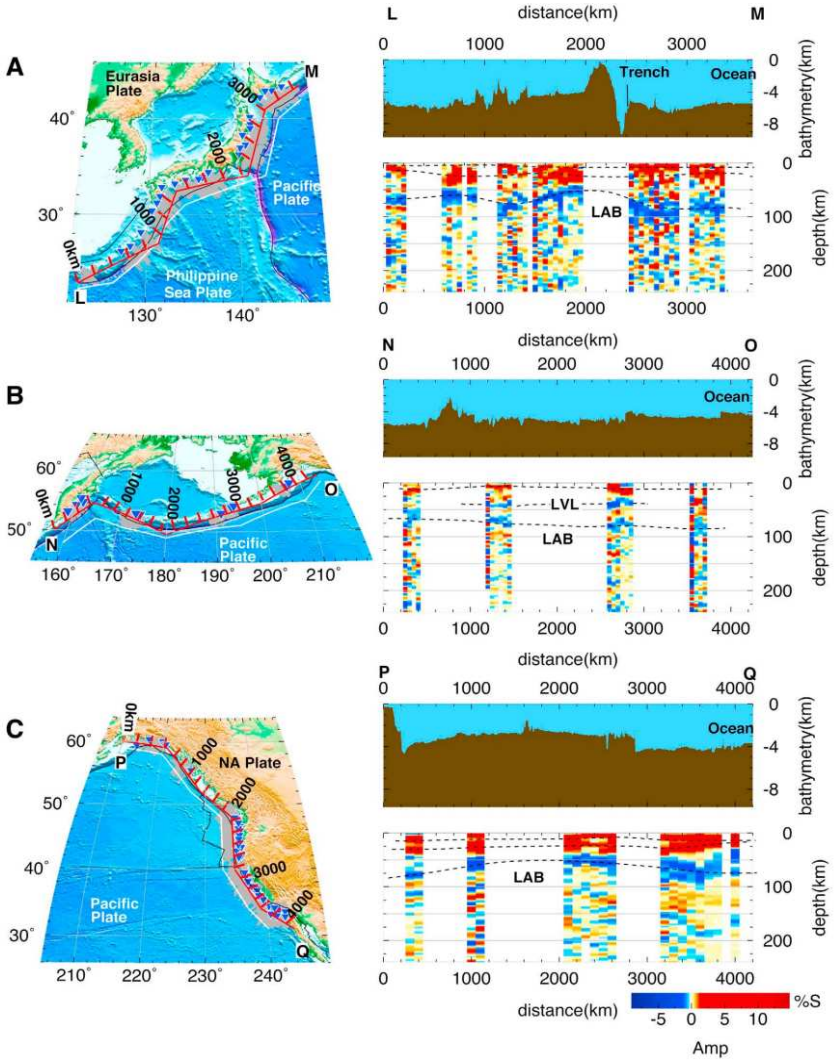

Figure 1.11: Study region maps and their corresponding S-receiver function (S-RF) image of the LAB obtained by *Kumar and Kawakatsu* (2011) at (A) Japan (B) Aleutian and (C) North American West coast on the Pacific seafloor. The The LAB has been interpreted from the S-RF as the transition from positive amplitues (red) to negative amplitudes (blue).

4. Seismic reflection studies: The BIRPS experiment (*McGeary and Warner*, 1985) was one of the first to image deep Earth reflections using active source seismic data in the continental lithosphere. The main reasons seismic methods are not used to image deeper structures is because of higher frequency content and a much weaker source. The signal-to-noise ratio associated with higher frequency content is attenuated rapidly in the Earth and is easily overwhelmed by the ambient seismic noise in deeper Earth. A recent study which was able to image the LAB at 120 Ma subduction zone beneath North Island, New Zealand, using seismic reflection is *Stern et al.* (2015) who used 500 kg of dynamite at each shot point to circumvent the source issue. They propose a 10 km thick LAB shear zone at 120 Ma subduction at depth of 70 - 80 km, with most of the volatiles coming from asthenosphere beneath the shear zone.

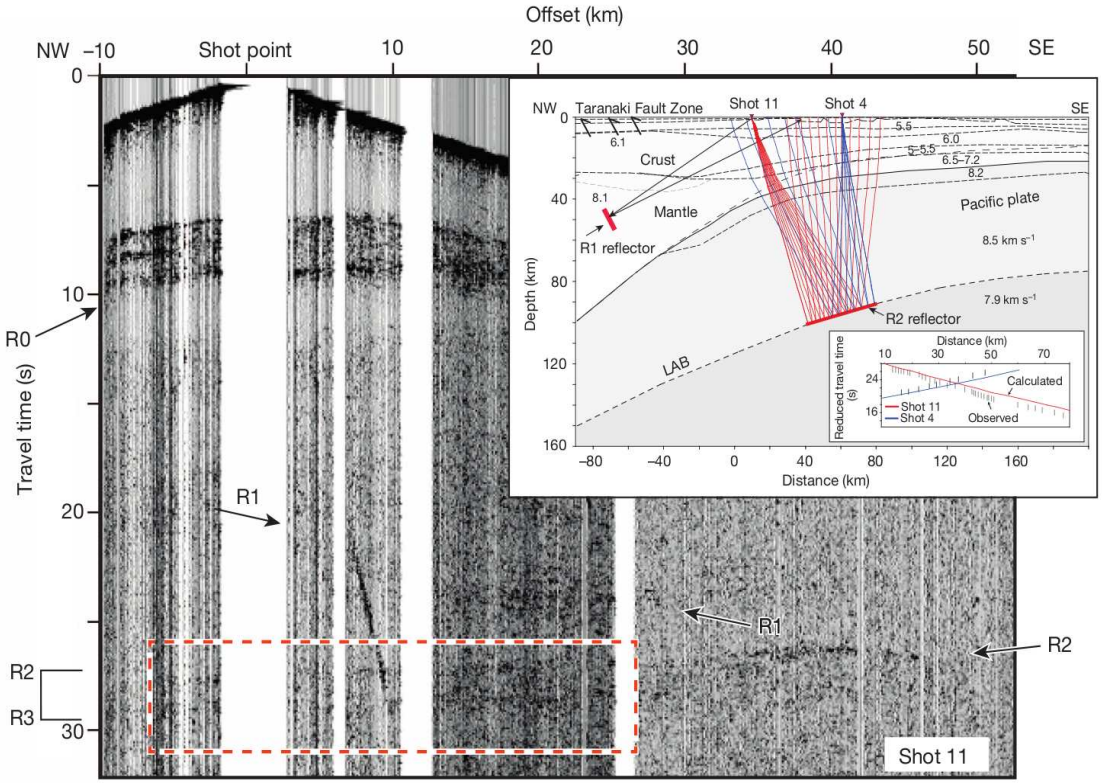

Figure 1.12: LAB imaged by seismic reflection studies: Image of the LAB reflections in a prestack shot record at the 120 Ma subduction setting offshore New Zealand (*Stern et al.*, 2015). The events R2 and R3 are interpreted to be reflections from a 10 km thick LAB shear zone rich in melt or water.

More recently, *Mehouachi and Singh* (2018) imaged a LAB channel across the St. Paul fracture zone in the equatorial Atlantic from the same dataset used in this thesis. They find the two reflections bounding a low velocity channel with a P-velocity change of ($\pm 8.5\% V_p$) and having an age dependency (figure 1.13). At South of St. Paul fracture zone where the age is 40 Ma, they find a 18 km thick channel at a depth of 72 km and on the North at 70 Ma of age, the thickness of the channel is found to decrease to 12 km and the depth increased to 88 km. They find the two reflections corresponding to 1260°C and 1355°C isotherms and that the total mass of water in the channel remaining same at both ages.

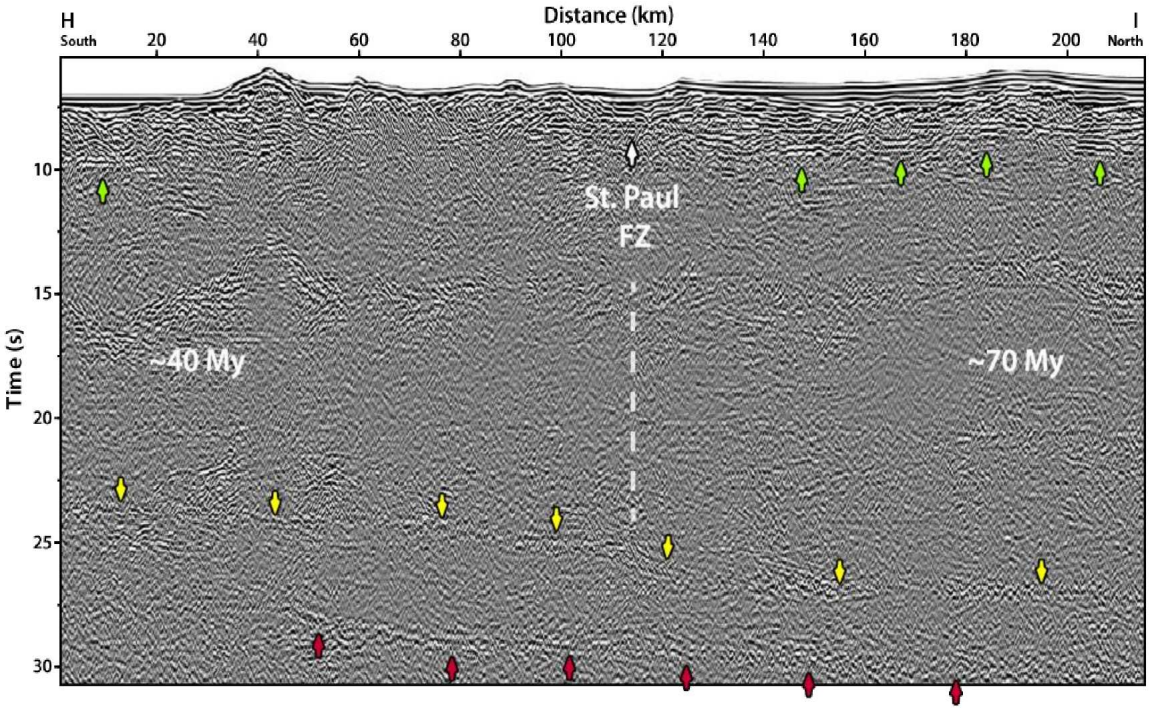

Figure 1.13: LAB imaged by seismic reflection studies: Image of the LAB reflections across St. Paul fracture zone in the equatorial Atlantic (*Mehouachi and Singh*, 2018). The two reflections (yellow and red arrows) bounding a low velocity LAB channel ($\pm 8.5\% V_p$) correspond to 1260°C and 1355°C isotherms. The LAB channel is interpreted to be age dependent as it is 18 km thick at 40 Ma and 12 km thick at 70 Ma. The corresponding depths are 72 and 88 km to the top of the LAB channel at 40 Ma and 70 Ma respectively.

5. Electrical methods: Among some of the recent studies, *Jones et al.* (2001) found a region of low resistivity <30 Ωm at depths of 80-100 km beneath the Archean slave craton. They interpreted it to dissolved hydrogen or graphitic carbon and found the low resistivity region to co-incide with geochemically defined ultradepleted harzburgitic layer. *Moorkamp et al.* (2010) performed a joint inversion using magnetotelluric, surface waves and receiver function data for the same region and found the low resistivity region to co-incide with a decrease in seismic velocity as well. The South African MagnetoTelluric EXperiment (SAMTEX) (*Evans et al.*, 2011) has imaged a decrease in resistivity at around 230 km beneath the Kaapvaal craton, though the study acknowledges that magnetotelluric data can not differentiate between a dry and rigid lithosphere or a slightly damp lithosphere (few hundred ppm of water). In the oceanic regime, *Naif et al.* (2013) imaged the LAB at Middle America trench at 23 Ma and propose the LAB to be a 25 km thick channel at depths of 45-70 km having 1.5-2 times lower resistivity than the lithosphere in the direction parallel to plate motion. The anisotropy of the resistivity measurements between the plate motion parallel and orthogonal directions affirms the presence of a higher conductivity channel.

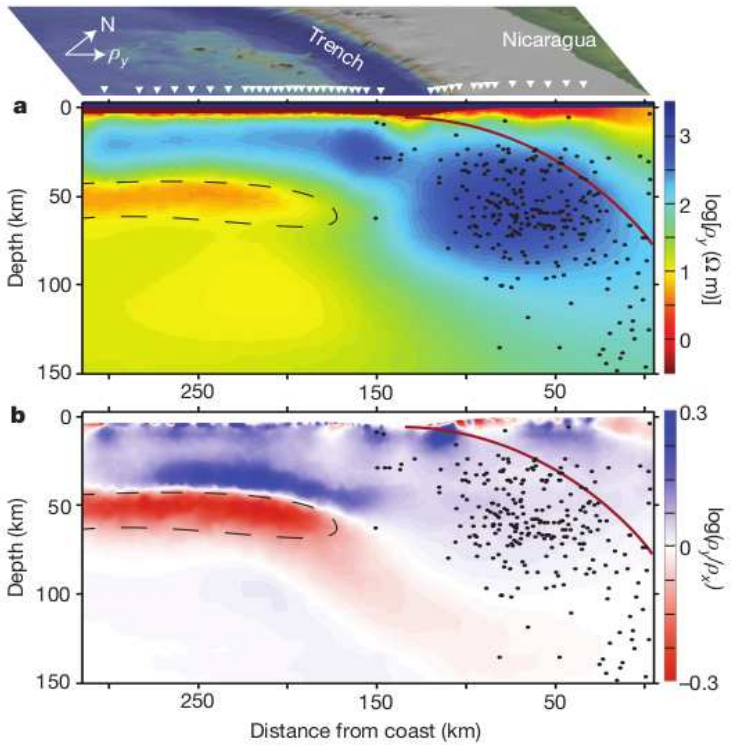

Figure 1.14: The electrical LAB channel as imaged by *Naif et al.* (2013) in the zone where Cocos plate subducts beneath the Carribean plate. The thickness of the channel is found to be 25 km having depths of 45-70 km at an age of 23 Ma.

1.5.3 Models of the oceanic LAB

The previous section focused mainly on the observations of the LAB by different means used within the geophysical community. In this section, I elaborate further the LAB models developed to explain the observations. Each new study tries to reconcile its observations with the previous studies.

The initial models proposed on the basis of vertical shear velocity contrast at the LAB account for the dependency of shear velocity on temperature (*Brune and Dorman*, 1963; *Priestley and Brune*, 1978) and propose a purely thermal model for the LAB. The LAB would then be the transition zone where there is a change from the heat conducting lithosphere to the adiabatic mantle. *Anderson and Sammis* (1970); *Hammond and Humphreys* (2000) proposed presence of melt could be also responsible for the shear velocity decrease, however it is shown by *Karato* (2014) that partial melting does not explain the observations. Inclusion of grain size in the thermal models (*Faul and Jackson*, 2005; *Priestley and MKenzie*, 2006) as well as addition of volatiles (*Karato and Jung*, 1998; *Karato*, 2012) have been proposed to explain the shear velocity decrease. *Karato* (2012) proposes a grain boundary sliding model facilitated by the presence of a sharp water gradient at the base of an age-independent LAB at ∼70 km depth. However, *Mehouachi and Singh* (2018) showed that a grain boundary sliding model sould be transparent on the P-wave seismic section, which was not the case according to their observations. A few more models of the oceanic LAB in recent times that have been proposed are discussed as follows.

The model proposed by *Kawakatsu et al.* (2009) on the basis of receiver function observation of the LAB at Japan-Pacific subduction assumes a rigid lithospheric plate floating on a partially molten asthenosphere consisting of horizontal meltrich layers embedded in a meltless mantle. This model has been termed as the melt lubricated *millefeuille* asthenosphere model and is able to explain the LAB observations from a small amount of melt.

On the basis of azimuthal anisotropy in the upper mantle, *Debayle and Ricard* (2013) observe the plate velocity to play a role in determining its magnitude. Slow spreading plates having velocities <30 mm/yr show much smaller azimuthal anisotropy as compared to intermediate 30-50 mm/yr spreading which is

attributed to small-scale convection patterns in the asthenosphere beneath slow moving plates. They also observe higher azimuthal anisotropy in the asthenosphere as compared to the lithosphere. They propose that anisotropy in the asthenosphere is mainly due to mantle-flow related lattice-prefered orientation of the olivine crystals whereas in the lithosphere, the reduced anisotropy is due to frozen melt lenses as also proposed by *Plomerova et al.* (2002). The transition between the two happens around the 1100°C isotherm (*Debayle and Ricard*, 2013). Figure 1.15 proposes a model of the oceanic LAB to summarize the receiver function, surface wave velocity and anisotropy studies, also attempting to distinguish between the LAB and the G-discontinuity (*Schmerr*, 2012).

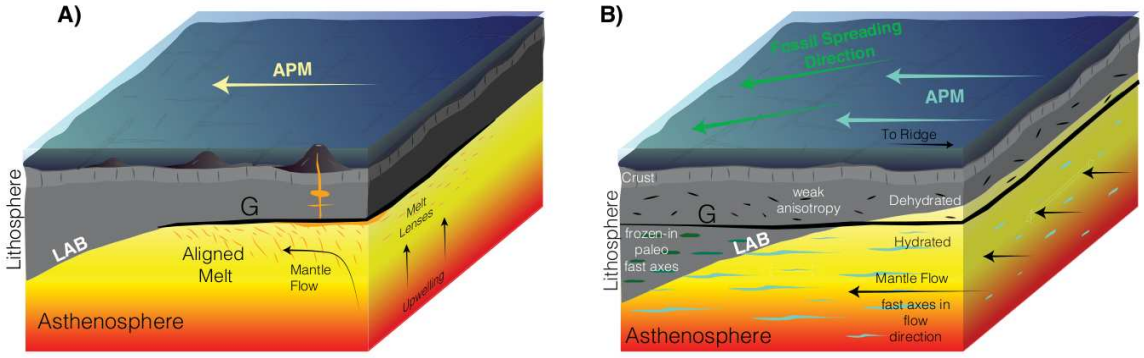

Figure 1.15: Model of LAB proposed by *Beghein et al.* (2014) to reconcile the surface wave azimuthal anisotropy, surface wave shear velocities and receiver function observations. An important feature is that a distinction is made between the LAB and the G-discontinuity. (A) Mantle upwelling beneath ridge axis creates melt which ponds at 80-100 km depth (*Sakamaki et al.*, 2013) and gets aligned in the direction of mantle flow, resulting in observed anisotropy. The LAB and the G are identical for younger ages after which the G is intermittently observed (*Schmerr*, 2012). (B) G is a chemical boundary layer between a weakly anisotropic, dry and a hydrated region having fossil-spreading alignment of olivine (*Karato*, 2012). The LAB represents the contrast between the dehydrated lithosphere and hydrated asthenosphere at younger ages and between frozen-melt having a paleo-spreading orientation and present-day mantle flow oriented olivine. APM refers to absolute plate motion.

Auer et al. (2015) attempts to reconcile all previously proposed models of LAB from surface wave velocity, surface wave anisotropy, RF and SS precursors as shown in figure 1.16. The model proposes an age-dependent thermo-mechanical base of lithosphere (LAB) which almost follows the 1200°C isotherm which flattens ∼200 km from the spreading ridge. The LAB respresents a discontinuity between the flow-oriented olivine and weakly anisotropic shape-oriented olivine. The G-discontinuity is different from the LAB and is at a constant depth of ∼60 km where the melt accumulates in ponds. Away from the ridge axis, it is intermittently imaged as frozen melt-lenses in the lithosphere may get re-heated due to hotspots or thermal anomalies. Few studies namely *Gaherty et al.* (1996, 1999); *Schmerr* (2012) have also imaged a discontinuity in the asthenosphere at constant depths of ∼150 km which represents a velocity decrease across and is intermittently imaged. It has been termed as the L-discontinuity. Beneath the spreading axis and the G- and L-discontinuities lies a zone of high radial anisotropy attributed to high melt mobility (ascending melt). This radial anisotropy is not observed away from the ridge axis. The azimuthal anisotropy is more prominent away from the ridge axis and is due to the different alignement patterns of olivine in the mantle across the LAB (*Beghein et al.*, 2014).

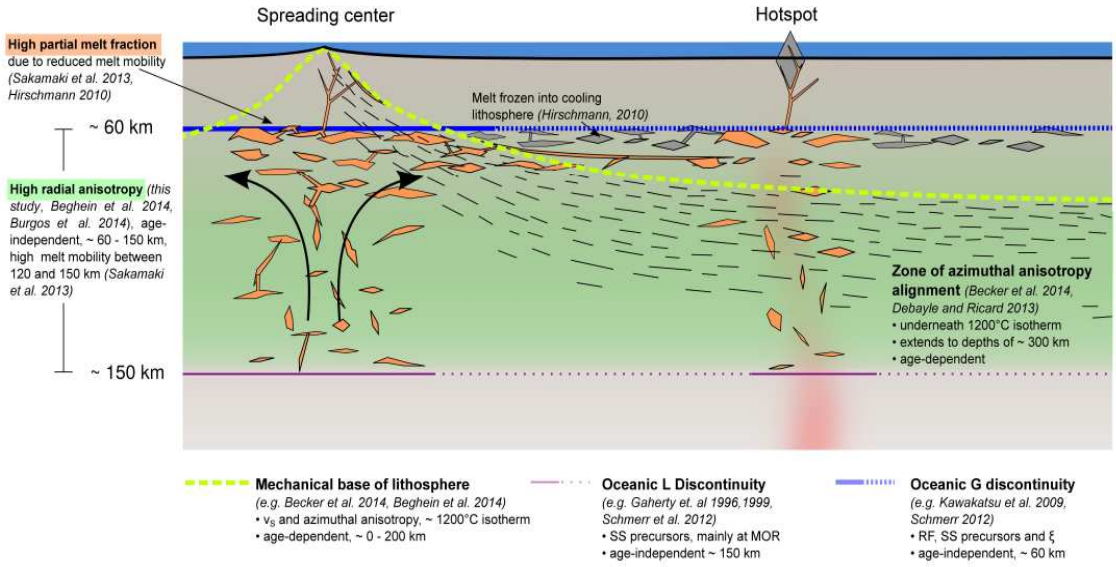

Figure 1.16: Model proposed by *Auer et al.* (2015) to reconcile previous models of seismological studies: Convective upwelling of mantle material and decompression melting at spreading centres forms basaltic oceanic crust (*Hirschmann*, 2010), whereas in deeper mantle partial melt accumulates in flow aligned, melt-rich channels whose depth is controlled by melt mobility (*Sakamaki et al.*, 2013). Melt from this melt rich channel spreads laterally and is frozen into the lithosphere at constant depth which depends on asthenospheric temperature and spreading rate. At hotspots and thermal anomalies, re-melting of this frozen melt may occur resulting in an intermittent LAB imaged by RF (*Schmerr*, 2012). The shape-prefered orientation of the frozen melt will result in radial anisotropy (*Kawakatsu et al.*, 2009) but may have a minor effect on azimuthal anisotropy. Flow induced lattice preferred orientation in upper asthenosphere will result in azimuthal anisotropy due to shearing in upper asthenosphere (*Becker et al.*, 2008; *Debayle and Ricard*, 2013).

There has been a recent shift towards the LAB being perceived as a channel from magneto-telluric (*Naif et al.*, 2013) and high-resolution seismic studies (*Stern et al.*, 2015; *Mehouachi and Singh*, 2018). These studies report an age-dependent (*Mehouachi and Singh*, 2018) channel 10-25 km thick, which would have been difficult to be observed by seismological studies due to low vertical resolution. An important finding of *Mehouachi and Singh* (2018) is that the mechanism of grain boundary sliding proposed by *Karato* (2012) does not affect the P-velocities (*Ghahremani*, 1980) and they propose the channel to be melt-rich stabilized by presence of volatiles as indicated by *Naif et al.* (2013); *Stern et al.* (2015) with most of the volatiles originating from a horizontal flux near the ridge axis as supported by recent modeling studies (*Keller et al.*, 2017). The horizontal flux of volatiles from the ridge is supported by the constant water content computed in the LAB channel ($90 \pm 35 ppm$) at different ages (*Mehouachi and Singh*, 2018).

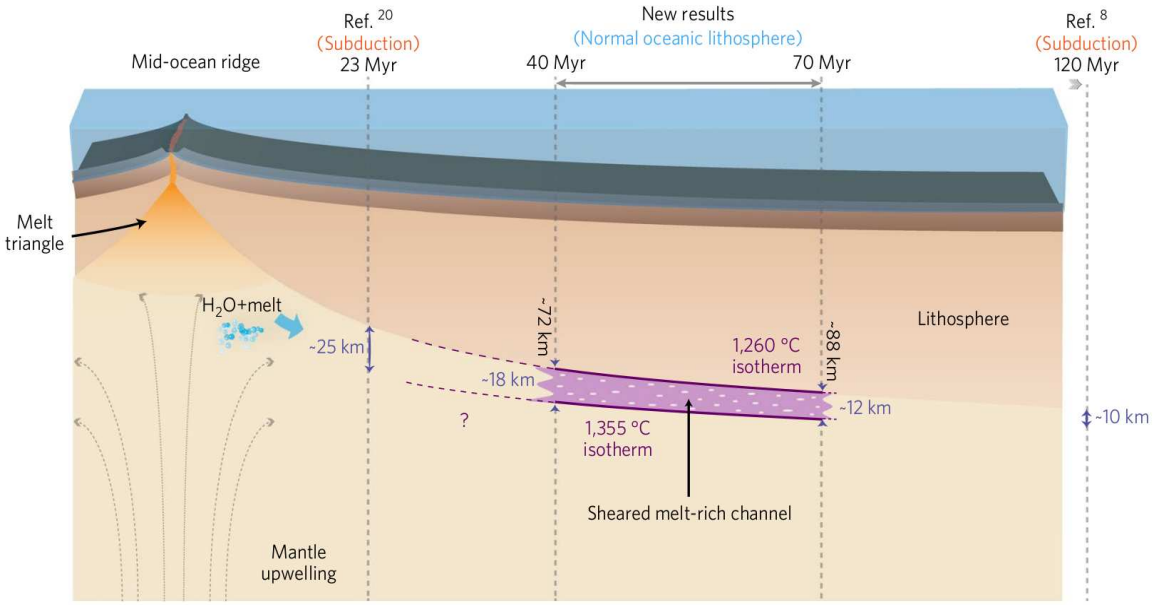

Figure 1.17: A model of the LAB channel as proposed by *Mehouachi and Singh* (2018): An age-dependent volatile-rich low velocity channel bounded by the isotherms 1260°C and 1355°C thins towards older oceanic lithosphere. The volatiles remain trapped in the channel after a sub-horizontal flux of the volatiles beneath the ridge axis. Results by *Naif et al.* (2013) and *Stern et al.* (2015) fit well to this model.

Some studies have also imaged a mid-lithospheric discontinuity in the continental cratons (*Selway et al.*, 2015; *Wirth and Long*, 2014; *Karato et al.*, 2015; *Tharimena et al.*, 2016). Very few studies have imaged frozen-in melt lenses in the oceanic lithosphere (*Ohira et al.*, 2018; *Qin et al.*, 2020), which can be considered equivalent to a mid-lithospheric discontinuity. However in this thesis, my main focus will be the LAB which has been referred to as the thermo-mechanical base of lithosphere above.

So far I have presented a picture of the lithospheric layering observed from previous studies and the various models proposed with a focus on oceanic lithosphere. Most of the seismology studies that have oberved the LAB suffer from the drawback of low vertical resolution and the recent studies from seismic reflection data have been limited to fracture zones/very old lithosphere at subduction zones. What remains unknown and uninvestigated is the structure and evolution of continuous normal oceanic lithosphere.

1.6 TransAtlantic ILAB project

To address the above limitations of the previous studies on the evolution of the upper oceanic crust and the lithosphere (LAB), the TransAtlantic Imaging of Lithosphere-Asthenosphere Boundary (ILAB) was designed. Two expeditions/experiments were carried out in the Equatorial Atlantic ocean - one in 2015 and another one in 2017. The 2015 expedition (also termed as ILAB expedition in this thesis) collected active source multi-channel multi-component 2-D seismic data along a ∼2775 km long profile as shown in figure 1.18. The 2017 expedition (also termed as LITHOS expedition in this thesis) collected co-located active source wide-angle seismic, conductive heatflow, parasound and high-resolution bathymetry along a flow line of the 2015 expedition. The parts of the profile lying on the fracture zones have been analysed for the LAB by *Mehouachi* (2019). This thesis focuses on the part of the profile covering 0-75 Ma on the African plate in figure 1.18. The details of the two expeditions and their data acquisitions are further elaborated below.

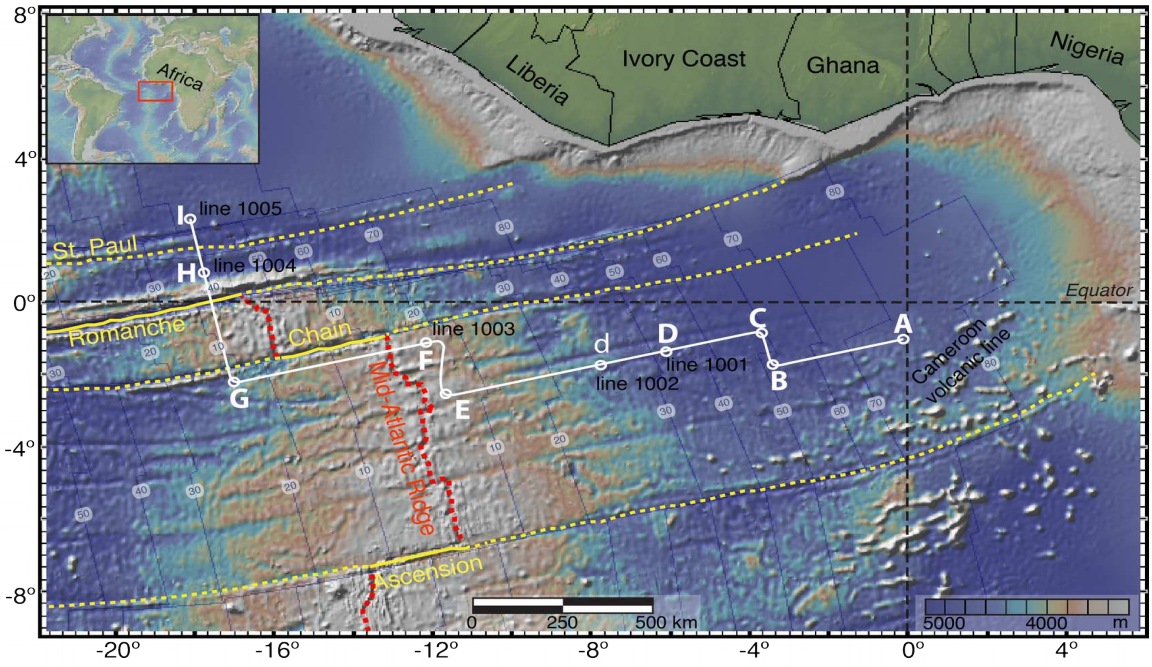

Figure 1.18: Study region of the TransAtlantic ILAB project showing the seismic profile in white (A-I). In this thesis, the part of the profile from point A at 75.6 Myr on the African plate to Mid-Atlantic ridge has been analysed. The profile from Mid-Atlantic ridge to point F is Leg 1; from point E at 1.8 Myr to point C at 46.7 Myr is Leg 2; from point B at 49.3 Myr to point A at 75.6 Myr is Leg 3. Change of recording length at point d. The part of the profile from the Mid-Atlantic ridge to point I on the South American plate has been analysed by *Mehouachi* (2019). Credit: *Milena Marjanović*.

1.6.1 2015 ILAB experiment

In March-April 2015, ∼1800 km of active-source multi-channel multi-component seismic data was acquired on-board M/V Western Trident of WesternGeco over oceanic lithosphere spanning 0-75 Myr (*Singh*, 2015). The 2D profile was acquired using the advanced Isometrix streamer (*Vassallo et al.*, 2013), consisting of 4 components - hydrophone (P) and geophone (A_x,A_y,A_z) at every 3.125 m over its entire lenth of 12 km. Figure 1.19 shows the Isometrix streamer and the multi-components. The hydrophone component records fluctuations in pressure (P) and the geophone components (A_x,A_y,A_z) record the amplitude and direction of the incoming energy. The long offset of 12 km makes it possible to record rays turning in the upper oceanic crust in older seafloor which have >5 km thick water column. An air-gun array comprising of 8 arrays of 6 air-guns each was used as a source. The resulting volume of the air-gun array was 10170 cubic inch (=167 litres) and is one of the largest used in the industry. The large volume of the air-guns was used to make sure that sufficient energy is generated to reach depths of 100 km. The record length

varied from 20-30 s two-way time (TWT) and was kept large enough to make sure energy from deeper parts of the lithosphere is captured. These parameters of data acquisition along with few others such as source and streamer depth are listed in table 1.3.

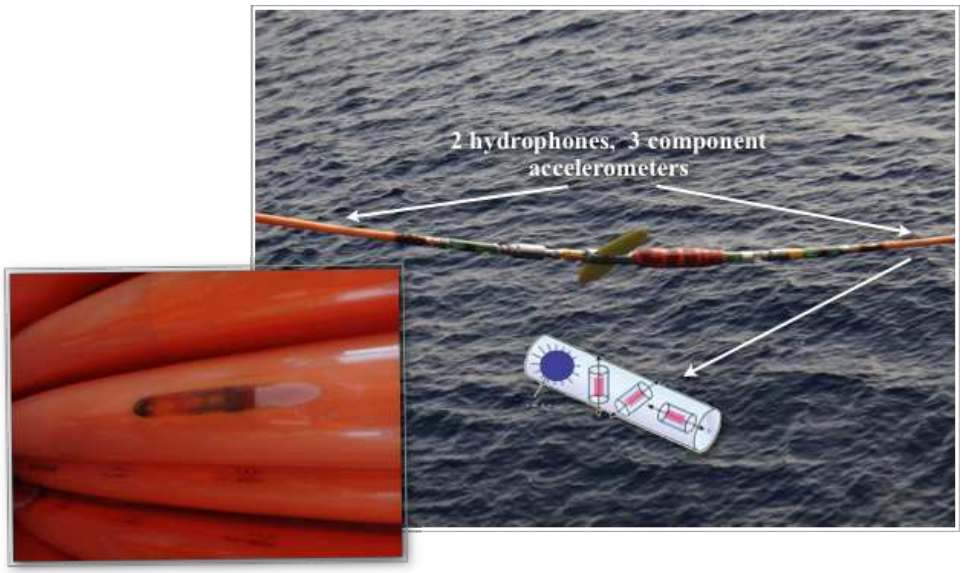

Figure 1.19: Isometrix streamer and the four components (P, A_x, A_y, A_z) used to acquire the seismic data. Credit: *Milena Marjanović.*

Table 1.3: Survey parameters of the multi-channel multi-component seismic data

Acquisition Parameter	Value
Components	4 (P, A_x, A_y, A_z)
Channels	3857
Channel spacing	3.125 m
Source	Airgun array (167 lt.)
Record length	20-30 s (changed at 26.7 Myr)
Sampling rate	2 ms
Receiver depth	25-30 m
Shot interval	50-75 m (changed at 26.7 Myr)
Source Depth	15 m

The data was collected from 0-75 Ma in the Equatorial Atlantic on the African plate in three-ridge perpendicular parts of the profile as shown in figure 1.18. These three-ridge perpendicular parts of the profile (also called flow lines) span a total of ∼1516 km with the individual profile lengths being: ∼156 km for the part of profile crossing the ridge-axis and spanning the Mid-Atlantic Ridge (zero-age) to 7.7 Ma on the African plate, ∼905 km for the longest leg of the profile from 1.8-46.7 Ma on the African plate, and ∼395 km for the part of the profile from 49.3-75.6 Ma and being nearest to the Cameroon volcanic line. It is important to mention here that I did not consider the turning radius during the ship's turns. As my objective was to provide variation with age, I did not consider the ridge-parallel parts of the profile (also called iso lines) in this study. I denote the three-ridge perpendicular profiles as Leg 1 (Mid-Atlantic ridge-7.7 Ma African), Leg 2 (1.8-46.7 Ma) and Leg 3 (49.3-75.6 Ma). The two ridge-parallel parts of the profile span ∼172 km between Leg 1 and Leg 2 and ∼112 km between Leg 2 and Leg 3 and have not been included in the study. The acquisition parameters of the survey with respect to the three ridge-perpendicular parts of the profile are listed in table 1.4. The parameters in leg 1 and distinct from leg 2 in terms of shot spacing and recording length and halfway along leg 2 at 26.7 Ma, the recording parameters again show a change as compared to leg 3 (table 1.4).

Table 1.4: Survey parameters of the three legs of the ridge-perpendicular parts of the seismic profile. All ages refer to ages on the African plate.

Leg No.	Age (Ma)	Record length (sec)	Shot spacing (m)	Streamer depth (m)
3	49.3 - 75.6	30.72	75	25
2	26.7 - 46.7	30.72	75	30
2	1.8 - 26.7	20.48	50	30
1	0 - 7.7	25	62.5	30

The recorded multi-channel seismic data from the 2015 expedition has reflections from various interfaces in the sub-surface such as seafloor, crust-mantle boundary (Moho) and the LAB. These reflections manifest as hyperbolic curves with offset. Several processing techniques such as those elaborated in chapter 2 are then used to correct the hyperbolic arrivals and obtain an image of the sub-surface. Wide-angle arrivals from the rays turning in upper oceanic crust are also recorded in the 12 km long streamer. These arrivals usually have a linear moveout with offset and contain the velocity information of the sub-surface. Techniques such as seismic tomography (chapter 2) are used to extract the P-velocity information from these arrivals. To enhance these arrivals (also called first arrivals) prior to performing tomography, sources and receivers are extrapolated down in the water-column from the sea-surface to close to the sea-floor. This is known as downward wavefield extrapolation (or downward continuation) and results in a better sub-surface coverage of the turning rays. Due to limitation of the streamer length in seismic reflection expedition such as these, the velocity information of the deeper parts of the crust and lithosphere remain unconstrained. The LITHOS 2017 expedition overcame this limitation by collecting co-located active-source wide-angle data as elaborated below.

1.6.2 2017 LITHOS experiment

In November-December 2017, ∼1000 km of active-source wide-angle seismic data, conductive heatflow measurements, parasound data and high resolution 11-km swath bathymetry was acquired along the Leg 2 of the MCS profile of the 2015 expedition (figure 1.18) spanning 0-50 Ma old lithosphere onboard the German research vessel Maria S. Merian (*Grevemeyer et al.*, 2018). The active source wide-angle seismic data was recorded on ocean-bottom hydrophones and ocean-bottom seismometers deployed on the seafloor at variable spacing ranging from 10-20 km depending on the lithosphere age. Maximum offsets of ∼1000 km were recorded on all the deployed ocean bottom instruments to constrain the crustal velocities, depth of crust-mantle boundary (Moho) and the upper mantle velocities. The analysis of the wide-angle seismic data of the 2017 LITHOS experiment is not a subject of this thesis and has been done by *Prof. Ingo Grevemeyer (GEOMAR)* and *Venkata Vaddineni (IPGP)*.

In addition to the active-source wide-angle seismic data, indirect measurements of vertical conductive heatflow were also made using a 5.4 m long probe as shown in figure 1.20. Along the 5.4 m length of the probe, 21 temperature sensors with a 0.001 K sensitivity were distributed uniformly. The probe was lowered from the ship's deck all the way down to the seafloor using a winch where it was coupled with the sediments (figure 1.20). The measurements were made at distinct ages from 0-50 Ma and at each age, 9-12 measurements at 1 km spacing were made. The location of these sites was chosen from the MCS data of the 2015 expedition where there existed sufficient sediment cover for the probes to be coupled. The probe measured the in-situ vertical temperature gradient and the thermal conductivity of the sediments, the product of which gives the vertical conductive heat flow. The individual measurements of the temperature gradient and thermal conductivity were transmitted to the ship in real time. Analysis of the heatflow data is being jointly carried out by *Prof. Heiner Villinger (Bremen university)* and myself. I elaborate further on the heatflow data in chapter 3 and use it to constrain the upper crustal properties.

Figure 1.20: The 5.4 m long heatflow measuring probe used in the LITHOS 2017 experiment (Credit: *Prof. Heiner Villinger*). The probe is being lowered from the ship deck to the seafloor through a winch cable. The vertical temperature gradient and the thermal conductivity are measured by the probe at each heatflow location.

Parasound data was also acquired in the 2017 experiment to provide a high resolution of the near-seafloor (10 meteres below the seafloor). Two primary pingers of frequency 18 kHz and 21 kHz were used to obtain a high resolution image of the seafloor and the resulting differential frequency of 3 kHz was used for imaging the near-surface sediments. 11-km swath high-resolution bathymetry was also measured onboard the 2017 experiment. The 11-km swath helped in interpreting some of the features along the profile, which otherwise could not be interpreted from a 2D seismic profile. I use the parasound and high-resolution bathymetry to check/validate such features in chapter 3. With an extensive amount of data collected from the 2015 ILAB and the 2017 LITHOS experiments, I now try to understand the study region which would help in interpretation of the results from these data.

1.7 Study region

The study region that the data has been collected on is the Equatorial African plate from 0-75 Ma formed at the Mid-Atlantic ridge. The bathymetric map is shown in figure 1.21 from *Olson et al.* (2014) along with MCS profile, the mid-Atlantic ridge plate boundary from *Bird* (2003) and the IODP borehole sites of Leg 108 and Leg 159. The West African craton and the Congo craton are thick continental lithospheric roots with an estimated thickness of 230 km (*Priestley and MKenzie*, 2006). Three prominent fracture zones (FZ) bound the region in the North: the St. Paul having an age contrast of 30 Ma (offset of 700 km), the Romanche having an age contrast of 45 Ma (900 km offset) and the Chain having an age contrast of 15 Ma (300 km offset). The southern end of the study region is bounded by the Ascension FZ. Two prominent island chains can be seen in proximity to the eastern end of profile on Leg 3: the St. Helena seamount chain and the Cameroon volcanic line. The Cameroon volcanic line has been proposed not to extend beyond 600 km from the African coast whereas the St. Helena seamount chain extends all the way to the present day location of St. Helena island further south. These volcanic chain islands are distinguished in terms of age, island chain pattern and swell height. Whereas the offshore part of Cameroon line closest to MCS profile is younger < 10 Ma (*Dunlop and Fitter*, 1979; *Fitton and Dunlop*, 1985), the oldest rocks >80-82 Ma (*O'Connor and le Roex*, 1992a) of St. Helena are found closest to the MCS profile. Also, as can be observed from the bathymetric map, the Cameroon islands have a linear pattern and the individual swells are much higher as compared to the St. Helena islands which are more widespread and have a lower swell height.

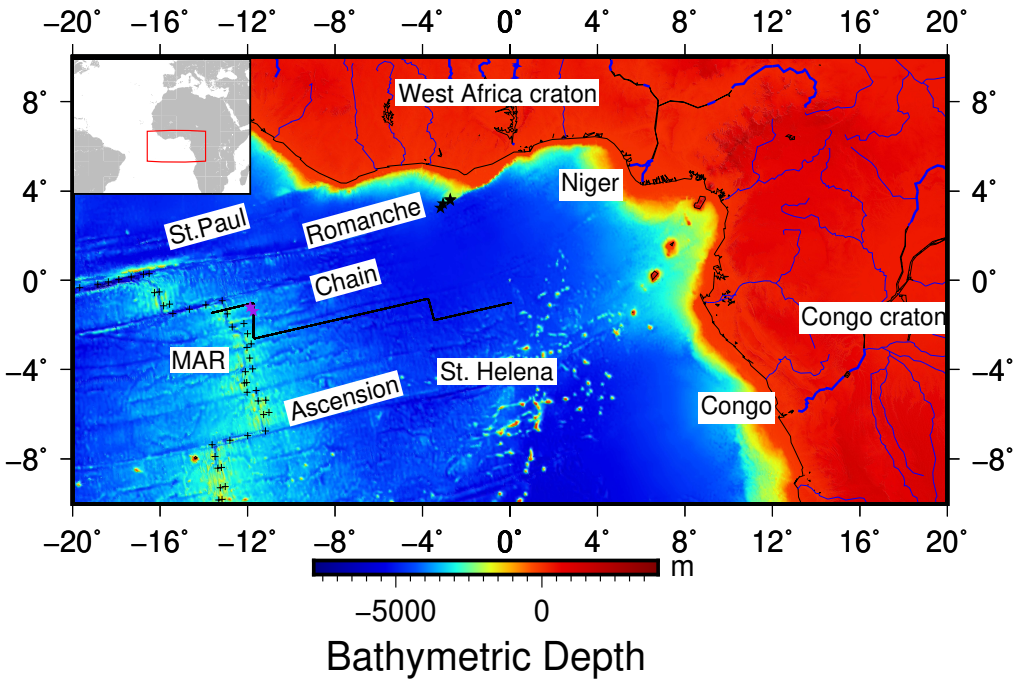

Figure 1.21: Bathymetric map of the study region (*Olson et al.*, 2014) with various features with an inset map (top left). The multi-channel seismic profile is labeled in black and extends from 4.5 Ma on the South American plate to 75.6 Ma on the African plate in three ridge perpendicular flow lines. The Mid-Atlantic ridge, which is the plate boundary between the African and the South American plate has been marked by + signs (*Bird*, 2003). The IODP borehole sites 662 and 663 of Leg 108 and sites 959-962 of Leg 157 have also been marked by purple stars and black stars respectively. The major and minor rivers in Africa have also been plotted in thick blue and thin blue respectively. The main fracture zones that offset the Mid-Atlantic ridge are St. Paul, Romanche and Chain in the North and Ascension fracture zone in the South. The Cameroon volcanic line (CVL) is a volcanic chain of islands that can be seen in a NE linear trend extending upto 600 km offshore Western Africa. A more scattered group of seamounts near the MCS profile is the St. Helena chain that extends upto the St. Helena hotspot much further south (not shown in map).

1.7.1 Geodynamic history and available information

The opening of the Atlantic ocean initiated by breaking up of the continental African and South American plates from the southern end near the Tristan hotspot around 150 Ma (*Granot and Dyment*, 2015). This northward propagating rift slowed down significantly near the equatorial region at ∼110 Ma (*Bonatti*, 1996) due to a thicker and 150°C colder lithosphere (*Bonatti et al.*, 1993). This developed extensive east-west fracturing zones which were further influenced by a slower African plate motion from 19-31 Ma (*O'Connor et al.*, 1999). The present day spreading rate at the Mid-Atlantic ridge is 16 mm/yr (*DeMets et al.*, 2010).

The age map of the study region, the associated error and the half-spreading rate are shown in figure 1.22a, b and c respectively. These datsets have been taken from the global database of *Müller et al.* (2008). It should be noted that the equatorial region is devoid of any magnetic anomalies which are used to invert for the seafloor ages. In absence of these magnetic anomalies, the ages have been estimated precisely in the North and South Atlantic and the ages have been determined thereof. The ages in the equatorial region are an interpolation of the ages in the North and South Atlantic and are not accurate. There is a mismatch with respect to some other studies which also determine global ages (*Cogné and Humler*, 2004). The half-spreading rates for the region are within 8-25 mm/yr as expected for a slow-spreading ridge like the mid-Atlantic ridge.

(a)

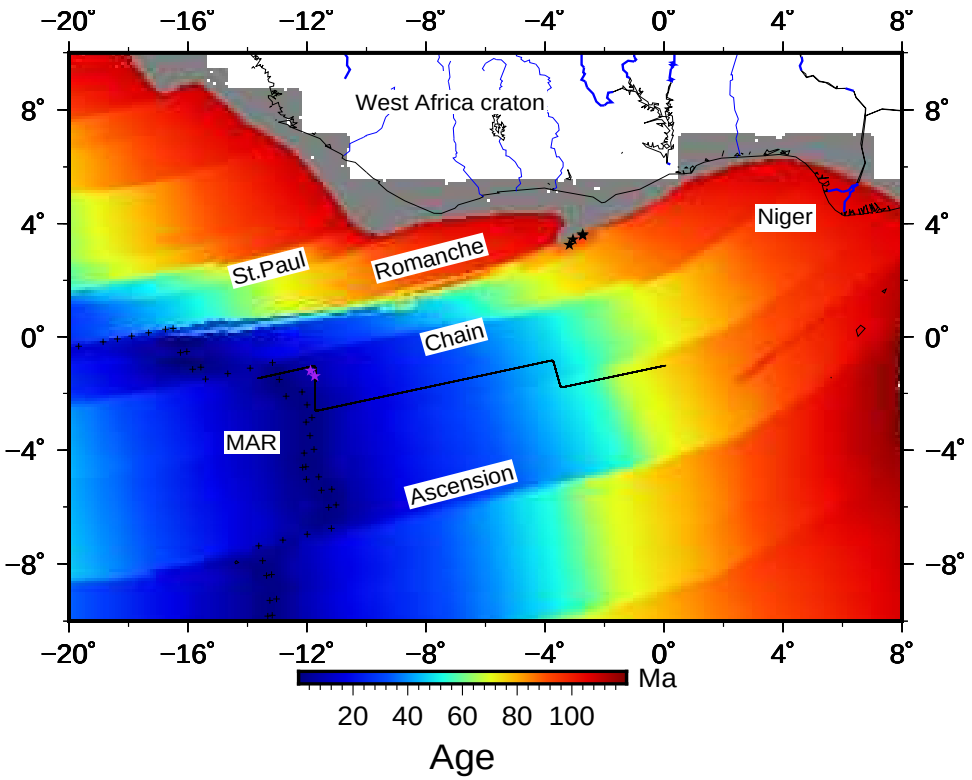
−20° −16° −12° −8° −4° 0° 4° 8°
8°
4°
0°
−4°
−8°
West Africa craton
Niger
St.Paul
Romanche
Chain
MAR
Ascension
Ma
20 40 60 80 100
Age

(b)

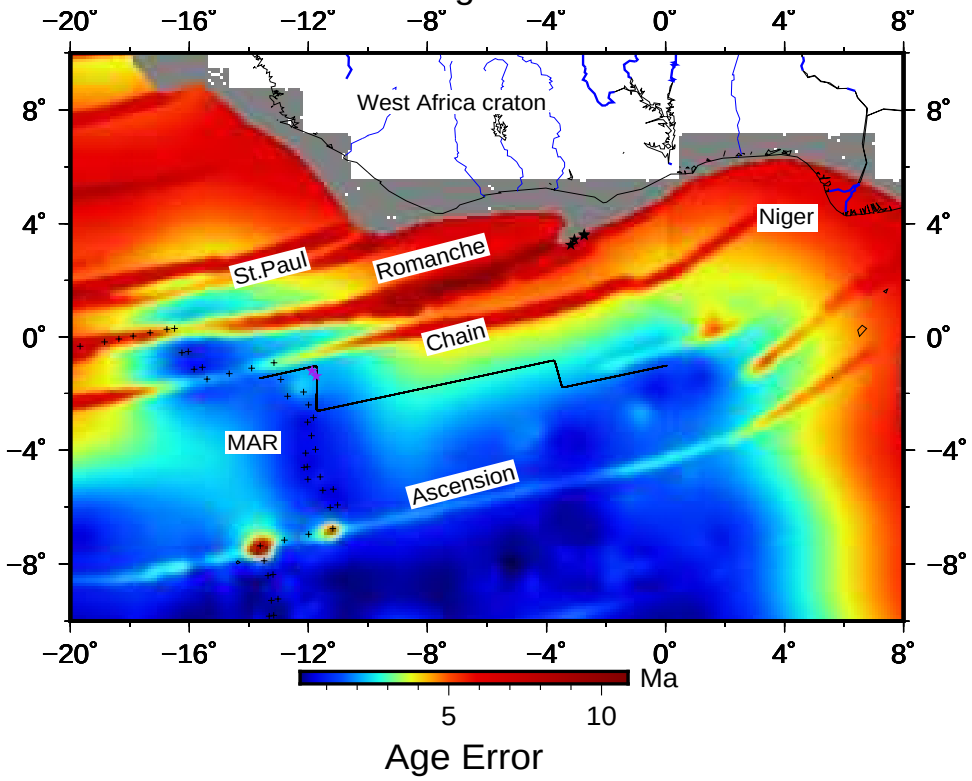
−20° −16° −12° −8° −4° 0° 4° 8°
8°
4°
0°
−4°
−8°
West Africa craton
Niger
St.Paul
Romanche
Chain
MAR
Ascension
Ma
5 10
Age Error

(c)

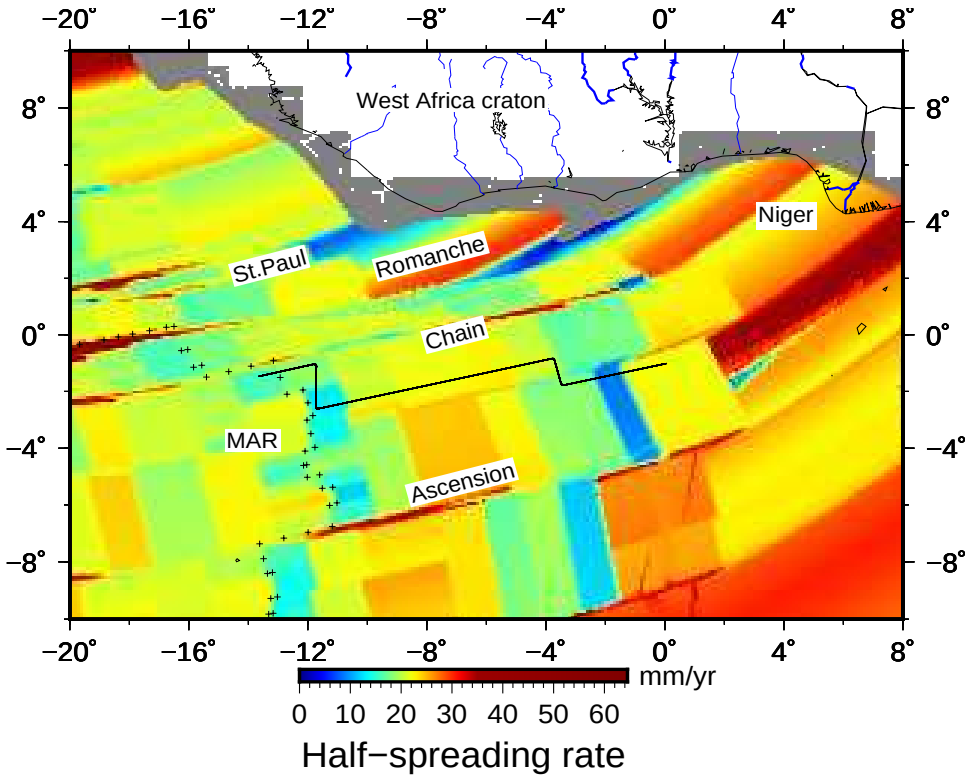

Figure 1.22: Age map (a), age eror map (b) and half-spreading rate (c) of the study region from *Müller et al.* (2008). The Mid-Atlantic ridge plate boundary is denoted by + signs and the IODP boreholes are shown as in figure 1.21

Available information about the study region on seismicity, sediment cover, gravity anomaly and heatflow is gathered below to have further information on the study region.

1. Seismicity: Seismicity in the region is most prominent at the ridge axis and the island chain of Cameroon and St. Helena as shown in figure 1.23. Earthquakes close to the ridge axis are shown with a focal mechanism (Harvard catalog) and are associated with the lithospheric generation at the mid-Atlantic ridge. The earthquakes on the island chains have been obtained from USGS open data and have magnitudes in the range 4-5. The cluster of 4 earthquakes at the edge of African continent along the Cameroon line is also the location of presently active Mount Cameroon.

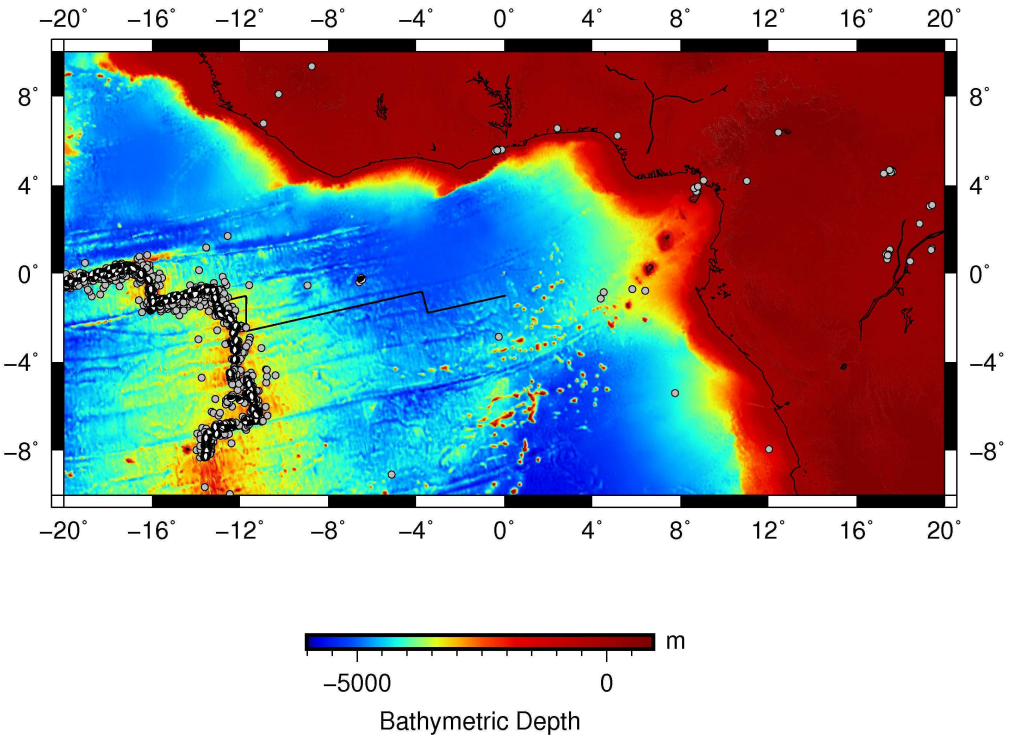

Figure 1.23: Seismicity map of the region with the bathymetry and features as shown in figure 1.21 (Credit: *Emma Gregory*). The solid gray circles denote the earthquake catalog from USGS whereas the beach ball focal mechanisms have been obtained from Harvard catalog. Apart from the Mid-Atlantic ridge, seismicity is also observed along the Cameroon Volcanic Line with all the earthquakes being shallower than 10 km.

2. Gravity measurements: These volcanic island chains also leave a footprint on the gravity anomalies as can be seen from the global free-air gravity anomaly map (*Sandwell et al.*, 2014) in figure 1.24. The individual swells have gravity anomaly in excess of +100 mgal and the surrounding region is isostically compensated by an anomaly of −50 mgal. I will expand more on this in chapter 4. The fracture zones and the median ridge valley exhibit negative gravity anomalies whereas their flanks are associated with a positive anomaly for isostatic compensation.

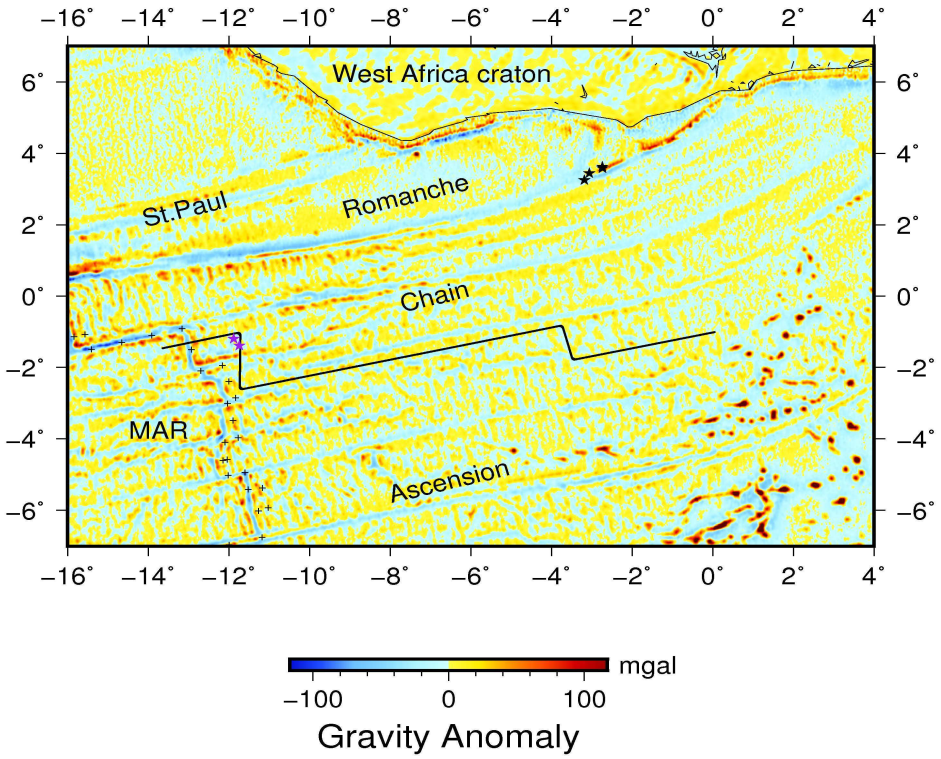

Figure 1.24: Free-air gravity anomaly map of the region with the MCS profile and different features as in figure 1.21 from *Sandwell et al.* (2014). The fracture zones and the Mid-Atlantic ridge are negative anomalies whereas the Cameroon line has positive gravity anomalies exceeding +100 mgal

3. Sediment cover: The MCS profile is most likely to be influenced by the Niger and the Congo rivers of Africa which are two of the major African rivers . As can be seen from the global sediment thickness map of *Whittaker et al.* (2013) in figure 1.25, the Niger river delta has a local accumulation of sediments reaching nearly 10 km in sediment thickness whereas the Congo river delta has a more widespread sediment distribution with sediment thickness peaking to 5 km. The contour of ∼2 km of sediment thickness can also be seen can be seen extending ∼1000 km from the African coast parallel to it. The IODP Leg 108 has sites 662 and 663 at ∼6 Ma old crust close to the profile as shown in figure 1.25. The drilling and scientific results from these boreholes is further investigated in chapter 3. The scientific results of borehole sites 959-962 of Leg 157 are more focused on the Ivory coast-Ghana passive transform margin and are not discussed as they do not relate to my thesis.

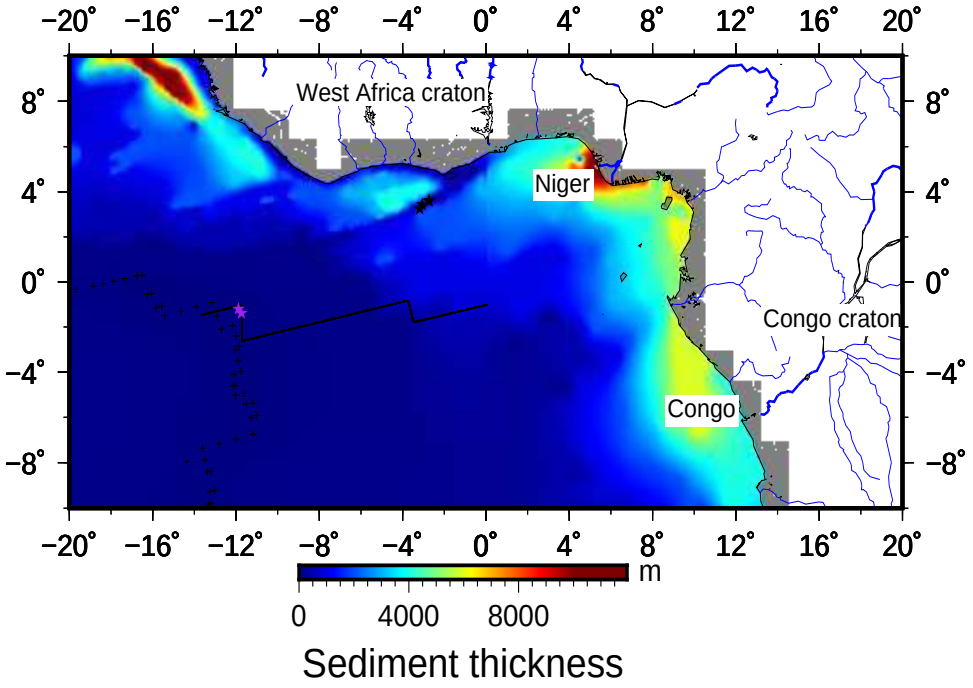

Figure 1.25: The global sediment thickness map from *Whittaker et al.* (2013) along with the MCS profile in black and the IODP boreholes marked by colored stars. The sediment thickness in the Niger river delta is higher and more localized as compared to the sediment thickness in the Congo river delta.

4. Surface heatflow: Another common geophysical observation made is that of surface heatflow. The surface heatflow measurements further constrains the evolution of crust and/or lithosphere. Figure 1.26(a) shows a compilation of all heatflow measurements in the Atlantic; (b) zooms in around the study region and (c) plots these heatflow measurements against expected cooling curve from *Hasterok* (2013). To add to this extensive dataset, heatflow data was further acquired in 2017 along Leg 2 of the MCS profile as discussed in the previous section.

(a)

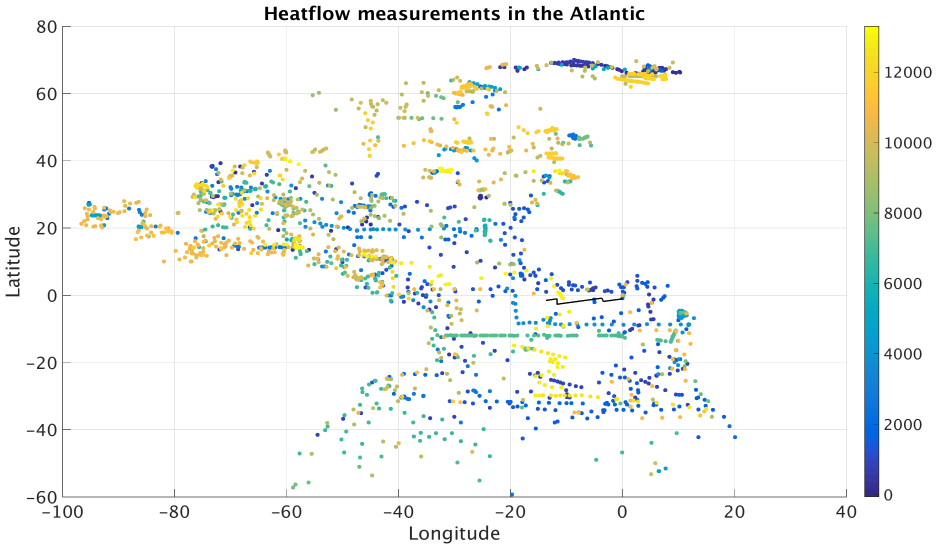

(b)

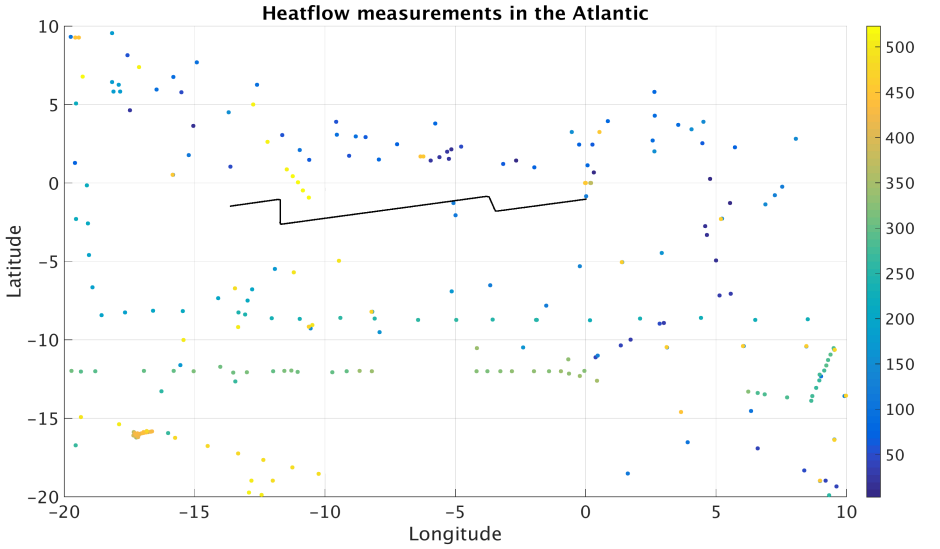

(c)

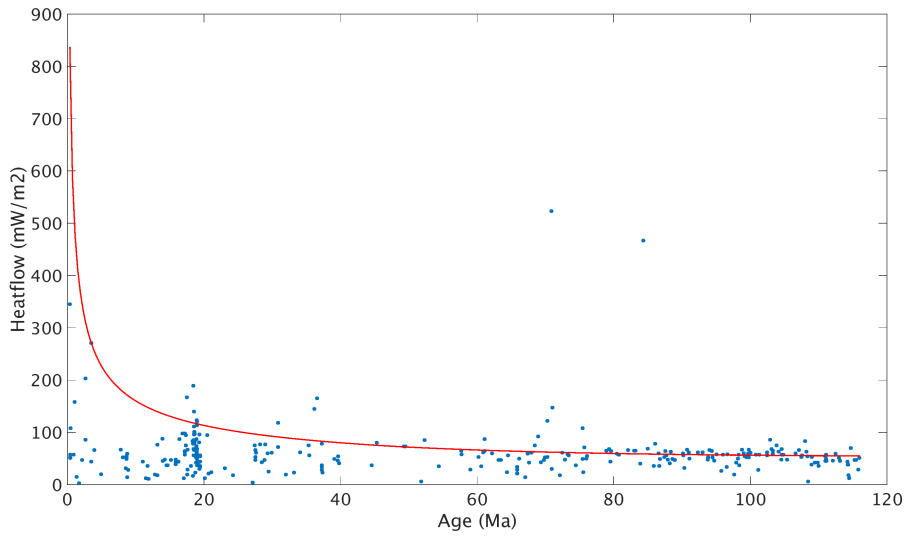

Figure 1.26: (a) A compilation of the various heatflow measurements made in the Atlantic ocean (Credit: *Heinrich Villinger*). The MCS profile is plotted in black. The colorscale represents the heatflow values in mW/m^2. (b) A zoom in shows the heatflow values extracted near the MCS profile. (c) A plot of the heatflow values in (b) with plate cooling model obtained from *Hasterok* (2013).

1.8 Objectives

With the limitations of the above models on upper oceanic crust and lithosphere-asthenosphere boundary defined as well as the study region explored, some of the questions that I attempt to address in this thesis are as follows:

1. How does the oceanic upper crust evolve from 0-75 Ma ? Is most of the evolution restricted within the first few Myr ? What is role of sediments in the evolution of the oceanic upper crust ?

2. How does the oceanic lithosphere evolve with age ? Is the Lithosphere-Asthenosphere boundary a simple boundary as shown by seismological studies or is it a more complex low velocity channel as shown by some recent studies ?

3. What happens to the lithosphere and LAB near mantle plumes ? What would be the effect of a mantle thermal anomaly on the lithosphere and the LAB ?

1.9 Thesis structure

This thesis attempts to address the question in section 1.8 over normal oceanic lithosphere from 0-75 Ma. I have divided the remainder of this thesis into five main chapters, the first focusing on data processing strategies for shallow upper crust and deeper Earth events, the second on evolution of upper crustal structure, the third and the fourth on evolution of the lithosphere and influence of volcanism/hot spots on the evolution of the lithosphere. The last chapter summarizes the observations and proposed models of upper oceanic crust and deeper Lithosphere-Asthenosphere boundary system. Every chapter, including this one, begins with its scientific summary both in French and English. The analysis and the results are then examined in detail in the sections in the chapter.

In chapter 2 , I focus on methodological aspects of procesing used in this thesis. First, I present detailed processing strategies on real data for upper oceanic crust, followed by techniques for imaging the Lithosphere-Asthenosphere Boundary (LAB).

In chapter 3, I present a systematic study of upper crustal structure along the ∼1500km long profile with more than ∼500 km of P-velocities obtained from high resolution tomography. The focus is on layer 2A and its relation to hydrothermal circulation. I then take advantage of the co-located heat flow and bathymetry data to provide a more comprehensive picture of the upper oceanic crust. In addition, I use the heat flow data to obtain constraints on the bulk-porosity-permeability relations in the upper crust.

In chapter 4, I specifially investigate the potential effects of hot spot/volcanism on the lithosphere with a case study on the Cameroon Volcanic line. In chapter 5, the lithosphere-asthenosphere boundary away from volcanism/influence of hot spots is examined.

I outline the scientific points in my thesis in chapter 6 and discuss the future prospectives of my work.

Chapter 2

Methodology and data processing

Dans ce chapitre, je donne une description théorique des différentes méthodologies et traitements de données qui ont été utilisés dans cette thèse. Pour imager la croûte supérieure à partir de données sismiques multitraces (MCS), un événement important appelé triplication de la couche 2A/2B dans les enregistrements sismiques est utilisé (*Harding et al.*, 1993). Pour comprendre à quoi ressemble une triplication de couche 2A/2B dans les regroupements de plans MCS, j'exécute une modélisation synthétique (*Shipp and Singh*, 2002) en utilisant une épaisseur variable de la colonne d'eau et des couches 2A et 2B. Cet événement 2A/2B est ensuite extrait dans le traitement des données sismiques pour obtenir une image de la sub-surface constituée de la frontière 2A/2B.

Après avoir obtenu les informations en temps double (TWT) à partir des images de la sub-surface, les vitesses d'ondes P de la croûte supérieure sont en outre obtenues en utilisant une procédure en deux étapes comprenant l'extrapolation du champ d'onde et la tomographie par temps de trajet basée sur les rais sismiques. L'extrapolation du champ d'onde vers le bas (*Berryhill*, 1984; *Arnulf et al.*, 2011) fait descendre les sources et les récepteurs de la surface de la mer vers le bas près du fond marin. Il est basé sur le principe de sommation de Kirchhoff et améliore les premières arrivées contenant des informations sur la structure de vitesse sous la surface. Le temps de trajet de ces premièresers arrivées est ensuite prélevé l'aide d'un algorithme de prélèvement semi-automatique et transmis à la tomographie à temps de trajet à rais. L'objectif de la tomographie est de mettre à jour un modèle de vitesse P de départ de telle sorte que les temps de trajet calculés des premières arrivées soient proches des temps de trajet observés dans les regroupements de plans extrapolés vers le bas. Elle est divisée en tracé de raispour calculer les temps de trajet synthétiques basés sur la méthode du chemin le plus court (*Moser et al.*, 1992) et l'inversion pour réduire l'inadéquation entre le temps de trajet calculé et observé des premières arrivées. Le modèle de vitesse d'ondes P de départ est mis à jour au fur et à mesure que l'inadéquation est réduite de la methode des moindres carrés possible (*Paige and Saunders*, 1982). L'application de ces techniques aux donnes réelles et l'interprétation des résultats sont traitées au chapitre 3.

De nouvelles techniques pour imager la limite lithosphère-asthénosphère (LAB) à partir des données MCS avec des exemples de données réelles sont présentées ci-dessous. Tout d'abord, le traitement embarqué approfondi effectué lors de l'expédition de 2015 par WesternGeco est présenté étape par étape. Le traitement des données consistant en une atténuation aléatoire du bruit, une réduction des images fantômes et une suppression des multiple est illustré. J'utilise ensuite les données traitées par WesternGeco et présente ma propre analyse des données. J'illustre que même après un traitement approfondi par WesternGeco, les données ne sont pas encore assez fines pour imaginer des structures terrestres plus profondes. J'essaie de supprimer le bruit de pendage linéaire des données et d'améliorer le contenu basse frquence (1,5-4 Hz) dans les domaines de décalage de prise de vue et de récepteur (*Partyka et al.*, 1999). Les données sont triées dans un domaine de décalage de point médian commun (CMP) où une interpolation de trace et un filtrage du nombre d'ondes sont effectués pour améliorer le rapport signal/bruit. Les meilleures vitesses d'empilement pour les réflexions de la LAB potentielles sont ensuite sélectionnées et une image de la sub-surface est obtenue. Cette image est ensuite améliorée par plusieurs techniques

d'amélioration du signal post-stack et dans les dernières étapes du traitement, je développe et applique une stratégie de traitement ciblée.

In this chapter, I give a theoretical description of the various methodologies and data processing that have been used in this thesis. For imaging the upper crust from multi-channel seismic (MCS) data, a prominent event termed as the layer 2A/2B triplication in the seismic records is used (*Harding et al.*, 1993). To understand how a layer 2A/2B triplication looks like in MCS shot gathers, I perform synthetic modelling (*Shipp and Singh*, 2002) using varying thickness of the water column and layers 2A and 2B. This 2A/2B event is then extracted in the seismic data processing to get an image of the sub-surface consisting of the 2A/2B boundary.

Having obtained the information in two-way time (TWT) from the sub-surface images, the P-velocities of the upper crust are further obtained using a two-step procedure consisting of wavefield extrapolation and ray-based travel-time tomography. Downward wavefield extrapolation (*Berryhill*, 1984; *Arnulf et al.*, 2011) brings down the sources and receivers from the sea-surface down close to the seafloor. It is based on Kirchhoff summation principle and enhances the first arrivals containing information about the sub-surface velocity structure. The travel-time of these first arrivals are then picked using a semi-automatic picking algorithm and passed onto ray-based travel-time tomography. The objective of the tomography is to update a starting P-velocity model such that the computed travel-times of the first arrivals are close to the observed travel-times in the downward extrapolated shot gathers. It is divided into ray-tracing to compute synthetic travel-times based on shortest path method (*Moser et al.*, 1992) and the inversion to reduce the misfit between the computed and observed travel time of the first arrivals. The starting P-velocity model is updated as the misfit is reduced in a least squares fashion (*Paige and Saunders*, 1982). The application of these techniques to real data and interpretation of results are left to chapter 3.

Novel techniques to image the Lithosphere-Asthenosphere Boundary (LAB) from the MCS data with real data examples are presented next. First, the extensive on-board processing performed on the 2015 expedition by WesternGeco is presented in a step-by-step manner. The data processing consisting of random noise attenuation, de-ghosting and de-multiple are illustrated. I then use the processed data by WesternGeco and present my own analysis of the data. I illustrate that even after extensive processing by WesternGeco, the data are not good enough to image deeper Earth structures. I try to remove linear dipping noise from the data and improve the low frequency content (1.5-4 Hz) in the shot-offset and receiver offset-domains (*Partyka et al.*, 1999). The data is sorted to common-midpoint (CMP) offset domain where trace interpolation and wavenumber filtering is performed to improve the signal-to-noise ratio. The best stacking velocities for the potential LAB reflections are then selected and an image of the sub-surface is obtained. This image is then improved upon by several post-stack signal enhancement techniques. In the last stages of processing, I develop and apply a target-oriented processing strategy.

2.1 Multi-channel seismic (MCS) data

Multi-channel seismic (MCS) data has been used extensively in this thesis. As described in the previous chapter, a 12 km long streamer with dense receiver spacing of 3.125 m was used to record the reflections. In marine seismic acquisitions, an end-on geometry is prefered in which the receivers are on one-side of the source whereas in land seismic acquisitions, a split-spread geometry is prefered in which the receivers are on both sides of the source. The difference between them is futher elaborated in chapter 5. The acquisition of multi-channels gives rise to a dimension termed as offset, which simply represents the distance between the source and the receivers. A seismic record of a single shot point is called a shot gather and consists of the recorded reflections in all the receivers of the streamer. An example of a shot gather (also termed as shot-offset domain) is shown in figure 2.1a,c. In the other case, the recording of a single channel having a fixed position with respect to all shots is called a receiver gather (or receiver-offset domain). The concept of shot and receiver gathers will be used in chapter 5 to create split-spread geometry gathers.

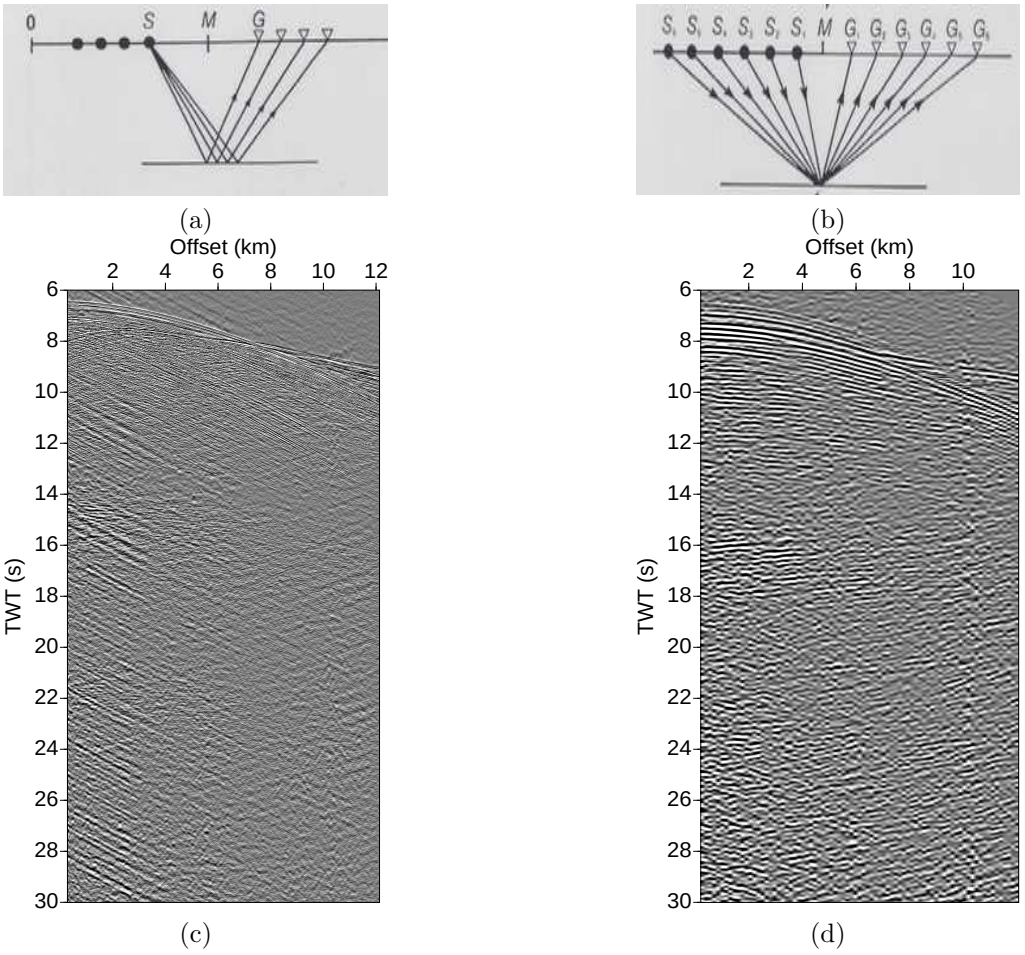

Figure 2.1: (a) The geometry of a MCS shot gather (shot-offset). A single source (S) is recorded in multiple receivers (G). (b) The geometry of a common mid-point (CMP) gather. Several source (S)-receiver (G) pairs at a common reflection point (common mid-point). (c) A MCS shot gather recorded on the 2015 cruise with 964 receivers at every 12.5 m. (d) A common mid-point (CMP) gather with 81 receivers at every 150 m. Note that the number of receivers in (d) is lesser than (c) and hence a lower resolution. Source for (a) and (b): *Research Gate*.

The shot and receiver gathers discussed above are not used for imaging the sub-surface. Instead they are sorted according to common mid-point (CMP) of the sub-surface. The common-mid-point (CMP) represents the point in the sub-surface which is being imaged by the sources and receivers. The dimension is then termed as (common mid-point-offset) CMP-offset and an example is shown in figure 2.1b,d. Whereas the data in shot-offset domain is used for estimating sub-surface velocity structure

(tomography), the data in CMP-offset domain is used for imaging the sub-surface. To obtain an image of the sub-surface from the CMP-offset records, the hyperbolic reflections are flattened according to a velocity termed as stacking or root mean square (RMS) velocity. This flattening is termed as Normal Moveout (NMO) correction and is given by the following equation.

$$t^2 = t_0^2 + \frac{x^2}{v^2}, \tag{2.1}$$

where t^2 is the two-way time of the reflection at an offset x, t_0^2 is the zero-offset two-way time of the reflection at zero-offset and v is the stacking/RMS velocity. Note that this equation is valid only only for flat reflecting interfaces in the sub-surface. Whereas the stacking/RMS velocity is a superficial imaging velocity, there are mathematical relations to extract the actual sub-surface P-velocities (also termed as interval velocities) from these stacking/RMS velocities. The above NMO correction on real data is illustrated in the following sections and the derivation of interval velocities from RMS velocities is elaborated in the next chapter. To increase the signal-to-noise ratio in sub-surface imaging, a common practice is to combine adjacent common mid-point (CMP) gathers to get a super gather termed as a super-CMP gather. The super-CMP gather has more number of traces as compared to a CMP gather and hence is used in imaging. The super-CMP gathers of the real data will be illustrated later in this chapter.

2.2 Upper crustal imaging

2.2.1 Identification of layer 2A in MCS data

The most prominent boundary in upper crust is the layer 2A/2B boundary identified as a triplication in the seismic records. Unlike a true reflection boundary, it is a high velocity gradient transition and hence can be only seen at wide angle (large offsets) in multi-channel seismic (MCS) records. In order to understand how a layer 2A triplication would manifest itself in MCS shot records, I first performed finite difference waveform modelling (*Shipp and Singh*, 2002). I first present a brief theoretical description of finite difference modelling followed by the results of layer 2A triplication. I also use the finite difference modelling to validate my tomography results for both surface and downward continued data in chapter 3.

The elastodynamic wave equation is represented in terms of stress (σ), strain (ε) and elastic modulus (C) in tensor notation as:

$$\sigma_{ij} = C_{ijkl}\varepsilon_{kl}. \tag{2.2}$$

In an elastic isotropic approximation as used here, the equation can be simplified and re-written as follows:

$$C_{ijkl} = \mu(\delta_{ik}\delta_{jl} + \delta_{il}\delta_{jk}) + \lambda\delta_{ij}\delta_{kl}, \tag{2.3}$$

where the λ and μ are the Lamé's parameters and δ_{ij} is the Kronecker delta function given by:

$$\delta_{ij} = 1 \quad if \quad i = j, \tag{2.4}$$

$$= 0 \quad if \quad i \neq j. \tag{2.5}$$

Substituting the equation 2.3 in 2.2, we obtain:

$$\sigma_{ij} = \lambda\delta_{ij}\varepsilon_{kk} + 2\mu\varepsilon_{ij}. \tag{2.6}$$

To expand the terms σ and ε in above equation, we use Newton's second law:

$$\sum F = m\frac{d^2u}{dt^2}. \tag{2.7}$$

For a volume V and surface S, the above equation 2.7 can be written as:

$$\int_V \rho\frac{\partial^2 u_i}{\partial^2 t}dV = \int_S \sigma_{ij}n_j dS + \int_V f_i dV, \tag{2.8}$$

where ρ is density and n is the normal to the surface. Replacing the surface integral by a volume integral in above equation 2.8 using divergence theorem and removing the integral signs, we get:

$$\rho\frac{\partial^2 u_i}{\partial^2 t} = \frac{\partial\sigma_{ij}}{\partial j} + f_i. \tag{2.9}$$

Substituting equation 2.6 in 2.9, we get:

$$\rho\frac{d^2u_i}{d^2t} = \lambda\frac{\partial\partial u_k}{\partial_j\partial_k}\delta_{ij} + \mu(\frac{\partial\partial u_i}{\partial_i\partial_j} + \frac{\partial\partial u_j}{\partial_i\partial_j}) + f_i. \tag{2.10}$$

Using Cartesian gather, the above equation 2.10 can be re-written in 2-D as:

$$\rho\frac{\partial^2u_x}{\partial^2t} = \frac{\partial\sigma_{xx}}{\partial x} + \frac{\partial\sigma_{xz}}{\partial z}, \tag{2.11}$$

$$\rho\frac{\partial^2u_z}{\partial^2t} = \frac{\partial\sigma_{xz}}{\partial x} + \frac{\partial\sigma_{zz}}{\partial z}, \tag{2.12}$$

$$\sigma_{xx} = (\lambda+2\mu)\frac{\partial u_x}{\partial x} + \lambda\frac{\partial u_z}{\partial z}, \tag{2.13}$$

$$\sigma_{zz} = (\lambda+2\mu)\frac{\partial u_z}{\partial z} + \lambda\frac{\partial u_x}{\partial x}, \tag{2.14}$$

$$\sigma_{xz} = \mu(\frac{\partial u_x}{\partial z} + \frac{\partial u_z}{\partial x}). \tag{2.15}$$

However, solving the above equations have been shown to be unstable in the case of solid-liquid boundary. A more efficient way is the staggered grid velocity-stress $v-\sigma$ formulation (*Virieux*, 1986):

$$\rho\frac{\partial v_x}{\partial t} = \frac{\partial\sigma_{xx}}{\partial x} + \frac{\partial\sigma_{xz}}{\partial z}, \tag{2.16}$$

$$\rho\frac{\partial v_z}{\partial t} = \frac{\partial\sigma_{xz}}{\partial x} + \frac{\partial\sigma_{zz}}{\partial z}, \tag{2.17}$$

$$\frac{\partial\sigma_{xx}}{\partial t} = (\lambda+2\mu)\frac{\partial v_x}{\partial x} + \lambda\frac{\partial v_z}{\partial z}, \tag{2.18}$$

$$\frac{\partial\sigma_{zz}}{\partial t} = (\lambda+2\mu)\frac{\partial v_z}{\partial z} + \lambda\frac{\partial v_x}{\partial x}, \tag{2.19}$$

$$\frac{\partial\sigma_{xz}}{\partial t} = \mu(\frac{\partial v_x}{\partial z} + \frac{\partial v_z}{\partial x}). \tag{2.20}$$

The above set of equations 2.16 are used to perform forward wavefield modelling. The conditions for the stability and convergence of these equations are given by the Courant-Friedrichs-Lewy condition (*Levander*, 1988):

$$dt < \frac{dx}{\sqrt{2}V_{max}}, \tag{2.21}$$

$$f_{max} < \frac{V_{min}}{5dx}, \tag{2.22}$$

where dt is the timestep and dx is the grid length used in modelling. V_{max} and V_{min} are the maximum and minimum velocities used in the model. f_{max} refers to the maximum frequency that can be modelled.

Previous studies have shown a layered velocity consisting of low gradient 2A-high gradient 2A-low gradient 2B (*Harding et al.*, 1993). The rays turning from low gradient regions of 2A and 2B are called prograde arrivals of 2A and 2B respectively. The rays turning from high gradient 2A, which is the interest here, is called retrograde arrival. First, I used the 1-D model of a water column-low gradient 2A-high gradient 2A-low gradient layer 2B to obtain the triplication. Then I varied the water column thickness and the transition zone thickness to see the shift on the triplication. I used a 10 Hz dominant frequency Ricker wavelet and a velocity model with a grid spacing of 6.25 m to perform the forward modelling. Figure 2.2 shows different cases to investigate the effect of water column thickness and 2A/2B transition zone thickness on the triplication.

The left panel of figure 2.2a shows the standard model with the following parameters: 4375 m water column thickness with P-velocity 1500 m/s; a 250 m low gradient 2A with P-velocity linearly increasing from 2250 m/s at top of 2A to 2500 m/s at bottom, a 312.5 m thick transition zone with P-velocity

linearly increasing from 2500 m/s at top to 6000 m/s at bottom; a 1250 m thick 2B with P-velocity 6000 m/s at top to 6230 m/s at bottom. No sediment cover was taken into account to simplify the modeling. V_p/V_s ratio was taken to be 1.73 following *Collier and Singh* (1998). The middle panel shows the seismic record obtained. The seafloor reflection starts at 5.9 s TWT and a weak layer 2B first arrival is seen beyond 6 km offset. To visualize the distribution of energy within the triplication, a zoom-in of the middle panel is plotted in the right panel. The triplication starts at 3 km offset and 6.6 s TWT with amplitudes increasing as we move to farther offsets. The peak amplitude occurs at 3.6 km offset and ∼6.7 s TWT. This almost co-incides with the onset of energy from 2B, though not clearly visible in the zoom-in wiggle plot. I now change the water column thickness to see the changes in the triplication.

Figure 2.2b shows the test performed with a increased water column thickness, keeping other parameters unchanged as in 2.2a. The increase in the water column by 312 m shifts the seafloor reflection at zero-offset to 6.3 s TWTT as seen from the middle panel. The zoom-in in the right panel shows the triplication starting at 3 km offset and at ∼7 s TWT with the peak occuring around 3.8 km offset and 7.15 s TWT. Comparing the position of peak energy in triplication with previous case, a vertical shift in time rather than a lateral shift in offset is more apparent due to thickening of water column. Addition of a low velocity column such as sediments will have the same effects of vertical time shift on the position of triplication. Now I will present the effect of transition zone thickness on the position of the triplication.

Figure 2.2c shows a 75 m thick transition zone keeping other parameters unchanged as in 2.2b. The triplication is found to be more distributed along the hyperbolic path as the narrow transition range represents more of a reflection. The peak amplitudes in the triplication are more spread out as well, covering 3.2-3.5 km offset and 6.9-7 s TWT. In comparison, figure 2.2d shows a 562.5 m thick transition zone keeping other parameters uncanged as in 2.2b. The triplication is found starting from 7.2 s TWT and 4 km offset similar to 2.2b. The peak of the triplication in this case is observed at 4.5 km offset and 7.3 s TWT in comparison to 3.8 km offset and 7.15 s TWT found for a thinner transition zone (250 m in 2.2b). This indicates that having an increased transition zone thickness will shift the triplication more in offset laterally than vertically in time.

(a)

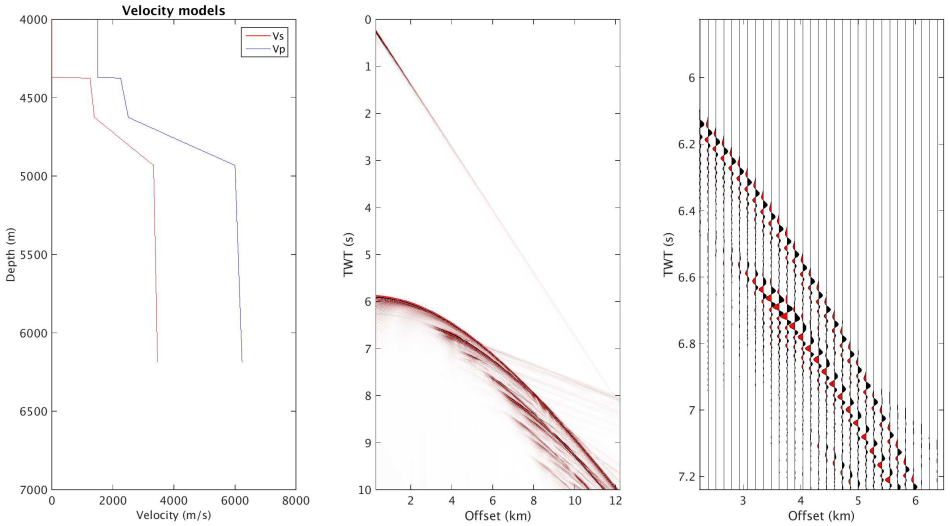
Velocity models
Vs
Vp
Depth (m)
Velocity (m/s)
TWT (s)
Offset (km)
TWT (s)
Offset (km)

(b)

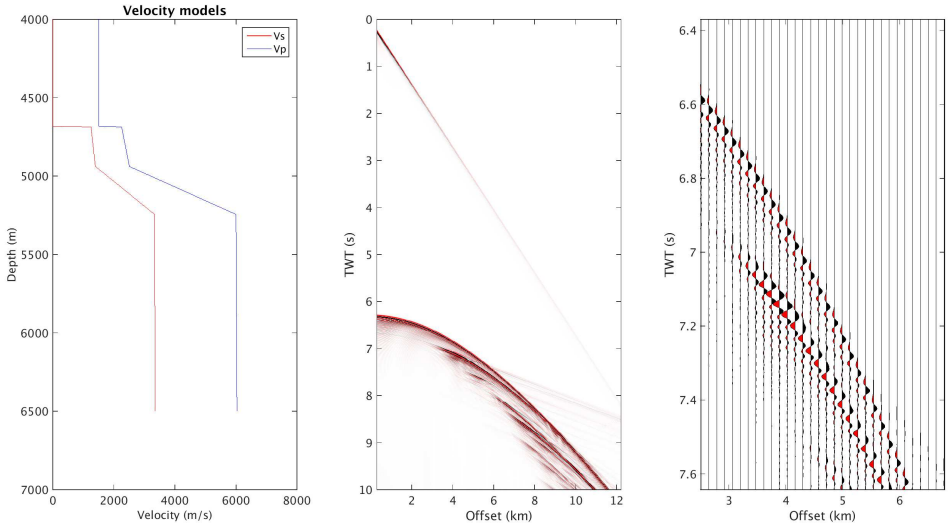
Velocity models
Vs
Vp
Depth (m)
Velocity (m/s)
TWT (s)
Offset (km)
TWT (s)
Offset (km)

(c)

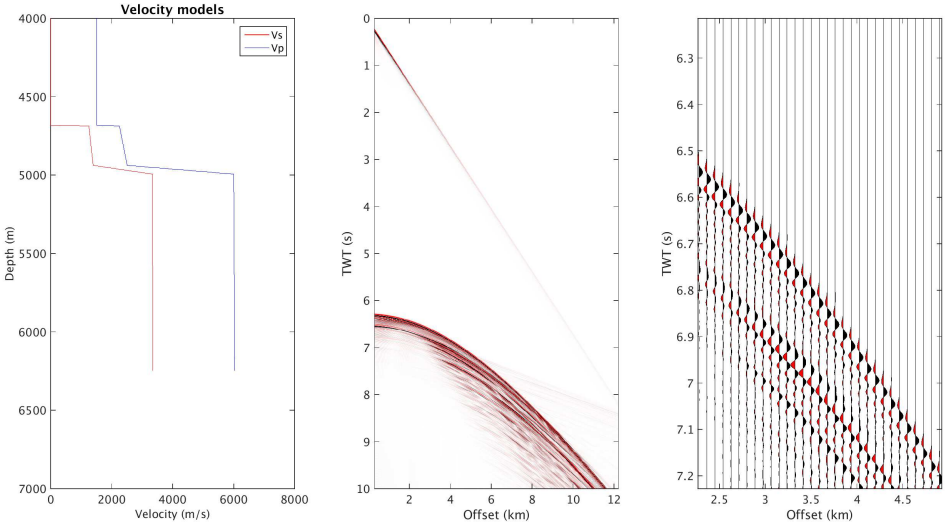
Velocity models
Vs
Vp
Depth (m)
Velocity (m/s)
TWT (s)
Offset (km)
TWT (s)
Offset (km)

(d)

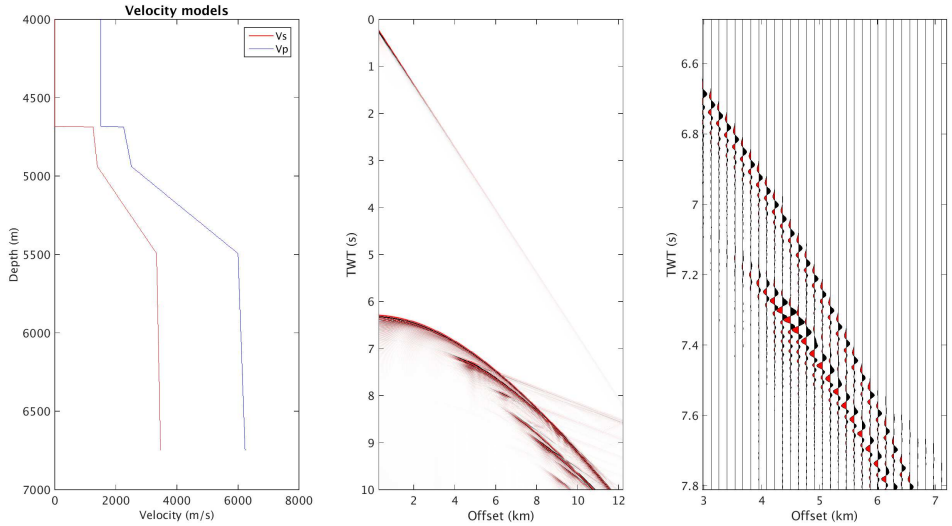

Figure 2.2: Finite difference modelling for investigating the triplication due to the high velocity gradient between 2A and 2B (*Shipp and Singh*, 2002). Each sub-figure shows the P- and S- 1-D models in the left panel, the seismic record in the middle panel and the zoom in of the record around the triplication in the right panel. (a) The standard case in which low gradient part of layer 2A has a thickness of 312.5 m and water column is 4375 m thick. (b) The water column thickness is increased by 312 m keeping other parameters unchanged as in (a). (c) The thickness of the transition zone is decreased to 75 m keeping other parameters unchanged as in (b). (d) The thickness of the transition zone is increased to 562.5 m keeping other parameters unchanged as in (b).

In summary, it is found that a thicker water column shifts the triplication more in time vertically and a thicker transition zone shifts the triplication more in offset laterally. Since the same source has been used in all cases above, length of the wavelet denoting the peak of the triplication can also be used as an additional constraint on differentiating the effects of a low velocity column and the transition zone. It is likely that rays turning through a thicker transition zone will be more attenuated in high frequency as compared to rays travelling through a thicker water column. This advance analysis has, however, not been carried out in this study as the purpose of the forward modeling has been primarily to identify the manifestation of layer 2A triplication in MCS shot records. In all the cases, the peak of energy has been to occur not at the cusp of triplication as claimed by other studies (*Harding et al.*, 1993) but shortly after it. In real data, identifying this event is far more challenging mainly due to scattering from the rough basement as found in a slow spreading regime like the equatorial African plate. Events simliar to triplication (bow-tie shape) can be replicated in features such as synclines (valleys). It is difficult to distinguish whether the energy is due to basement morphology or actually due to high velocity gradient at base of 2A.

2.2.2 Seismic data processing for layer 2A

The data was sorted in common-mid point (CMP) domain to image the layer 2A. After identifying the layer 2A event in previous section in real CMP gathers, the analysis for layer 2A was performed twice along the whole profile. In the first, a composite stacking technique was employed in which the near and far offset stacks were formed separately. The near offset stack contained the seafloor and the basement images while the far offset stack contained the layer 2A triplication. Normal Move-out correction (NMO) was performed by using different stacking velocities of basement and layer 2A event. However, different stacking velocities for basement and layer 2A event caused a NMO stretch at wide angle thus affecting the far offset stack containing the layer 2A triplication. In the new processing scheme, a single stacking velocity for layer 2A event was used for NMO correction instead of separate velocities for basement and layer 2A event. The choice of the best imaging velocity was made visually as shown in figure 2.3. After correcting the CMP-offset gathers with the best stacking velocity, a single stack was created after isolating

the layer 2A event as shown in figure 2.4.

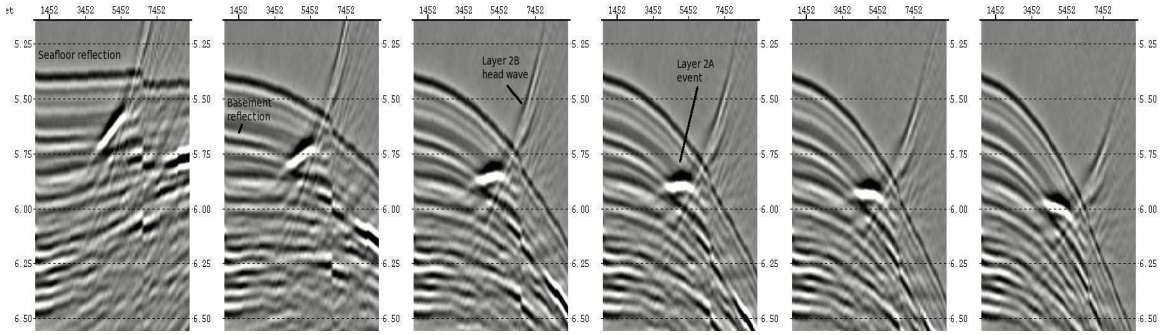

Figure 2.3: Choice of best stacking (imaging) velocity for layer 2A event on a NMO-corrected common mid-point (CMP) gather. Stacking velocities used for NMO correction from left: 1500 m/s, 1600 m/s, 1700 m/s, 1800 m/s, 1900 m/s and 2000 m/s. The desirable image should have a flattened layer 2A event and so the best imaging velocity of 1800 m/s is used (3rd from right). The horizontal axis in all panels is the offset in metres and the vertical axis is the two-way time.

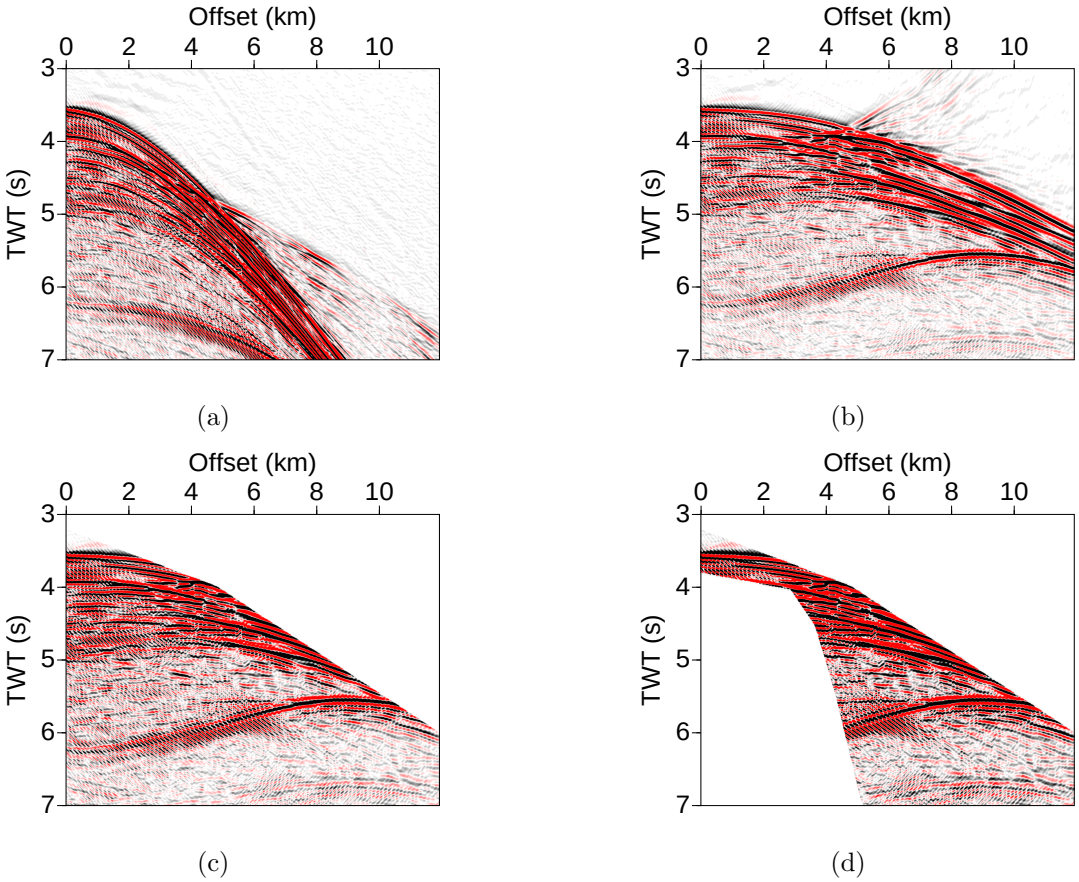

Figure 2.4: Processing steps for layer 2A event: (a) A super-CMP gather. (b) NMO corrected super-CMP gather with the best flattening velocity for the layer 2A event. The NMO velocities have been determined from a suite of super-CMP gathers corrected with different NMO velocites and constant velocity stacks up to the offset range where the triplication is observed. Note a single velocity has been used for NMO correction instead of separate velocities for seafloor and layer 2A event in order to avoid NMO stretching which would most affect the shallow wide angle energy. (c) The first arrivals which are under corrected have been muted out in this step. (d) A top mute removing the moveout of the seafloor just above the layer 2A event and an inner trace mute to remove energy arriving prior to the layer 2A/2B event have also been applied. The data is then stacked. Note that due to the processing being focused exclusively on layer 2A, the events beneath layer 2A are not reliable for interpretation. The post-stack processing includes band pass filter 0-1-35-40 Hz, constant water velocity time migration to provide a uniform image and seafloor mute.

Some automatic techniques for finding the best stacking velocity are commonly used (such as semblance) but are applicable only for true reflections. Since layer 2A event is not a true reflection and occurs only at larger offsets, such automatic techniques could not be used for layer 2A and hence a visual analysis had to be performed for choosing the best stacking velocity that would flatten the layer 2A event (figure 2.3). However, different stacking velocities for a visually flattened triplication yield different times on the stacked section for the layer 2A event. Hence I also carried out an uncertainty estimation of the stacking velocities on the two-way time of the layer 2A event. Figure 2.5 shows the estimated uncertainties in two-way time of the layer 2A event when stacking velocities are ranged from 1700-1900 m/s in figure 2.3. Note that the layer 2A event seems reasonably flattened in figure 2.3 for the different stacking velocities from 1700-1900 m/s. Figure 2.5 shows the difference of ±100 m/s in the stacking velocities correspond to a two-way time difference of ±70 ms of the layer 2A event. A velocity of 4.5 km/s for the base of layer 2A yields a depth uncertainty of ±315 m for an uncertainty of 70 ms TWTT. In case of smooth bathymetry variation as in the easternmost part of the profile, a reduced variation in stacking velocities yields an uncertainty of ±30 ms which would correspond to an depth uncertainty of ±165 m for velocities of ∼5 km/s.

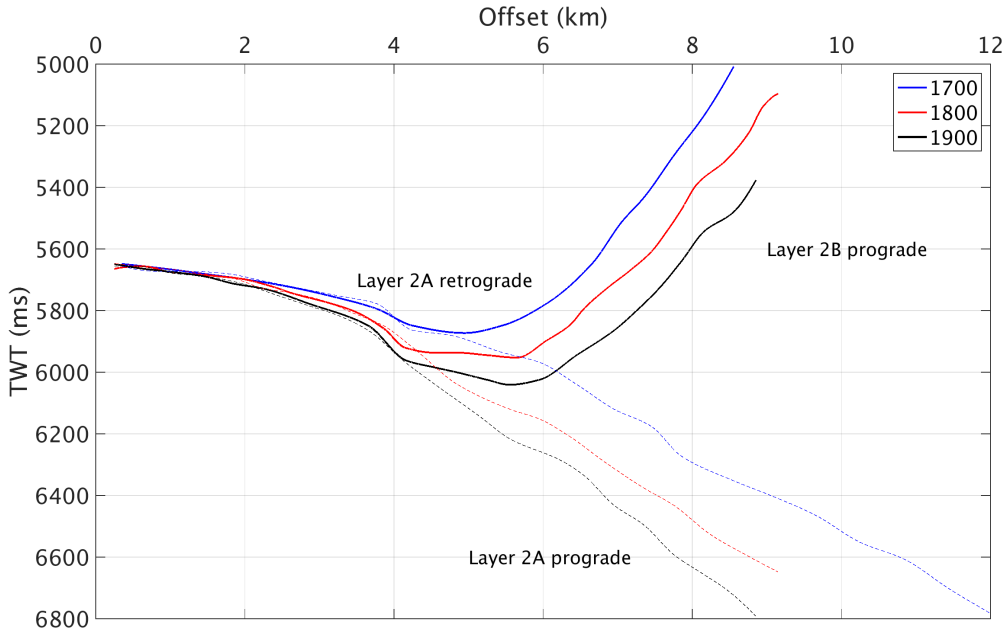

Figure 2.5: Uncertainty estimation: A rough bathymetry yields more variable stacking velocities which cause an uncertainty of ±70 ms TWTT for the layer 2A event. In regions where a relatively smoother basement is observed like that at 75 Ma, an uncertainty of ±30 ms TWTT is found for the layer 2A event. The Layer 2A prograde arrivals refer to rays turning from low gradient part of layer 2A whereas the Layer 2A retrograde arrivals refer to rays turning from high gradient part of layer 2A. Similarly, layer 2B prograde arrivals refer to rays turning from (low gradient part of) layer 2B.

2.3 High-resolution tomography for upper crust

The previous section deals with imaging the layer 2A event in multi-channel seismic (MCS) data. The MCS data also contain first arrivals, which are rays turning in the upper oceanic crust. For extracting the sub-surface P-velocity information from these first arrivals, the technique of tomographic inversion is used. Recent studies such as *Arnulf et al.* (2011) have developed a two-step strategy of high-resolution tomography in which the conventional downward wavefield extrapolation is done prior to tomography. In the following pages, I discuss the methodological aspects of the downward wavefield extrapolation and tomography but before it, I illustrate the geometry of the MCS data.

2.3.1 Data regularization for wavefield extrapolation

Prior to performing wavefield extrapolation, it is necessary to ensure that an uniform geometry of the sources and receivers is present. The data regularization was performed to address two main things: offset regularization and interpolating missing shots.

An analysis of the original geometry was performed to determine the non-uniformity in the geometry. Due to source and receiver lines not being in-line and having some lateral offset as shown in figure 2.6a, the offset increment for the first ∼100 receivers is <12.5 m as shown in figure 2.6b.

(a)

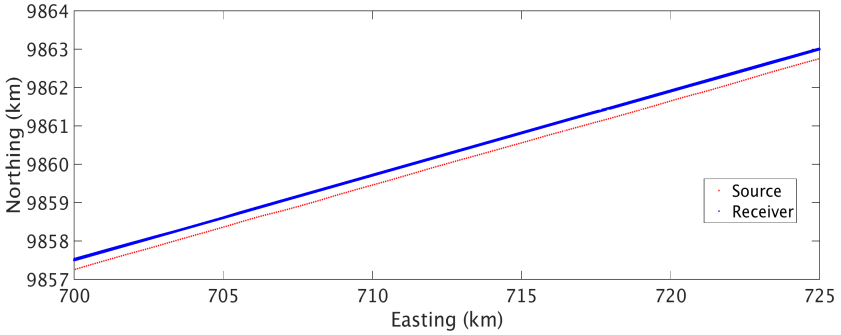

(b)

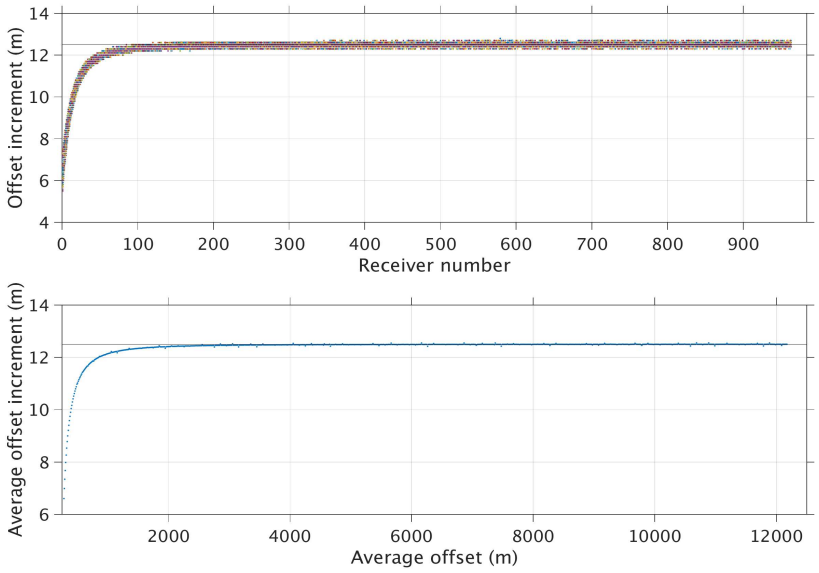

(c)

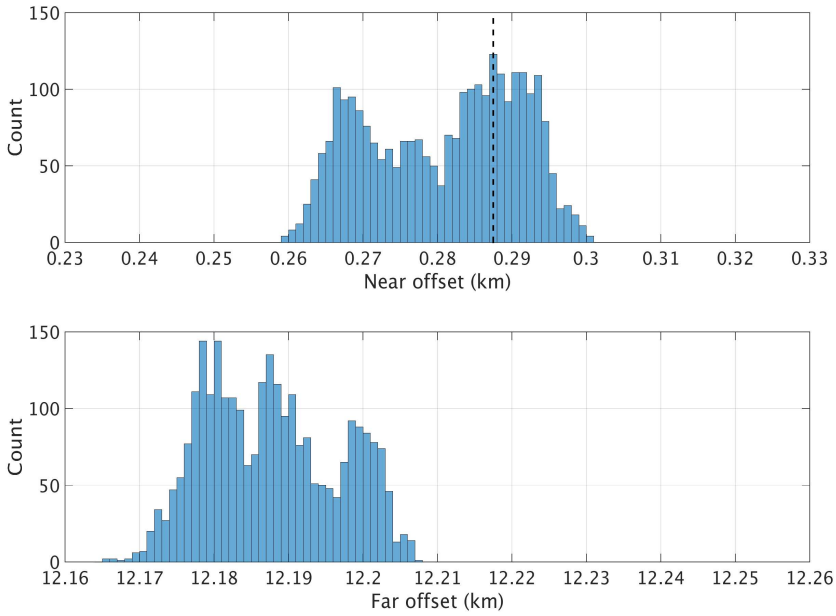

Figure 2.6: Analysis of headers of raw data: (a) The streamer geometry shows the non-uniform offset increment caused by sources and receivers not being in the same straight line as shown in (b). (c) A near offset value was fixed at 0.2875 km in the new offset pattern (vertical black dashed line) and 10-16 receivers were dropped. In case the ship was turning, more receivers were dropped to maintain linearity of the source-receiver geometry.

A new offset pattern was formed in which the sources and receivers were in-line and the offset increment was fixed at a constant 12.5 m. The near offset headers were analyzed and a value of 287.5 m was fixed

as shown in figure 2.6c. The original receivers closest to the new offset pattern were chosen to create the new geometry. This resulted in dropping about 10-16 receivers at near offset and the total number of receivers dropped from 964 to 948-954 with the streamer length remaining the same at 12.2 km. In regions where the ship was turning, for instance at 46.7 Ma, the number of receivers in the new offset pattern were further reduced to 904 to keep the linearity of the source-receiver geometry. Figure 2.7 shows the data before and after the geometry regularization. A near-offset zoom in of one of shots is shown to highlight the difference between the trace spacing (offset increment) between the new and the old geometry pattern.

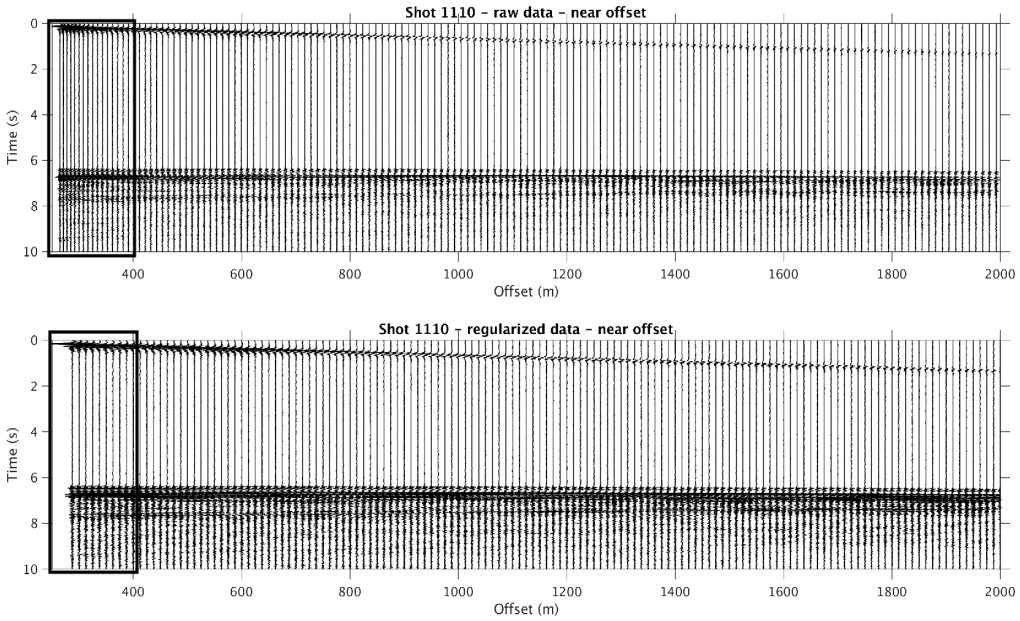

Figure 2.7: Offset regularized data before (top) and after (below): The difference is most prominent in the first 400 m of the offset as highlighted (black rectangle) where 10-16 traces were dropped to obtain regularized data. A uniform offset increment can be observed after geometry regularization (below).

For performing tomography, it was necessary to choose a part of the data with the least missing shots. There were ∼50 shots missing in the profile. On the other hand, regions with anomalous topography were to be avoided if the definition of normal oceanic crust was to be kept. Therefore, missing shots were interpolated in the common-offset domain so as to avoid having data gaps in the velocity models obtained from tomography (*Hanchao Jian, personal communication*).

In order to avoid energy loss at zero-offset, a near-offset extrapolation strategy was used in which the first 1 km of the shot gather was extrapolated to negative offsets by simply mirroring. This modified shot gather was then tapered as usual in both offset at near and far offsets and time at just before the first arrival and end of record length. The procedure is described in figure 2.8. The tapering is essential so as to avoid artifacts in the downward continuation procedure. The near-offset extrpolation strategy helps to preserve energy at zero offset which is useful for both first arrivals and seafloor reflections. This was performed for both pass 1 and pass 2 of downward continuation described in the next section.

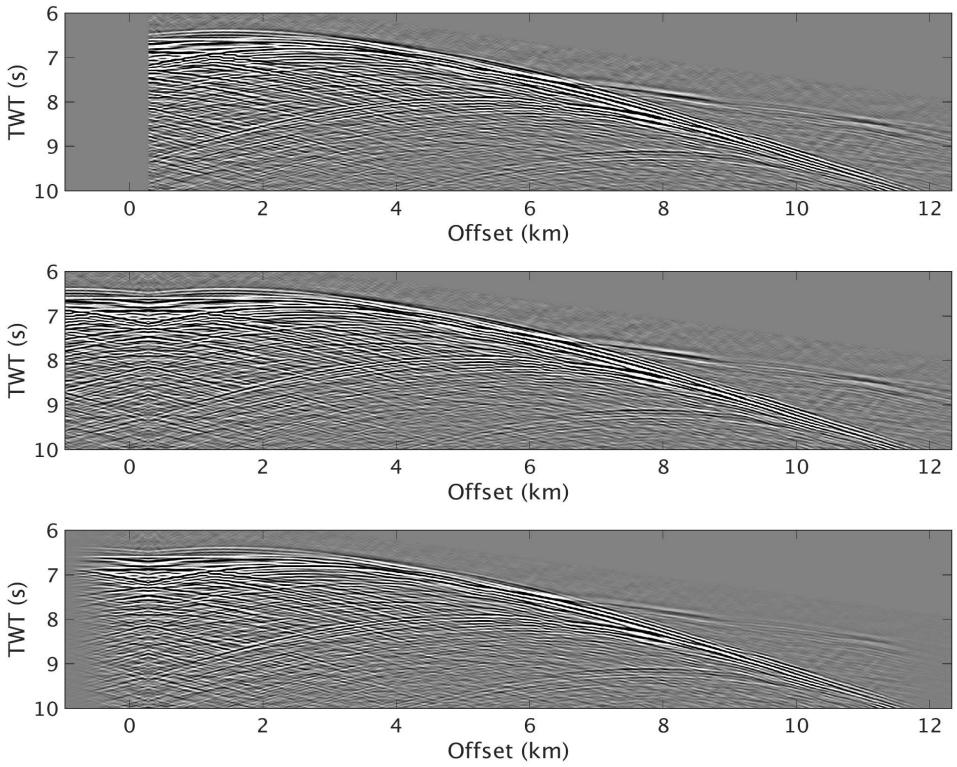

Figure 2.8: Modification of a shot gather shown prior to wavefield extrapolation: The top panel represents the original shot gather; appending energy at the beginning of the shot gather by taking a mirror image of the shot gather at 0.2875 km as shown in middle panel; the bottom panel shows the offset and time tapered shot gather from previous step to input to downward continuation. A similar strategy was used for receiver gathers in pass 2 of downward continuation.

2.3.2 Downward continuation (or downward wavefield extrapolation)

Seismic migration can be considered as a succession of wavefield extrapolation in steps of dz to the required depth of the subsurface reflection. Several techniques for performing seismic migration have been documented. These include, finite difference implementation, kirchhoff integration scheme, etc (summarized in *Berkhout* (1981)). However, the underlying principle of seismic migration is wavefield extrapolation which simply means to extrapolate the wavefields to a new datum from a given datum. Wavefield extrapolation is an important step for enhancing the first arrivals which turn in the upper oceanic crust. It was first proposed for post-stack data by *Berryhill* (1979) and for pre-stack data by *Berryhill* (1984) (figure 2.9) and has been implemented in many recent studies involving analysis of the upper oceanic crust (*Arnulf et al.*, 2011). Here a Kirchhoff integration scheme has been used to implement wavefield extrapolation of pre-stack seismic data using a constant water velocity of 1.496 km/s. The pre-stack seismic data is usually downward continued in two distinct passes: first in which receivers (shot gathers) are extrapolated down (called pass 1) and second in which shots (receiver gathers) are extrapolated down (called pass 2).

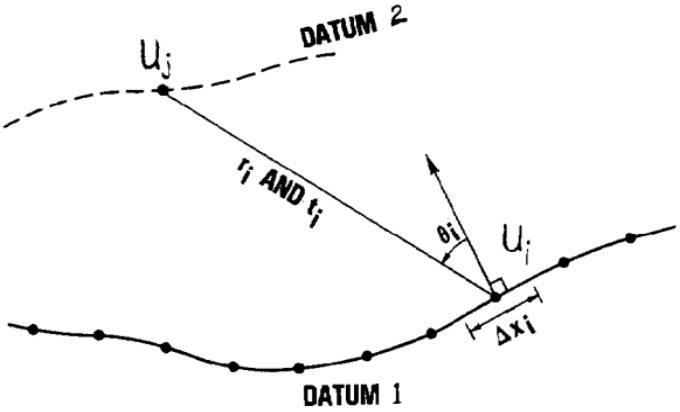

Figure 2.9: Wavefield extrapolation as proposed by *Berryhill* (1984). A virtual wavefield at a datum 2 is constructed using the wavefields at datum 1. The parameters described here are used in equation 2.23.

$$U_j(t) = \frac{1}{\pi} \sum_i \Delta x_i \cos\theta_i \frac{t_i}{r_i} [U_i(t - t_i) * F_i]. \tag{2.23}$$

where $U_j(t)$ is the wavefield at the j^{th} location on the new datum; $U_i(t)$ is the wavefield of the i^{th} receiver on the original datum; F_i is a weighting function that depends on the location of the i^{th} receiver on the original datum; r_i,t_i,θ_i are the distance, travel-time and angle respectively along the raypath joining the i^{th} receiver on the original datum with the j^{th} receiver on the new datum; Δx_i is the receiver spacing on the original datum. Note that $U_i(t-t_i)$ is the time shifted version of the i^{th} receiver wavefield on the original datum. This is implemented practically by convolving the original wavefield $U_i(t)$ with a time delay function while correcting for geometrical spreading and 3D to 2D conversion.

The datum for wavefield extrapolation is usually a smoothed version of the seafloor and above it. A smoothed version is necessary for better shot to shot continuity in the first arrivals and to taper the effect of sudden topographic changes. The depth of the new datum should be as close to the seafloor as possible whilst avoiding surface waves. A datum very close to the seafloor may generate surface waves. Another factor to choose the smoothing extent and the depth of the datum was to ensure that the raypaths between the original and the new datum travel in the water and not through solid rock. A visual check of the raypaths between the original and the new datum was also performed in order to ensure it. An erraneous datum in which raypaths pass through solid rock will give artifacts which would eventually map into the tomography models. This is especially useful in regions such as fracture zones, where high bathymetric gradients are observed. Figure 2.10a shows the raypaths for three distinct shot gathers between the original and downward continued datum for pass 1 in which the receivers are being extrapolated down. Figure 2.10b shows the raypaths for three distinct receiver gathers between the original and downward continued datum for pass 2 in which the shots are being extrapolated down. Figure 2.11 shows the downward extrapolation at the ridge axis, where extra care had to be taken owing to the bathymetry variations. The raypaths for all receivers (shot gathers) between the original and the new datum are plotted in figure 2.11a whereas raypaths for all shots (receiver gathers) between the original and the new datum are plotted in figure 2.11b.

(a)

(b)

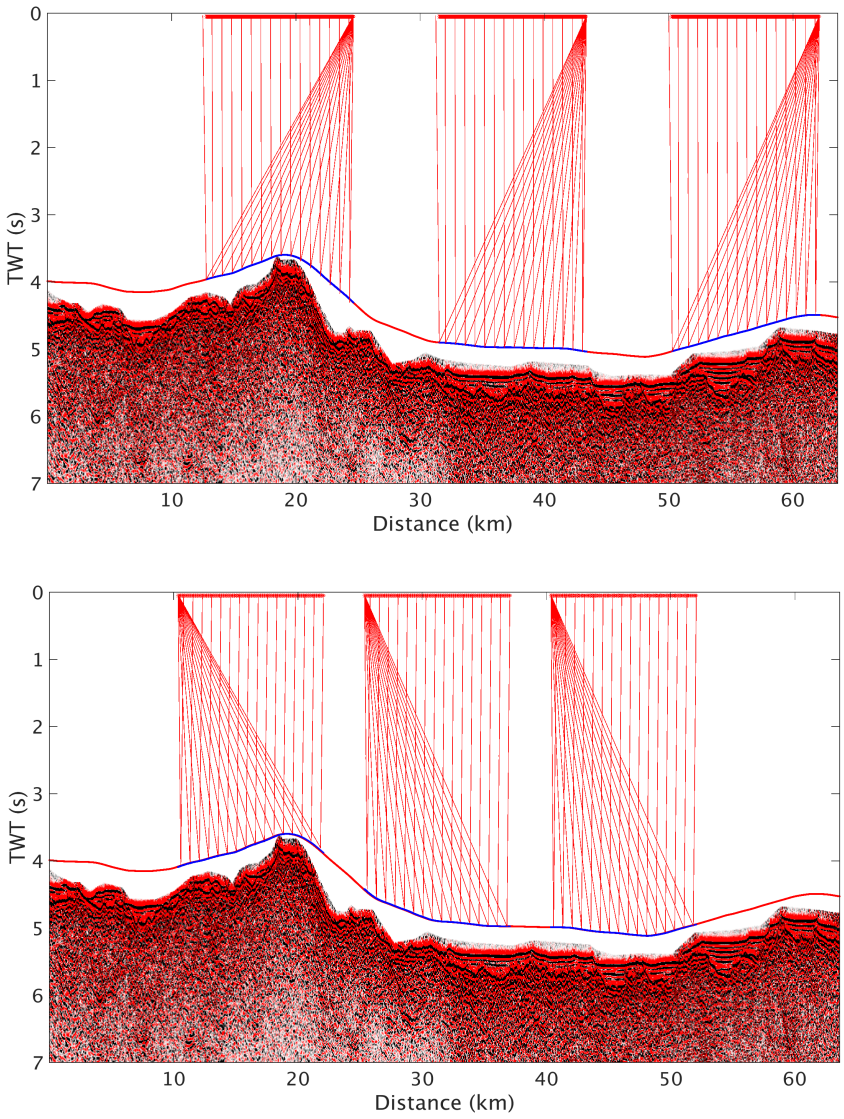

Figure 2.10: (a) A visual check for the raypaths in pass 1 of downward continuation shown at three distinct locations, each corresponding to length of a streamer (12 km). The receiver wavefields are being downward continued from the surface to a datum near the seafloor. Note that the streamer is moving from right to left (decreasing distance on the image) and hence the contributing wavefields are maximum for the virtual receiver (on the new datum) at the near-offset end of the streamer (left end). The contributing receiver wavefields, governed by Fresnel zone width, decrease for virtual receivers at higher offsets along the streamer length and are minimum for virtual receiver at the farthest end of the streamer (right here)(b) The same check for raypaths in pass 2 of downward continuation at three distinct locations. The source wavefields are being downward continued from the surface to the same datum here. Note the reversal of contributing wavefields for the virtual receivers at near offset end and far offset end of streamer.

(a)

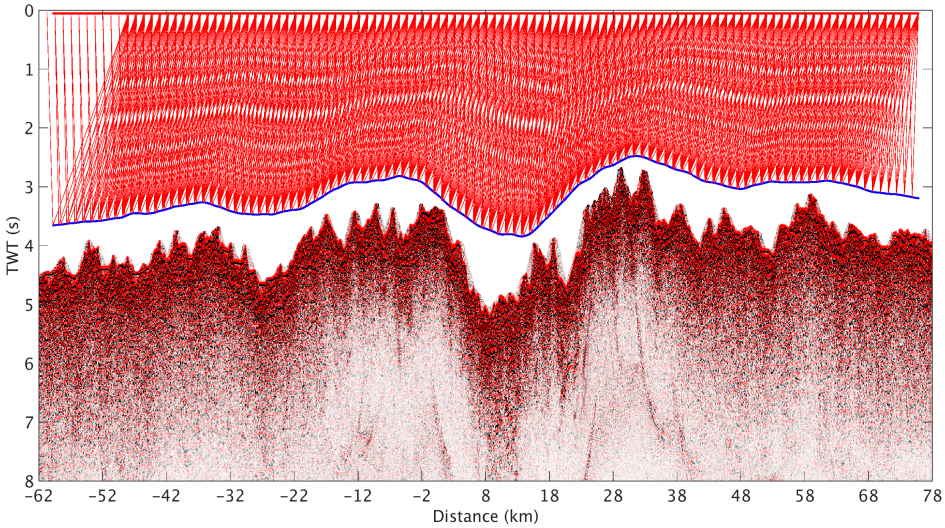

(b)

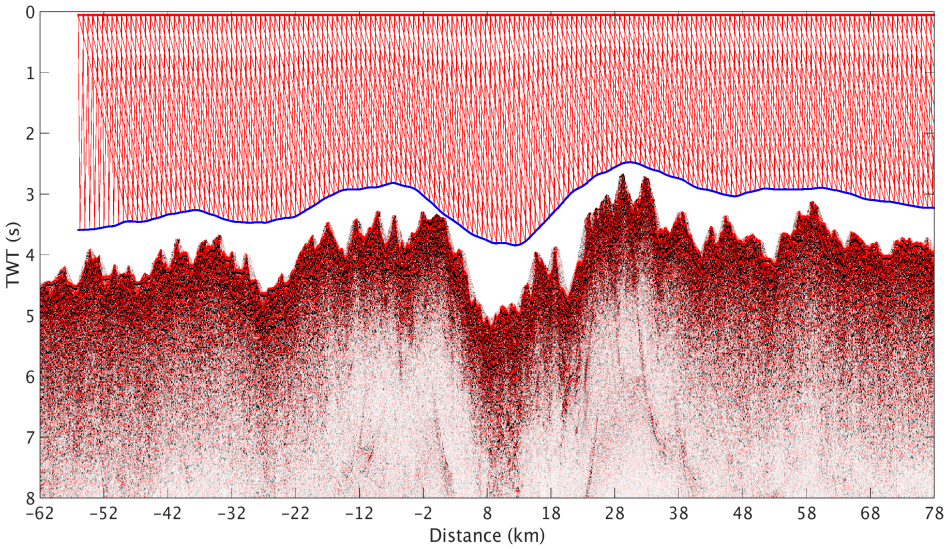

Figure 2.11: (a) Raypaths in sea-water during pass 1 of downward continuation of the seismic data near the ridge axis plotted for every 100th receiver (of 954) of every 100th shot. The receiver wavefields (at a spacing of 12.5 m) are being downward continued here. The median valley of the ridge axis is at ∼9 km. (b) Raypaths in sea-water during pass 2 of downward continuation plotted for every 100th shot (of 954) of every 10th receiver. The shot wavefields (at a spacing of 62.5 m) are being downward continued here.

The first step is to shift the original wavefields in time corresponding to the time delay between the original wavefield and the new wavefiled along the raypaths. The original wavefields lying within a fresnel zone for a particular virtual wavefield are then assigned a weight which takes the shape of the hamming window and is then stacked. The hamming window weighting function ensures smooth tapering of the wavefields away from the stationary point while the maximum contribution comes from the stationary point which is the closest original wavefield to the virtual wavefield.

The 2-pass strategy employed in downward continuing is further elaborated. In the first pass, the traces in groups of shot gathers are extrapolated down to the depth of the receivers and in the second, the same traces are sorted in receiver gathers and extapolated to the depth of the shots. The extrapolated gather after the second pass is re-sorted back to shot-offset domain. The first arrival is much better enhanced as it covers more region in the upper oceanic crust as compared to the original wavefields as shown in figure 2.12. The prestack ensemble has to be frequency filtered to account for non-alising. The aliasing frequency represents the maximum frequency over which aliasing will occur. It is represented by the ratio of dip range of kirchhoff operator and trace spacing in the ensemble. The dip range of

the kirchhoff operator is usually the range of slowness considered during wavefield extrapolation. This parameter is elaborated in more detail in chapter 5. In the first pass in which the shot gathers are usually extrapolated, the trace spacing is the receiver spacing =12.5 m, the aliasing frequency is high enough (=133 Hz) to downward continue without low-pass filtering. In the second pass, in which the receiver gathers (shots) are usually extrapolated, the trace spacing is the shot spacing (ranging from 50-75 m) which gives an aliasing frequency filtering is to be performed. In this case, the shot spacing of 50-75 m limited the aliasing frequency to ∼20 Hz.

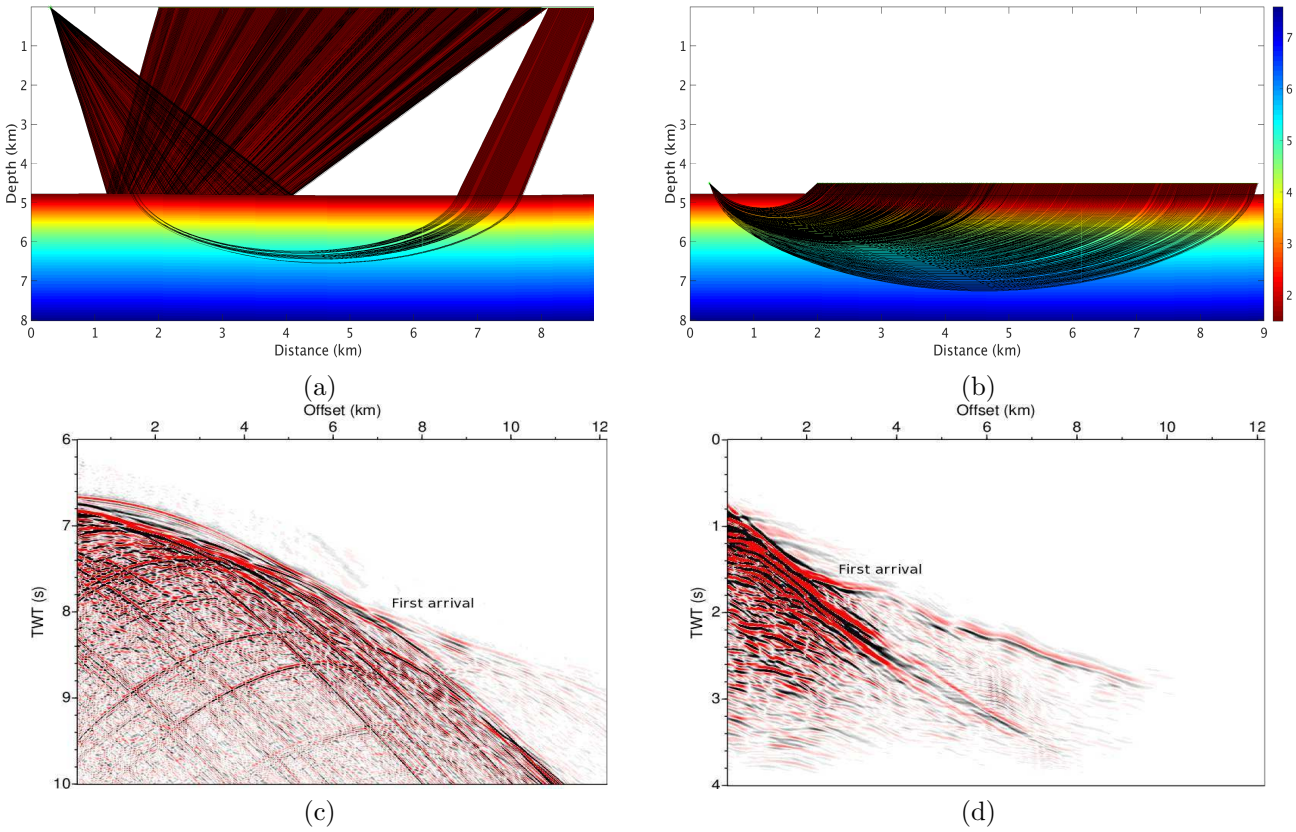

Figure 2.12: Ray coverage of first arrivals (turning rays) before (a) and after (b) downward continuation. The corresponding shot gathers before (c) and after (d) downward continuation. Note that the first arrival covers a larger range of offset after downward continuation in (d) as compared to before downward continuation in (c). This figure summarizes the advantages of downward continuation.

2.3.3 Travel-time tomography

Following downward continuation, I performed travel-time tomography using the iterative method of *Van Avendonk et al.* (2004) to obtain upper crustal P-velocities at distinct ages using the enhanced first arrivals of the shot gathers (figure 2.12d). In this chapter, I give a brief description of the theoretical concept of tomography (forward and inverse) and leave the applications to chapter 3.

1. High-frequency approximation of the wave equation

   The elasto-dynamic wave equation can be solved by methods that fall under three main categories: numerical techniques such as finite difference, integral techniques such as Kirchhoff summation and high-frequency approximations. Here I have used the high-frequency approximation of the wave gather. By approximating the wave to be of infinitely high frequency (i.e. a ray), we assume the medium through which the wave is travelling to be locally homogenous as compared to the wavelength of the wave. This also implies that only the region that the ray traverses would be affected as opposed to the finite-frequency approaches in which a volume surrounding the wavepath is affected. The basic theory behind the high frequency approximation is described here:

The acoustic wave equation in frequency domain (i.e. Helmholtz equation) can be described in terms of pressure P, frequency of the pressure wave ω, velocity of the pressure wave c, Laplacian operator Δ and space vector $\mathbf{x}$ as:

$$\Delta P(\mathbf{x},\omega) = \frac{-\omega^2}{c^2(\mathbf{x})} P(\mathbf{x},\omega). \tag{2.24}$$

A solution is given by:

$$P(\mathbf{x},\omega) = A(\mathbf{x},\omega) S(\omega) e^{-i\omega T(\mathbf{x})}. \tag{2.25}$$

The amplitude term $A(\mathbf{x},\omega)$ can be further expanded in the form of a Taylor Expansion in $1/(i\omega)$

$$A(\mathbf{x},\omega) = \sum_{n=0}^{+\infty} \frac{A_n(\mathbf{x})}{(i\omega)^n}. \tag{2.26}$$

Putting the last two equations in the acoustic wave equation above, we get

$$\frac{-\omega^2}{c^2(\mathbf{x})} \sum_{n=0}^{+\infty} \frac{A_n(\mathbf{x})}{(i\omega)^n} = -\omega^2 (\nabla T(\mathbf{x}))^2 \sum_{n=0}^{+\infty} \frac{A_n(\mathbf{x})}{(i\omega)^n} + i\omega \sum_{n=0}^{+\infty} \frac{2\nabla T(\mathbf{x}) \cdot \nabla A_n(\mathbf{x}) + \Delta T(\mathbf{x}) A_n(\mathbf{x})}{(i\omega)^n} + \sum_{n=0}^{+\infty} \frac{\Delta A_n(\mathbf{x})}{(i\omega)^n}. \tag{2.27}$$

Comparing the $i\omega$ terms as per their powers, we get

$$(i\omega)^2 \qquad \frac{1}{c^2(\mathbf{x})} = (\nabla T(\mathbf{x}))^2, \tag{2.28}$$

$$(i\omega)^1 \qquad 0 = 2\nabla T(\mathbf{x}) \cdot \nabla A_0(\mathbf{x}) + \Delta T(\mathbf{x}) A_0(\mathbf{x}), \tag{2.29}$$

$$(i\omega)^0 \qquad 0 = 2\nabla T(\mathbf{x}) \cdot \nabla A_1(\mathbf{x}) + \Delta T(\mathbf{x}) A_1(\mathbf{x}) + \Delta A_0(\mathbf{x}), \tag{2.30}$$

.....

$$(i\omega)^{-n} \qquad 0 = 2\nabla T(\mathbf{x}) \cdot \nabla A_{n+1}(\mathbf{x}) + \Delta T(\mathbf{x}) A_{n+1}(\mathbf{x}) + \Delta A_n(\mathbf{x}). \tag{2.31}$$

The first equation in this series is the Eikonal equation and involves the travel time associated with the high-frequency approximation. The second equation related the amplitude to the travel time and is known as the Transport equation. Here, I only use the Eikonal equation to compute the travel times.

In implementation of the Eikonal equation, the two-point ray tracing problem is common. It consists of two points (a source and a receiver) which have to satisfy the ray trajectory while the slowness of the medium is unknown. This type of optimization problem is solved using a shooting approach,

a bending approach or a continuation approach. In a shooting approach, an initial ray is shot from the starting point with an a-priori slowness vector and then the slowness vector is updated until the ray crossing the ending point. In the bending approach, an initial trajectory crossing the two points is varied until it satisfies the ray equation. In the continuation approach, an initial ray is shot between the two points with a simple velocity model which is then updated according to the velocity model until the exact velocity model is introduced. The numerical solution of the eikonal equation was first introduced by *Reshef and Kosloff* (1986) and *Vidale* (1988). This was followed by a several new studies which improved the speed, robustenss and stability. Apart from the numerical solution, another category of algorithms were developed based on Fermat's principle, for instance the shortest path method (*Moser et al.*, 1992). The idea was simply to find the shortest traveltime between two points. The modern numerical eikonal solvers came into existence shortly after in 1992. The shortest travel time method combined with the ray bending method as used in *Van Avendonk et al.* (1998, 2004) has been used here.

2. Inversion of long-wavelength velocity models

After tracing rays through a initial slowness grid, the residual between the synthetic and picked travel times are optimized, thereby updating the velocity model. The optimization method is non-linear and is linearized by a local gauss-newton approximation and uses a LSQR solver (*Paige and Saunders*, 1982) which is suited for sparse least-squares problems.

Assuming that d is the data residual between synthetic travel time (t_{syn}) and the picked or observed travel time (t_{pk}), the following equations are obtained:

$$d = G\delta m, \tag{2.32}$$

where G is the Frechet matrix of first derivates of the travel time residual, d, with respect to model parameter perturbation, δm. The model parameter perturbation, δm, comprises of the background slowness perturbations, δu_0, the interface depth perturbation, δr_k and the perturbation in the slowness change across the interface, δu_k for the k^{th} interface. Here only the background slowness change, u_o, and the slowness change across the sediment/crust ($k = 2$) or water/crust boundary ($k = 1$) is inverted for. The inversion equation then becomes:

$$F(\delta m) = \left\| \begin{vmatrix} C_d^{\frac{-1}{2}}(G\delta m - d) \\ \lambda D(m + \delta m) \\ \gamma I \delta m \end{vmatrix} \right\|^2, \tag{2.33}$$

$$\tag{2.34}$$

where C_d is the data covariance matrix computed from the picking uncertainties, λ is one of the Tikhonov regularization parameter applied to the roughness matrix, D, of the first-order derivatives (not used here) or the second-order derivatives. The second order derivatives are only used here so as to obtain a smooth model as opposed to first order derivatives which would give a flat model. The smoothing of the second-order derivatives of the updated model, $m + \delta m$, is carried out as opposed to the initial model, m, to prevent the solution from being biased towards the initial model. γ is the other Tikhonov regularization parameter which is responsible for damping of the update δm.

The misfit, χ^2, is then evaluated as

$$\chi^2 = \frac{1}{N} \sum_{i=1}^{N} C_d^{-1}(t_{pk} - t_{syn})^2, \tag{2.35}$$

where N is the number of data (picked traveltimes). In practice, the above χ^2 is too expensive to compute. Hence the approximate least-squares estimate, $\delta\hat{m}$ is used instead of the true δm in equation as shown:

$$\chi^2 \approx \frac{1}{N} \left|\left| C_d^{\frac{-1}{2}} (G\delta\hat{m} - d) \right|\right|^2 . \tag{2.36}$$

Due to the non-uniqueness and ill-posed nature of the inverse problem, the inversion is performed iteratively in which the χ^2 is gradually reduced to 1. There exists a trade-off in choosing the desired misfit, χ^2, and the model roughness, γ for every iteration. The L-curve test was performed to choose an optimum misfit and roughness by choosing the point of maximum curvature of the L-curve (*Hansen and OLeary*, 1993).

2.4 Imaging the Lithosphere-Asthenosphere boundary (LAB)

Imaging the Lithosphere-Asthenosphere boundary (LAB) over a lithosphere formed at a slow spreading mid-oceanic ridge is challenging due to the rugged basement topography and subsequent seafloor scattering. Additionally, rapid attenuation of high frequency energy and low signal-to-noise ratio also make it challenging to image structures in deeper Earth using seismic reflection data. Many of the techniques discussed above to image the shallower upper crustal events fail for deeper Earth events. To circumvent the issues, the dataset was acquired using one of the largest airgun sources (10170 cubic inch or 167 litres) available in the industry. Extensive processing of the data aimed at noise removal and improving signal-to-noise ratio for deeper Earth was implemented which I discuss below.

2.4.1 On-board processing (Western Geco)

The on-board processing was carried out by Western Geco and aimed to remove noise, multiples and enhance the frequency bandwidth. These are illustrated one-by-one below.

1. Random noise attenuation: anomalous ampitude bursts of energy incoherent in different domains (shot-offset, receiver-offset etc.) were attenuated as shown in figure 2.13.

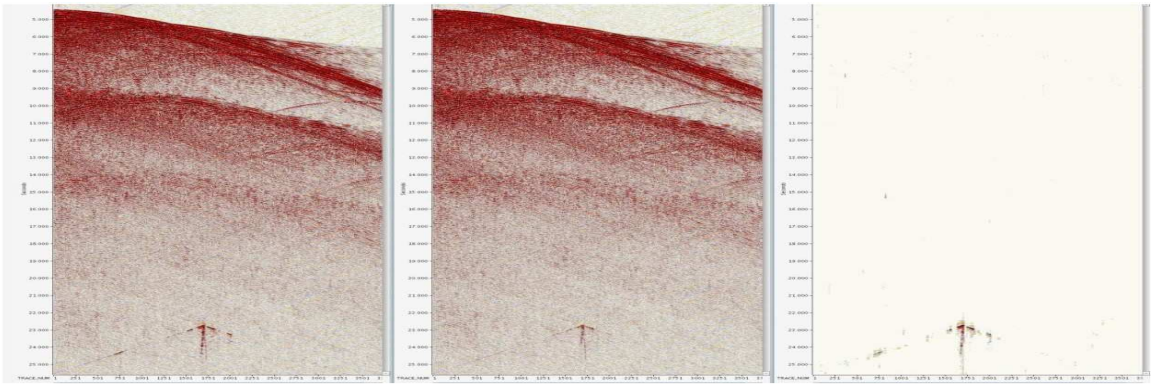

Figure 2.13: Left: Original shot gather (P-component) with an anomalous amplitude at ∼23 s. Middle: Same shot gather with attenuated amplitude of the noise. Right: Difference between original shot gather (left) and attenuated shot gather (middle). The anomalous amplitude has been removed. Source: *Western Geco processing reports*

2. Optimal de-ghosting by $P - V_z$ summation: A ghost reflection in the seismic is the reflection from the water surface recorded shortly after the primary reflection as shown in figure 2.14a. The pressure (P) and the vertical velocity (V_z) component record this ghost reflection with opposite polarities while the primary reflection is recorded with the same polarity as shown in figure 2.14a. The ghost reflection creates notches in the frequency spectra (*Vassallo et al.*, 2013) as shown in figure 2.14c. By summing the pressure (P) and vertical velocity (V_z) components, the ghost reflection is removed as shown in figure 2.14b. This technique is called de-ghosting. The vertical velocity, V_z, is obtained by integration of the vertical acceleration component, A_z, recorded in the geophone. This is simply added to the P-component to obtain the resulting $P - V_z$ component of the shot gather as shown in figure 2.15.

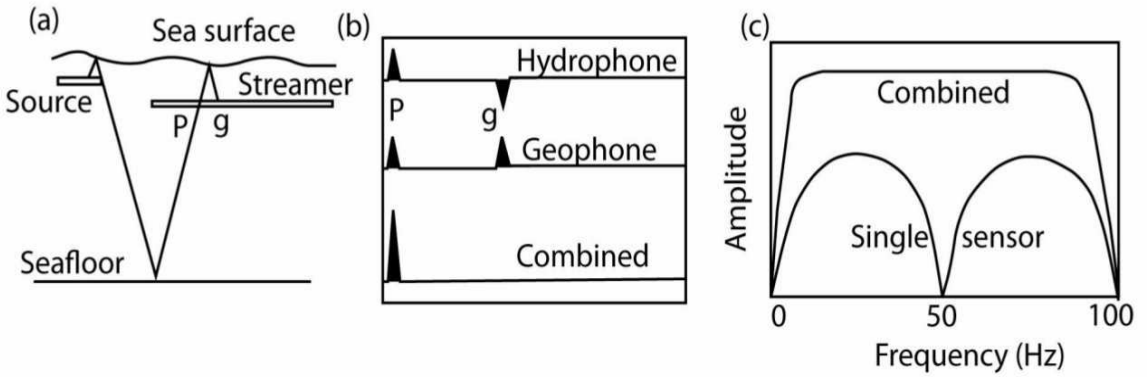

Figure 2.14: (a) The raypaths of primary (p) and ghost (g) reflection. The ghost reflection is reflected from the water surface from the source side and receiver side. (b) The recording of the primary (p) and ghost (g) reflection on the geophone (vertical velocity) and hydrophone (pressure). Note the primary and ghost reflections are recorded with opposite polarities in pressure and vertical velocity component, so their summation removes the ghost and enhances the primary reflection. (c) Original and enhanced frequency spectra by deghosting (*Vassallo et al.*, 2013). Credit: *Satish Singh*.

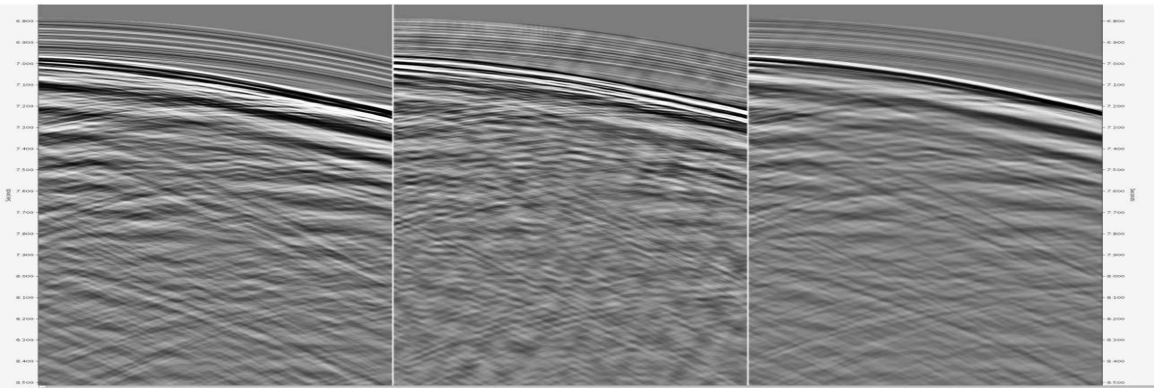

Figure 2.15: Left: P-component shot gather. Middle: V_z-component of the same shot gather. Right: Combined $P - V_z$ component. Note enhanced primary reflection and reduced reverberations in combined $P - V_z$ component just below the primary reflection. Source: *WesternGeco processing reports*

3. Calibrated marine source to eliminate shot-to-shot variations from source arrays. This was done by estimating far-field signature using the near-field hydrophones and comparing it with a reference signature. Debubble was then performed to remove the bubble energy followed by zero-phasing of the data. The effect of the processing steps can be seen in the near seafloor traces of the stack section as shown in figure 2.16.

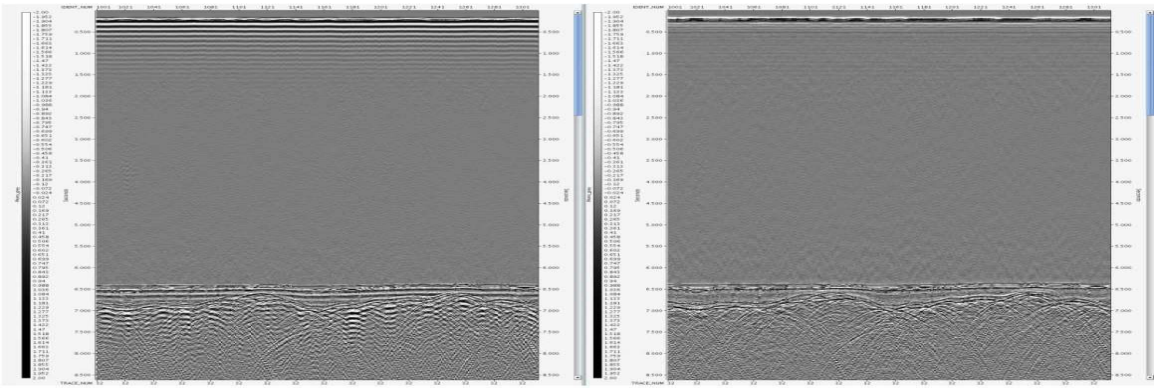

Figure 2.16: Left: Seafloor of stack section after deghosting. Right: After calibrated marine source, debubble and zero-phasing. Note that the seafloor is sharper after calibrated marine source, debubble and zero phasing. Source: *WesternGeco processing reports*

4. Array forming and resampling: Every 4 receivers of the original streamer spaced at 3.125 m were combined to create a single receiver wavefield with new receiver spacing at 12.5 m. Before combining, an anti-aliasing wavenumber filter was applied followed by a correction to flatten the approximately hyperbolic reflecton events. The data was also resampled in time dimension from 2 ms to 8 ms to reduce the data size. The effect of array forming is best viualized by observing the frequency-wavenumber (F-K) spectra of the resulting shot gathers as showin in figure 2.17.

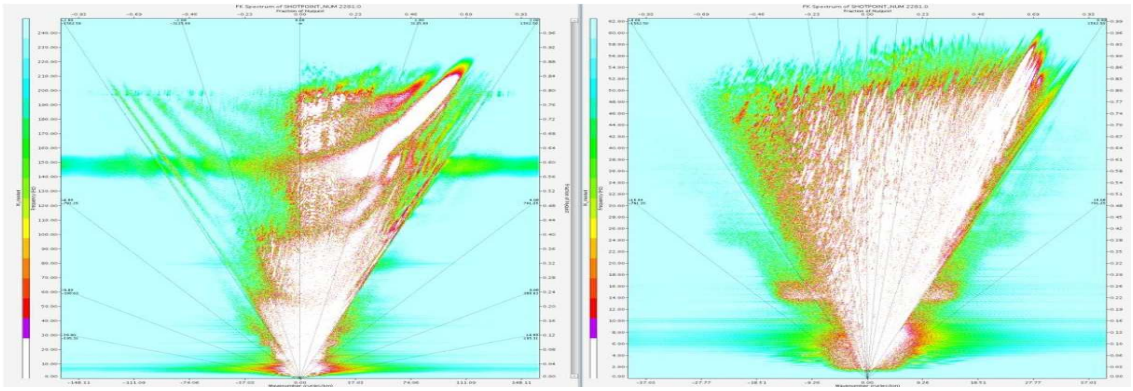

Figure 2.17: Left: Frequency-wavenumber (F-K) plot of a shot gather before array forming. Right: Frequency-wavenumber (F-K) plot of same shot gather after array forming. Note that the larger region in the F-K plots denotes better signal-to-noise ratio. The horizontal-axis represents wavenumber and vertical axis represents frequency. Source: *WesternGeco processing reports*

5. Multiple removal (demultiple): Multiples are reverberations in the water column of the reflected energy as shown in figure 2.18a. Multiples of shallow reflections such as seafloor and basement can hinder the deeper reflections. An example of multiples on a shot gather is shown in figure 2.18b.

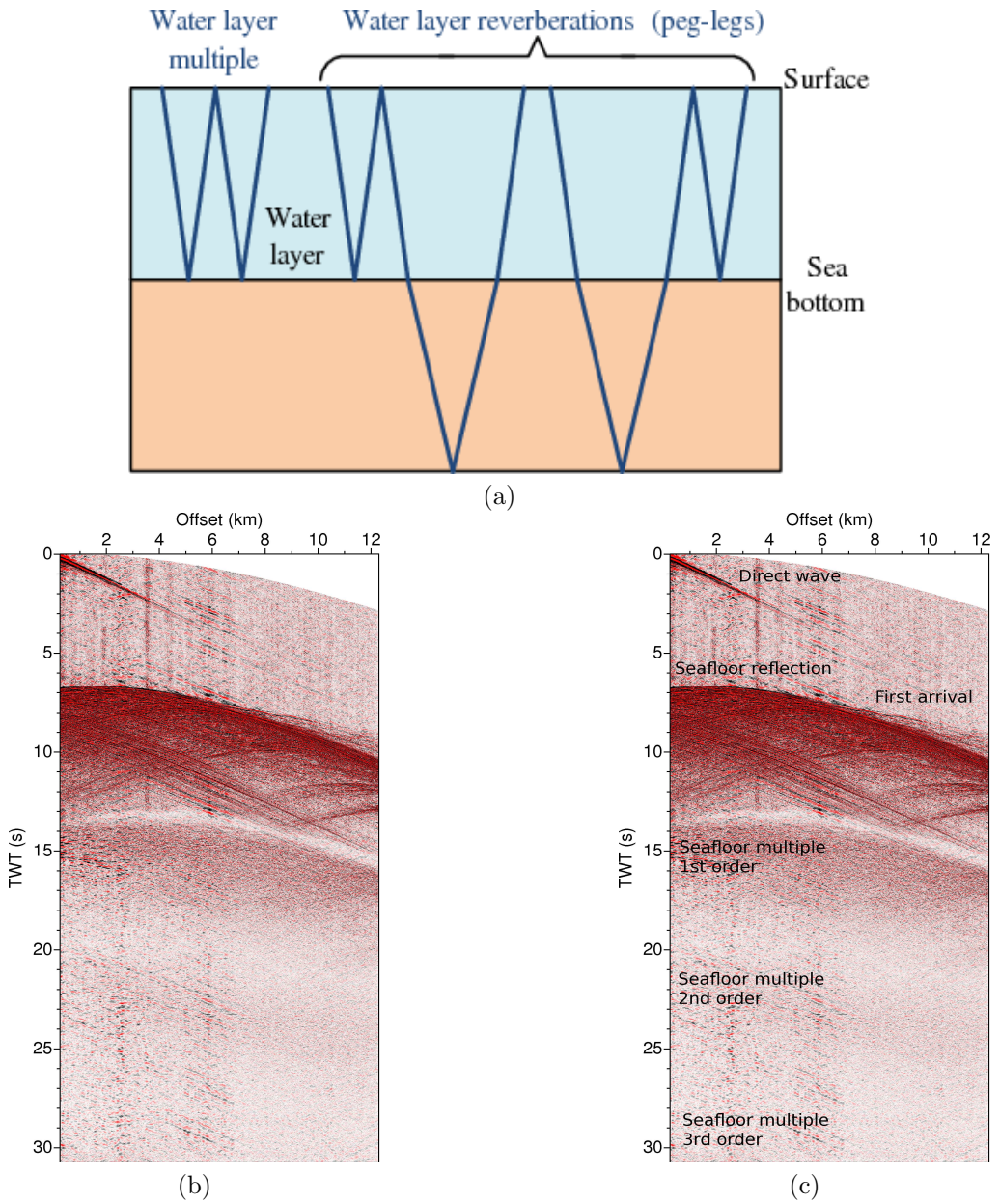

Figure 2.18: (a) Sketch depicting multiples in the water column (*Carvalho et al.*, 2018). (b) Real shot gather from 2015 ILAB cruise. (c) The different events along with 1st, 2nd and 3rd order water bottom multiples have been marked in (b). The number of times it bounces off the water surface is the order of the multiples.

In order to remove the multiple reflections of shallow events that would potentially hinder the actual deeper events, a suite of processing was carried out by WesternGeco. The application of these techniques (Schlumberger Geosolutions proprietary) are briefly illustrated below.

- Generalized surface multiple prediction: Multiples are modeled from input data using auto-convolution without taking into account bathymetry and are subtracted from real data using adaptive least-squares. The resulting effect on a shot gather is shown in figure 2.19.

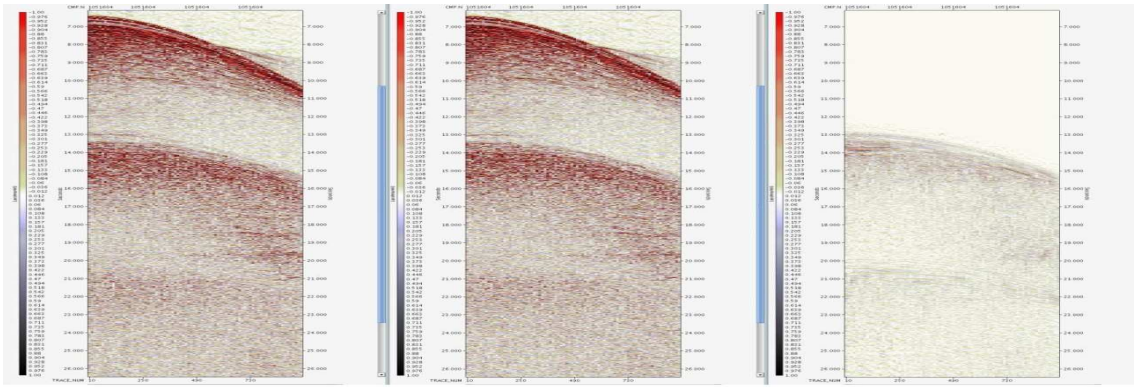

Figure 2.19: Left: Shot gather before Generalized surface multiple prediction. Middle: same shot gather after generalized surface multiple prediction. Right: Difference. Note that the multiples have been attenuated. Source: *WesternGeco processing reports*

- Weighted least-squares radon: This technique exploits the differences between the moveout of a primary event and its multiple in a moveout corrected common-midpoint gather. A high-resolution Radon transform is used to distinguish between the primary and its multiple in the tau-p (delay time-slowness) domain. A high-resolution Radon transform is achieved over a conventional Radon transform by using a time-variant weighting scheme applied during the transform. In order to supply a suitable velocity for correcting the hyperbolic moveout, an extensive velocity analysis was performed. An example shot gather illustrating the process is shown in figure 2.20.

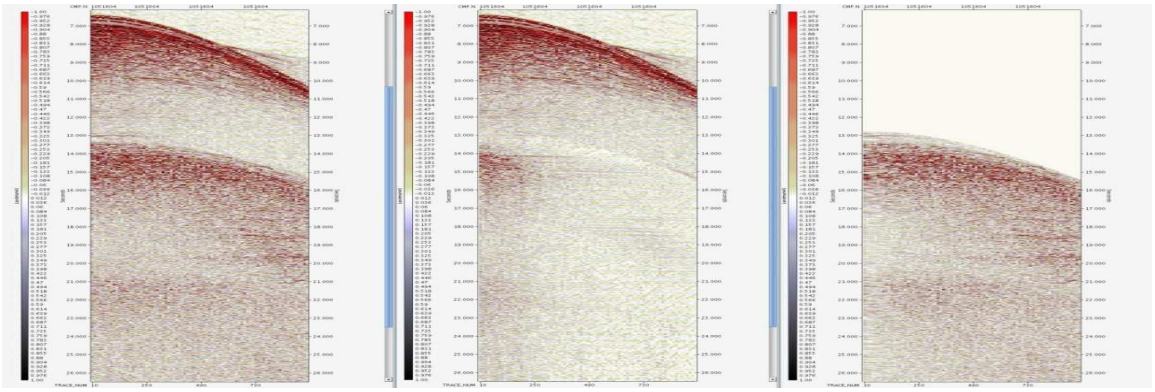

Figure 2.20: Left: Shot gather. Middle: same shot gather after multiple removal using weighted least squares radon. Right: Difference. Note that the multiples have been attenuated. Source: *WesternGeco processing reports*

- Post-Radon Isolating multiple techniques: Apparently, even after the application of the generalized surface multiple removal and weighted least squares, residual multiple energy is still found in the data especially at zero offsets where moveout does not have an effect on the primary and multiple energies. The last demultiple strategy used by WesternGeco was post-radon isolating multiple. Unlike the previous technique which relies on a velocity model, this technique uses spectral decomposition to remove the time-invariant residual multiple energy. The effect of this technique can be seen in a stack section in figure 2.21.

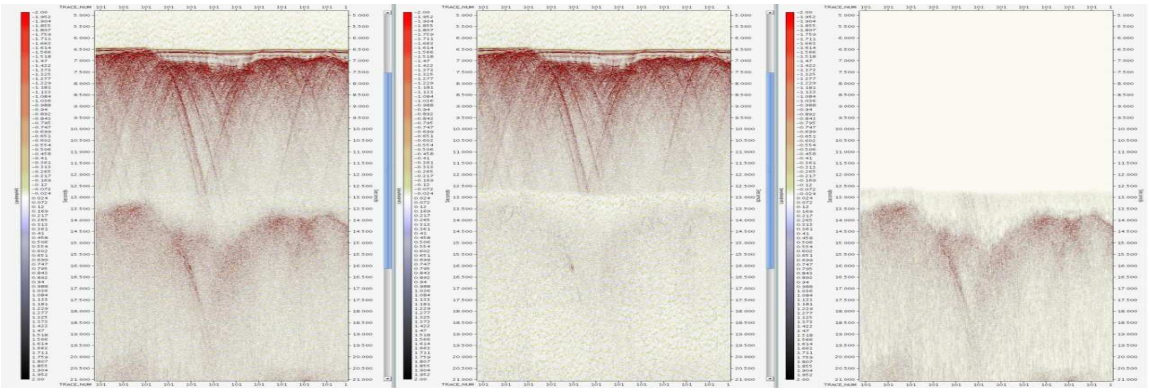

Figure 2.21: Left: Stack section. Middle: same stack section after post-radon isolating multiple removal. Right: Difference between the original stack section and after multiple removal. Source: *WesternGeco processing reports*

In addition to the above processing steps, Kirchhoff pre-stack time migration was also performed by WesternGeco. However, the resulting migrated data was found to have migration smiles that were hindering deeper Earth events. Hence I used the output shot gathers after the above demultiple sequence for further processing.

I present in the remainder of this chapter, techniques to improve the signal-to-noise ratio in challenging low frequency environments. I present specifically those techniques which were found to be successful in improving the signal-to-noise ratio rather than all techniques that were attempted. These are broadly divided into pre-stack enhancement (shot-offset and CMP-offset domains) followed by post-stack enhancement. I compare the same sample of real data at different processing steps namely, after processing in shot-offset domain (figure 2.26), after processing in common-mid-point (CMP)-offset domain (figure 2.32), after processing in post-stack domain (figure 2.33) and after the final target-oriented processing (figure 2.37).

2.4.2 Removal of dipping noise events

In almost all the shot gathers, a strong amplitude dipping events was observed in the near offset over the entire record length of the shot gathers. These events had a velocity corresponding to 1700 - 1800 m/s. I used the linear moveout correction with these velocities to flatten the events first and then filtered them out using a windowed f-k filter of dimensions 61 traces by 61 time samples (= 762.5 m $\times$ 0.48 s). The application of linear moveout correction resulted in the complete removal of energy above 7 s at 12 km offset (as shown by the white space in figure 2.22b. After the application of removal of near offset dipping energy, I found the energy dipping in the opposite direction at far offsets to have become visible (figure 2.22b). This would be associated to some receiver side noise as compared to the source side noise I just removed. To remove that, I first performed a reversal of offsets (new offset = (old offset $\times -1$) + length of streamer) so that the energy was transposed to near offset. This near offset energy can then be removed by another linear moveout correction followed by f-k filtering rejection. After reversing the offsets, I found this energy corresponding to velocities 2300 - 2400 m/s. However, I observed application of this second linear moveout correction removes energy completely above 5 s at the near offset as can be seen in figure 2.22c. This implied if the seafloor is shallower than 5 s, it will be affected. A simple solution to this problem was to use receiver gathers instead of shot gathers for the second linear moveout correction. In the receiver-offset domain, no reversal of offsets was performed and dipping events could be removed without affecting the energy at 5 s. This was done for younger ages where seafloor was shallower than 5 s (=3.75 km).

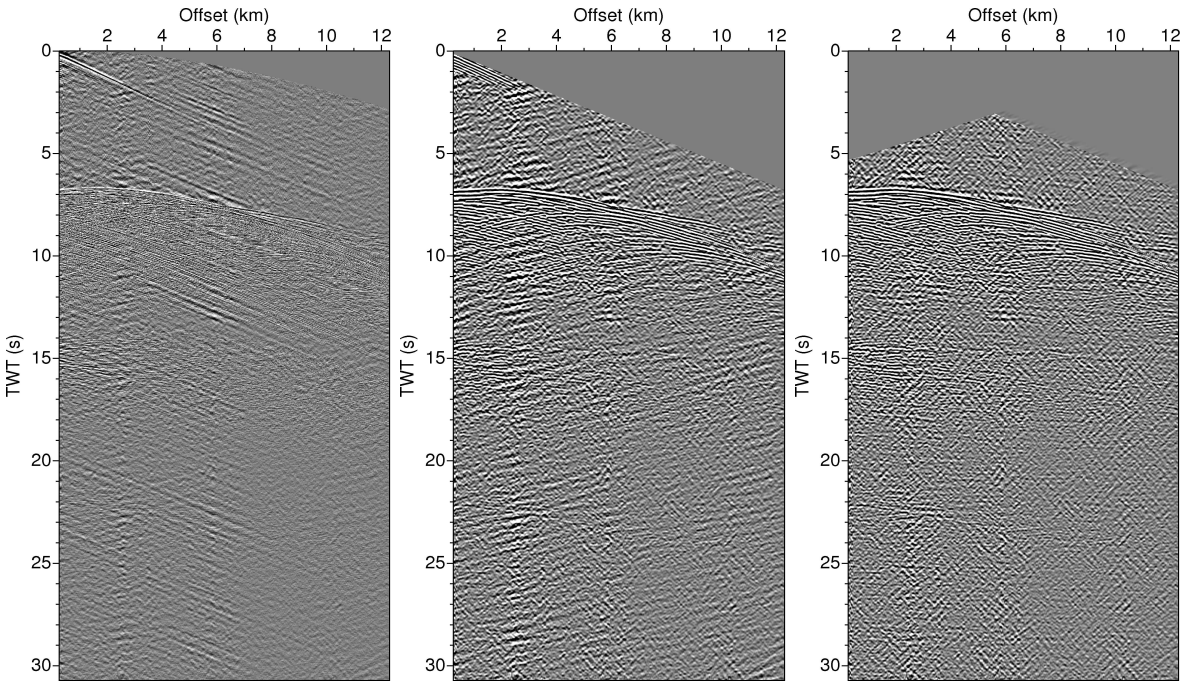

Figure 2.22: Removal of linear dipping events in shot (and receiver) domains (see text): (a) The original shot gather (b) Linear dipping events (1700-1800 m/s) at near offset removed and (c) linear dipping events (2300-2400 m/s) at far offset removed. Note successive removal of energy near seafloor in (b) and (c). A low pass filter (1.5-6 Hz) has also been applied.

The steeply dipping events now prominent in figure 2.22c were attenuated by a frequency-wavenumber (F-K) filter and I also performed time-frequency decomposition to edit bad traces in shot gathers. The final shot gather after the application of frequency-wavenumber filtering and time-frequency decomposition is shown in figure 2.23b.

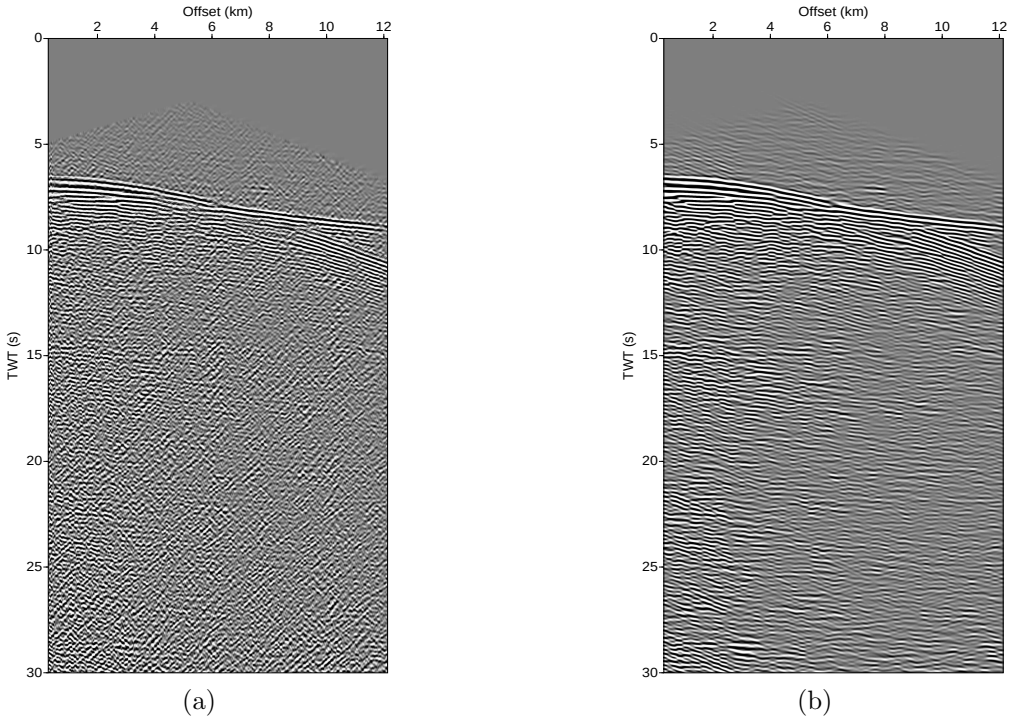

Figure 2.23: (a) Shot gather after removal of linear dipping noise as in fgure 2.22c. (b) Same shot gather after application of frequency-wavenumber filtering to be passed on to for further processing.

2.4.3 Low frequency enhancement

The analysis of the stacked data after the above processing made it clear that a boost of low frequency was needed in order to see events. The minimum frequency in the data was 1.5 Hz. In addition to above linear noise removal, a low frequency filter from 1.5-6 Hz was applied. The frequency spectra of the resulting shot gathers is shown in figure 2.24a. There was a need to boost energies in the spectra from 1.5-4 Hz. This low frequency enhancement was performed by time-variant spectral balancing of seismic data via time-frequency decomposition with Gabor-Morlet wavelets being used for the wavelet transforms (*Partyka et al.*, 1999). The Morlet's modification (*Morlet et al.*, 1982) of the original Gabor-wavelet transform (*Gabor*, 1946) in the time-domain (t)is denoted by ($G_j(t)$) and corresponds to:

$$G_j(t) = e^{-a_j t^2} e^{iw_j t}, \tag{2.37}$$

$$\text{where} \quad a_j = \frac{ln(2)w_j}{4\pi^2}, \tag{2.38}$$

where w_j is the frequency of the j_{th} wavelet. This can be represented in the frequency domain (w) as:

$$G_j(w) = \int_{-\infty}^{+\infty} G_j e^{iw_j t} dt = \sqrt{\frac{\pi}{a_j}} e^{-(w-w_j)^2/4a_j}, \tag{2.39}$$

with the parameters the same as described before. The width of the j_{th} wavelet in time domain (Δt_j) and in frequency domain (Δw_j) can be related to the frequency w_j as:

$$\Delta t_j = \frac{k_1}{w_j}, \tag{2.40}$$

$$\text{and} \quad \Delta w_j = \frac{k_2}{w_j}. \tag{2.41}$$

The values of k_1 and k_2 above can be found by approximating

$$e^{\frac{-a_j \Delta t_j^2}{4}} = \frac{1}{2}, \tag{2.42}$$

or in the frequency domain equivalently

$$e^{\frac{-\Delta w_j^2}{4}} = \frac{1}{2}. \tag{2.43}$$

The above approximation gives, $k_1 = 4\pi$ and $k_2 = \frac{2ln(2)}{\pi}$. The primary user inputs for the Gabor-Morlet wavelet transform are the beginning (w_1) and ending (w_2) central frequency and the number of frequency bands this range would be divided into. Based on the analysis of the frequency spectra of the shot gathers in figure 2.24a, I used the beginning and ending central frequency as 2 Hz and 5 Hz, with the range being divided into 12 smaller frequency bands.

The frequency spectra before and after of the shot gather is given in figure 2.24. A more symmetrical distribution of energies can be observed from 1.5-6 Hz in figure 2.24b as compared to a which would boost up the deep reflections.

(a)

(b)

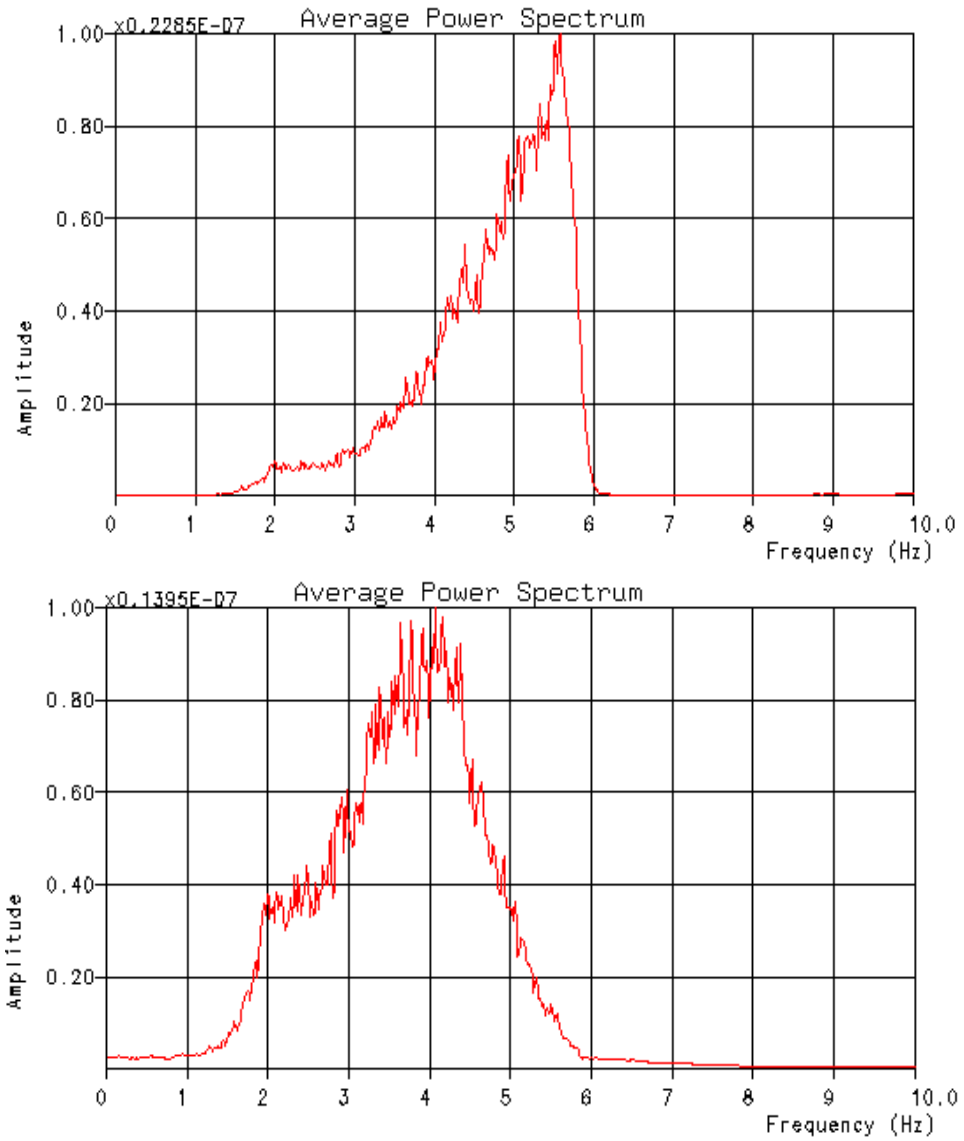

Figure 2.24: Frequency spectra of a shot gather before (a) and after (b) low frequency enhancement. The lower frequencies in the range 2-4 Hz have been improved after the low frequency enhancement.

The data were then sorted into receiver gathers to further suppress noise using time-variant band-limited noise suppression. In the frequency band 0-1.5 Hz, the noise is scaled down by a factor of 0.5 and artifacts are reduced by a smoothing operator. A preliminary velocity analysis for deeper events was performed using super-CMP gathers. Semblance based velocity analysis was out of question due to low signal to noise ratio. Individual events on super-CMP gathers were very difficult to identify and stacking velocities approximately 6-8 km/s were picked at 20-30 s TWT. Constant velocity stacks at different stacking velocities are shown in figure 2.25. Subsequently the data was stacked after NMO correction using the best velocities and is shown in figure 2.26a.

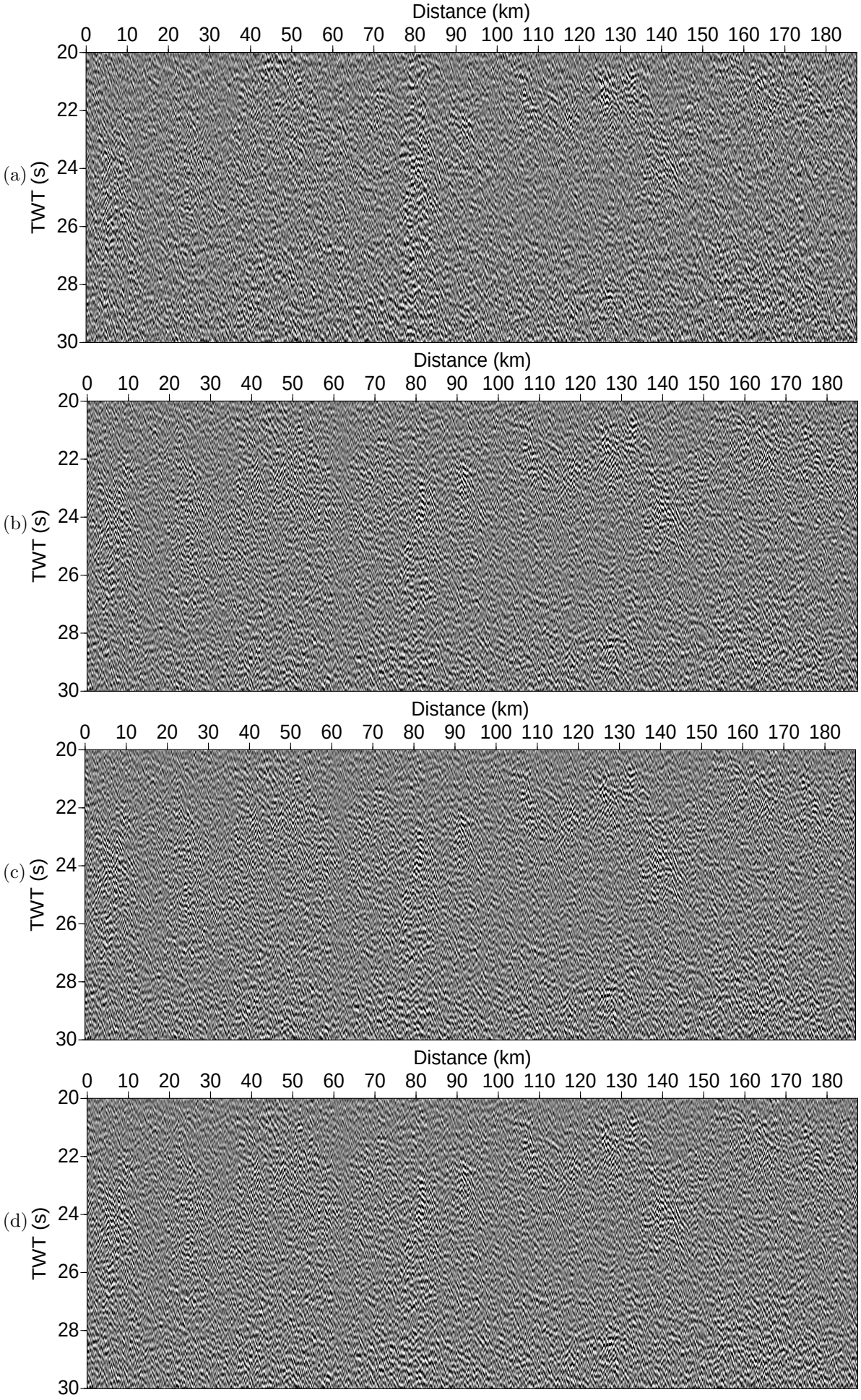

Figure 2.25: Constant velocity stack sections at different stacking velocities: (a) 2500 m/s (b) 5000 m/s (c) 7500 m/s (d) 10000 m/s. Same stack section as in figure 2.26 is shown.

Application of a strong windowed dip filter in post-stack processing on figure 2.26a is shown in figure 2.26b. Not much improvement is observed after post-stack dip filtering and I had to search for other ways to improve the best stack section obtained so far in figure 2.26a.

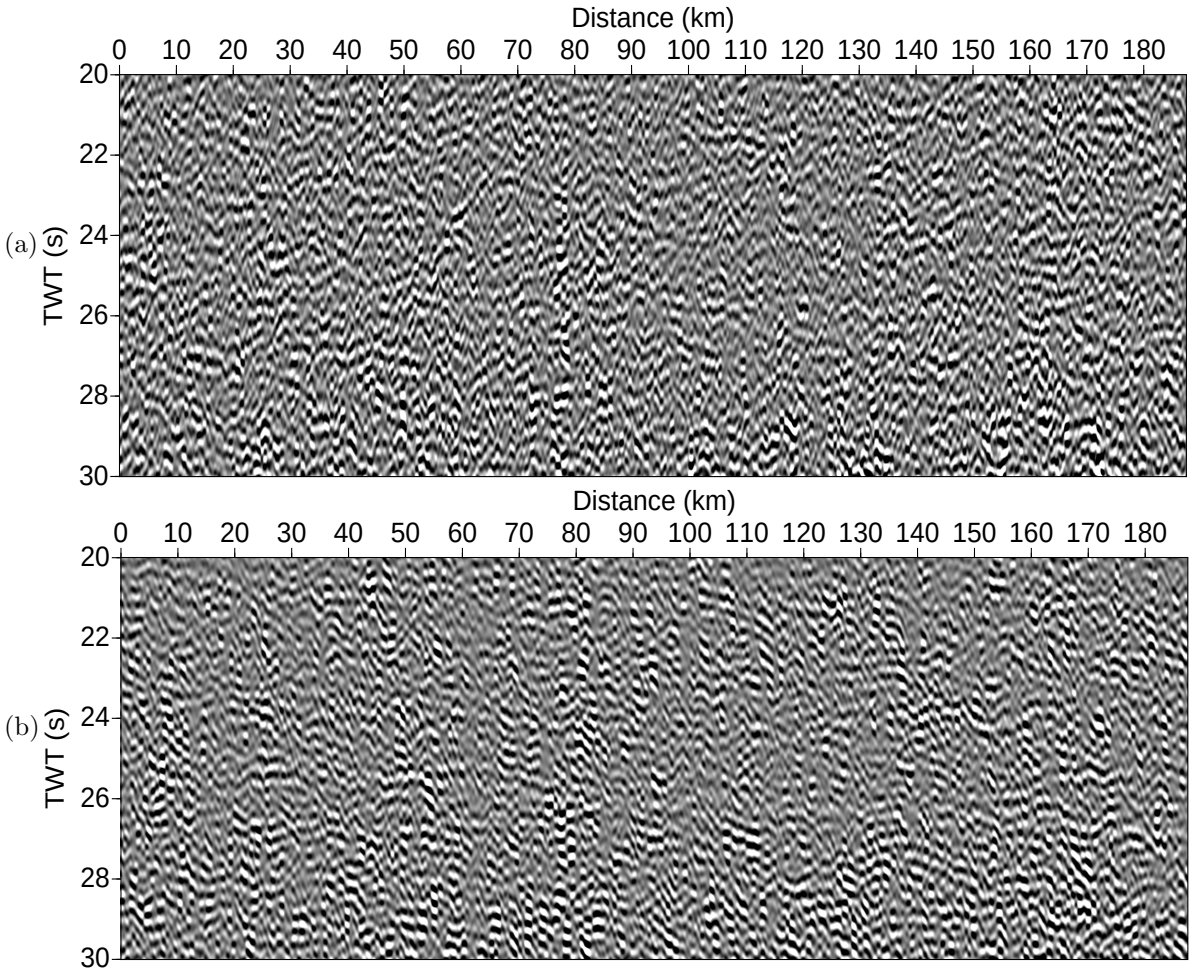

Figure 2.26: (a) Stacked data after linear noise removal and low frequency boost-up in shot (and receiver) domain, velocity analysis (figure 2.25) and NMO correction. (b) Application of a strong dip filter in post-stack processing

I tried several amplitude and frequency processing techniques including those mentioned in *Mehouachi and Singh* (2018) and (*Mehouachi*, 2019) but the improvement was not significant. I also downward continued the pre-stack data to see any improvements in the image using the two-pass strategy as described in section 2.3.2. Figure 2.27 compares the stacked data in (a) and the downward continued stacked data in (b) for a part of the profile. Note that there is a loss of data equal to streamer length in the process of downward continuation. Due to downward continuation being essentially an iteration of seismic migration, the output consisted of (migration) smiles, rendering the image even worse than before.

(a)

(b)

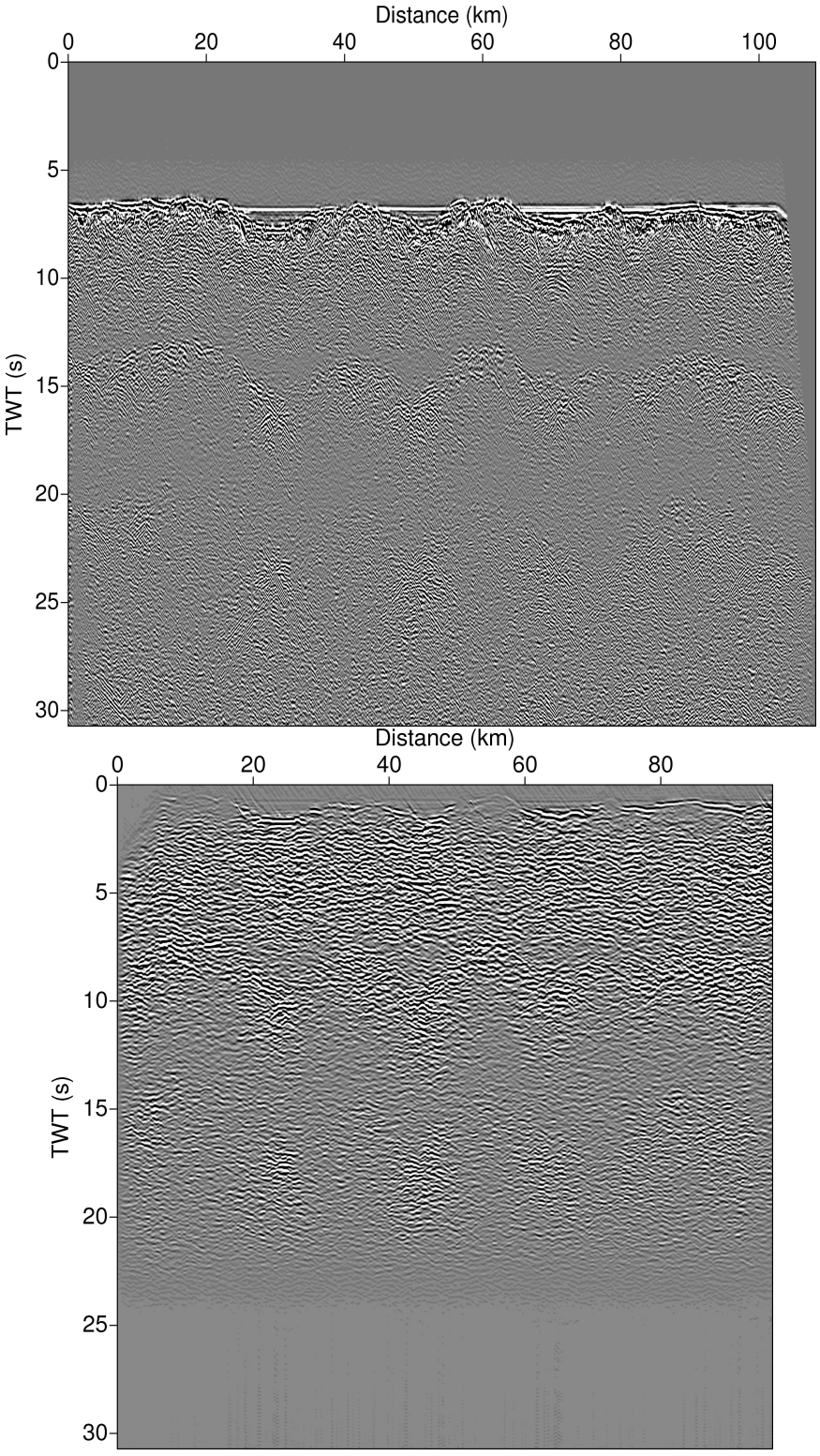

Figure 2.27: (a) Stacked data after NMO correction. (b) Stacked data after downward continuation of pre-stack gathers (two-pass) followed by NMO correction. The loss of data by a streamer's length in (b) is due to the process of downward continuation. Note that deeper earth events are not enhanced by downward continuation.

It was clear from figure 2.26 that all the discontinuous events may not be real and have to filtered out on some criteria. Additionally, the diffraction tails were rendering the events as discontiuous and had to be removed without seismic migration. To estimate how the LAB from previous studies would manifest on a P-wave seismic section, I performed synthetic modelling (*Shipp and Singh*, 2002) using the velocity

model shown in figure 2.28. I represented the LAB according to the 1300°C isotherm (*Artemieva*, 2006) with a 10% velocity drop and a constant mantle gradient to reach velocities 8.1-8.4 km/s at the 1300°C isotherm. Additionally, as the notion of a LAB channel was being developed around the same time, I took an additional second reflection into the modelling whose depth was nearly 90 km throughout the profile. I assumed a 10% P-velocity drop in the region between the two reflections.

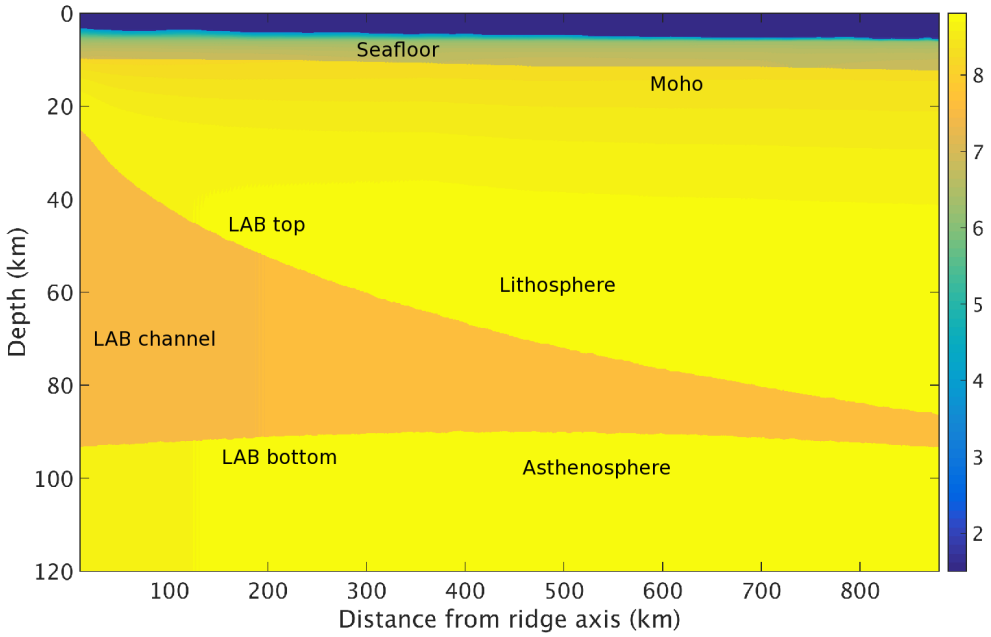

Figure 2.28: Velocity model used for estimation of LAB at distinct ages on the MCS profile. LAB is assumed to be the 1300°C isotherm with a 10% P-velocity reduction in the channel. The western end of the model corresponds to 2 Ma with the lithospheric thickness being ∼15 km and the eastern end of the model corresponding to 47 Ma with a lithospheric thickness of 72 km. The crust has been assumed to be 6 km throughout.

The shot gathers shown in figure 2.4.3 were then estimated at 100 km increments from 2 Ma. The estimated moveout of the LAB reflection is 0.2 s at offsets greater than 6 km at 2 Ma as seen in figure 2.4.3a. This moveout reduces drastically as the reflection moves deeper at increasing ages due to flattening of the LAB. The moveout of the reflection in the CMP domain would be double of that in the shot domain. An important finding from figure 2.4.3 is that events away from the ridge-axis are most likely expected to be flat in MCS records. With this finding, I proceed to further enhance flat (zero wavenumber) events in different domains of the MCS data.

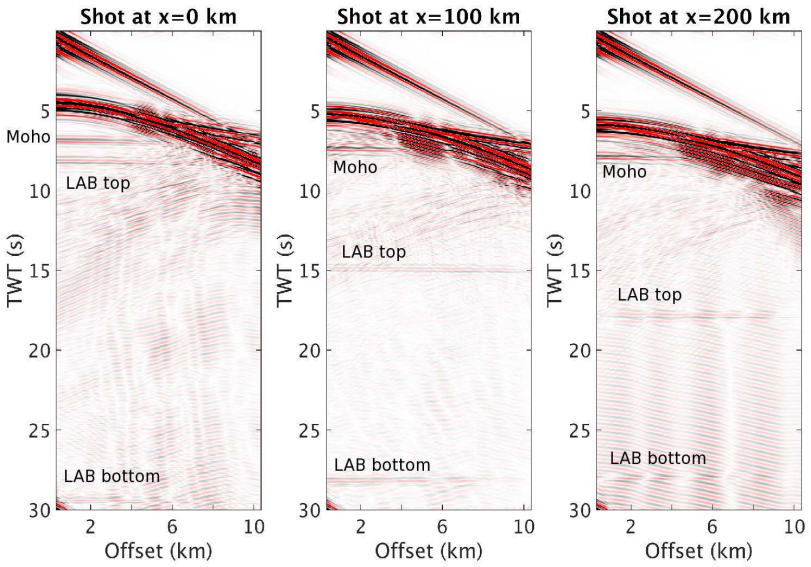

(a)

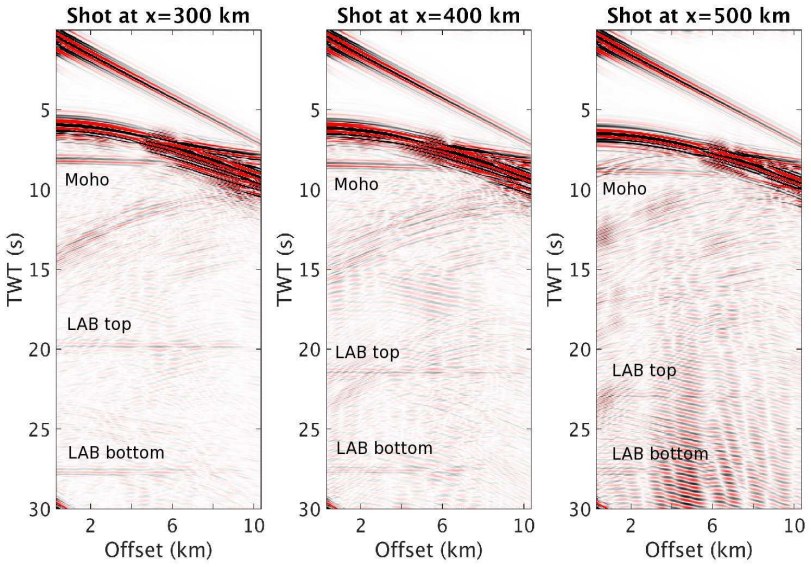

(b)

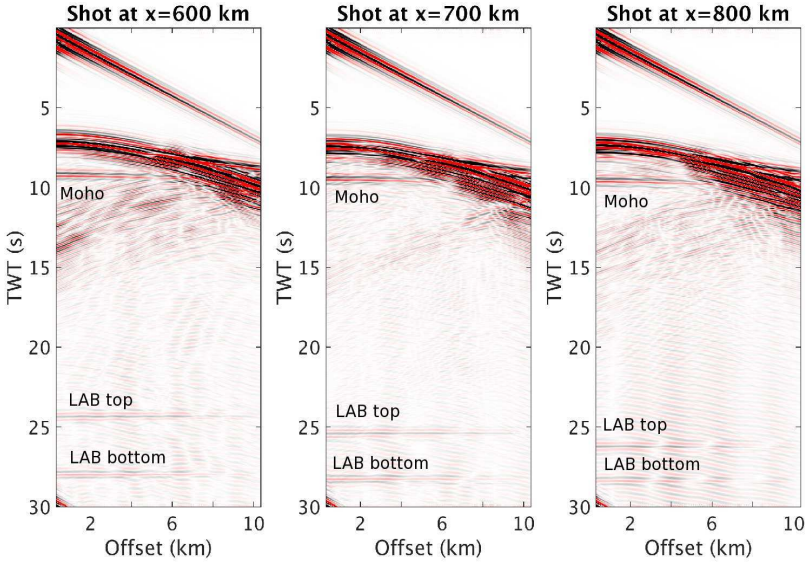

(c)

Figure 2.29: Shots modeled at labeled distances from 2 Ma using the velocity model in figure 2.28. Ricker wavelet of dominant frequency 3 Hz was used. In all cases, the Moho reflection and the reflections corresponding to top and base of the LAB channel can be seen.

2.4.4 Enhancing flat events in the offset-interpolated CMP

I initally tried to further enhance flat events in the shot-offset and receiver-offset domains but found that the reflections were less focused when stacked. The solution was to focus on the common-mid-point (CMP) domain. In order to improve the signal to noise ratio, *Mehouachi and Singh* (2018) suggests using super-CMP gathers instead of CMP gathers to increase the fold and hence improve the signal to noise ratio. However, my experience with super-CMP gathers while performing velocity analysis made me question the suggested improvement by using super-CMP gathers. As an alternative, I used offset-interpolated CMP gathers such that the fold was equivalent to a super-CMP gather. I used the in-built workflow module of the Echos Paradigm software to perform the offset interpolation which I describe briefly. The input traces of the CMP gather are interpolated along coherent dips within a 2000 m $\times$ 50 ms window. This window size along with values of several following parameters was selected after doing an extensive trial of a suite of parameter values. Since the focus was mainly on flatter events, I set the range of dips to be scanned as $\pm$10 ms/trace in the original CMP gathers which had a trace spacing of 150 m. A semblance plot is created in which the coherency is a function of dip and time. A 120 ms coherency smoothing window is also used to stabilize the semblance. The peak coherencies are then found and interpolated according to their exact dip ranges and sorted in order of highest to lowest.

A simple comparison between the super-CMP gather and an offset interpolated CMP gather (of the same CMP gather) can be seen in figure 2.30. A higher signal-to-noise ratio is seen in an offset interpolated CMP gather as compared to a super-CMP gather. Subsequently, I ended up using an offset interpolated CMP gather.

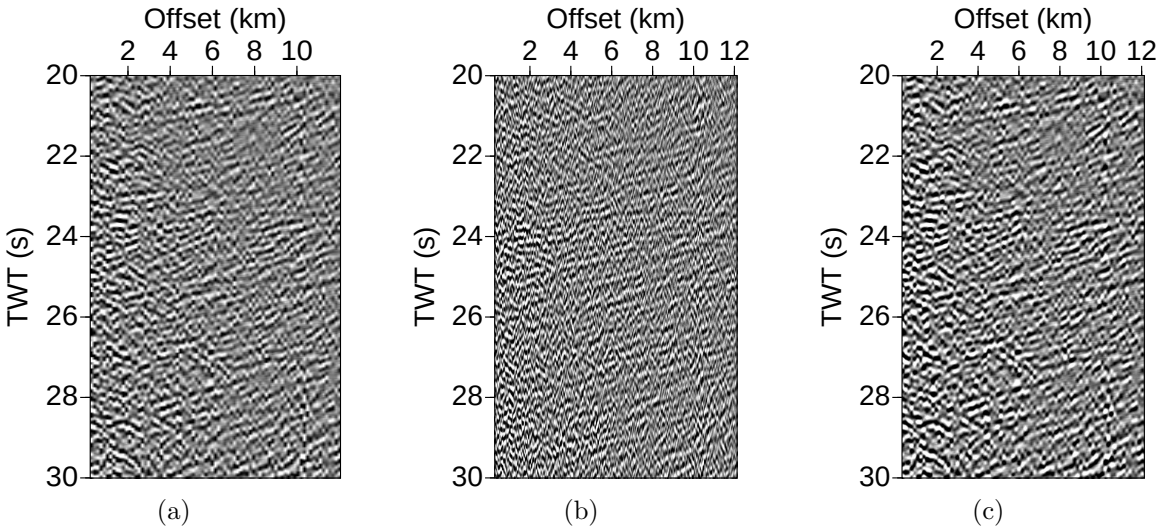

Figure 2.30: (a) Original CMP gather (b) Super-CMP gather (c) Offset-interpolated CMP gather. Both super-CMP and offset-interpolated CMP gather have the same frequency content and have been corrected with same stacking velocities for uniformity in comparison. Note better signal-to-noise ratio in (c) compared to (b) and (a).

After forming offset-interpolated CMP gathers and NMO correction using refined stacking velocities, I investigated in further filtering out of the non-flattening events by different means:

1. Karhunen-Loeve (KL) transform: This technique has been is based on eigen-image decomposition of an image and filtering out the undesired events. It has been applied to seismic for random noise attenuation (*AL-YAHYA*, 1991). A covariance matrix is formed first by taking dot products of all pairs of the pairs of traces in the gather. The eigenvectors and their corresponding eigenvalues are computed for this matrix. Enhancement of flat events is then performed by reconstructing the data using only first 2 eigenvectors and their eigenvalues. Inclusion of all eigenvectors scaled to their eigenvalues will reconstuct the original dataset. This transform is based on the assumption that non-flat events are mostly noise (diffraction tails) and so the input gather must the target events as flat as possible.

2. Wavenumber filtering: The flat events can be looked upon as energy corresponding to zero-wavenumber in the f-k domain. I used this filter to enhance the zero-wavenumber energy with a window size of 21 traces (out of a total of 972 traces in ensemble). Although the computational time increases with a smaller window size like the one used here, artifacts are reduced. On the other hand, having a larger window size would introduce artifacts but have smaller computational time.

A comparison between the two schemes is shown in figure 2.31. The KL transform is more time consuming and apparently renders the image pixelated in comparison to wavenumber filtering.

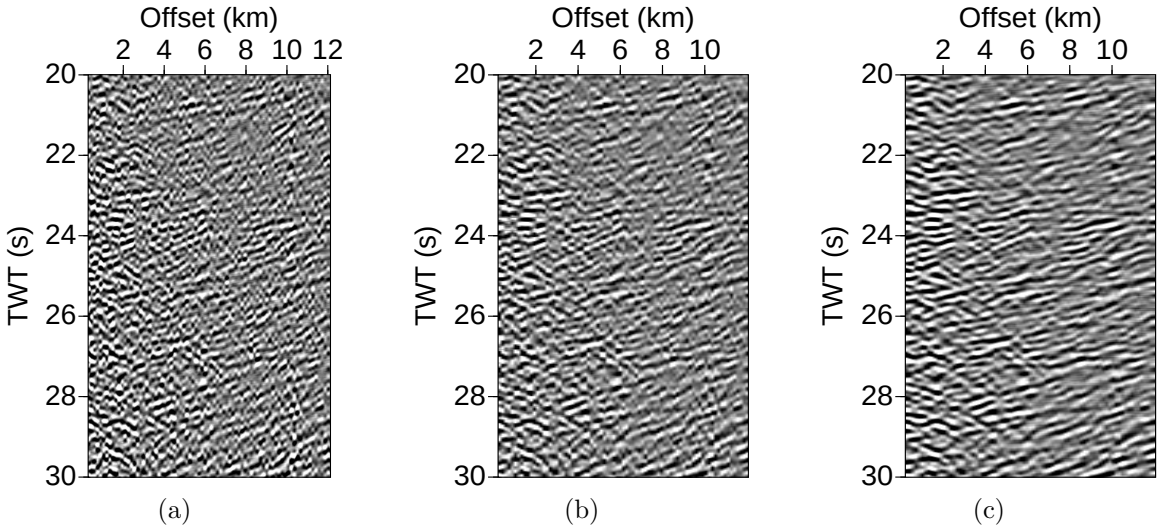

Figure 2.31: (a) Offset interpolated CMP gather as in figure 2.30c (b) KL-transform applied on the offset interpolated CMP gather. Only the first 2 eigenvectors and corresponding eigenvalues are used in reconstructing the image. (c) Windowed Wavenumber filtering applied on the offset-interpolated CMP gather with same window size as (b).

At this stage, NMO correction using a more refined velocity model followed by stacking is shown in figure 2.32. Some improvement can be observed in the stacked section after adding the above processing steps as compared to figure 2.26.

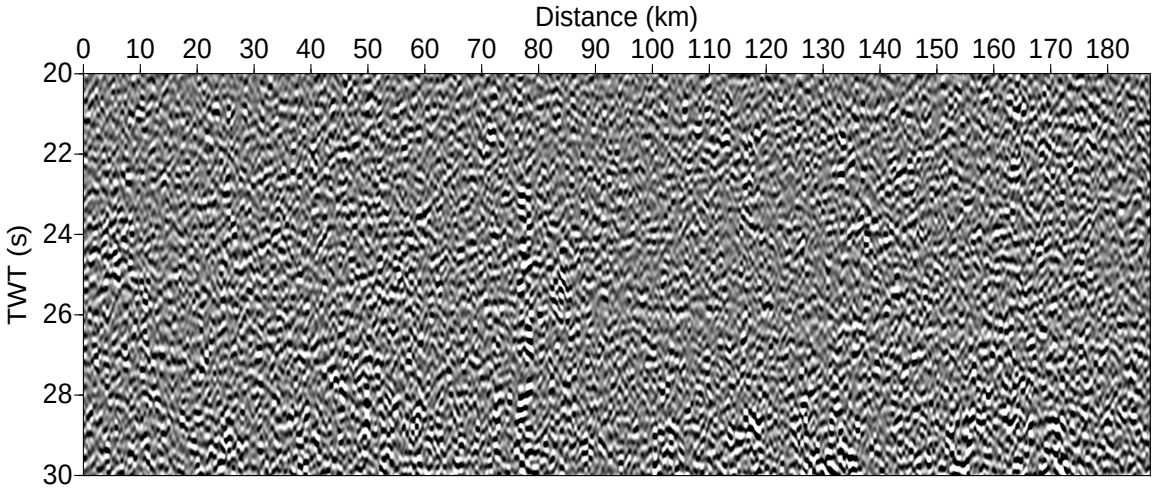

Figure 2.32: Stacked data after enhancing the flat events in offset-interpolated CMP domain, refined velocity analysis and NMO correction and post-stack processing. Compare with figure 2.26a.

I also attempted a workflow consisting of an iterative offset interpolation of a CMP gather, wavenumber filtering and partial stacking. The idea behind the iterative worflow was to enhance flat events repeatedly but proved to be time consuming considering the amount of data that had to be processed (∼1400 km). Hence I proceeded with enhancing the flat events in the stack section obtained in figure 2.32.

2.4.5 Enhancing flat events in the post-stack domain

The post-stack processing in previous sections and used in figures 2.26, 2.32 mainly consist of low pass filtering to reduce the frequencies down to 5 Hz, low frequency boost-up and windowed dip filtering with feedback. Additionally, some of the in-built processing modules in Paradigm Echos provided an improvement almost immediately. These include but are not limited to:

1. Time-variant band-limited noise suppression: After decomposing data into coherent and non-coherent signals, the time-variant noise suppression thresholds the non-coherent signals with the coherent signals
2. Windowed frequency-space (F-X) deconvolution was performed iteratively in the range 2-5 Hz
3. A frequency based noise suppression from 0-2 Hz and 5-10 Hz to attenuate diffraction tails
4. Next a dip based windowed coherency search and search for maximum coherency of dips ranging from 0.5 to +1 ms/m was performed. 50% percent of this maximum coherency energy was added back to the data to highlight the reflections of dipping interest
5. Further, a windowed frequency-wavenumber(F-K) transformation of the data was performed and the amplitude of each sample in the F-K spectrum was then raised to power of 2 before being inverse transformed into the offset-time(X-T) domain.

The stack section obtained by the addition of above post-stack processing is shown in figure 2.33. An improvement can be seen in reflection in highlight.

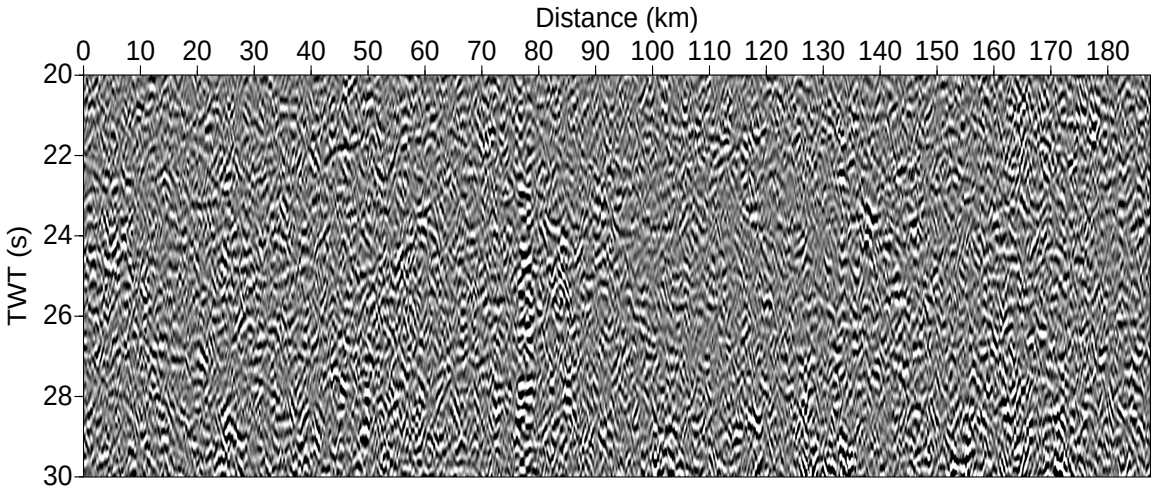

Figure 2.33: Stacked data after post-stack processing (see text). Compare with figure 2.32.

So far the processing I have performed has been by hit and trial of the various workflow modules available in the industrial software, Paradigm Echos. But as seen in the figure 2.33, further improvement is needed to bring out the event that has been in highlight. A simple spherical divergence gain did not suffice for enhancing the reflection. For this reason, I implemented in the final stages of my processing, a target oriented processing strategy.

The basic aim of target oriented processing is to search for the most coherently dipping energy within a given region around the prospective reflection. To accomplish the same, I used the Kuwahara filter (*Bartyzel*, 2016) which has been shown to be superior to the conventional mean/median filter in the way that it preserves edges in addition to smoothing. Essentially the region or offset-time $(x - t)$ window around a particular point in the image is divided into several sub-windows of varying dimensions, from $\Delta t_{min}, \Delta x_{min}$ to $\Delta t_{max}, \Delta x_{max}$. In each of these sub-windows, the mean and the variance of the amplitudes constituting that window is computed. Then the variances are sorted in a descending order and the window with minimum variance (maximum coherency) is assigned the highest weight followed by

the the next most coherent window. In this manner, the coherent windows are sorted and are assigned weights with the weight function being a cosine taper.

To exemplify, a maximum size of 7 × 3 point window is assumed around any given poing in the image. The actual dimension of this window is (7-1) × trace spacing = 37.5 m by (3-1) × time spacing = 16 ms. This 7 × 3 point window is sub-divided into all possible window sizes from 2 × 2 to 7 × 3. This gives a total of 135 windows for the coherency to be searched for around any given point. In each of these 135 windows, the variance is computed and the variances of all these 135 windows is sorted in a descending order. Then a cosine taper function of 135 points is applied to the mean of the respective 135 windows as a weighting function. A scalar can be applied to the weighting function to further boost up the amplitudes.

Another parameter that comes into play is the expected dip of the reflection. When the search in the above manner is complete over a point in the image, the following point in the image around which the minimum variance (maximum coherency) is searched for depends on this parameter. An obvious alternative is to manually pick each and every point on the prospective reflection around which most coherent energy is to be searched for, but that would extremely bias the results. Subsequently the minimum and maximum window sizes, the expected dip of the reflection and the initial position of the window are the only parameters required. I performed a number of tests on the synthetic gathers with the optimum window size and the dip parameter as shown in figures 2.34, 2.35.

The optimum window size is first tested keeping the dip parameter constant. The results are shown in figure 2.34. A synthetic event with a constant dip is created (figure 2.34a) and sufficient gaussian noise is added until the event is almost completely masked (figure 2.34b). Then the dependency of the filtering on different window sizes is examined. These window sizes range from 11 × 11 (figure 2.34c)to 61 × 61 (figure 2.34d). A better resolved event is seen for a larger window size as compared to a smaller window size.

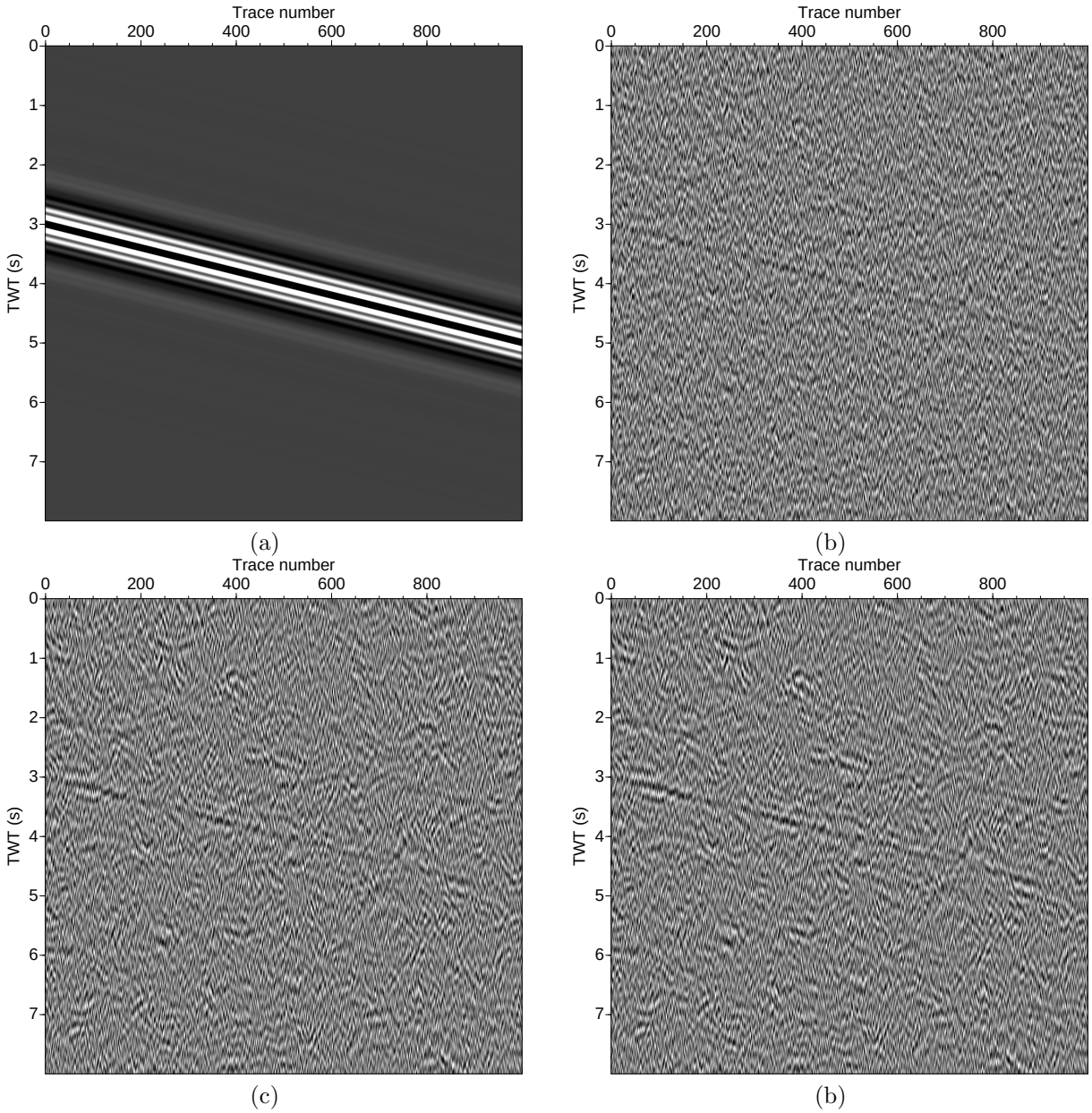

Figure 2.34: (a) Constant dipping synthetic event (b) Gaussian noise added until the event is sufficiently masked (c) Recovered reflection using target-oriented processing and window size of 11 × 11. (d) Recovered reflection using target-oriented processing and window size of 61 × 61. Larger window size in (d) is able to better recover the reflection. Same amplitude scale in (b),(c) and (d).

For investigating the dependency on the dip parameter, a synthetic gather consisting of several conficting dips (0,4 and 10 ms/trace) is considered as shown in figure 2.35a. Sufficient gaussian noise was added to mask the dips completely as shown in figure 2.35b. Different dipping events were then recovered using an optimum window size (figure 2.35c,d,e). It can be seen from figure 2.35e that events having a high dip are not recovered well.

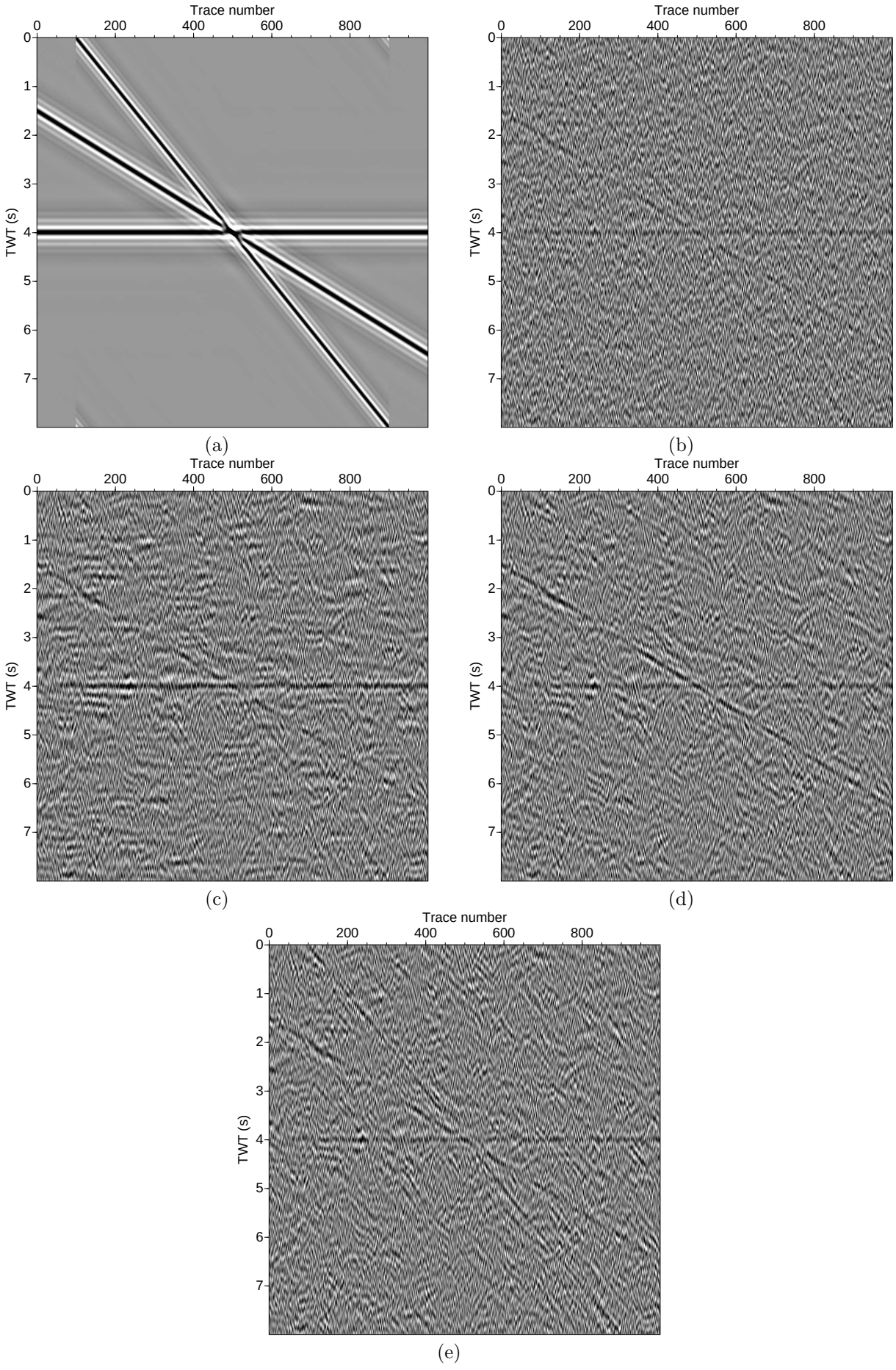

Figure 2.35: (a) Conficting dips (0, 4 and 10 ms/trace) synthetic events (b) Gaussian noise added until the events are sufficiently masked (c) Recovered reflection using target-oriented processing and dip close to 0 ms/trace (d) Recovered reflection using target-oriented processing and dip close to 4 ms/trace (e) Recovered reflection using target-oriented processing and dip close to 10 ms/trace. Same amplitude scale in (b),(c) and (d) and (e).

I also tested the strategy on a complex sigmoid model as shown in figure 2.36. The original seismic image is shown in figure 2.36a and is masked sufficiently by addition of gaussian noise in figure 2.36b. The recovered image using an a-priori knowledge of the dip of the event is sown in figure 2.36c. It can be seen that the linear patterns in the image have been recovered to some extent. However, without any a-priori knowledge of the expected dip of the reflection, a wide-range of dips to be scanned for is provided next in figure 2.36d. Since the dips are rapidly changing, the traget-oriented processing fails to recover the pattern in the image. In fact, the linear pattern at the top of the sigmoidal pattern is better recovered when exclusively those dips are searched for (figure 2.36c) as compared to searching for a wide range of dips in figure 2.36d.

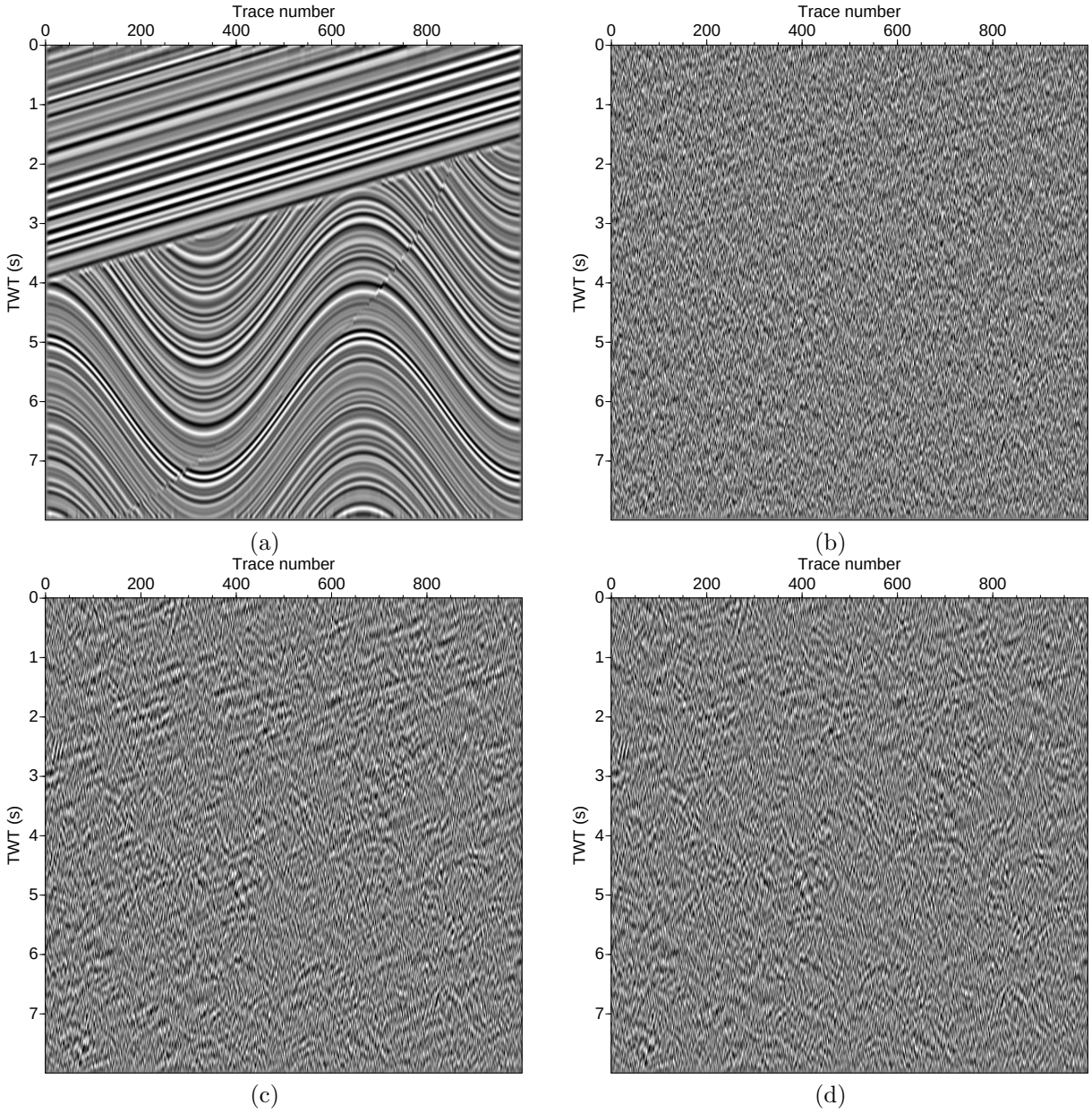

Figure 2.36: (a) A complex sigmoidal pattern having linear dipping events on top (b) Gaussian noise added until the signal to noise ratio is sufficiently low (c) Recovered image using target-oriented processing and with a specified dip corresponding to that of the linear pattern. (d) Recovered image using target-oriented processing and a wide range of dips to be searched for. Same amplitude scale in (b),(c) and (d).

The synthetic tests performed above are enough to know about the shortcomings of the target-oriented processing strategy. These are two-fold: (a) A sufficiently high signal to noise ratio (threshold) is needed; (b) Events having only a constant dip are better enhanced as compared to events which have rapidly

changing dips. These two shortcomings hold regardles of the choice of the dip parameter and the window size. Additionally the target-oriented processing fails is the dip of the event is very high. As will be seen in chapter 5, this technique fails where the dip of the LAB is changing abruptly and/or is having a very low signal-to-noise ratio.

Due to the extensive search being carried out in this filtering, it is computationally time taking. This is the primary reason that I apply it on a region around a reflection rather than the whole seismic image. For application to real data, instead of searching in each and every window dimension, I search only among specific dimensions of rectangular windows to reduce the computational time. To further reduce computational time, I split the entire seismic image with a CMP spacing of 6.25 m into several data sets with increased CMP spacing and decreased number of CMP traces. These were then merged after the filtering was done on each of the seismic images in a parallel manner. Before applying it to each seismic image, the amplitudes were squared and scaled up to remove the bias due to negative amplitudes. The original polarity of the amplitudes are considered after the filtering is done and by running a positive to negative polarity transition search along the enhanced amplitudes using the same dip, the final reflection image is obtained as shown in figure 2.37.

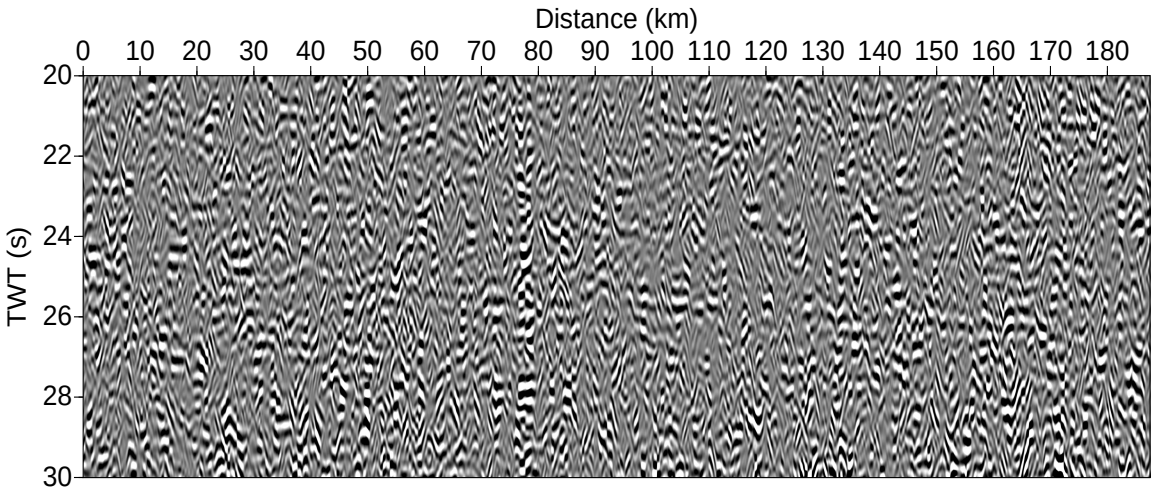

Figure 2.37: Final stacked data after application of data-adaptive Kuwahara filtering (see text). Compare with figure 2.33. The reflection can be seen dipping from ∼24 s TWT at 0 km distance to ∼26 s TWT at 160 km distance.

Chapter 3

Aging of upper oceanic crust

Jusqu'à très récemment, les longueurs des flûtes dans les données de sismique réflexion n'étaient pas assez longues pour capturer les premières arrivées en eaux profondes (>5 km). Par la suite, la plupart des études sur la croûte océanique supérieure étaient basées sur des études sismiques grand angle qui ont une faible résolution dans la croûte supérieure. Les forages fournissent des informations précises sur la croûte océanique supérieure, mais leur âge est limité. En raison du manque de données sur les âges de la croûte mature (>40 Ma), l'évolution de la croûte océanique supérieure a été limitée à ∼10 Ma (*Carlson*, 2004). La croûte océanique supérieure est divisée en une couche 2A et une couche sous-jacente 2B. La couche 2A est principalement composée de coulées de lave extrusives et a une vitesse des ondes P plus faible que la couche sous-jacente 2B. L'interprétation de la couche 2B et de la frontière de la couche 2A/2B est débattue. Dans certaines études, la couche 2B est considérée comme un complexe filonien dykes verticaux ou commes des coulées de lave intrusives (*Harding et al.*, 1993) tandis que dans d'autres, elle est interprétée comme une unité modifiée hydrothermalement (*Vera et al.*, 1990). Certaines études proposent une combinaison des deux dans différentes régions d'étude (*Christeson et al.*, 2010; *Carlson*, 2011) mais ne fournissent pas une image intégrée des observations.

Pour surmonter les limitations exposées ci-dessus, j'ai analysé la croûte océanique supérieure de 0 à 75 Ma à partir des données MCS. Tout d'abord, j'ai identifié l'événement de la couche 2A dans les enregistrements sismiques sur la base de la modélisation de la forme d'onde dans le chapitre 2. Cet événement de la couche 2A est observé tout au long de 0 à 75 Ma dans la croûte océanique supérieure et indique un gradient de vitesse élevé à la base de la couche 2A. Pour obtenir les images de la sous-surface et les informations en temps bidirectionnel (seconde temps double, ou TWT), j'ai effectué un traitement des données sismiques comme décrit dans le chapitre 2. En choisissant le fond marin, le socle et l'événement de la couche 2A de 0 à 75 Ma à partir des images de la sub-surface, j'obtiens l'épaisseur des sédiments et l'épaisseur de la couche 2A en TWT. J'ai observé que l'épaisseur de la couche 2A TWT diminue rapidement de ∼500 ms TWT à l'axe de la ride (zéro-âge) à ∼300 ms hors axe. Les incertitudes dans la couche d'imagerie 2A sont de ±30-70 ms TWT. Ensuite, pour obtenir les vitesses d'ondes P de la croûte supérieure, j'exécute la procédure en deux étapes d'extrapolation de champ d'onde vers le bas et de tomographie par temps de parcours, comme décrit dans le chapitre 2.

A l'axe, les vitesses d'ondes P de ∼2,5 km/s obtenues, augmentent rapidement à ∼4 km/s en 4 Ma. J'observe que les vitesses d'ondes P au sommet de la croûte sont des <4,5 km/s à tous les âges, l'essentiel de l'évolution se produisant entre 0 et 4 Ma. L'épaisseur TWT de la couche 2A à partir des images de sub-surface est ensuite utilisée pour obtenir l'épaisseur de la couche 2A en utilisant les vitesses de tomographie. Par la suite, une épaisseur de ∼900 m pour la couche 2A est observée à l'axe de la ride, et diminue rapidement à ∼770 m à 4 Ma et diminue encore à ∼600 m à 15 Ma. Les incertitudes des estimations de profondeur correspondent à ±165-365 m. Deux taux d'amincissement distincts de 0-4 Ma et 4-15 Ma de la couche 2A sont observés et respectivement attribués à la circulation hydrothermale de haute température (active) et de basse température (passive). Au-delà de 15 Ma, peu de changements d'épaisseur physique de la couche 2A sont observés. Il est intéressant de noter

que l'épaisseur des sédiments augmente rapidement loin de l'axe, et est négligeable à ∼170 m à 4 Ma. L'estimation des taux de dépôt pour l'épaisseur des sédiments (*Alibés et al.*, 1996) décompactés (∼240 m pour une épaisseur actuelle de ∼170 m) correspond à 47 mm/ka et correspond bien aux données du forage IODP 108, site 662-663 results (*Ruddiman and Janecek*, 1989). Ces réutilisations indiquent que l'augmentation rapide de l'épaisseur de la couverture sédimentaire et la réduction de l'intensité de la chaleur pour la circulation hydrothermale loin de l'axe de la ride limitent l'étendue de la circulation hydrothermale active jusqu'à 4 Ma.

On observe que les vitesses d'ondes P au sommet de la couche 2B augmentent progressivement de ∼4,5 km/s sur l'axe de la ride à ∼5,5 km/s jusqu'à 46 Ma. Il s'agit du premier ensemble de données qui enregistre une augmentation des vitesses de la couche 2B jusqu'à 46 Ma, car la plupart des études précédentes ont limité l'évolution de la couche 2B à 0,5 Ma (*Newman et al.*, 2011). Cette augmentation implique également la pénétration d'eau de mer dans la couche et que l'altération hydrothermale ne se limite pas à la couche 2A mais se prolonge bien en- dessous. Les estimations de la porosité des couches 2A et 2B à partir de leurs vitesses P respectives (*Taylor and Singh*, 2002) indiquent que les porosités deduites du forage (*Carlson*, 2011, 2014a) et de la gravité (*Holmes and Johnson*, 1993) sont observées si la couche 2A a des fissures trois fois plus fines que la couche 2B. Cela explique également un gradient de vitesses élevé dans la couche 2A par rapport à la couche 2B, car des fissures plus minces montrent une augmentation plus forte de la vitesse des ondes P lorsqu'elles sont scellées (*Wilkens et al.*, 1991) en raison de phénomènes tels que l'altération hydrothermale.

Des vitesses d'ondes P typiques de ∼5,9 km/s sont observées hors axe à des profondeurs de 1 km sous le socle. Celles-ci se sont avérées être proches des vitesses d'ondes P dans les complexes filoniens de dykes verticaux, issues d'études de forage (*Carlson*, 2011). En comparant les vitesses d'ondes P de la couche 2B avec les vitesses d'ondes P situées 1 km au-dessous du plancher océanique/du sous-sol, on observe que, même à l'âge zéro, les vitesses sont similaires. À un âge plus avancé, les vitesses de la couche 2B deviennent nettement inférieures à celles situées 1 km en dessous du socle. Cela implique que la couche 2B correspond à de dykes verticaux à l'âge zéro. Hors axe, elle est susceptible d'être une limite d'altération hydrothermale dans la coulée de lave. L'augmentation rapide des vitesses de la couche 2A jusqu'à 4 Ma et l'augmentation progressive des vitesses de la couche 2B jusqu'à 46 Ma indiquent que des fissures plus minces se scellent rapidement dans la jeune croûte océanique et que des fissures plus épaisses se scellent progressivement avec l'âge en raison de la circulation hydrothermale (*Shaw*, 1994).

J'utilise également les données de flux de chaleur conductrices colocalisées de l'expédition de 2017 pour valider mon hypothèse d'un système hydrothermal continu à partir des vitesses d'ondes P issues de la tomographie. Les données de flux de chaleur observées se révèlent être inférieures au flux de chaleur hors axe prévu à des âges distincts. Cette différence de flux de chaleur prévu et observé est attribuée à la redistribution latérale de la chaleur due à la circulation de l'eau de mer, ce qui implique à son tour que la circulation hydrothermale se poursuit hors axe comme proposé. J'utilise également une approximation analytique de la loi de Darcy (*Fisher et al.*, 2003) pour calculer les perméabilités globales à partir des mesures de flux de chaleur. Avec les porosités estimées à partir de la tomographie des vitesses d'ondes P et des perméabilités d'ensemble à partir de mesures de flux de chaleur, je compare les valeurs de perméabilité d'ensemble à la porosité avec certains modèles existants de théorie de la percolation. À l'exception de l'analyse des données de flux de chaleur, ce chapitre a été publié dans *Geochemistry,Geophysics,Geosystems* (https://doi.org/10.1029/2019GC008577).

Until very recently, the streamer lengths in seismic reflection data were not long enough to capture the first arrivals in deep waters (>5 km). Subsequently, most of the previous studies on upper oceanic crust were based on wide-angle seismic studies, which have a low resolution in the upper crust. Boreholes provide accurate information on the upper oceanic crust but are limited in age. Due to lack of data for mature crustal ages (>40 Ma), the evolution of upper oceanic crust has been limited to ∼10 Ma (*Carlson*, 2004). The upper oceanic crust is divided into layer 2A and the underlying layer 2B. The layer 2A is primarily composed of extrusive lava flows and has a lower P-velocity that the underlying layer 2B. The interpretation of layer 2B and the layer 2A/2B boundary have been both debated upon. In some studies, the layer 2B is considered to be the sheeted dyke layer or the intrusive lava flow (*Harding et al.*, 1993) whereas in others it is interpreted to be a hydrothermally altered unit within the lava flow (*Vera et al.*, 1990). Some studies propose a combination of the two at different study regions (*Christeson et al.*, 2010; *Carlson*, 2011) but do not provide an integrated picture of the observations.

To overcome the above limitations, I analysed 0-75 Ma upper oceanic crust from the MCS data. First, I identified the layer 2A event in seismic records based on the waveform modeling in chapter 2. This layer 2A event is observed throughout 0-75 Ma in the upper oceanic crust and indicates a high velocity gradient at the base of layer 2A. To obtain the sub-surface images and the information in two-way time (TWT), I performed seismic data processing as described in chapter 2. By picking the seafloor, the basement and the layer 2A event from 0-75 Ma from the sub-surface images, I obtain the sediment TWT thickness and the layer 2A TWT thickness. I observed that the layer 2A TWT thickness rapidly decreases from ∼500 ms TWT at the ridge-axis (zero-age) to ∼300 ms off-axis. The uncertainities in imaging layer 2A are obtained as ±30-70 ms TWT. Then to obtain the upper crustal P-velocities, I perform the two-step procedure of downward wavefield extrapolation and travel-time tomography as described in chapter 2.

At the ridge-axis, P-velocities of ∼2.5 km/s are obtained which rapidly increase to ∼4 km/s by 4 Myr. I observe P-velocities at top of the crust to be <4.5 km/s at all ages with most of the evolution happening from 0-4 Ma. The TWT thickness of layer 2A from the sub-surface images is then used to obtain the physical thickness of layer 2A using the tomography velocities. Subsequently, a ∼900 m thick layer 2A is observed at the ridge-axis which rapidly thins to ∼770 m at 4 Myr and further thins to ∼600 m at 15 Myr. The uncertainties in the depth estimates correspond to ±165-365 m. Two distinct thinning rates from 0-4 Myr and 4-15 Myr of layer 2A are observed and attributed to high temperature (active) and low temperature (passive) hydrothermal circulation. Beyond 15 Myr, not much change in physical thickness of layer 2A is observed. Interestingly, the sediment thickness rapidly increases away from the ridge-axis where it is negligible to ∼170 m at 4 Myr. The estimated deposition rates for the decompacted (*Alibés et al.*, 1996) sediment thickness (∼240 m for present day thickness of ∼170 m) corresponds to 47 mm/kyr and matches well with the IODP borehole 108 site 662-663 drilling results (*Ruddiman and Janecek*, 1989). These results indicate that the rapidly increasing thick sediment cover and the reducing intensity of heat for hydrothermal circulation away from ridge-axis limit the extent of active hydrothermal circulation until 4 Myr.

P-velocities at top of the layer 2B are observed to be gradually increasing from ∼4.5 km/s at the ridge-axis to ∼5.5 km/s until 46 Myr. This is the first dataset that records an increase in layer 2B velocities until 46 Myr, as most of the previous studies limited the evolution of layer 2B to 0.5 Ma (*Newman et al.*, 2011). It also implies seawater penetration and hydrothermal alteration is not limited to layer 2A and extends well below it. Porosity estimates of layer 2A and 2B from their respective P-velocities (*Taylor and Singh*, 2002) indicate that the borehole (*Carlson*, 2011, 2014a) and seafloor gravity-based (*Holmes and Johnson*, 1993) porosities are observed from this data set if layer 2A has three times thinner cracks than layer 2B. This also explains for a high-velocity gradient in layer 2A relative to layer 2B as thinner cracks show a sharper increase in P-velocity when sealed (*Wilkens et al.*, 1991) due to phenomena such as hydrothermal alteration.

Typical P-velocities of ∼5.9 km/s are observed off-axis at depths of 1 km below the basement. These have been found to be close to the P-velocities of sheeted dykes from borehole studies (*Carlson*, 2011). By comparing the P-velocities of layer 2B with the P-velocities 1 km below the seafloor/basement, it is observed that while at zero-age the velocities are similar, at older ages the layer 2B velocities become

distinguishably lower than the velocities 1 km below the basement. This implies that the layer 2B corresponds to sheeted dykes at zero-age and off-axis is likely to be a hydrothermal alteration boundary within the lava flow. The rapid increase of layer 2A velocities until 4 Myr and the gradual increase in layer 2B velocities until 46 Myr indicate that thinner cracks seal rapidly in young oceanic crust and thicker cracks gradually seal with age due to hydrothermal circulation (*Shaw*, 1994).

I also use the co-located conductive heatflow data from 2017 expedition to validate my hypothesis of a continuous hydrothermal system from tomography P-velocities. The observed heatflow data is found to be lower than the predicted heatflow off-axis at distinct ages. This difference in predicted and observed heatflow is attributed to lateral redistribution of heat due to circulating seawater, which in turn implies that the hydrothermal circulation continues off-axis as proposed from tomography results. I also use an analytic approximation of the Darcy's law (*Fisher et al.*, 2003) to compute the bulk permeabilities from the heat-flow measurements. With the porosities estimated from tomography P-velocities and bulk permeabilities from heatflow measurements, I compare the porosity-bulk permeability values with some existing models of percolation theory. With the exception of the analysis of heatflow data, this chapter has been published in *Geochemistry,Geophysics,Geosystems* (https://doi.org/10.1029/2019GC008577).

3.1 Introduction

Chapter 1 introduces the limitations of the existing studies of the upper oceanic crust. These include lack of data for mature crustal ages and lack of resolution in uppermost crust from existing wide-angle data. The TransAtlantic ILAB 2015 expedition overcame these limitations by acquiring active source multi-channel seismic reflection (MCS) data using a 12 km long streamer sampling oceanic lithosphere from 0-75 Ma (chapter 1). In this chapter, I analyse ∼1400 km of the MCS data for determining age-related variations of the sediment and upper oceanic crust.

The three ridge-perpendicular parts of the profile were extracted (refered to as Leg 1, Leg 2 and Leg 3 and described in chapter 1) as the objective was to consider a variation with age. The water-velocity (1.5 km/s) migrated stack section is shown in figure 3.1 for the three Legs of the profile. This minimal processed seismic image gives information about the seafloor, sediment cover and basement topography.

To create a single continuous flow line from 0-75.6 Ma, the three Legs of the MCS data were combined together. Leg 1 (0-7.7 Ma) and Leg 2 (1.8-46.7 Ma) had overlapping age ranges from 1.8-7.7 Ma and hence the part of Leg 1 from 1.8-7.7 Ma has been omitted from this study and was carried out by *Hanchao Jian (IPGP)*. The resulting Leg 1 (0-1.8 Ma) along with Leg 2 (1.8-46.7 Ma) and Leg 3 (49.3-75.6 Ma) are illustrated by black lines in figure 3.2. Also shown in red lines are the regions where downward continuation and tomography have been performed (discussed later in section 3.7). Figure 3.2 also shows in cross marks the distinct conductive heatflow meaurements made in the 2017 LITHOS expedition as described in chapter 1 (discussed later in section 3.12).

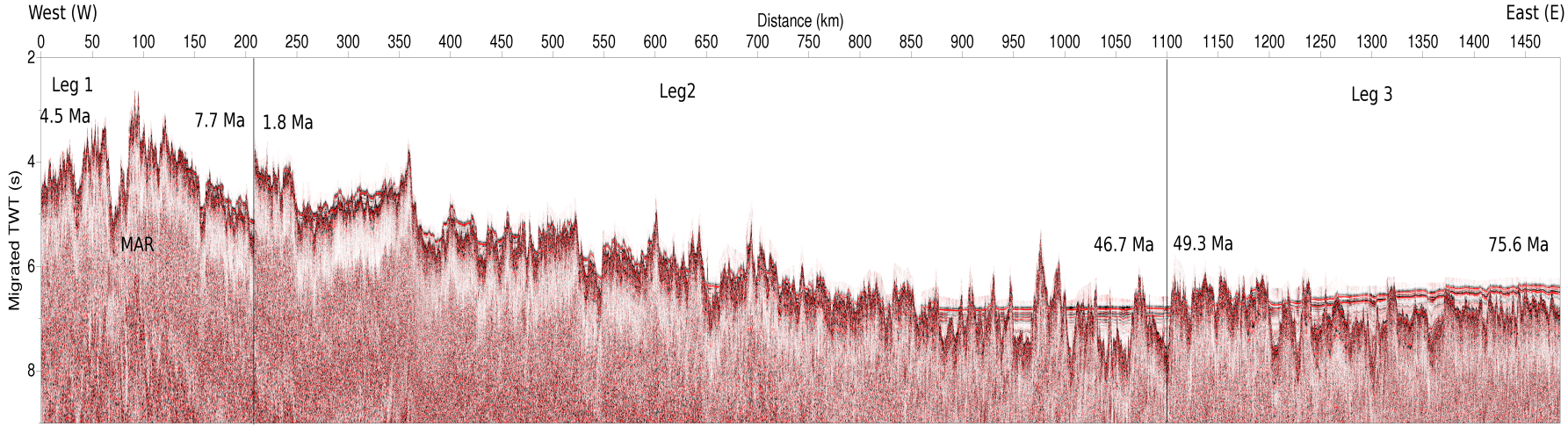

Figure 3.1: Water-velocity (1.5 km/s) migrated stack section combined for all three Legs (ridge perpendicular profiles). The distance 0 km represents an age of 4.5 Ma on the South American plate. At ∼70 km, the median valley of the ridge axis is seen. Leg 1 ends at ∼200 km distance at an age of 7.7 Ma on the African plate. Leg 2 begins at ∼200 km distance and an age of 1.8 Ma on the African plate and continues until a distance of ∼1100 km which represents an age of 46.7 Ma. Leg 3 begins at ∼1100 km and continues until almost 1500 km distance spanning an age range of 49.3 Ma to 75.6 Ma. Only 0-1.8 Ma of Leg 1 was considered and combined with Leg 2 and Leg 3 to form a continuous flow line from 0-75.6 Ma (see text).

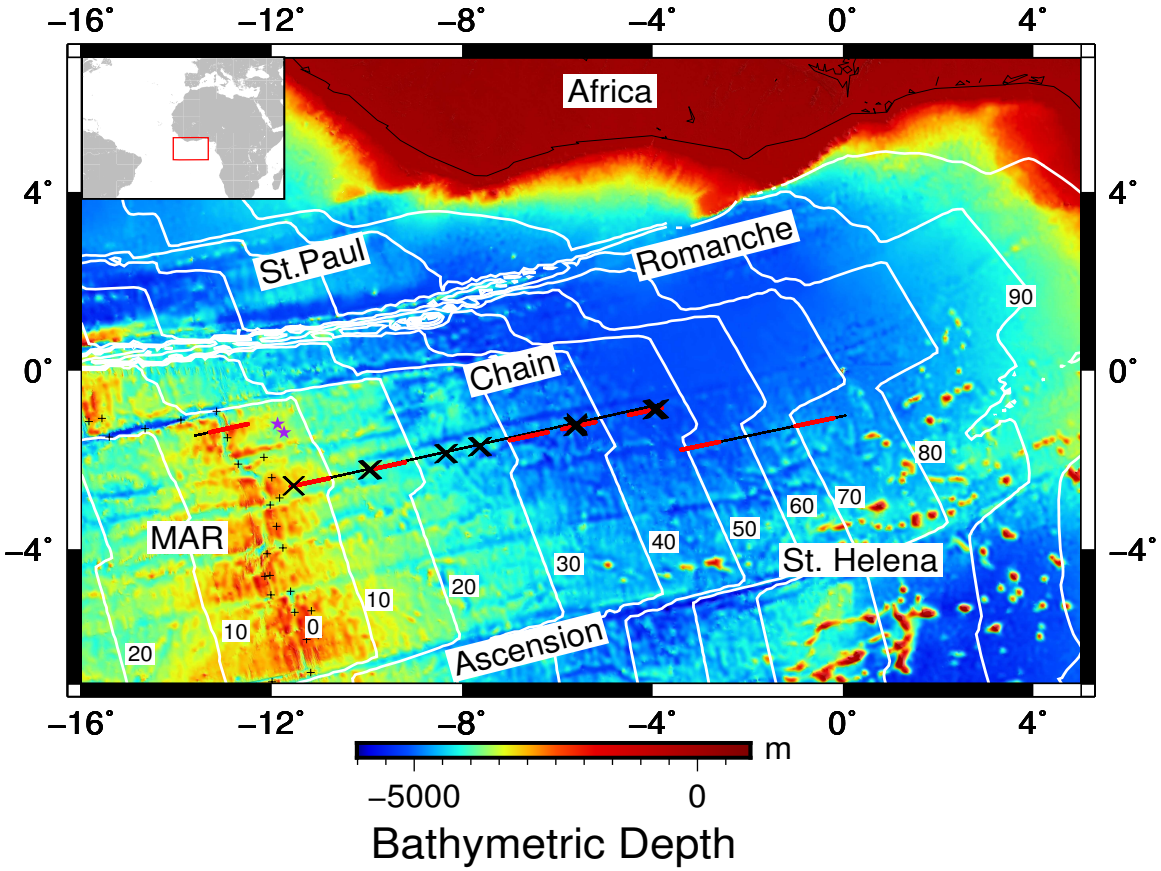

Figure 3.2: Bathymetric map of the study region (*Olson et al.*, 2014) showing the ridge-perpendicular parts of the multi channel seismic profile in black. The red parts of the profile indicate where downward continuation and tomography have been performed. The cross marks denote the locations of conductive heatflow measurements from LITHOS cruise. The IODP Leg 108 sites 662 and 663 (*Ruddiman and Janecek*, 1989) have been marked by purple stars. The age contours have been plotted at every 10 Ma in white from *Müller et al.* (2008).

3.2 Seafloor and basement morphology

After obtaining a continuous flow line from 0-75.6 Ma (figure 3.2) I picked the seafloor and the basement all along the profile from figure 3.1 (omitting the overlapping profile from 1.8-7.7 Ma) and depth converted using water velocity (1.5 km/s) and sediment velocity (discussed shortly in the next section). This is shown in figure 3.3b. The median valley of the ridge-axis has now been placed at 0 km distance. The distance of the single continuous flow line is almost 1300 km and has been used for analysis in this whole thesis. The basement morphology as seen throughout the profile is quite rough, which is typical of crust formed at slow spreading ridges (*Ranero et al.*, 1997). A distinguishing feature of slow-spreading centres is a median valley at the ridge-axis in comparison to fast spreading centres which are marked by an uplift at the ridge-axis. The basement topography seems to have three distinct steps of subsidence: 50-180 km, 200-370 km and 370-500 km. The region of 50-180 km is characterized by an uplift rather than a subsidence. Another distinct feature that is observed is the onset of a sudden thick sediment cover starting at 650 km. I elaborate more on the sediments shortly in the next section (section 3.3).

Figure 3.3a also shows the half-spreading rate extracted along the MCS profile in figure 3.3b from *Müller et al.* (2008) (red solid line). The 2.6 Myr age gap between Leg 2 (ending at 46.7 Myr) and Leg 3 (starting at 49.3 Myr) is visible in figure 3.3a (blue solid line) at ∼900 km distance. The present half-spreading rate is 16 mm year^{-1}, which is in good agreement with other plate spreading models such as NUVEL-1 (*DeMets et al.*, 2010). Farther away from the ridge-axis, the half-spreading rate ranges between the upper limit of 23 mm year^{-1} at 610-780 km distance and a lower limit of 9 mm year^{-1} at 1030-1100 km distance. These values lie in the lower end of two extremes - 28°S East Pacific Rise, which is the fastest spreading centre and where the half-spreading rate reaches 150 mm year^{-1} (*Arora et al.*, 2011), and the Gakkel Ridge, which is the slowest spreading centre and where the half-spreading rate is ∼6 mm year^{-1} (*Jokat et al.*, 2003).

(a)

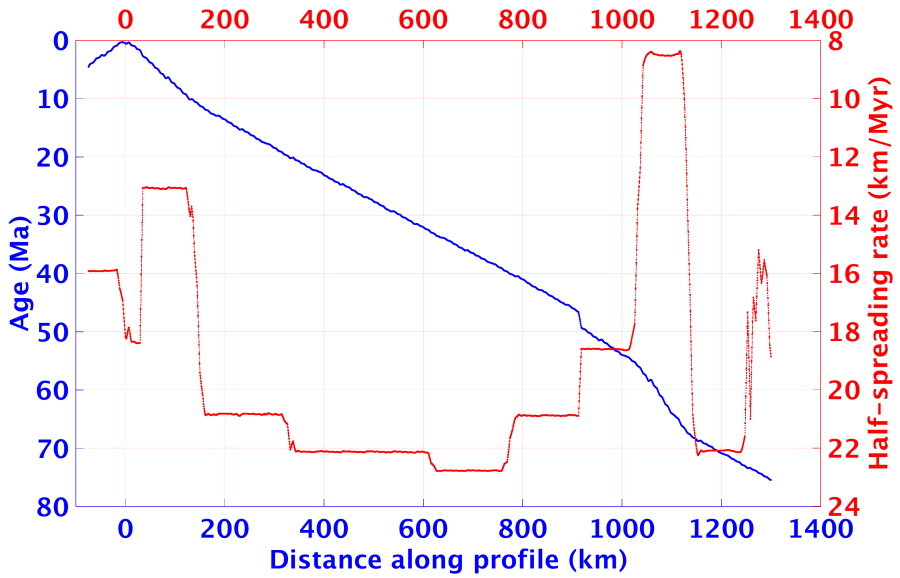

(b)

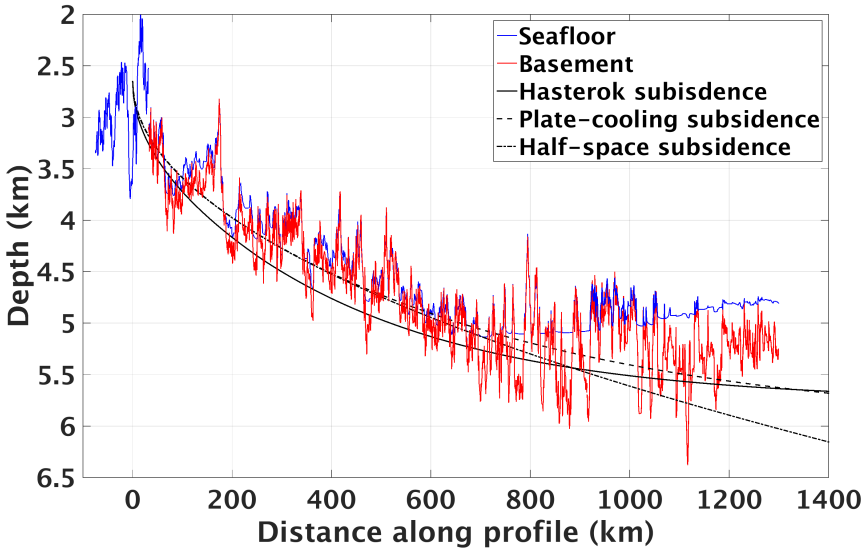

Figure 3.3: (a) The seafloor age and half-spreading rate along the profile obtained from *Müller et al.* (2008). (b) The seafloor and basement along the whole profile is shown along with different subsidence models (described in text and introduced in chapter 1).

From 650 km onwards in figure 3.3b, the seafloor flattens and rises towards the older lithosphere, which could be due to the thickening of the sediments near the African margin. However, there are large topographic features between 750-1300 km, not covered by the sediments. Interestingly, there lies two chains of seamounts to the east of our profile - St. Helena and Cameroon Volcanic Line as introduced in chapter 1. It is possible that these features might have been formed due to these volcanic chains. Furthermore, there is also a slight decrease in the average basement depth between 900-1300 km, possibly due to mantle upwelling and higher thermal anomaly associated with the adjacent volcanic chains. This subject is further investigated in depth in chapter 4.

The variation of basement topography from 0-75 Ma in figure 3.3b can be compared with subsidence models as introduced in chapter 1. The spreading rate for the plate cooling model (chapter 1) is taken from figure 3.3a as 16.8 mm/yr (mean value). The different subsidence models (half-space, plate cooling) depend on the ridge-axis (zero-age) depth (denoted by d_r in chapter 1). The ridge-axis depth for these subsidence models was obtained by taking the least squares fit of the subsidence with the basement topography from 0-46.7 Ma. The basement topography from 49.3-75.6 Ma (Leg 3) was not taken as it became apparent that it was not following the subsidence trend and was uplifted relative to the rest of the profile from 0-46.7 Ma. The least squares ridge-axis depth is found to be 2653±20 m, which lies within

the range of values proposed by most other studies mentioned above (2500±200 m) and is strikingly similar to the value proposed by *Crosby and McKenzie* (2009) of 2652 m on the basis of global residual gravity and topography. A modification of the half-space subsidence (*Hasterok*, 2013) has advantages over other subsidence curves as explained in chapter 1 and has been used here. Hence the best fit curve in a least squares sense to the basement subsidence of the MCS profile from 0-46.7 Ma is given by the equation:

$$d(t) = 2653 + 414.5\sqrt{t} \quad \text{if} \quad t \leq 17.4 \quad \text{Myr} \tag{3.1}$$

$$d(t) = 5762 - 2520e^{-0.034607t} \quad \text{if} \quad t > 17.4 \quad \text{Myr} \tag{3.2}$$

The above subsidence curve is plotted in figure 3.3b in black solid line for a ridge-axis depth of ∼2653 m. With respect to this subsidence model, I computed a mean uplift of 270±20 m in the Leg 3 of the profile from 49.3-75.6 Ma. I further follow up on this in chapter 4 and infer scientifically.

In order to look at some of the basement features more closely, I took the help of co-located high resolution bathymetry from the 2017 LITHOS cruise. For instance, two close seamounts as observed on the MCS profile at ∼800 km distance were resolved to be a 11-km diameter seamount caldera from the co-located bathymetry data. This is shown in figure 3.4a. It can be seen that this feature was not formed at the ridge axis due to no-correlation with spreading rate in figure 3.3a. Whether this feature is linked to adjacent volcanic chains further east is the subject of chapter 4. Another feature at ∼180 km distance which marks the transition from basement uplift to basement subsidence was also not found to be correlated to the plate spreading and hence must not have been formed at the ridge-axis. This is shown in figure 3.4b. Further work on this feature is being carried out by *Venkata Vaddineni, IPGP*.

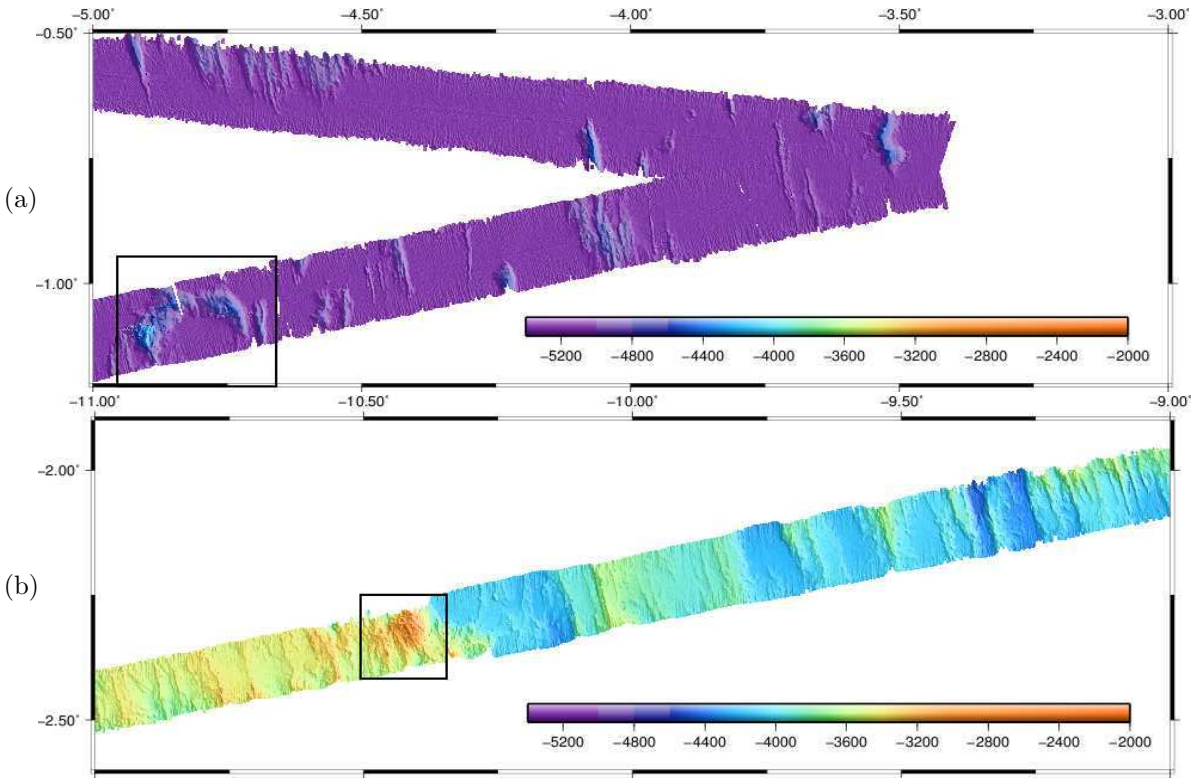

Figure 3.4: (a) High resolution 11-km swath bathymetry image from the 2017 LITHOS cruise at ∼800 km distance in figure 3.3b and (b) at ∼180 km distance in figure 3.3b. The features elaborated in text are highlighted in black rectangles. 0.5° of longitue/latitude represents 55 km along track distance. Credit: *Ingo Grevemeyer*.

3.3 Sediment cover

Figures 3.1 and 3.3b show the sediment distribution with age along the MCS profile. No sediment cover is observed at the ridge-axis followed by a fluctuating sediment cover in the basement valleys. The LITHOS cruise in 2017 had also collected Ocean bottom seismometer (OBS) data along the same profile from 0-50 Ma. A study was carried out to correlate the sediment thickness and the corresponding P-to-S delay observed in the OBS data due to the sediment column (*Ferrante et al.*, 2020). Figure 3.5 shows the comparison between the P-to-S delay due to sediments observed in the OBS and the sediment two-way time thickness observed in the MCS. The mostly positive correlation from the wide-angle OBS data set of the 2017 LITHOS expedition and the 2015 ILAB MCS data set further supports the estimates of sediment thickness obtained in this study.

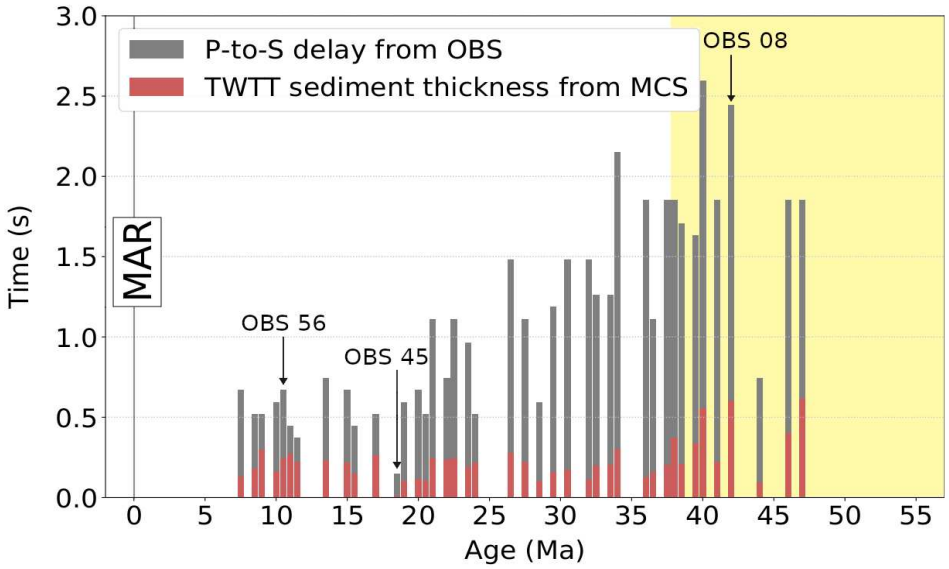

Figure 3.5: Correlating the sediment thickness in two-way time from MCS data from 2015 ILAB expedition and the P-to-S delay observed on co-located wide-angle OBS data from 2017 LITHOS expedition due to sediments. Each bar represents an OBS. Figure 3 in *Ferrante et al.* (2020).

The MCS profile has a jump from Leg 1 to Leg 2 at 1.8 Ma with the two Legs being offset laterally by ~172 km (chapter 1). While the ridge-axis is covered in Leg 1 of the MCS profile, Leg 2 does not cover the ridge-axis and begins from 1.8 Ma old lithosphere (figure 3.2). In order to ensure that my results are equally valid for the ridge axis beyond Leg 2, I analysed the available parasound data for the 0-50 Ma old lithosphere co-inciding with Leg 2 from 1.8-46.7 Ma which was acquired on the 2017 LITHOS expedition. While a thick sediment cover could be found at 47 Ma (figure 3.6b), no sediments could be found at the ridge axis (figure 3.6a) just like the ridge axis from the MCS profile on Leg 1. Hence similar sediment thickness is observed in MCS data on ridge-axis crossing profile in Leg 1 that I have used and the parasound data on ridge-axis crossing profile in Leg 2.

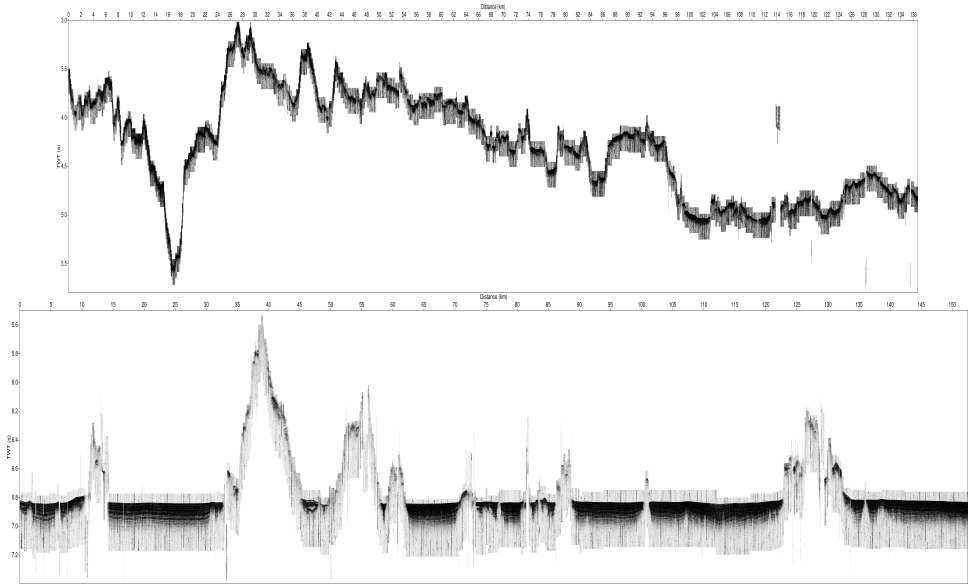

Figure 3.6: High resolution images at 3 kHz of the near surface from Parasound data. (a) The image at the ridge-axis crossing the Leg 2 of the profile and (b) the image at the 47 Ma. A sediment cover is not visible at the ridge axis similar to my observed at the ridge axis on Leg 1 traversed by the MCS profile. Hence the sedimentation curve is valid though it spans a jump at 1.8 Ma from Leg 1 to Leg 2.

In order to obtain a physical thickness of the sediments, I performed semblance-based velocity analysis to estimate the sediment velocities from pre-stack seismic data in regions with a flatter basement morphology. The average sediment P-velocities were then obtained by Dix conversion (*Dix*, 1955) of root mean square (RMS) velocities at distinct ages and have been mentioned in table 3.1. The estimated uncertainty in these velocities is ±25 m/s. No clear trend of the sediment velocities with age is distinguishable. These sediment velocities in table 3.1 have been used to depth convert the sediment two-way time thickness from figure 3.3b and is shown in Figure 3.7.

Table 3.1: Sediment P-velocities at distinct ages as obtained by Dix inversion (*Dix*, 1955) of stacking velocities

Age (Ma)	Sediment P-velocities (m/s)
75	1850
50	1820
46	1820
38	1765
30	1712
23	1643
15	1685
4	1784

I also extracted the sediment thickness from the global dataset (*Whittaker et al.*, 2013) along the MCS profile shown in black curve in Figure 3.7. A higher sediment thickness from 2-38 Myr and a lower sediment thickness in the rest of the profile is observed as compared to the global study of *Whittaker et al.* (2013). Lastly, I also plot the sediment deposition rates from *Agius et al.* (2018) in the Equatorial Atlantic from P-to-S seismic phase conversion at sediment-crust boundary. Whereas Figure 3.5 shows a good correlation between P-to-S delay and my estimated sediment thickness, the same is not observed for *Agius et al.* (2018), who acknowledge their estimated rates of deposition to be a lower limit. However, the sediments observed today have been compacted and hence do not represent the thickness at the time of deposition. To compute the decompacted sediment thickness, I used the relation from *Agius et al.* (2018) which is based on *Alibés et al.* (1996): decompacted thickness = 0.6974*compacted thickness$^{1.1507}$. Decompacted sediments at the time of formation can be ∼40% thicker as compared to the compacted sediments as observed today (*Alibés et al.*, 1996). *Agius et al.* (2018) estimate sediment deposition rates

of 5 mm/kyr for seafloor younger than 10 Myr and 1.2 mm/kyr for older seafloor. I observe much higher rates of sedimentation of 47 mm/kyr for the first 4 Myr with the decompacted sediment thickness reaching a maximum of ∼240 m for a compacted sediment thickness of ∼170 m. This is in agreement with the IODP Leg 108 cores drilled on sites 662 and 663 (Figure 3.2) (*Ruddiman and Janecek*, 1989), which sampled sediments to 200 m depth and estimated rates of deposition between 30-50 mm/kyr (*Ruddiman et al.*, 1989a).

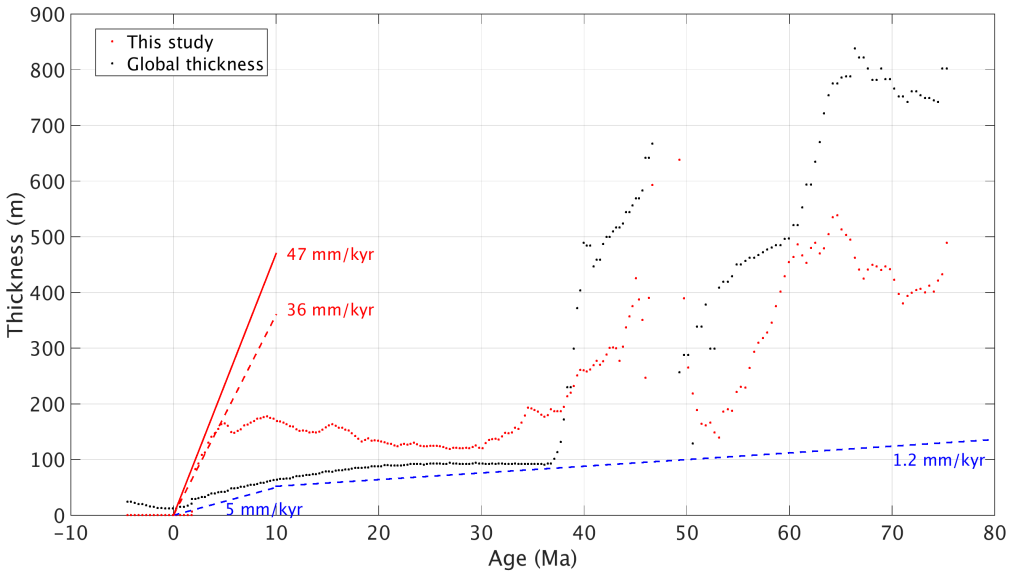

Figure 3.7: Sediment thickness obtained in this study (red curve) and its variation with age. Global sediment thickness estimates from *Whittaker et al.* (2013) are shown in black. The sedimentation rates for both compacted and decompacted sediments (*Alibés et al.*, 1996) is also plotted in dashed red and solid red respectively. Also shown in blue dashed lines are sediment deposition rates from *Agius et al.* (2018) in the Equatorial Atlantic from P-to-S seismic phase conversion at sediment-crust boundary.

The sediment thickness increases rapidly for the first 4 Myr, and decreases slightly up to 30 Myr, and then again increases linearly up to 75 Myr (Figure 3.7), suggesting that the sediments up to 30 Myr are of pelagic origin whereas those from 30-75 Myr might have hemipelagic/turbiditic origin. *Khripounoff et al.* (2003) report activities of turbidity currents in the Congo-Angola continental shelf extending 760 km from the river mouth to the abyssal plain with a down-slope of more than 5100 m and covering an estimated area of 0.3 million km^2. *Ittekkot* (1988) showed that 65% of the total organic matter is refractory and is carried into the deep-ocean by mid-water transport (*Walsh*, 1988), so it can be inferred that the eastern end of the seismic profile is under the influence of the Congo deep sea fan. I further examine the relationship between the paleo-sedimentation rates in the Atlantic, paleoclimatic conditions of north-western Africa and wind-driven coastal upwelling, the glacial-interglacial period and oceanic productivity of organic matter (planktons) and the fluctuations in carbon dioxide reserves in the atmosphere and the deep ocean.

The high sedimentation rate (47 mm/kyr) for the first 4 Myr could be due to increased glaciation (*Ravelo et al.*, 2004) and/or high eolian dust fluxes from Africa to the Atlantic (*Ruddiman et al.*, 1989b). An expanded sea-ice cover in the high latitudes during the last glacial maximum led to a decrease in the ocean productivity of organic matter and caused wind-driven upwelling along the north-east Atlantic coast which in turn caused an increased ocean productivity in the lower latitudes. Furthermore, *Sarnthein et al.* (1988) proposed a near-surface large-scale lateral advection of organic matter from higher latitudes to lower latitudes which also caused lowering of the sea-surface temperatures. They also attribute the large-scale carbon dioxide depletion of the deep ocean reserves and the corresponding increase of atmospheric carbon dioxide to the onset of the deglaciation period wherein a decline of low-latitude upwelling and productivity was observed. This short term change was in contrast to the long term increase of

atmospheric carbon dioxide (*Sigman and Boyle*, 2000). *Wagner* (2000) found an increase in marine organic matter by 20-60% in the glacial conditions at site 663 as compared to the interglacial conditions and related it to stronger oceanic upwelling during the late Quarternary glacial periods. North Africa exhibited arid climatic conditions since the Tortonian stage (∼7-11 Ma) (*Zhang et al.*, 2014) and the Passat and Harmattan wind systems are known to carry huge amounts of lithogenic dust in response to glacial-interglacial cycles from dry African areas to deep sea settings (*deMenocal*, 1995; *F. Ruddiman and M. Pokras*, 1993). More recently, the disintegration of the ice-sheets during the last ∼14000 years and the resulting fresh water input to the oceans has been shown to decrease the productivity of the North Atlantic deep water and sea-surface temperature anomalies, creating extreme arid conditions in Northern Africa (*Street-Perrott and Perrott*, 1990). *Wagner* (2000) found a 60% increase in terrigenious organic matter at site 663 during the glacial period corresponding to an increase in eolian dust fluxes. Total organic content has been found to be higher in upwelling site 658 as compared to non-upwelling sites 657 and 659 at the north-west African coast (*Stein et al.*, 1986). The higher organic content is attributed to higher fluvial deposits and dense vegetation cover, prior to 3.1 Ma, after which north-western Africa experienced more arid conditions.

The negative gradient slope in the sediment thickness with age between 10 to 30 Myr could be explained due to compaction. Strong bottom thermohaline intrusions as found in the North Atlantic deep waters (*Sheen et al.*, 2012) could erode the sediments, decreasing the sediment thickness. Another possibility is that most of the sediments are deposited near the ridge axis by strong current within the ridge axis and upwelling and deposition of sediments just outside of the axial valley. In this scenario, there would have been a slight increase in the sedimentation between 30 and 5 Myr.

A thicker sediment cover beyond 35 Myr is observed in which the sediment thickness almost doubles as compared to younger ages. The global sediment thickness map (*Whittaker et al.*, 2013) also finds a sudden change starting at ∼37 Ma and the variation from 37-75 Ma in the sediment thickness is also similar to our results, although it overestimates the sediment thickness by 300-400 m as compared to our results. This increased sediment cover correlates well with the sedimentation flux history of the Congo river delta which shows a higher sediment flux from 2500-3000 km^3/Myr from 5-35 Myr to <500 km^3/Myr beyond 35 Myr (*Paul et al.*, 2014a). Figure 3.8 shows the sedimentation histories of the Niger and the Congo rivers and an increase in the sediment flux of the Congo river at ∼35 Myr.

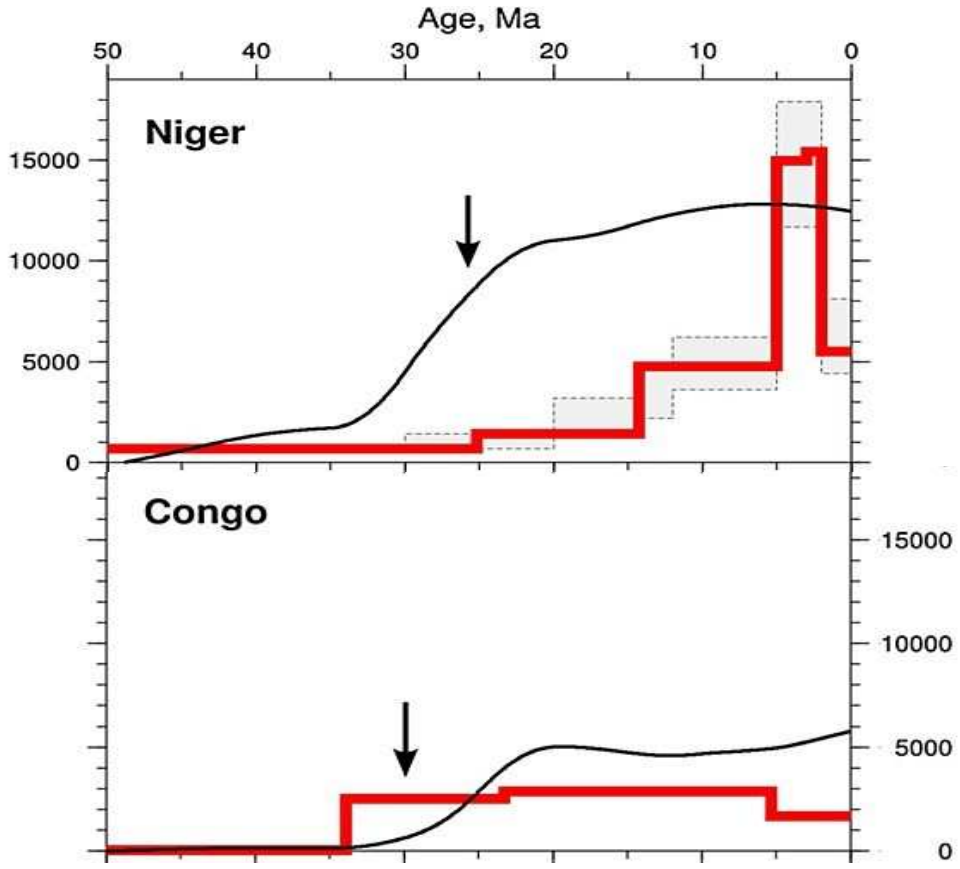

Figure 3.8: Sedimentation flux histories of the Niger (top) and Congo (bottom) rivers from *Paul et al.* (2014b). The vertical axis represents the sediment flux in km^3/Myr. The red solid line is sediment flux computed from seismic reflection profiles and well log, gray areas represent the uncertainty and the black lines are sediment flux calculated from modelling tributaries within catchment. The arrows denote the onset of clastic sedimentation.

3.4 Layer 2A in seismic records

Having visualized the triplication in synthetic shot gathers in chapter 2, I proceeded to identify layer 2A triplications in seismic records. The super-common-midpoint (super-CMP) gathers were created by combining 8-12 adjacent common-midpoint (CMP) gathers together. These super-CMP gathers were dip filtered to enhance the triplications. Figure 3.9 shows the super-CMP gathers near the ridge axis and the triplications in the zoom-in wiggle plots (right panels). I choose to show the TWT in reduced TWT so as to better enhance the triplication. Figure 3.9 shows the super-CMP gathers at different distance from the median valley on the ridge-axis. In figure 3.9a, 9 km from the ridge-axis on the South American plate, a strong amplitude arrival at 4.2 km offset and 4 s of reduced TWTT is interpreted to be the cusp of the Layer 2A/2B triplication. The bathymetry is updip relative to the streamer and a clear layer 2B arrival sloping downward is also seen clearly. In figure 3.9b which is at the median valley of the ridge-axis, energy arriving at 4 km offset and 5.5 s of reduced TWTT is interpreted to be cusp of the Layer 2A/2B triplication. A weak layer 2B arrival can be seen sloping upward starting at 6 km offset and 5.6 s TWTT since the bathymetry is downdip relative to the streamer. In figure 3.9c on the African plate at $\sim$1 Ma age, a similar arival to figure 3.9a with a strong amplitude arriving at 4 km offset and 3.5 s TWTT is interpreted to be the layer 2A arrival.

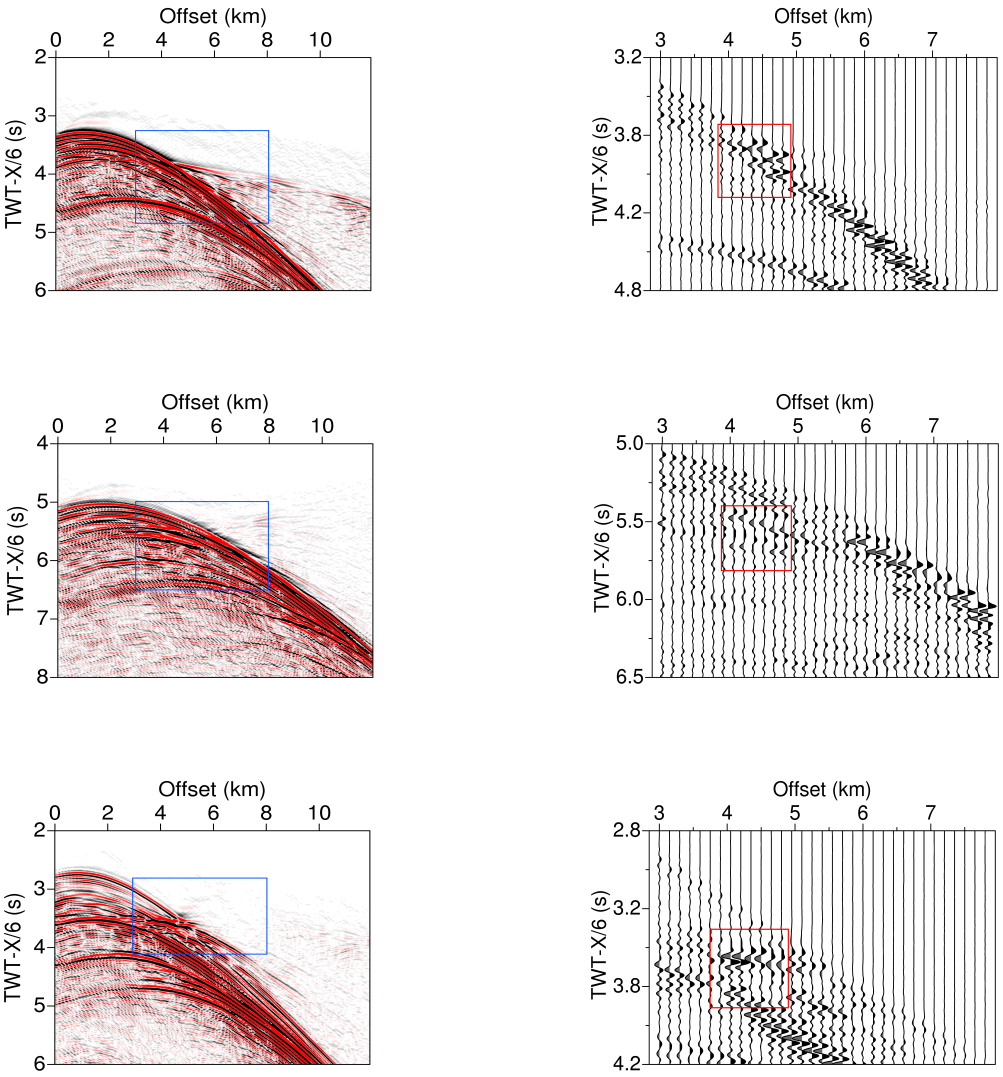

Figure 3.9: Super-CMP gathers at different locations from the ridge axis: (a) At the ridge flank on the South American plate 9 km from the ridge axis and at 2 km on the seismic section (figure 3.11b). (b) At the valley of the ridge axis and 9 km on the seismic section (figure 3.11a). (c). At the ridge flank on the African plate at 20 km from the ridge axis and at 29 km on the seismic section (figure 3.11b). The blue rectangled region has been zoomed as corresponding wiggle plots in the right panel, which highlights the triplications (rectangled in red). A reduction velocity of 6 km/s has been used for better visualization.

I also investigated the presence of layer 2A triplication at other ages, all along ∼1500 km profile. The left panel of figure 3.10 shows super-common-mid point (CMP) gathers at five different locations, at the median valley of the ridge axis (0 Ma), at ∼16 Ma, ∼31 Ma, ∼50 Ma and ∼70 Ma. The super-CMP gathers were obtained by combing eight neighboring CMP-gathers and dip filtered to remove the noise. A close examination of these data indicates the presence of triplications associated with the high velocity gradient at the base of layer 2A (right panel of figure 3.10). As one progresses towards mature oceanic crust, the effect of a thicker water column and a sediment cover move the triplication to farther offsets. At zero age, figure 3.10a, the triplication is seen to be at 4-4.5 km offsets and 5.5-6 km at 75 Ma (figure 3.10e). As found from the finite-difference modelling in chapter 2, the shifting of the triplications to farther offsets could be either due to a lower gradient (a thicker transition zone equivalently) at base of layer 2A and/or increased thickness of the water column and sediment layer.

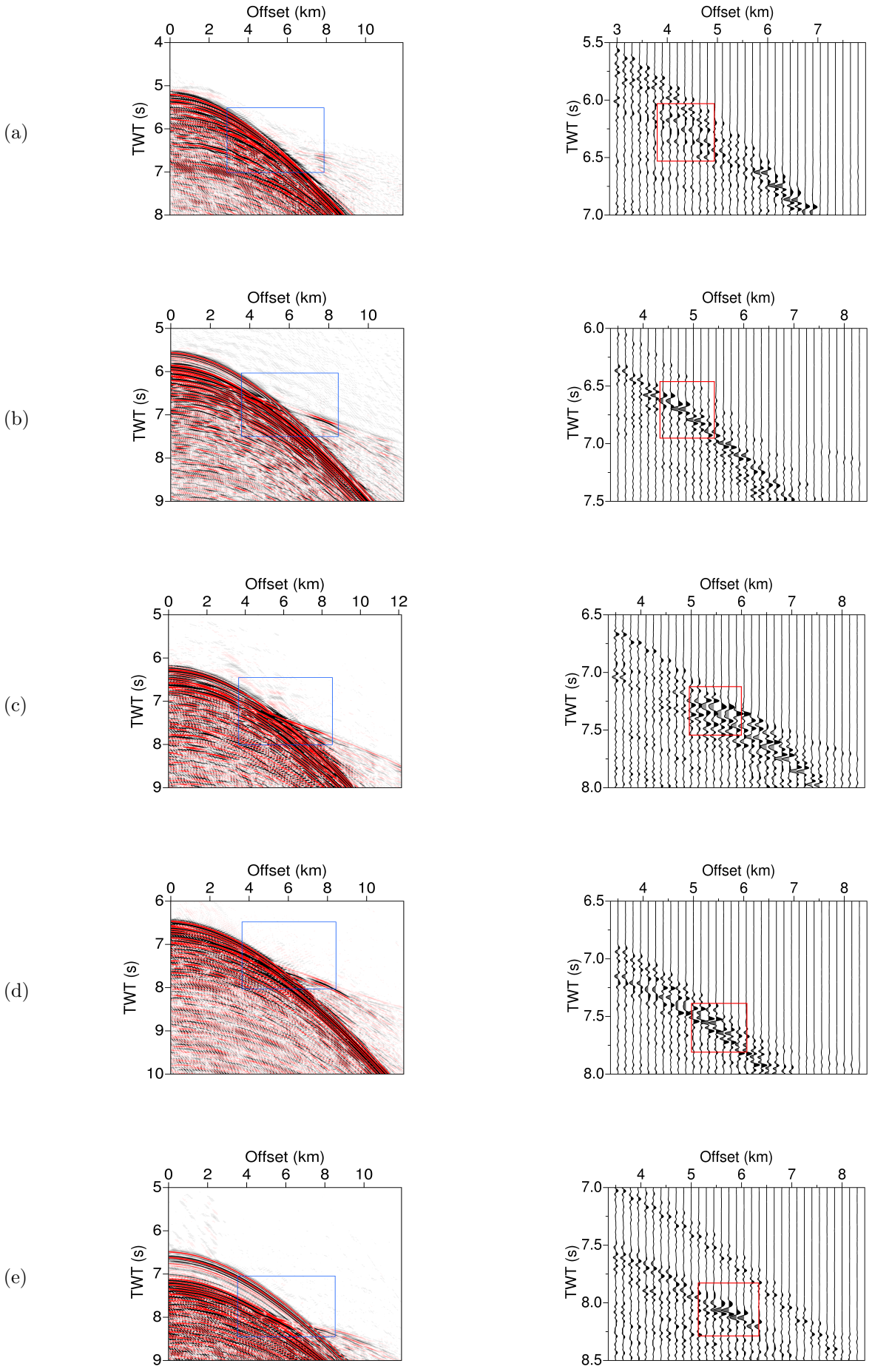

Figure 3.10: The left panel consists of dip-filtered super-common-midpoint (super-CMP) gathers showing layer 2A triplication at different crustal ages: (a) the median valley of the ridge axis (zero age) ; (b) 16 Ma ; (c) 31 Ma ; (d) 50 Ma and (e) 70 Ma. A shift in triplication can be observed towards the farther offsets as the age increases. The blue rectangled region has been expanded to highlight the triplication in the right panel (rectangled in red). The amplitudes in the right panels are much reduced.

3.5 Layer 2A images

Seismic reflection data were processed (chapter 2) to obtain the seismic image of Layer 2A from the CMP gathers at distinct ages as shown in Figures 3.11 and 3.12. I briefly describe the layer 2A events in each of the individual stack sections at distinct ages.

At the ridge axis, the median valley is observed at 5.2 s TWTT with a clear reflection of layer 2A at ∼500 ms TWTT below the seafloor (bsf) (Figure 3.11a). Due to the rugged bathymetry, the layer 2A is intermittently imaged beneath the ridge flanks at ∼550 ms bsf. The uncertainty in the layer 2A thickness is ±70 ms. Figure 3.11c shows the seismic image at 15.6-17.8 Ma with a rugged basement topography covered with up to 450 ms TWTT thick sediments. A strong amplitude layer 2A/2B event is imaged at 300 ms ± 70 ms TWTT below the basement almost throughout the profile with the thinnest in the valley at 52 km. Figure 3.11d shows the seismic image at 30.4-33.4 Ma having a rugged basement topography and a veneer of thin (100-150 ms) sediment covering the basement. The imaging of the layer 2A event is best in the western part of the profile. The layer 2A event is also imaged beyond 25 km distance with weaker amplitudes and where the basement is relatively flat. The seismic TWTT thickness of the layer 2A varies between 320-370 ms TWTT. However, towards the eastern end of the profile, the imaging of the layer 2A event is poor. The profile at 49.9-52.2 Ma has basement morphology similar to that at 30 Ma and has a thin layer of sediment (Figure 3.11e). There are three prominent basement valleys - at 15 km, at 40 km and at 57 km on the profile with sediment thickness varying between 300 ms and 200 ms TWTT. The layer 2A event can be observed (300 ms TWTT below the basement) throughout the profile with varying amplitudes. Figure 3.11f shows the seismic section at 68.6-71.9 Ma, which is at the eastern end of the profile, having an average of ∼500 ms TWTT thick sediment cover, with the maximum being 700 ms at the central basement valley from 27-32 km on the profile. The layer 2A event is weak, less continuous and lies roughly ∼300 ms ± 30 ms below the basement.

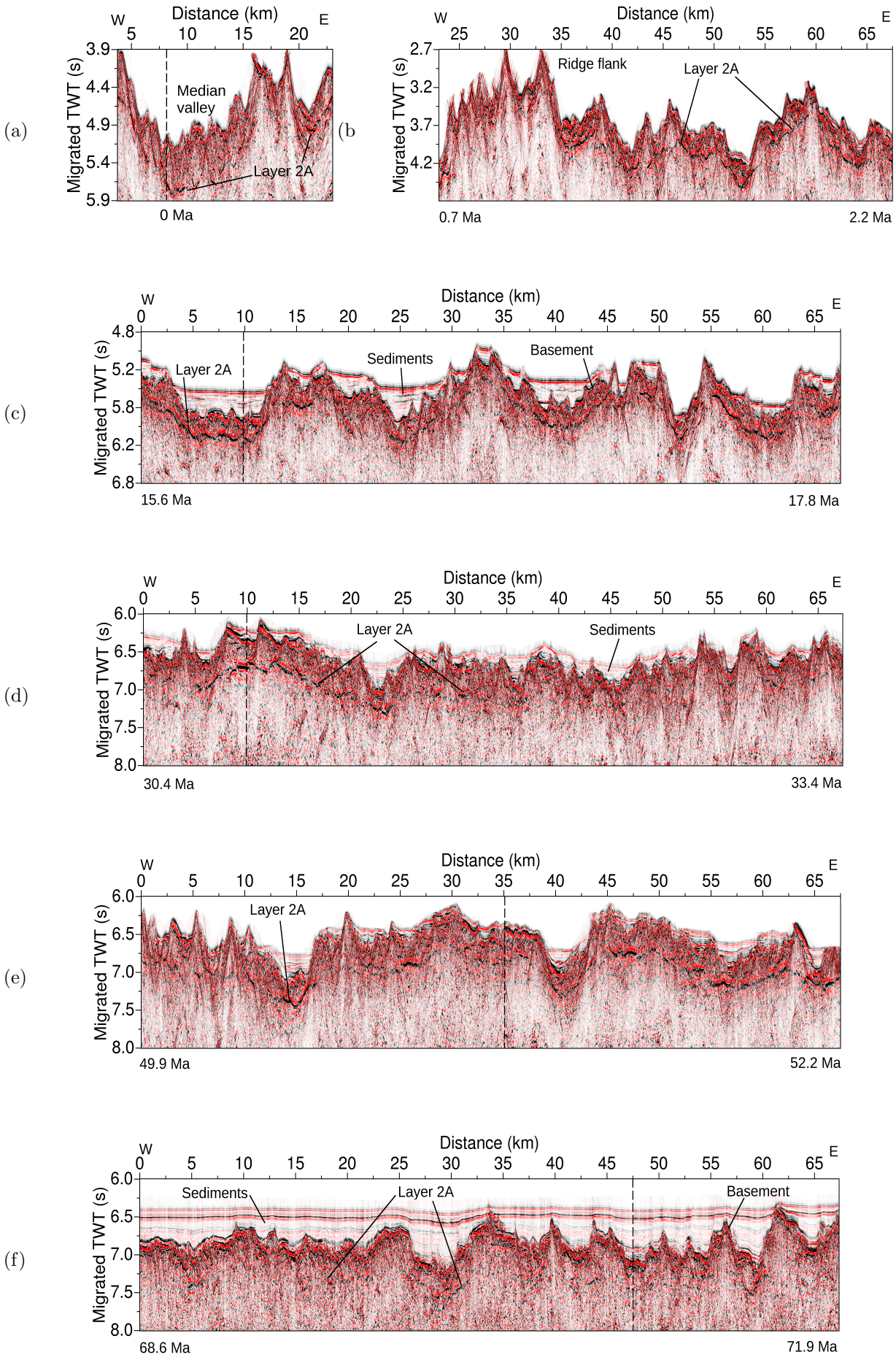

Figure 3.11: Post-stack seismic sections showing the layer 2A event at different crustal ages: (a) Median valley of the ridge-axis ; (b) 0.7 Ma to 2.2 Ma; (c) 15.6 to 17.8 Ma ; (d) 30.4 to 33.4 Ma ; (e) 49.9 to 52.2 Ma and (f) 68.6 to 71.9 Ma. The black dashed line shows the location of the super-CMP gathers in Figure 3.10.

(a)

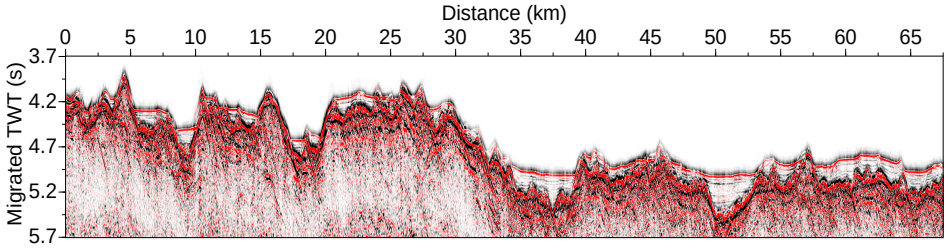

(b)

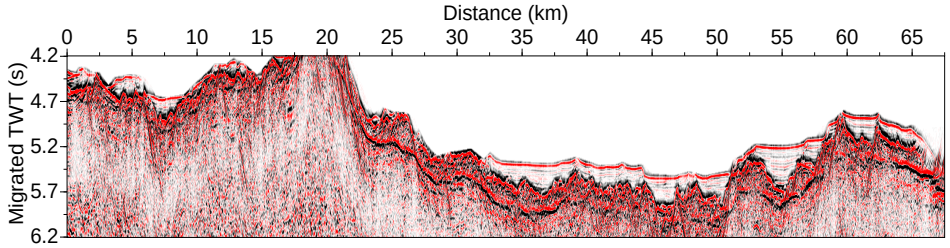

(c)

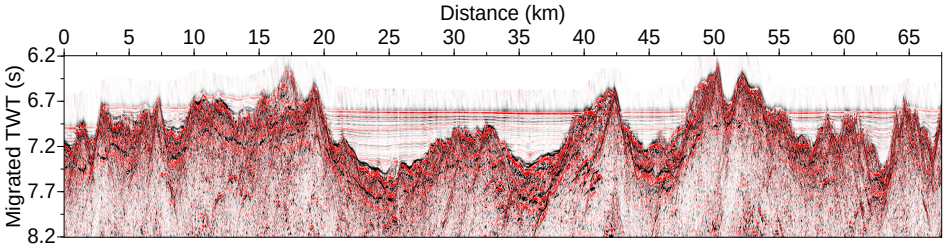

(d)

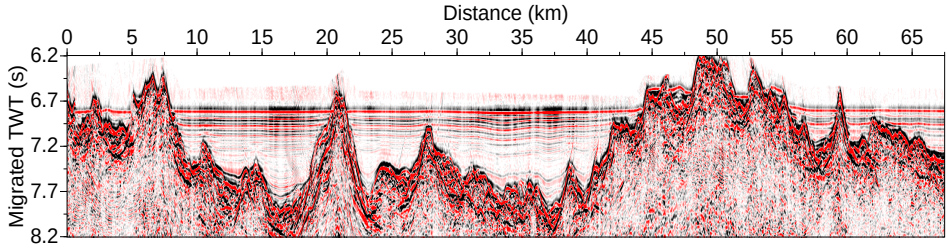

Figure 3.12: Additional layer 2A images at distinct ages: (a) 3.1-6.3 Ma; (b) 11.2-14.7 Ma; (c) 35.1-38.9 Ma; (d) 43.7-46 Ma.

After obtaining the best possible images of the layer 2A event at distinct ages as shown in Figures 3.11 and 3.12, I picked the layer 2A event in two-way time to obtain its variation from 0-75 Ma, similar to my seafloor and basement picks in figure 3.3. The seafloor, basement and layer 2A event picks for the whole profile are shown in Figure 3.13a. The variation of seafloor and basement topography along with basement subsidence have been previously discussed in section 3.2.

(a)

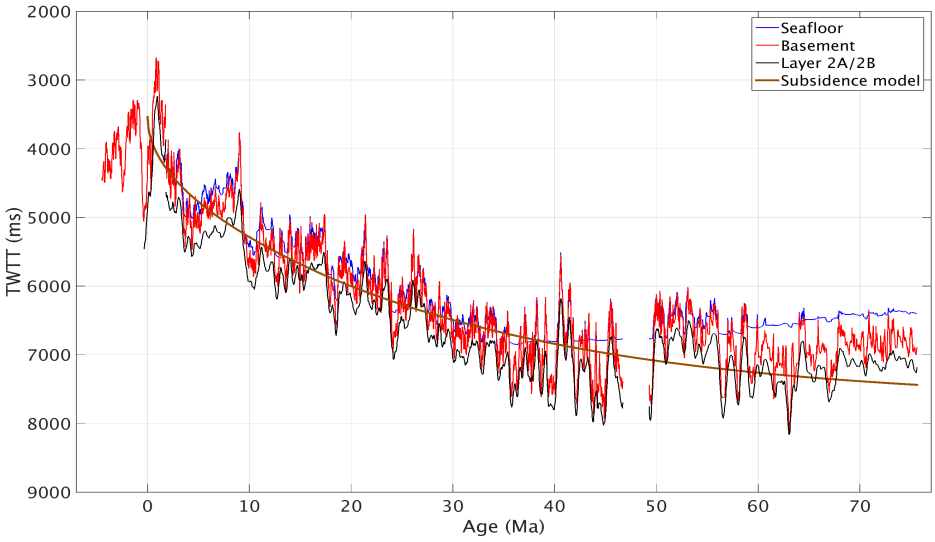

(b)

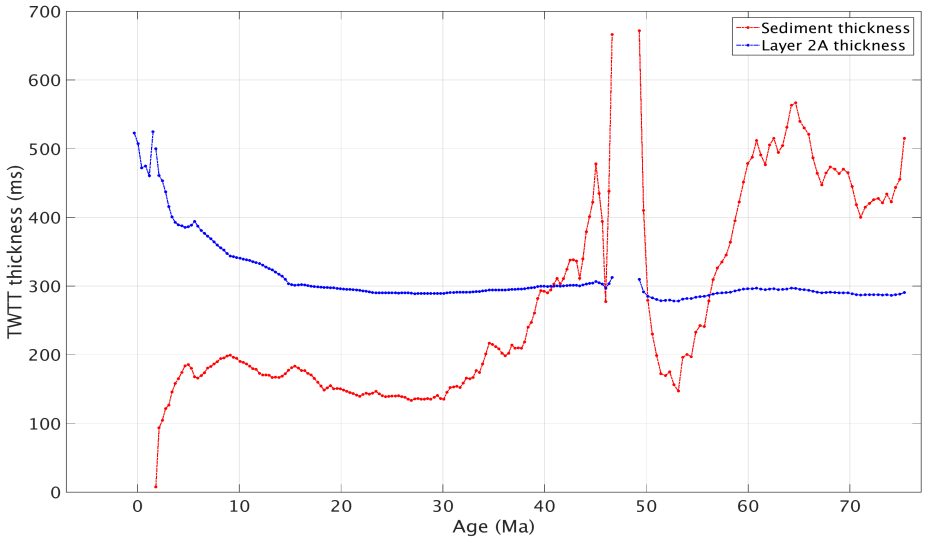

Figure 3.13: (a) Age versus two-way travel time plots for seafloor, basement and layer 2A/2B across the ridge-perpendicular segments of the profile. The ridge axis corresponds to zero age. The subsidence of the oceanic crust can be observed as one moves away from the ridge axis. The theoretical subsidence model has been plotted on the basis of *Hasterok* (2013). Onset of a thicker sediment cover can be seen at 35 Ma on the African plate. An uplifted basement can be seen at 75 Ma which is near the Cameroon Volcanic Line. (b) A smoothed version of sediment thickness and layer 2A thickness computed from (a). A gradual increase in sediment cover thickness can be observed as one moves away from the ridge axis with the maximum thickness being ∼ 500 ms TWT at 65 Ma. The layer 2A TWTT thickness rapidly decreases from 500 ms at zero age to 350 ms at 10 Ma and reaches a minimum of 280 ms at ∼25 Ma. The seismic TWT thickness of layer 2A derived from the stack sections has an uncertainty of ±30 ms where the basement is relatively flat and ±70 ms where the basement is rugged (chapter 2).

Figure 3.13b shows a smoothed version of the layer 2A and sediment TWT thickness for the whole profile. A decrease in the TWTT thickness of seismic layer 2A is seen with increasing age. At the ridge axis, a ∼500 ms TWTT thick seismic layer 2A is observed. The layer 2A thickness decreases rapidly to ∼350 ms up to ∼10 Myr, then linearly decreases to 300 ms at 15 Myr and reaches to a minimum of 280 ms TWTT at 25 Myr. A slight increase is observed beyond 25 Myr until 45 Myr, which then remains constant up to the end of the profile at about 300 ms. The sediment thickness linearly increases with age until 4 Myr, with a peak at 9 Myr (200 ms) and decreases to ∼140 ms during the next 20 Myr. From 30 Myr onwards, a linear increase is observed with the maximum sediment thickness reaching to ∼470 ms TWTT at 45 Ma. An anomalous increase in the sediment thickness around 49 Myr is due to the large distance from the Congo river along this segment of the profile. The mean sediment thickness at the

end of the profile is 450-500 ms TWTT. Interestingly, a strong correlation is observed in the increase of sediment cover and decrease in layer 2A thickness within the first 4 Myr.

The next step was to obtain P-velocities to further constrain the evolution of the upper oceanic crust and to convert the two-way travel time information obtained to depth which I describe below.

3.6 Interval velocity estimation from stacking velocities

Similar to estimation of sediment P-velocities from root mean square (RMS) velocities by Dix inversion (*Dix*, 1955) in section 3.3, I used the Dix inversion to estimate the layer 2A P-velocities from RMS velocities of basement and layer 2A triplications. The Dix inversion (*Dix*, 1955), described shortly, estimates the interval velocities from the RMS velocities obtained from imaging the seismic data. However, it has a drawback of being valid only for flat (zero dip) reflections. The interval velocities for the whole profile and the depth converted layer 2A thickness is shown in figure3.14. To simplify the computation and given the amount of data I was having, I did not consider the effect of basement dip and assumed stacking velocities to be the same as the RMS velocities.

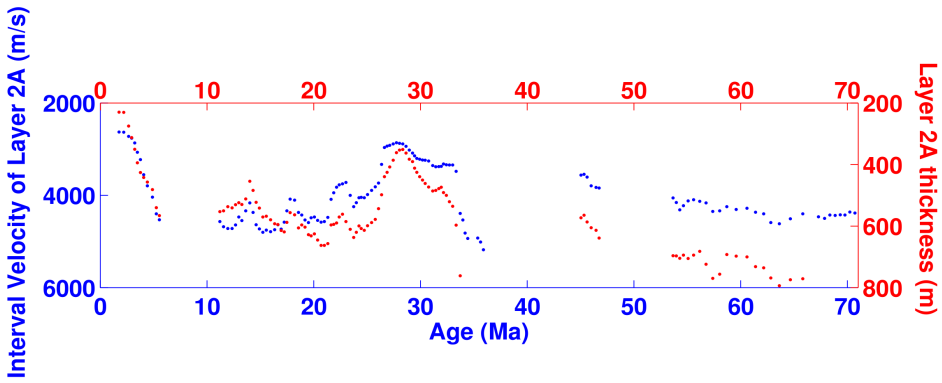

Figure 3.14: Interval velocity as obtained from Dix inversion of stacking velocity for layer 2A for the whole profile in blue. Also shown is the depth converted physical thickness in red.

Rohr (1994) first estimated layer 2A velocities from Dix inversion of stacking velocities at Juan de Fuca ridge but these velocities were found to be over-estimated by 1 km/s by *Nedimović et al.* (2008).

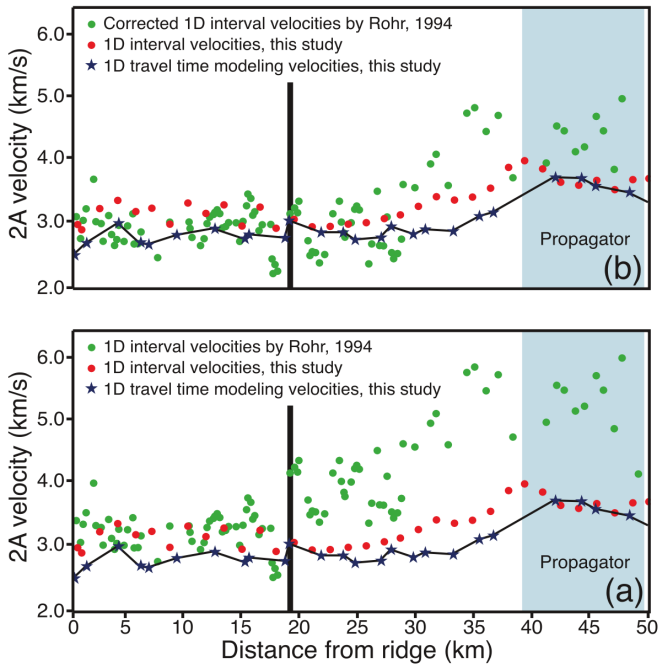

Figure 3.15: A comparison of the velocities obtained by different means for layer 2A at the Juan de Fuca ridge (*Nedimović et al.*, 2008). The green dots in the above panel (b) show the corrected layer 2A velocities as compared to (a), which show the original layer 2A velocities determined by Dix inversion (*Dix*, 1955) by *Rohr* (1994).

It was clear that the estimates of interval velocity from RMS velocities by Dix inversion was not good.

To investigate this further, I performed a test to what offset the Dix inversion works.

3.6.1 Reliability of Dix inverted velocities

The Dix inversion is valid only for true reflections in a flat layer model of the Earth and uses the zero-offset two-way time along with the root mean square (RMS) velocities to estimate the interval velocities. We consider two events at zero-offset times t_{01} and t_{02} arising from two reflectors in the subsurface.

Considering the two reflections stack with velocities v_1 and v_2 respectively, their RMS velocities would be equal to the stacking velocities as the dip, θ, $= 0$ and $v_{rms} = \frac{v_{stack}}{cos\theta}$. The Dix inversion (*Dix*, 1955) then becomes,

$$v_{int} = \sqrt{\frac{v_2^2 t_{02} - v_1^2 t_{01}}{t_{02} - t_{01}}}. \tag{3.3}$$

Note zero-offset times have been used. A reflection can be considered the limiting case where $\frac{dv}{dz}\big|_{dz=0}$. The base of the layer 2A, which is a high velocity gradient region, can be represented as $\frac{dv}{dz}$ with $dz > 0$. The introduction of a gradient shifts the reflection to greater offsets (X). Hence a question arises : to what offsets is Dix inversion valid ? In order to examine it, I replace the zero-offset two-way time terms in the Dix equation with the non-zero offset two-way time.

$$v_{int} = \sqrt{\frac{v_2^2 t_2 - v_1^2 t_1}{t_2 - t_1}}. \tag{3.4}$$

The non-zero offset two-way time of the two events, t_1 and t_2, are related to the zero-offset times, t_{01} and t_{02}, by the NMO equation,

$$t_i^2 = t_{0i}^2 + \frac{X^2}{v_i^2}, \tag{3.5}$$

which can be simplified as,

$$t_i = t_{0i} + \frac{X^2}{2 v_i^2 t_{0i}}, \tag{3.6}$$

where $i = 1, 2$ and v_i is the stacking velocity which is the same as the RMS velocity used in Dix formula. I neglect the higher orders of the NMO equation for the simplicity of computation. I denote equation 3.4 by zero-offset or the original Dix equation and equation 3.7 by the offset corrected Dix equation.

Substituting the above equation in the Dix formula and re-arranging, we get,

$$v_{int} = \sqrt{\frac{v_2^2 t_{02} - v_1^2 t_{01} + \frac{X^2}{2t_{02}} - \frac{X^2}{2t_{01}}}{t_{02} - t_{01} + \frac{X^2}{2v_2^2 t_{02}} - \frac{X^2}{2v_1^2 t_{01}}}}. \tag{3.7}$$

Note that by replacing the zero-offset two-way time by the non-zero offset two-way time and the NMO equation in equation 3.5, the offset term X has been introduced in equation 3.7. In order to check upto which offset terms, the Dix equation is valid, I kept v_1 at 1.5 km/s (stacking velocity of seafloor/basement) and varied X from 0 to 12 km and v_2 from 1.5 km/s to 3 km/s (stacking velocity of layer 2A event). t_{01} and t_{02} are the zero-offset times of the seafloor/basement and the 2A event respectively which are not directly estimated from pre-stack data. The results of layer 2A two-way time thickness estimated are

shown in figure 3.16 and are obtained between 0.3-0.5 s. I use these values for $t_{02} - t_{01} = \Delta t$. First I show the Dix inversion results in equation 3.4 (figure 3.16(a)) for a reasonable range of interval velocities which I then test it against the offset corrected Dix formula in equation 3.7 (figure 3.16(b,c)) for two end-members of $\Delta t = 0.3, 0.5$s.

(a)

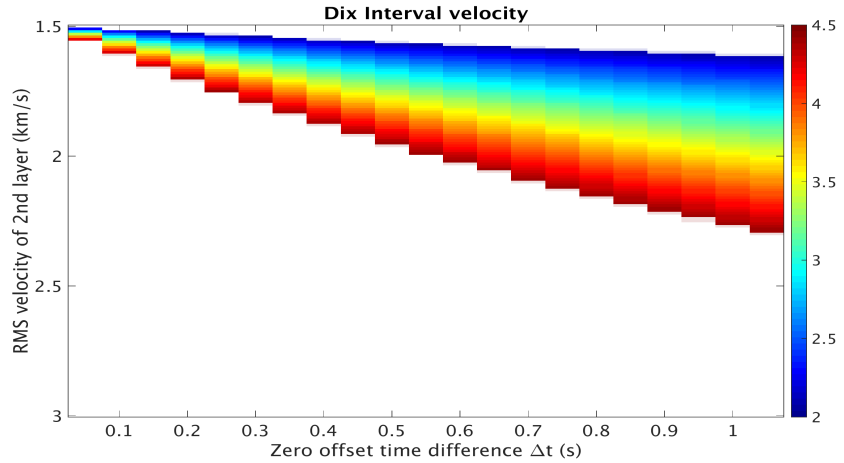

(b)

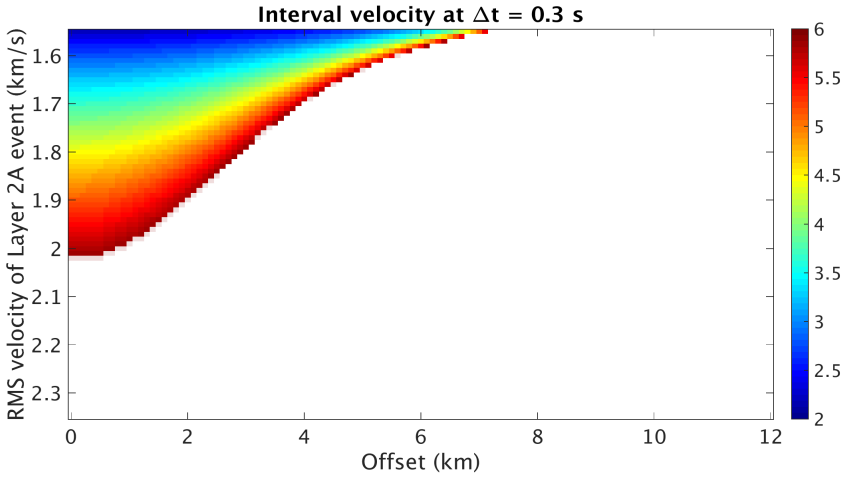

(c)

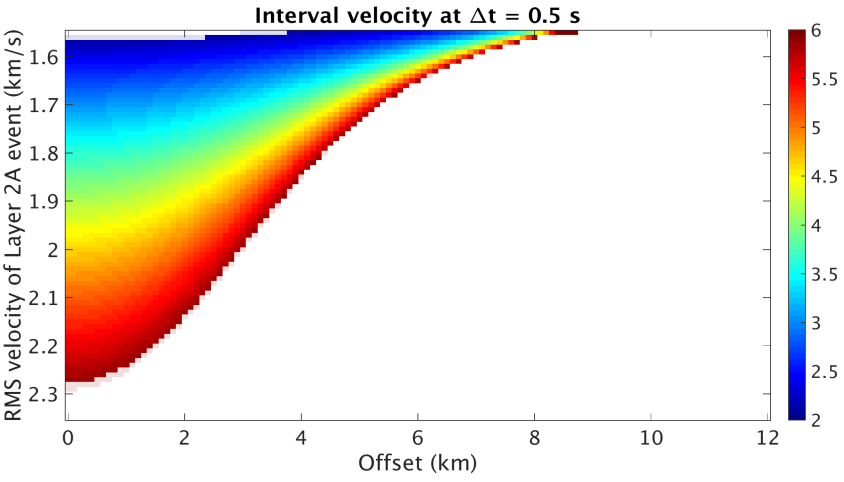

Figure 3.16: (a) Zero-offset Dix interval velocities as a function of $t_{02} - t_{01} = \Delta t$ and v_2 (see text). The colorbar indicates the range of reliable interval velocities (2 - 6 km/s) and corresponding pairs of Δt and v_2 can be deduced. The offsets corresponding to these pairs are then deduced from the offset corrected Dix formula. Two end-members are tested at (b) Δt =0.3s and (c) Δt =0.5s.

At Δt =0.3s, the offset corrected Dix formula in figure 3.16b shows reasonable interval velocities for layer 2A corresponding to v_2 =1.55-2 km/s at zero-offset. However at larger offsets, the range of RMS velocities for layer 2A event (v_2) which gives a reasonable layer 2A velocity narrows down significantly.

Most of the layer 2A triplication occur at offsets >4 km as seen in figures 3.10 and 3.9. At this offset range, RMS velocities for layer 2A event between 1.6-1.7 km/s would provide reasonable results. Figure 3.16c shows that a wider range of RMS velocities at zero-offset corresponding to v_2 =1.55-2.2 km/s gives reasonable interval velocities for layer 2A. This corresponds to Δt =0.5 s which is observed at the ridge-axis and has the maximum thickness of layer 2A event (figures 3.13b) along the whole profile. At farther offsets, the range of valid RMS velocities is narrowed down similar to that in figure 3.16b. Though RMS velocities obtained in the range 1.6-1.7 km/s do show reasonable interval velocities for layer 2A event in the offset range 4-6 km in figures 3.16b and c, the dipping basement topography and presence of sediment cover in real data make the range of RMS velocities exceed 1.7 km/s. Hence there was a need to have more reliable estimation of P-velocities. As described in chapter 2, I used a recently developed method of downward wavefield extrapolation (*Arnulf et al.*, 2011) followed by high resolution tomography to achieve most accurate results.

3.7 High resolution tomography models

Prior to performing tomography, downward continuation was carried out along several regions of the profile (red lines in figure 3.2) to enhance the first arrival as described in chapter 2. The following figure 3.17 shows downward continued super-CMP gathers corresponding to the super-CMP gathers shown in figure 3.10. In all cases of figure 3.17, the first arrival is now visible at 1-2 km offsets as compared to 4-5 km offsets in figure 3.10. This enhancement of the first arrival is due to the sources and receivers being brought down closer to the seafloor and the resulting better sub-surface ray coverage in the process of downward continuation. Note that while figure 3.17 shows downward continued super-CMP gathers, the picking of the first arrivals was performed on downward continued shot gathers for tomography.

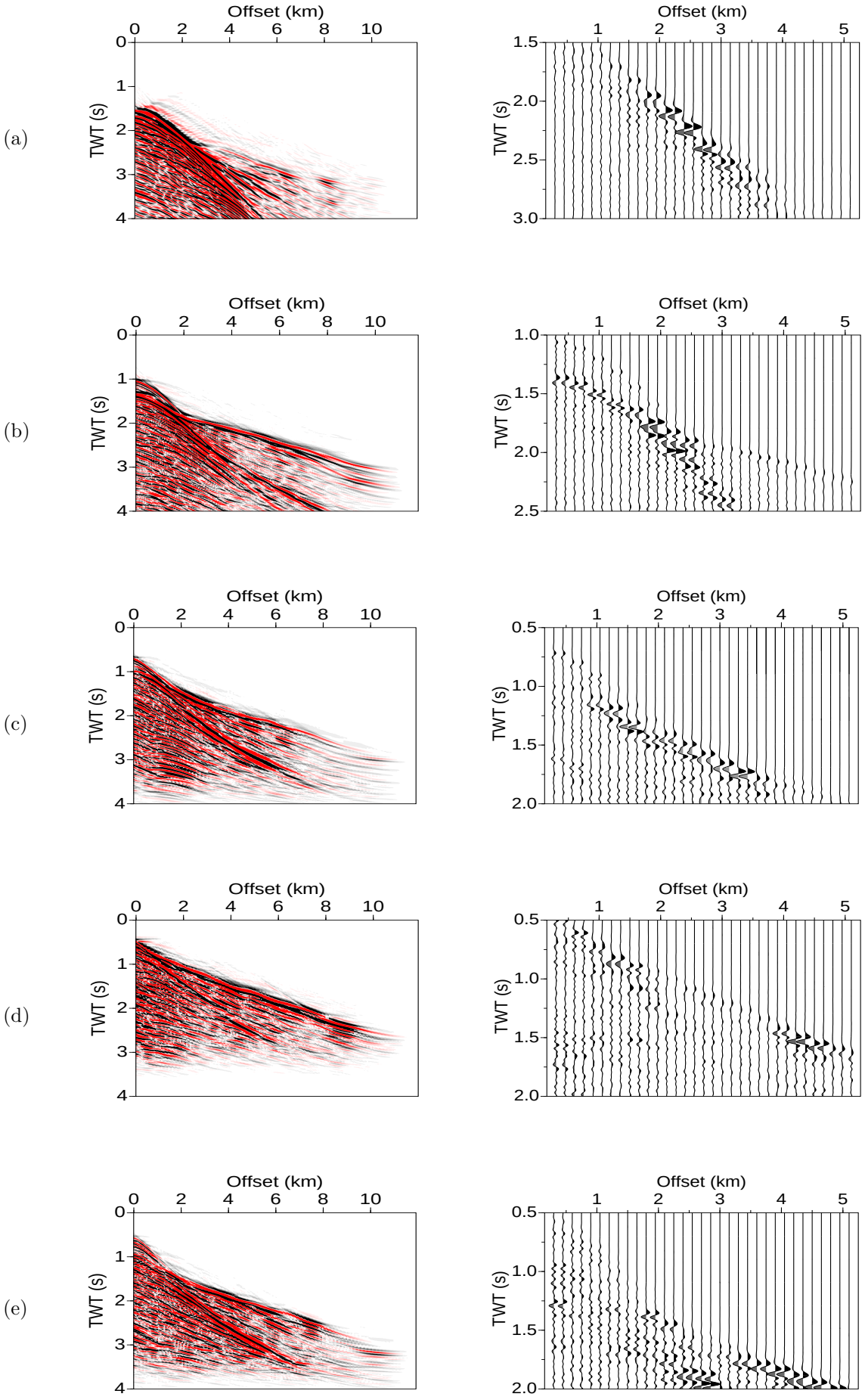

Figure 3.17: Downward continued super-CMP gathers corresponding to super-CMP gathers of Figure 3.10 at different crustal ages: (a) the median valley of the ridge axis (zero age); (b) 16 Ma; (c) 31 Ma; (d) 50 Ma and (e) 70 Ma. The first arrival is much enhanced now as there is better ray coverage through the uppermost oceanic crust. The first 5 km offset of the left panels have been expanded in the right panels.

Ray-based travel-time tomography of the enhanced first arrivals on the downward continued shot gathers was then performed to extract information of the P-velocities of the upper crust (*Van Avendonk et al.*, 2004). The theoretical background for travel-time tomography inversion has been described in chapter 2. I picked the first arrivals of the downward continued shot gathers every by 150 m (every 2nd shot at 75 m spacing and every 3rd shot at 50 m spacing) except at the ridge axis where I picked at every 125 m (every 2nd shot at 62.5 m spacing). As the objective was to present an age related variation of P-velocities, each shot was not picked for first arrivals to save time. Although the initial plan was to perform tomography at 0 Ma, 15 Ma, 30 Ma , 50 Ma and 75 Ma only, other locations such as 3 Ma, 46 Ma and 47 Ma were chosen later to provide a more comprehensive picture of the crust (red lines in figure 3.2). Moreover, these locations were specifically chosen as they were co-inciding with the heatflow locations. A total of ∼3000 shots were picked along the whole profile. A semi-automatic picking strategy was adopted to facilitate shot-to-shot continuity. The final two-way travel time picks were subject to corrections based on frequency filtering effect, source signature delay and zero-phasing performed by WesternGeco. The zero-phasing during the processing by WesternGeco was estimated by stacking the aligned direct wave signals in the raw data. A linear moveout correction with a velocity of 1.496 km/s was used to best align the direct wave signals. The stacking of these signals was then performed to estimate the time shift. A time shift of ∼15 ms was found as shown in figure 3.18a. This was taken into account and added to the picks. Next the shift in first arrivals due to low frequency filtering was also performed as shown in figure 3.18b. A shift of ∼10 ms was observed due to the low frequency filtering which was again taken into account. The source signature provided by WesternGeco was used to identify the source signature delay which was ∼50 ms. Hence a total of ∼75 ms was added to the picks.

An initial velocity model was obtained by hanging a 1D velocity profile corresponding to the ages in the Atlantic from a smoothed seafloor/basement picked from the seismic stack sections. The 1D velocity model for 30, 50 and 70 Ma old oceanic crust was taken from *White et al.* (1992) whereas for younger crust the velocity model was taken from *Dunn et al.* (2005). A constant sediment velocity at distinct age range was taken from table 3.1. In order to perform raytracing, the graphing grid was kept at 12.5 m spacing which is the same as the receiver spacing in the streamer. The number of grid points to be affected surrounding the raypath was kept as 15 in both the horizontal and vertical directions with a angle increment of 0.05°. This implied an area of 187.5 m × 187.5 m was to be affected surrounding the raypath at any given point of time. A lower value of the surrounding grid points to be affected would have decreased the computational time, but would have sampled the upper crust less densely. Grid points having slowness lower than 1.2 s/km were only sampled. This would correspond to a velocity of 0.833 km/s for the near surface S-waves.

Some tests were performed to ensure optimum range of these parameters: smoothing of the seafloor and basement interfaces, second order smoothing, horizontal to vertical smoothing ratio, inversion grid spacing and size of the Huygens' secondary point scatterer. In implementation, the Huygens' secondary point scatterer is the number of grid points surrounding the raypath which are affected by the traversing ray. I found adequate sampling of the upper crust with a forward star size of 15 grid node points by 15 grid node points. A higher forward star increased the computational time but did not yield better results. For determining an optimum size of the inversion grid, different grid sizes were tested: 150 m × 25 m, 300 m × 50 m and 500 m × 100 m. The lower limit of 150 m lateral spacing was fixed since the shots were picked every 150 m. No significant changes in the results were found when the inversion grid size was increased from 150 m × 25 m to 300 m × 50 m while a decrease in the computational time was observed. The largest grid spacing yielded poorer results and the inversion grid spacing was fixed as 300 m × 50 m. It was also observed that smoothing the basement or the seafloor interfaces should be kept to a minimum as higher smoothing yielded ray deficit regions below the interface which would then be filled with higher velocities during the inversion. The smoothing of the interfaces was performed using a moving average window of 300 m. The result was similar when a gaussian window of the same length was used instead of the moving average window. However, at the ridge axis and at 15.6-17.8 Ma, the smoothing of the seafloor and basement had to be increased to ensure sufficient ray coverage beneath the seafloor and basement. Furthermore, the initial downward continued datum at 15.6-17.8 Ma had

(a)

(b)

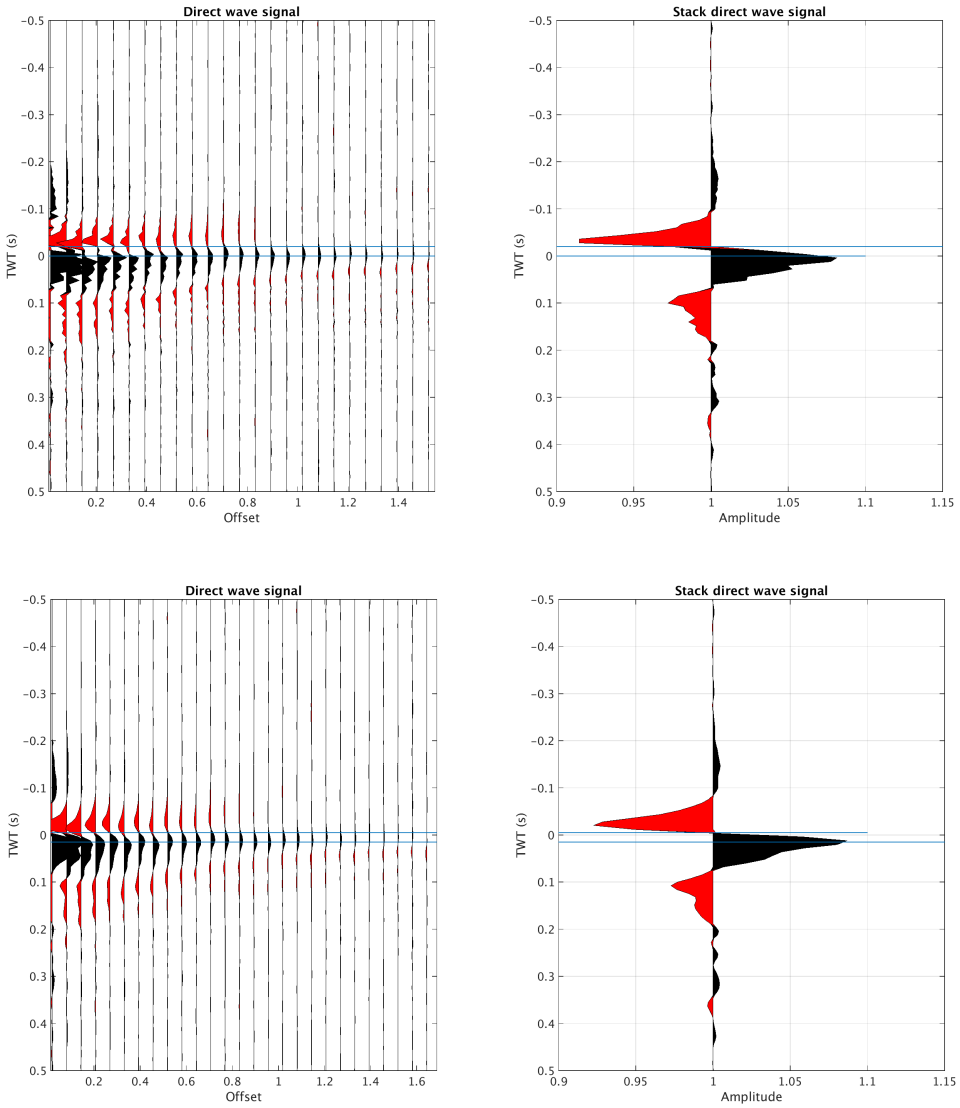

Figure 3.18: Estimating time shifts in first arrivals due to (a) zero-phasing of the data and (b) low frequency filtering. The time shift between the zero-crossing (red to black) and the peak of the first arrival (both denoted by solid blue lines) has been used to correct the first arrivals.

to be smoothed even more and downward continuation and first arrival picking performed again. The difference between the first arrival picks corresponding to the data downward continued to two different datums has been shown in figure 3.19.

(a)

(b)

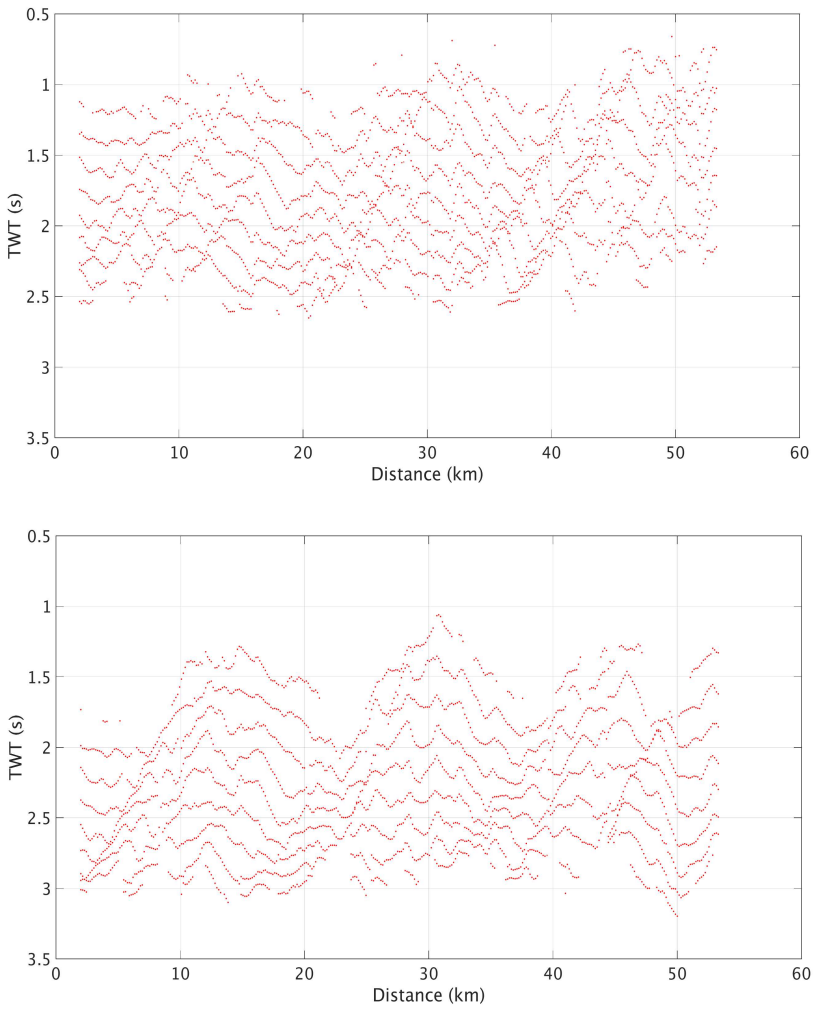

Figure 3.19: First arrival picks plotted at 15.6-17.8 Ma for each shot at every 1 km offset. (a) When data is downward continued to a smoothed version of the seafloor 0.2-0.3 km above it. (b) When data downward continued to a more flatter datum above the seafloor.

The uncertainty in the first arrival picks was kept as 20 ms for the ridge axis and 15.6-17.8 Ma due to the rugged bathymetry whereas it was kept as 15 ms for all other ages except 68.6-71.9 Ma, where it was 10 ms owing to the thick sediment cover and smoother basement topography. Consecutive inversion runs were carried out to avoid the avoid the convergence in a local minima. The first inversion run had a starting 1D model from previous studies (*White et al.*, 1992; *Dunn et al.*, 2005) which was then converged to minimum misfit (χ^2) ensuring adequate smoothing and damping. The smoothing parameter (λ) is usually kept 4 times higher than the damping parameter (γ) in tomographic inversion (*Hanchao Jian, personal communication*). As my aim was to obtain smooth models which would not only facilitate the depth conversion of layer 2A/2B picks but also suppress the local effects at each age, I kept a higher horizontal/vertical ratio in smoothing to obtain laterally smoothed models. The final model at the end of the inversion run was then stacked to obtain a 1D velocity model for the next inversion run. The process was repeated until no further update of the velocity model was observed. The minimum misfit model obtained at the end of the last inversion run was considered the final velocity model for that age range.

Figures 3.20 and 3.21 show the high resolution tomography results at distinct ages. The black dashed line is the depth converted layer 2A/2B boundary from figures 3.11 and 3.12 and using the velocities of the corresponding tomography velocities in figures 3.20 and 3.21. Before I proceed to interpret the

tomography models, I perform a two-step validation of the tomography models: checkerboard test and synthetic seismogram modeling in section 3.8.

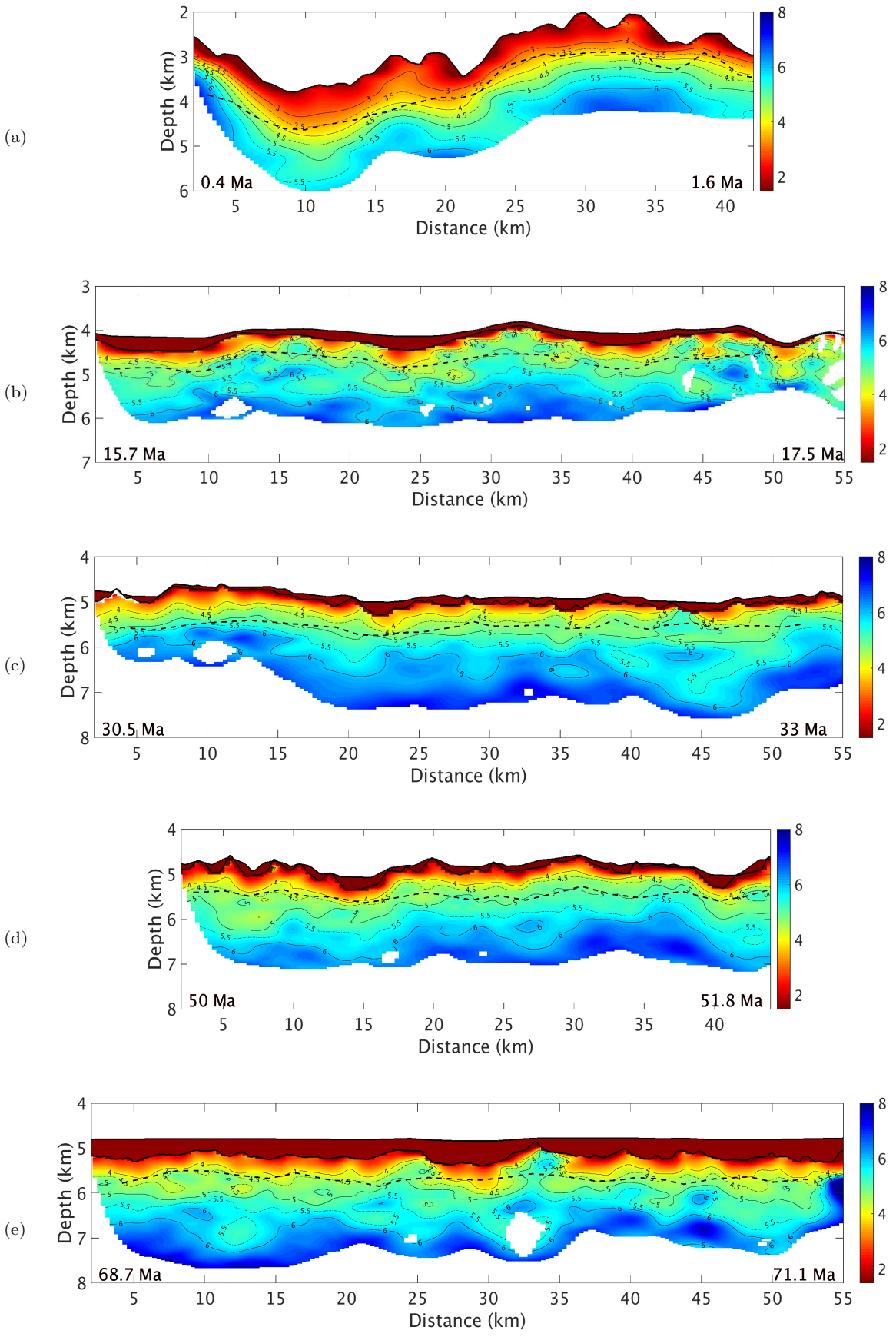

Figure 3.20: Tomography inversion results at distinct ages corresponding to sections of Figure 3.11. The interface corresponds to a smoothed version of the seafloor and basement. The black dashed line corresponds to depth converted layer 2A/2B from the seismic using laterally smoothed tomography velocities. Regions where the ray coverage is quite low have been masked. Sediment velocities have been estimated using RMS velocity analysis from seismic. The distances are plotted with respect to the seismic sections in Figure 3.11.

(a)

(b)

(c)

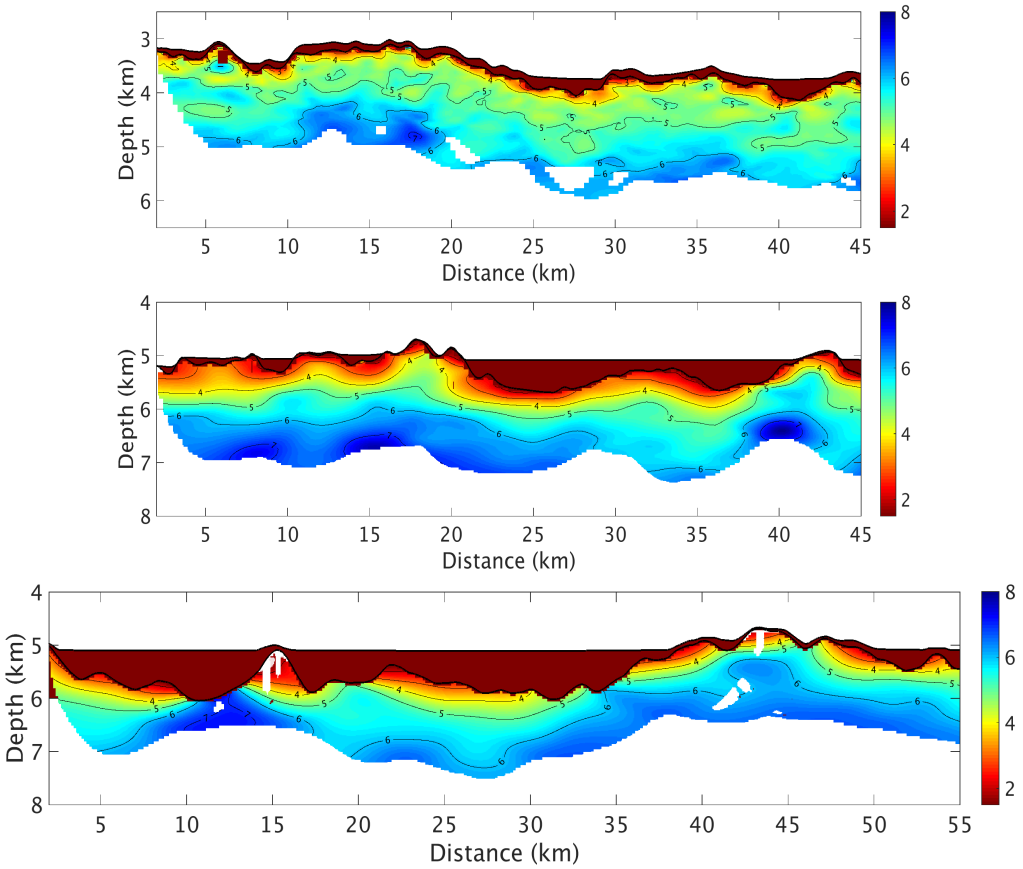

Figure 3.21: Additional tomography inversion results at distinct ages corresponding to Figure 3.12a,c and d. The interface corresponds to a smoothed version of the seafloor and basement. Regions where the ray coverage is quite low have been masked. Sediment velocities have been estimated using RMS velocity analysis from seismic. The distances are plotted with respect to the seismic sections in Figure 3.12.

3.8 Validation of tomography models

Before proceeding with the usual validation tests, it was necessary to perform a more basic check: ray coverage and reduction of travel time residuals. Unless there was sufficient ray coverage and two-way time residual reduction, the tomography models may not have converged to the true minimum and would not represent the true subsurface velocities. Figure 3.22 shows the ray coverage diagrams for the tomography models for distinct ages corresponding to figure 3.20. The ray coverage is usually determined by the parameter derivative weight sum (DWS) (*Van Avendonk et al.*, 2004), which is the sum of all columns of the Fretchet derivative matrix and an indicator of the ray coverage. A better ray coverage is observed at 30.5-33 Ma and 50-51.8 Ma as compared to other ages though a sufficiently good ray coverage is observed at all ages in the top 1-1.5 km of the upper crust. Figure 3.23 shows the initial (red) and final (blue) residuals of the tomographic inversion, along with the uncertainties. A good reduction of the residuals is achieved in all the ages, most apparent at the ridge axis where the initial residuals are very large (figure 3.23a).

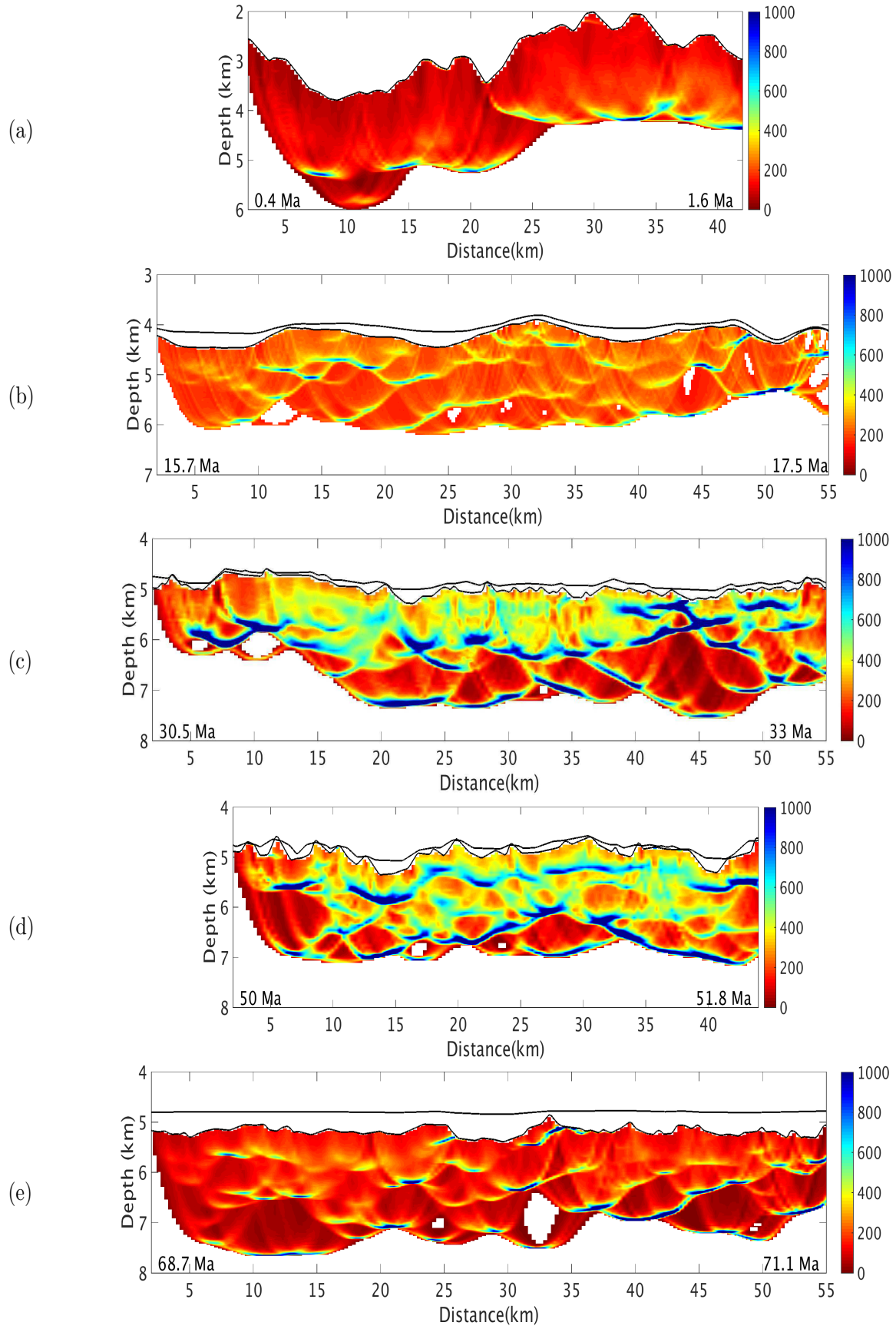

Figure 3.22: Derivative sum diagrams for the distinct ages. The derivative weight sum is obtained by summing along the columns of the Fretchet derivative matrix and is indicative of the ray coverage (*Van Avendonk et al.*, 2004). A good ray coverage is observed through the uppermost 1-1.5 km of the oceanic crust in all cases.

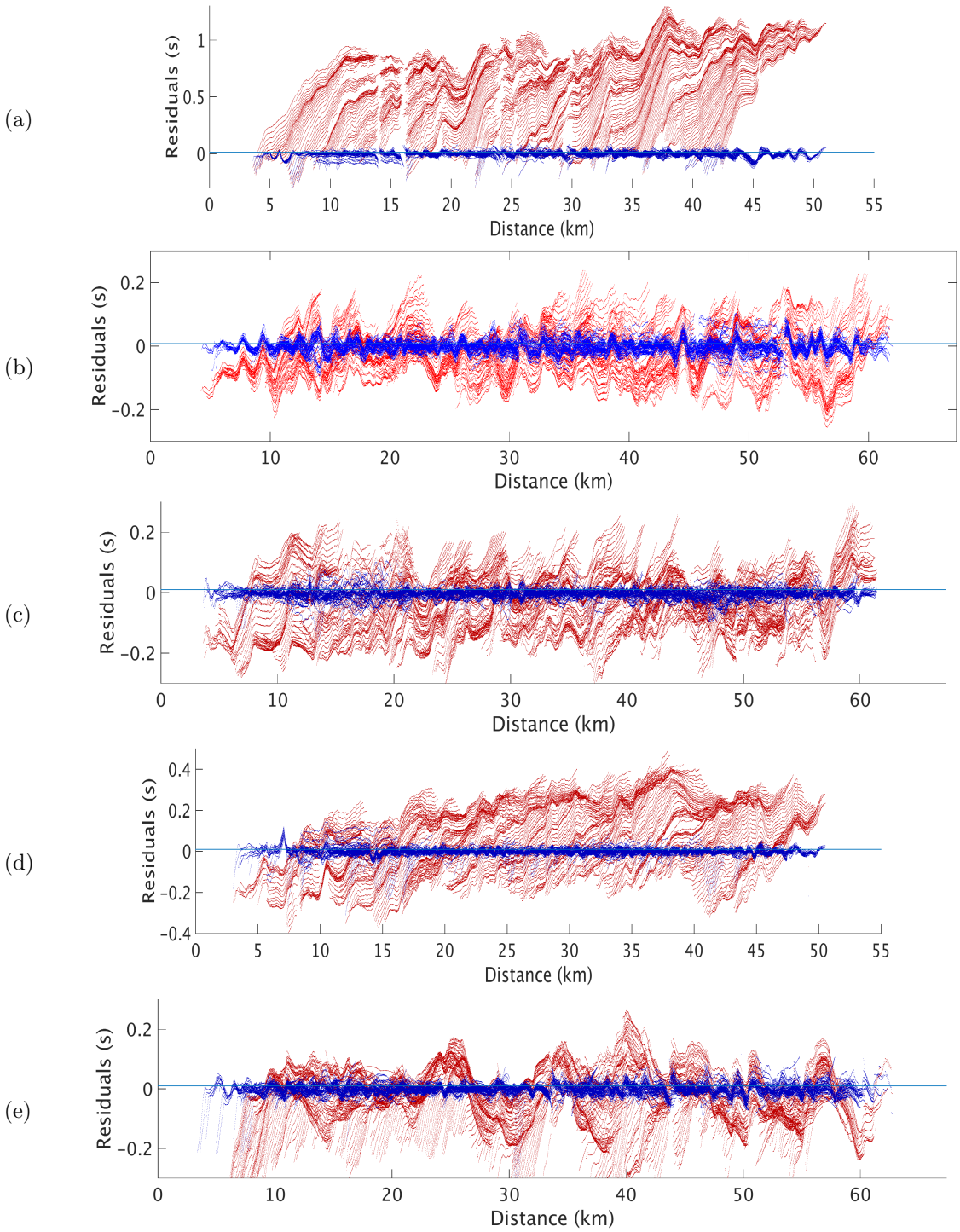

Figure 3.23: Initial (red) and final residuals (blue) of tomographic inversion for the distinct ages. Note the data has been acquired from right to left. The vertical scale has been adjusted to plot the full range of initial residuals. The mean of the final travel time residuals at the distinct ages is : (a) 23 ms; (b) 21 ms; (c) 18 ms (d) 14 ms (e) 16 ms whereas the corresponding uncertainties are : (a) 20 ms; (b) 20 ms; (c) 15 ms; (d) 15 ms; (e) 10 ms

3.8.1 Checkerboard tests

In order to assess the resolution of tomography, checkerboard tests were performed for different anomaly sizes as shown in figure 3.24 and 3.25. Four different gaussian anomaly sizes: 2 km × 2 km, 1.5 km × 1.5 km, 1 km × 1 km, 0.5 km × 0.5 km with 5% velocity perturbation were tested. The tests were performed at the ridge axis (figure 3.24) and at 68.6-71.9 Ma (figure 3.25) where a thick sediment cover is observed. The checkerboard tests for resolution in both cases yield a limit of 0.5 km anomalies with

5% velocity perturbation.

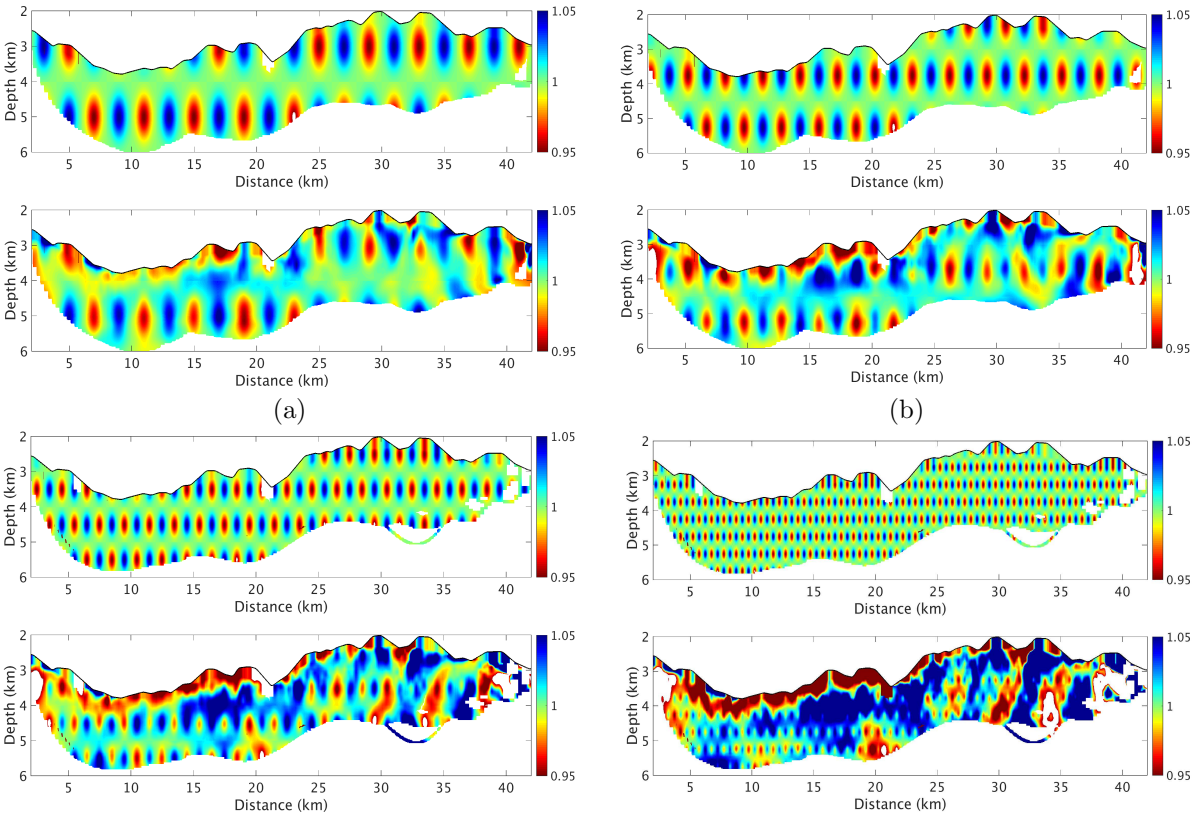

Figure 3.24: Checkerboard test for resolution at the ridge axis: (a) Top panel shows the 2km × 2km checkerboard pattern and below is the recovered; (b) 1.5km × 1.5km pattern and the recovered (below); (c) 1km × 1km pattern and the recovered (below); (d) 0.5 km × 0.5 km pattern and the recovered (below). All anomalies are 5% velocity perturbations. The limiting resolution from this test is the dimension of 0.5-1 km of an anomaly having 5%.

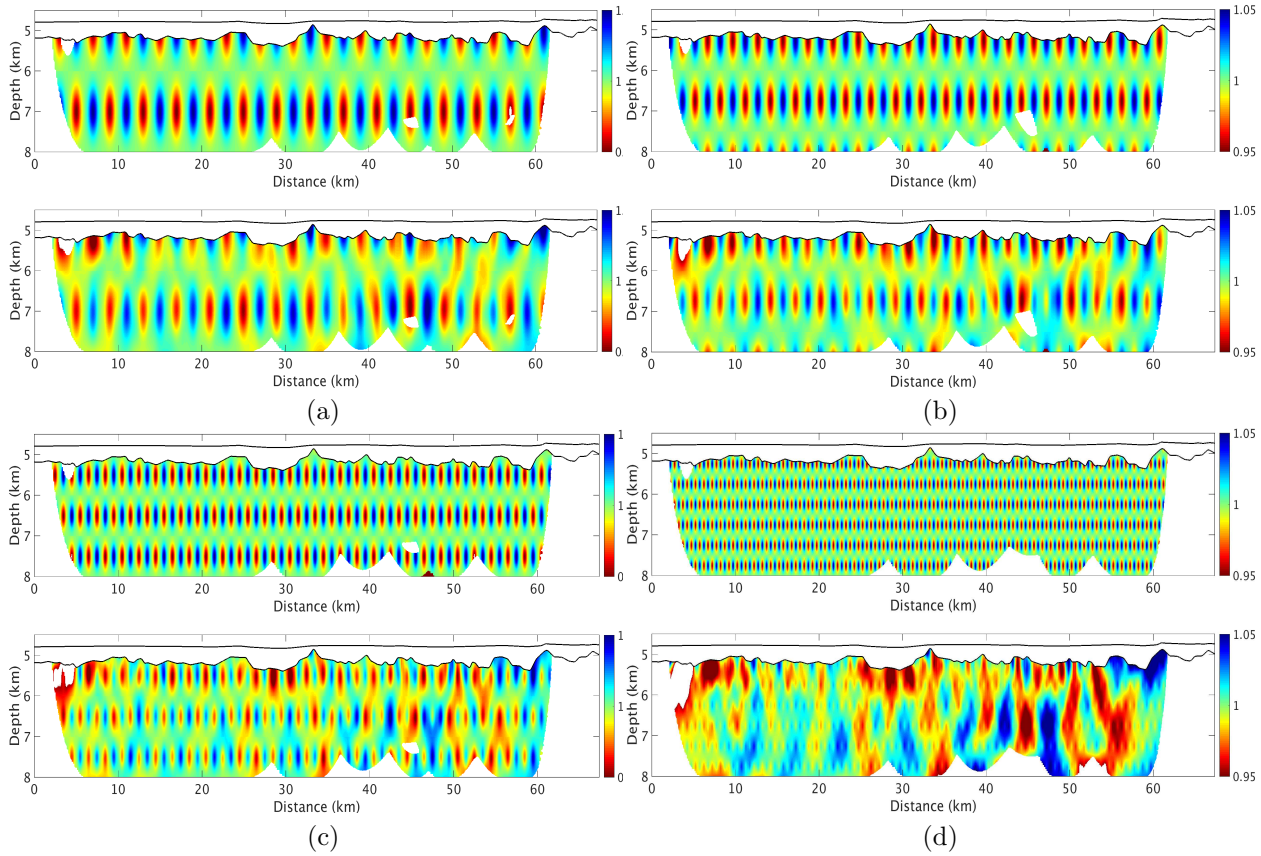

Figure 3.25: Checkerboard test for resolution at 68.6-71.9 Ma: A thick sediment cover overlies the basement. (a) Top panel shows the 2km × 2km checkerboard pattern and below is the recovered; (b) 1.5km × 1.5km pattern and the recovered (below); (c) 1km × 1km pattern and the recoverd (below); (d) 0.5 km × 0.5 km pattern and the recovered (below). All anomalies are 5% velocity perturbations. The limiting resolution from this test is the dimension of 0.5-1 km of an anomaly having 5%.

3.8.2 Synthetic elastic forward waveform modeling

I also performed synthetic waveform modeling of both downward continued and surface data using the tomography models and did a comparison with the corresponding real shot gathers at same location. I used a V_p/V_s ratio of 1.73 corresponding to a Poisson's ratio of 0.25 as found 200 m below the seafloor at fast spreading East Pacific rise by *Collier and Singh* (1998). The velocity model was discretized into a 12.5 m grid and a Ricker wavelet of 10 Hz dominant frequency was used for generating the synthetic seismogram. This was performed for both downward continued (Figure 3.27) and surface data (Figure 3.26) at distinct ages.

Figure 3.26 shows comparison between the synthetic (left) and real surface (original; without downward continuation) data at distinct ages. The different events have been marked in the gathers. Note that the direct wave, which is clear in synthetic gathers, has been muted in the real shot gathers. A good match can be observed between the slopes of the first arrivals and the position of the triplication.

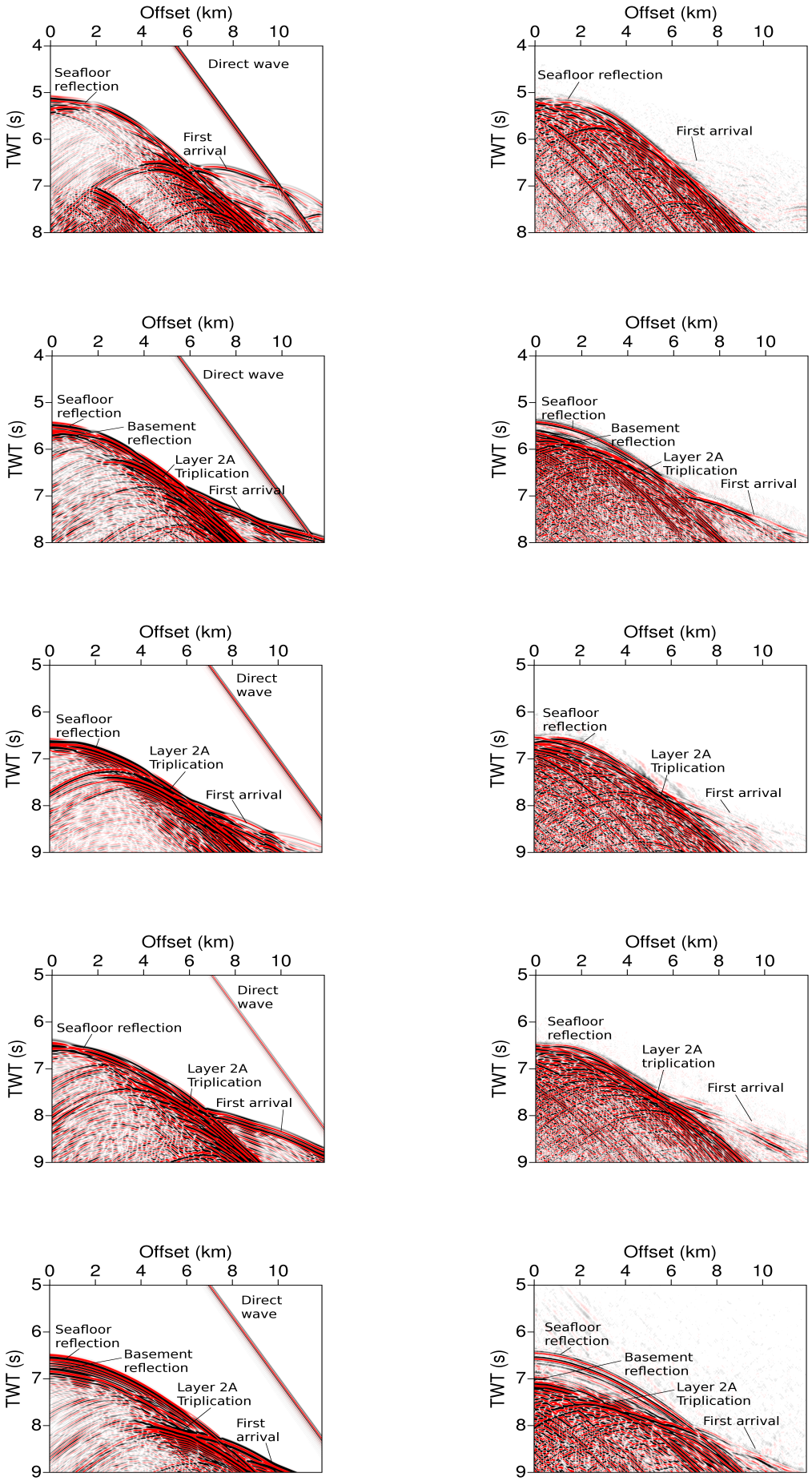

Figure 3.26: Final synthetic and real shot gathers for surface data at distinct ages. The different arrivals on the seismic section have been marked. A good match between the first arrivals and position of the triplication can be found at all crustal ages between synthetic and real data.

The left panel of Figure 3.27 shows plots of the synthetic downward continued shot gathers and the right panels show the real downward continued shot gathers at the same location. Though a smoother version of bathymetry was used to perform tomography, a good match between the first arrivals is observed between the synthetic and real data. Note that triplication in real data is not very clear due to downward continuation procedure, which unfolds the triplication. In almost all the ages, a distinct linear moveout arrival is seen appearing after the first arrival (P-refraction) in the real shot gathers and may correspond to the S-refraction. If it corresponds to the S-refraction, then the S-velocities are lower than expected and ratio of P-velocity and S-velocity is < 1.73.

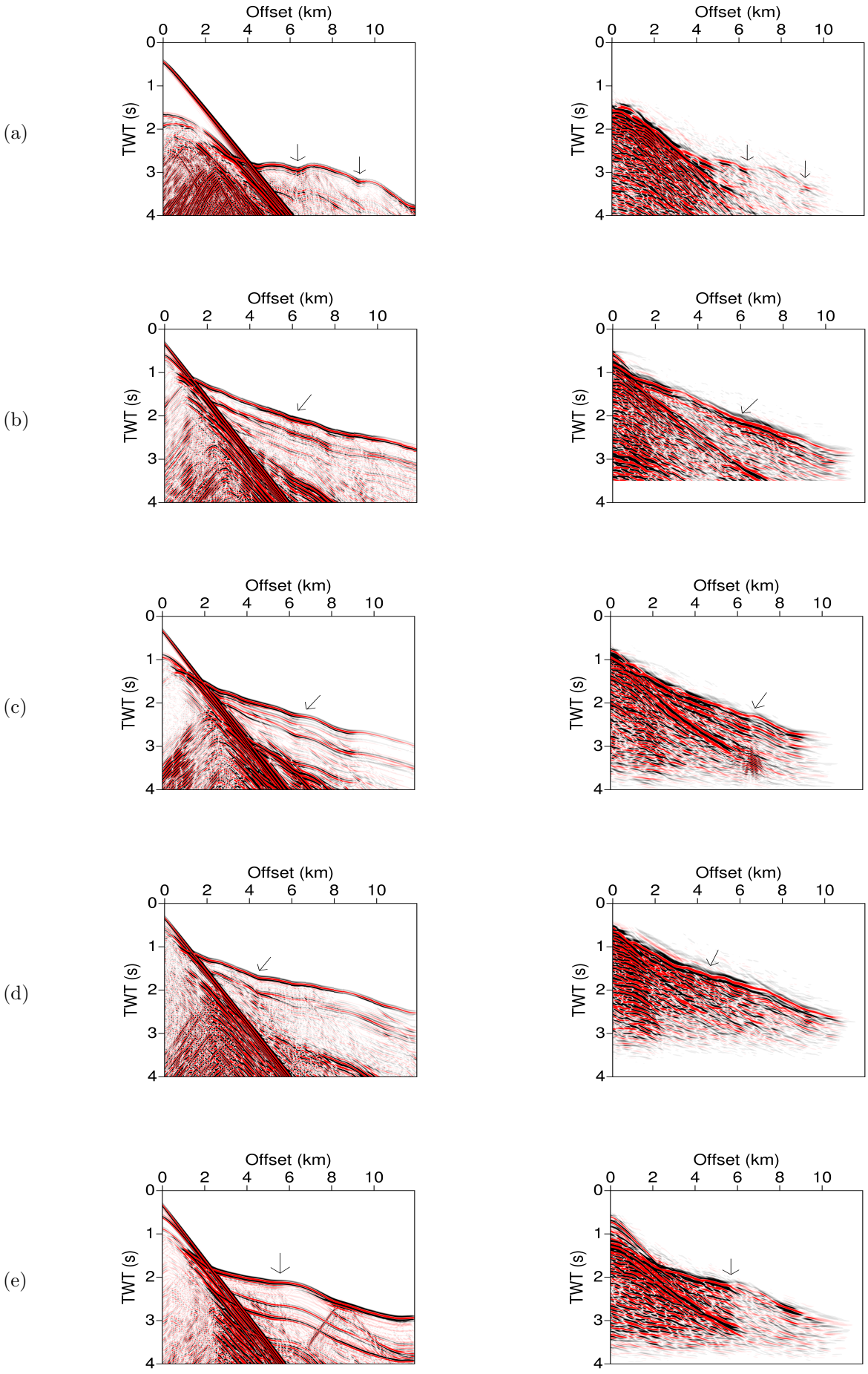

Figure 3.27: Final synthetic and real shots gathers for downward continued data at distinct ages. A Ricker source wavelet of dominant frequency of 10 Hz has been used for elastic modelling of the synthetic shot gathers. A good match can be found between the synthetic and real gathers indicating a good reliability of tomography models. V_p/V_s ratio has been taken to be 1.73 from *Collier and Singh* (1998).

3.9 Interpretation of tomography models

Having validated my tomography results, I now proceed to a combined interpretation of my seismic images in figure 3.11 and the corresponding tomography models in figure 3.20. One of the first steps was to use the tomography velocities from figure 3.20 to depth convert the layer 2A/2B boundary observed in the seismic images. A 1D velocity profile at each CMP location in figure 3.20 was used to compute the depth of the 2A/2B boundary which would correspond to the observed two-way time/thickness in the seismic stack sections in figure 3.11. The dashed black curves in figure 3.20 denote the depth converted layer 2A/2B boundary obtained. Uncertainties in depth (mentioned below) were taken into account from both the seismic and tomography models.

At the ridge axis, the median valley has a velocity of 2.5 km/s (Figure 3.20a) and the adjacent ridge flanks have a slightly higher velocity reaching ∼3 km/s near the seafloor. The layer 2A/2B boundary lies at 820±315 m beneath the median valley, corresponding to the reflection image at 500 ms (Figure 3.11a). At the ridge flanks, from 27-32 km distance range, the layer 2A seismic reflection at 550 ms maps to 900±315 m depth and to a mean velocity of 4 km/s. The tomography results for the 15.6-17.8 Ma profile indicate a mean Layer 2A velocity of 4 km/s with the base of the reflected layer 2A at ∼580±275 m below the basement and lying roughly along the 5 km/s velocity contour (Figure 3.20b). The tomography results for the 30.4-33.4 Ma region show smoothly varying velocities below the basement of ∼3.9 km/s (Figure 3.20c). The layer 2A/2B reflection boundary maps to 530±230 m and corresponds to a velocity contour of ∼5 km/s. Due to rougher bathymetry on the western end of the profile, the ray coverage is limited to 1.5 km below the seafloor. On the eastern end, a better penetration of rays is observed due to relatively smoother basement topography and a thicker sediment cover. The tomography results at 49.9-52.2 Ma indicate the mean velocity in the range of 3.8-4.1 km/s with velocities reaching 5.3 km/s within 1 km below the basement (Figure 3.20d). Figure 3.20e shows the tomography results at 68.6-71.9 Ma showing smoothly varying velocities of 3.8-4 km/s below the basement. The depth converted layer 2A/2B boundary is at 520±135 m below the basement and corresponds to a mean velocity of 5 km/s. An overall deeper penetration of rays is observed as compared to other ages due to the thick sediment cover reducing the back scattering from the rough basement.

3.9.1 Estimation of Layer 2A and 2B velocities

I now try to use the high resolution P-velocities obtained in figure 3.20, 3.21 to estimate velocities for layers 2A and 2B. It should be mentioned here that velocities below the basement, which would correspond to low gradient part of 2A at the top of layer 2A, have been termed as layer 2A velocities. Instead of taking velocities just immediately below the basement, velocities in the top 200 m below the basement have been vertically averaged along the tomography models to estimate the layer 2A velocities. This was done to suppress local basement topographic variations and the subsequent ray coverage variations. The layer 2B velocities termed here refer to velocities along the layer 2A/2B boundary or at top of the layer 2B. As mentioned before, the 1D tomography velocity-depth profiles at each CMP location were taken from figure 3.20 and were converted to two-way travel time-depth 1D profiles using 'vint2t' function of CREWES library which estimates 1D travel-time depth profiles from interval velocity-depth profiles. The two-way travel-time thickness estimated from the seismic in figure 3.11, 3.12 was then used to used estimate depths at which this layer 2A/2B boundary would be mapped onto the velocity models in figure 3.20. Velocities for layer 2B were then picked along this depth converted 2A/2B boundary.

It was necessary that the depth of layer 2A/2B boundary estimated from tomography velocities and the seismic two-way time, also correspond to a high gradient in the velocity models by the definition of layer 2A/2B boundary (chapter 2). To visualize the high gradient in the velocity models at which the rays would turn sharply, I used ray-tracing on the final velocity models in figure 3.20 to identify the turning point of the rays. Turning point of the the rays arriving at 0-4 km offset is shown in figure 3.28a and those arriving at 4-8 km offset is shown in figure 3.28b. The patches represent the depths at which the rays turn. The black dashed lines are the depth converted layer 2A/2B boundary from tomography

velocities as in figure 3.20. Ideally, the colored patches which represent the turning point of the rays should have been present along/very near this boundary. However, this is not found to be the case in figure 3.28 in which the rays are found to be turning well above and below this boundary. A reason for not being able to distinguish a high velocity gradient would be the inherent smoothing in tomography. The conventional model of low gradient 2A-high gradient 2A-low gradient 2B has been smoothed out and subsequently rays turning sharply from a particular depth range cannot be distinguished in figure 3.28.

(a)

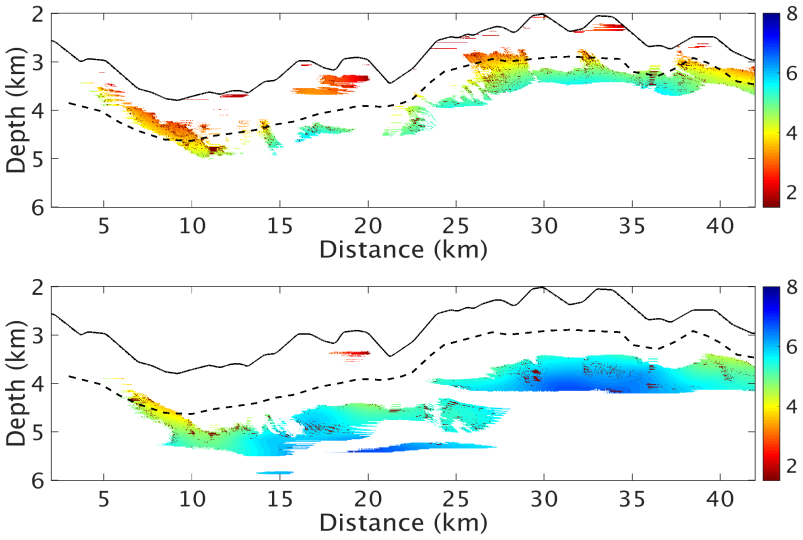

(b)

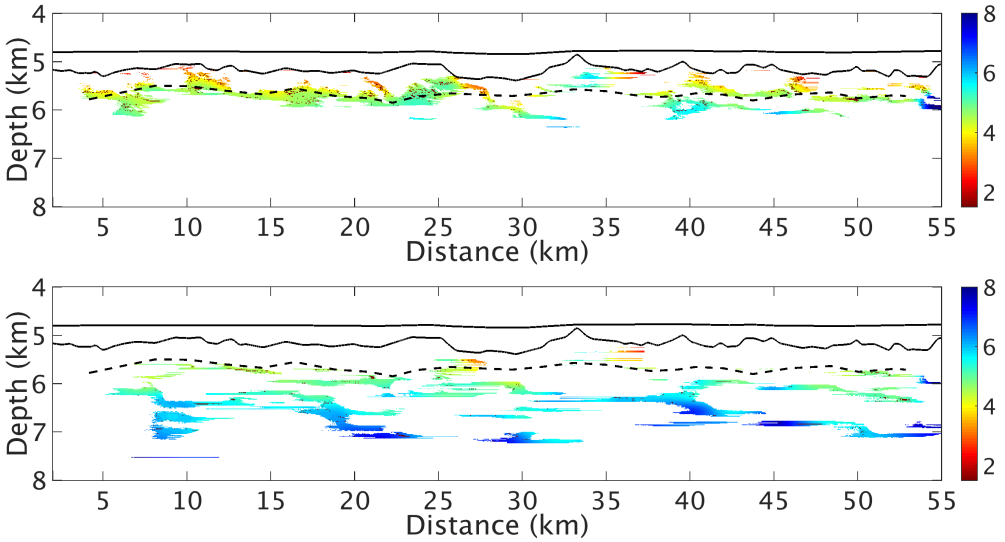

Figure 3.28: P-velocities corresponding the turning points of the rays in the tomography models at two distinct ages in figure 3.20: (a) 0-1.6 Ma and (b) 68.6-71.9 Ma. For each age range, the top panel shows the turning depths of rays arriving at 0-4 km ofset range and bottom panel shows turning depths of rays arriving at 4-8 km offset range.

Alternately, I computed the vertical velocity gradients without the turning rays and from the tomography models itself. The vertical velocity gradients corresponding to the tomograhy models in figure 3.20 are shown in figure 3.29. The black dashed curves are the depth converted layer 2A/2B boundaries as in figure 3.20. As in the previous case of turning rays, the low gradient part of layer 2A is not distinguishable from the high gradient part of layer 2A. However on further examination, a correlation is observed between the layer 2A/2B boundary and the high gradient 2A-low gradient 2B transition. In figure 3.29a, there exists a low gradient region (<1/s of 2A) at 10-11 km distance followed by a higher gradient region (2-2.5/s of 2B) beneath. This high gradient region extends over a depth range of ∼0.5 km and is followed again by a low gradient region (∼1/s of 2B). Hence a low gradient 2A-high gradient 2A-low gradient

2B pattern has been highlighted at the median valley of the ridge-axis. Beneath the ridge flanks, the high gradient of 2B reaches to ∼4.5/s. The layer 2A/2B as mapped lies approximately at the base of the higher gradient region and has an uncertainty of ∼0.3 km. At other older ages, the layer 2A/2B boundary correlates with the high gradient 2A-low gradient 2B transition at some regions for instance, at 2-15 km distance in figure 3.29b. The upper 450-500 m below the basement consists of a high gradient region (>5/s), which is followed by a low gradient region (<2/s). At 30.4-33.4 Ma, the vertical velocity gradient (Figure 3.29c) suggests that the base of the high gradient region corresponds to 2-2.5/s. The boundary between the low gradient layer 2B and the high gradient base of layer 2A is not well resolved in the central part of the profile (Figure 3.29c). Similarly, figure 3.29d shows a high velocity gradient (>5/s) observed in the near surface almost throughout the profile with its base (1.5-2/s) lying roughly 500±165 m below the basement. In figure 3.29e, a good correlation between 2A/2B boundary and high gradient 2A-low gradient 2B transition (∼3/s) for almost throughout the profile is observed. The base of the high gradient region does not transition steeply into the low gradient layer 2B, leading to a weak layer 2A reflection image (Figure 3.11e).

Figure 3.30 shows the 1D profiles of velocity (figure 3.20 and velocity gradients (figure 3.29) at those locations at all ages at which the 2A/2B boundary shows a good match to the distinct gradient regions of 2A and 2B. In figure 3.30a, at x=21.5 and 36 km (blue and black curves), a distinction can be made between high gradient 2A and low gradient 2B regions and the layer 2A/2B (dashed lines) lie approximately at this boundary. At the median valley (red curve), the match is not so good and the 2A/2B event lies below the transition (red dashed curve). In figure 3.30e, at the selected distances, x=13.5 and 40 km (red and black), we find a low gradient just below the basement followed by a high gradient region. This high gradient region again changes to a low gradient region at approximately the depth of the layer 2A/2B boundary (dashed lines). The low gradient corresponds to upper part of layer 2A and the bottom is high gradient which is again followed by low gradient part of layer 2B. At some distances such as x=20 km (blue), the low gradient part of layer 2A is not distinguishable from the high gradient below and appears merged due to the smoothing effect of tomography.

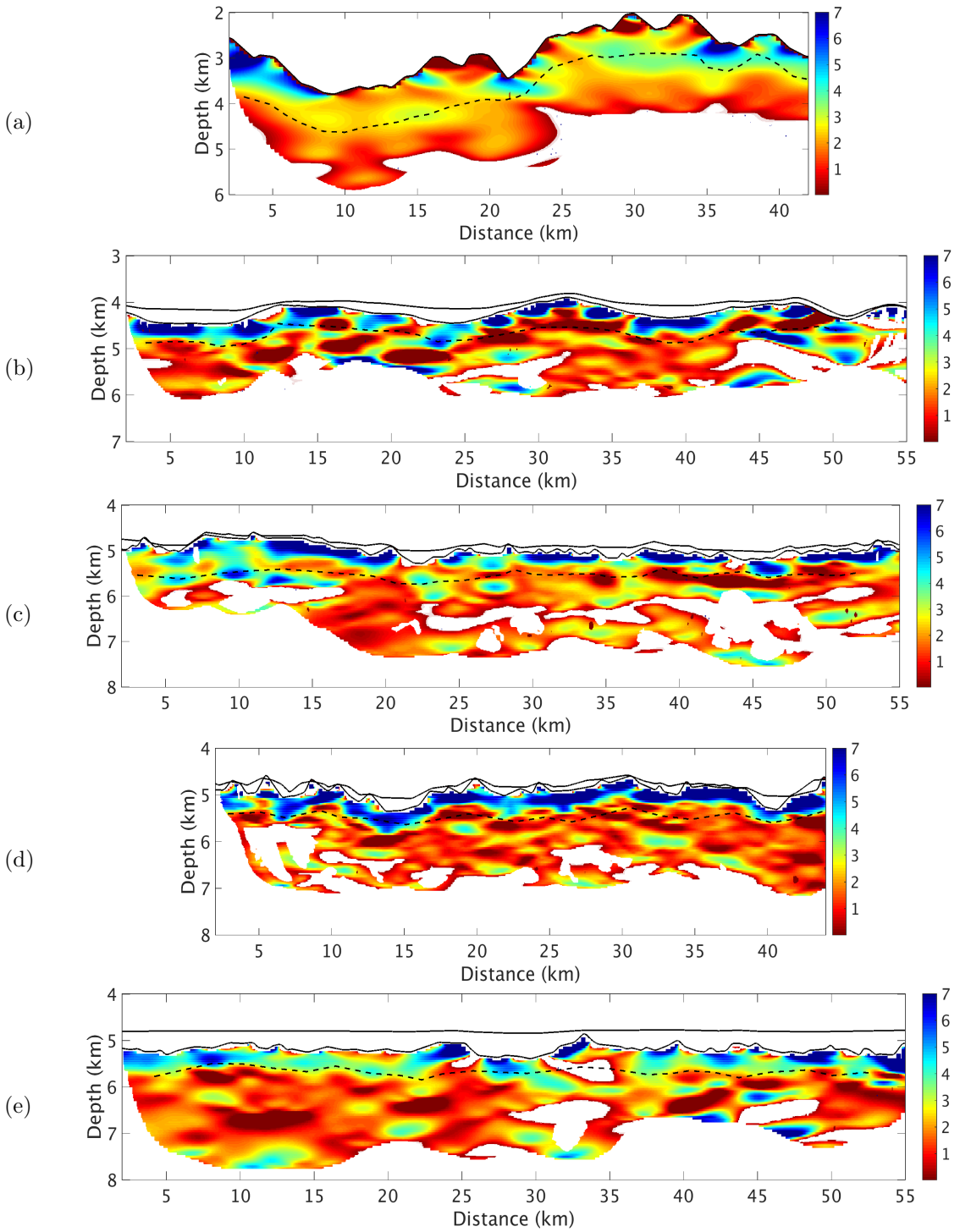

Figure 3.29: Vertical velocity gradient profiles from Figure 3.20. The dashed curves represent the layer 2A/2B boundary which have been depth converted from the seismic records using tomography velocities. At all ages, the layer 2A/2B boundary shows a good match with the base of the high vertical velocity gradient region in the upper oceanic crust and varies from 2.5-4/s at the ridge axis to a more variable 2-5/s at other ages.

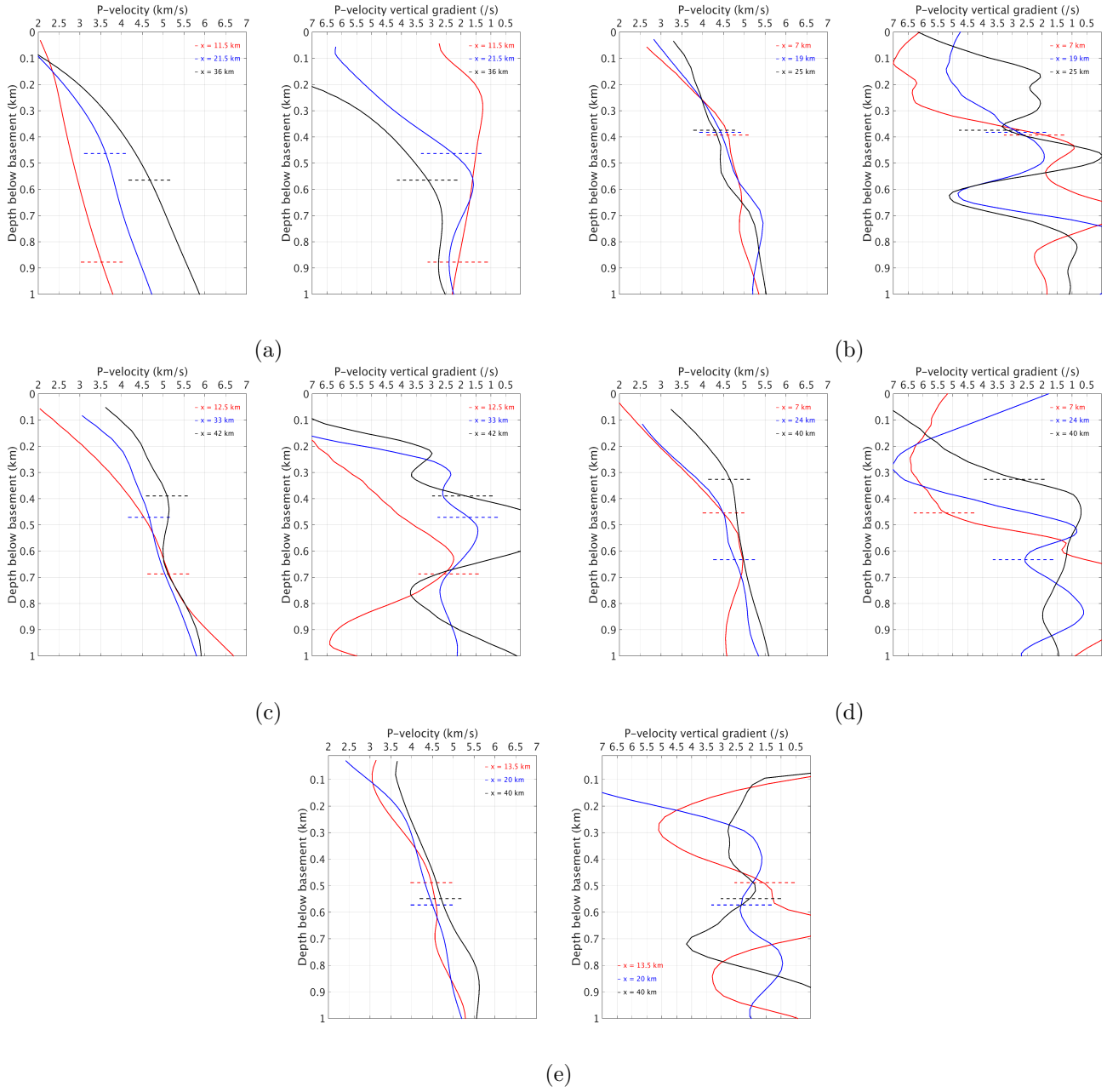

Figure 3.30: 1-D velocity and vertical velocity gradient profiles corresponding to distinct ages from figure 6 are shown by solid curves at distinct distances on the models denoted by x. The dashed curves represent the layer 2A/2B boundary (also from figure 3.20) which have been depth converted from the seismic records using tomography velocities. The low gradient part of layer 2A can be distinguished from the high gradient at the base of layer 2A at some ages (b,d and e) and the layer 2A/2B boundary can be identified as the base of high gradient region of layer 2A at almost all ages.

To summarize, a low gradient 2A-high gradient 2A-low gradient 2B pattern can be distinguished at some ages such as figure 3.30b, d and e. The 2A/2B boundary shows a good match with the high gradient 2A-low gradient 2B transition at least at one location at all ages. At other locations, the smoothing effect of tomography and/or the actual reduction of gradients may be responsible for mismatch observed. Having provided an insight into the correlation of layer 2A/2B boundary with the gradient transition in the velocity models, I now proceed to look at the age-related variations of layer 2A and 2B velocities. P-velocities for layer 2A and 2B were averaged at every 1 Myr (10-16 km) from the tomography models at distinct ages in figure 3.20 to estimate velocities at 24 Myr data points out of 75 Myr. The resulting global-age variation of the P-velocities is shown in Figure 3.31. Additionally, P-velocities at 1 km below the basement was averaged and plotted to get more information from the tomography models.

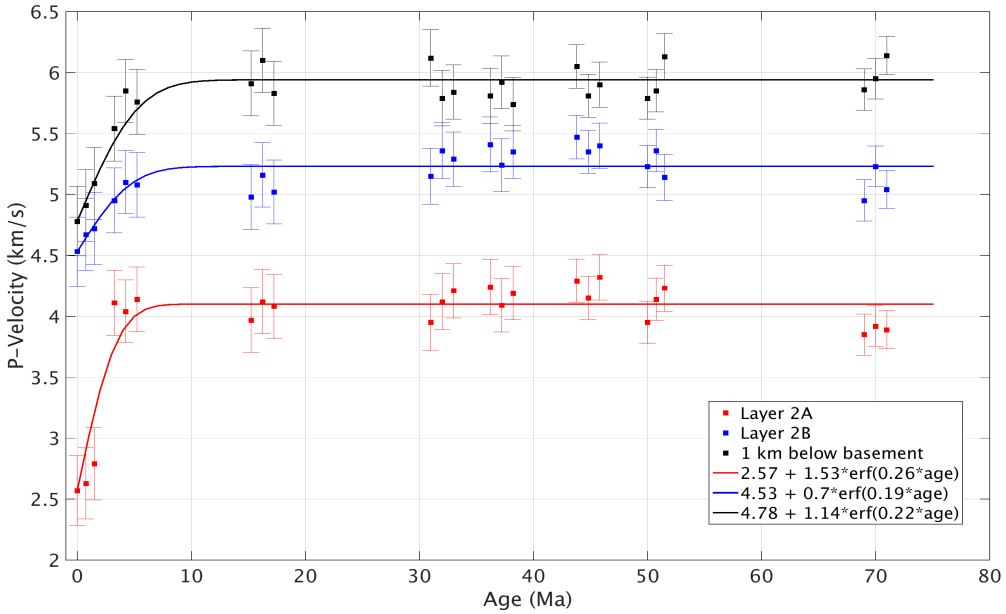

Figure 3.31: P-velocities of layer 2A (red), 2B (blue) and at 1 km below the basement (black) plotted as a function of age. At each region where tomography has been performed (Figure 3.20), velocities 200 m below the basement were picked for layer 2A and along the layer 2A/2B boundary for layer 2B at every 1 Ma. The uncertainties in the velocities are denoted by the error bars respectively. The best fitting polynomial curves for P-velocities are shown by solid lines and correspond to modifications of the relation proposed by *Grevemeyer and Weigel* (1996). The velocities become statistically constant beyond 4 Ma and is 4.1±0.4 km/s for Layer 2A, 5.2±0.5 km/s for Layer 2B, and 5.9±0.5 km/s for 1 km below the basement.

The age variation of the P-velocities in figure 3.31 depicts most of the changes happening within the first 4 Myr with the velocities changing slightly thereafter. A slight decrease in velocities to ∼3.8 km/s is observed at 75 Ma. The layer 2B velocities show smaller variations with velocities ranging in between 4.5-5.5 km/s. Similar to Layer 2A, most of the increase in velocities happens in the first 4 Myr. A modification of the velocity-age variation from *Grevemeyer and Weigel* (1996) was found to have an excellent fit to the velocities of layer 2A:

$$v_{2A} = 2.57 + 1.53erf(0.26t) \tag{3.8}$$

where t is the age in Myr and erf refers to the errorfunction. The statistical parameters justifying the fit are the coefficient of determination $(r^2) = 0.87$ and root mean square error $(r.m.s.e.) = 0.18$ km/s. The equation originally used by *Grevemeyer and Weigel* (1996) to explain the layer 2A velocities with age from OBH data was: $2.1 + 0.58erf(0.04t)$. However, they acknowledge the relation is a simple empirical approximation due to the paucity of the data. In the South Atlantic, using MCS data and same methodology of wavefield extrapolation followed by tomography, *Kardell et al.* (2018) found layer 2A velocities continuously increasing with age, unlike here where most of the evolution is limited to first 4 Myr. They proposed a 5th-order polynomial function to explain velocity variation for 0-14 Ma: $-3.272 \times 10^{-5}t^5 + 12 \times 10^{-4}t^4 - 14.1 \times 10^{-3}t^3 + 2.04 \times 10^{-2}t^2 + 4.695 \times 10^{-1}t + 2.331$ and a logarithmic function to explain the velocities from 0-70 Ma: $log_{29}t + 3.4$. However in this study, the equation 3.8 implies statistically constant values of the layer 2A velocities = 4.1 ± 0.4 km/s beyond 4 Ma. Similarly, for velocities for layer 2B and at 1 km below the basement, the equations 3.9 and 3.11 provide a good fit.

$$v_{2B} = 4.53 + 0.7erf(0.19t) \tag{3.9}$$

$$\text{with} \quad r^2 = 0.69 \quad \text{and} \quad r.m.s.e. = 0.13 \tag{3.10}$$

$$v_{1k} = 4.78 + 1.14erf(0.22t) \tag{3.11}$$

$$\text{with} \quad r^2 = 0.88 \quad \text{and} \quad r.m.s.e. = 0.12 \tag{3.12}$$

3.10 Porosity estimation

The increase of velocities with depth in the uppermost oceanic crust has been well known. There is lack of evidence of increasing metamorphic grade with depth in basalts (*Andrews*, 1977). There is also evidence that metamorphism may not necessarily increase the velocity of basalts (*Fox et al.*, 1973; *Christensen*, 1970). The pressure and temperature coefficients of basalts are too small to be accounted for the increase in velocity with depth as observed (*Murase and McBIRNEY*, 1973). Hence the main predominating factor which can account for the increase of velocity with depth in basalts is the pore and crack geometry. *Wilkens et al.* (1991) show the importance of aspect ratios of crack porosity on seismic velocities. According to this study, a small porosity with a high aspect ratio can cause a much greater reduction in velocity as compared to a spheroidal inclusion with the same porosity.

There have been several studies on the influence of micro-structure on the rock elastic properties. There are three main theories in this regard and are termed the composite medium theories. *Hashin* (1962) and *Hashin and Shtrikman* (1963) approximate the composite material using concentric spheres giving upper and lower bounds on the elastic moduli of the composite material (Hasin-Shtrikman limits). The self consistent approximation (SCA) uses the solution of a single inclusion and approximates the interaction of many inclusions (*Cleary et al.*, 1980). On the other hand, the differential effective medium (DEM) scheme recomputes the elastic moduli of the composite material at the increment of each inclusion (*Budiansky*, 1965; *Hill*, 1965). It also takes into account the alignment of the inclusions (*Te Wu*, 1966). The disordered orientation of inclusions does not show decrease in the P-velocity with increasing porosity whereas the aligned orientation of the inclusions shows a sharper decrease in P-velocity with porosity. A good review of these techniques can be found in *Berryman* (1992) and *Berge et al.* (1993).

Following *Wilkens et al.* (1991), another important parameter that influences the P-velocity-porosity relationship is the inverse aspect ratio of the pores. The inverse aspect ratio is defined as the ratio of polar to equatorial radius. Thus a high inverse aspect ratio pore would be more prolate, i.e. elongated in the poles. Using a P-velocity of basalts at 0% porosity and 200 MPa pressure as 6.4 km/s (*E Johnston et al.*, 1995), the effect on increasing porosity is seen on P-velocity for the different schemes is shown in Figure 3.32. In the two cases, the pores are assumed to be void and filled with seawater within a background basalt matrix.

(a)

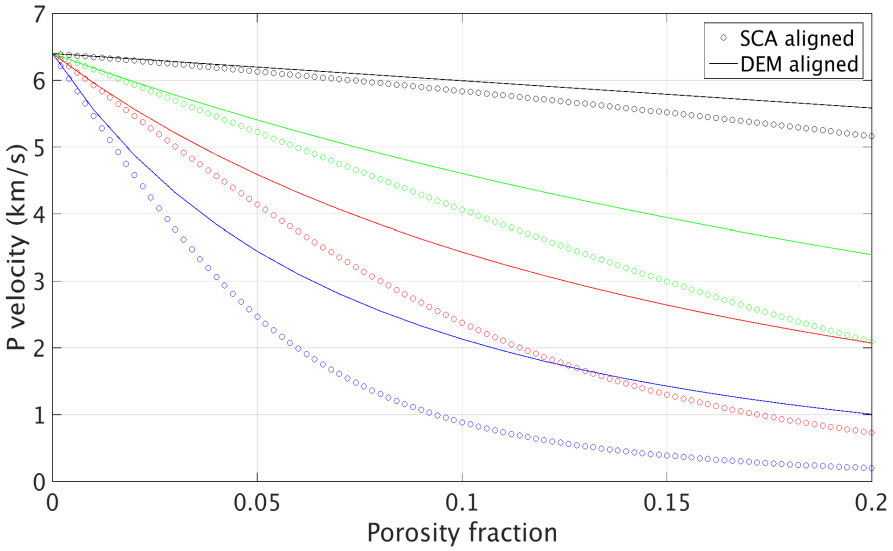

(b)

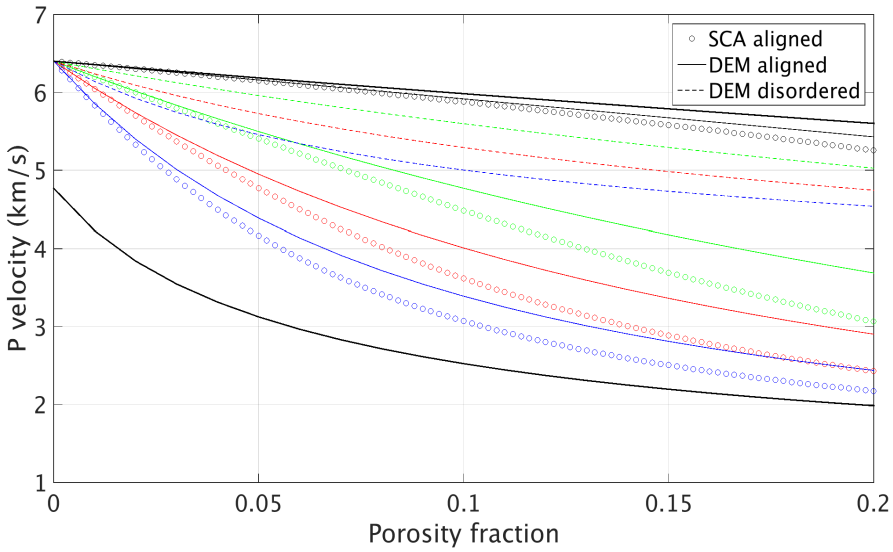

Figure 3.32: The SCA and DEM (aligned, disordered) porosities for different aspect ratios: 1(black), 5(green), 10(red) and 20(blue) for: (a) voids and (b) seawater in a background matrix of basalt. Also shown in thick black lines in (b) are the upper and lower Hashin-Shtrikman bounds of elastic moduli of basalt (*Hashin*, 1962; *Hashin and Shtrikman*, 1963).

I first estimated the porosity variations in both depth and distance for each of the high resolution tomography P-velocity models obtained in section 3.9. Figure 3.33 shows the porosity variations for the SCA scheme for two ages: 30.4-33.4 Ma and 68.6-71.9 Ma. But due to smoothing in tomography models, I do not examine fine-scale porosity-depth variations, but instead only large-scale porosity-age variation in layers 2A and 2B, similar to velocity-age variation in figure 3.31.

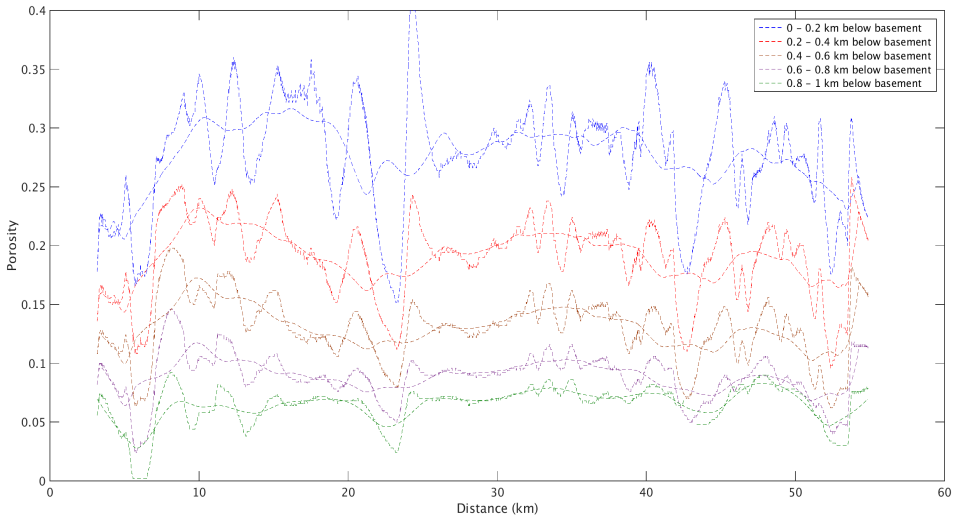

(a)

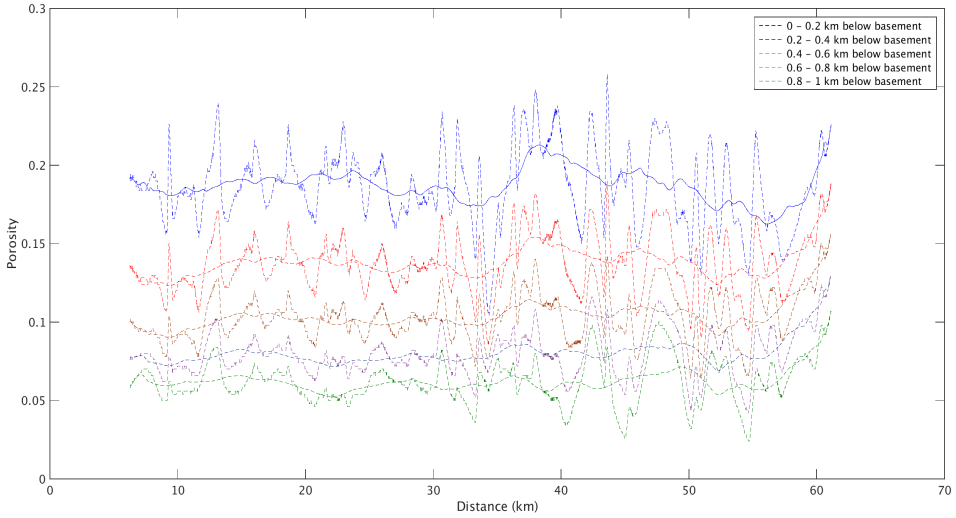

(b)

Figure 3.33: The SCA scheme porosities for (a) 30.4-33.4 Ma and (b) 68.6-71.9 Ma in a background matrix of basalt. The vertically averaged porosities and their variation in distinct depth intervals is shown in dashed lines and a laterally smooth version with a 3 km moving average filter is shown by solid lines.

Effective medium theory (*Taylor and Singh*, 2002) proposes a combination of the SCA and DEM methods to estimate a better constrained velocity-porosity relationship and has been used to compute the porosity filled with gas in fore-arc basins (*Huot and Singh*, 2018). *Taylor and Singh* (2002) also state that DEM can be used as a stand-alone option to compute the stiffness matrix of a composite whose micostructure comprises a background host phase (basalt) containing inclusions of the second phase (seawater) at any composition. I used zero-porosity P-velocity (intercept velocity) of basalt as 6.74 km/s based on borehold modelling studies (*Carlson*, 2014b). *Wilkens et al.* (1991) proposed an upper limit of 7.11 km/s for the P-velocity of an unaltered zero-porosity basalt, which was found to be reduced to 6.74 km/s due to alteration by *Carlson* (2014b). Cracks and pores further lower the P-velocities in the range observed in the tomography results. The density of zero-porosity basalt was taken as 2930 kg/m^3 from borehold modelling of holes 504B and 1256D (*Carlson*, 2014a). For simplicity, I did not consider the seafloor gravity derived density-age variation as proposed by *Holmes and Johnson* (1993): $\rho = 2.62t^{0.045}$. The P-velocity-density relation for basalts proposed by *Carlson and Herrick* (1990) did not sow a good match to our results and so were not used ($\rho = (3.81 \pm 0.02) - (6 \pm 0.1)/V_p$).

A poisson's ratio value of 0.28 at the seafloor and 0.25 at 200 m below the seafloor was found by *Collier and Singh* (1998) at East Pacific Rise. The upper limit of Poisson's ratio was taken from (*Christensen*, 1996) as 0.3. For a P-velocity of 6.74 km/s, a Poisson'ratio varying from 0.25-0.3 yielded intercept S-velocities from 3.574 km/s to 3.896 km/s. A quick test was performed between these two intercept S-velocities and the resulting difference was found to be insignificant and within 0.01 porosity fraction. Hence I chose the value of 0.25 as the poisson's ratio from *Collier and Singh* (1998) which yielded $V_p/V_s = 1.73$. Another assumption I made was to assume the pore spaces being completely filled with seawater (ρ_w =1030 kg/m^3, V_p =1.5 km/s and V_s =0 km/s) and no voids.

As mentioned previously, porosity depends not only on the P-velocity but also on the inverse aspect ratio. In addition to it, the choice of the method (SCA vs DEM) played a role in estimating the porosities from P-velocities. First, I used the above parameters to highlight the difference between the two methods as shown in figure 3.34. Next I look into some of the previous studies to resolve the porosity-inverse aspect ratio ambiguity.

(a)

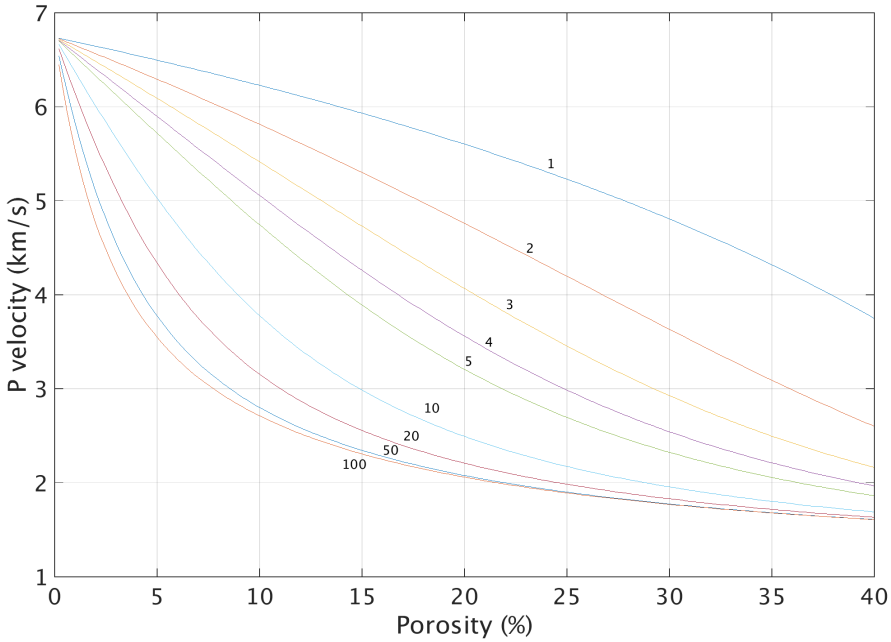

(b)

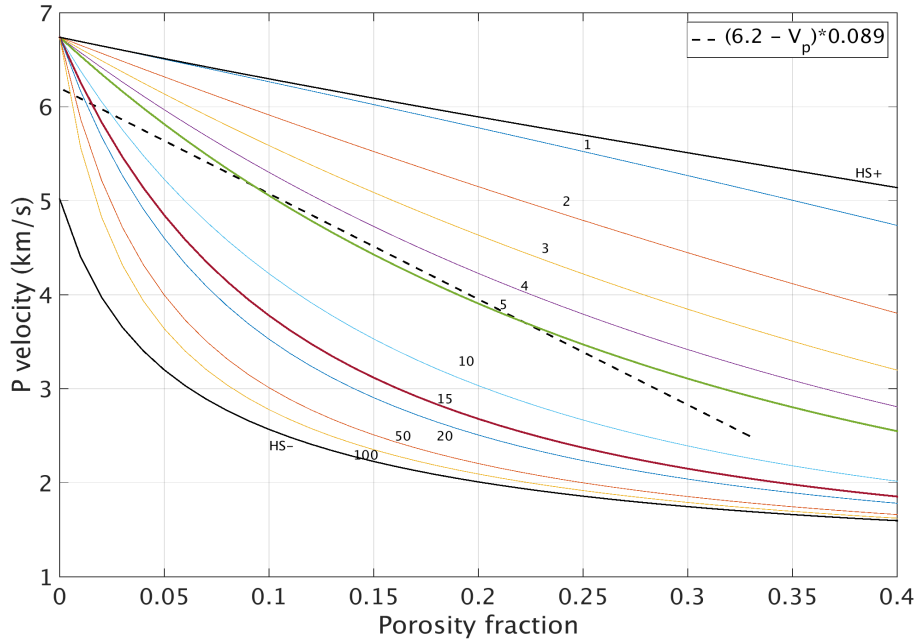

Figure 3.34: Effect of increasing inclusion of seawater in pore-spaces of a background basalt matrix for different aspect ratios for: (a) SCA scheme and (b) DEM aligned scheme. Based on borehole modelling, the best fitting equation for velocity-porosity (dashed black curve) matches an inverse aspect ratio of 5 in the DEM scheme (see text). HS+ and HS− represent the upper and lower bounds of elastic moduli of basalt (*Hashin*, 1962; *Hashin and Shtrikman*, 1963).

The compilation by *Carlson* (2014a) shows the porosities of the upper and lower lavas to be ranging from 5.4-9.8% at boreholes 504B and 1256D with the mean porosity being ∼8%. Boreholes at younger crust such as Endeavor and Blanco FZ have porosities ∼21% at zero age which decreases to 13% at 0.63 Ma. *Holmes and Johnson* (1993) also observe similar porosity variations from 23.2% at the ridge-axis to 11.3% at 0.73 Ma. *Grevemeyer and Bartetzko* (2004) find a 10% decrease in porosity by 15 kyr but as *Carlson* (2014a) notes, there is no correlation of porosity with age beyond 0.2 Ma at the Endeavor segment. At the Reykjanes Ridge segment of the MAR, the crustal porosity has been found to decrease from ∼25% to ∼7% at 1 km depth (*Greer et al.*, 2002). This porosity-depth variation trend is also observed from figure 3.33.

With the porosity estimates from the previous studies, the choice of both the method and inverse aspect ratio became simpler. The DEM scheme explains the zero-age velocities for 2A (2.57 km/s from figure 3.34) within the reasonable range of porosities (∼20%) using a higher inverse aspect ratio (∼15). The SCA scheme gives an inverse aspect ratio of ∼10 to explain the zero-age velocities with porosities (∼20%). For layer 2B, an inverse aspect ratio of 5 shows porosities ∼8% at older ages for both the SCA and DEM schemes. Thus in order to explain our P-velocities with a reasonable porosities, inverse aspect ratios in the range of 5-15 (DEM) or 4-10 (SCA) are obtained. The values of the inverse aspect ratio proposed by *Carlson* (2010) for modeling extrusives at boreholes 504B and 1256D are 10 and ∼14 respectively. Moreover, a modification of the P-velocity-porosity relation proposed by *Carlson* (2014a):

$$\phi = (6.2 - V_p) * 0.089 \tag{3.13}$$

showed a very good match to inverse aspect ratio of 5 using the DEM scheme. The parameters justifying the fit are coefficient of determination, $r^2 = 0.69$ and root mean square error, $r.m.s.e. = 0.0098$. Hence, the DEM scheme was preferred as it more closely matched borehole results. For layer 2B an inverse aspect ratio of 5 showed excellent fits as sown in figure 3.34. Layer 2A and 2B porosities were computed using the P-velocities from figure 3.31 and the velocity-porosity relation from figure 3.34b. For layer 2B, an inverse aspect ratio of 5 was used, as discussed above. For layer 2A, two different inverse aspect ratios were considered as described below and shown in figure 3.35.

An inverse aspect ratio of 5 for layer 2A yielded very high porosities as compared to previous porosity estimates of the extrusives. Also, it did not show a good match to the best fit velocity-porosity relation as was obtained for layer 2B ($r^2 = 0.14$ and $r.m.s.e. = 0.0336$). But upon varying the inverse aspect ratio of layer 2A to 15, a good match with porosities of layer 2B (inverse aspect ratio of 5) and with those of previous studies was obtained. So while one way of perceiving layer 2A/2B boundary was change in the porosities using the same aspect ratio, another way was change in the aspect ratio to obtain similar porosities. In visualizing the layer 2A/2B as a change in inverse aspect ratio, I quantified an estimate of three times thinner cracks in layer 2A (inverse aspect ratio=15) as compared to layer 2B (inverse aspect ratio=5). So, the change in velocities from layer 2A to layer 2B could be explained by filling of thinner cracks in 2A without much significant change in porosity between layers 2A and 2B.

(a)

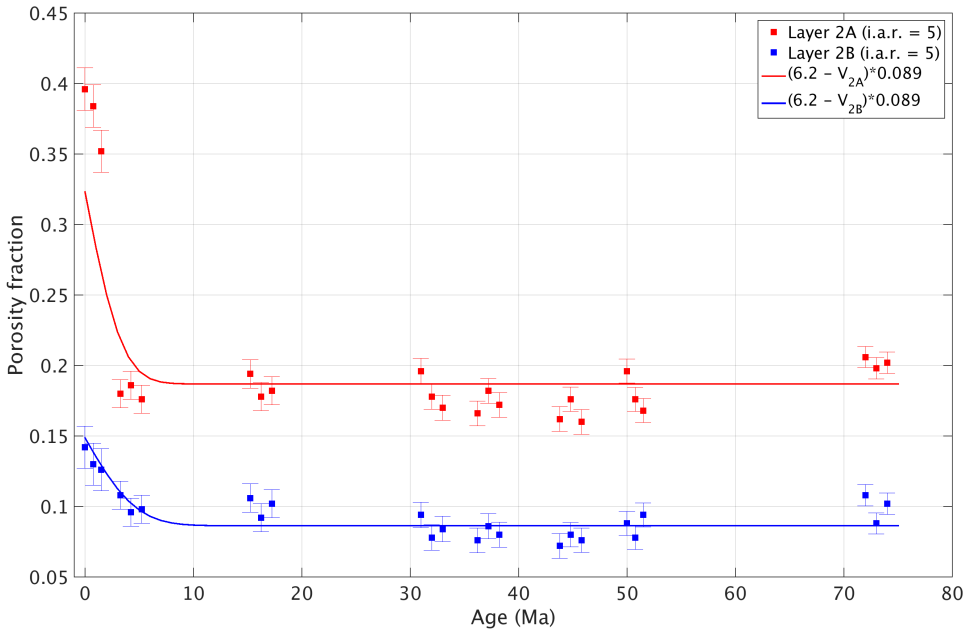

(b)

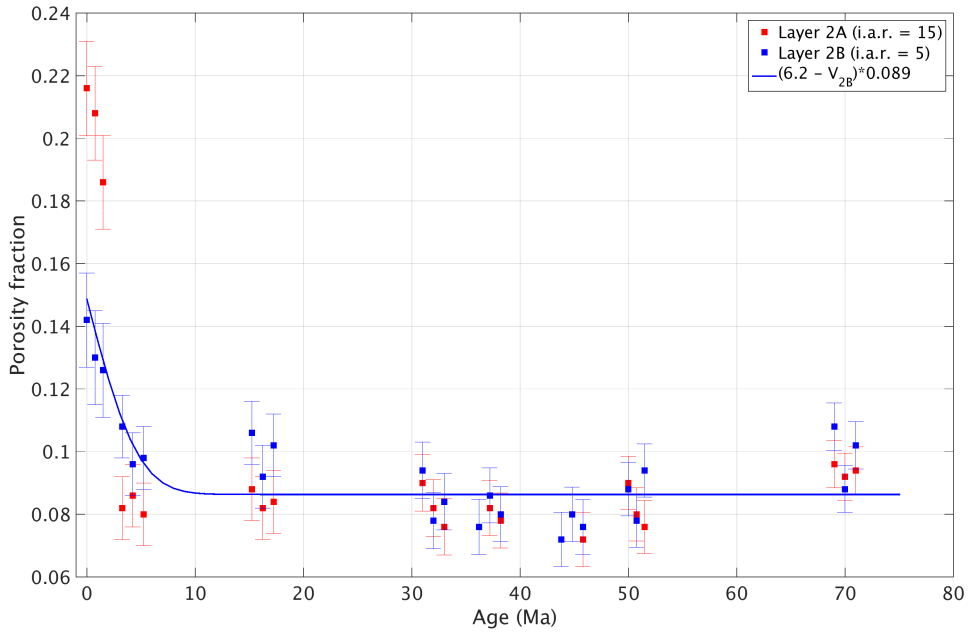

Figure 3.35: Layer 2A and Layer 2B porosities computed from figure 3.31 using: (a) inverse aspect rato of 5 for both 2A and 2B and (b) inverse aspect ratio of 5 for layer 2B and 15 for layer 2A.

The zero-age porosity for layer 2A is ∼21% which decreases to ∼14% at depths of ∼850 m corresponding to layer 2A/2B boundary. Away from the ridge-axis, the porosities for both layer 2A and along 2A/2B boundary lie in the range of 7-11% which match the porosity estimates from previous studies. The key point from the porosity analysis on this data set has not been the porosities itself, but the inverse aspect ratios used to obtain the porosities such that they match the previous estimates. This is elaborated when defining the layer 2A/2B boundary in the next section.

3.11 Inferences on upper crustal properties and processes

In the previous sections, I have obtained adequate information from seismic imaging, P-velocity, velocity gradients and porosity analyses for the upper crust. Here, I attempt to provide an unified view of these upper crustal properties along with their variation with age and the processes which affect them.

3.11.1 Layer 2A P-velocities at zero-age

An increase in P-velocity from 2.57±0.28 km/s at zero-age to 2.79±0.28 km/s by ∼1.5 Myr is found in figure 3.31. The P-velocity obtained at zero-age at 35°N Mid-Atlantic ridge is 2.3 km/s and increases to >2.7 km/s within ∼2 Myr (*Hussenoeder et al.*, 2002a). At 8-9°S Mid-Atlantic ridge, a mean layer 2A velocity of 2.74±0.24 km/s close to zero-age has been obtained by modeling of wide-angle data (*Minshull et al.*, 2003). At the Lucky Strike segment, zero-age velocities are found in the range 2.2-3 km/s (*Arnulf et al.*, 2011) whereas *Kardell et al.* (2018) find velocities of ∼2.4 km/s in the South Atlantic. A comparison of layer 2A zero-age P-velocities is shown in table 3.2. The results in this study at zero-age are in good agreement with most of the studies in the slow-spreading Mid-Atlantic ridge.

Table 3.2: Comparison of zero-age layer 2A P-velocity at different spreading centers

Study	Spreading center	Zero-age P-velocity (km/s)
Hussenoeder et al. (2002a)	35°N MAR	2.3
Minshull et al. (2003)	8-9°S MAR	2.74
Arnulf et al. (2011)	Lucky Strike segment MAR	2.2-3
Kardell et al. (2018)	30°S MAR	2.4
Navin et al. (1998)	Reykjanes segment MAR	2.6
Nedimović et al. (2008)	Juan de Fuca Ridge	2.3-2.5
Hussenoeder et al. (2002b)	17°S East Pacific Rise	2.1-2.4
This study	2°S MAR	2.57

MAR is the slow-spreading Mid-Atlantic Ridge

3.11.2 Off-axis Layer 2A P-velocities

The top of the crust is always found to have velocities less than 4.5 km/s throughout the profile with velocities reaching 4.1 km/s within 4 Myr as shown in figure 3.31. The proposed velocity-age variation in equation 3.8 is relatively more rapid as that observed by *Kardell et al.* (2018), who observe velocities reaching ∼4.2 km/s by 6 Ma. This rapid increase of velocities is attributed to active hydrothermal circulation and deposition of precipitates, leading to closure of the pore-spaces. This is also related to rapid thickening of sediments within the first 4 Myr (figure 3.7), which would act as a blanket and cease active hydrothermal circulation. The sediment blanketing could allow the hydrothermal fluids to stay longer in the crust and increasing the precipitate, as indicated by the increase of velocity. However, basement outcrops are exposed very frequently along the profile as seen in the seismic in figure 3.1. Hence, more important than sediment blanketing is the reduced heat available for hydrothermal circulation and precipitation away from the ridge axis. This reduced heat flow results in reduced kinetic energy of the circulating water in the upper crust and therefore slows down and limits its interactions with the host rock. This can be considered a less vigorous form of hydrothermal circulation, which is termed as passive hydrothemal circulation. Passive, off-axis hydrothermal circulation is characterized by low Rayleigh numbers indicating a much steadier flow as compared to the turbulent flow observed in on-axis active hydrothermal systems.

Kardell et al. (2018) observe velocities reaching ∼4.9 km/s at 58 Ma and propose low-temperature hydrothermal circulation causing continuing evolution of layer 2A. However, I find layer 2A velocities become statistically constant at 4.1±0.4 km/s beyond 4 Myr, similar to *Grevemeyer and Weigel* (1996). A clear trend can not be identified beyond 4 Ma as the velocities show a slight decrease at 16 Myr and an increase at 35-45 Myr with a local effect again reducing the velocities at 75 Ma. The local effect reducing the velocities to ∼3.8 km/s near 70 Ma may be due to thermal anomaly from adjacent volcanic chains.

Fluid circulation has been demonstrated in crust as old as 106 Ma on the Atlantic ocean floor (*Fisher and Von Herzen*, 2005). As discussed in chapter 1, the northward propagating rift between the African and South American plates slowed down considerably in the Equatorial Atlantic, causing differences in evolution of the African Plate in the Equatorial Atlantic and the South American Plate in the South Atlantic. This difference in evolution of the two distinct study regions is apparent from the lower layer 2A velocities in this study as compared to *Kardell et al.* (2018).

3.11.3 Layer 2A thickness at zero-age

Figure 3.13b shows the variation of seismic two-way travel time (TWTT) thickness of layer 2A with age. It decreases from 500±70 ms at the ridge axis to 300±30 ms at 15 Ma and continues until 75 Ma. Regions having a thicker sediment cover and flatter basement morphology provide good layer 2A images and better constrain its thickness. Local thickening and thinning of the seismic layer 2A are observed beneath bathymetric valleys and seamounts as seen in figure 3.11. To estimate the physical thickness of layer 2A from the two-way time thickness, the P-velocities from tomography in figure 3.31 was simply multiplied by the one-way thickness in figure 3.13b. The resulting variation of physical thickness of layer 2A with age is shown in figure 3.36. This is described below and a comparison with the other studies is also made.

At the ridge-axis, the thickness of layer 2A is variable and lies in the range of 750-900 m±315 m with the maximum thickness being ∼900 m at ∼1 Ma beneath the ridge flanks (figure 3.36). This is close to layer 2A thickness estimated at the Lucky Strike segment of the Mid-Atlantic ridge (*Combier et al.*, 2015), the hotspot influenced Reykjanes segment (*Navin et al.*, 1998) and near the Ascension islands (*Minshull et al.*, 2003). The thickness obtained by these individual studies as well as the thickness at other spreading centers and their variation with age have been described in chapter 1. In the South Atlantic, *Estep et al.* (2019) estimate layer 2A thickness of ∼1000 m near the ridge-axis from the same seismic experiment as *Kardell et al.* (2018).

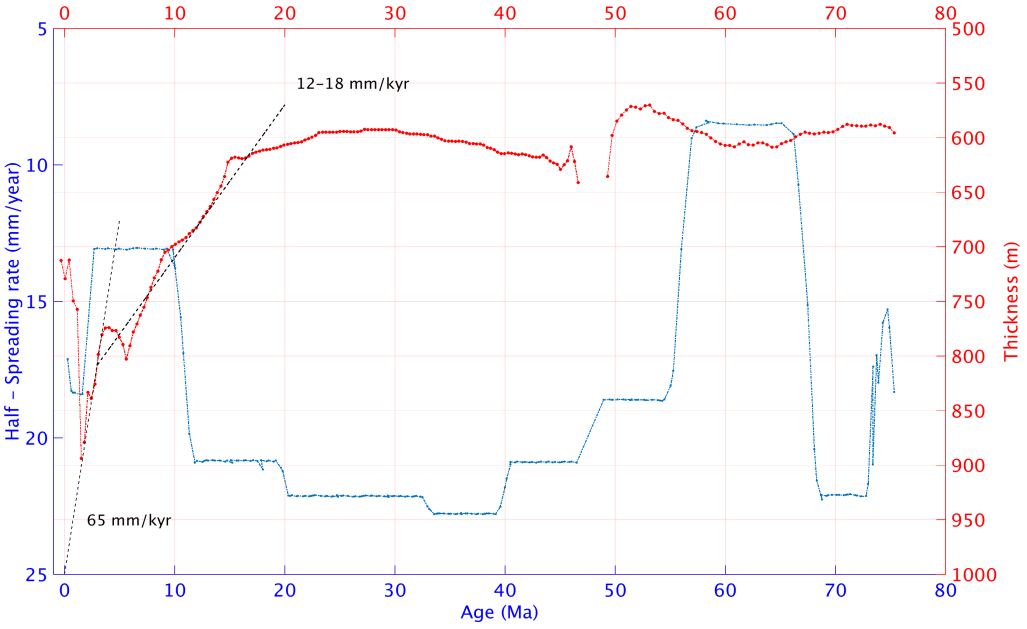

Figure 3.36: Variation of Layer 2A thickness (red) with age and half-spreading rate (blue) (*Müller et al.*, 2008) in the Equatorial Atlantic. Black dashed lines show two distinct thinning rates which have been identified as corresponding to the distinct age ranges. The upper bound of uncertainty on the thickness of layer 2A is ±315 m and is found in regions of rugged bathymetry and the lower bound of uncertainty in regions of relatively flatter bathymetry is ±165 m.

3.11.4 Off-axis layer 2A thickness

In the South Atlantic, *Estep et al.* (2019) estimate layer 2A thickness of ∼1000 m near the ridge-axis and a mean thickness of 759±326 m for crust aged 0-7 Myr in the South Atlantic. They do not observe layer 2A thinning systematically with age and find an increase in layer 2A thickness at 15-31 Ma. However, I find a decrease in layer 2A thickness from a maximum of ∼900 m near the ridge-axis to ∼770m at 4 Myr and estimate a thinning rate of 65 mm/kyr in figure 3.36. This corresponds to the regime of rapid sedimentation from 0-4 Myr (figure 3.7). From 4-15 Myr, a further reduction in layer 2A thickness is seen without a clear trend and estimated thinning rates vary from 12-18 mm/kyr. Beyond 15 Myr there is not much change in the layer 2A thickness and we estimate thickness in the range of 570-620 m with an uncertainty ranging from ±365 m to ±165 m. These thickness values are similar to off-axis thickness of layer 2A at other spreading centers (*Hussenoeder et al.*, 2002a). It is very likely that the two distinct thinning rates are linked to how hydrothermal circulation is influencing the uppermost crust as described in the following.

The off-axis thinning of layer 2A at slow spreading ridges can be explained by considering sea-water circulating to greater depths at the ridge-axis where no sediments are present and the upper crust is faulted due to tectonic extension (figure 3.11a). Heat from base of the lithosphere would be higher as it is shallower near the ridge-axis and would result in increased hydrothermal circulation and precipitation of minerals at depths corresponding to layer 2A/2B boundary observed in this study. Away from the ridge-axis, a rapidly thickening sediment cover accompanied by reduced heat supply due to subsidence of the base of lithosphere may restrict the depths of penetration of the hydrothermal fluids. The thickness variation, derived from the P-velocities variation, again suggest that the regime from 0-4 Myr may be influenced by active hydrothermal circulation which decreases away from the ridge axis and passive hydrothermal circulation may influence the crust from 4-15 Myr. As a result, a higher thinning rate of 65 mm/kyr is observed from 0-4 Ma followed by a more gradual thinning of 12-18 mm/kyr from 4-15 Ma. Locally, the layer 2A thickness may also be affected by a heat source which metamorphoses the lavas and hence decrease the thickness. An alternate explanation attributes the off-axis thinning to tectonic reasons with the layer 2A erupted as a volcanic mound at the ridge axis and then faulted, thinned and transported off-axis (*Macdonald*, 1982; *Combier et al.*, 2015).

Estep et al. (2019) do not observe layer 2A event in the seismic beyond 48 Myr which they attribute to rough basement topography and/or the closure of pore spaces lying below the threshold to be seen in seismic records. However, layer 2A event is intermittently imaged in this study until 75 Myr, indicating that the pore spaces are not fully closed in the uppermost lavas and that there still exists an observable change in the uppermost lavas and the underlying altered lavas. Along with *Estep et al.* (2019) and other studies on the Mid-Atlantic ridge, the results of this study suggest that thickness of layer 2A is established at the ridge-axis in slow spreading centers such as Mid-Atlantic ridge. Unlike fast spreading ridges such as East Pacific rise where a rapid thickening takes place (*Harding et al.*, 1993; *Vera and Diebold*, 1994) or at intermediate spreading centers such as Juan de Fuca ridge (*Canales et al.*, 2005) and Galapagos spreading center (*Blacic et al.*, 2004) where gradual off-axis thickening is observed, these results indicate that off-axis thinning is observed in slow spreading centers and off-axis thickness of layer 2A (∼600 m) is similar to those at other spreading centers (*Hussenoeder et al.*, 2002a).

The above quantification of thinning of layer 2A is valid assuming the spreading rate is independent of layer 2A thickness and most of the crustal thickness variations are linked to lower crustal (layer 3) thickness variations, as proposed by *Mutter and Mutter* (1993). Usually, a much variable crustal thickness is observed in a slower spreading rate (*Chen*, 1992; *Lizarralde et al.*, 2004) as compared to faster spreading rates. Slow spreading rates are observed at 3-10 Myr, ultraslow spreading rate at 57-65 Myr and intermediate spreading rates at 12-46 Myr for the study region as computed by *Müller et al.* (2008). Similar to observations of *Estep et al.* (2019), layer 2A thickness does not correlate with the spreading rate as shown in figure 3.36. If the thickness of layer 2A were completely produced at the ridge-axis and unaffected by hydrothermal circulation, there must be a correlation between the spreading rate and the layer 2A thickness. The absence of a correlation between the spreading rate and layer 2A

thickness implies influence of process such as hydrothermal circulation to account for thinning of layer 2A. It is fair to assume a uniformly thick layer 2A being produced at the ridge axis with hydrothermal circulation thinning layer 2A to different degrees depending on whether it is in younger crust (active) or older crust (passive).

3.11.5 Variation of layer 2B P-velocities with age

The velocities along the 2A/2B boundary show an increase in velocities ranging from ∼4.5 km/s at zero-age to a maximum of ∼5.5 km/s in older oceanic crust (figure 3.31). Similar to layer 2A, the velocities in layer 2B are found to increase rapidly within first 4 Myr from ∼4.5 km/s at zero age to 5.1 km/s at 4 Myr. Whereas velocities in layer 2A become statistically constant at 4.1±0.4 km/s beyond 4 Myr, velocities in layer 2B show slightly more variations. A gradual increase from ∼5.1 km/s at 4 Myr to a maximum of ∼5.5 km/s at 36-46 Myr could be due to an off-axis increase in the depth of penetration of the circulating fluids involved in hydrothermal circulation. This gradual increase of layer 2B velocities with age until ∼40 Myr is an unique and important observation from this data set. In most of the studies described in the following paragraph, the evolution of layer 2B has been limited to much younger ages. This increase in velocities at 36-46 Myr is followed by the lowering of velocities to ∼5.2 km/s at 51 and 70 Myr.

In the South Atlantic, *Kardell et al.* (2018) observe layer 2B velocities of 5 km/s close to the ridge axis, which varies slightly within the first 12 Myr and find velocities reaching 5.5 km/s more rapidly at ∼20 Myr. At the intermediate spreading Juan de Fuca ridge, *Newman et al.* (2011) propose a rapid evolution of layer 2B velocities to 5.2±0.3 km/s within 0.5 Myr from crustal formation. However, *Christeson et al.* (2012) finds velocities in upper part of layer 2B in the range 4.7-4.9 km/s with a average value of 4.8±0.25 km/s at young fast and intermediate spreading centers. The inconsistent values of layer 2B velocities in these studies may be due to differences in methods of estimation or due to differences in geological settings of the regions. The range of layer 2B velocities beyond 4 Myr observed in this study can be approximated as 5.2±0.5 km/s which is close to the data compiled by *Houtz and Ewing* (1976), who estimate mean layer 2B velocities in the Atlantic as 5.13±0.38 km/s and matches with the observed velocities at Juan de Fuca (*Newman et al.*, 2011).

3.11.6 What is the layer 2A/2B boundary ?

An important observation from figure 3.31 is that velocities at top of layer 2B do not exceed 5.8 km/s, which is the lowest velocity observed in dikes at boreholes 504B and 1256D (*Carlson*, 2014a). This is also found from seismic data compiled by *Carlson* (2018), who proposes the dike section to be layer 2C as originally observed by *Houtz and Ewing* (1976). At depths of 1 km below the basement, we find velocities in the range 4.8-5.1 km/s at the ridge-axis and a more variable 5.5-6.2 km/s at older ages from figure 3.31. This implies that the dike section is reached within 1 km below the top of the crust. The lower velocities in the dike section at zero age are possibly due to higher temperatures near the ridge-axis and are close to velocities observed at the layer 2A/2B boundary. The distinction between 2A/2B velocities and velocities 1 km below basement becomes clear away from the ridge axis. The velocity-age variation 1 km below the basement is given by the best fitting curve $V(t) = 4.78 + 1.14erf(0.22t)$ which become statistically constant at 5.9±0.5 km/s beyond 4 Myr. Additionally, estimated porosities for the top of layer 2B (figure 3.35) using an inverse aspect ratio of 5 show a good match to the porosities in the extrusive section observed in boreholes (*Carlson*, 2014a). Hence, it would be safe to conclude from our results that the layer 2A/2B boundary could be a lava/dike transition at the ridge-axis and a hydrothermal alteration boundary within the extrusive section away from the ridge.

Figure 3.35 helps further to understand the layer 2A/2B boundary in terms of grain size and porosity. Whereas the same aspect ratio for layer 2A and 2B helps visualizing 2A/2B boundary as a porosity boundary in figure 3.35a, it does not show a good match to the borehole observations as mentioned in section 3.10. Hence, the inverse aspect ratio used in computing the porosities for layers 2A and 2B has been adjusted to fit the borehole observations as shown in figure 3.35b. The increase in velocity from

layer 2A to layer 2B may then be caused by a change in the concentration of thin cracks, rather than porosity itself. The filling up of three times thinner cracks in layer 2A (inverse aspect ratio of 15) due to hydrothermal alteration would produce a relatively large velocity increase (*Wilkens et al.*, 1991) compared to layer 2B (inverse aspect ratio of 5). So, the 2A/2B boundary can be visualized as representing the change from a layer populated by thin cracks (2A) to a layer populated by relatively three times thicker cracks (2B).

3.11.7 Summary

The results of this study indicate the possibility of a continuous hydrothermal system from the ridge axis to the mature oceanic crust (∼15 Ma) with passive hydrothermal circulation systems becoming dominant beyond 4 Ma (figure 3.37). The active hydrothermal systems found near the ridge axis, which are associated with smoker fields and high temperature vents cause a rapid increase in layer 2A velocities. These circulations are characterized by high Rayleigh numbers, which exceed the critical Rayleigh number indicating turbulent fluid motion and precipitate massive sulphide deposits as secondary minerals (*Alt*, 1988; *Humphris*, 1998; *Elderfield*, 1988). The high sedimentation rate away from the ridge-axis would restrict the depth of penetration of the hydrothermal fluids and thereby reducing the layer 2A thickness. Off-axis, heat from the base of lithosphere is reducing due to cooling of the lithospheric plate leading to passive hydrothermal circulation, which is found to be dominant beyond 4 Myr and until 15 Myr at which layer 2A reaches typical off-axis thickness values. A gradual increase in layer 2B velocities in observed until ∼46 Myr, which may be due to depth of the hydrothermally circulating fluids. Recent results of the Oman drilling project (*Harris et al.*, 2017) have found evidence of a hydrothermally altered lower crust indicating the depth of penetration of hydrothermal fluids in the lower crust. The layer 2A/2B boundary is proposed to be a lava/dike transition on-axis and a hydrothermal alteration boundary within the extrusive section off-axis. These results match well with the model proposed by *Shaw* (1994), in which the thin cracks preferentially close at shallow depths (in layer 2A) in young oceanic crust by hydrothermal alteration while thicker cracks at greater depths (layer 2B) gradually seal with age also by hydrothermal deposition. This explains the gradual increase of layer 2B velocities with age and layer 2A having thinner cracks as compared to layer 2B.

Fluid circulation may continue in the basement beyond 15 Myr without significantly influencing layer 2A velocities and thickness. Basement outcrops, having higher permeability ($10^{-13}m^2$) than sediments ($10^{-15}m^2$), act as discharge and recharge sites for passive hydrothermal systems and fluid circulation (*Harris et al.*, 2004; *Villinger et al.*, 2002). The vertical gravity gradient map of the study region shows a large number of fracture zones through which fluids may seep into the crust easily. The recharge and discharge outcrops can be separated by as much as 50 km as observed at the Juan de Fuca Ridge (*Fisher et al.*, 2003). Apart from *Kardell et al.* (2018) who support the idea of long lasting hydrothermal circulation, *Baker et al.* (1991) suggest a large scale lateral advection of seawater through basaltic oceanic crust on the basis of isotopic pore water composition of overlying sediments in equatorial Pacific ocean over an age spanning 15 Ma to 70 Ma. They find average residence time of seawater in basement is computed to be 20,000 years with an inferred pore fluid velocity between 1 and 10 m/yr. Anomalous heat flow values have been found at 83 Ma Atlantic seafloor (*Embley et al.*, 1983) and local thermal anomalies such as these may create sufficient lateral pressure gradients for onset of local hydrothermal systems. Additionally, the slope of the seafloor/basement plays a crucial role in determining the direction of fluid flow (*Johnson et al.*, 1993; *Wang et al.*, 1997). Models of hydrothermal circulation have been demonstrated to be consistent with observations in crust as old as 106 Ma in the Atlantic (*Fisher and Von Herzen*, 2005).

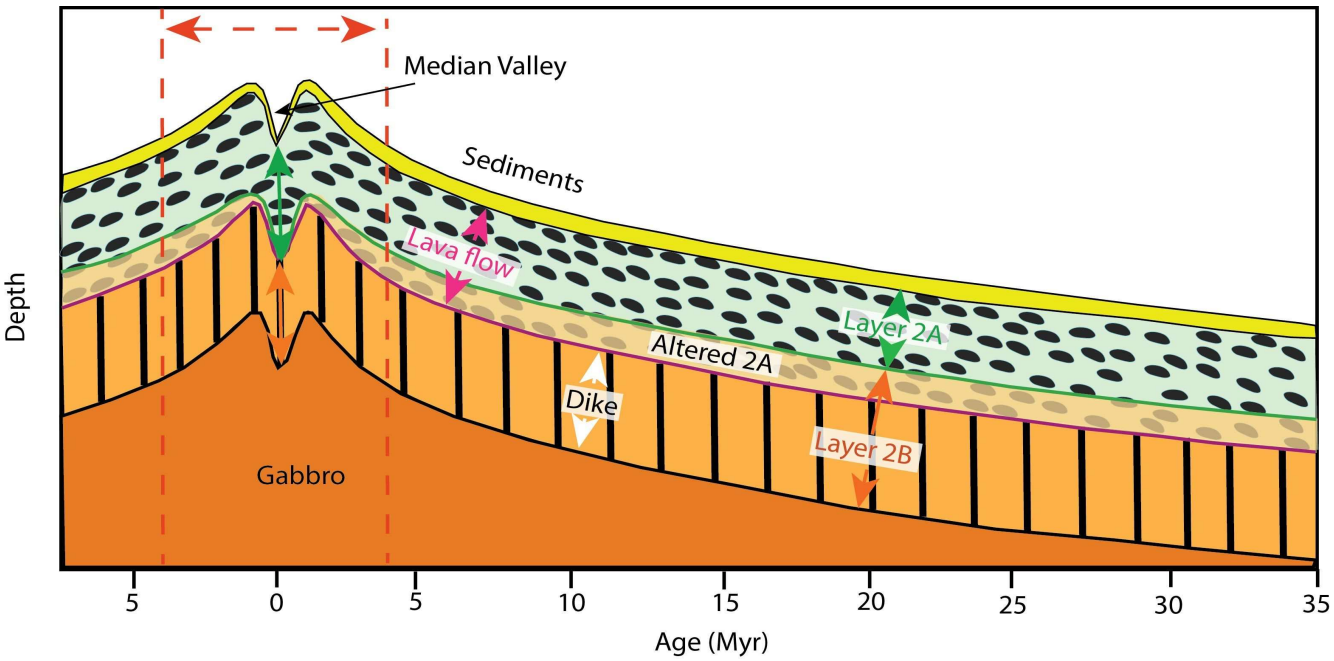

Figure 3.37: Schematic sketch showing layer 2A persisting as a basaltic layer even at mature crustal ages. Active hydrothermal circulation is limited to first 4 Ma, after which passive hydrothermal circulation becomes dominant. After 15 Ma, hydrothermal circulation stops influencing the layer 2A, although fluid circulation may continue with the basement outcrops serving as recharge and discharge sites. Local effects like increase in P-velocity may be due to passive hydrothermal systems. The Layer 2A/2B boundary is a lava/dike contact at the ridge axis, whereas it is a hydrothermal alteration boundary above the dikes in older crust. Note that the image is not to scale.

This unique dataset has co-located heatflow and multi-channel seismic (as compared to previous heatflow studies which use single channel seismic) and I realized I have an opportunity to validate the implication of hydrothermal circulation system made above. In the remainder of this chapter, I further analyze the co-located heat-flow dataset and used it to estimate the bulk permeabilities. I then compare the porosity-permeabilty estimates with models of percolation theory.

3.12 Co-located heat flow data

As introduced in chapter 1, heatflow measurements at distinct age ranges were made in the 2017 LITHOS expedition. The distinct heatflow measurements made relative to the 2015 MCS profile is shown in figure 3.2. At each age range, 9-12 measurements were made at spacing of ∼1 km apart at regions having at least some sediment cover where the heatflow probes could be coupled with the ground. Instead of measuring heatflow directly, vertical temperature gradient ($\frac{dT}{dz}$) and thermal conductivity (k) measurements were made at each probe site and the resulting conductive heatflow, q, was obtained by the expression:

$$q = k\frac{dT}{dz}. \tag{3.14}$$

3.12.1 Validating hydrothermal systems

Surface heatflow measurements have been commonly used to determine presence of hydrothermal systems (*Fisher et al.*, 2003). Sites where observed heatflow is lower than the predicted value are termed as recharge sites, where cold seawater enters the crust and redistributes the heat laterally. Discharge sites are those where the heated seawater exits the crust and the resulting heatflow is higher than the predicted. Some recent studies such as *Marjanović et al.* (2017) based on high-resolution P-velocity models from full waveform inversion have been able to obtain signatures of the hydrothermal pathways of seawater between the recharge and discharge sites.

Previous studies have also used a comparison between predicted and observed heatflow measurements to see until what age hydrothermal circulation influences the crust. Under the influence of hydrothermal circulation, the observed heatflow would be usually less than the predicted heatflow due to lateral redistribution of heat. Eventually, with increasing age, sediment cover and reducing intensity of hydrothermal circulation, the predicted heatflow would match the observed surface heatflow. This age has been called as the 'sealing age' and has ranged anywhere from 10 Myr (*Grevemeyer and Weigel*, 1996; *Carlson*, 1998) to 65 Myr (*Stein and Stein*, 1994). However, in the previous section, a continuous hydrothermal/fluid circulation system of varying intensity from 0-75 Myr has been implied since the top of the crust is never fully 'sealed'. Hence, to validate the implications of the previous section, I make a comparison between on-board surface heatflow measurements and the predicted heatflow values. In order to compute the predicted surface heatflow at distinct ages, $q(t)$, I use the model by *Hasterok* (2013):

$$q(t) = 506.7\sqrt{t} \quad \text{if} \quad t \leq 48.1 \quad \text{Myr}, \tag{3.15}$$

$$q(t) = 53 + 106e^{-0.034607t} \quad \text{if} \quad t > 48.1 \quad \text{Myr}. \tag{3.16}$$

Figure 3.38 shows the individual on-board heatflow measurements at each age range with respect thickness of sediments from section3.3. Sediments play a role in influencing the heatflow measurements and hence have to be taken into account. An increasingly thick sediment cover will have a reduced heatflow measurement due to higher dissipation of heat in the sediments for a constant heat source. This results in an inverse relation between sediment thickness and surface heatflow measurement provided the heat source is constant/laterally invariant (*Davis et al.*, 1999). The absence of this inverse relation implies that the sub-basement heat source is not constant and is varying from one heatflow location to another.

Given the narrow age range of the heatflow measurements at one site in figure 3.38, the predicted surface heatflow from the above equation has been plotted at a constant age which corresponds to the mean of the age range of the heatflow. Note that the predicted heatflow from the above equation does not take into account the sediment cover. In the presence of sediment cover, the predicted heatflow would be reduced. In order to make a fair comparison between surface heatflow measurements and the predicted heatflow (without sediment cover), only those heatflow measurements which have been acquired over

negligible sediment cover should be taken into account. With this in mind, I first compare the measured heatflow at each age range where there is minimal sediment cover with the predicted heatflow and then proceed to check the inverse relation between the heatflow meaurements and sediment thickness.

Figure 3.38a corresponds to an age range of 2.86-3.1 Ma and a measurement corresponding to zero sediments is observed to be ∼50 mW/m^2 lies significantly below the predicted value of ∼290 mW/m^2. Following from the discussion in the previous section, this age range corresponds to the regime of active hydrothermal circulation. Hence, the predicted heatflow is reduced by ∼240 mW/m^2 due to heat being redistributed laterally and the site being close to a recharge site. The heatflow measurements are scattered and do not show an inverse relation with the sediment thickness as there is a heatfow value of 140 mW/m^2 at 220 m thick sediment cover. This may imply that there is an increased local heat source beneath this measurement or this site is very close to a discharge site.

In figure 3.38b which corresponds to ∼15 Myr, relatively less scattering is observed in the heatflow measurements compared to 3.38a. In figure 3.36, layer 2A is observed to continue to thin until 15 Myr after which its thickness becomes constant. This regime has been attributed to passive hydrothermal systems/fluid circulation. Although a reduction of ∼100 mW/m^2 in the surface heatflow relative to the predicted heatflow is observed, absence of a minimal sediment cover heatflow site does not enable to validate presence of passive hydrothermal systems.

The measurement at negligible-sediment cover at ∼23 Myr shows a value of 25 mW/m^2 in figure 3.38c, which is considerably less than the predicted heatflow value of ∼110 mW/m^2. This difference again validates that the heatflow is being laterally redistributed in crust old as 23 Myr due to seawater recharge and validating the proposed hypothesis of fluid circulation in older crust. Again the absence of an inverse correlation between sediment thickness and heatflow measurements is observed, with one heatflow meaurement at 140 m thick sediments being 170 mW/m^2 and exceeding the predicted heatflow. This implies for either local radiogenic heat sources or the site being close to a discharge site.

At 27 Myr, the predicted heatflow is at ∼95 mW/m^2 and two distinct heatflow meaurements in negligible sediment cover show varying heatflow values as seen in figure 3.38d. One of these measurements is very close to the predicted heatflow which may imply that no fluid cirulation is present at the site. It is also possible that the site is locally influenced by some heat source or is very close to a dischare site. With the exception of that one particular heatflow location, other sites do show significant reduction as compared to the predicted heatflow.

A very good example of the inverse correlation between the sediment thickness and heatflow measurement is seen in figure 3.38e. This implies for a locally invariant/constant heat source beneath the heatflow measurement sites. Also, it is interesting to note that the heatflow measured at the sediment free site is almost thrice the predicted value of ∼80 mW/m^2. On comparing with figure 3.38f, it can be seen again that the heatflow measurement on the sediment-free site exceeds the predicted heatflow value of ∼75 mW/m^2. The two distinct heatflow sites in figure 3.38e and f are separated by ∼8.7 Myr and both indicate towards a higher than predicted heatflow. A possiblity, like the previous cases, is that these two sites are near to/correspond to seawater discharge sites. Another possibility is an overall higher heat flow/thermal anomaly in this region. It is also interesting to note that in figure 3.38g, which represents a heat flow close to 3.38f, a higher heatflow value for the same sediment cover thickness as compared to 3.38f can be observed. This confirms a higher heat flow/thermal anomaly in the region starting from 36 Myr with the magnitude of thermal anomaly increasing beyond 45 Myr. It is interesting to note that an onset of a thicker sediment cover can also be observed from 36 Myr and that the MCS tomography results in figure 3.21c point towards a high velocity anomaly in the subsurface.

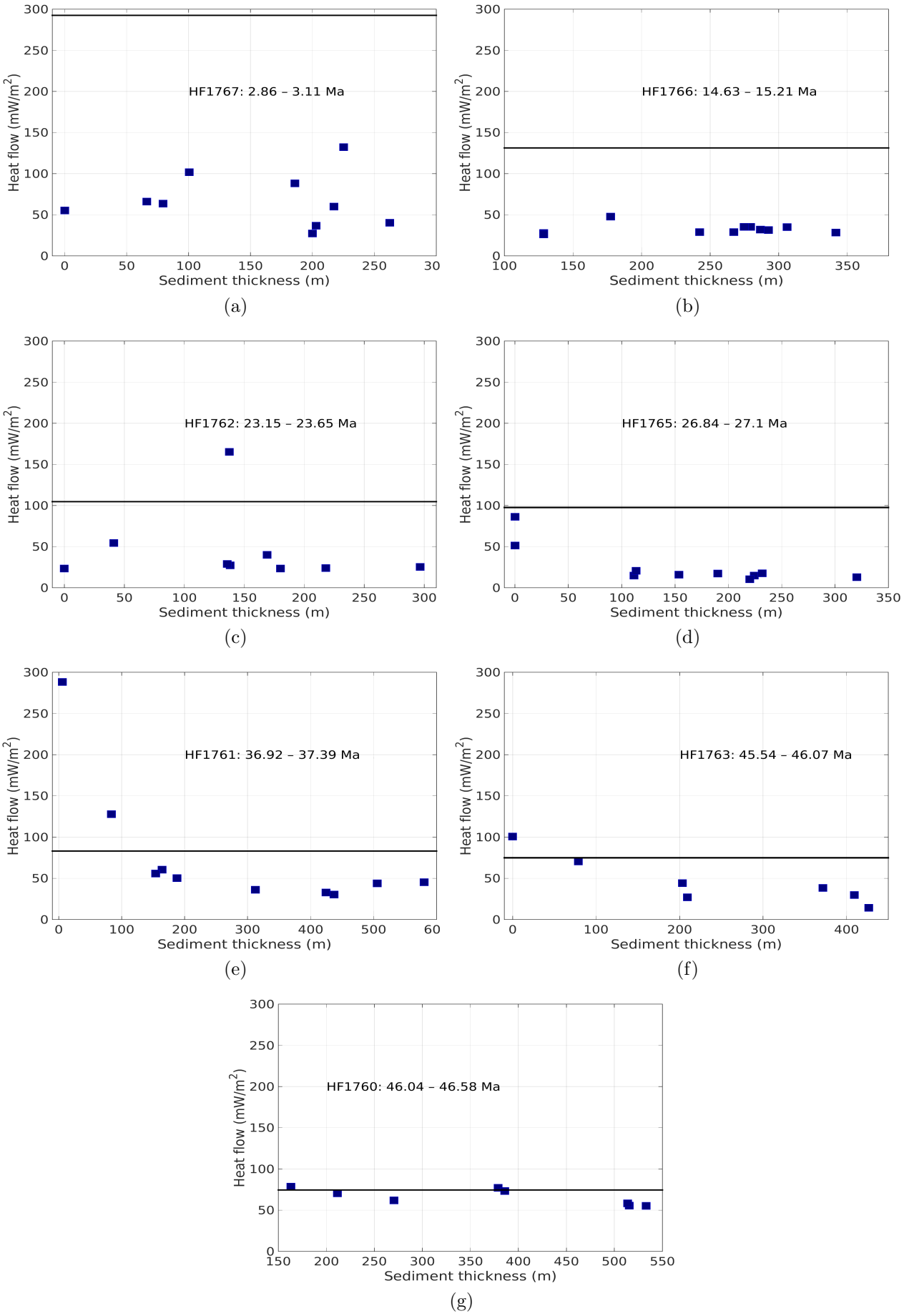

Figure 3.38: Heat flow measured values onboard LITHOS cruise (blue squares) at distinct ages versus the sediment thickness estimates from MCS analysis in 3.3. Also shown is the predicted heatflow from top of the crust (black line) from the proposed model in *Hasterok* (2013) for the corresponding age.

In summary, comparing the heatflow measurements at sediment free sites with predicted values have validated that heat is being re-distributed in the sub-surface at all ages. Most of the sediment free sites have lower heatflow measurements compared to predicted values indicating that these are recharge sites where cold seawater is entering the crust. Other sites where a high heatflow is measured may correspond to discharge sites. However, identifying recharge and discharge sites was not the main objective of the analysis. Instead these comparisons have shown that the heatflow data strongly supports the proposed hypothesis of hydrothermal systems. Another interesting observation from this comparison is the increased heatflow beyond 36 Myr which may be due to the St Helena and Cameroon volcanic chains as is also suggested from the bathymetric features and sediment cover.

3.12.2 Permeability estimation

Here I try to estimate permeability from the heatflow measurements using Darcy's law. It should be stated here that the term permeability refers to bulk permeability, which is usually higher than the in-situ permeabilities measured in packer experiments (*Fisher*, 1998). *Fisher and Becker* (2000) proposed a simple analytical model to reconcile the variation of permeability measurements with age. They used a simple hydrothermal system as shown in in figure 3.39 with the governing equations of the system described in equation 3.17.

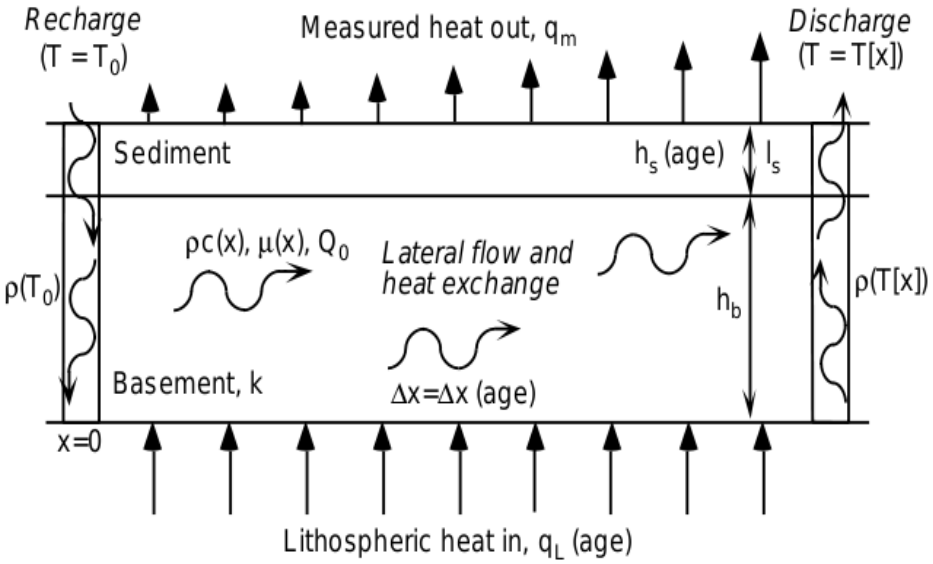

Figure 3.39: A schematic sketch from *Fisher and Becker* (2000) explaining the various parameters of equation 3.17, also from *Fisher and Becker* (2000)

$$\frac{q_m}{q_l} = 1 - exp\left(\frac{-\lambda_s \Delta x}{Q_0 h_s h_b \rho(T) c}\right), \tag{3.17}$$

$$\text{where} \quad Q_0 = \frac{-kdP}{\mu(T)dx}, \tag{3.18}$$

$$\text{where} \quad \mu(T) = ((((T-20) \times 1.551e^{-2} + 1)^{-1.572} \times 1e^{-3}, \tag{3.19}$$

$$\text{and} \quad \rho(T) = 1029 - 0.06308T - 0.0028136T^2. \tag{3.20}$$

In the above equation and the figure, q_m is the measured heat output, q_l is the expected heat flow, λ_s is the sediment thermal conductivity, Δx is distance that varies with crustal age, Q_0 is volume flux per cross sectional area of advecting fluids, h_s is sediment thickness, h_b is the crustal thickness through which the fluids flow, ρ is the temperature dependent density of the advecting fluid, c is the specific heat of the advecting fluids, k is the permeability, μ is the temperature dependent dynamic viscosity of the

Table 3.3: Estimates of basement temperature at distinct ages from mean measurements of sediment thickness, vertical temperature gradient and bottom water temperatures at each age range

Age (Ma)	Sediment thickness (m)	$\frac{dT}{dz}$ (m°C/m)	T_0 (°C)	T (°C)
3	154	71.735	2.46	15.82
14.8	248	35.54	2.35	13.51
23.4	146	50.7	2.28	11.51
26.9	156	29.749	2.12	7.05
37.1	286	80.7	2.21	18.21
45.8	243	51.5	2.5	10.85
46.3	371	77.19	2.19	31.75

advecting fluid, $\frac{dP}{dx}$ is the lateral pressure gradient and T is the temperature of the advecting fluid. The equations relating the viscosity and density of the advecting fluid to temperature is taken from *Schoofs and Hansen* (2000). The density equation has been modified from *Schoofs and Hansen* (2000) to better fit the seafloor depths observed in the MCS profile in figure 3.3b (corresponding to 20-50 MPa).

The heatflow measurements, q_m, and the predicted heatflow ,q_l from equation 3.15 are known as described previously. A direct measurement of the sediment thermal conductvity, λ_s, has also been made at the heatflow sites and has a mean value of 0.9 $Wm^{-1}K^{-1}$. From MCS analysis, constraints on sediment thickness, h_s, and aquifer thickness ,h_b, can be placed. The unaltered lava flow (Layer 2A) thickness shown in figure 3.36 can be well approximated to be the aquifer thickness, h_b. To estimate the temperature of the seawater, T, which is used in computing the viscosity and density, I used the measurements of vertical temperature gradient ($\frac{dt}{dz}$) and temperature measurements at top of the sediments (T_0), along with the sediment thickness in the following expression:

$$T = h_s \frac{dT}{dz} + T_0. \tag{3.21}$$

This equation would ideally give the temperature at top of the basement which should be the same as the temperature of the advecting fluid through it. Table 3.3 shows a rough estimate of the basement temperature from the mean measurements at each age. It can be observed that the basement temperature first decreases away from ridge axis and then increases beyond 36 Myr as we move towards older age.

Assuming specific heat of seawater as 4200 J/kg/°C, the only parameters that remain unconstrained to compute the permeability ,k, are Δx and the lateral pressure gradient, $\frac{dP}{dx}$. Both these parameters depend on location and spacing between the recharge and discharge sites as shown in figure 3.39. The analysis performed previously does give an insight into the sites which could potentially serve as recharge and discharge sites. However, which pair of recharge and discharge sites form a hydrothermal system can not be identified with the current sparse 2-D heatflow data set. I approximate these parameters in the two cases: one in which sewater enters the crust at ridge-axis and exits through one of the measured heatflow sites. This would correspond to large-scale hydrothermal cells. In the other case, I assume that the distance between recharge and discharge sites is 1-100 km corresponding to small-scale hydrothermal cells. Δx is taken as one-half of dx as assumed in several settings (*Baker et al.*, 1991; *Davis et al.*, 1999). dP is assumed to be hydrostatic pressure gradient between the recharge and discharge sites and $= \Delta\rho(T)g(h_s + h_b)$ where g is the acceleration due to gravity and h_s, h_b are the sediment and Layer 2A (basement acquifer) thickness respectively.

The permeability estimates of the first case considered are shown in figure 3.40a. As stated above, this case considers ridge-axis as the recharge site and the heatflow measurements at distinct ages as discharge site. The ridge-axis parameters for basement temperature, T, has been extrapolated from above table 3.3 to 20°C. Sediment thickness at the ridge-axis is found from MCS analysis to be zero and thickness of the aquifer is the thickness of the layer 2A, which is found from the MCS to be ∼900 m. The mean values of these parameters have been taken from the heatflow measurements at individual sites and the resulting permeabilities calculated from equation 3.17. Note that permeability values are expressed in the order of

magnitude rather than an accurate value similar to previous studies. Different approaches to estimation of permeability have yielded values varying from 10^{-9} to 10^{-22} m^2 (*Fisher*, 1998). The estimates shown in figure 3.40a are closer to the indirect estimates from borehole temperature and flow meter logs (*Fisher*, 1998).

(a)

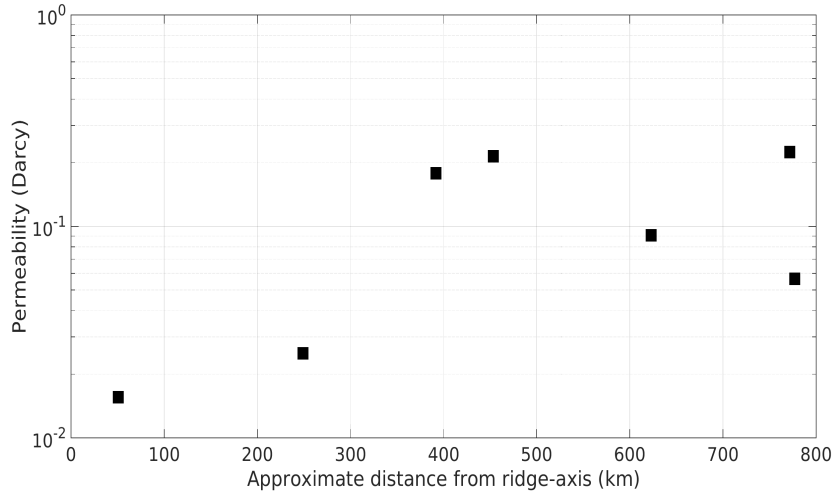

(b)

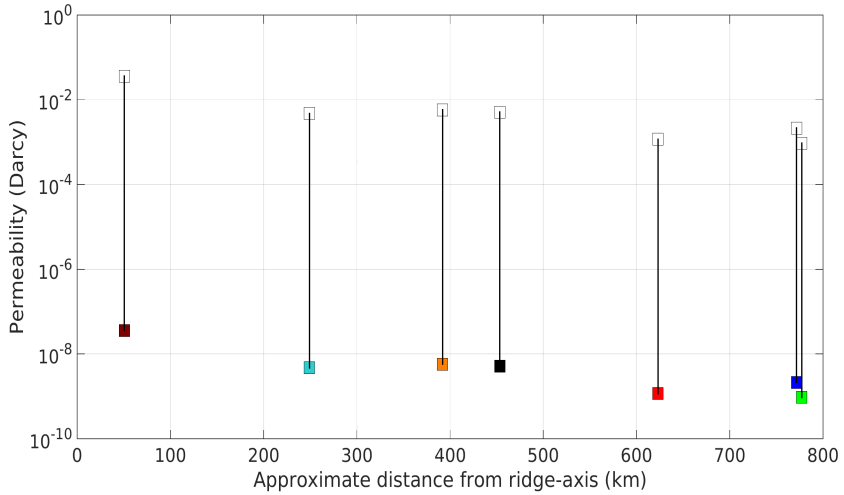

(c)

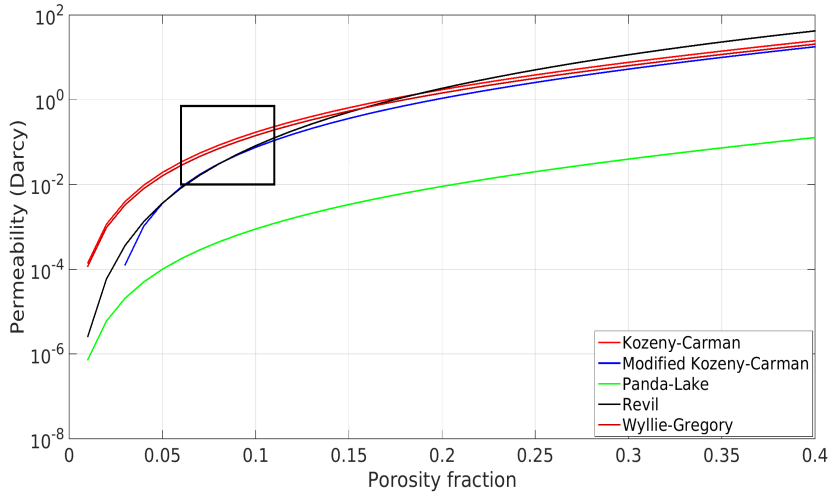

Figure 3.40: Estimated permeabilities from heatflow and MCS measurements in Darcy from equation 3.17. 1 Darcy = 10^{-12}m^2. (a) Assuming the ridge-axis is the recharge site where seawater enters oceanic crust and is discharged at the site of heatflow measurement. (b) Assuming the distance between the recharge and discharge sites vary from 100 m (filled square) to 100 km (empty square) at each heatflow location. A mean estimate of the various parameters at each heatflow location have been considered. (c) Percolation theory models of porosity-permeability relationships from *Mukerji and Dvorkin* (2009) assuming an average grain size of 250 micron. The black rectangular region denotes the porosity-permeability estimates from the MCS and the co-located heatflow data in this study.

Figure 3.40b shows the second case in which smaller scale hydrothermal cells are considered. The distance between the recharge and discharge sites has been assumed to vary from 0.1-100 km and the

maximum and minimum values of sediment cover thickness, basement temperature and measured heat flow at each site have been taken to compute the lateral pressue gradient, dP, between the recharge and discharge sites. Due to the samller size of the hydrothermal cells considered, a reduction in the bulk permeability estimates as compared to figure 3.40a can be observed.

Lastly, I make an attempt to correlate the porosity estimates from section 3.10 and the permeabilty estimates from above with the existing porosity-permeability relations for basaltic rocks. Since the existing relations have been mostly derived from laboratory experiments, a comparison with the above results can be useful to validate them. I have considered five main percolation theory relations from *Mukerji and Dvorkin* (2009) - Kozeny-Carman, Modified Kozeny-Carman, PandaLake, Revil E. and Wylie-Gregory models. These are shown in figure 3.40c for a grain size of 250 micron. The range of porosity estimates obtained in section 3.10 and figure 3.35 is 6-11% with mean off-axis porosity for both layers 2A and 2B being ∼8%. The corresponding permeabilites from figure 3.40b range from 10^{-2} to $10^{-1}\mathrm{m}^2$ assuming the upper limit of permeabilities from 100 km wide hydrothermal systems. Though the estimates of permeability in figure 3.40a,b are very rough, a large-scale convection of hydrothermal systems as assumed in figure 3.40a gives a better match to the permeabilities from percolation theory as compared to small-scale convection of hydrothermal systems in figure 3.40a. This indicates the possibility of large-scale hydrothermal systems with spacing between recharge and discharge sites exceeding ∼100 km as proposed in previous sections.

Chapter 4

Effect of mantle thermal anomaly on the Lithosphere-Asthenosphere boundary (LAB)

La limite de la lithosphère-asthénosphère (LAB) intéresse les géophysiciens depuis sa découverte (*Gutenberg*, 1926, 1948, 1955, 1959). Des études récentes basées sur la sismologie telles que les fonctions récepteur (*Kawakatsu et al.*, 2009; *Kumar and Kawakatsu*, 2011), la vitesse de cisaillement des ondes de surface (*Maggi et al.*, 2006; *Auer et al.*, 2014), l'anisotropie des ondes de surface (*Burgos et al.*, 2014) ont pu estimer la profondeur de la LAB. Cependant, la résolution verticale de la LAB de ces études est faible et une limite nette ne peut pas être déduite. En utilisant les données MCS, j'ai d'abord analysé les événements terrestres plus profonds dans le profil 50-75 Ma, qui a une topographie de socle relativement lisse et une couverture sédimentaire plus épaisse par rapport au reste du profil.

Suite au traitement des données pour la LAB décrit dans le chapitre 2, j'ai réussi à obtenir une image P de haute résolution de la LAB de 50 à 75 Ma. Cette réflexion est caractérisée par un contraste de vitesse d'ondes P négatif (∼8.8%) indiquant des vitesses d'ondes P plus faibles en dessous de la réflexion. Elle est plongé vers des âges plus avancés à partir du temps bidirectionnel de ∼22 s (TWT) à 50 Myr à ∼27 s TWT à 75 Myr, compatible avec les modèles de refroidissement des plaques. De plus, un événement ∼2 s TWT sous le socle est observé partout et est interprété comme la limite croûte-manteau ou le Moho. La superposition des réflexions multiples du fond marin, du socle et du Moho prouve que la réflexion de la LAB observée est réelle et sans rapport avec ces multiples. De plus, j'ai estimé les glissements latéraux et corrélé avec la réflexion de la LAB. La réflexion de la LAB est ensuite convertie en profondeur seconde temps double en utilisant les vitesses d'ondes P de la tomographie et une vitesse d'ondes P maximale de 8,5 km/s dans le manteau (*Stern et al.*, 2015; *Mehouachi and Singh*, 2018). La réflexion de la LAB correspond à des profondeurs de 68 à 86 km, moins profondes que la LAB imagée dans la zone de fracture de St Paul (*Mehouachi and Singh*, 2018). Le choix des vitesses d'ondes P maximales du manteau de 8,4 à 8,65 km/s déplace la réflexion de la LAB dans les limites d'incertitude de ±2 km. Après avoir testé un certain nombre de modèles de refroidissement à demi-espace et de refroidissement de plaques, la réflexion de la LAB correspondait le mieux à l'isotherme ∼1130°C du modèle de refroidissement à demi-espace. Cette réflexion se révèle être ∼5-7 km moins profonde et donc plus froide par rapport à une étude récente faite plus au nord dans la zone de fracture de St Paul où la LAB était de 1260°C isotherme (*Mehouachi and Singh*, 2018). De plus, aucune autre réflexion plus profonde (*Naif et al.*, 2013; *Stern et al.*, 2015; *Mehouachi and Singh*, 2018) n'est observée dans la région d'étude.

On observe que le socle de la région d'étude est soulevé de ∼400 m en moyenne par rapport au modèle de subsidence demi-espace (*Audhkhasi and Singh*, 2019). Ce soulèvement du socle indique un manteau/asthénosphère plus chaud et une température excessive de ∼125°C est associée au soulèvement du socle (*Hartley et al.*, 2011). Une autre preuve d'un manteau plus chaud provient de l'anomalie

de bouguer du manteau résiduel dans la région d'étude, qui diminue vers 75 Ma, bien que l'épaisseur de la croûte reste presque constante à 5,7-6,2 km. Par conséquent, la faible réflexion de la LAB et l'élévation du socle témoignent d'un manteau/asthénosphère plus chaud dans cette région d'étude. Fait intéressant, cette partie du profil est proche des affleurements les plus anciens de la chaîne volcanique de Sainte-Hélène (80-82 Ma) et les plus jeunes affleurements de la ligne volcanique du Cameroun (1-10 Ma) contraints à partir de datations radioactives (*O'Connor and le Roex*, 1992b). Une queue de panache de 280 K a été imagée sous le mont Cameroun à ∼1000 km de notre profil et est supposée être la queue de panache de la ligne volcanique du Cameroun (*Reusch et al.*, 2010). Les affleurements de la ligne volcanique du Cameroun deviennent plus jeunes vers l'océan et donc vers notre profil. De plus, des études tomographiques anisotropes ont montré un écoulement mantellique radial depuis l'extérieur du mont Cameroun vers le profil à des profondeurs de ∼110 km. Ces résultats suggèrent un écoulement asthénosphérique à grande échelle de la ligne volcanique du Cameroun vers la région d'étude. Le flux mantellique apporte avec lui l'anomalie thermique du manteau associée au point chaud camerounais et influence la lithosphère et la LAB le long de notre profil. Il est probable que l'anomalie thermique a abaissé le solidus de la LAB de 1260°C à 1130°C et les hétérogénéités gelées formées en raison du panache de Sainte-Hélène sont à nouveau en fusion et s'accumulent aux profondeurs de la LAB observées. Au moment de la rédaction de cette thèse, cet article a été soumis à *Geophysical Research Letters* et est en cours de révision.

The Lithosphere-Asthenosphere Boundary (LAB) has been a subject of interest to geophysicists ever since its discovery (*Gutenberg*, 1926, 1948, 1955, 1959). Recent studies based on seismology such as receiver functions (*Kawakatsu et al.*, 2009; *Kumar and Kawakatsu*, 2011), shear-wave speed of surface waves (*Maggi et al.*, 2006; *Auer et al.*, 2014), surface wave anisotropy (*Burgos et al.*, 2014) have been able to estimate the LAB depths. However, the vertical resolution of the LAB from these studies is low and a sharp LAB cannot be inferred. Using the MCS data I first analyzed the deeper Earth events in the 50-75 Ma profile, which has favorable imaging conditions of a relatively smooth basement topography and a thicker sediment cover as compared to the rest of the profile.

Following the data processing for LAB described in chapter 2, I successfully obtained a high-resolution P-image of the LAB from 50-75 Ma. This reflection is characterized by a negative P-velocity contrast (∼8.8%) indicating lower P-velocities below the reflection and is observed to be dipping towards older ages from ∼22 s two-way time (TWT) at 50 Myr to ∼27 s TWT at 75 Myr, consistent with plate cooling models. Additionally, an event ∼2 s TWT below the basement is observed throughout and is interpreted as the crust-mantle boundary or the Moho. Superimposing the water-bottom multiple reflections of seafloor, basement and Moho prove that the observed LAB reflection is real and unrelated to these multiples. Additionally, I also estimated side-swipes and correlated with the LAB reflection, but in vain. The LAB reflection is then depth converted from TWT to depth using P-velocities from tomography and maximum P-velocity of 8.5 km/s in the mantle (*Stern et al.*, 2015; *Mehouachi and Singh*, 2018). The LAB reflection is found to correspond to depths of 68-86 km, which is shallower than the LAB imaged at St Paul fracture zone (*Mehouachi and Singh*, 2018). The choice of maximum mantle P-velocities from 8.4-8.65 km/s shifts the LAB reflection within the uncertainty limits of ±2 km. After testing a number of half-space and plate cooling models, the LAB reflection best fitted the ∼1130°C isotherm of the half-space cooling model. This reflection is found to be ∼5-7 km shallower and hence colder as compared to a recent study further north at St Paul fracture zone where the LAB was 1260°C isotherm (*Mehouachi and Singh*, 2018). Additionally no second deeper reflection (*Naif et al.*, 2013; *Stern et al.*, 2015; *Mehouachi and Singh*, 2018) is observed in the study region.

The basement in the study region is observed to be uplifted by a mean of ∼400 m with respect to half-space subsidence model (*Audhkhasi and Singh*, 2019). This basement uplift is indicative of a hotter mantle/asthenosphere and an excess temperature of ∼125°C is associated with the basement uplift (*Hartley et al.*, 2011). Further evidence of a hotter mantle comes from the residual mantle bouguer anomaly in the study region, which is found to decrease towards 75 Ma though the crustal thickness remains almost constant at 5.7-6.2 km. Hence shallowing of the LAB reflection and uplift of the basement are evidence of a hotter mantle/asthenosphere in this study region. Interestingly, this part of the profile is close to oldest outcrops of the St Helena volcanic chain (80-82 Ma) and to the youngest outcrops of the Cameroon volcanic line (1-10 Ma) as found from radioactive dating (*O'Connor and le Roex*, 1992b). A 280 K plume tail has been imaged beneath Mt Cameroon at ∼1000 km from our profile and is postulated to be the plume tail of Cameroon volcanic line (*Reusch et al.*, 2010). The outcrops of Cameroon volcanic line have been shown to decrease in age towards the ocean and also towards our profile. Further, anisotropic tomographic studies have shown mantle flow radiating outwards from Mt Cameroon towards out profile at depths of ∼110 km. These results suggest a large scale-asthenospheric flow from Cameroon volcanic line towards the study region. The mantle flow brings along with it the mantle thermal anomaly associated with Cameroon hotspot and is found to influence the lithosphere and the LAB along our profile. It is likely that the thermal anomaly has increased the mantle temperatures and the frozen-in heterogeneities formed due to the St Helena plume are re-melting and accumulating at the observed LAB depths. At the time of writing this thesis, this article has been submitted to *Geophysical Research Letters* and is currently under review.

4.1 Volcanism in the Equatorial Atlantic offshore West Africa

A number of parallel, NE-trending volcanic chains and topographic highs can be observed offshore West Africa (north to south) : Canary islands, Cape Verde rise, Sierra Leone rise, Cameroon volcanic line, Walvis ridge and St. Helena seamount chain with an spacing of 1500 - 1800 km between them. Previous studies have pointed out similar characteristics between these volcanic chains and topographic highs including $\sim 30^{\circ}$ NE trend, inconsistent age progressions (*Morgan*, 1983), crustal uplift exceeding 1 km, intraplate volcanism and anomalously high heat flow values. *Herman et al.* (1977) collected more than 400 heat flow measurements between the Azores-Gibraltar ridge and the Walvis ridge and propose that the eastern Atlantic offshore West Africa is underlain by an anomalous thin lithosphere. It was observed from the analysis of basement topography and sediment cover from the MCS profile in chapter 3 that an uplift of the basement and sediments is observed (elaborated later in section 4.7) towards the eastern end of the profile. This trend is also observed at the Canary islands and Cape Verde islands (*Grunau et al.*, 1975), with the uplifted sediments being exposed at few places (*Stillman*, 1987; *Rothe*, 1990). The age of volcanism and uplift has been proposed to begin in the Oligocene (34 - 23 Ma) and continue until the Miocene (23 - 5 Ma) (*Meyers et al.*, 1998), although some studies propose ∼60 Ma as the start of volcanism (*Holik et al.*, 1991).

McNutt (1988); *Courtney and White* (1986) proposed that to explain the geophysical observations of these basement uplift and elevated heatflows in these areas, a convective mantle plume originating in the asthenosphere must be taken into account. Apart from the idea of a mantle plume responsible for these features, some authors explain them to be due to hotlines formed by upwelling in the convecting mantle below. *Meyers et al.* (1998) explain these volcanic features by the model proposed by *Richter and Parsons* (1975). According to the model, convection cells between the LAB and the 670 km discontinuity with their axes parallel to the spreading direction of the lithospheric plate. As the convection in adjacent cells is in opposite directions, the upwelling mantle brings the deep mantle material, enriched in large-ion lithophile elements to the base of the lithospheric plate, leading to decompression melting and formation of volcanic chains.

The Cameroon line is 620 km from the eastern end of the MCS profile at 75.6 Ma. Some authors believe that the source of Cameroon line is the hotspot below the present day St. Helena island (*Morgan*, 1972, 1983; *Duncan and Richards*, 1991; *Wilson*, 1992). However, as pointed out by *Meyers et al.* (1998), there is no evidence of crustal uplift at St. Helena island unlike that observed at Cameroon line. Also, there exists an age discrepancy in the volcanic rocks from the two islands (*O'Connor and le Roex*, 1992a). The oceanward end of Cameroon line is relatively young (< 10 Ma) while the rocks from some of the nearby island are 80-82 Ma old (*O'Connor and le Roex*, 1992a), which are 20 Myr younger to the surrounding seafloor ages (figure 4.1). Further south-east along the St. Helena line, the ages of the volcanic rocks have been found to be 52.2 Ma. This suggests that the youngest end of the Cameroon line and the oldest end of the St. Helena chain is closest to our profile as seen in figure 4.1. Seismic tomography of shear waves (*Zhang and Tanimoto*, 1992) and geochemical studies (*Schilling*, 1985; *Schilling et al.*, 1985) have pointed out a low velocity channel channel ∼100-200 km deep transporting materials from St. Helena hotspot to the ridge axis further west. Volcanism can also be observed along Ascension fracture zones which can be explained by the fracture zone being a reactivated shear zone (the Central African shear zone) due to the plume and sporadic volcanism follows (*Fairhead*, 1988; *Fairhead and Binks*, 1991). The source of these volcanics may be the Ascension and St. Helena hotspots, which are far away from the eastern end of my profile as shown in figure 4.2. Therefore, I mainly focus on the Cameroon Volcanic line, which I elaborate further.

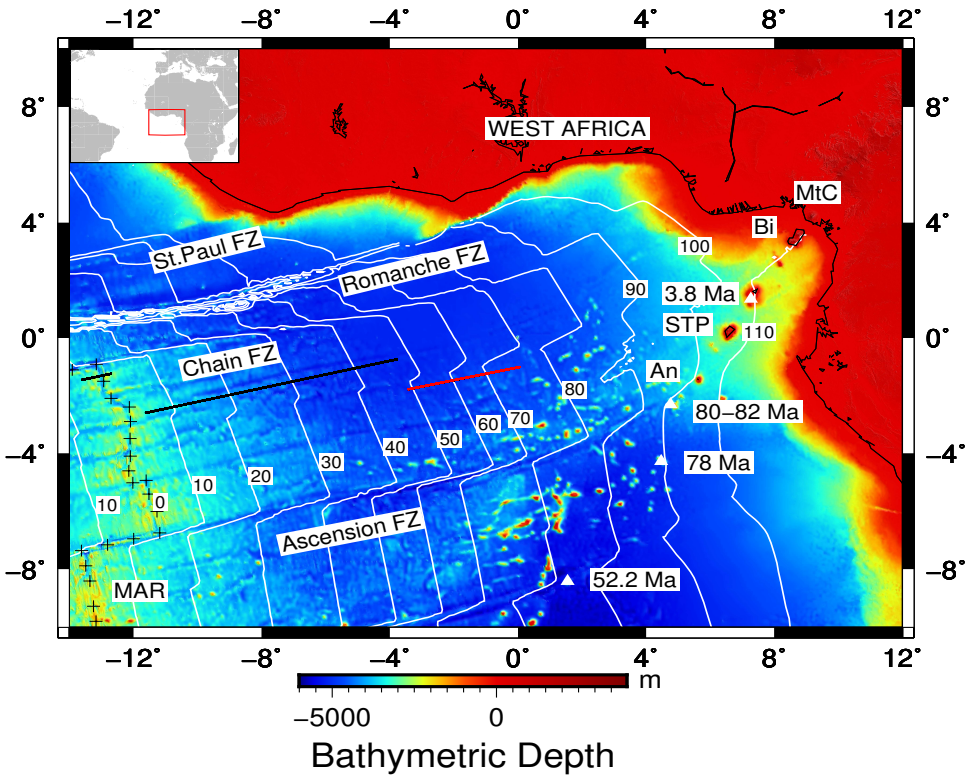

Figure 4.1: Study region showing the profile from 49.3-75.6 Ma as a red line. The white triangles along with their ages denote the seamounts dated by *O'Connor and le Roex* (1992b). Oldest outcrops of St Helena chain and youngest outcrops of Cameroon volcanic line lie close to the profile. Refernce distances from end of the profile at 75.6 Ma: 550 km for the 80-82 Ma outcrop, 840 km for 52 Ma old outcrop, 850 km for 3.8 Ma outcrop. The Ascension fracture zone (FZ) offsets the MAR causing an age contrast of ∼10 Myr. *An*: Annobon Island, *STP*: Sao Tome and Principe Islands, *Bi*: Bioko Island and*MtC*: Mount Cameroon.

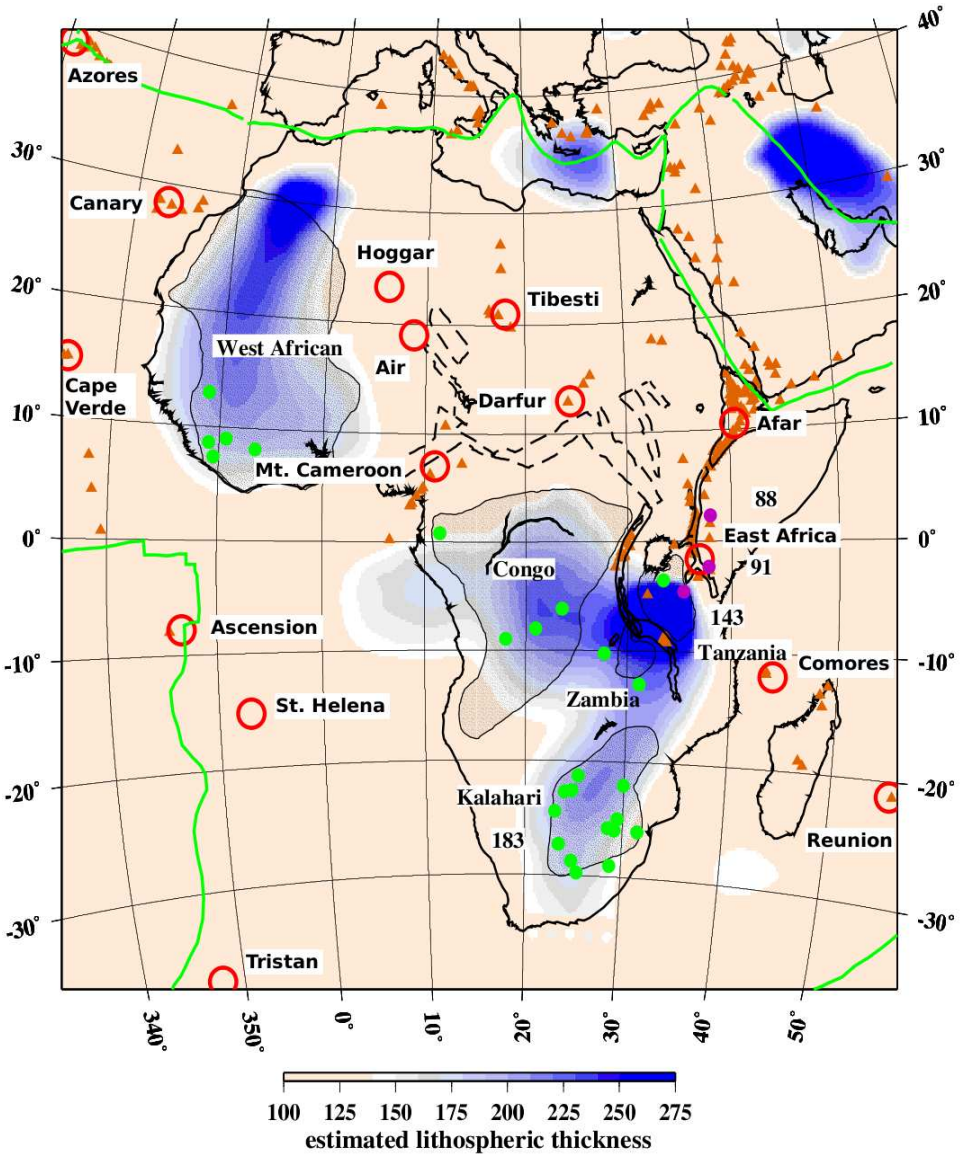

Figure 4.2: Lithospheric thickness of the African plate obtained from shear wave velocities from surface wave tomography (*Priestley and MKenzie*, 2006) and the relationship between shear wave velocities and temperature (modified from *Priestley and Tilmann* (2009)). The triangles denote sites of recent volcanic centres and the red circles the present-day hotspot locations. To be noted is the thinner oceanic lithosphere along the Cameroon line between the West Africa and the Congo cratons, where lithospheric thickness reaches 230 km.

4.2 Cameroon Volcanic line

The Cameroon Volcanic line (CVL) is a ∼1600 km long, linear chain of seamounts in Western equatorial Africa oriented in a SW-NE direction with ∼1000 km of them being on continental Cameroon and the other ∼600 km being in the ocean. There are four major islands in increasingly oceanward direction: Bioko, Principe, Sao Tome and Annobon (or Pagalu) as can be seen in figure 4.1. Some of the previous studies consider three prominent oceanic islands only: Principe, Sao Tome and Annobon (*Lee et al.*, 1994) whereas some include Bioko and Annobon also (*Ngounouno et al.*, 2005). The continental end of the Cameroon line terminates in a Y-shaped structure into Adawamas, Biu and Jos volcanic complexes (*Fitton*, 1980, 1983). The oldest rocks of the CVL date back to 42 Ma (*Marzoli et al.*, 1999, 2000) and are located in the continental regime with Mount Cameroon in the Cameroon province being a currently active volcano and considered to be the present hotspot location. Earthquakes of magnitude ∼4.9 have been recorded in the past 40 years near Mount Cameroon with the most recent eruption being in 2000 (USGS data release). Near the islands of Sao Tome and Principe, earthquakes of magnitude 4.4-4.8 have been recorded in 2010, 2016 and 2018 (chapter 1). The eruption rates for the CVL over the last 30 - 40 Ma have been in the range 2-3$\times 10^{-2}$ $m^3 s^{-1}$ which is 40 times lower as compared to other hotspots (*Milelli et al.*, 2012). There is no consistent age pattern along the CVL that could be explained by a fixed hotspot motion such as the St. Helena chain (*Morgan*, 1983). In the oceanic regime, the CVL exhibits an overall trend of decreasing age oceanward (*Lee et al.*, 1994) though the Bioko, Sao Tome and Annobon volcanics have been dated to be younger than 1 Ma and volcanics in the Principe island being no older than 30 Ma (*Dunlop and Fitter*, 1979; *Fitton and Dunlop*, 1985; *Ngounouno et al.*, 2001; *Njilah et al.*, 2004; *Ngounouno et al.*, 2005). *Rankenburg et al.* (2004) also find continental signatures in the isotopic compositions of CVL oceanic lavas while *Lee et al.* (1996); *Teitchou et al.* (2011) propose similar composition of unmetasomatized sub-continental lithospheric and sub-oceanic lithosphere which further complicates their origin. The global free-air gravity anomaly over the region (chapter 1) shows measurements in excess of of +100 mgal at the exposures of the island chain with an overall negative gravity anomaly ∼50 mgal surrounding these outcrops, to account for the mass deficit. This is even higher than the gravity anomalies of 50-70 mgal at the ridge flanks of the ridge axis. However, *Colli et al.* (2016) show that a large-scale excess of gravity may not neccessarily accompany a dynamic topography. *Meyers et al.* (1998) collected gravity and magnetic data and observed higher ampitude anomalies relating them to uplift of the basement. Adjacent to the uplifted regions, the high amplitude magnetic anomalies were found to be absent which was attributed to Cretaceous quiet period and thick sediment cover exceeding 4 km in some places.

On the basis of structural geological analysis of remote sensing data, *Moreau et al.* (1987); *Déruelle et al.* (1987) deduced the CVL to be a complex volcanotectonic feature comprising of en echelon tension gashes related to sinistral transcurrent shear in the lithsophere. *Meyers and Rosendahl* (1991) acquired MCS reflection data with a 6 km long streamer on the CVL and found crustal uplift, rather than volcanism, to be responsible for the formation of the elevated topographic expression of the CVL as illustrated in figure 4.3. They found the crust in the region to be uplifted by as much as 3 km at Principe island forming a crustal arch perpendicular to the CVL. By mapping an unconformity in the sediments created due to the uplift (T_{40} in figure 4.3) and gravity modelling, *Meyers et al.* (1998) proposed that the melt intrusion was accompanied by reheating of the mantle to depths of 40 km to uplift the crust. The reheating of the oceanic lithosphere upto depths of 40 km is proposed to explain the upward bending of the oceanic crust (due to asthenospheric upwelling) exceeding the flexural rigidity of the lithosphere. In other words, reheating of the oceanic lithosphere would alter its elastic properties such that it supports the crustal uplift of the order of 1 km. Reheating of the oceanic lithosphere is also supported by higher present-day heatflow measurements. The theory behind melt intrusion comes from their gravity modelling study in which *Meyers et al.* (1998) introduce a wedge-shaped material of lower density ($\delta\rho = -0.1$ g/cm^3) within the mantle peridotite (ρ =3.4 g/cm^3) at depths of 20-40 km. However, this density contrast cannot be solely explained by reheating of the peridotite as it would require the low density material to have an excess temperature of +1225°C as $\frac{\rho_2}{\rho_1} = 1 - \Delta T \alpha$. To model the density contrast only by introduction

of partial melt would require a volumetric addition of 25% of melt, which again is unreasonable. Hence, *Meyers et al.* (1998) proposed a combination of introduction of partial melt and reheating the lithosphere to explain the crustal uplift and high heatflow measurements, the source of which is inferred to be within the sub-lithospheric mantle (*McNutt*, 1988; *Courtney and White*, 1986). This is well supported by geochemical studies which find more radiogenic uppermantle ratios of $^{87}Sr/^{86}Sr$ and $^{206}Pb/^{204}Pb$ in Cameroon volcanic rocks and suggest the source to be in the asthenosphere (*Dunlop and Fitter*, 1979; *Fitton and Dunlop*, 1985; *Fitton*, 1987) although a study based on $^{3}He/^{4}He$ ratio argues against a deep mantle plume origin (*Aka et al.*, 2004). As described in the previous section, *Meyers et al.* (1998) proposed a model combining Rayleigh-Bernard convection cells (*Richter and Parsons*, 1975) between the LAB and 670 km discontinuity which brings up the asthenospheric material and volcanism due to decompression melting gives rise to the African hotlines namely the Canary islands, Cape Verde rise, Sierra Leone rise, Cameroon volcanic line, Walvis ridge and St. Helena seamount chain.

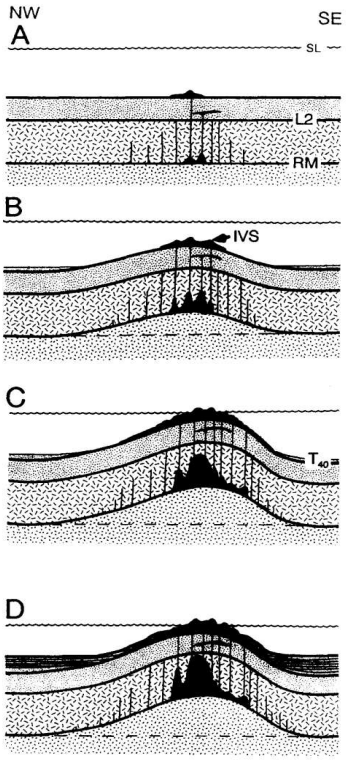

Figure 4.3: Model of crustal uplift creating the Cameroon volcanic line as proposed by *Meyers et al.* (1998). SL is the sea-level, L2 is the top of basement, RM is the Moho reflection and IVS is the intercalated volcanics and sediments. (A) The volcanism began as early as the Oligocene when a thick sedimentary cover had alreday developed. (B) The crustal uplift that began in the late Oligocene but peaked in Miocene (C). The peak in uplift has created an unformity in the sediments, labeled T_{40}. (D) Topographic features of the Cameroon line as seen today.

More recently, *Reusch et al.* (2010) performed body wave tomography from teleseismic events recorded on 32 stations over a 2 year time period from 2005-2007 in the Cameroon Broadband Seismic Experiment (*Tibi et al.*, 2005) and imaged a tabular low-velocity anomaly directly beaneath CVL extending from depths of 50-300 km. The lower depth extent of this low velocity anomaly is not limited to 300 km and may extend further. The P- and S-velocity perturbations range from -1 to -2% and -2 to -3%, respectively. The -2 to -3 % perturbation in the S-velocity is attributed to a temperature increase of 280 K (with 0.8 m/s/K for a grain size of 10 mm and 100 km depth and $1300°C$ as proposed by*Faul and Jackson* (2005); *Wiens et al.* (2008)) within the low velocity anomaly assuming the decrease in shear velocity solely due to temperature. This temperature difference of 280 K is close to the 230 K temperature difference deduced between the convective boundary layer and the LAB by *Lévy and Jaupart* (2011) in eastern North America. *Reusch et al.* (2010) then evaluates all the previous models proposed for the origin of

the CVL against this observation as elaborated as follows.

Models including a single plume as proposed by *Morgan* (1983); *Lee et al.* (1994); *Burke* (2001) are flatly rejected due to apparent age inconsistency among the islands of CVL although *Burke* (2001) attributes the age inconsistency to onset of small-scale (∼100 km) upper mantle convection at 30 Ma due to a relatively slower motion (33%) of the African plate (*O'Connor et al.*, 1999). In another plume-based model proposed by *Griffiths and Campbell* (1990), a ∼100-200 km diameter plume tail feeds a plume head which flattens at the LAB over an area ∼1000-2000 km in diameter at ∼40 Ma. Though the plume head impinged at the LAB would not be present today due to entrainment in mantle convection (*Nyblade and Sleep*, 2003), the plume tail may still be present due to slower movement of the African plate since 30 Ma (*O'Connor et al.*, 1999), feeding warm mantle material to the base of lithosphere and creating a ∼50-100 km thick low-velocity zone (*Nyblade and Sleep*, 2003). Though feasible, this model is also rejected by *Reusch et al.* (2010) as it is much shallower than the observed depths (50-300 km) of tabular low-velocity zone imaged. In yet another plume based model proposed by *Ebinger and Sleep* (1998), the possibility of the thinned lithosphere between the West African and Congo cratons to act as a transporting medium to carry warm mantle material from the Afar plume (figure 4.2) to the CVL is examined. Assuming the plume to have impinged on the LAB at 45 Ma, it would have reached the CVL at 5 Ma assuming the transport to be in a 100 km thick LAB channel ∼100-200 km deep (*Ebinger and Sleep*, 1998). This does not adhere to the observation of a 50-300 km low-velocity channel and hence is ruled out by *Reusch et al.* (2010) though they acknowledge the vertical smearing of ∼100 km in their tomography images.

The model proposed by *Fairhead* (1988); *Fairhead and Binks* (1991) considers sporadic volcanism along the reactivated Central African shear zone to have resulted in CVL and other volcanic lines in the equatorial Atlantic. The Central African shear zone was formed at ∼110 Ma during the opening up of the Atlantic when the north-ward propoagating rift reached the thicker, colder lithosphere in the equatorial Atlantic (*Bonatti*, 1996). Since some later studies examined volcanic rocks along the CVL to be of much younger age and due to lack of information regarding the low velocity anomaly, this model is not able to explain the observations of the CVL. Another non-plume source model based on edge-driven convection (*King and Anderson*, 1995, 1998) attempts to explain higher shear wave velocities in the mantle transition zone beneath the West African and East South American cratons. They take into account the lithospheric thickness variations between the Congo craton and the adjacent thinner 'mobile' lithosphere. The source of warm material is kept fixed beneath the continental craton as in previous studies to explain the absence of the effect of plate motion on the CVL. As the warm mantle material moves along the edge (LAB) from the thicker cratonic lithosphere to the thinner 'mobile' lithosphere, it undergoes decompression melting and results in the formation of volcanism. This model accounts for a possibly 50-300 km thick mobile belt carrying warm mantle material dipping towards the thick cratonic lithosphere but it does not explain the no-dipping vertical low velocity channel imaged by *Reusch et al.* (2010). In a variant of the same model, the same authors (*King and Ritsema*, 2000; *King*, 2007) propose that the edge-flow may result in an upwelling-downwelling pattern due to the temperature variations between the cold, cratonic lithosphere and adjacent warmer 'mobile' lithosphere. The upwelling would occur at the 'mobile' lithosphere which would very well explain the observed vertical low velocity channel observed by *Reusch et al.* (2010) and the downwelling at the cratonic Congo lithosphere. *Reusch et al.* (2010) propose that along the axis of CVL, the edge-flow model of *King and Anderson* (1995, 1998) occurs in which the 'mobile' lithosphere is the oceanic lithosphere and orthogonal to the CVL in the continental regime, the latter upwelling-downwelling model proposed by (*King and Ritsema*, 2000; *King*, 2007) takes place in which the 'mobile' lithosphere is the thinned continental lithosphere between West African and Congo cratons (*Ebinger and Sleep*, 1998) as also imaged by shear wave velocity studies (*Priestley and Tilmann*, 2009). Figure 4.4 shows a sketch of proposed scheme from *Reusch et al.* (2010).

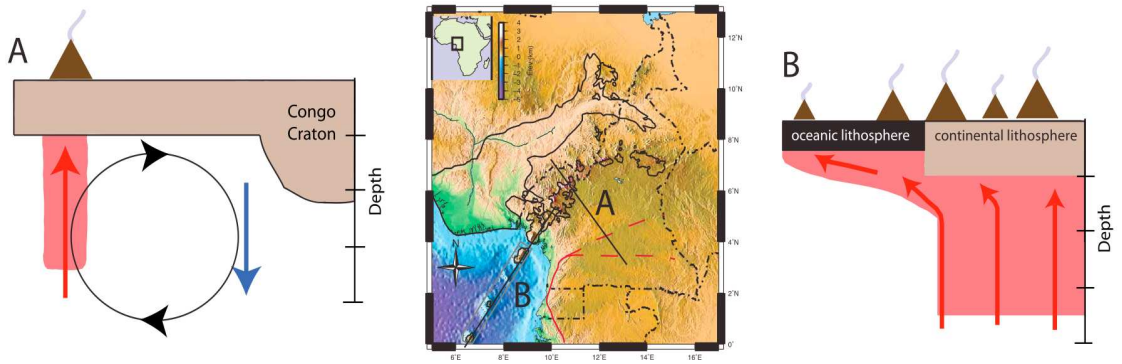

Figure 4.4: The scheme proposed for formation of Cameroon Volcanic line by *Reusch et al.* (2010) to explain their observation of a 50-300 km low velocity tabular column from beneath the CVL from body wave tomography: (A) upwelling-downwelling model (*King and Ritsema*, 2000; *King*, 2007) along the thick Congo craton and the thinner continental lithosphere with downwelling happening at the thicker cratonic lithosphere and (B) edge-flow model (*King and Anderson*, 1995, 1998) along the oceanic-cratonic lithosphere with the melt moving towards thinner oceanic lithosphere which explains the overall oceanward decreasing age.

To see the depth extent of the low velocity zone beneath the CVL as proposed by *Reusch et al.* (2010), *Reusch et al.* (2011) used P-to-S receiver functions stacks from the same 32 teleseismic stations over the same 2 year period (*Tibi et al.*, 2005). Though they imaged the upper bound (410 km discontinuity) and lower bound (670 km discontinuity) of the mantle transition zone, they found that the mantle transition zone thickness beneath the CVL (215±10 km) is no different from that beneath adjacent regions and lies well within the global estimates 242-260 km (*Flanagan and Shearer*, 1998; *Chevrot et al.*, 1999; *Lawrence and Shearer*, 2006). Usually the hotspots have been associated with deep thermal anomalies in the mantle (*Lawrence and Shearer*, 2006; *Courtier et al.*, 2007) and variations in the mantle transition zone thickness have been correlated with thermal structure of the mantle (*Bina and Helffrich*, 1994). However, to reconcile their observations from body wave tomography and receiver functions, *Reusch et al.* (2011) propose that the 280 K hotter, low-velocity zone does not extend upto the 410 km discontinuity beneath the CVL as there is no apparent change in the transition zone thickness. *Meyers et al.* (1998) do not consider the 410 km discontinuity but the more prominent 670 km discontinuity as the lower boundary for mantle convection responsible for forming the CVL.

Ngako et al. (2006) proposed the possibility of the existence of more than one plume sources and the CVL resulting from the complex interaction of at least two plumes and lithospheric fractures. *Milelli et al.* (2012) proposed a oscillatory upwelling and downwelling mechanism to explain a lithospheric instability origin for the CVL. They consider the Y-shaped termination of the CVL at the continental end and on the basis of laboratory experiments, observe the upwelling (and downwelling) patterns within the asthenosphere (a low viscosity medium) arising from the base of lithosphere (modeled as a denser fluid). The instability at the base of lithosphere arises due to cooling from the top (modeled as heating the dense fluid from bottom) which then induces asthenospheric upwelling (modeled as bouyant mantle material spreading out radially while rising above). The radial spreading of the bouyant material would occur along the strike of the upwelling towards the oceanic domain whereas it is laterally confined towards the continental end, which explains the Y-shaped termination. Their experiments shed more light on the edge-flow model proposed by *Reusch et al.* (2010) and also explains the isotopic compositions of continental signatures found in CVL oceanic lavas (*Rankenburg et al.*, 2004).

Recent studies on crustal radial anisotropy from ambient noise tomography (*Ojo et al.*, 2017) have observed negative radial anisotropy ($V_{sv} > V_{sh}$) in upper and middle continental crust and a positive radial anisotropy ($V_{sv} < V_{sh}$) in the lower continental crust. They attribute the observed anisotropy to fossil microcracks or metamorphic foliations due to the upwelling of plume material. *Adams et al.* (2015) performed Rayleigh wave phase tomography on the data aquired during Cameroon Broadband Seismic Experiment (*Tibi et al.*, 2005) and confirmed the observations of *Reusch et al.* (2010) who performed body

wave tomography on the same dataset. Additionally, they observed widespread infiltration or erosion of the continental lithosphere beneath the CVL caused by mantle upwelling and edge-flow convection (*Reusch et al.*, 2010) or lithospheric instabilites at the egde of the African continent (*Milelli et al.*, 2012). However, their observations were unable to resolve between the two candidate models of upwelling-downwelling (*King and Anderson*, 1998; *Reusch et al.*, 2010) and lithospheric instability (*Milelli et al.*, 2012). Irrespective of the origin of the CVL, it is likely to have an effect on the lithosphere and the LAB in the region of the MCS profile.

4.3 Seismic image from 50-75 Ma

Due to the Leg 3 of the MCS profile being closest to the volcanic chains and having a thicker sediment cover and relatively flatter basement morphology (chapter 3), I started data processing on it first. Following the processing for deeper Earth events as described in chapter 2, I obtained the following high resolution image for the profile as shown in the following figure 4.5a. An event intermittently imaged around 2 s two-way time (TWT) below the seafloor is observed and is interpreted to be the crust-mantle boundary (Moho). A deeper event from ∼23 s two-way time (TWT) to ∼27.5 s TWT can be seen dipping towards older age and is a potential candidate for the base of lithosphere (LAB). A quick analysis for polarity indicates that the deeper reflection has a polarity reversed to that of the seafloor as shown in figure 4.5b.

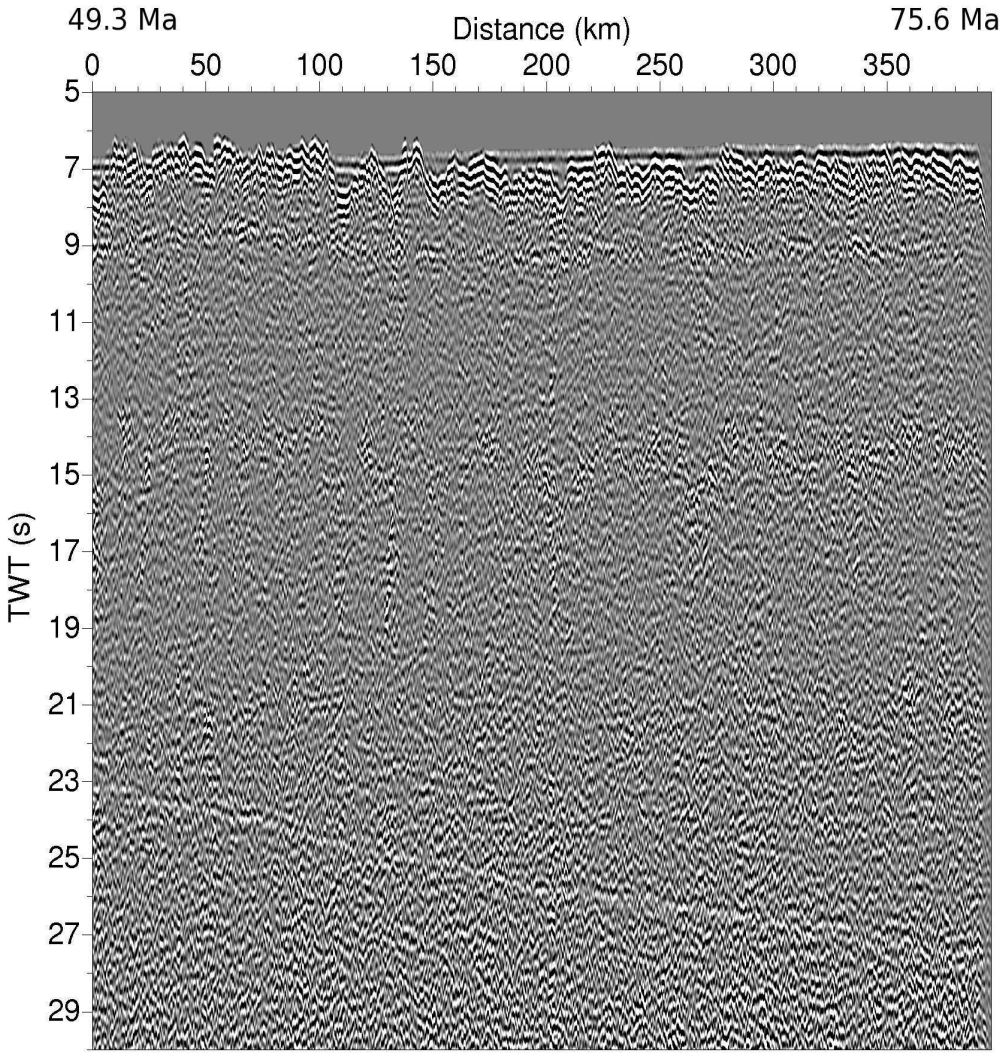

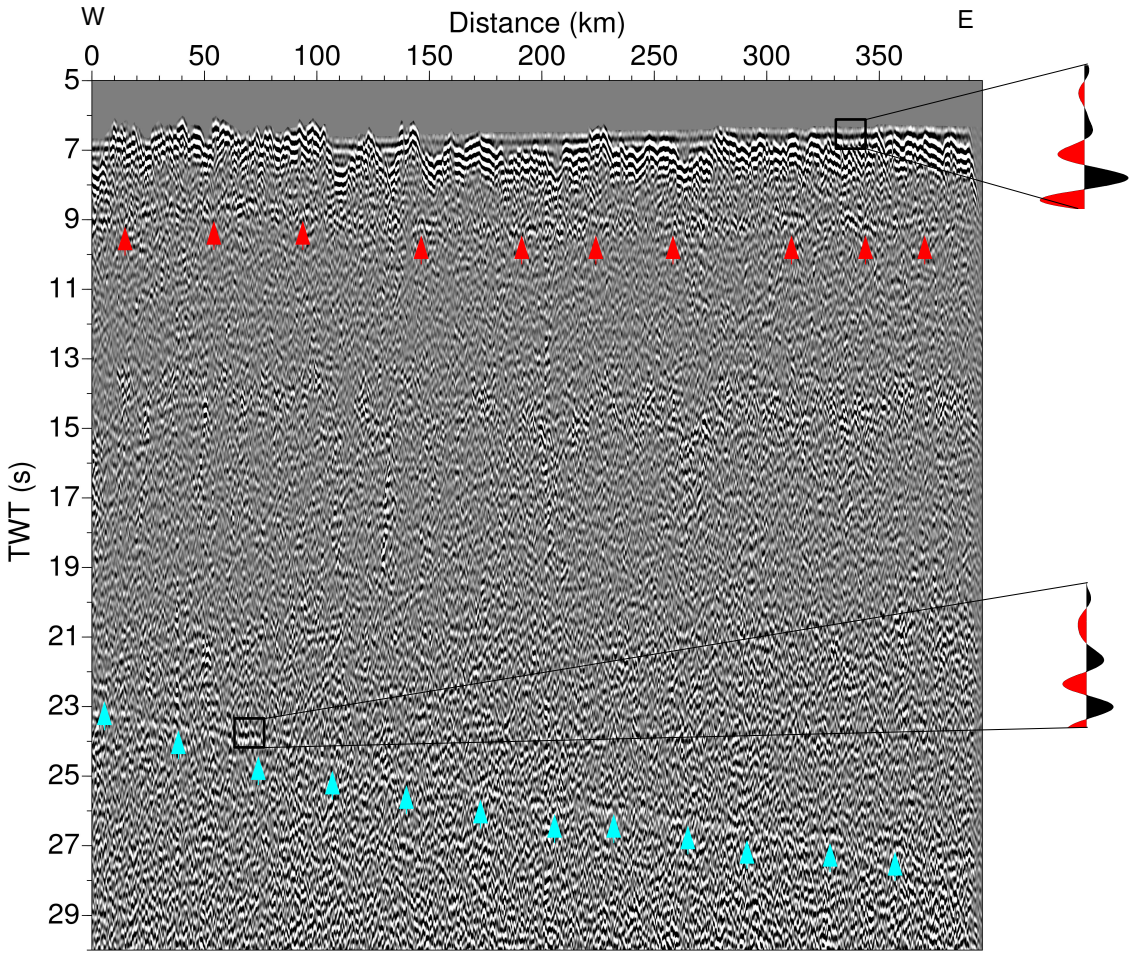

Figure 4.5: (a) Final processed uninterpreted seismic section of the Leg 3 from 49.3 Ma in West to 75.6 Ma in East. (b) Interpreted seismic image showing Moho (red) and LAB (cyan) with polarity of seafloor and LAB reflections.

4.4 LAB reflection in time

The first step was to confirm the veracity of the deeper reflection. To do this, I first overlaid the water-bottom multiples of prominent events. There would be a large number of multiples from various events and hence I mainly consider the water-bottom multiples of three prominent reflections - seafloor (green), basement (cyan) and the Moho (yellow) are found not to coincide with the imaged reflection as shown in figure 4.6. The multiples are observed to be sub-horizontal and rough but the imaged reflection is dipping smoothly towards older ages. This rules out the reflection to be a water-bottom multiple of the seafloor, basement or the Moho.

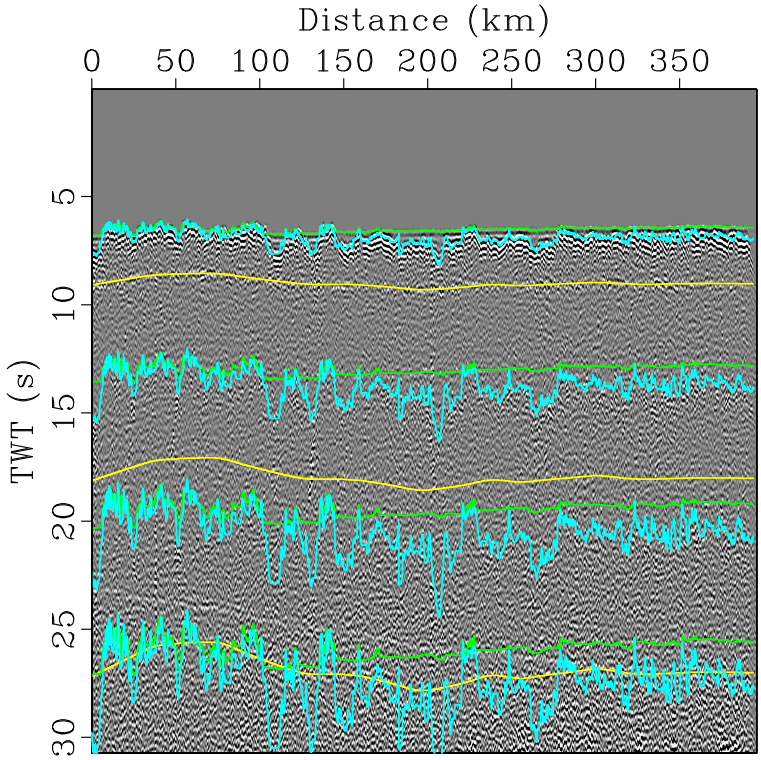

Figure 4.6: Seismic section superimposed with seafloor (green), basement (cyan) and Moho (yellow) multiples.

4.4.1 Estimating side-swipes

The MCS profile has been acquired in a 2D manner, but sometimes reflections from out of the 2D plane get captured. These out of the plane reflections are called side-swipes. I attempted to compute side-swipes over the part of the profile from 49.3-75.6 Ma using the 15-arc second global bathymetric map (*Olson et al.*, 2014). Two main constraints were used to compute side-swipes - the record length of the seismic (30 s TWT) and the likelihood (reflectance) for a bathymetric point to be mapped in the plane of zero-offset seismic. I used a co-located source-receiver pair (common mid-point) instead of the actual source and receiver positions due to computational constraints. I used common-mid-points spaced every 500 m along the whole profile instead of taking ever common mid-point at every 6.25 m. The possible bathymetric points on the 3D seafloor (*Olson et al.*, 2014) that could potentially be imaged as side-swipes are filtered first according to the record length (30 s TWT) in water (P-velocity of 1.5 km/s). This is illustrated in figure 4.7a. Those bathymetric points having a TWT of >30 s from the common mid-point cannot be imaged and hence are filtered out. In the next constraint, surface normal vectors to each of these bathymetric points in figure 4.7a are computed as shown in figure 4.7b. A dot product of each of the surface normal vectors with the vector joining the common mid-point and the bathymetric point (of that surface normal vector) is computed in figure 4.7c. Note that the dot product will give a measure of linearity of the surface normal vector with the common mid-point. This measure of linearity (normalized

dot product) can be considered as a likelihood (probability) of the bathymetric point to reflect energy back to the common mid-point. By selecting only those bathymetric points having a high probability (>0.95) of reflecting back are taken into account. The filtered bathymetric points using this two-step strategy is shown for the entire profile in figure 4.8a and their corresponding mapped TWT in the profile is shown in figure 4.8b.

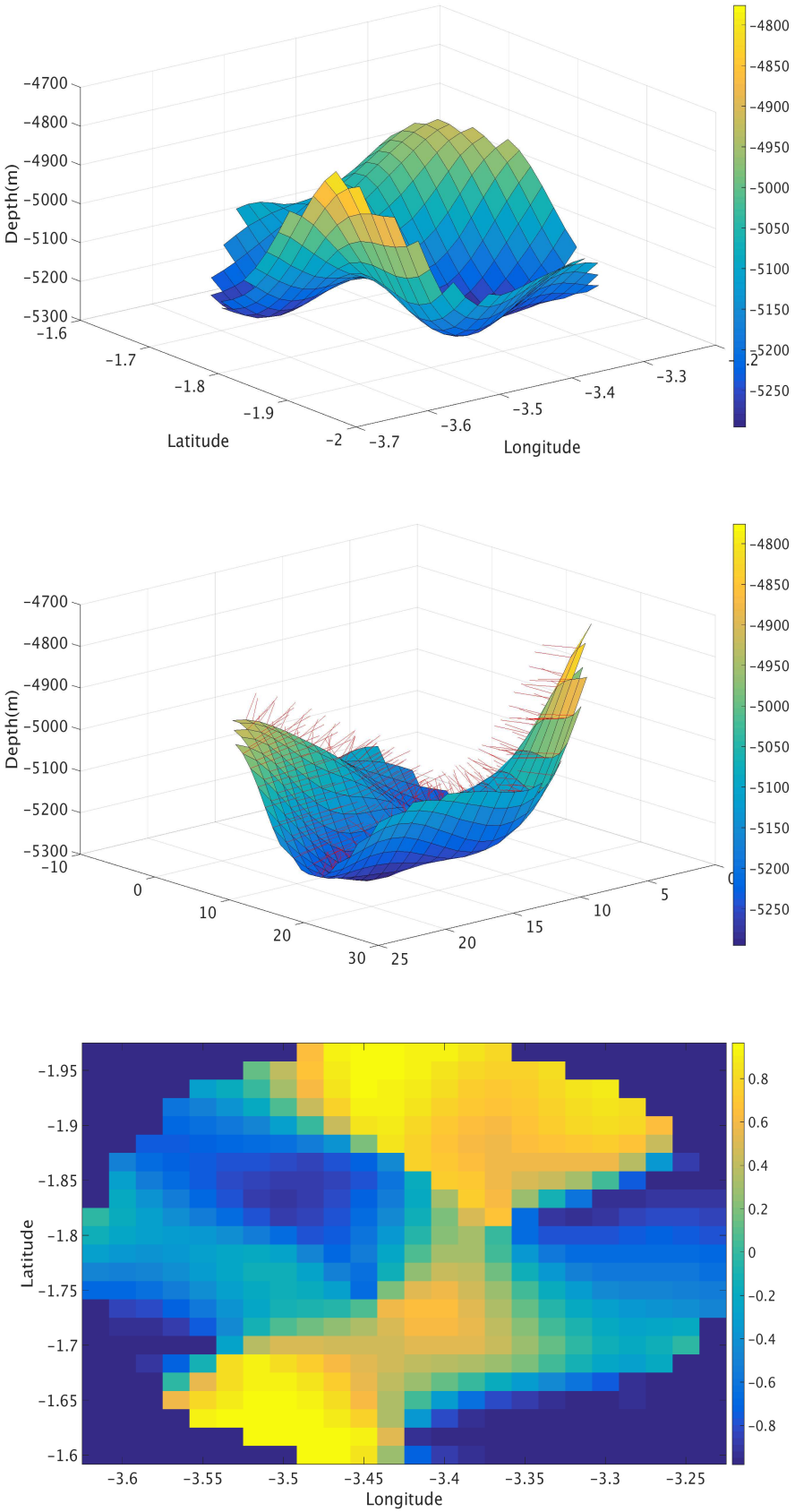

Figure 4.7: Strategy for estimating side-swipes: (a) First, the record length (30 s TWT) is used as a constraint to filter out the possible bathymetric points that can contribute as a side-swipe. (b) For he second constraint, Surface normal vectors to each of these bathymetric points are created. (c) Then the dot product of each of these surface-normal vectors with the vector joining the surface common mid-point and the bathymetric point is computed and assigned a likelihood function to that bathymetric point. Only points having a high probablity (>0.95) of reflecting back are taken into account.

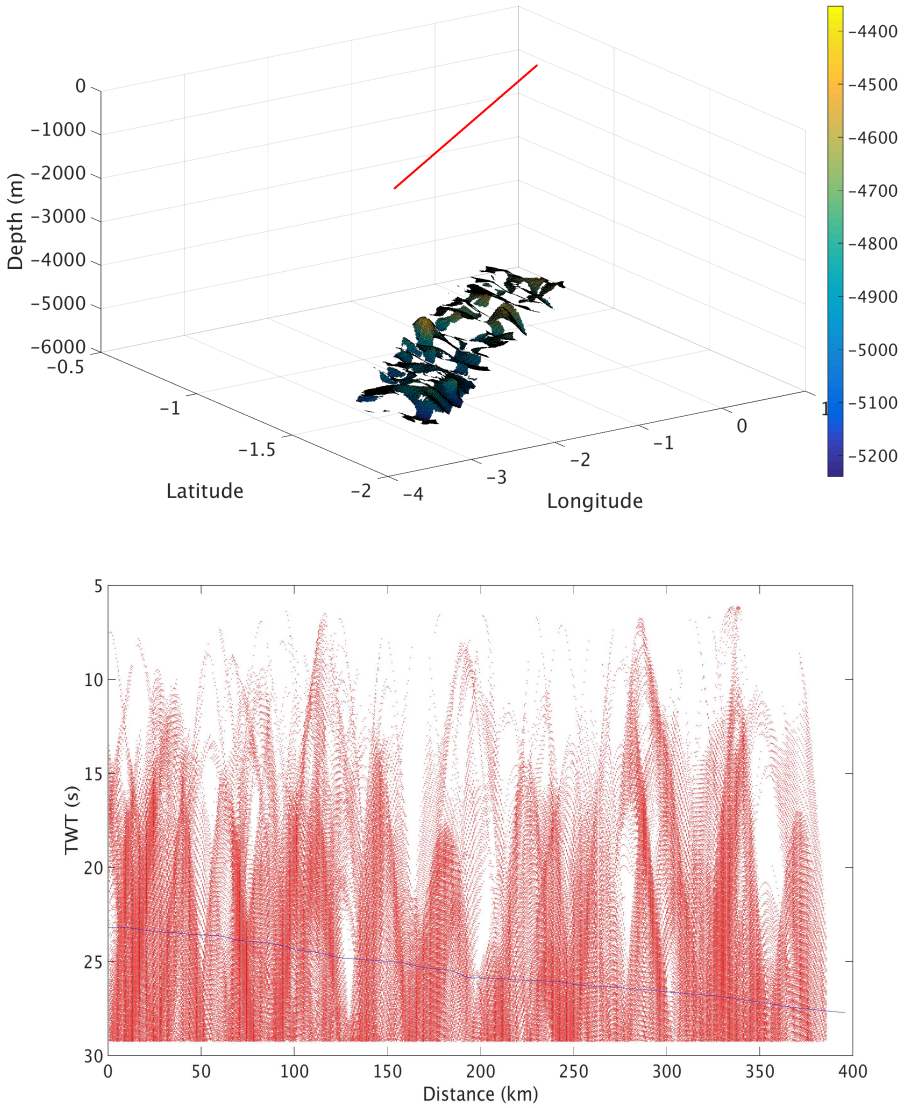

Figure 4.8: Estimated side swipes for Leg 3 from 15 arc second global bathymetry grid (*Olson et al.*, 2014): (a) Possible bathymetric points have been filtered on the basis of two-step strategy described in text. The red line is the MCS profile on the surface. (b) The two-way time from these bathyemtric points have been plotted (red) against the two-way time of the reflection (blue) in question.

The above analysis shows that the imaged reflection does not correspond to the water-bottom seafloor, basement and Moho multiples. Quantitative estimation of side-swipes does not concentrate the out of the plane reflection points over the imaged reflection. It is very likely that this reflection is indeed the base of the lithosphere (LAB).

4.4.2 P-velocity drop estimation

Polarity analysis has shown that this reflection corresponds to a velocity drop (figure 4.5b), characterized by reduction of amplitudes at this interface. *Mehouachi and Singh* (2018) consider the top of the LAB channel as the freezing front and estimate a drop of ∼8.5% at the LAB. The expected impedance contrast at each interface (seafloor and LAB) is described in table 4.1.

Due to seafloor and the LAB as most continuous reflections and having more prominent impedance contrasts as compared to other reflections (Moho etc.), I consider only the relative amplitudes of the seafloor and the LAB reflections. As shown in figure 4.9, I picked several points along the seafloor and the LAB reflections to correlate with the values obtained in the above table. To estimate the P-velocity drop from the impedance contrast values and the picked reflection points, I followed the methodology

Table 4.1: Estimates of P-velocity (V_p), density (ρ) and reflectivity coefficient ($Z = V_p\rho$) from MCS data at distinct interfaces observed on the seismic

Layer	$V_p(m/s)$	$\rho(kg/m^3)$	$Z(kg/m^2s)$
Water	1500	1	1500
Sediments (decompacted)	1650	1.2	1980
Layer 2A	4000	2.67	10680
Lithosphere (above LAB at 75 Ma)	8500	3.3	28050

used in *Qin and Singh* (2015); *Mehouachi and Singh* (2018). The amplitudes in figure 4.9 were corrected for spherical divergence and intrinsic attenuation (A) using the following relation.

$$A = A_0 exp^{\frac{-\pi f t}{Q}} \tag{4.1}$$

where A_0 is the seafloor amplitude, f is the dominant frequency, t is the two-way time and Q is the quality factor taken as 1000 (*Qin and Singh*, 2015; *Mehouachi and Singh*, 2018).

The incident energy is partly reflected and partly transmitted on an interface. The reflected energy is denoted by the reflection coefficient,R, which depends on the impedance contrast of the two media separated by the interface: $R = (Z_2 - Z_1)/(Z_2 + Z_1)$. Applying it to seafloor and LAB reflection interfaces, one gets the formulation:

$$R_{LAB} = \frac{R_{SF} A_{LAB}}{(1 - R_{SF}) A_{SF}} \tag{4.2}$$

where A_{LAB} and A_{SF} are the estimated amplitudes at the LAB and seafloor interfaces respectively, R_{LAB} and R_{SF} are the reflection coefficients of the LAB and seafloor interfaces respectively. R_{LAB} can then be used to estimate P-velocity below the LAB reflection. Assuming density in the lithosphere and asthenosphere is same (=3300 kg/m^3), R_{LAB} can be directly used to estimate the velocity below the LAB if the velocity above the LAB is known. The variation of estimated P-velocity drop with age is shown in figure 4.10. The mean estimated P-velocity drop for the profile is found to be 8.8%, close to the 8.5% found by *Mehouachi and Singh* (2018). Note since densities are assumed to be unchanged across LAB, this P-velocity drop of 8.8% represents the maximum P-velocity drop possible.

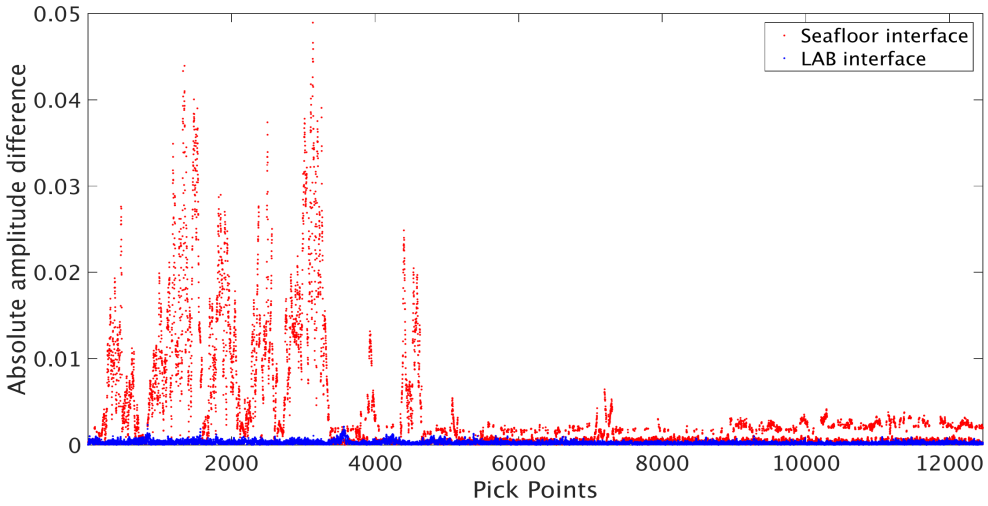

Figure 4.9: The seismic amplitudes along the seafloor and LAB reflections were picked on seismic section (without any gain) to determine the relative change in impedance contrast. More than 12000 pick points were identified at the polarity reversals of the seafloor and LAB reflections from 49.3-75.6 Ma. The seafloor from 49.3-61 Ma comprises of rugged basement topography and can be seen with higher amplitudes due to higher impedance contrast at the water-basement interface as compared to the water-sediment interface beyond 61 Ma.

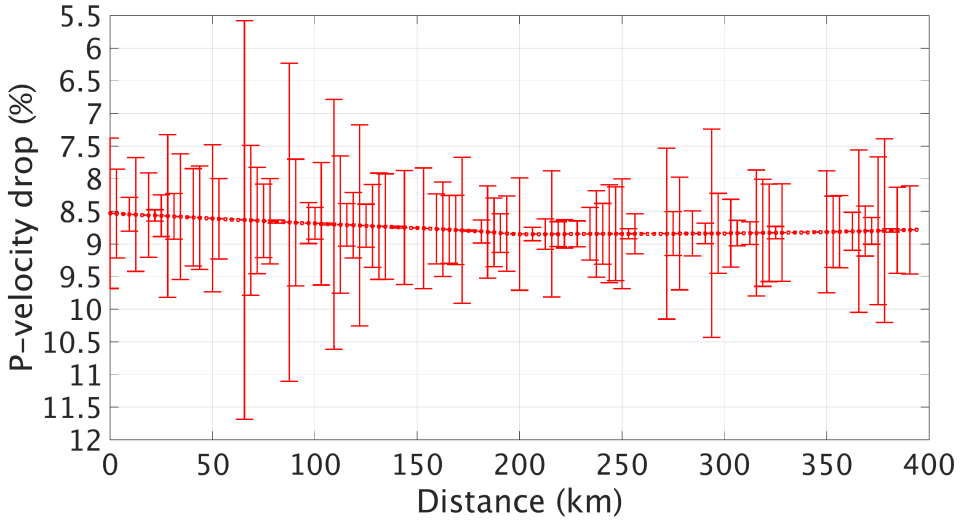

Figure 4.10: The P-velocity drop across the LAB reflection corresponding to the picked points in figure 4.9 and the values used in table 4.1. The reference reflection taken for the computation is the seafloor and the methodology used is the the same as *Qin and Singh* (2015); *Mehouachi and Singh* (2018).

4.5 Depth conversion of the LAB reflection

In order to make interpretation, I converted my seismic section from two-way time in figure 4.5 to depth. A reliable P-velocity model was needed for the depth conversion. The P-velocity model from global database (*Pasyanos et al.*, 2014), along the MCS profile was not found reliable as the LAB reflection was observed to be dipping towards 50 Ma (figure 4.11), contrary to our results. In the absence of any other source for P-velocities, I used the following P-velocities.

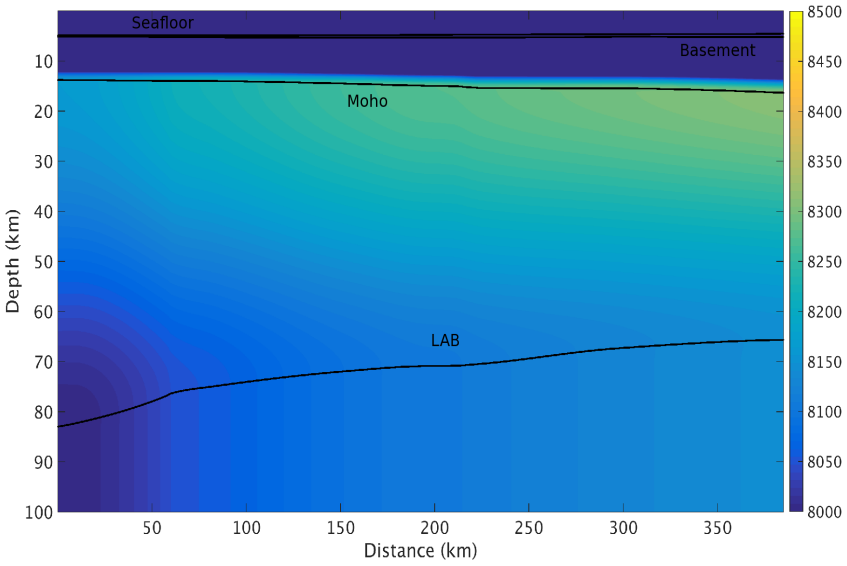

Figure 4.11: The mantle gradient of the P-velocity and the Moho, LAB reflections (black) from the seismology model LITHOS1.0 along the MCS profile from *Pasyanos et al.* (2014). The zero distance corresponds to Western end of MCS profile at 49.3 Myr and the 400 km distance corresponds to the Eastern end of the MCS profile at 75.6 Myr.

I used my tomography results for the upper 2 km of the crust at 50.9-52.9 Ma and 68.9-71.6 Ma (chapter 3) and laterally interpolated the velocities in between. The mean crustal thickness was taken as 6.3 km (*Lianjun Li, personal communication*) and I extrapolated velocities to 6.8-7 km/s at the base of crust (*White et al.*, 1992). The seafloor, basement, Moho, and the LAB reflection was then picked from the seismic and smoothed 20 km laterally to avoid depth conversion artifacts. Below the Moho, I used a velocity of 8 km/s (*White et al.*, 1992) and linearly extrapolated to a maximum mantle velocity of 8.5 km/s. This maximum mantle velocity of 8.5 km/s was taken from *Stern et al.* (2015); *Mehouachi and Singh* (2018). However, recent active source studies have shown velocities in the spreading direction to reach 8.65 km/s (*Ohira et al.*, 2018). Assuming a linear mantle velocity and the seismic two-way time (t_{LAB}) as a constraint on lithospheric thickness, minimum and maximum mantle velocities (v_{min}, v_{max}) can be related to the thickness of lithospheric mantle (z_{LAB}) as:

$$z_{LAB} = \frac{t_{LAB}(v_{max} - v_{min})}{2log_e(\frac{v_{max}}{v_{min}})} \tag{4.3}$$

By using v_{min} as 8 km/s and t_{LAB} known from figure4.5, v_{max} between 8.4-8.65 km/s give an uncertainty of ± 2 km in the thickness of lithospheric mantle and hence the depth of LAB reflection. I used the higher end of maximum mantle velocities as the profile is in the plate spreading direction as opposed to orthogonal spreading direction where the maximum mantle velocities are slightly lower (*Zhikai Wang, personal communication*). The 1-D velocity model obtained in this fashion was smoothed in depth to avoid sudden jumps in velocities which could create artifacts in the seismic image and is shown in figure 4.12. Unlike *Mehouachi and Singh* (2018), who used a variable mantle gradient to fix the velocity at the LAB to be 8.5 km/s, I used a constant mantle gradient with velocity above the reflection being 8.5

km/s at 75 Ma and 8.38 km/s at 50 Ma. This is reasonable as the mantle gradient is not expected to change much due to aging of the lithosphere.

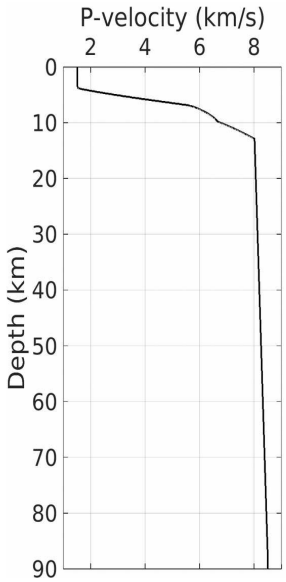

Figure 4.12: 1-D P-velocity model used for depth conversion of the LAB reflection. Linearly increasing mantle velocities with a constant gradient has been assumed such that the maximum mantle velocity reaches 8.5 km/s at 75 Ma. A smooth version of seafloor, basement, Moho and LAB reflection have been used in the model to avoid artifacts. The same 1-D model has ben used along the entire length of the profile for simplicity.

Lastly, I also resampled the seismic data in time (figure 4.5) from 8 ms to 2 ms to avoid stretching and compression during depth conversion. The full depth converted seismic and the zoom-in on the LAB reflection is shown in figure 4.13a and b respectively.

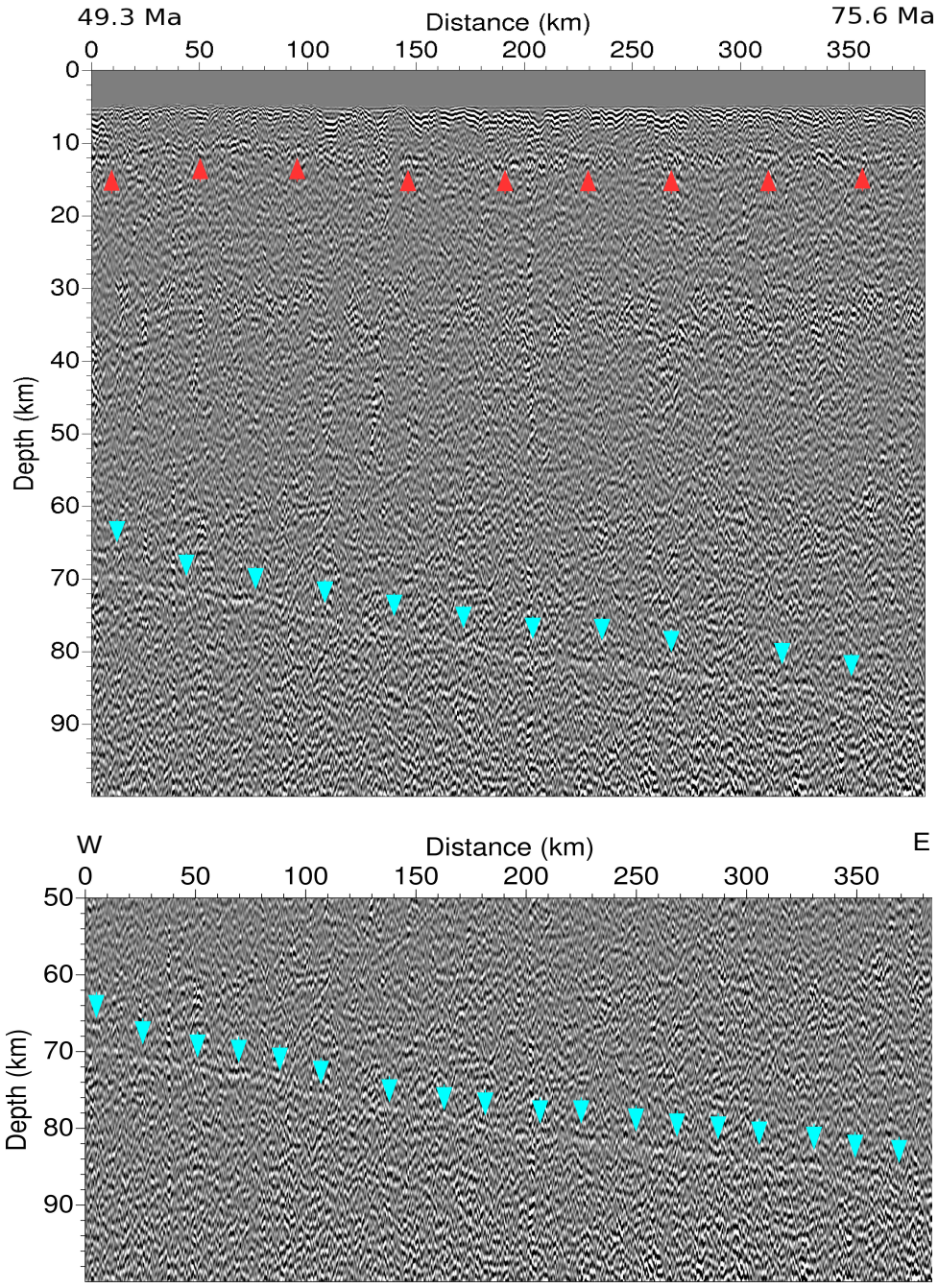

Figure 4.13: (a) Full depth converted seismic image with a zoom-in on the (b) LAB reflection from ∼68 km depth to ∼86 km depth. The uncertainty in the depth of the LAB reflection is ±2 km.

I compared the LAB depths from all available literature between 49.3-75.6 Ma lithosphere. Figure 4.14 shows the comparison with the global seismology model along the MCS profile (*Pasyanos et al.*, 2014), the receiver function studies in the Pacific plate at different ages (*Kumar and Kawakatsu*, 2011) and the seismic reflection study at St. Paul fracture zone (*Mehouachi and Singh*, 2018). Whereas the seismology and receiver function studies show inconsistent variation of LAB depths with age, the seismic reflection study shows a deeper and less steeply dipping reflection imaged distinctly at lithospheric ages 40,50 and 70 Ma. Interestingly, two out of the five receiver function results (*Kumar and Kawakatsu*, 2011) are consistent with our results (at 50 Myr and 60 Myr in figure 4.14) and two others are consistent with the global seismology model LITHOS 1.0 (at 70 Myr and 73 Myr in figure 4.14). These results indicate that the velocities used for depth conversion are significant for defining the LAB.

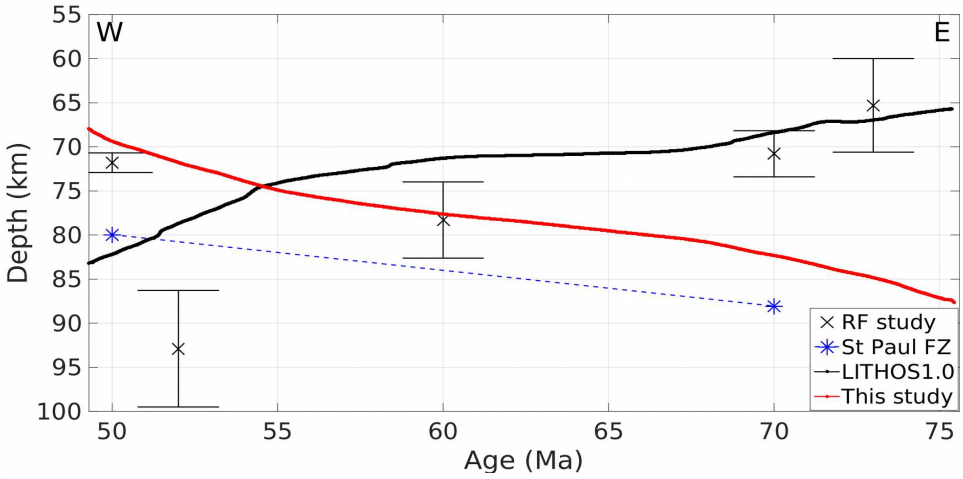

Figure 4.14: The LAB reflection in depth (this study) compared with other studies in the same age range: seismology (*Pasyanos et al.*, 2014), receiver function studies (*Kumar and Kawakatsu*, 2011) and seismic reflection (*Mehouachi and Singh*, 2018). Note that the latter study at St Paul fracture zone is only able to constrain the depths at distinct ages of 40, 50 and 70 Ma lithosphere (shown by blue stars). Uncertainty in LAB reflection (red) is ±2 km.

4.6 Estimation of thermal boundary of the LAB

Mehouachi and Singh (2018) associate the LAB with the 1260°C isotherm as a solidus below which the melt is frozen. The plate-cooling model they use to estimate this temperature is *McKenzie et al.* (2005) which best fit their data. However, the study region in their case had been a fracture zone, unlike continuous oceanic lithosphere as in this case. Subsequently, I re-investigated in depth the various plate cooling models and the best fitting thermal boundary. The thermal structure of the lithosphere is described by half-space and plate-cooling models as introduced in chapter 1. The difference between these models can be visualized in figure 4.15.

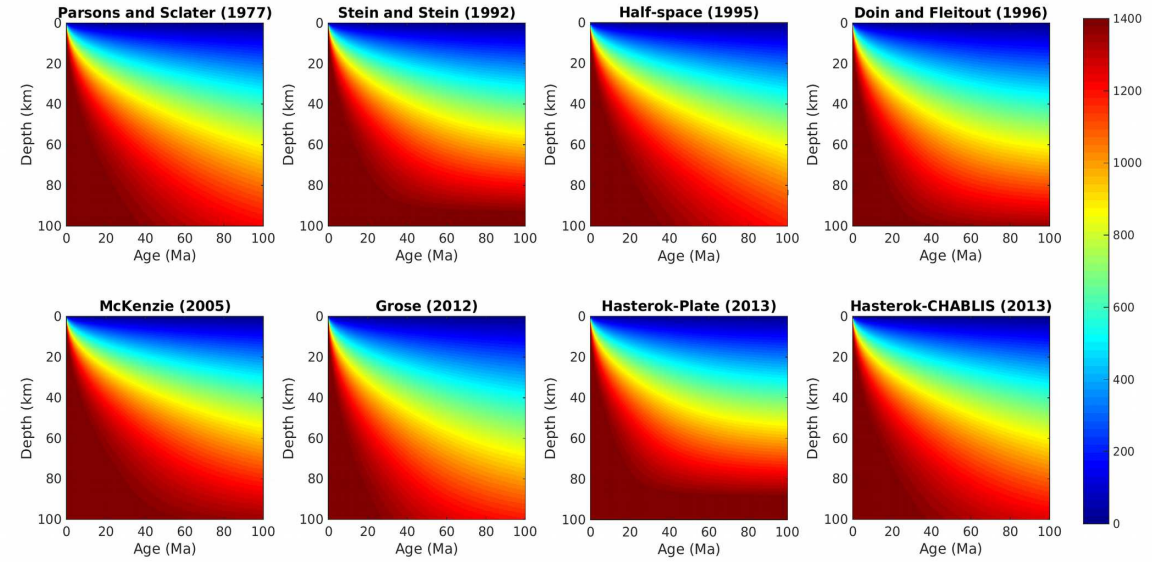

Figure 4.15: Various half-space and plate-cooling models published in literature (described in chapter 1). The temperature distribution with depth and age is plotted until 1400°C.

The differences between the various models in figure 4.15 become prominent at greater depths corresponding to the imaged LAB reflection in our region. By testing all the models shown in figure 4.15, I found a good match of the observed LAB reflection to three particular models - the half-space model (1130°C isotherm), the PS77 model (1135°C isotherm) and the Hasterok-CHABLIS model (1140°C). These are shown in figure 4.16. Additionally, the 1260°C isotherm for the study region is also plotted which was estimated to be the temperature corresponding to the LAB at St Paul fracture zone (*Mehouachi and Singh*, 2018). It can be seen clearly that the reflection in this study is steeper and shallower than the 1260°C isotherm. The LAB reflection corresponds to 1130±20°C in this study.

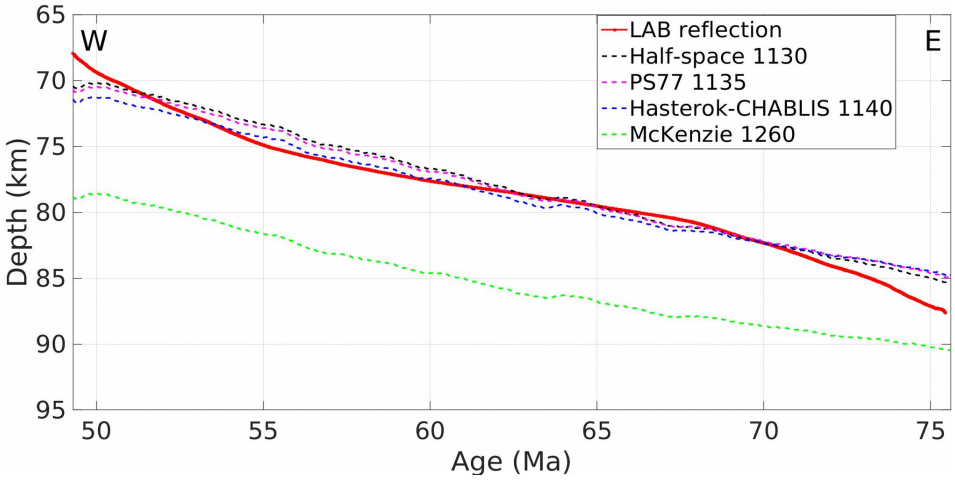

Figure 4.16: The LAB reflection in depth (red) with the best fitting isotherms of different models. Laterally smoothed seafloor and basement depths were added to the different models in figure 4.15 to compare with the LAB reflection. Also shown in dashed green is the LAB temperature of 1260°C estimated at St Paul fracture zone (*Mehouachi and Singh*, 2018).

It must be mentioned here that a laterally smoothed version of the basement topography (top of lithospheric plate) having a temperature of 2°C (T_0) was assumed in the above calculations. A discrepancy between the imaged LAB reflection and the isotherms can be observed at the two ends of the profile, at 49.3-51 Myr in the West and 70-75.6 Myr in the East. This discrepancy implies that whereas the top of the lithospheric plate (basement) is formed by extrusive processes such as those described in chapter 3, the base of the plate (LAB) is formed by completely different processes, such as melt accumulation. Due to absence of co-located heatflow measurements for this Leg of the profile, I did not make any assumptions about the temperature at the basement, although temperatures at the basement have been found to reach 20°C at the eastern end of Leg 2 of the profile as discussed in chapter 3.

4.7 Basement uplift

As noted in the basement topography analysis in chapter 3 that the easternmost part of the profile is uplifted with respect to subsidence models. The various subsidence models such as half-space and plate-cooling have been described in chapter 1. I analysed the regional bathymetry to find evidence of basement uplift. By removing the sediment thickness of the region (*Whittaker et al.*, 2013) from the bathymetry (*Olson et al.*, 2014), the basement topography is obtained. The predicted basement topography from half-space subsidence is then obtained (chapter 1) with the seafloor ages from *Müller et al.* (2008). The difference between the predicted and observed basement topography is shown in figure 4.17 and it can be seen while the maximum uplift due to the volcanic chains is South of the MCS profile from 49.3-75.6 Myr, the MCS profile itself is near the edge of being influenced by the volcanic uplift.

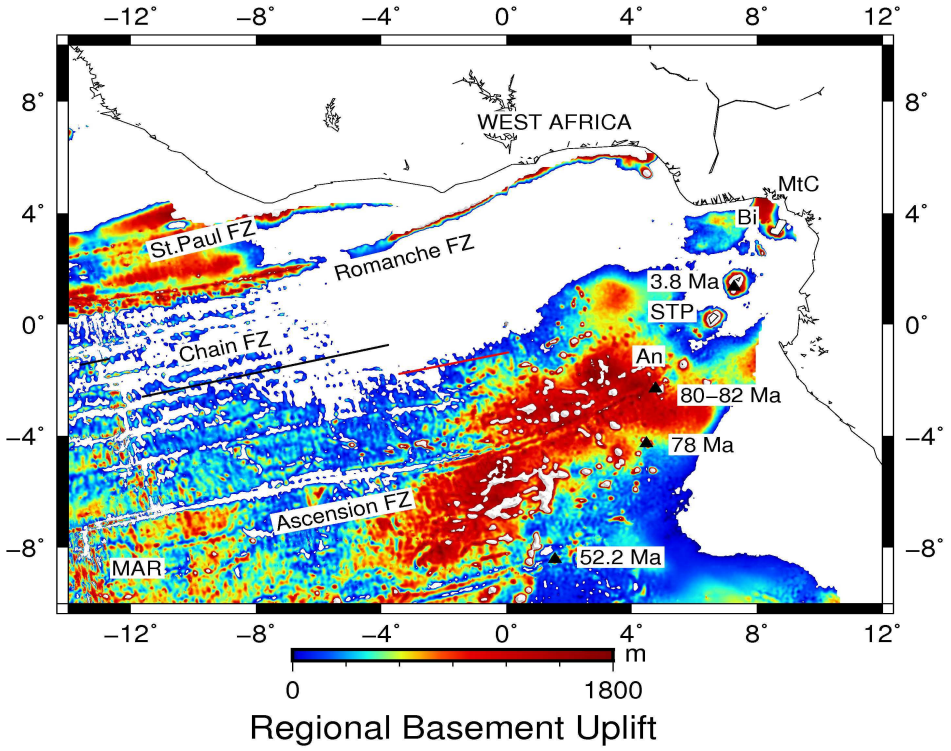

Figure 4.17: The basement uplift of the Equatorial Atlantic on the African plate with respect to half-space cooling model. The global sediment cover from *Whittaker et al.* (2013) has been removed from the global bathymetry data set from *Olson et al.* (2014) to obtain the global basement topography. The half-space subsidence corresponding to seafloor ages from *Müller et al.* (2008) have then been computed using a ridge-axis depth of 2655±20 m with respect to least squares fitting of the subsidence to the observed basement topography from 0-50 Ma. Most of the uplift can be seen concentrated to the south of the MCS profile (shown in red) and the MCS profile is near the edge of the uplift.

A ridge-axis depth of ∼2653 m (rounded to 2655±20 m) for the subsidence models has been obtained in the analysis of the basement topography in chapter 3. The mean uplift I observe from 49.3-75.6 Ma is 270±20 m with respect to Hasterok's subsidence curve (*Hasterok*, 2013) and 290±20 m with respect to half-space subsidence model, not including the bending of the plate due to sediments. In order to account for the effect of this sediment loading, I use the relation proposed by *Adam et al.* (2005) and applied to Juan de Fuca subduction plate (*Han et al.*, 2016). If δd is the bending of the lithospheric plate due to a h_s thick sediment cover and ρ_w=1030, ρ_s=1500, ρ_m=3300 are the densities of the water, sediments and the mantle in kg/m^3 respectively, then these parameters are isostatically related by (*Adam et al.*, 2005).

$$\delta d = \frac{\rho_s - \rho_w}{\rho_m - \rho_w} h_s \tag{4.4}$$

Numerical modeling results suggest that this relation is valid for plates having an elastic thickness <20 km. The elastic thickness as shown by *Anderson* (1995) corresponds to ∼650°C isotherm. *Watts and Burov* (2003) examine the relation between the seismogenic lithospheric thickness (i.e. earthquakes depths) and elastic plate thickness and conclude that though there is no direct correlation between these parameters, their range overlaps. I assume the elastic thickness of the lithosphere from 49.3-75.6 Ma is <20 km and the sediments density is 1.5 kg/m^3 for a ∼500 m thick sediment cover as compared to 2 kg/m^3 (*Han et al.*, 2016) used in subduction zone settings where the sediment cover is 2-3 km thick. This gives an additional basement uplift of ∼110 m from the above relation which implies that the basement would have been uplifted by 110 m more if the sediment cover were to be removed. The total mean uplift of the basement then becomes 290 m + 110 m = 400 m with respect to half-space subsidence model. The sediment unloaded basement uplift with respect to plate cooling model is ∼360 m and with respect to Hasterok's subsidence curve (*Hasterok*, 2013) is ∼375 m. The 2D variation of the basement and its uplift with respect to subsidence models is shown in figure 4.18.

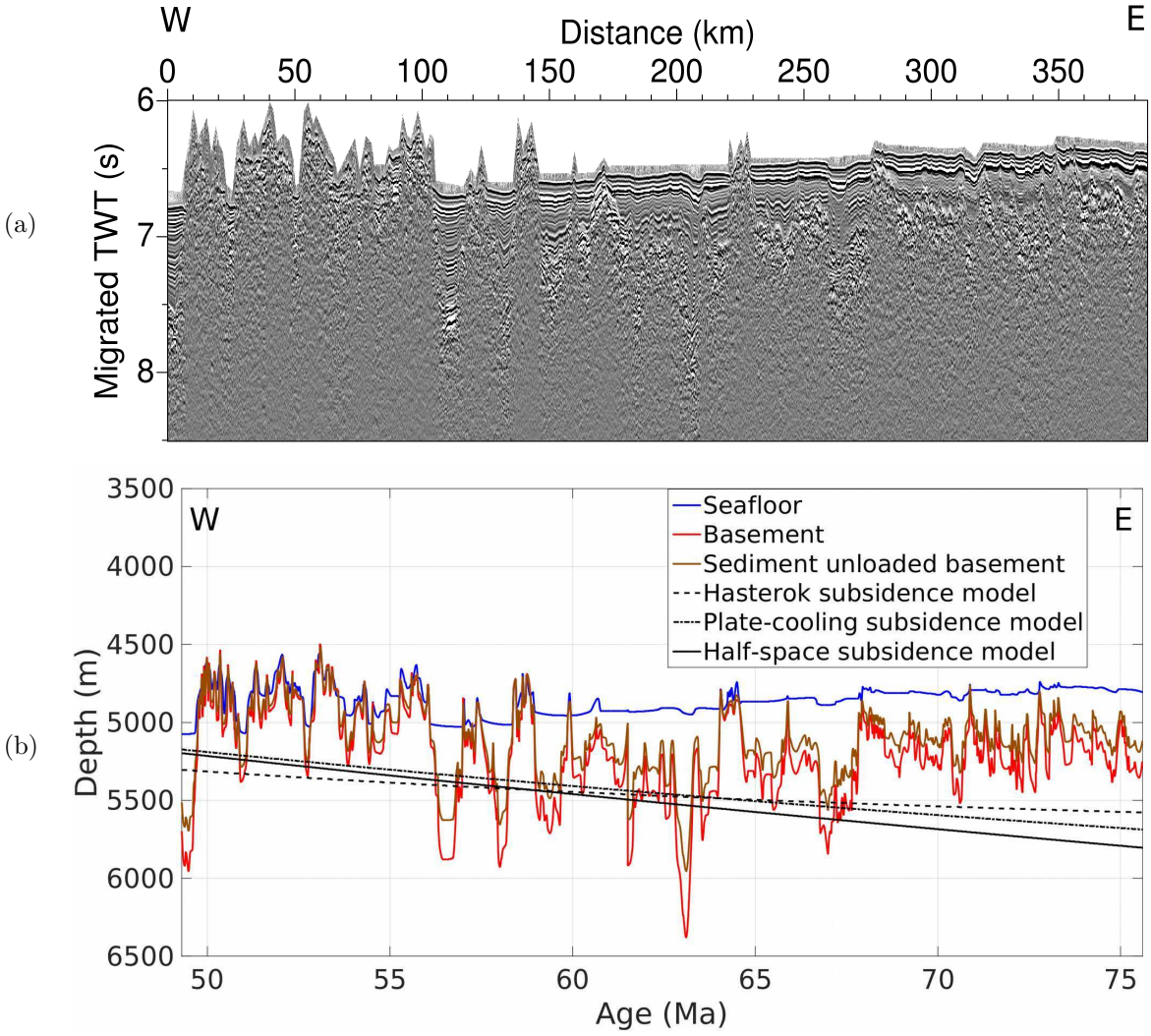

Figure 4.18: (a) Time migrated seismic section of the near surface showing seafloor and basement fom 50-75 Ma. (b) Line diagram of the seafloor, basement and sediment unloaded basement with respect to subsidence modles (see text). Water and sediment P-velocities as 1.5 km/s and 1.65 km/s respectively have been used to depth convert the interfaces from the seismic in (a). The mean uplift of the sediment unloaded basement with respect to half-space subsidence model is ∼400 m.

4.7.1 Evidence of hotter mantle/asthenosphere

Hartley et al. (2011); *Hoggard et al.* (2016) propose an isostasy model in which they correlate the observed dynamic topographic on the Earth's surface with the temperature perturbation within the convection

cells in the asthenosphere needed to cause the uplift. The notion of an asthenospheric ocean has long been prevalent in the seismological community and has been recently imaged by means of waveform tomography (*Fichtner et al.*, 2009; *French et al.*, 2013). The uplift, U, caused by a temperature perturbation of ΔT within an asthenospheric channel of thickness h, and ambient temperature T_0 on a lithosphere with thermal expansion coefficient α is given by:

$$U = \frac{h\alpha\Delta T}{1 - \alpha T_0} \tag{4.5}$$

The main parameter which influences the thermal perturbation from the above equation is the asthenospheric channel thickness and the thermal perturbation is almost invariant to the ambient asthenospheric temperature. Using α =3.3e^{-5}°C $^{-1}$ and ambient asthenospheric temperatures T_0 =1400°C (*Sarafian et al.*, 2017) in an asthenospheric channel of h =100 km (*French et al.*, 2013), an uplift, U =400± 20 m would create an average excess temperature perturbation of ∼125± 20°C. This excess temperature when added to the estimated LAB temperature of 1130°C, gives an estimate of ∼1255°C, which is very close to 1260°C estimated by *Mehouachi and Singh* (2018). The basement uplift with respect to plate-cooling subsidence (360 m) and Hasterok's subsidence (375 m) give an excess temperature perturbation of ∼110-115°C.

It would be interesting to correlate the slope of the imaged reflection with the excess temperature variation along the profile. Using the above equation for estimating the excess temperature from basement uplift in figure 4.18b, the variation can be seen in figure 4.19. It can be seen that until 65 Myr, the excess temperature required is close to 100°C, but increases beyond from 100°C to ∼240°C at 75 Myr. This is because the uplift increases rapidly at the eastern end of the MCS profile at 75 Myr (figure 4.18b). Also worth reminding here is that the excess temperature of the plume tail imaged beneath Mt. Cameroon is around 280°C (*Reusch et al.*, 2010) and also mantle flows at depths of ∼110 km in the direction of CVL from anisotropic tomography studies (*Silveira and Stutzmann*, 2002) have been observed.

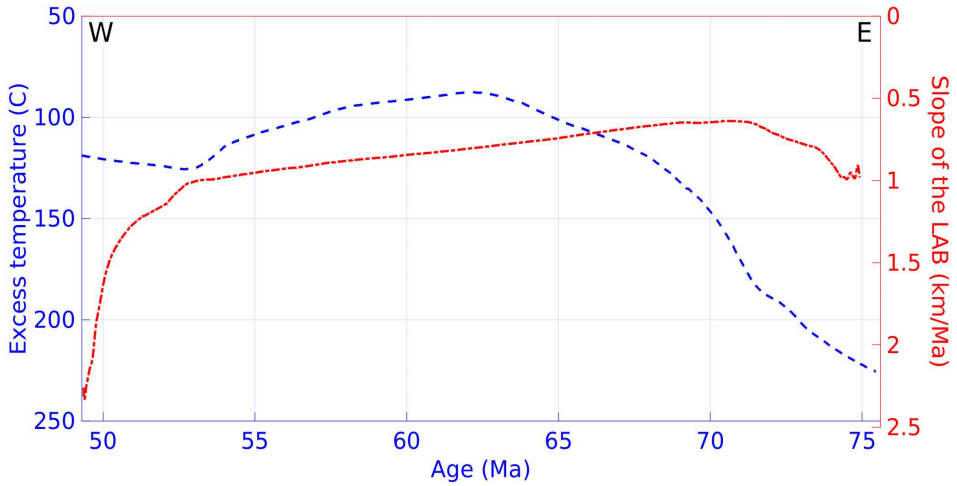

Figure 4.19: The excess temperature along the profile (dashed blue) compared with the slope of LAB reflection (dashed red).

The results so far have indicated towards a hotter asthenosphere compensating the lower temperature of the LAB estimated in this study as compared to previous studies (*Mehouachi and Singh*, 2018). Further evidence of a hotter mantle underneath the MCS profile comes from analysis of residual mantle bouguer anomaly (RMBA). The mantle bouguer anomaly was firstly obtained by removing from the free-air gravity anomaly (*Sandwell et al.*, 2014), the gravitational effects of water-sediment and sediment-crust interfaces (*Parker*, 1973). The gravitational effect of lithosphere plate cooling was modeled (*Kuo and Forsyth*, 1988) and removed further to get the residual mantle bouguer anomaly (*Lianjun Li, personal communication*). The resulting variation of the RMBA in mgal along the profile is shown in figure 4.20 in

solid blue. A continuous decrease in the RMBA is observed from 50-75 Ma. This decrease may correspond to crustal thinning or to a hotter mantle. However, detailed analysis of crustal thickness (*Lianjun Li, personal communication*), indicate that the crustal thickness shows a slight increase towards 75 Myr and its values are within those observed for normal oceanic crust (dashed red in figure 4.20). This rules out crustal thinning as a reason for decreasing RMBA along the profile and instead suggests a hotter mantle.

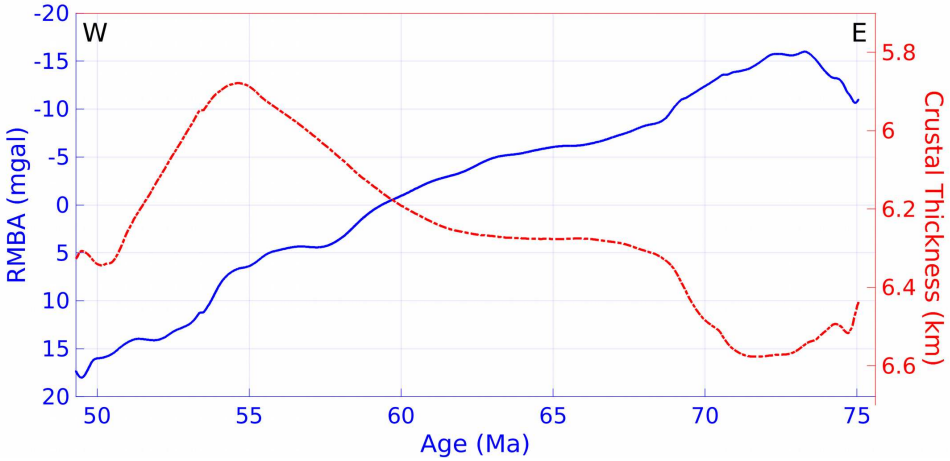

Figure 4.20: The variation along the profile of the residual mantle bouguer anomaly or RMBA (solid blue) compared with the crustal thicknes (dashed red). Though RMBA keeps decreasing, the crustal thickness does not, implying for a hotter mantle. Credit: *Lianjun Li.*

This analysis indicates a hotter mantle in this study region and support the idea of a large-scale thermal anomaly in this region. In the next section, I discuss the possible sources of these anomalies.

4.8 Plume-LAB interaction

The basic introduction to hotspots and mantle plumes has been described in chapter 1. Here I attempt to examine in particular, the interaction of a mantle plume with the LAB and subsequent formation of hotspots. The MCS profile is at an angle of ∼45°C to the axis of Cameroon line. Previous studies have imaged a low velocity anomaly anomaly at 50-300 km depths beneath the CVL and proposed an edge-flow model in which the plume head is spreading towards the oceanic lithosphere (*Reusch et al.*, 2010). The African lithospheric plate is moving at slow rate of 20 mm/yr towards the direction of the spreading plume. This provides motivation to study the interaction of the mantle plumes with the lithosphere and the LAB, which I elaborate in this section. There have been three mechanisms proposed to explain the geophysical observations of hotspot swells:

1. The dynamic pressure (buoyancy flux) created by the plume material causes upwelling in the asthenosphere and supports the uplift of the lithospheric plate. The lithospheric thickness would remains unchanged in this case and heat flow measurements would not be affected. This model is known as the dynamic support model and has been proposed by *Morgan* (1971); *McKenzie et al.* (1980); *Parsons and Daly* (1983); *Watts et al.* (1985).

2. Another popular model (*Detrick and Crough*, 1978; *Menard and McNutt*, 1982) is the thermal rejuvenation of the lithospheric plate due to heating from the impingment of the plume head. The thermal rejuvenation would cause thinning and weakening of the lithospheric plate and high surface heatflow values would be expected.

3. Another possibility is the underplating of lithospheric plate by extracted basaltic melt from the plume head. This would result in a thicker than normal lithosphere with possibility of higher mantle velocities in the underplating which is comprised of the residue of the plume material (*Boyd and Meyer*, 1979; *Robinson*, 1988; *Phipps Morgan et al.*, 1995). This mechanism is likely to be an after effect of the passage of a plume rather during the passage of a plume beneath the lithosphere.

4.8.1 Numerical models

Laboratory experiments and numerical solutions offer a good estimate of the processes happening in the subsurface. There have been several studies that attempt to explain midplate hotspot swells by means of numerical solutions. The parameters corresponding to best fit results to the observed geoid topography, heatflow and occasionaly gravity anomalies are then presented. In most of these models, a plume initiates as a Rayleigh-Taylor instability in a thermal boundary layer and rises through the mantle, forming a spherical head with a thinner tail connecting it to the source (conduit). On approaching the LAB, it starts flattening depending on decrease in buoyancy force near the surface, the vicinity of the surface, rheological contrast and reaction of the resistant LAB (*dAcremont et al.*, 2003). The main parameters considered in the modeling are the diameter of the plume tail, asthenospheric viscosity, Rayleigh number, lithospheric velocity, temperature and density contrast of upwelling plume relative to surrounding asthenosphere. *Thoraval et al.* (2006) performed numerical modelling for a fast moving plate such as the Pacific plate and found the 1200°C isotherm to be uplifted by 10-40 km while the 800°C isotherm was completely unperturbed.

Figure 4.21 shows the effect of a mantle plume on the LAB as compiled by *Renkin and Sclater* (1988). The interaction depends on whether the LAB is considered a cooling half-space isotherm or a plate-cooling model isotherm with a viscous thermal boundary layer beneath. In the case of a cooling half-space isotherm (left in figure 4.21), it is re-heated and is resest to a younger age. The subsidence then continues beyond the influence of hotspot and re-aging occurs. In the case of a plate-cooling model (right in figure 4.21), the plume spreads in the shape of a mushroom head at the LAB causing uplifting and thinning.

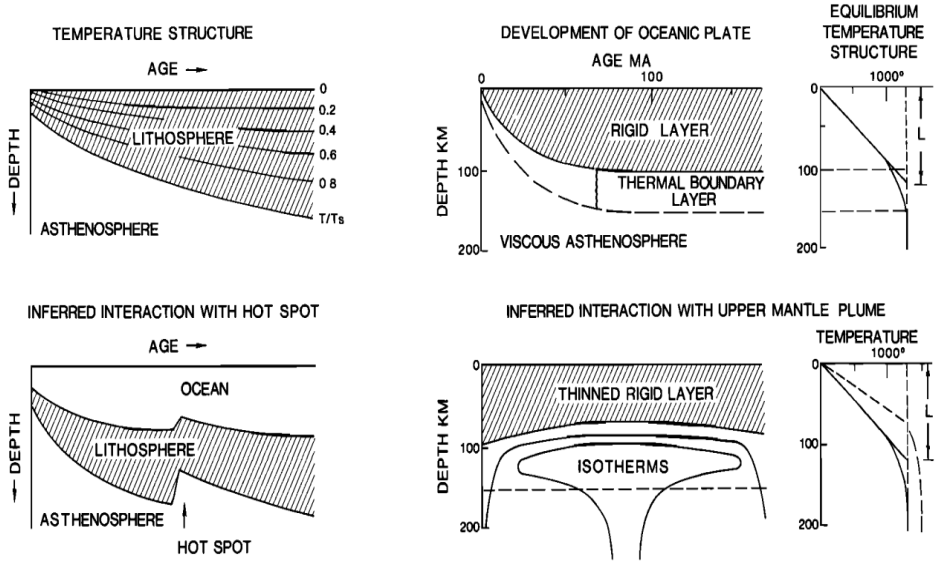

Figure 4.21: Possible interactions of the upwelling plume with the LAB depending on whether the LAB is a half-space (left) or a plate cooling isotherm (right) (*Renkin and Sclater*, 1988).

To further examine the interaction of mantle plume with the old lithosphere, I compare with other hotspot tracks namely the Cape Verde rise (130 Ma), Reunion hotspot track in the Indian ocean between the Mascarene basin (66 Ma-45 Ma) and Madagascar basin (83 Ma-60 Ma) and the Hawaiian island chain in the Pacific (90-100 Ma). I do not consider the Iceland hotspot track or the young Juan de Fuca ridge, as they are an example of a ridge-hotspot interaction whereas I am interested in old lithosphere-hotspot interaction.

4.8.2 Cape Verde rise

The Cape Verde rise exhibits one of the extreme cases of oceanic midplate volcanism with the regional depth and geoid anomaly being 2.4 km and 12 m respectively (*McNutt*, 1988). A 35% increase in thermal gradient is observed on-swell relative to expected heatflow from heat-flow meausurements (*Courtney and White*, 1986). *McNutt* (1988) deduced that in order to achieve the geoid and heatflow anomalies, temperatures in excess of 1500°C must have been maintained in the lithosphere at least for 20 Myr. As such temperatures are unreasonable within the lithosphere, they deduce that at least some part of the Cape Verde rise is due to the bouyancy flux due to upwelling plume. They also acknowledge a simple conduction model cannot account for the reheating of the lithosphere and somehow the fast spreading Pacific plate is thinned more easily as compared to the slow spreading of the African plate. By means of numerical modeling, *Courtney and White* (1986) also rule out a purely lithospheric reheating model for the Cape Verde rise and consider a mushroom-shaped convective plume emanating from the 670 km discontinuity with 1500 km wide upwelling and downwelling zones. From wide-angle tomography results, *Pim et al.* (2008) do not observe high velocities in lower crust nor low velocities in upper mantle and rule out crustal underplating and a depleted swell root, concuring with the aforementioned dynamic support and lithospheric reheating model.

4.8.3 Hawaiian plume

The Hawaiian island chain is a well documented example of the result of the passage of the oceanic lithosphere over a mantle hotspot. The presence of a mantle thermal plume beneath Hawaii has been demonstrated by geochemical (*Hofmann*, 1997; *WATSON and McKenzie*, 1991), gravity (*Ribe and Christensen*, 1994) and seismic studies (*Li et al.*, 2000). It has been suggested that the root of the Hawaiian hotspot is the core-mantle boundary from variations in the mantle transition zone thickness (*Li et al.*, 2000) and shear-wave velocity and anisotropy in the lowermost mantle (*Russell et al.*, 1998). *Li et al.*

(2000) find the thickness of the mantle transition zone bounded by 410 km and 660 km discontinuities to thin by 30-50 km beneath the Hawaiian island and attribute it to a thermal anomaly of 200-350°C inside the plume (*Bina and Helffrich*, 1994).

From S-wave receiver function technique, *Li et al.* (2004) found a 100-110 km thick lithosphere under the Hawaiian island which thins to 50-60 km thick at the end of the island chain. It is proposed that the plume head got impinged at the base of lithosphere beneath the present day Hawaiian island with the lithosphere moving at a speed of 70-80 mm/yr. Normal lithospheric thickness corresponding to 90-100 Ma old lithosphere is observed beneath the Hawaiian island where the impingement begins. As the plate moves away, gradual reheating of the lithosphere due to the impinged lab material thins it and during the next 3-4 Myr, the lithosphere becomes half of its thickness as observed at the end of the Hawaiian seamount chain which is 400 km away from the active Hawaiian island. Figure 4.23 illustrates the thinning as described here. From S-to-P receiver functions, *Rychert et al.* (2013) found the plume upwelling beneath Hawaiian island offset 100 km towards the west and challenge the vertical upwelling model beneath the Hawaiian island.

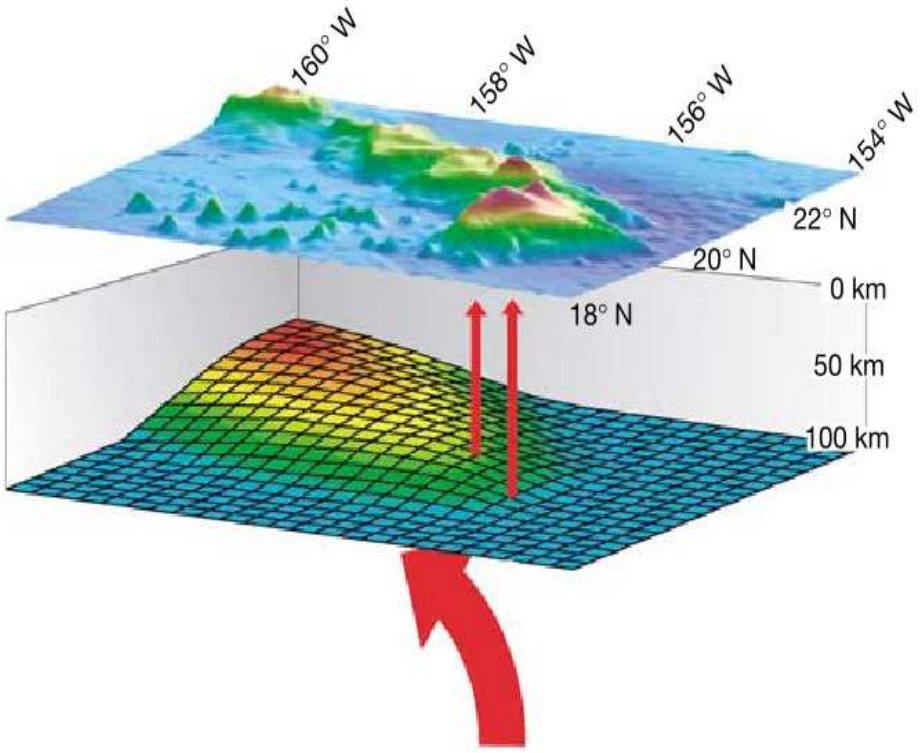

Figure 4.22: Thinning and de-ageing of the lithosphere and shallowing of the seismic LAB as described from S-RF by *Li et al.* (2004). The plume head impinges beneath the present day Hawaiian island and is dragged off in the direction of plate motion as described by red arrow. At 400 km away towards the end of the Hawaiian chain, the plume material thins the lithosphere to half of its original thickness.

4.8.4 Reunion hotspot track

Another well studies example is the Reunion hotspot swell in the Indian ocean extending from the Reunion island to the Mascarene plateau. *Bonneville et al.* (1997) acquired heatflow data and observed a 6-8 mW/m^2 increase in the regional heat flow. It is proposed that the mantle plume lies beneath the present day Reunion island where the lithosphere is thermally unaffected as indicated by flexural rigidity whereas the lithosphere beneath the Mascarene plateau has been thinned and weakened (1-2 orders of magnitude lower than normal lithosphere) by means of reheating by plume impingement. The higher heat flow values support the reheating of the lithosphere and its thinning and thermal rejuvenation. This model proposed is strikingly similar to the model for Hawaiian hotspot track.

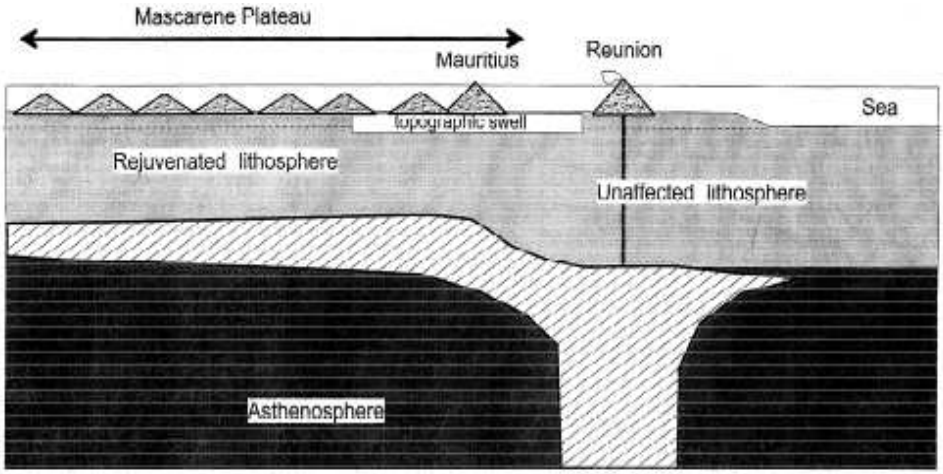

Figure 4.23: Thinning and de-ageing of the lithosphere and shallowing of the seismic LAB as described from seafloor gravity and surface heatflow measurements by *Bonneville et al.* (1997). The plume head impinges beneath the present day Reunion island and thins, weakens and re-heats the lithosphere observed beneath the Mascarene plateau.

The above two hotspot tracks fall under the category of primary plumes or superplumes which have an origin at the core-mantle boundary. They propose a similar model of the plume head impinging at the LAB and being dragged of in the plate spreading direction. Over a period of time, the impinged melt thins and thermally rejuvenates the lithosphere resulting in higher heat flow at the surface. In another example of the Canary islands, *Canales and Dañobeitia* (1998) attribute the swell to a thermal anomaly resulting from a low-viscosity convective layer in the lowermost part of oceanic lithosphere and shallowest asthenosphere. With the possible mechanisms of the plume-lithosphere interaction discussed, I now try to fit the observations in this chapter with the existing models of Cameroon volcanic line.

4.9 Thermal anomaly due to Cameroon Volcanic Line

The observations in this chapter can be summarized as follows: A shallower LAB associated with a lower solidus of 1130°C compared to solidus of 1260°C observed at St. Paul fracture zone, uplift of the basement with a mean of ∼400 m, excess temperature in the asthenosphere corresponding to a mean of 125°C, hotter mantle from RMBA measurements. The effect of the thermal anomaly is seen increasing towards 75 Myr near the volcanic chains. From the discussion on Cameroon volcanic line in section 4.2, it is likely that the thermal anomaly from Cameroon line has influenced the LAB along the MCS profile, increasing the mantle temperature and thinning the lithosphere by 5-7 km. Figure 4.24 summarizes this chapter.

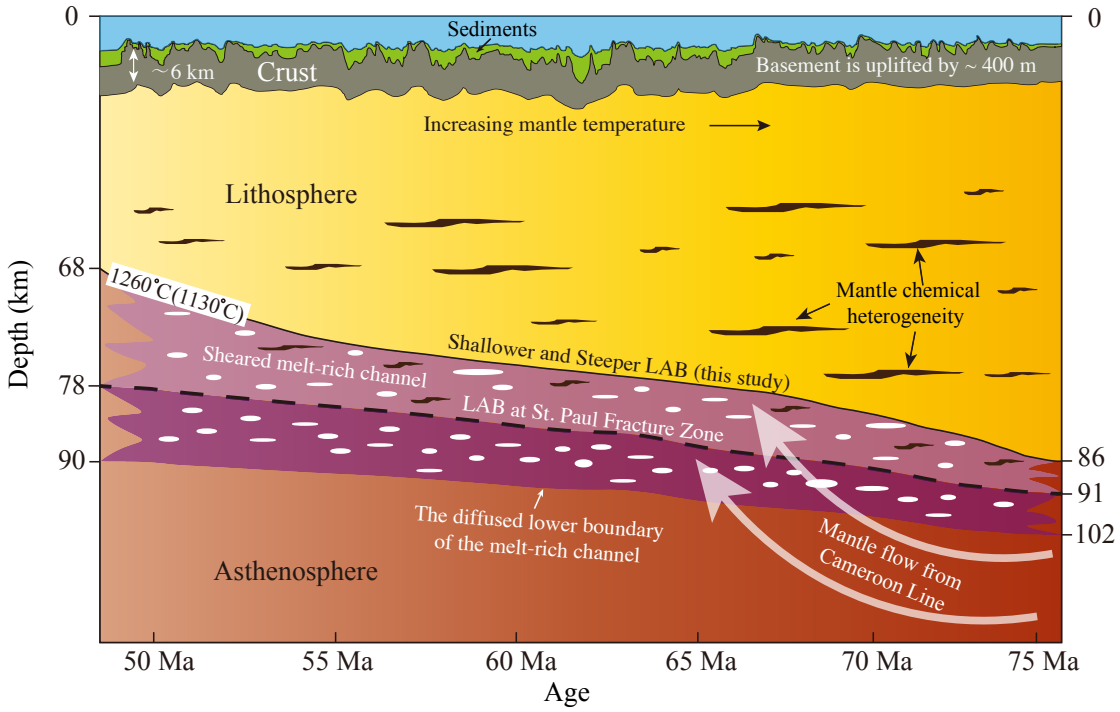

Figure 4.24: Schematic diagram depicting potential effects of a mantle thermal anomaly. The lithosphere-asthenosphere boundary (LAB) imaged in this study is shallower and steeper compared with the LAB imaged at St. Paul fracture zone at same oceanic lithosphere age (*Mehouachi and Singh*, 2018). The mantle thermal anomaly from the Cameroon line results in lowering of the solidus corresponding to the LAB from 1260°C at St Paul fracture zone (*Mehouachi and Singh*, 2018) to 1130°C isotherm in this study. The horizontal ellipsoids represent sheared melt bands in the melt-rich channel (*Mehouachi and Singh*, 2018). Re-heating and re-melting of the pre-existing chemical heterogeneities (dark shaded lenses) introduced by the passage of St. Helena Hotspot is likely due to recent thermal anomaly from the Cameroon line.

Unaffected mantle transition zone thickness (*Reusch et al.*, 2011) and limited depth extent of the plume tail (*Reusch et al.*, 2010) of the Cameroon line rule out the possibility of the plume material originating from the core-mantle boundary or the 670 km discontinuity. However, *Meyers et al.* (1998); *Anderson* (2000); *Courtillot et al.* (2003) proposed that plumes arising without thermal instabilities due to asthenospheric convection are linked to tensile stresses in the lithosphere and decompression melting. Moreover, there is a evidence of low shear velocities extending to depths The excess temperature of the plume tail estimated by *Reusch et al.* (2010) is 280°C beneath the Mt. Cameroon whereas a mean excess temperature of 125°C at ∼1000 km away from the plume tail has been estimated here. It is likely that this excess temperature is due to flow either in the melt-rich channel (*Mehouachi and Singh*, 2018) or in the asthenosphere below or in both. The presence of long distance asthenospheric flow has been proposed between the La Reunion Island and the Central Indian ridge (*Barruol et al.*, 2019). Moreover, anisotropic

tomography studies have shown the presence of 1% anisotropy at depths of 110 km radiating from Mt Cameroon (*Silveira and Stutzmann*, 2002), indicating mantle flow.

It is also likely that this thermal anomaly is reminiscent of the rejuvenated oceanic lithosphere already influenced by the St Helena plume, which passed the area 50-80 Myr ago. However, the seamounts associated with the St Helena plume spread over ∼500 km wide zone covering 30 Myr of oceanic lithosphere, and our eastern end of the profile lies close to the western limit of these seamounts. It is possible that the passage of the St Helena plume has introduced chemical heterogeneity in the lithospheric mantle, which is being re-melted due to a small thermal anomaly originating from the Cameroon plume (Figure 4.24). A chemically heterogeneous mantle would melt more easily due to the presence of a mantle thermal anomaly (*Anderson*, 2006; *Hirschmann et al.*, 2009). The re-melted heterogeneities would have a tendency to migrate towards a younger and shallower lithosphere north of the Ascension fracture zone and accumulate at the imaged LAB reflection. If there exists a LAB channel as pointed out by some recent studies (*Naif et al.*, 2013; *Stern et al.*, 2015; *Mehouachi and Singh*, 2018), it is likely that the base of the channel got diffused due to the incoming anomaly (figure 4.24). The absence of earthquakes deeper than 10 km in the study region (chapter 1) also support the large-scale thermal anomaly proposed in this study as a colder lithosphere would likely have much deeper earthquakes.

Chapter 5

LAB image on 2-47 Ma old lithosphere

Le chapitre précédent illustre l'effet d'une anomalie thermique du manteau sur la lithosphère et la limite lithosphère-asthénosphère (LAB). Les observations de 50 à 75 Ma correspondent à une région anormale qui est influencée par la ligne volcanique du Cameroun et la chaîne de Sainte-Hélène. Pour présenter une image complète de la LAB, une analyse du profil 2-47 Ma à l'écart des chaînes volcaniques est présentée dans ce chapitre. Un certain nombre de zones de fracture et de discontinuités non transformées/failles pseudo-transformées se trouvent dans cette région d'étude. Ce profil est divisé en deux sections, 2-27 Ma et 27-47 Ma, avec un changement de durée d'enregistrement à 27 Ma. De 2 à 27 Ma, l'image sismique P obtenue à partir du traitement mentionné dans le chapitre 2 montre plusieurs événements localement discontinus qui pourraient potentiellement être des seuils de fusion gelés/partiellement fondus. Un candidat très probable pour la LAB est identifié et correspond à une lithosphère de ∼25 km d'épaisseur à 2 Ma et ∼50 km de lithosphère d'épaisseur à 16 Ma. Ces résultats indiquent une lithosphère plus épaisse dans la région d'étude par rapport à celle de la plaque sud-américaine (*Mehouachi*, 2019) et de la ride Juan de Fuca (*Qin et al.*, 2020) au même âge.

On observe que l'événement LAB interprété de 2 à 27 Ma continue avec même pendage quobservé de 27 à 47 Ma. Cependant, les variations d'amplitude de l'événement LAB de 27 à 47 Ma sont beaucoup plus élevées, ce qui pourrait indiquer que des lentilles de magma s'accumulent à ces profondeurs. L'événement LAB correspond à des profondeurs de 58 km sous le plancher océanique à 27 Ma et de 74 km à 47 Ma. Il est associé à une baisse de vitesse des ondes P et correspond probablement à l'isotherme 1300°C. Fait intéressant, une réflexion apparemment indépendante de l'âge avec un contraste de vitesse des ondes P positif se trouve à des profondeurs constantes de ∼80 km au-dessous du fond marin. Il est probable que la réflexion supérieure interprétée comme la LAB représente le haut d'un canal et la réflexion inférieure indépendante de l'âge correspond à la base de ce même canal. Des evidences d'un canal sous-lithosphérique ont été trouvées dans les zones de fracture (*Mehouachi and Singh*, 2018) et les zones de subduction (*Naif et al.*, 2013; *Stern et al.*, 2015). Ce canal dissocie le manteau lithosphérique sus-jacent du manteau asthénosphérique sous-jacent et est riche en volatils et en matériel partiellement fondu (*Hirschmann*, 2010; *Mehouachi and Singh*, 2018). Certaines différences sont constatées lors de la comparaison de la profondeur et de l'épaisseur du canal imagée avec les autres études (*Naif et al.*, 2013; *Stern et al.*, 2015; *Mehouachi and Singh*, 2018) mais une tendance commune de l'amincissement du canal avec l'âge est observée. Je présente enfin une méthode pour améliorer le rapport signal/bruit lors de l'imagerie d'événements terrestres plus profonds.

The preceding chapter illustrates the effect of a mantle thermal anomaly on the lithosphere and the Lithosphere-Asthenosphere Boundary (LAB). The observations from 50-75 Ma correspond to an anomalous region, which is influenced by Cameroon volcanic line and St Helena chain. To present a comprehensive picture of the LAB, an analysis of the profile 2-47 Ma away from the volcanic chains is presented in this chapter. A number of fracture zones and non-transform discontinuities/pseudo-transform faults are found in this study region from 2-47 Ma. The profile from 2-47 Ma is divided into 2-27 Ma and 27-47 Ma with a change in recording length at 27 Ma. From 2-27 Ma, the obtained seismic P-image from the processing mentioned in chapter 2 shows several locally discontinuous events which could potentially be frozen-in/partially molten melt sills. A very likely candidate of the LAB is identified and is found to correspond to ∼25 km thick lithosphere at 2 Myr and ∼50 km thick lithosphere at 16 Myr. These results are indicative of a thicker lithosphere in the study region compared to that at South American plate (*Mehouachi*, 2019) and Juan de Fuca ridge (*Qin et al.*, 2020) at the same age.

The interpreted LAB event from 2-27 Ma is observed to continue with the same dip from 27-47 Ma. However, the amplitude variations in the LAB event from 27-47 Ma are much higher indicating it could possibly be melt lenses accumulating at those depths. The LAB event corresponds to depths of 58 km depth below seafloor at 27 Myr and 74 km below seafloor at 47 Myr. It is associated with a P-velocity drop and likely corresponds to the 1300°C isotherm. Interestingly, an apparently age-independent reflection with a positive P-velocity contrast is found at constant depths of ∼80 km below the seafloor. It is likely that the upper reflection interpreted as LAB represents the top of a channel and the age-independent lower reflection corresponds to the base of the channel. Evidence of a sub-lithospheric channel has been found at fracture zones (*Mehouachi and Singh*, 2018) and subduction zones (*Naif et al.*, 2013; *Stern et al.*, 2015). This channel decouples the overlying lithospheric mantle from the underlying asthenospheric mantle and is rich in volatiles and partially molten melts (*Hirschmann*, 2010; *Mehouachi and Singh*, 2018). Some discrepancies are found when comparing the depth and the thickness of the imaged channel with the other studies (*Naif et al.*, 2013; *Stern et al.*, 2015; *Mehouachi and Singh*, 2018) but a common trend of channel thinning with age is observed. I lastly present a potential notion for improving the signal to noise ratio in imaging deeper Earth events.

5.1 Profile from 2-47 Ma

The MCS profile from 1.8-46.7 Myr (denoted by rounded values of 2-47 Myr in this chapter for simplicity) is re-introduced by the red line in figure 5.1a. Halfway along the profile, at ∼27 Myr, a change of recording parameters takes place as desribed in chapter 1. The record length changes from 20 s two-way time (TWT) from 2-27 Myr to 30 s TWT from 27-47 Myr and the shot spacing changes from 50 m from 2-27 Myr to 75 m from 27-47 Myr. The decision to reduce the record length for younger lithosphere was made as a thinner lithosphere would be expected for younger lithosphere. The effect of reducing the shot spacing for younger lithosphere should result in having a relatively higher signal-to-noise ratio as the fold (number of traces) in the common-midpoint (CMP) domain will increase.

The region around the MCS profile from 2-47 Myr consists of several fracture zones (first order discontinuity) and non-transform discontinuities/pseudo-transform faults (second order discontinuity) which become more apparent from the vertical gravity gradient map in figure 5.1b. Almost parallel to the MCS profile from ∼15-47 Myr and ∼50 km north to the profile is the Charcot fracture zone. The Charcot fracture zone does not appear to be present for lithosphere younger than ∼15 Myr and from ∼2-8 Myr, there appears to be a non-transform discontinuity co-inciding with the MCS profile. At ∼15 Myr, the MCS profile is intersected by what appears to be another second order discontinuity in the direction orthogonal to plate spreading. From ∼25-35 Myr, another second-order discontinuity runs parallel and close to the profile. The origin of these first-order and second-order discontinuities is likely to be due to the slower rifting between equatorial Africa and South American plates at ∼110 Ma as discussed in chapter 1. The purpose of describing the first-order and second-order discontinuities close to the profile has been to show the region is highly heterogenous and imaging deeper Earth structures would be challenging as well as to examine any possible correlations of these discontinuities with the deeper Earth structures.

(a)

(b)

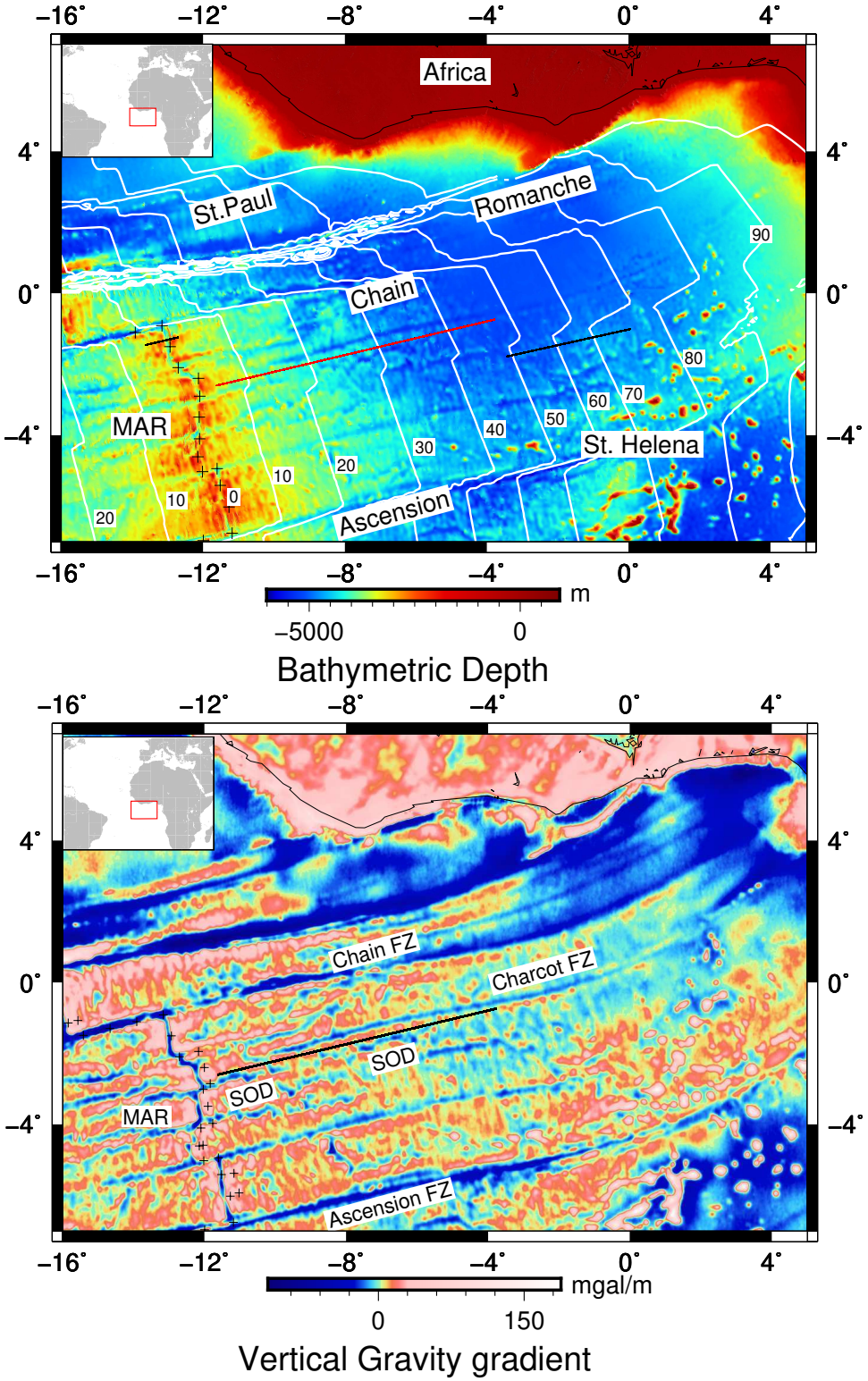

Figure 5.1: (a) Bathymetric depth of the study region and the MCS profile from 1.8-46.7 Ma as a red line. (b) Vertical gravity gradient of the study region (*Credit: Venkata Vaddineni*) and the same MCS profile from 1.8-46.7 Ma as a black line. The MCS profile from 1.8-46.7 Ma is very close to the Charcot fracture zone in the North and has several second order discontinuities (pseudo-transform faults/non transform discontinuities) in the South. *SOD: second-order discontinuity.*

Seismic reflection experiments such as this one will often yield a high resolution image of the subsurface and subsequently, several events will be imaged. However, rather than interpreting all these various events, only those selected events which could be potentially the Moho/LAB (based on polarity, continuity and dip of the event) have been focused on.

5.2 Seismic image from 27-47 Ma

Following the processing described in chapter 2 which is based primarily on enhancing flat events, the subsurface image of the profile from 27-47 Myr was obtained as shown in figure 5.2a. As compared to the seismic image from 49.3-75.6 Myr in the previous chapter, which had a frequency content of 1.5-6 Hz, the frequency content for this part of the profile had to be reduced to 1.5-4 Hz to get the best image. The record length is 30 s TWT and a thick sediment cover can be seen starting from 670 km distance, which corresponds to ∼36 Myr. Several deeper events can be observed and only those which can be observed over considerable distances are interpreted.

(a)

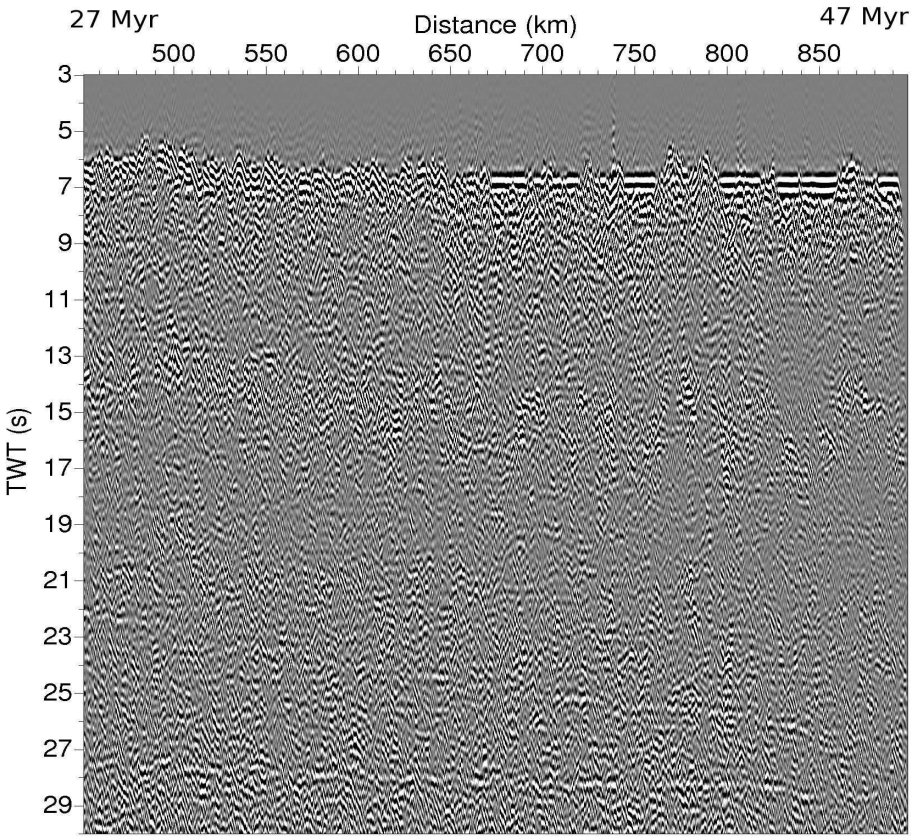

(b)

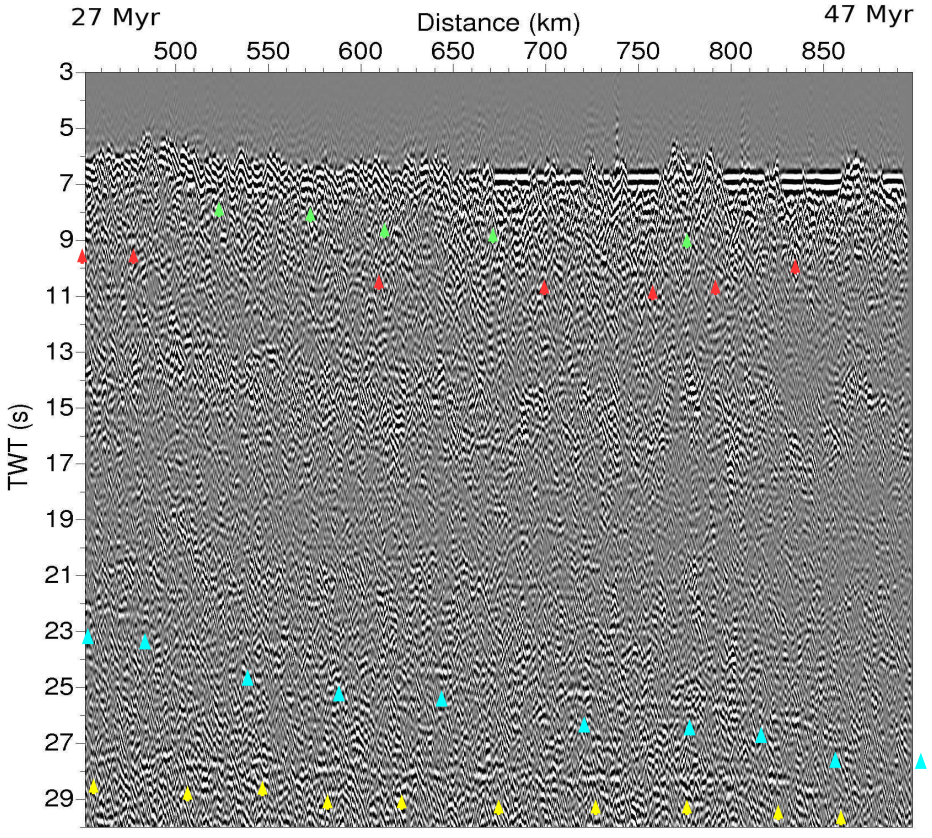

Figure 5.2: (a) Final processed uninterpreted seismic image from 27-47 Myr. Note the frequency content is 1.5-4 Hz. (b) Interpreted seismic image from 27-47 Myr. Cyan arrows denote the potential base of lithosphere (LAB) and yellow arrows denote the base of the channel. See text for full interpretation.

Figure 5.2b shows the various events identified. A shallow event ∼1-1.5 s TWT below the seafloor (green arrows) can be observed from ∼500 km distance range to ∼800 km distance range. A deepening of this event corresponing to the onset of sediment cover at 670 km distance is also observed. This event is too deep to be the layer 2A and could be potentially the Moho or the crust-mantle boundary. Another event (red arrows) can be observed starting at 9 s TWT at 0 km distance range and almost 2 s below the seafloor. This event is poorly imaged between 500-600 km distance range and can be imaged intermittently 600 km distance onwards. It appears to be 4 s TWT below the seafloor at 600 km distance and 3 s TWT below the seafloor from 700-800 km distance range. Between 800-850 km, shallowing of the event by ∼1 s TWT is observed. Polarity analysis of this event indicates it represents a positive P-velocity contrast, making it another likely candidate of the Moho.

Deeper in the seismic image, an event dipping towards the older age can be observed. This event (marked by cyan arrows) appears to start at 22 s TWT at 450 km distance corresponding to 27 Myr and is observed to be dipping to almost 24 s TWT at 550 km. The image of the event between 550-650 km is poor and intermittently imaged bright reflection spots beyond 650 km become visible. The event dips towards older ages and is at ∼26 s TWT at 800 km distance. Between 800-850 km distance, the event is observed to locally dip sharply to ∼27 s TWT but it again observed at 26 s TWT at 900 km distance. Polarity analysis of this event at selected locations indicate that it represents a negative P-velocity contrast. This observation, combined with age-dependency of this reflection makes it a very likely candidate to be the base of the lithosphere (LAB). Owing to its continually dipping nature, it is unlikely to correspond to a water-bottom multiple of the seafloor/basement. Depth conversion using the same velocities as in chapter 4 indicate that this reflection dips from ∼58 km at 27 Myr to ∼72 km (±2-3 km uncertainty) at 47 Myr below the seafloor. From the sea-surface, the depths of the reflection correspond to ∼64 km at 27 Myr to ∼80 km at 47 Myr. This reflection corresponds to ∼1300°C according to plate cooling models (chapter 1).

5.2.1 Comparison with LAB at 50-75 Myr

It is also interesting to compare the LAB reflection observed in figure 5.2 with that in the leg 3 of the profile from 49.3-75.6 Ma in the previous chapter. In the preceding chapter, the interpreted LAB reflection corresponded to ∼1130°C isotherm. Overall the LAB is observed to be dipping from ∼22 s TWT at 27 Myr to ∼26 s TWT at 47 Myr in figure 5.2b as compared to ∼22.5 s TWT at 49 Myr to ∼27 s TWT at 75 Myr in the previous chapter. This indicates a deeper LAB and hence a higher temperature of the LAB along the profile from 27-47 Myr. A deeper LAB could be due to a colder lithosphere in the vicinity of the fracture zones and second order discontinuities as seen in figure 5.1b. However, no correlation between some of the second-order discontinuities in older part of the profile such as the one between 25-35 Myr (figure 5.1)b and the LAB reflection (figure 5.2) can be observed. The thermal anomaly from the volcanic chain of Cameroon and the subsequently re-melted heterogeneities of St Helena plume (chapter 4) do not seem to cause the same shallowing effect on the LAB from 27-47 Myr. This again could be attributed to the first- and second-order discontinuities potentially blocking the thermal anomalies. The higher heatflow observed in chapter 3 beyond 36 Myr and co-located with the profile in figure 5.1 is most probably unrelated to the thermal anomalies from the volcanic chains.

5.2.2 Evidence for LAB channel

Interestingly, another event at almost 28 s TWT (yellow arrows) can be observed throughout 27-47 Myr in figure 5.1b. It is unlikely that this event corresponds to a water-bottom multiple as it is almost flat in contrast to the rugged nature of the basement topography, which would be further exaggerated in the higher order multiples. Depth conversion using same velocities as in chapter 4 indicate that this reflection corresponds to a depth of ∼80 km below the seafloor and ∼86 km below the sea-surface. This apparently age-independent discontinuity has a positive polarity contrast indicating an increase in P-velocities across the reflection. It is likely that this event is the base of the LAB channel whereas the upper dipping reflection coresponds to the top of the LAB channel (*Mehouachi and Singh*, 2018).

The channel is supposedly rich in volatiles such as water, carbon dioxide (*Mehouachi and Singh*, 2018) that helps to stabilize carbonatite/silicate melts (*Hirschmann et al.*, 2009; *Hirschmann*, 2010) in this channel. The upper bounding reflection could be considered as the freezing front (solidus) between the lithosphere and the channel and the lower bounding reflection as the shearing front (*Mehouachi and Singh*, 2018)between the channel and the asthenosphere. The thickness of the channel in two-way time (TWT) is ∼6 s at 27 Myr and close to 2 s at 47 Myr. Taking into account the depth estimates of the upper reflection as ∼58 km at 27 Myr to ∼72 km at 47 Myr and for the lower reflection as ∼80 km (all values below seafloor), the thickness of channel is estimated close to 22 km at 27 Myr and 8 km at 47 Myr.

5.2.3 Comparison with other studies

At St Paul fracture zone which spans an age contrast of 40/70 Myr, *Mehouachi and Singh* (2018) imaged a ∼18 km thick-channel at 40 Myr and a ∼12 km thick-channel at 70 Myr. From figure 5.2, at 750 km distance, which corresponds to ∼40 Myr, and the above calculations of channel thickness, a ∼12 km thick channel is observed at the same age of 40 Myr. This indicates the channel is thinner in this study region as compared to that in the St Paul fracture zone. Upon further comparing the individual depth of the reflections at 40 Myr, the upper reflection is found to be ∼74 km below the sea-surface and the lower reflection is found to be ∼86 km below the sea-surface. The corresponding values observed by *Mehouachi and Singh* (2018) at 40 Myr are ∼72 km for the upper reflection and ∼90 km for the lower reflection below the sea-surface. This indicates that while the upper reflection is imaged at similar depths at St Paul fracture zone and our profile, the lower reflection is imaged slightly shallower along our profile hence thinning the channel by 4-6 km. A thinner channel likely indicates lower content of volatiles and melt in the LAB channel as compared to *Mehouachi and Singh* (2018).

Naif et al. (2013) observed a 25 km thick channel at 23 Myr old subducting lithosphere ranging from 45-70 km below the sea-surface. The 25 km thick channel at 23 Myr old lithosphere is close to the 22 km thick channel at 27 Myr in this study and indicates the thinning of the channel with age as proposed by *Mehouachi and Singh* (2018). However, the depths of the channel found by *Naif et al.* (2013) is 45-70 km from sea-surface at 23 Myr as compared to 64-86 km below the sea-surface at 27 Myr in this study. This discrepancy may be due to several factors. Magnetotelluric studies such as *Naif et al.* (2013) have much lower resolution compared to seismic reflection studies. Furthermore, the lithosphere in *Naif et al.* (2013) was formed in an ultra-fast spreading environment and lies in the vicinity of a subduction zone, which could affect the thermal regime and nature of the LAB. *Stern et al.* (2015) imaged a 10 km thick channel at a 120 Ma old subducting lithosphere ranging from 70-80 km depths below the oceanic basement. The study region in *Stern et al.* (2015) is again a subduction zone and may be affected by subduction zone processes. However, along our profile, the channel is observed to thin rapidly from ∼22 km at 27 Myr to ∼8 km at 47 Myr with the variation being due to the dipping of the top of the channel while the base of the channel remains fixed at ∼86 km below the sea-surface. These comparisons show that there could be significant variations in the nature of the LAB depending on the study region (subduction zone or mid-oceanic ridge) and other factors such as mantle anomaly and spreading rate.

5.3 Seismic image from 2-27 Ma

Imaging the base of the lithosphere at the youngest part of the profile was especially challenging. The limitations of the present processing scheme as described in chapter 2, were requiring a threshold signal-to-noise ratio, especially due to strong seafloor scattering, and inability to account for steeply/abruptly varying dipping reflections. This processing strategy was less likely to produce a good quality image, yet I discuss the obtained image from the same processing and its interpretation in figure 5.3. It is likely that the improved image will have the same events in figure 5.3b but with a better signal-to-noise ratio after overcoming the above limitations. The final processed uninterpreted image is shown in figure 5.3a. Similar to figure 5.2a, the frequency content has been reduced to 1.5-4 Hz to get the best possible results.

(a)

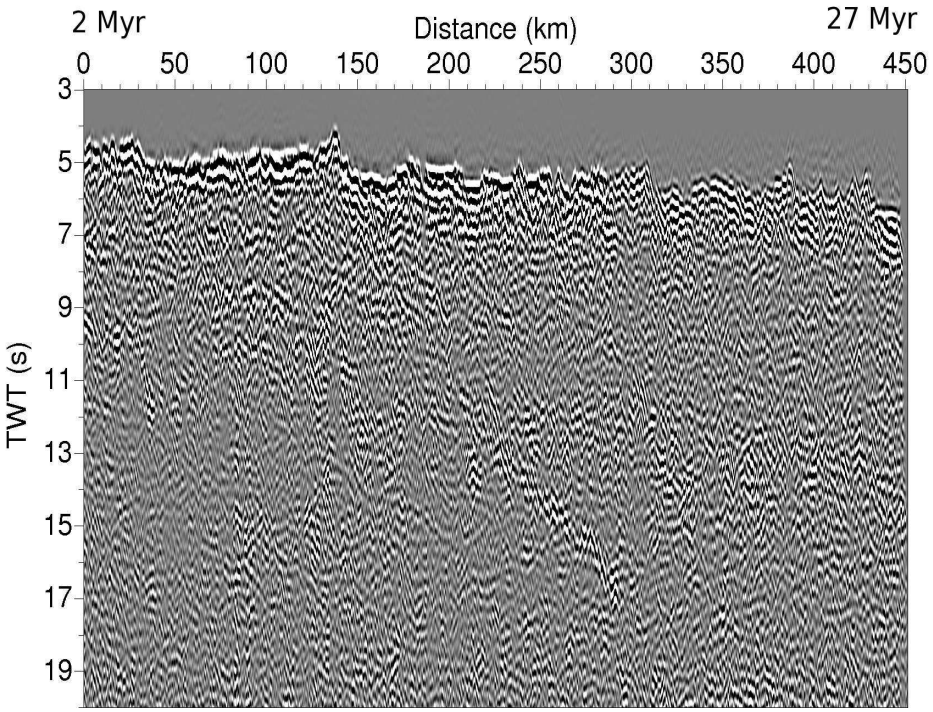

(b)

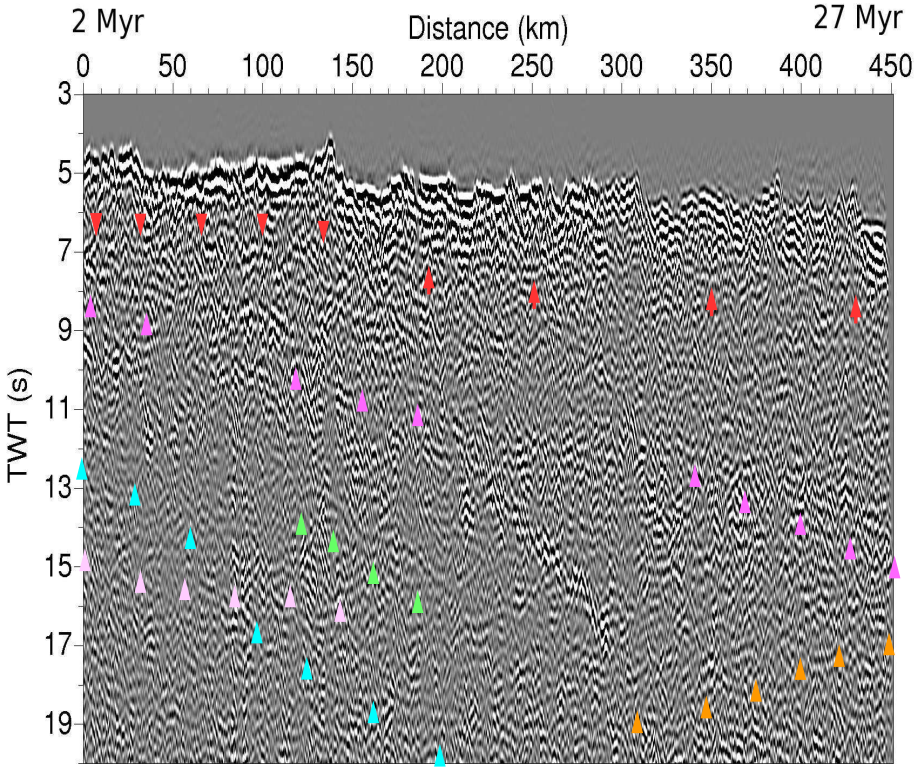

Figure 5.3: (a) Final processed uninterpreted seismic image from 2-27 Myr and (b) Interpreted seismic image from 2-27 Myr. Cyan arrows depict th potential base of lithosphere (LAB). See text for full interpretation.

Figure 5.3b shows the interpreted image with several events marked. A reflection intermittently imaged around 2 s two-way time (TWT) below the seafloor (marked by red arrows) and starting at 7 s TWT at 0 km distance is potentially the crust-mantle boundary or the Moho. Starting just below the potential Moho reflection, at 7 s TWT at 0 km distance is another reflection dipping towards older

ages (magenta arrows). This event is well imaged until 100 km distance where it reaches 9 s TWT, then re-appears at 350 km distance at ∼11 s TWT and continues dipping to ∼14 s TWT at 450 km distance which corresponds to 27 Myr. However, this event is not well imaged in the seismic section 27-47 Myr as seen in figure 5.2. Also, the reflection appears to be to close to the Moho at 2 Myr (0 km distance) and hence is unlikely to represent the LAB.

A bright reflection energy spot is identified at ∼12 s TWT (cyan arrows) and is found dipping towards older ages. The dipping part is not well imaged and can be loosely traced along the cyan arrows. Another very clear event found to be dipping towards older age can be seen from ∼120-200 km distance range (green arrows). Whether it is related to the event at ∼12 s TWT is not well answered due to the poor continuity of the event. It is interesting to note that both these events (cyan and green) have a negative polarity contrast and likely represent the base of the lithosphere. A number of horizontal events can be seen below the proposed LAB reflection at 12 s TWT at 2 Myr. One such event is seen starting at 14 s TWT at 0 km distance (light magenta arrows) and continuing until almost 200 km distance. Another event (not marked) could be seen starting at 15 s TWT but not so consistently imaged. It is likely that these horizontal events correspond to sheared melt lenses originating from a horizontal flux near the ridge-axis (*Keller et al.*, 2017). Some imaged events dipping in opposite direction (orange arrows) and showing no continuity in the older part of the profile from 27-47 Myr are left open for interpretation.

A good candidate for the base of the lithosphere is the event at ∼12 s TWT at 2 Myr (cyan arrows) in figure 5.3. The event, though poorly imaged beyond 70 km (cyan arrows), can be loosely followed to ∼20 s TWT at 250 km distance, which almost corresponds to 16 Myr. This event should be continuous with the one observed in figure 5.2b at ∼22 s TWT at 27 Myr. It is interesting to note that the dip of the LAB reflection spans 4 s TWT in the age span of 20 Myr from 22 s at 27 Myr to 26 s at 47 Myr (figure 5.2b). Assuming the event observed in figure 5.3 at 20 s TWT at 16 Myr (cyan arrows) is the same event as the one at 22 s TWT at 27 Myr in figure 5.2b, it implies the event spans 2 s TWT in the age span of 11 Myr from 16-27 Myr. This assumption is very likely to be valid as the event spans the same TWT in the same age span in both 16-27 Myr (2 s TWT in 11 Myr) and 27-47 Myr (4 s TWT in 20 Myr or equivalently 2 s TWT in ∼11 Myr).

The above interpretation is most likely to represent the cyan arrows in figure 5.3b as the base of the lithosphere or the LAB. This rules out the event marked in green arrows in figure 5.3b as the base of the lithosphere. In that case, the event marked by green arrows represents potential frozen-in melt lenses within the lithosphere. Whereas the dip of the LAB is about ∼2 s TWT every 10 Myr beyond 16 Myr as discussed above, it can be seen that the LAB (cyan arrows) in figure 5.3b dips from ∼12 s TWT at 2 Myr to 20 s TWT at 16 Myr. This means a span of 8 s TWT every 14 Myr or 2 s TWT every 3.5 Myr until 16 Myr as compared to 2 s TWT every 10 Myr beyond 16 Myr. This reduction in the dip of the LAB with age makes it consistent to plate cooling models. The LAB fom 27-47 Myr in figure 5.2b was assigned the 1300°C isotherm and it is likely the event interpreted as LAB in figure 5.3b as cyan arrows also represents the same isotherm.

P-velocities at top of mantle are known from co-located wide angle seismic tomography to be around 7.6 km/s at 2 Myr which increase to 8 km/s at 16 Myr (*Venkata Vaddineni, personal communication*). Assuming the Moho (red arrows) at ∼7 s TWT, a 6 km/s average crustal velocity for a 6 km thick crust and velocities at top of mantle age-dependent from 7.6-8 km/s from co-located wide-angle tomography, the event interpreted as LAB in figure 5.3b and marked as cyan arrows corresponds to a lithosphere almost ∼25 km thick at 2 Myr with the lithospheric mantle being close to 19 km thick. This extends to a ∼50 km thick lithosphere at 16 Myr (250 km distance) with the lithospheric mantle being ∼44 km thick. As discussed above, it is likely that the same event continues to be observed at 58 km thick lithosphere at 27 Myr and 72 km thick lithosphere at 47 Myr (cyan arrows in figure 5.2b).

5.3.1 Comparison with other studies

Mehouachi (2019) attempted to image the LAB from the MCS data set on the South American plate. *Mehouachi* (2019) improved upon a multi-parameter stacking operator termed as offset-continuation

operator (*Coimbra et al.*, 2016) by-passing the requirement of accurate velocity and slope in the time-space (t-x) domain. The operator was subsequently termed as offset-continuation dip-moveout operator (OC-DMO) and was applied to the MCS profile crossing the ridge-axis and into the South American plate as shown in figure 5.4a. This part of the MCS profile spans a range of 0-26 Myr and is close to the Chain transform fault. However as *Mehouachi* (2019) notes the profile is unikely being influenced by its thermal effect based on thermal modeling studies (*Behn et al.*, 2007).

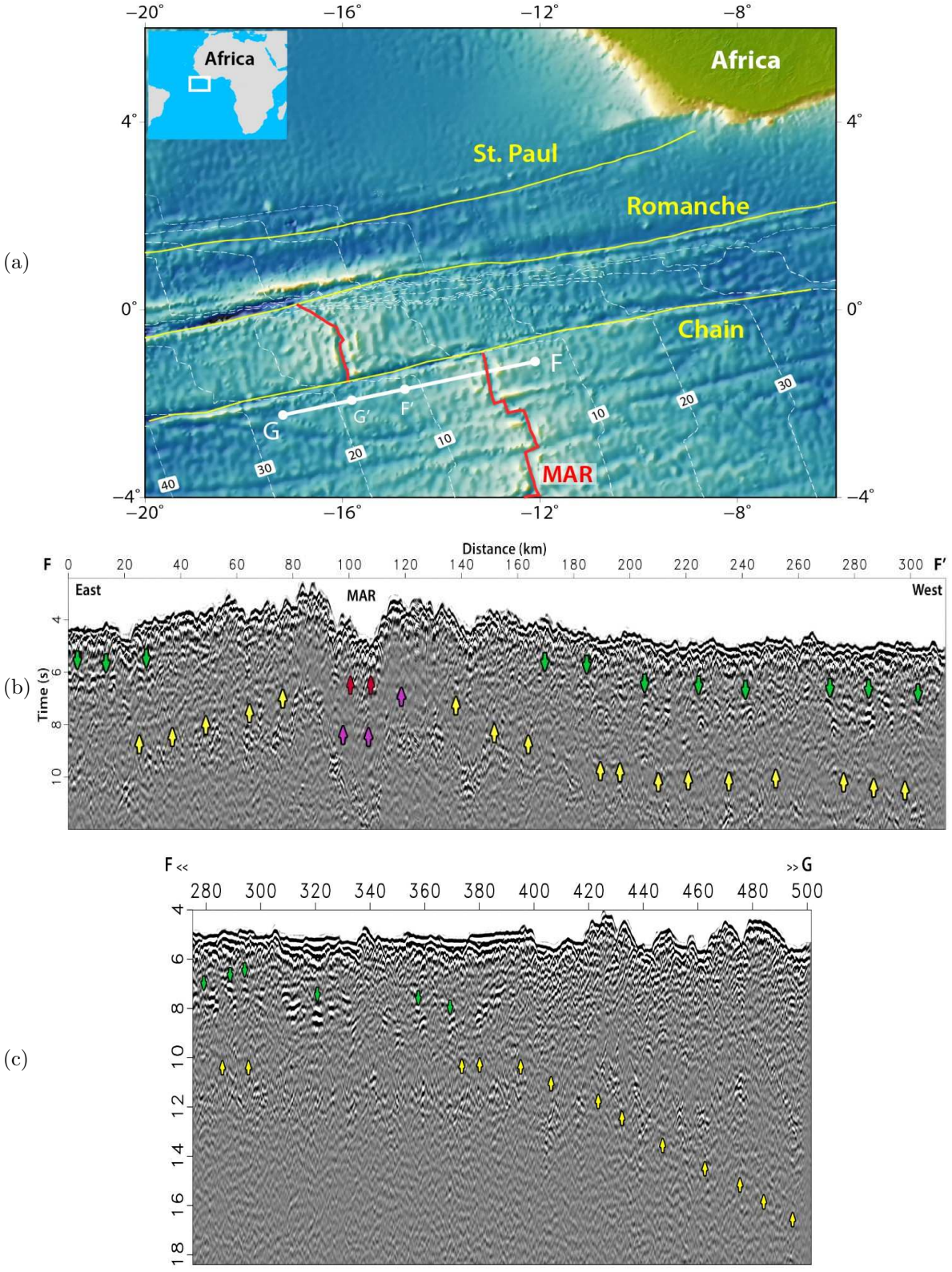

Figure 5.4: (a) Study region on the South American plate with the MCS profile from F-G and reference ages: F (6 Myr, African plate), F′ (12 Myr), G′ (18 Myr), G (26 Myr). (b) Final processed interpreted image from 6 Myr on African plate (F) to 12 Myr on South American plate (F′). The yellow arrows mark the potential LAB reflection, the green arrows mark the potential Moho reflection, the red arrows mark the potential magma chamber and the magenta arrows mark uninterpreted but identified events. (c) Final interpreted image from ∼11 Myr (West) to ∼20 Myr (East). Yellow arrows mark potential LAB reflection and green arrows mark potential Moho reflections. Source: *Mehouachi* (2019).

The MCS profile from 0-12 Myr shown in figure 5.4b shows a reflection ∼3 s two-way time (TWT) below the seafloor at ∼140 km distance which rapidly deepens to ∼6 s TWT below the seafloor at ∼180

km distance (yellow arrows). This approximately translates to 10 km below the seafloor at ∼2 Myr and 22 km below the seafloor beyond ∼5 Myr. Flattening of the reflection is observed until ∼400 km distance in figure 5.4c which corresponds to ∼16 Myr beyond which the reflection is seen to dip towards older age reaching ∼10 s TWT below the seafloor at ∼500 km distance which corresponds to ∼20 Myr. This corresponds to ∼40 km below the seafloor at 20 Myr.

Using an average crustal velocity of 6 km/s for a 6 km thick crust and same range of age-dependent mantle P-velocities from 7.6-8 km/s as above, preliminary lithospheric age-thickness values obtained from the above observations on South American plate are: 10 km at 2 Myr, 22 km between 5-16 Myr and rapid deepening to 40 km at 20 Myr. To explain the flattening of the LAB between 5-16 Myr, thermal effect due to transform faults is ruled out beyond 40 km from the transform fault (*Behn et al.*, 2007). Instead *Mehouachi* (2019) attributes a relatively flatter bathymetry in the same range corresponding to the observed flatter LAB reflection.

In comparison, the results on the African plate from 2-27 Myr in figure 5.3b show a 25 km thick lithosphere at 2 Myr. This is more than the double estimated at the same age on the South American plate. Assuming a 6 km thick crust leaves us with a 19 km thick lithospheric mantle on the African plate versus a 4 km thick lithospheric mantle on the South American plate. Such a high asymmetry is unlikely and the reasons are difficult to speculate. Beyond 2 Myr and until 5 Myr, the reflection observed in figure 5.3b is seen dipping towards older age and corresponds to a lithospheric thickness of ∼30 km at 5 Myr. The lithospheric thickness at 5 Myr on the South American plate is 22 km as described above. Similarly in comparison to lithospheric thickness of 40 km at 20 Myr on the South American plate, a lithospheric thickness of ∼52 km is observed at the same age on the African plate. This indicates the lithospheric mantle on the African plate is overall thicker than that on the South American plate closer to the transform faults.

Qin et al. (2020) used a novel imaging strategy to find the LAB on a 0.51-2.67 Myr old lithospheric plate from wide-angle seismic data on the Endeavor segment of intermediate spreading Juan de Fuca ridge. They found two sub-horizontal reflections at depths of ∼11 and 14.5 km below the seafloor at 0.51-2.67 Myr and proposed either of the two hypothesis: the top reflection is the LAB and the bottom reflection is a partially molten sill or both the top and bottom are frozen-in melt sills and the LAB is deeper following the 1200°C isotherm. In the first case when the reflection at 11 km below the seafloor is considered as the LAB, mechanisms of mantle thermal anomaly, sediment blanketing and rigorous hydrothermal circulation are invoked to explain the flatness of the LAB between 0.5-2.67 Myr lithosphere. The depth of reflection at 11 km is strikingly similar to that observed on the South American plate by *Mehouachi* (2019) at the same age of ∼2 Myr, however in the latter case, the reflection is found to be dipping steeply from 0.5-2.67 Myr. With regard to these studies, a much thicker lithosphere at 2 Myr (∼25 km) is imaged on the African plate in figure 5.3b. In the second possibility, *Qin et al.* (2020) propose a deeper LAB reflection at 2 Myr following the 1200°C isotherm with their two observed reflections corresponding to frozen-in melt sills. This interpretation is more supporting to our results of a thicker lithosphere at 2 Myr. It is likely that the geological setting of the region (bounded by fracture zones, non-transform faults etc) influence the depth of the LAB and the thickness of the lithosphere.

5.4 Need for better processing strategies

The results so far obtained have been based on the application of several amplitude and frequency based filters or target-oriented processing (chapter 2) which aim to superficially enhance a potential reflection. As described in chapter 2, the processing workflow depends a lot on the threshold signal to noise ratio and variation of the dip of the reflection. A lower signal to noise ratio as well as rapidly varying dip of the reflection that could be possible at young lithosphere make it difficult for the existing processing strategies to work. This indicates a two-fold need: to include dip-based processing strategies in pre-stack seismic data and to develop a processing technique that does not depend on the threshold signal to noise ratio. Techniques for incorporating the dip of the reflection can be carried out by OC-DMO (*Mehouachi*, 2019). In the remainder of this chapter, I examine a potential notion to improve the signal to noise ratio.

5.4.1 Using reciprocity to create split-spread gathers

The different geometries in land/marine seismic data acquisitions are illustrated in figure 5.5. In marine sesimic acquisition systems such as the one in this project, an end-on geometry is common (in which receivers are at one end of the source) due to practical difficulties of having a split-spread arrangement. On the other hand, a split-spread geometry involves receivers on both sides of the source and is common in land acquisition systems. In practice, it would be desirable to have a split-spread geometry as the subsurface coverage in a single shot recording is more than an end-on geometry.

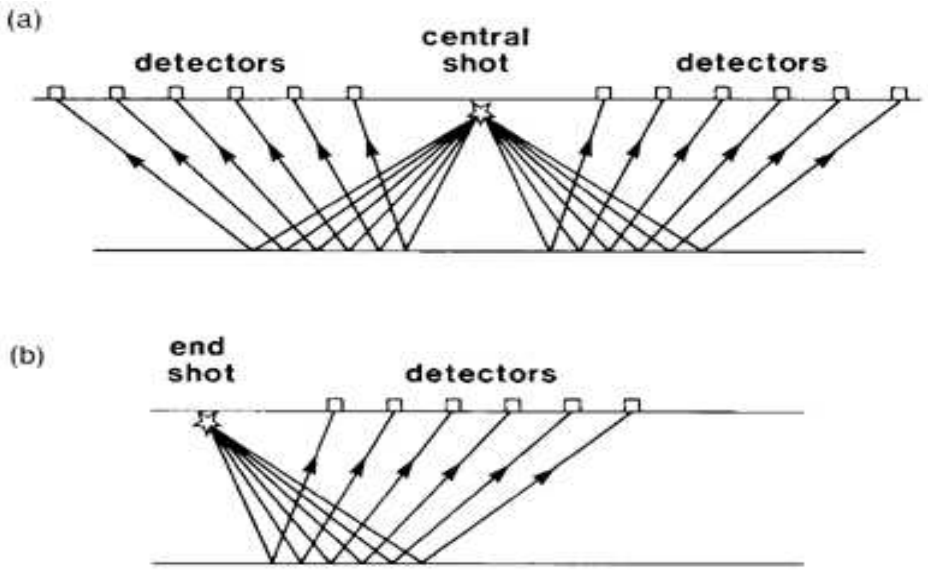

Figure 5.5: (a) A split-spread recording arrangement. The receivers are on both sides of the source. More common in land acquisition systems. (b) An end-on recording arrangement. The receivers are on one side of the source. More common in marine acquisition systems. Source: *Geophysics for Practicing Geoscientists (GitHub)*

The reciprocity theorem states that by interchanging the source and receiver positions, the Green's function or the response of the subsurface does not change (*Aki and Richards*, 2002). This theorem can be used to construct split-spread gathers from end-on gathers in marine seismic data as illustrated in figure 5.6. The original shot gathers acquired in an end-on geometry is shown in figure 5.6a. The source is at one end and the receivers in the streamer follow behind. For the same recording position, a receiver gather can be conceived as the recording of several shots on a fixed receiver position as shown in figure 5.6b. Note using reciprocity here, the source can be visualized as a receiver and the receiver as a source, making the receiver gather a shot gather. The idea then is to simply combine the shot gather in figure 5.6a and the receiver gather at the same position in figure 5.6b to obtain the split-spread gather as shown in figure 5.6c. Note that this again can be visualized using reciprocity as a source in the middle

with receivers at both ends as shown in figure 5.6d.

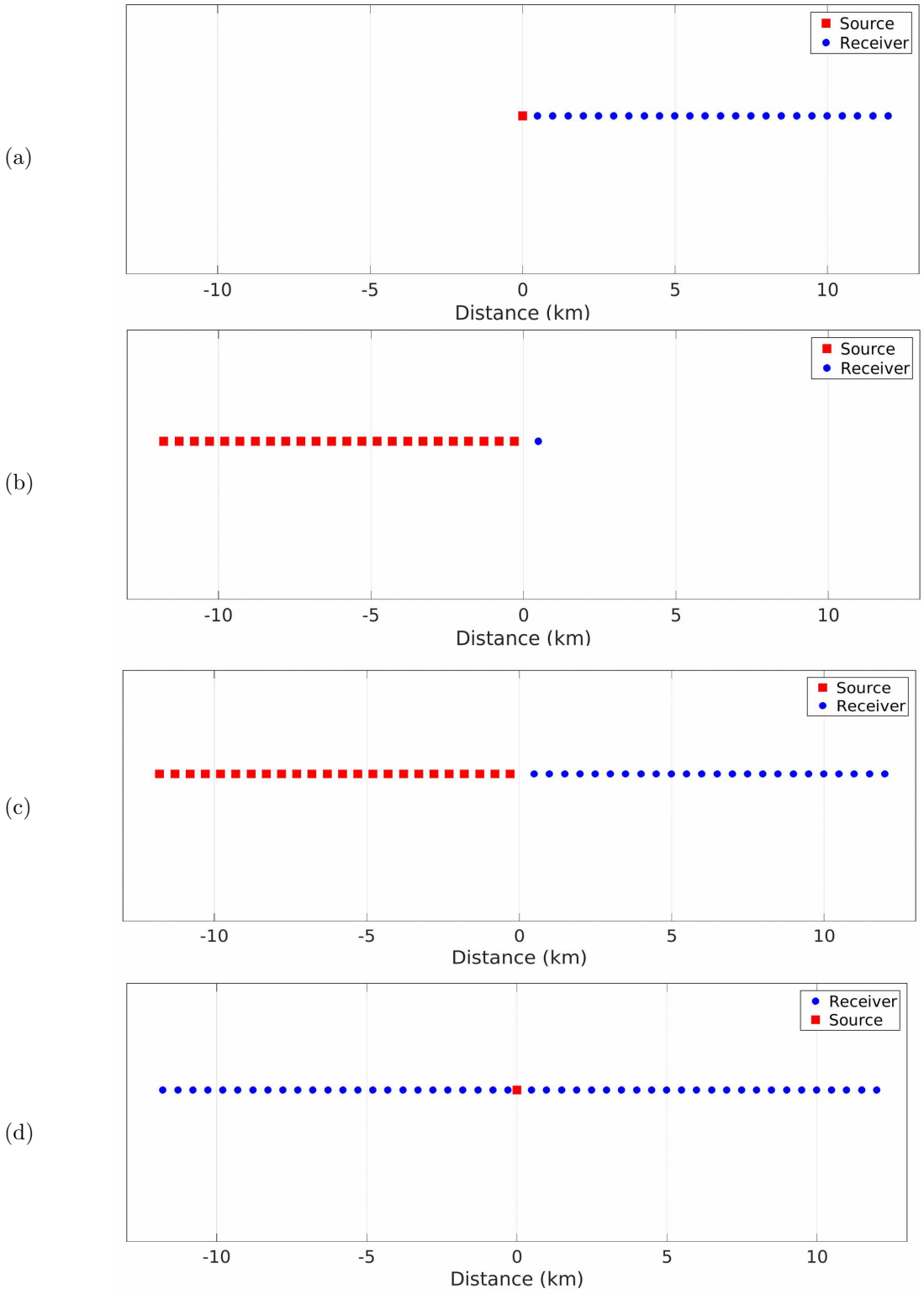

Figure 5.6: (a) A single shot followed by a number of receivers constitutes a shot gather in an end-on geometry. (b) A single (fixed) receiver of a number of shots constitutes a receiver gather. (c) Combining the shot gather and receiver gather at the same location results ina split-spread gather. (d) The split spread gather can be viewed as a central source with receivers at both ends using reciprocity.

Figure 5.7 shows the application to real data. Figure 5.7a shows the shot gather originally acquired as in figure 5.6a and figure 5.7b shows the receiver gather at the same location and corresponds to geometry shown in figure 5.6b. This receiver gather was obtained by sorting the dataset from shot-offset to receiver-offset domains. Applying reciprocity and combining the two, a split-spread gather is obtained as shown

in figure 5.7c and corresponding to the geometry in figure 5.6d.

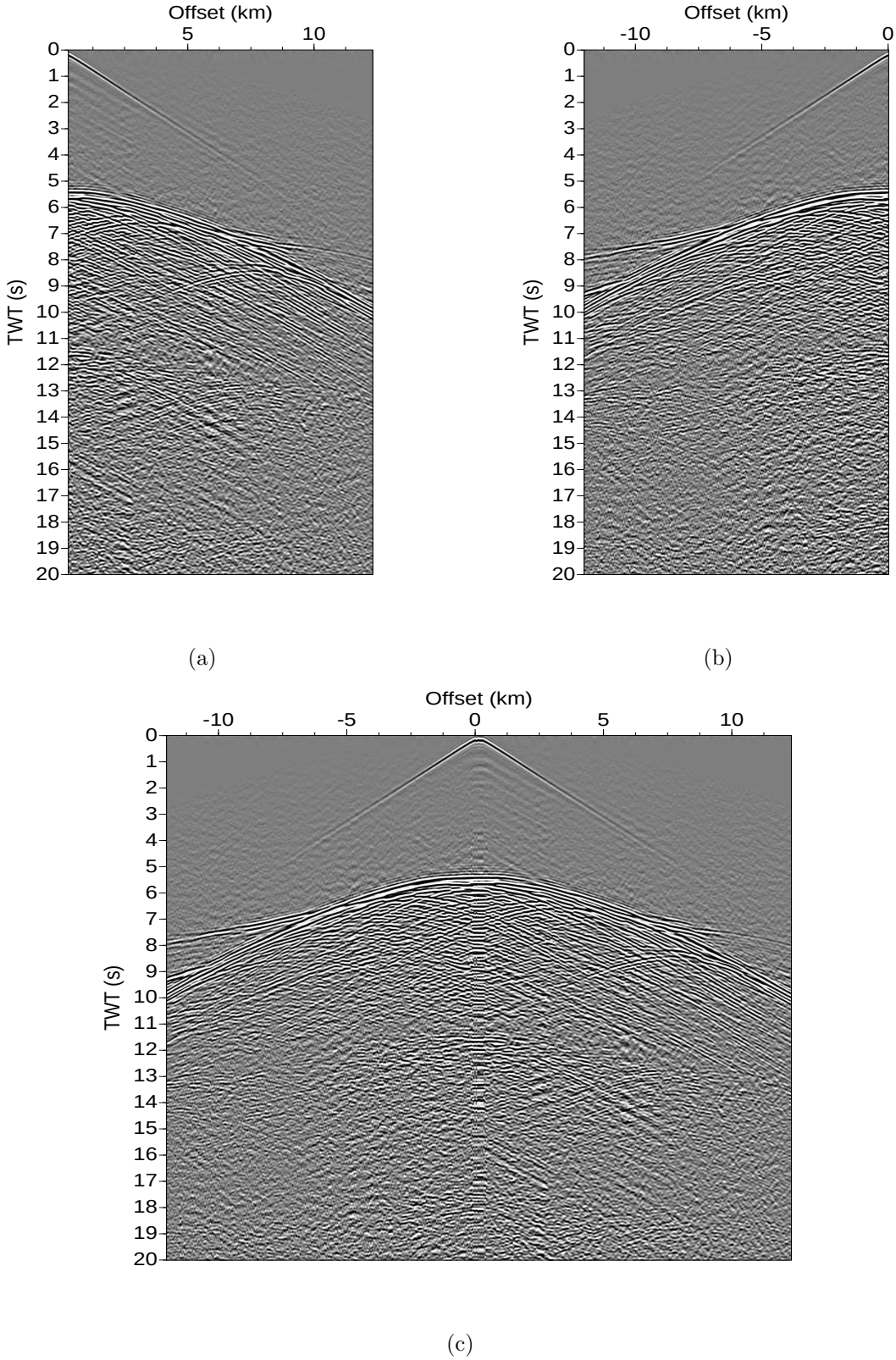

Figure 5.7: (a) A single shot gather corresponding to the geometry shown in figure 5.6a. (b) A single (fixed) receiver gather at the same location corresponding to the geometry shown in figure 5.6b. (c) Combining the shot gather and receiver gather in (a) and (b) gives a split-spread gather corresponding to the geometry in figure 5.6d.

The split-spread gathers formed as above will be able to better handle dips as they cover a subsurface extent of 12 km compared to 6 km in end-on gathers. As a result, a higher signal to noise ratio is expeted

when these gathers are stacked. Though the split-spread gathers described above can themselves be used for imaging, I re-visit wavefield extrapolation for a further potential improvement which I illustrate below.

5.4.2 Downward wavefield extrapolation of split-spread gathers

The previous attempt at using wavefield extrapolation for imaging deeper reflections made in chapter 2 did not consider split-spread gathers neither did it experiment with the parameters involved in wavefield extrapolation. I first illustrate below the extrapolation parameter I vary to improve the results and then show the difference in the extrapolation results by varying that parameter.

The principle behind downward continuation is that the wavefield at a point on a new datum can be obtained from the combination of wavefields from receivers on a previous datum (*Berryhill*, 1984). Instead of taking all the receiver wavefields from the original datum, only those receiver wavefields lying within a certain distance range from the point of extrapolation are taken into account. This distance is usually taken as 1.5 times the Fresnel zone radius, given by $\sqrt{\frac{z\lambda}{2}}$ where z is the vertical depth of extrapolation and λ is the seismic wavelength. Figure 5.8a illustrates the concept of Fresnel zone. The receiver wavefield (blue lines) having the maximum contribution is the closest to the position at which the wavefield is desired (red asterisk) and the contribution from other receiver wavefields decreases as the distance from the position on the new datum increases. This is known as the stationary point theorem (*Aki and Richards*, 2002).

(a)

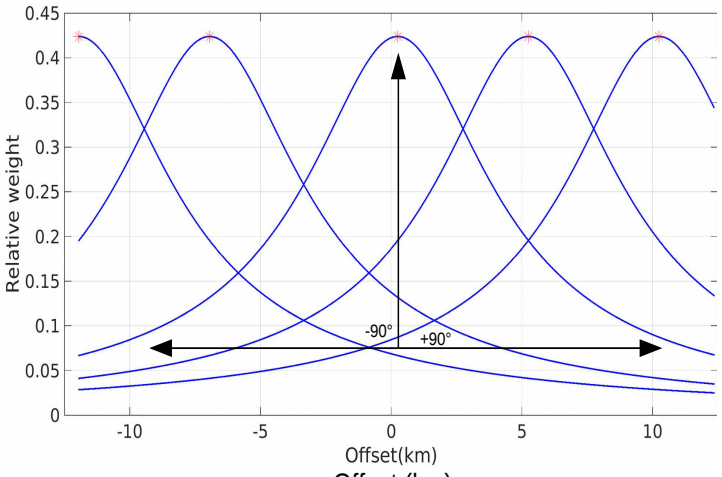

(b)

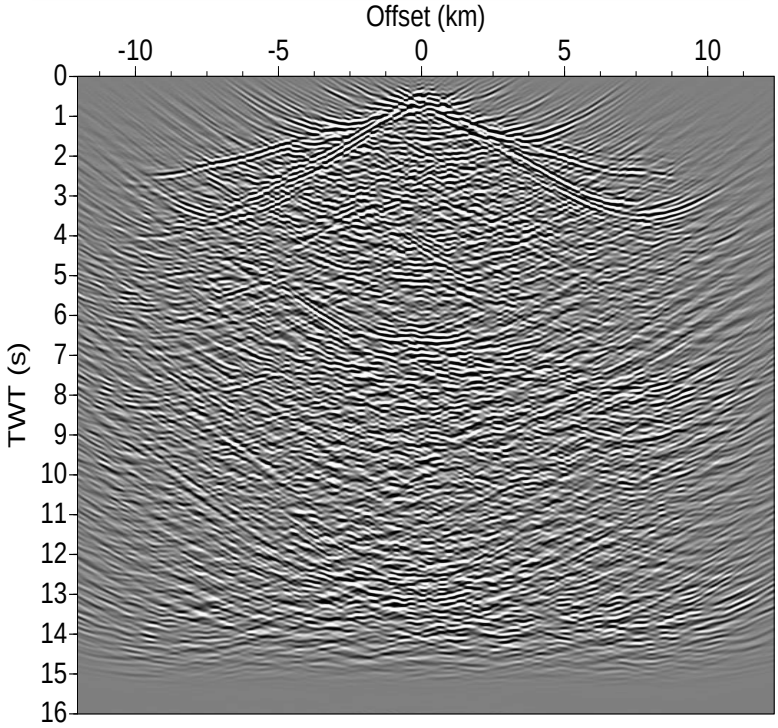

Figure 5.8: (a) The range of receiver wavefields on original datum (blue solid line) used to generate the wavefield at the position on the new datum (red asterisk). Shown are the contributing wavefields for five locations on the new datum at offsets -12 km, -7 km, 0 km, 5 km and 10 km. Note that the range of contributing wavefileds is the full Fresnel zone width and yields an extrapolation operator of $-90°$ to $+90°$. (b) The downward extrapolated split-spread gather from figure 5.7c using the range of contributing receiver wavefields from (a).

An important observation from figure 5.8a is that the contributing wavefields span the entire offset range of the split-spread gather [-12.5 12.5] km in comparison to an end-on gather where offset range is limited to [0 12.5] km. The resulting extrapolated split-spread gather is shown in figure 5.8b. Artifacts in the shape of smiles, termed as 'migration smiles' can be seen masking the first arrivals as well as deeper reflections.

To avoid the above artifacts, I first changed the range of contributing wavefields such that the extrapolated wavefields at negative offsets were formed from contributing wavefields only at negative offsets an extrapolated wavefields at positive offsets were formed from contributing wavefields only at positive offsets. This is shown in figure 5.9a and the resulting extrapolated split-spread gather can be seen in figure 5.9b. The 'migration smiles' are relatively reduced and the first arrivals are clearer.

(a)

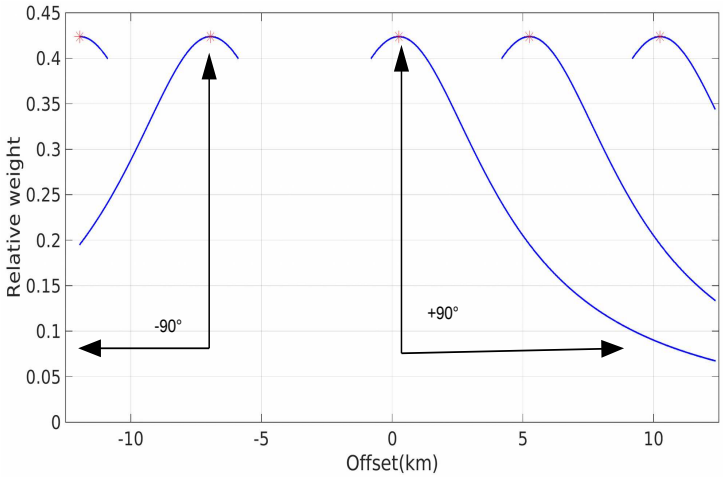

(b)

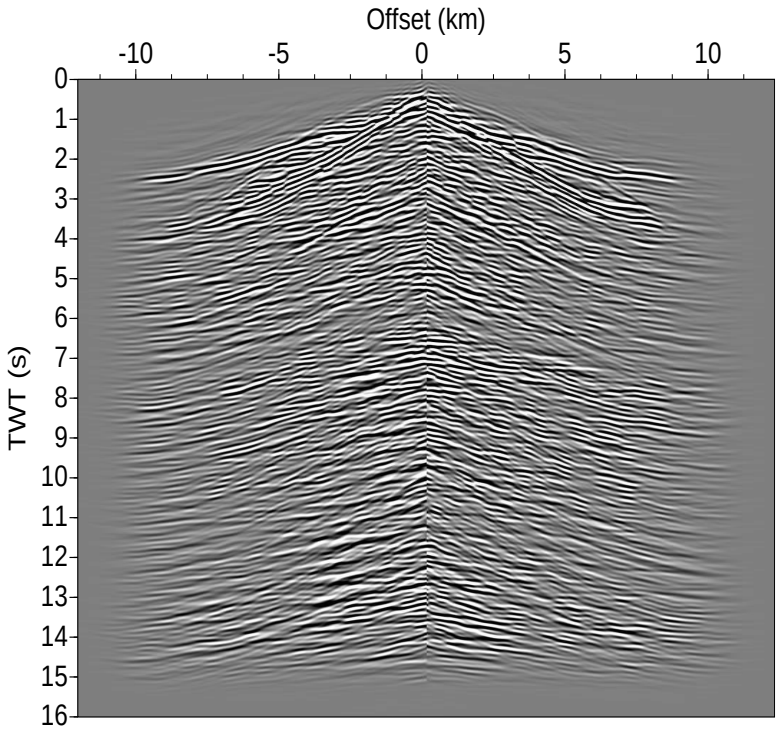

Figure 5.9: (a) The range of receiver wavefields on original datum (blue solid line) used to generate the wavefield at the position on the new datum (red asterisk). Range of contrbuting wavefields reduced to 0 to 90° for positive offsets and -90 to0° for negative offsets. (b) The downward extrapolated split-spread gather from figure 5.7c using the range of contributing receiver wavefields from (a).

However, using only selective offsets as above renders the resulting extrapolated split-spread gather discontinuous at zero-offset as can be observed in figure 5.9b. So whereas such an extrapolated split-spread gather can be used for travel-time tomography of first arrivals to obtain a better ray coverage, it is unlikely to be used for imaging due to conflicting dips in negative and positive offsets. To avoid that, I made another modification to the range of contributing offsets for wavefield extrapolation. I reduced the upper limit of contributing offsets from the previous 90° to 10°. This is shown in figure 5.10a and the resulting extrapolated split-spread gather is shown in figure 5.10b.

(a)

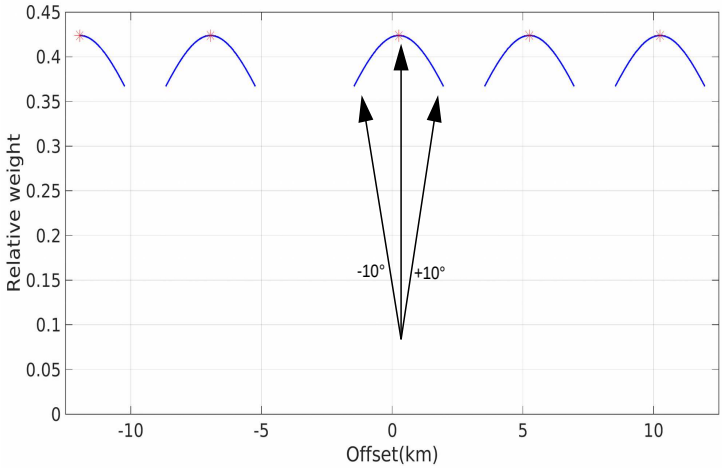

(b)

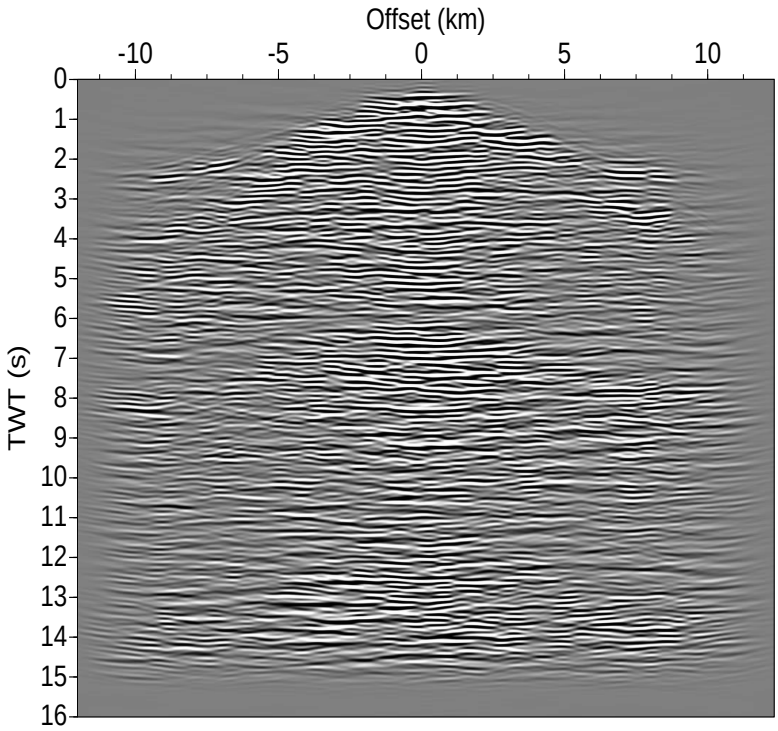

Figure 5.10: (a) The range of receiver wavefields on original datum (blue solid line) used to generate the wavefield at the position on the new datum (red asterisk). The range of contributing wavefields has been reduced to -10° to $+10^\circ$ for all offsets. (b) The downward extrapolated split-spread gather from figure 5.7c using the range of contributing receiver wavefields from (a).

The extrapolated split-spread gather obtained in figure 5.10b has poorly constructed first arrivals but better wavefield continuities at zero-offset, as opposed to figure 5.9. By muting the unwanted arrivals as shown in figure 5.11b, it can be used for further processing. At the moment, application of the proposed method to the real data for the youngest part of the lithosphere is a work in progress.

(a)

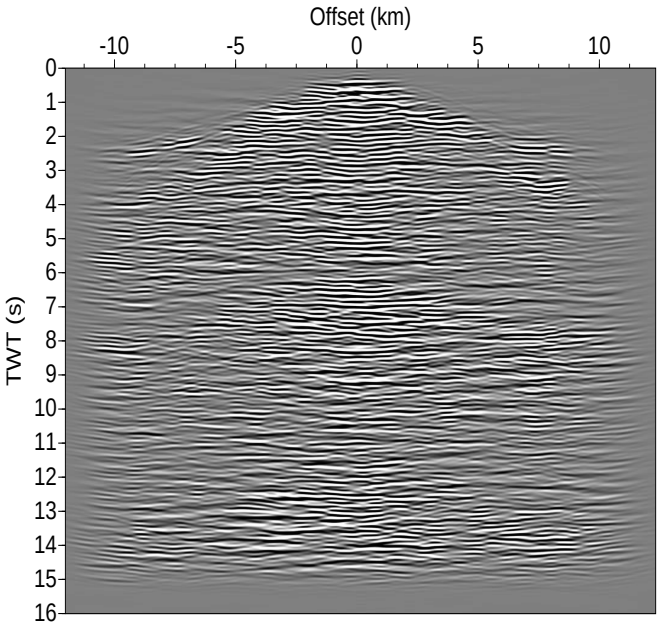

(b)

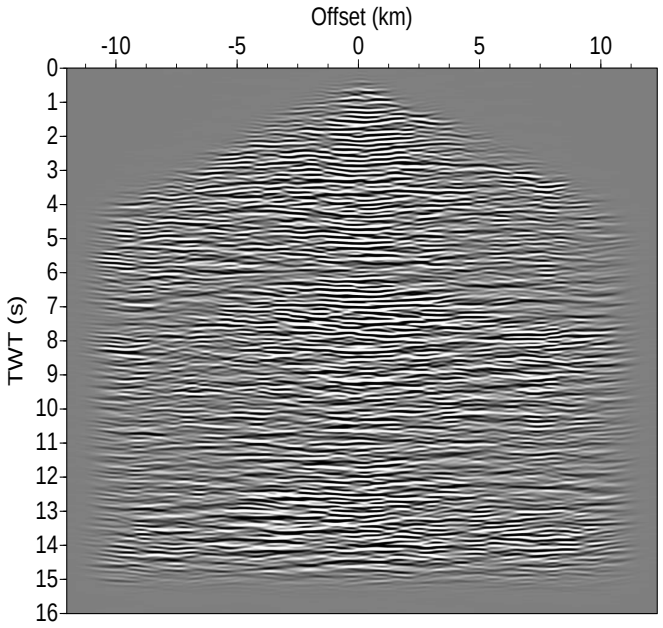

Figure 5.11: (a) Downward extrapolated split-spread gather from figure 5.10b (b) Muting approapriate arrivals to carry out further processing.

5.5 Summary

The profile from 2-47 Myr is bounded by Charcot fracture zone in the North and several non-transform discontinuities/pseudo transform faults. The processed seismic image obtained from 2-27 Myr shows evidence of a ∼25 km thick lithosphere at 2 Myr and a LAB reflection dipping towards older age. Beyond 2 Myr, the LAB image is poor but can be observed dipping sharply to ∼50 km thick lithosphere at 16 Myr. However from 27-47 Myr, the LAB reflection is observed again and is dipping towards older ages, roughly corresponding to 1300°C isotherm. Additionally a second deeper reflection is also observed and appears to be age-independent at a constant depth of ∼80 km below the seafloor. Polarity analysis indicates the upper dipping reflection having a negative polarity and the bottom age-independent reflection having a positive polarity. This indicates that a sub-lithospheric LAB channel bounded a age-dependent freezing front and an age-independent shearing front is present. A schematic sketch of the LAB channel extrapolated to the ridge-axis is shown in figure 5.12. The LAB channel decouples the overlying lithosphere from the underlying asthenosphere, hence giving a new perspective on plate tectonics. The channel is expected to be rich in volatiles, mainly water (*Mehouachi and Singh*, 2018) and carbon dioxide (*Hirschmann et al.*, 2009; *Hirschmann*, 2010), which are needed to stabilize melts within the channel. Most of these volatiles have a horizontal flux near the ridge-axis as supported by modelling studies (*Keller et al.*, 2017).

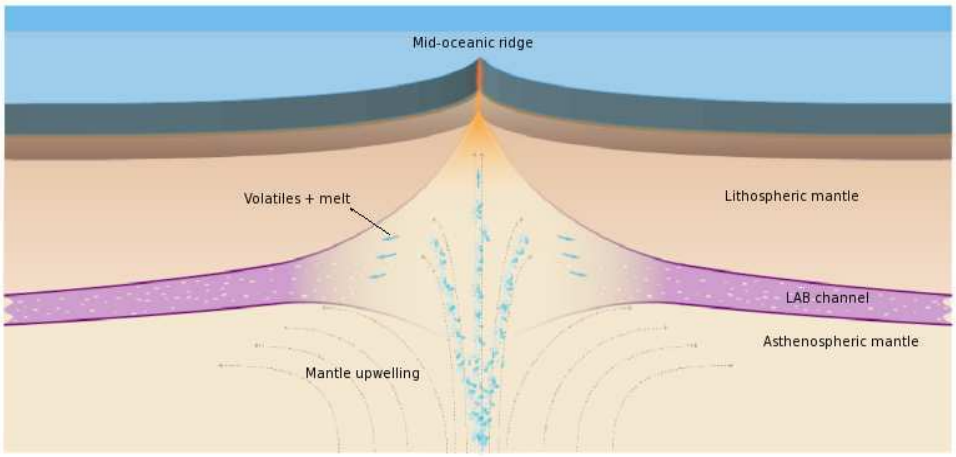

Figure 5.12: Sketch showing a sub-lithospheric volatile-rich LAB channel decoupling the lithosphere from the asthenosphere (*Credit: Satish Singh*). The upper reflection corresponds to 1300°C isotherm at older lithospheric ages and bottom reflection corresponds to an age-independent discontinuity intermittently imaged.

Chapter 6

Conclusions and Perspectives

Ce chapitre résume comment cette thèse a contribué au progrès de la science. En analysant l'ancienne croûte océanique supérieure de 0 à 75 Ma à partir de données sismiques à canaux multiples (MCS) de haute qualité, une nouvelle perspective sur l'évolution de la croûte océanique supérieure est obtenue et les implications pour les systèmes hydrothermaux continus sont proposées. Un traitement avancé pour les événements terrestres plus profonds a été développé et testé avec succès sur des données réelles. L'analyse des limites de la lithosphère et de l'asthénosphère (LAB) de 50 à 75 Ma a permis de délimiter une image P à haute résolution de la LAB, ainsi que de montrer les effets d'une anomalie thermique du manteau sur la lithosphère et la LAB. Le profil 2-47 Ma, situé loin des chaînes volcaniques, montre la présence d'un canal LAB et d'une lithosphère plus épaisse à 2 Ma dans cette région d'étude. Les observations de la LAB dans des régions anormales et relativement normales dans cette thèse exposent un nouveau paradigme sur les processus géodynamiques dans le manteau supérieur.

.

This chapter summarizes in plain language how this thesis has contributed to the advancement of science. By analyzing 0-75 Ma old upper oceanic crust from high quality multi-channel seismic (MCS) data, a new perspective on evolution of upper oceanic crust is obtained and the implications for continuous hydrothermal systems have been made. Advanced processing for deeper Earth events has been developed and tested successfully on real data. Analysis for Lithosphere-Asthenosphere Boundary (LAB) from 50-75 Ma has demarcated a high resolution P-image of the LAB, as well as showing the effects of a mantle thermal anomaly on the lithosphere and LAB. The profile from 2-47 Ma, away from volcanic chains, shows evidence of a LAB channel and a thicker lithosphere at 2 Ma in this study region. The observations of the LAB at anomalous and relatively normal regions in this thesis have given a new paradigm on the geodynamic processes in the upper mantle.

6.1 General conclusions

In this thesis, I have attempted to provide a comprehensive picture of the Equatorial Atlantic lithosphere on the African Plate from 0-75 Ma formed at the slow spreading Mid-Atlantic ridge. This has been broadly divided into the study of upper crust by means of both seismic imaging and upper crustal velocities and the study of deeper reflections, particularly the Lithosphere-Asthenosphere boundary (LAB). I have used multi-channel multi-component 12 km long streamer seismic data and co-located heatflow data, parasound data and high resolution bathymetry to interpret my results better.

Chapter 3 shows upper crustal images and P-velocities that have been obtained from the MCS profile at 0-75 Ma. An observation of the basaltic lava layer 2A is made throughout the profile from pre-stack, post-stack seismic data. To get further information, high resolution travel-time tomography is performed at distinct ages. It is concluded that the layer 2A is present throughout the profile and implications for hydrothermal and fluid circulations are made. Analysis of co-located heat flow data supports the hypothesis of continuing hydrothermal circulations in the older upper crust. Estimates of porosity and permeability and comparison with models of percolation theory also point towards large-scale hydrothermal systems.

In chapters 4 and 5, I image the Lithosphere-Asthenosphere Boundary (LAB). Only a single coherent reflection is seen at 50-75 Ma dipping towards 75 Ma and I first prove that the LAB imaged at 50-75 Ma is real and not a multiple or a sideswipe using high resolution bathymetry. The effects of the Cameroon mantle thermal anomaly are then examined by considering the uplifted lithosphere at 50-75 Ma and the shallower LAB. From 27-47 Ma, an upper and a lower reflection could be identified having opposite polarity contrasts. These events are likely bounding a LAB channel which decouples the lithospheric mantle above the channel from the asthenospheric mantle below the channel. Some events have been imaged from 2-27 Ma and a potential event has been interpreted to be the LAB. These results are then compared with those of similar age lithosphere but closer to the Chain Transform fault on the South American plate and on the young Juan de Fuca plate. A thicker lithosphere at younger ages is observed in this study region as compared to other studies.

The analysis has given me the following answers to the questions posed in chapter 1.

6.1.1 Evolution of upper oceanic crust

1. How does the oceanic upper crust evolve from 0-75 Ma ? Is most of the evolution restricted within the first few Myr ? Do the sediments play an important role in the evolution of the crust ?

   Most of the evolution of the upper oceanic crust happens within first 4 Myr, beyond which a thick sediment cover and reduced heat supply away from ridge-axis reduce the intensity of hydrothermal circulation. Seismic imaging shows layer 2A thickness decreases rapidly whereas an increase in P-velocity is observed away from ridge-axis. High temperature (active) and low temperature (passive) hydrothermal alteration minerals such as greenschist facies and zeolite facies respectively can seal the pore-spaces causing an increase in velocity with depth. Off-axis, exposed basement outcrops could serve as the recharge and discharge site for hydrothermal convection. Co-located heatflow data validates this proposed hypothesis as the observed heatflow is much lower than the predicted heatflow. Top ∼600 m of crust is never fully sealed. The layer 2A/2B boundary is a lava-dyke contact at the ridge-axis and represents an hydrothermal alteration front within the lava flow away from the ridge-axis. Layer 2A has three times thinner cracks and subsequently a higher velocity gradient than layer 2B.

6.1.2 Evolution of the Lithosphere

2. How does the oceanic lithosphere evolve with age ? Is the Lithosphere-Asthenosphere boundary a simple boundary as shown by seismological studies or is it a more complex low velocity channel as shown by some recent studies ?

There is evidence of a reflection ∼26 km below the seafloor at 2 Ma lithosphere and dipping towards the older ages. Starting at 27 Myr, the base of the lithosphere (LAB) becomes prominent again and is observed at ∼58 km below the seafloor. In addition to the LAB, a second deeper reflection is also imaged at ∼80 km below the seafloor. Preliminary polarity analysis indicates a LAB channel with the upper reflection being close to ∼1300°C isotherm and the lower channel being an age-independent discontinuity. The LAB channel decouples the above lithosphere from the underlying asthenosphere and is likely to be rich in volatiles that would facilitate the stability of melts in the channel. A deeper and a thinner LAB channel observed in this study compared to other studies indicates that the channel likely has lower water/melt content as compared to those in other study regions.

3. What happens to the LAB near mantle plumes ? What would be the effect of a mantle thermal anomaly in case of a melt starved plume ?

   Thinning of the lithosphere, shallowing of the LAB and absence of the base of the channel is observed due to mantle thermal anomaly from the Cameroon line. A sharper image of the LAB is obtained possibly due to melt-accumulation of the re-melted heterogeneities of the older St Helena plume. The LAB is assigned a isotherm of 1130°C compared to 1300°C observed away from the volcanic chains. Additionally uplift of the basement, decreasing residual mantle bouguer anomaly is also observed indicating higher mantle/asthenospheric temperatures.

6.2 Perspectives and further work

1. The high-resolution tomography results can be further used to perform seismic full-waveform inversion. This would further enhance the fine-scale structures in the velocity models of the upper oceanic crust. A common limitation of the computationally expensive local optimization based full-waveform inversion is having a starting model as close as possible to the true model.

2. The porosity and bulk permeability estimates of the upper oceanic crust and their age related variations can be used to perform modeling of hydrothermal convection systems to further understand the mechanism of filling up of pore-spaces.

3. Ongoing work is focusing on providing an integrated picture of the P-images from multi-channel seismic data and the P-velocities from co-located active-source wide-angle tomography of the upper mantle.

4. Improvement in P-images obtained for the youngest part of the profile is also ongoing. These require inclusion and appropriate processing of dipping reflections in the pre-stack seismic data as well as innovative strategies such as using split-spread downward continued data for better subsurface coverage.

The ultimate aim of this thesis has been to contribute further to and address the limitations of the existing studies of the upper oceanic crust and the deeper Lithosphere-Asthenosphere seismic structure. This thesis shows an experiment which has been successful in imaging the base of the lithosphere at oceanic lithosphere formed at a slow spreading center. To obtain a broader view of the LAB system, similar experiments should be conducted at oceanic lithosphere formed at other spreading centers, especially fast spreading centers such as East Pacific Rise where imaging conditions would be better. Techniques for imaging the LAB from seismic reflection data as in this thesis and from wide-angle seismic data as in *Qin et al.* (2020) could be used together to provide a better image and understanding of the LAB system. Tools such as geodynamic modeling could help in understanding and explaining the observations reported in this thesis and develop an integrated picture of the LAB system with previous seismological models.

Bibliography

Adam, C., V. Vidal, and A. Bonneville (2005), Mifil: A method to characterize seafloor swells with application to the south central pacific, *Geochemistry, Geophysics, Geosystems*, *6*(1).

Adams, A. N., D. A. Wiens, A. A. Nyblade, G. G. Euler, P. J. Shore, and R. Tibi (2015), Lithospheric instability and the source of the cameroon volcanic line: Evidence from rayleigh wave phase velocity tomography, *Journal of Geophysical Research: Solid Earth*, *120*(3), 1708–1727.

Agius, M., N. Harmon, C. Rychert, S. Tharimena, and J.-M. Kendall (2018), Sediment characterization at the equatorial mid-atlantic ridge from p-to-s teleseismic phase conversions recorded on the pi-lab experiment, *Geophysical research letters*, *45*(22), 12–244.

Aka, F. T., K. Nagao, M. Kusakabe, H. Sumino, G. Tanyileke, B. Ateba, and J. Hell (2004), Symmetrical helium isotope distribution on the cameroon volcanic line, west africa, *Chemical Geology*, *203*(3-4), 205–223.

Aki, K., and P. G. Richards (2002), *Quantitative seismology*.

AL-YAHYA, K. M. (1991), Application of the partial karhunen-loève transform to suppress random noise in seismic sections 1, *Geophysical prospecting*, *39*(1), 77–93.

Alibés, B., M. Canals, B. Alonso, S. Lebreiro, P. Weaver, et al. (1996), Quantification of neogene and quaternary sediment input to the madeira abyssal plain.

Alt, J. C. (1988), Hydrothermal oxide and nontronite deposits on seamounts in the eastern pacific, *Marine Geology*, *81*(1-4), 227–239.

Anderson, D. L. (1995), Lithosphere, asthenosphere, and perisphere, *Reviews of Geophysics*, *33*(1), 125–149, doi:10.1029/94RG02785.

Anderson, D. L. (2000), The thermal state of the upper mantle; no role for mantle plumes, *Geophysical Research Letters*, *27*(22), 3623–3626.

Anderson, D. L. (2005), Scoring hotspots: The plume and plate paradigms, *SPECIAL PAPERS-GEOLOGICAL SOCIETY OF AMERICA*, *388*, 31.

Anderson, D. L. (2006), Speculations on the nature and cause of mantle heterogeneity, *Tectonophysics*, *416*(1-4), 7–22.

Anderson, D. L., and C. Sammis (1970), Partial melting in the upper mantle, *Physics of the Earth and Planetary Interiors*, *3*, 41–50.

Andrews, A. (1977), Low temperature fluid alteration of oceanic layer 2 basalts, dsdp leg 37, *Canadian Journal of Earth Sciences*, *14*(4), 911–926.

Arnulf, A., S. Singh, A. Harding, G. Kent, and W. Crawford (2011), Strong seismic heterogeneity in layer 2a near hydrothermal vents at the mid-atlantic ridge, *Geophysical Research Letters*, *38*(13).

Arnulf, A., A. Harding, G. Kent, S. Singh, and W. Crawford (2014), Constraints on the shallow velocity structure of the lucky strike volcano, mid-atlantic ridge, from downward continued multichannel streamer data, *Journal of Geophysical Research: Solid Earth*, *119*(2), 1119–1144.

Arora, K., A. Cazenave, E. R. Engdahl, R. Kind, A. Manglik, S. Roy, K. Sain, and S. Uyeda (2011), *Encyclopedia of solid earth geophysics*, Springer Science & Business Media.

Artemieva, I. M. (2006), Global 1× 1 thermal model tc1 for the continental lithosphere: implications for lithosphere secular evolution, *Tectonophysics*, *416*(1-4), 245–277.

Audhkhasi, P., and S. C. Singh (2019), Seismic structure of the upper crust from 075 ma in the equatorial atlantic ocean on the african plate using ultralong offset seismic data, *Geochemistry, Geophysics, Geosystems*, *20*(12), 6140–6162, doi:10.1029/2019GC008577.

Auer, L., L. Boschi, T. Becker, T. Nissen-Meyer, and D. Giardini (2014), Savani: A variable resolution whole-mantle model of anisotropic shear velocity variations based on multiple data sets, *Journal of Geophysical Research: Solid Earth*, *119*(4), 3006–3034.

Auer, L., T. W. Becker, L. Boschi, and N. Schmerr (2015), Thermal structure, radial anisotropy, and dynamics of oceanic boundary layers, *Geophysical Research Letters*, *42*(22), 9740–9749, doi:10.1002/2015GL066246.

Baker, P. A., P. M. Stout, M. Kastner, and H. Elderfield (1991), Large-scale lateral advection of seawater through oceanic crust in the central equatorial pacific, *Earth and Planetary Science Letters*, *105*(4), 522–533.

Barclay, A. H., D. R. Toomey, and S. C. Solomon (1998), Seismic structure and crustal magmatism at the mid-atlantic ridge, 35 n, *Journal of Geophysical Research: Solid Earth*, *103*(B8), 17,827–17,844.

Barrell, J. (1914), The Strength of the Earth's Crust, *Journal of Geology*, *22*, 289–314, doi:10.1086/622155.

Barruol, G., K. Sigloch, J.-R. Scholz, A. Mazzullo, E. Stutzmann, J.-P. Montagner, S. Kiselev, F. Fontaine, L. Michon, C. Deplus, and J. Dyment (2019), Large-scale flow of indian ocean asthenosphere driven by runion plume, *Nature Geoscience*, *12*, doi:10.1038/s41561-019-0479-3.

Bartyzel, K. (2016), Adaptive kuwahara filter, *Signal, Image and Video Processing*, *10*(4), 663–670, doi:10.1007/s11760-015-0791-3.

Becker, T. W., B. Kustowski, and G. Ekström (2008), Radial seismic anisotropy as a constraint for upper mantle rheology, *Earth and Planetary Science Letters*, *267*(1-2), 213–227.

Beghein, C., K. Yuan, N. Schmerr, and Z. Xing (2014), Changes in seismic anisotropy shed light on the nature of the gutenberg discontinuity, *Science*, *343*(6176), 1237–1240.

Behn, M. D., M. S. Boettcher, and G. Hirth (2007), Thermal structure of oceanic transform faults, *Geology*, *35*(4), 307–310.

Berge, P. A., J. G. Berryman, and B. P. Bonner (1993), Influence of microstructure on rock elastic properties, *Geophysical Research Letters*, *20*(23), 2619–2622.

Berkhout, A. (1981), Wave field extrapolation techniques in seismic migration, a tutorial, *Geophysics*, *46*(12), 1638–1656.

Berryhill, J. R. (1979), Wave-equation datuming, *Geophysics*, *44*(8), 1329–1344.

Berryhill, J. R. (1984), Wave-equation datuming before stack, *Geophysics*, *49*(11), 2064–2066.

Berryman, J. G. (1992), Single-scattering approximations for coefficients in biots equations of poroelasticity, *The Journal of the Acoustical Society of America*, *91*(2), 551–571.

Bina, C. R., and G. Helffrich (1994), Phase transition clapeyron slopes and transition zone seismic discontinuity topography, *Journal of Geophysical Research: Solid Earth*, *99*(B8), 15,853–15,860.

Bird, P. (2003), An updated digital model of plate boundaries, *Geochemistry, Geophysics, Geosystems*, *4*(3).

Blacic, T. M., G. Ito, J. P. Canales, R. S. Detrick, and J. Sinton (2004), Constructing the crust along the galapagos spreading center 91.3–95.5 w: Correlation of seismic layer 2a with axial magma lens and topographic characteristics, *Journal of Geophysical Research: Solid Earth*, *109*(B10).

Bock, G. (1994), Synthetic seismogram images of upper mantle structure: No evidence for a 520-km discontinuity, *Journal of Geophysical Research: Solid Earth*, *99*(B8), 15,843–15,851.

Bonatti, E. (1996), Anomalous opening of the equatorial atlantic due to an equatorial mantle thermal minimum, *Earth and planetary science letters*, *143*(1-4), 147–160.

Bonatti, E., M. Seyler, and N. Sushevskaya (1993), A cold suboceanic mantle belt at the earth's equator, *Science*, *261*(5119), 315–320.

Bonneville, A., R. P. Von Herzen, and F. Lucazeau (1997), Heat flow over reunion hot spot track: Additional evidence for thermal rejuvenation of oceanic lithosphere, *Journal of Geophysical Research: Solid Earth*, *102*(B10), 22,731–22,747.

Boyd, F. R., and H. O. Meyer (1979), *The mantle sample: inclusions in kimberlites and other volcanics*, vol. 2, American Geophysical Union.

Brune, J., and J. Dorman (1963), Seismic waves and earth structure in the canadian shield, *Bulletin of the Seismological Society of America*, *53*(1), 167–209.

Budiansky, B. (1965), On the elastic moduli of some heterogeneous materials, *Journal of the Mechanics and Physics of Solids*, *13*(4), 223–227.

Burgos, G., J.-P. Montagner, E. Beucler, Y. Capdeville, A. Mocquet, and M. Drilleau (2014), Oceanic lithosphere-asthenosphere boundary from surface wave dispersion data, *Journal of Geophysical Research: Solid Earth*, *119*(2), 1079–1093.

Burke, K. (2001), Origin of the cameroon line of volcano-capped swells, *Journal of Geology - J GEOL*, *109*, 349–362, doi:10.1086/319977.

Calvert, A. (1995), Seismic evidence for a magma chamber beneath the slow-spreading mid-atlantic ridge, *Nature*, *377*(6548), 410–414.

Canales, J., and J. Dañobeitia (1998), The canary islands swell: a coherence analysis of bathymetry and gravity, *Geophysical Journal International*, *132*(3), 479–488.

Canales, J. P., R. S. Detrick, S. M. Carbotte, G. M. Kent, J. B. Diebold, A. Harding, J. Babcock, M. R. Nedimović, and E. Van Ark (2005), Upper crustal structure and axial topography at intermediate spreading ridges: Seismic constraints from the southern juan de fuca ridge, *Journal of Geophysical Research: Solid Earth*, *110*(B12).

Carlson, R. (1998), Seismic velocities in the uppermost oceanic crust: Age dependence and the fate of layer 2a, *Journal of Geophysical Research: Solid Earth*, *103*(B4), 7069–7077.

Carlson, R. (2004), Seismic properties of layer 2a at 11 ma: Results of a vertical seismic profile at ocean drilling program site 1243, *Geophysical research letters*, *31*(17).

Carlson, R. (2010), How crack porosity and shape control seismic velocities in the upper oceanic crust: Modeling downhole logs from holes 504b and 1256d, *Geochemistry, Geophysics, Geosystems*, *11*(4).

Carlson, R. (2011), The effect of hydrothermal alteration on the seismic structure of the upper oceanic crust: Evidence from holes 504b and 1256d, *Geochemistry, Geophysics, Geosystems*, *12*(9).

Carlson, R. (2014a), The influence of porosity and crack morphology on seismic velocity and permeability in the upper oceanic crust, *Geochemistry, Geophysics, Geosystems*, *15*(1), 10–27.

Carlson, R. (2014b), The effects of alteration and porosity on seismic velocities in oceanic basalts and diabases, *Geochemistry, Geophysics, Geosystems*, *15*(12), 4589–4598.

Carlson, R. (2018), Ocean crustal seismic layer 2c, *Geochemistry, Geophysics, Geosystems*, *19*(9), 3084–3096.

Carlson, R., and C. Herrick (1990), Densities and porosities in the oceanic crust and their variations with depth and age, *Journal of Geophysical Research: Solid Earth*, *95*(B6), 9153–9170.

Carvalho, H. S., F. Shams, R. Ferrari, and L. Boccato (2018), Application of extreme learning machines and echo state networks to seismic multiple removal, in *2018 International Joint Conference on Neural Networks (IJCNN)*, pp. 1–8, IEEE.

Cazenave, A., A. Souriau, and K. Dominh (1989), Global coupling of earth surface topography with hotspots, geoid and mantle heterogeneities, *Nature*, *340*(6228), 54.

Chen, Y. J. (1992), Oceanic crustal thickness versus spreading rate, *Geophysical Research Letters*, *19*(8), 753–756.

Chevrot, S., L. Vinnik, and J.-P. Montagner (1999), Global-scale analysis of the mantle pds phases, *Journal of Geophysical Research: Solid Earth*, *104*(B9), 20,203–20,219.

Christensen, N. I. (1970), Possible greenschist facies metamorphism of the oceanic crust, *Geological Society of America Bulletin*, *81*(3), 905–908.

Christensen, N. I. (1996), Poisson's ratio and crustal seismology, *Journal of Geophysical Research: Solid Earth*, *101*(B2), 3139–3156.

Christensen, N. I., and M. H. Salisbury (1972), Sea floor spreading, progressive alteration of layer 2 basalts, and associated changes in seismic velocities, *Earth and Planetary Science Letters*, *15*(4), 367–375.

Christensen, U. (1995), Effects of phase transitions on mantle convection, *Annual Review of Earth and Planetary Sciences*, *23*(1), 65–87.

Christeson, G. L., G. Kent, G. Purdy, and R. Detrick (1996), Extrusive thickness variability at the east pacific rise, 9–10 n: Constraints from seismic techniques, *Journal of Geophysical Research: Solid Earth*, *101*(B2), 2859–2873.

Christeson, G. L., K. D. McIntosh, and J. A. Karson (2007), Inconsistent correlation of seismic layer 2a and lava layer thickness in oceanic crust, *Nature*, *445*(7126), 418.

Christeson, G. L., J. A. Karson, and K. D. McIntosh (2010), Mapping of seismic layer 2a/2b boundary above the sheeted dike unit at intermediate spreading crust exposed near the blanco transform, *Geochemistry, Geophysics, Geosystems*, *11*(3).

Christeson, G. L., J. V. Morgan, and M. R. Warner (2012), Shallow oceanic crust: Full waveform tomographic images of the seismic layer 2a/2b boundary, *Journal of Geophysical Research: Solid Earth*, *117*(B5).

Cleary, M. P., S.-M. Lee, and I.-W. Chen (1980), Self-consistent techniques for heterogeneous media, *Journal of the Engineering Mechanics Division*, *106*(5), 861–887.

Cogné, J.-P., and E. Humler (2004), Temporal variation of oceanic spreading and crustal production rates during the last 180 my, *Earth and Planetary Science Letters*, *227*(3-4), 427–439.

Coimbra, T. A., A. Novais, and J. Schleicher (2016), Offset-continuation stacking: Theory and proof of concept, *Geophysics*, *81*(5), V387–V401.

Colli, L., S. Ghelichkhan, and H.-P. Bunge (2016), On the ratio of dynamic topography and gravity anomalies in a dynamic earth, *Geophysical Research Letters*, *43*(6), 2510–2516.

Collier, J., and S. Singh (1998), Poisson's ratio structure of young oceanic crust, *Journal of Geophysical Research: Solid Earth*, *103*(B9), 20,981–20,996.

Combier, V., T. Seher, S. C. Singh, W. C. Crawford, M. Cannat, J. Escartín, and D. Dusunur (2015), Three-dimensional geometry of axial magma chamber roof and faults at lucky strike volcano on the mid-atlantic ridge, *Journal of Geophysical Research: Solid Earth*, *120*(8), 5379–5400.

Condie, K. C. (2001), *Mantle plumes and their record in Earth history*, Cambridge university press.

Courtier, A. M., M. G. Jackson, J. F. Lawrence, Z. Wang, C.-T. A. Lee, R. Halama, J. M. Warren, R. Workman, W. Xu, M. M. Hirschmann, et al. (2007), Correlation of seismic and petrologic thermometers suggests deep thermal anomalies beneath hotspots, *Earth and Planetary Science Letters*, *264*(1-2), 308–316.

Courtillot, V., A. Davaille, J. Besse, and J. Stock (2003), Three distinct types of hotspots in the earths mantle, *Earth and Planetary Science Letters*, *205*(3-4), 295–308.

Courtney, R. C., and R. S. White (1986), Anomalous heat flow and geoid across the cape verde rise: evidence for dynamic support from a thermal plume in the mantle, *Geophysical Journal International*, *87*(3), 815–867.

Cronan, D., and S. Wakefield (1994), Pelagic fluxes and sedimentation, *Journal of the Geological Society*, *151*(2), 349–350.

Crosby, A., and D. McKenzie (2009), An analysis of young ocean depth, gravity and global residual topography, *Geophysical Journal International*, *178*(3), 1198–1219.

Crough, S. T. (1983), Hotspot swells, *Annual Review of Earth and Planetary Sciences*, *11*(1), 165–193.

Cummins, P., B. Kennett, J. Bowman, and M. Bostock (1992), The 520 km discontinuity?, *Bulletin of the Seismological Society of America*, *82*(1), 323–336.

Daly, R. A. (1940), *Strength and Structure of the Earth*, Prentice-Hall New York.

Davies, G. F. (1988), Ocean bathymetry and mantle convection: 1. large-scale flow and hotspots, *Journal of Geophysical Research: Solid Earth*, *93*(B9), 10,467–10,480, doi:10.1029/JB093iB09p10467.

Davis, E., and C. Lister (1974), Fundamentals of ridge crest topography, *Earth and Planetary Science Letters*, *21*(4), 405–413.

Davis, E., D. Chapman, K. Wang, H. Villinger, A. Fisher, S. Robinson, J. Grigel, D. Pribnow, J. Stein, and K. Becker (1999), Regional heat flow variations across the sedimented juan de fuca ridge eastern flank: Constraints on lithospheric cooling and lateral hydrothermal heat transport, *Journal of Geophysical Research: Solid Earth*, *104*(B8), 17,675–17,688.

Debayle, E., and Y. Ricard (2013), Seismic observations of large-scale deformation at the bottom of fast-moving plates, *Earth and Planetary Science Letters*, *376*, 165–177.

deMenocal, P. B. (1995), Plio-pleistocene african climate, *Science*, *270*(5233), 53–59, doi:10.1126/science.270.5233.53.

DeMets, C., R. G. Gordon, and D. F. Argus (2010), Geologically current plate motions, *Geophysical Journal International*, *181*(1), 1–80.

Déruelle, B., J. N'ni, and R. Kambou (1987), Mount cameroon: an active volcano of the cameroon line, *Journal of African Earth Sciences (1983)*, *6*(2), 197–214.

Detrick, R., J. Collins, R. Stephen, and S. Swift (1994), In situ evidence for the nature of the seismic layer 2/3 boundary in oceanic crust, *Nature*, *370*(6487), 288.

Detrick, R. S., and S. T. Crough (1978), Island subsidence, hot spots, and lithospheric thinning, *Journal of Geophysical Research: Solid Earth*, *83*(B3), 1236–1244.

Dix, C. H. (1955), Seismic velocities from surface measurements, *GEOPHYSICS*, *20*(1), 68–86, doi:10.1190/1.1438126.

Doin, M., and L. Fleitout (1996), Thermal evolution of the oceanic lithosphere: an alternative view, *Earth and Planetary Science Letters*, *142*(1-2), 121–136.

Duncan, R. A., and M. Richards (1991), Hotspots, mantle plumes, flood basalts, and true polar wander, *Reviews of Geophysics*, *29*(1), 31–50.

Dunlop, H., and J. Fitter (1979), A k-ar and sr-isotopic study of the volcanic rocks of the island of principe, west africaevidence for mantle heterogeneity beneath the gulf of guinea, *Contributions to Mineralogy and Petrology*, *71*(2), 125–131.

Dunn, R. A., V. Lekić, R. S. Detrick, and D. R. Toomey (2005), Three-dimensional seismic structure of the mid-atlantic ridge (35 n): Evidence for focused melt supply and lower crustal dike injection, *Journal of Geophysical Research: Solid Earth*, *110*(B9).

dAcremont, E., S. Leroy, and E. B. Burov (2003), Numerical modelling of a mantle plume: the plume head–lithosphere interaction in the formation of an oceanic large igneous province, *Earth and Planetary Science Letters*, *206*(3-4), 379–396.

E Johnston, J., G. Fryer, and N. I Christensen (1995), Velocity-porosity relationships of basalts from the east pacific rise, *142*, doi:10.2973/odp.proc.sr.142.106.1995.

Eaton, D. W., F. Darbyshire, R. L. Evans, H. Grütter, A. G. Jones, and X. Yuan (2009), The elusive lithosphere–asthenosphere boundary (lab) beneath cratons, *Lithos*, *109*(1-2), 1–22.

Ebinger, C. J., and N. Sleep (1998), Cenozoic magmatism throughout east africa resulting from impact of a single plume, *Nature*, *395*(6704), 788.

Ekström, G. (2011), A global model of love and rayleigh surface wave dispersion and anisotropy, 25-250 s, *Geophysical Journal International*, *187*(3), 1668–1686.

Ekström, G., and A. M. Dziewonski (1998), The unique anisotropy of the pacific upper mantle, *Nature*, *394*(6689), 168.

Elderfield, H. (1988), The oceanic chemistry of the rare-earth elements, *Philosophical Transactions of the Royal Society of London. Series A, Mathematical and Physical Sciences*, *325*(1583), 105–126.

Embley, R. W., M. A. Hobart, R. N. Anderson, and D. Abbott (1983), Anomalous heat flow in the northwest atlantic: A case for continued hydrothermal circulation in 80-my crust, *Journal of Geophysical Research: Solid Earth*, *88*(B2), 1067–1074.

Estep, J., R. Reece, D. A. Kardell, G. L. Christeson, and R. L. Carlson (2019), Seismic layer 2a: Evolution and thickness from 0- to 70-ma crust in the slow-intermediate spreading south atlantic, *Journal of Geophysical Research: Solid Earth*, *0*(0), doi:10.1029/2019JB017302.

Evangelidis, C., T. Minshull, and T. Henstock (2004), Three-dimensional crustal structure of ascension island from active source seismic tomography, *Geophysical Journal International*, *159*(1), 311–325.

Evans, R. L., A. G. Jones, X. Garcia, M. Muller, M. Hamilton, S. Evans, C. J. S. Fourie, J. Spratt, S. Webb, H. Jelsma, and D. Hutchins (2011), Electrical lithosphere beneath the kaapvaal craton, southern africa, *Journal of Geophysical Research: Solid Earth*, *116*(B4), doi:10.1029/2010JB007883.

F. Ruddiman, W., and E. M. Pokras (1993), Influences of high- and low-latitude processes on african terrestrial climate: Pleistocene eolian records from equatorial atlantic ocean drilling program site 663, *Paleoceanography*, *8*, 209–242, doi:10.1029/93PA02688.

Fairhead, J. (1988), Mesozoic plate tectonic reconstructions of the central south atlantic ocean: the role of the west and central african rift system, *Tectonophysics*, *155*(1-4), 181–191.

Fairhead, J., and R. Binks (1991), Differential opening of the central and south atlantic oceans and the opening of the west african rift system, *Tectonophysics*, *187*(1-3), 191–203.

Faul, U. H., and I. Jackson (2005), The seismological signature of temperature and grain size variations in the upper mantle, *Earth and Planetary Science Letters*, *234*(1-2), 119–134.

Ferrante, G., C. Thomson, V. Vaddineni, P. Audhkhasi, and S. Singh (2020), Characterization of converted s-waves from sediment-basement interface in deep-sea sediments, article submitted to Geophysical Journal International.

Fichtner, A., B. L. Kennett, H. Igel, and H.-P. Bunge (2009), Full seismic waveform tomography for upper-mantle structure in the australasian region using adjoint methods, *Geophysical Journal International*, *179*(3), 1703–1725.

Fisher, A., and K. Becker (2000), Channelized fluid flow in oceanic crust reconciles heat-flow and permeability data, *Nature*, *403*(6765), 71–74.

Fisher, A., E. Davis, M. Hutnak, V. Spiess, L. Zühlsdorff, A. Cherkaoui, L. Christiansen, K. Edwards, R. Macdonald, H. Villinger, et al. (2003), Hydrothermal recharge and discharge across 50 km guided by seamounts on a young ridge flank, *Nature*, *421*(6923), 618.

Fisher, A. T. (1998), Permeability within basaltic oceanic crust, *Reviews of Geophysics*, *36*(2), 143–182.

Fisher, A. T., and R. P. Von Herzen (2005), Models of hydrothermal circulation within 106 ma seafloor: Constraints on the vigor of fluid circulation and crustal properties, below the madeira abyssal plain, *Geochemistry, Geophysics, Geosystems*, *6*(11).

Fitton, J. (1980), The benue trough and cameroon linea migrating rift system in west africa, *Earth and Planetary Science Letters*, *51*(1), 132–138.

Fitton, J. (1987), The cameroon line, west africa: a comparison between oceanic and continental alkaline volcanism, *Geological Society, London, Special Publications*, *30*(1), 273–291.

Fitton, J., and H. Dunlop (1985), The cameroon line, west africa, and its bearing on the origin of oceanic and continental alkali basalt, *Earth and Planetary Science Letters*, *72*(1), 23–38.

Fitton, J. G. (1983), Active versus passive continental rifting: evidence from the west african rift system, *Tectonophysics*, *94*(1-4), 473–481.

Flanagan, M. P., and P. M. Shearer (1998), Global mapping of topography on transition zone velocity discontinuities by stacking ss precursors, *Journal of Geophysical Research: Solid Earth*, *103*(B2), 2673–2692.

Fox, P. J., E. Schreiber, and J. Peterson (1973), The geology of the oceanic crust: compressional wave velocities of oceanic rocks, *Journal of Geophysical Research*, *78*(23), 5155–5172.

French, S., V. Lekic, and B. Romanowicz (2013), Waveform tomography reveals channeled flow at the base of the oceanic asthenosphere, *Science*, *342*(6155), 227–230.

Gabor, D. (1946), Theory of communication. part 1: The analysis of information, *Journal of the Institution of Electrical Engineers-Part III: Radio and Communication Engineering*, *93*(26), 429–441.

Gaherty, J. B., T. H. Jordan, and L. S. Gee (1996), Seismic structure of the upper mantle in a central pacific corridor, *Journal of Geophysical Research: Solid Earth*, *101*(B10), 22,291–22,309, doi:10.1029/96JB01882.

Gaherty, J. B., M. Kato, and T. H. Jordan (1999), Seismological structure of the upper mantle: a regional comparison of seismic layering, *Physics of the Earth and Planetary Interiors*, *110*(1-2), 21–41.

Ghahremani, F. (1980), Effect of grain boundary sliding on anelasticity of polycrystals, *International Journal of Solids and Structures*, *16*(9), 825–845.

Granot, R., and J. Dyment (2015), The cretaceous opening of the south atlantic ocean, *Earth and Planetary Science Letters*, *414*, 156–163.

Greer, A. A., M. C. Sinha, and L. M. MacGregor (2002), Joint effective medium modelling for co-incident seismic and electromagnetic data, and its application to studies of porosity structure at mid-ocean ridge crests, *LITHOS Science Report*, *4*, 103–120.

Grevemeyer, I., and A. Bartetzko (2004), Hydrothermal ageing of oceanic crust: inferences from seismic refraction and bore hole studies, *Hydrogeology of Oceanic Lithosphere*, pp. 128–150.

Grevemeyer, I., and W. Weigel (1996), Seismic velocities of the uppermost igneous crust versus age, *Geophysical Journal International*, *124*(2), 631–635.

Grevemeyer, I., S. C. Singh, H. Villinger, C. Papenberg, P. Audhkhasi, V. Vaddineni, L. Gomez de la Pena, N. Kaul, and H. Schröder (2018), LITHOS-iLAB - an 1100 km long seismic and heat flow transect in the equatorial Atlantic Ocean, covering 0 to 50 Ma oceanic lithosphere, in *EGU General Assembly Conference Abstracts*, EGU General Assembly Conference Abstracts, p. 6969.

Griffiths, R. W., and I. H. Campbell (1990), Stirring and structure in mantle starting plumes, *Earth and Planetary Science Letters*, *99*(1-2), 66–78.

Grose, C. J. (2012), Properties of oceanic lithosphere: Revised plate cooling model predictions, *Earth and Planetary Science Letters*, *333*, 250–264.

Grunau, H., P. Lehner, M. Cleintuar, P. Allenbach, and G. Bakker (1975), New radiometric ages and seismic data from fuerteventura (canary islands), maio (cape verde islands), and são tomé (gulf of guinea), in *Progress in geodynamics*.

Gung, Y., and B. Romanowicz (2002), Superplumes from the core–mantle boundary to the base of the lithosphere: evidence from q tomography, *Science*, *296*, 513–516.

Gutenberg, B. (1926), Untersuchungen zur frage, bis zu welcher tiefe die erde kristallin ist, *Zeitschrift für Geophysik*, *2*, 24–29.

Gutenberg, B. (1948), On the layer of relatively low wave velocity at a depth of about 80 kilometers, *Bulletin of the Seismological Society of America*, *38*(2), 121–148.

Gutenberg, B. (1955), Low-velocity lithosphere channel, *Geological Society of America Bulletin*, *66*(9), 1203–1204.

Gutenberg, B. (1959), The asthenosphere low-velocity layer, *Annals of Geophysics*, *12*(4), 439–460.

Hammond, W. C., and E. D. Humphreys (2000), Upper mantle seismic wave velocity: Effects of realistic partial melt geometries, *Journal of Geophysical Research: Solid Earth*, *105*(B5), 10,975–10,986, doi: 10.1029/2000JB900041.

Han, S., S. M. Carbotte, J. P. Canales, M. R. Nedimović, H. Carton, J. C. Gibson, and G. W. Horning (2016), Seismic reflection imaging of the juan de fuca plate from ridge to trench: New constraints on the distribution of faulting and evolution of the crust prior to subduction, *Journal of Geophysical Research: Solid Earth*, *121*(3), 1849–1872.

Hansen, P. C., and D. P. OLeary (1993), The use of the l-curve in the regularization of discrete ill-posed problems, *SIAM Journal on Scientific Computing*, *14*(6), 1487–1503.

Harding, A. J., G. M. Kent, J. Orcutt, et al. (1993), A multichannel seismic investigation of upper crustal structure at 9 n on the east pacific rise: Implications for crustal accretion, *Journal of Geophysical Research: Solid Earth*, *98*(B8), 13,925–13,944.

Harris, M., B. Zihlmann, D. Mock, T. Akitou, D. A. H. Teagle, K. Kondo, J. R. Deans, L. Crispini, E. Takazawa, J. A. Coggon, and P. B. Kelemen (2017), Hydrothermal Alteration of the Lower Oceanic Crust: Insight from OmanDP Holes GT1A and GT2A., *AGU Fall Meeting Abstracts*.

Harris, R. N., A. T. Fisher, and D. S. Chapman (2004), Fluid flow through seamounts and implications for global mass fluxes, *Geology*, *32*(8), 725–728.

Hartley, R. A., G. G. Roberts, N. White, and C. Richardson (2011), Transient convective uplift of an ancient buried landscape, *Nature Geoscience*, *4*(8), 562.

Hashin, Z. (1962), The elastic moduli of heterogeneous materials, *Journal of Applied Mechanics*, *29*(1), 143–150.

Hashin, Z., and S. Shtrikman (1963), A variational approach to the theory of the elastic behaviour of multiphase materials, *Journal of the Mechanics and Physics of Solids*, *11*(2), 127–140.

Hasterok, D. (2013), A heat flow based cooling model for tectonic plates, *Earth and Planetary Science Letters*, *361*, 34–43.

Hasterok, D., D. Chapman, and E. Davis (2011), Oceanic heat flow: Implications for global heat loss, *Earth and Planetary Science Letters*, *311*(3-4), 386–395.

Herman, B. M., M. G. Langseth, and M. A. Hobart (1977), Heat flow in the oceanic crust bounding western africa, *Tectonophysics*, *41*(1-3), 61–77.

Hill, M. (1957), Recent geophysical exploration of the ocean floor, *Physics and Chemistry of the Earth*, *2*, 129–163.

Hill, R. (1965), Theory of mechanical properties of fibre-strengthened materialsiii. self-consistent model, *Journal of the Mechanics and Physics of Solids*, *13*(4), 189–198.

Hillier, J. K., and A. Watts (2005), Relationship between depth and age in the north pacific ocean, *Journal of Geophysical Research: Solid Earth*, *110*(B2).

Hirschmann, M. M. (2010), Partial melt in the oceanic low velocity zone, *Physics of the Earth and Planetary Interiors*, *179*(1), 60 – 71, doi:https://doi.org/10.1016/j.pepi.2009.12.003.

Hirschmann, M. M., T. Tenner, C. Aubaud, and A. Withers (2009), Dehydration melting of nominally anhydrous mantle: The primacy of partitioning, *Physics of the Earth and Planetary Interiors*, *176*(1-2), 54–68.

Hofmann, A. W. (1997), Mantle geochemistry: the message from oceanic volcanism, *Nature*, *385*(6613), 219.

Hofmeister, A. (1999), Mantle values of thermal conductivity and the geotherm from phonon lifetimes, *Science*, *283*(5408), 1699–1706.

Hofmeister, A. (2005), Dependence of diffusive radiative transfer on grain-size, temperature, and fe-content: Implications for mantle processes, *Journal of Geodynamics*, *40*(1), 51–72.

Hoggard, M. J., N. White, and D. Al-Attar (2016), Global dynamic topography observations reveal limited influence of large-scale mantle flow, *Nature Geoscience*, *9*(6), 456.

Holik, J. S., P. D. Rabinowitz, and J. A. Austin Jr. (1991), Effects of canary hotspot volcanism on structure of oceanic crust off morocco, *Journal of Geophysical Research: Solid Earth*, *96*(B7), 12,039–12,067, doi:10.1029/91JB00709.

Holmes, M. L., and H. P. Johnson (1993), Upper crustal densities derived from sea floor gravity measurements: Northern juan de fuca ridge, *Geophysical Research Letters*, *20*(17), 1871–1874.

Houtz, R., and J. Ewing (1976), Upper crustal structure as a function of plate age, *Journal of Geophysical Research*, *81*(14), 2490–2498.

Humphris, S. E. (1977), The hydrothermal alteration of oceanic basalts by seawater., Ph.D. thesis, Massachusetts Institute of Technology.

Humphris, S. E. (1998), Rare earth element composition of anhydrite: implications for deposition and mobility within the active tag hydrothermal mound, in *Proceedings-Ocean Drilling Program Scientific Results*, pp. 143–162, National Science Foundation.

Humphris, S. E., T. McCollom, H. Vents, and M.-O. Ridges (1998), The cauldron beneath the sea floor, *Oceanus*, *41*(2), 18.

Huot, G., and S. C. Singh (2018), Seismic evidence for fluid/gas beneath the mentawai fore-arc basin, central sumatra, *Journal of Geophysical Research: Solid Earth*, *123*(2), 957–976, doi:10.1002/2017JB014849.

Hussenoeder, S. A., G. M. Kent, and R. S. Detrick (2002a), Upper crustal seismic structure of the slow spreading mid-atlantic ridge, 35 n: Constraints on volcanic emplacement processes, *Journal of Geophysical Research: Solid Earth*, *107*(B8).

Hussenoeder, S. A., R. S. Detrick, G. M. Kent, H. Schouten, and A. J. Harding (2002b), Fine-scale seismic structure of young upper crust at 17 20 s on the fast spreading east pacific rise, *Journal of Geophysical Research: Solid Earth*, *107*(B8).

Hyndman, R., and M. Drury (1976), The physical properties of oceanic basement rocks from deep drilling on the mid-atlantic ridge, *Journal of Geophysical Research*, *81*(23), 4042–4052.

Ittekkot, V. (1988), Global trends in the nature of organic matter in river suspensions, *Nature*, *332*(6163), 436.

Johnson, H. P., K. Becker, and R. Von Herzen (1993), Near-axis heat flow measurements on the northern juan de fuca ridge: Implications for fluid circulation in oceanic crust, *Geophysical Research Letters*, *20*(17), 1875–1878.

Jokat, W., O. Ritzmann, M. C. Schmidt-Aursch, S. Drachev, S. Gauger, and J. Snow (2003), Geophysical evidence for reduced melt production on the arctic ultraslow gakkel mid-ocean ridge, *Nature*, *423*(6943), 962–965.

Jones, A. G., I. J. Ferguson, A. D. Chave, R. L. Evans, and G. W. McNeice (2001), Electric lithosphere of the Slave craton, *Geology*, *29*(5), 423–426, doi:10.1130/0091-7613(2001)029⟨0423:ELOTSC⟩2.0.CO;2.

Karato, S.-i. (2012), On the origin of the asthenosphere, *Earth and Planetary Science Letters*, *321*, 95–103.

Karato, S.-i. (2014), Does partial melting explain geophysical anomalies?, *Physics of the Earth and Planetary Interiors*, *228*, 300–306.

Karato, S.-i., and H. Jung (1998), Water, partial melting and the origin of the seismic low velocity and high attenuation zone in the upper mantle, *Earth and Planetary Science Letters*, *157*, 193–207, doi:10.1016/S0012-821X(98)00034-X.

Karato, S.-i., T. Olugboji, and J. Park (2015), Mechanisms and geologic significance of the mid-lithosphere discontinuity in the continents, *Nature geoscience*, *8*(7), 509.

Kardell, D. A., G. L. Christeson, J. D. Estep, R. S. Reece, and R. L. Carlson (2018), Long-lasting evolution of layer 2a in the western south atlantic: Evidence for low-temperature hydrothermal circulation in old oceanic crust, *Journal of Geophysical Research: Solid Earth*.

Karson, J. A. (2002), Geologic structure of the uppermost oceanic crust created at fast-to intermediate-rate spreading centers, *Annual Review of Earth and Planetary Sciences*, *30*(1), 347–384.

Karson, J. A., and G. L. Christeson (2003), Comparison of geologic and seismic structure of uppermost fast-spreading oceanic crust: Insights from a crustal cross-section at the hess deep rift, in *Heterogeneity in the Crust and Upper Mantle*, pp. 99–129, Springer.

Katsura, T. (1995), Thermal diffusivity of olivine under upper mantle conditions, *Geophysical Journal International*, *122*(1), 63–69.

Kawakatsu, H., P. Kumar, Y. Takei, M. Shinohara, T. Kanazawa, E. Araki, and K. Suyehiro (2009), Seismic evidence for sharp lithosphere-asthenosphere boundaries of oceanic plates, *Science*, *324*(5926), 499–502.

Keller, T., R. F. Katz, and M. M. Hirschmann (2017), Volatiles beneath mid-ocean ridges: Deep melting, channelised transport, focusing, and metasomatism, *Earth and Planetary Science Letters*, *464*, 55–68.

Kennett, B., and E. Engdahl (1991), Traveltimes for global earthquake location and phase identification, *Geophysical Journal International*, *105*(2), 429–465.

Kennett, B., and T. Furumura (2015), Toward the reconciliation of seismological and petrological perspectives on oceanic lithosphere heterogeneity, *Geochemistry, Geophysics, Geosystems*, *16*(9), 3129–3141.

Khripounoff, A., A. Vangriesheim, N. Babonneau, P. Crassous, B. Dennielou, and B. Savoye (2003), Direct observation of intense turbidity current activity in the zaire submarine valley at 4000 m water depth, *Marine Geology*, *194*(3-4), 151–158.

King, S. D. (2007), Hotspots and edge-driven convection, *Geology*, *35*(3), 223–226.

King, S. D., and C. Adam (2014), Hotspot swells revisited, *Physics of the Earth and Planetary Interiors*, *235*, 66–83.

King, S. D., and D. L. Anderson (1995), An alternative mechanism of flood basalt formation, *Earth and Planetary Science Letters*, *136*(3-4), 269–279.

King, S. D., and D. L. Anderson (1998), Edge-driven convection, *Earth and Planetary Science Letters*, *160*(3-4), 289–296.

King, S. D., and J. Ritsema (2000), African hot spot volcanism: small-scale convection in the upper mantle beneath cratons, *Science*, *290*(5494), 1137–1140.

Korenaga, T., and J. Korenaga (2008), Subsidence of normal oceanic lithosphere, apparent thermal expansivity, and seafloor flattening, *Earth and Planetary Science Letters*, *268*(1-2), 41–51.

Kumar, P., and H. Kawakatsu (2011), Imaging the seismic lithosphere-asthenosphere boundary of the oceanic plate, *Geochemistry, Geophysics, Geosystems*, *12*(1), doi:10.1029/2010GC003358.

Kumar, P., X. Yuan, R. Kind, and G. Kosarev (2005), The lithosphere-asthenosphere boundary in the tien shan-karakoram region from s receiver functions: Evidence for continental subduction, *Geophysical Research Letters*, *32*(7), doi:10.1029/2004GL022291.

Kuo, B.-Y., and D. W. Forsyth (1988), Gravity anomalies of the ridge-transform system in the south atlantic between 31 and 34.5 s: Upwelling centers and variations in crustal thickness, *Marine Geophysical Researches*, *10*(3-4), 205–232.

Lawrence, J. F., and P. M. Shearer (2006), A global study of transition zone thickness using receiver functions, *Journal of Geophysical Research: Solid Earth*, *111*(B6).

Le Pichon, X., R. Houtz, C. L. Drake, and J. E. Nafe (1965), Crustal structure of the mid-ocean ridges: 1. seismic refraction measurements, *Journal of Geophysical Research*, *70*(2), 319–339.

Lee, C.-T. A. (2003), Compositional variation of density and seismic velocities in natural peridotites at stp conditions: Implications for seismic imaging of compositional heterogeneities in the upper mantle, *Journal of Geophysical Research: Solid Earth*, *108*(B9), doi:10.1029/2003JB002413.

Lee, C.-T. A., A. Lenardic, C. M. Cooper, F. Niu, and A. Levander (2005), The role of chemical boundary layers in regulating the thickness of continental and oceanic thermal boundary layers, *Earth and Planetary Science Letters*, *230*(3), 379 – 395, doi:https://doi.org/10.1016/j.epsl.2004.11.019.

Lee, D.-C., A. N. Halliday, J. G. Fitton, and G. Poli (1994), Isotopic variations with distance and time in the volcanic islands of the cameroon line: evidence for a mantle plume origin, *Earth and Planetary Science Letters*, *123*(1-3), 119–138.

Lee, D.-C., A. N. Halliday, G. R. Davies, E. J. Essene, J. G. Fitton, and R. Temdjim (1996), Melt enrichment of shallow depleted mantle: a detailed petrological, trace element and isotopic study of mantle-derived xenoliths and megacrysts from the cameroon line, *Journal of Petrology*, *37*(2), 415–441.

Levander, A. R. (1988), Fourth-order finite-difference p-sv seismograms, *Geophysics*, *53*(11), 1425–1436.

Lévy, F., and C. Jaupart (2011), Temperature and rheological properties of the mantle beneath the north american craton from an analysis of heat flux and seismic data, *Journal of Geophysical Research: Solid Earth*, *116*(B1).

Lewis, B. (1978), Evolution of ocean crust seismic velocities, *Annual Review of Earth and Planetary Sciences*, *6*(1), 377–404.

Li, X., R. Kind, K. Priestley, S. Sobolev, F. Tilmann, X. Yuan, and M. Weber (2000), Mapping the hawaiian plume conduit with converted seismic waves, *Nature*, *405*(6789), 938.

Li, X., R. Kind, X. Yuan, I. Wölbern, and W. Hanka (2004), Rejuvenation of the lithosphere by the hawaiian plume, *Nature*, *427*(6977), 827.

Lizarralde, D., J. B. Gaherty, J. A. Collins, G. Hirth, and S. D. Kim (2004), Spreading-rate dependence of melt extraction at mid-ocean ridges from mantle seismic refraction data, *Nature*, *432*(7018), 744.

Macdonald, K. C. (1982), Mid-ocean ridges: Fine scale tectonic, volcanic and hydrothermal processes within the plate boundary zone, *Annual Review of Earth and Planetary Sciences*, *10*(1), 155–190, doi:10.1146/annurev.ea.10.050182.001103.

Maggi, A., E. Debayle, K. Priestley, and G. Barruol (2006), Multimode surface waveform tomography of the pacific ocean: a closer look at the lithospheric cooling signature, *Geophysical Journal International*, *166*(3), 1384–1397.

Marjanović, M., N. Fuji, S. C. Singh, T. Belahi, and J. Escartín (2017), Seismic signatures of hydrothermal pathways along the east pacific rise between 9 16 and 9 56 n, *Journal of Geophysical Research: Solid Earth*, *122*(12), 10–241.

Marzoli, A., P. R. Renne, E. M. Piccirillo, C. Francesca, G. Bellieni, A. J. Melfi, J. B. Nyobe, and J. N'ni (1999), Silicic magmas from the continental cameroon volcanic line (oku, bambouto and ngaoundere): 40 ar-39 ar dates, petrology, sr-nd-o isotopes and their petrogenetic significance, *Contributions to Mineralogy and Petrology*, *135*(2-3), 133–150.

Marzoli, A., E. Piccirillo, P. Renne, G. Bellieni, M. Iacumin, J. Nyobe, and A. Tongwa (2000), The cameroon volcanic line revisited: petrogenesis of continental basaltic magmas from lithospheric and asthenospheric mantle sources, *Journal of Petrology*, *41*(1), 87–109.

McGeary, S., and M. Warner (1985), Seismic profiling the continental lithosphere, *Nature*, *317*(6040), 795.

McKenzie, D., A. Watts, B. Parsons, and M. Roufosse (1980), Planform of mantle convection beneath the pacific ocean, *Nature*, *288*(5790), 442.

McKenzie, D., J. Jackson, and K. Priestley (2005), Thermal structure of oceanic and continental lithosphere, *Earth and Planetary Science Letters*, *233*(3-4), 337–349.

McKenzie, D. P. (1967), Some remarks on heat flow and gravity anomalies, *Journal of Geophysical Research*, *72*(24), 6261–6273.

McNutt, M. (1988), Thermal and mechanical properties of the cape verde rise, *Journal of Geophysical Research: Solid Earth*, *93*(B4), 2784–2794.

Mehouachi, F. (2019), Nature of the oceanic lithosphere across the equatorial fracture zones in the atlantic ocean, Ph.D. thesis, Institut de Physique du Globe de Paris.

Mehouachi, F., and S. C. Singh (2018), Water-rich sublithospheric melt channel in the equatorial atlantic ocean, *Nature Geoscience*, *11*(1), 65.

Melbourne, T., and D. Helmberger (1998), Fine structure of the 410-km discontinuity, *Journal of Geophysical Research: Solid Earth*, *103*(B5), 10,091–10,102.

Menard, H., and M. McNutt (1982), Evidence for and consequences of thermal rejuvenation, *Journal of Geophysical Research: Solid Earth*, *87*(B10), 8570–8580.

Meyers, J. B., and B. R. Rosendahl (1991), Seismic reflection character of the cameroon volcanic line: Evidence for uplifted oceanic crust, *Geology*, *19*(11), 1072–1076.

Meyers, J. B., B. R. Rosendahl, C. G. Harrison, and Z.-D. Ding (1998), Deep-imaging seismic and gravity results from the offshore cameroon volcanic line, and speculation of african hotlines, *Tectonophysics*, *284*(1-2), 31–63.

Milelli, L., L. Fourel, and C. Jaupart (2012), A lithospheric instability origin for the cameroon volcanic line, *Earth and Planetary Science Letters*, *335-336*, 80 – 87, doi:https://doi.org/10.1016/j.epsl.2012.04.028.

Minshull, T., N. Bruguier, and J. Brozena (2003), Seismic structure of the mid-atlantic ridge, 8–9 s, *Journal of Geophysical Research: Solid Earth*, *108*(B11).

Montagner, J.-P., and T. Tanimoto (1991), Global upper mantle tomography of seismic velocities and anisotropies, *Journal of Geophysical Research: Solid Earth*, *96*(B12), 20,337–20,351.

Montelli, R., G. Nolet, F. Dahlen, G. Masters, E. R. Engdahl, and S.-H. Hung (2004), Finite-frequency tomography reveals a variety of plumes in the mantle, *Science*, *303*(5656), 338–343.

Moorkamp, M., A. G. Jones, and S. Fishwick (2010), Joint inversion of receiver functions, surface wave dispersion, and magnetotelluric data, *Journal of Geophysical Research: Solid Earth*, *115*(B4), doi:10.1029/2009JB006369.

Moreau, C., J.-M. Regnoult, B. Déruelle, and B. Robineau (1987), A new tectonic model for the cameroon line, central africa, *Tectonophysics*, *141*(4), 317–334.

Morgan, J. P., and Y. J. Chen (1993), The genesis of oceanic crust: Magma injection, hydrothermal circulation, and crustal flow, *Journal of Geophysical Research: Solid Earth*, *98*(B4), 6283–6297.

Morgan, W. J. (1971), Convection plumes in the lower mantle, *Nature*, *230*(5288), 42.

Morgan, W. J. (1972), Deep mantle convection plumes and plate motions, *AAPG bulletin*, *56*(2), 203–213.

Morgan, W. J. (1983), Hotspot tracks and the early rifting of the atlantic, in *Developments in Geotectonics*, vol. 19, pp. 123–139, Elsevier.

Morlet, J., G. Arens, E. Fourgeau, and D. Glard (1982), Wave propagation and sampling theorypart i: Complex signal and scattering in multilayered media, *Geophysics*, *47*(2), 203–221.

Moser, T., G. Nolet, and R. Snieder (1992), Ray bending revisited, *Bulletin of the Seismological Society of America*, *82*(1), 259–288.

Mukerji, T., and J. Dvorkin (2009), *The Rock Physics Handbook 2ed*, Cambridge University Press.

Müller, R. D., M. Sdrolias, C. Gaina, and W. R. Roest (2008), Age, spreading rates, and spreading asymmetry of the world's ocean crust, *Geochemistry, Geophysics, Geosystems*, *9*(4).

Murase, T., and A. R. McBIRNEY (1973), Properties of some common igneous rocks and their melts at high temperatures, *Geological Society of America Bulletin*, *84*(11), 3563–3592.

Mutter, C., and J. Mutter (1993), Variations in thickness of layer 3 dominate oceanic crustal structure, *Earth and Planetary Science Letters*, *117*, 295–317, doi:10.1016/0012-821X(93)90134-U.

Naif, S., K. Key, S. Constable, and R. Evans (2013), Melt-rich channel observed at the lithosphere–asthenosphere boundary, *Nature*, *495*(7441), 356.

Navin, D., C. Peirce, and M. Sinha (1998), The ramesses experimentii. evidence for accumulated melt beneath a slow spreading ridge from wide-angle refraction and multichannel reflection seismic profiles, *Geophysical Journal International*, *135*(3), 746–772.

Nedimović, M. R., S. M. Carbotte, J. B. Diebold, A. J. Harding, J. P. Canales, and G. M. Kent (2008), Upper crustal evolution across the juan de fuca ridge flanks, *Geochemistry, Geophysics, Geosystems*, *9*(9).

Newman, K. R., M. R. Nedimović, J. P. Canales, and S. M. Carbotte (2011), Evolution of seismic layer 2b across the juan de fuca ridge from hydrophone streamer 2-d traveltime tomography, *Geochemistry, Geophysics, Geosystems*, *12*(5).

Ngako, V., E. Njonfang, F. T. Aka, P. Affaton, and J. M. Nnange (2006), The north–south paleozoic to quaternary trend of alkaline magmatism from niger–nigeria to cameroon: complex interaction between hotspots and precambrian faults, *Journal of African Earth Sciences*, *45*(3), 241–256.

Ngounouno, I., C. Moreau, B. Déruelle, D. Demaiffe, and R. Montigny (2001), Petrology of the alkaline undersaturated complex of kokoumi (cameroon), *BULLETIN-SOCIETE GEOLOGIQUE DE FRANCE*, *172*(6), 675–686.

Ngounouno, I., B. Déruelle, R. Montigny, and D. Demaiffe (2005), Petrology and geochemistry of monchiquites from tchircotche (garoua rift, north cameroon, central africa), *Mineralogy and Petrology*, *83*(3-4), 167–190.

Njilah, I., H. Ajonina, K. Kamgang, and M. Tchindjang (2004), K-ar ages, mineralogy, major and trace element geochemistry of the tertiary-quaternary lavas from the ndu volcanic ridge nw cameroon, *African Journal of Science and Technology*, *5*(1).

Nyblade, A. A., and N. H. Sleep (2003), Long lasting epeirogenic uplift from mantle plumes and the origin of the southern african plateau, *Geochemistry, Geophysics, Geosystems*, *4*(12).

O'Connor, J., P. Stoffers, P. van den Bogaard, and M. McWilliams (1999), First seamount age evidence for significantly slower african plate motion since 19 to 30 ma, *Earth and Planetary Science Letters*, *171*(4), 575–589.

O'Connor, J. M., and A. P. le Roex (1992a), South atlantic hot spot-plume systems: 1. distribution of volcanism in time and space, *Earth and Planetary Science Letters*, *113*(3), 343–364.

O'Connor, J. M., and A. P. le Roex (1992b), South atlantic hot spot-plume systems: 1. distribution of volcanism in time and space, *Earth and Planetary Science Letters*, *113*(3), 343 – 364, doi:https://doi.org/10.1016/0012-821X(92)90138-L.

Ohira, A., S. Kodaira, G. F. Moore, M. Yamashita, T. Fujiwara, Y. Kaiho, S. Miura, and G. Fujie (2018), Active-source seismic survey on the northeastern hawaiian arch: insights into crustal structure and mantle reflectors, *Earth, Planets and Space*, *70*(1), 1–16.

Ojo, A. O., S. Ni, and Z. Li (2017), Crustal radial anisotropy beneath cameroon from ambient noise tomography, *Tectonophysics*, *696*, 37–51.

Olson, C. J., J. J. Becker, and D. T. Sandwell (2014), A new global bathymetry map at 15 arcsecond resolution for resolving seafloor fabric: SRTM15_PLUS, *AGU Fall Meeting Abstracts*, OS34A-03.

Paige, C. C., and M. A. Saunders (1982), Lsqr: An algorithm for sparse linear equations and sparse least squares, *ACM Transactions on Mathematical Software (TOMS)*, *8*(1), 43–71.

Parker, R. (1973), The rapid calculation of potential anomalies, *Geophysical Journal International*, *31*(4), 447–455.

Parsons, B., and S. Daly (1983), The relationship between surface topography, gravity anomalies, and temperature structure of convection, *Journal of Geophysical Research: Solid Earth*, *88*(B2), 1129–1144.

Parsons, B., and J. G. Sclater (1977), An analysis of the variation of ocean floor bathymetry and heat flow with age, *Journal of geophysical research*, *82*(5), 803–827.

Partyka, G., J. Gridley, and J. Lopez (1999), Interpretational applications of spectral decomposition in reservoir characterization, *The leading edge*, *18*(3), 353–360.

Pasyanos, M. E., T. G. Masters, G. Laske, and Z. Ma (2014), Litho1.0: An updated crust and lithospheric model of the earth, *Journal of Geophysical Research: Solid Earth*, *119*(3), 2153–2173, doi:10.1002/2013JB010626.

Paul, J. D., G. G. Roberts, and N. White (2014a), The african landscape through space and time, *Tectonics*, *33*(6), 898–935, doi:10.1002/2013TC003479.

Paul, J. D., G. G. Roberts, and N. White (2014b), The african landscape through space and time, *Tectonics*, *33*(6), 898–935, doi:10.1002/2013TC003479.

Peirce, C., M. Sinha, S. Topping, and C. Gill (2007), Morphology and genesis of slow-spreading ridgesseabed scattering and seismic imaging within the oceanic crust, *Geophysical Journal International*, *168*(1), 59–89.

Phipps Morgan, J., W. J. Morgan, Y.-S. Zhang, and W. H. Smith (1995), Observational hints for a plume-fed, suboceanic asthenosphere and its role in mantle convection, *Journal of Geophysical Research: Solid Earth*, *100*(B7), 12,753–12,767.

Pim, J., C. Peirce, A. Watts, I. Grevemeyer, and A. Krabbenhöft (2008), Crustal structure and origin of the cape verde rise, *Earth and Planetary Science Letters*, *272*(1-2), 422–428.

Plomerova, J., D. Kouba, and V. Babuska (2002), Mapping the lithosphere-asthenosphere boundary trough changes in surface-wave anisotropy, *Tectonophysics*, *358*, 175–185, doi:10.1016/S0040-1951(02)00423-7.

Priestley, K., and J. Brune (1978), Surface waves and the structure of the great basin of nevada and western utah, *Journal of Geophysical Research: Solid Earth*, *83*(B5), 2265–2272.

Priestley, K., and D. MKenzie (2006), The thermal structure of the lithosphere from shear wave velocities, *Earth and Planetary Science Letters*, *244*(1), 285 – 301, doi:https://doi.org/10.1016/j.epsl.2006.01.008.

Priestley, K., and F. Tilmann (2009), Relationship between the upper mantle high velocity seismic lid and the continental lithosphere, *Lithos*, *109*(1-2), 112–124.

Purdy, G., L. Kong, G. Christeson, and S. Solomon (1992), Relationship between spreading rate and the seismic structure of mid-ocean ridges, *Nature*, *355*(6363), 815.

Qin, Y., and S. C. Singh (2015), Seismic evidence of a two-layer lithospheric deformation in the indian ocean, *Nature communications*, *6*, 8298.

Qin, Y., S. C. Singh, I. Grevemeyer, M. Marjanović, and R. W. Buck (2020), Thin versus thick lithosphere beneath the young juan de fuca plate, *Nature Communications*, in press.

Raitt, M. (1963), The crustal rocks, *The sea*, *3*, 85–102.

Ranero, C. R., E. Banda, and P. Buhl (1997), The crustal structure of the canary basin: Accretion processes at slow spreading centers, *Journal of Geophysical Research: Solid Earth*, *102*(B5), 10,185–10,201.

Rankenburg, K., J. Lassiter, and G. Brey (2004), The role of continental crust and lithospheric mantle in the genesis of cameroon volcanic line lavas: constraints from isotopic variations in lavas and megacrysts from the biu and jos plateaux, *Journal of Petrology*, *46*(1), 169–190.

Ravelo, A., D. H Andreasen, M. Lyle, A. Olivarez Lyle, and M. Wara (2004), Regional climate shifts caused by gradual global cooling in the pliocene epoch, *Nature*, *429*, 263–7, doi:10.1038/nature02567.

Renkin, M. L., and J. G. Sclater (1988), Depth and age in the north pacific, *Journal of Geophysical Research: Solid Earth*, *93*(B4), 2919–2935, doi:10.1029/JB093iB04p02919.

Reshef, M., and D. Kosloff (1986), Migration of common-shot gathers, *Geophysics*, *51*(2), 324–331.

Reusch, A. M., A. A. Nyblade, R. Tibi, D. A. Wiens, P. J. Shore, A. Bekoa, C. T. Tabod, and J. M. Nnange (2011), Mantle transition zone thickness beneath cameroon: evidence for an upper mantle origin for the cameroon volcanic line, *Geophysical Journal International*, *187*(3), 1146–1150.

Reusch, M. M., A. A. Nyblade, D. Wiens, P. J. Shore, A. Bekoa, C. Tabod, and J. M. Nnange (2010), Upper mantle structure beneath cameroon from body wave tomography and the origin of the cameroon volcanic line, *Geochemistry, Geophysics, Geosystems*, *11*, doi:10.1029/2010GC003200.

Revenaugh, J., and T. H. Jordan (1991), Mantle layering from scs reverberations: 2. the transition zone, *Journal of Geophysical Research: Solid Earth*, *96*(B12), 19,763–19,780.

Ribe, N., and U. Christensen (1994), Three-dimensional modeling of plume-lithosphere interaction, *Journal of Geophysical Research: Solid Earth*, *99*(B1), 669–682.

Richter, F. M., and B. Parsons (1975), On the interaction of two scales of convection in the mantle, *Journal of Geophysical Research*, *80*(17), 2529–2541.

Robinson, E. M. (1988), The topographic and gravitational expression of density anomalies due to melt extraction in the uppermost oceanic mantle, *Earth and planetary science letters*, *90*(2), 221–228.

Rohr, K., B. Milkereit, and C. Yorath (1988), Asymmetric deep crustal structure across the juan de fuca ridge, *Geology*, *16*(6), 533–537.

Rohr, K. M. (1994), Increase of seismic velocities in upper oceanic crust and hydrothermal circulation in the juan de fuca plate, *Geophysical research letters*, *21*(19), 2163–2166.

Rothe, P. (1990), Sediments on volcanic islandson the importance of the exception, in *Sediments and Environmental Geochemistry*, pp. 29–47, Springer.

Ruddiman, W., M. Sarnthein, J. Backman, J. Baldauf, W. Curry, L. Dupont, T. Janecek, E. Pokras, M. Raymo, B. Stabell, et al. (1989a), 29. late miocene to pleistocene evolution of climate in africa and the low-latitude atlantic: Overview of leg 108 results1, in *Proceedings of the Ocean Drilling Program Scientific Results*, vol. 108, pp. 463–484.

Ruddiman, W., M. Sarnthein, J. Backman, J. Baldauf, W. Curry, L. Dupont, T. Janecek, E. Pokras, M. Raymo, B. Stabell, R. Stein, and R. Tiedemann (1989b), *29. Late Miocene to Pleistocene Evolution of Climate in Africa and the Low-Altitude Atlantic: Overview of Leg 108 Results*, vol. 108, pp. 463–484, doi:10.2973/odp.proc.sr.108.173.1989.

Ruddiman, W. F., and T. R. Janecek (1989), Biogenic and terrigeneous components in Pliocene-Pleistocene sediments of the equatorial Atlantic, doi:10.1594/PANGAEA.746239, supplement to: Ruddiman, WF; Janecek, TR (1989): Pliocene-Pleistocene biogenic and terrigenous fluxes at equatorial Atlantic Sites 662, 663, and 664. In: Ruddiman, W; Sarnthein, M; et al. (eds.), Proceedings of the Ocean Drilling Program, Scientific Results, College Station, TX (Ocean Drilling Program), 108, 211-240, https://doi.org/10.2973/odp.proc.sr.108.165.1989.

Russell, S. A., T. Lay, and E. J. Garnero (1998), Seismic evidence for small-scale dynamics in the lowermost mantle at the root of the hawaiian hotspot, *Nature*, *396*(6708), 255.

Rychert, C., K. Fischer, and S. Rondenay (2005), A sharp lithosphere-asthenosphere boundary imaged beneath eastern north america, *Nature*, *436*, 542–5, doi:10.1038/nature03904.

Rychert, C. A., and P. M. Shearer (2011), Imaging the lithosphere-asthenosphere boundary beneath the pacific using ss waveform modeling, *Journal of Geophysical Research: Solid Earth*, *116*(B7).

Rychert, C. A., N. Schmerr, and N. Harmon (2012), The pacific lithosphere-asthenosphere boundary: Seismic imaging and anisotropic constraints from ss waveforms, *Geochemistry, Geophysics, Geosystems*, *13*(9).

Rychert, C. A., G. Laske, N. Harmon, and P. M. Shearer (2013), Seismic imaging of melt in a displaced hawaiian plume, *Nature Geoscience*, *6*(8), 657.

Sakamaki, T., A. Suzuki, E. Ohtani, H. Terasaki, S. Urakawa, Y. Katayama, K.-i. Funakoshi, Y. Wang, J. W. Hernlund, and M. D. Ballmer (2013), Ponded melt at the boundary between the lithosphere and asthenosphere, *Nature Geoscience*, *6*(12), 1041.

Sandwell, D. T., R. D. Müller, W. H. Smith, E. Garcia, and R. Francis (2014), New global marine gravity model from cryosat-2 and jason-1 reveals buried tectonic structure, *Science*, *346*(6205), 65–67.

Sarafian, E., G. A. Gaetani, E. H. Hauri, and A. R. Sarafian (2017), Experimental constraints on the damp peridotite solidus and oceanic mantle potential temperature, *Science*, *355*(6328), 942–945, doi: 10.1126/science.aaj2165.

Sarnthein, M., K. Winn, J.-C. Duplessy, and M. R. Fontugne (1988), Global variations of surface ocean productivity in low and mid latitudes: Influence on co2 reservoirs of the deep ocean and atmosphere during the last 21,000 years, *Paleoceanography and Paleoclimatology*, *3*(3), 361–399.

Schilling, J., G. Thompson, R. Kingsley, and S. Humphris (1985), Hotspotmigrating ridge interaction in the south atlantic, *Nature*, *313*(5999), 187.

Schilling, J.-G. (1985), Upper mantle heterogeneities and dynamics, *Nature*, *314*(6006), 62.

Schmerr, N. (2012), The gutenberg discontinuity: Melt at the lithosphere-asthenosphere boundary, *Science*, *335*(6075), 1480–1483, doi:10.1126/science.1215433.

Schoofs, S., and U. Hansen (2000), Depletion of a brine layer at the base of ridge-crest hydrothermal systems, *Earth and Planetary Science Letters*, *180*(3-4), 341–353.

Schreiber, E., and P. J. Fox (1977), Density and p-wave velocity of rocks from the famous region and their implication to the structure of the oceanic crust, *Geological Society of America Bulletin*, *88*(4), 600–608.

Seher, T., W. C. Crawford, S. C. Singh, M. Cannat, V. Combier, and D. Dusunur (2010), Crustal velocity structure of the lucky strike segment of the mid-atlantic ridge at 37 n from seismic refraction measurements, *Journal of Geophysical Research: Solid Earth*, *115*(B3).

Selway, K., H. Ford, and P. Kelemen (2015), The seismic mid-lithosphere discontinuity, *Earth and Planetary Science Letters*, *414*, 45–57.

Shaw, P. R. (1994), Age variations of oceanic crust poisson's ratio: Inversion and a porosity evolution model, *Journal of Geophysical Research: Solid Earth*, *99*(B2), 3057–3066.

Shearer, P. M. (1991), Constraints on upper mantle discontinuities from observations of long-period reflected and converted phases, *Journal of Geophysical Research: Solid Earth*, *96*(B11), 18,147–18,182.

Sheen, K., N. White, C.-c. Caulfield, and R. Hobbs (2012), Seismic imaging of a large horizontal vortex at abyssal depths beneath the sub-antarctic front, *Nature Geoscience*, *5*, 542–546, doi:10.1038/ngeo1502.

Shipp, R. M., and S. C. Singh (2002), Two-dimensional full wavefield inversion of wide-aperture marine seismic streamer data, *Geophysical Journal International*, *151*(2), 325–344.

Sigman, D. M., and E. A. Boyle (2000), Glacial/interglacial variations in atmospheric carbon dioxide, *Nature*, *407*(6806), 859.

Silveira, G., and E. Stutzmann (2002), Anisotropic tomography of the atlantic ocean, *Physics of the Earth and Planetary Interiors*, *132*(4), 237–248.

Singh, S. (2015), European research council funds 2d ultra-deep seismic reflection data acquisition across the atlantic ocean, *first break*, *33*(6).

Singh, S. C., W. C. Crawford, H. Carton, T. Seher, V. Combier, M. Cannat, J. P. Canales, D. Düsünür, J. Escartin, and J. M. Miranda (2006), Discovery of a magma chamber and faults beneath a mid-atlantic ridge hydrothermal field, *Nature*, *442*(7106), 1029.

Sleep, N. H. (1990), Hotspots and mantle plumes: Some phenomenology, *Journal of Geophysical Research: Solid Earth*, *95*(B5), 6715–6736.

Staudigel, H. (2003), Hydrothermal alteration processes in the oceanic crust, *Treatise on geochemistry*, *3*, 659.

Stein, C. A., and S. Stein (1992), A model for the global variation in oceanic depth and heat flow with lithospheric age, *Nature*, *359*(6391), 123.

Stein, C. A., and S. Stein (1994), Constraints on hydrothermal heat flux through the oceanic lithosphere from global heat flow, *Journal of Geophysical Research: Solid Earth*, *99*(B2), 3081–3095.

Stein, R., H. Ten Haven, R. Littke, J. Rullkotter, and D. Welte (1986), 21. accumulation of marine and terrigenous organic carbon at upwelling site 658 and nonupwelling sites 657 and 659: Implications for the reconstruction of paleoenvironments in the eastern subtropical atlantic through late cenozoic times1, in *Proceedings of the Ocean Drilling Program: Scientific results*, vol. 108, p. 361, The Program.

Steinberger, B. (2000), Plumes in a convecting mantle: Models and observations for individual hotspots, *Journal of Geophysical Research: Solid Earth*, *105*(B5), 11,127–11,152.

Stern, T. A., S. A. Henrys, D. Okaya, J. N. Louie, M. K. Savage, S. H. Lamb, H. P. Sato, R. Sutherland, and T. Iwasaki (2015), A seismic reflection image for the base of a tectonic plate, *Nature*, *518*, 85–88.

Stillman, C. (1987), A canary islands dyke swarm: implications for the formation of oceanic islands by extensional fissural volcanism, *Mafic dyke swarms. Edited by HC Halls and WF Fahrig. Geological Association of Canada, Special Paper*, *34*, 243–255.

Street-Perrott, F. A., and R. A. Perrott (1990), Abrupt climate fluctuations in the tropics: the influence of atlantic ocean circulation, *Nature*, *343*(6259), 607.

Taylor, M., and S. Singh (2002), Composition and microstructure of magma bodies from effective medium theory, *Geophysical Journal International*, *149*(1), 15–21.

Te Wu, T. (1966), The effect of inclusion shape on the elastic moduli of a two-phase material, *International Journal of solids and structures*, *2*(1), 1–8.

Teitchou, M., M. Grégoire, R. Temdjim, R. Ghogomu, C. Ngwa, and F. Aka (2011), Mineralogical and geochemical fingerprints of mantle metasomatism beneath nyos volcano (cameroon volcanic line), *Geological Society of America Special Papers*, *478*, 193–210.

Tharimena, S., C. A. Rychert, and N. Harmon (2016), Seismic imaging of a mid-lithospheric discontinuity beneath ontong java plateau, *Earth and Planetary Science Letters*, *450*, 62–70.

Thoraval, C., A. Tommasi, and M.-P. Doin (2006), Plume-lithosphere interaction beneath a fast moving plate, *Geophysical research letters*, *33*(1).

Tibi, R., A. Larson, A. Nyblade, P. Shore, D. Wiens, J. Nnange, C. Tabod, and A. Bekoa (2005), A broadband seismological investigation of the cameroon volcanic line, in *AGU Fall Meeting Abstracts*.

Tivey, M. A., H. P. Johnson, C. Fleutelot, S. Hussenoeder, R. Lawrence, C. Waters, and B. Wooding (1998), Direct measurement of magnetic reversal polarity boundaries in a cross-section of oceanic crust, *Geophysical research letters*, *25*(19), 3631–3634.

Toomey, D. R., G. Purdy, S. C. Solomon, and W. S. Wilcock (1990), The three-dimensional seismic velocity structure of the east pacific rise near latitude 9 30 n, *Nature*, *347*(6294), 639.

Turcotte, D. L., and G. Schubert (2002), *Geodynamics*, Cambridge university press.

Van Avendonk, H. J., A. J. Harding, J. A. Orcutt, and J. S. McClain (1998), A two-dimensional tomographic study of the clipperton transform fault, *Journal of Geophysical Research: Solid Earth*, *103*(B8), 17,885–17,899.

Van Avendonk, H. J., D. J. Shillington, W. S. Holbrook, and M. J. Hornbach (2004), Inferring crustal structure in the aleutian island arc from a sparse wide-angle seismic data set, *Geochemistry, Geophysics, Geosystems*, *5*(8).

Vassallo, M., K. Eggenberger, D.-J. van Manen, A. Özbek, and P. Watterson (2013), Broadband and beyond with marine towed streamers, *The Leading Edge*, *32*(11), 1356–1365.

Vera, E., J. Mutter, P. Buhl, J. Orcutt, A. Harding, M. Kappus, R. Detrick, and T. Brocher (1990), The structure of 0-to 0.2-my-old oceanic crust at 9 n on the east pacific rise from expanded spread profiles, *Journal of Geophysical Research: Solid Earth*, *95*(B10), 15,529–15,556.

Vera, E. E., and J. B. Diebold (1994), Seismic imaging of oceanic layer 2a between 9 30 n and 10 n on the east pacific rise from two-ship wide-aperture profiles, *Journal of Geophysical Research: Solid Earth*, *99*(B2), 3031–3041.

Vidale, J. (1988), Finite-difference calculation of travel times, *Bulletin of the Seismological Society of America*, *78*(6), 2062–2076.

Vidale, J. E., and H. M. Benz (1992), Upper-mantle seismic discontinuities and the thermal structure of subduction zones, *Nature*, *356*(6371), 678.

Viličić, D., M. Kuzmić, S. Bosak, T. Šilović, E. Hrustić, and Z. Burić (2009), Distribution of phytoplankton along the thermohaline gradient in the north-eastern adriatic channel; winter aspect, *Oceanologia*, *51*(4), 495.

Villinger, H., I. Grevemeyer, N. Kaul, J. Hauschild, and M. Pfender (2002), Hydrothermal heat flux through aged oceanic crust: where does the heat escape?, *Earth and Planetary Science Letters*, *202*(1), 159–170.

Virieux, J. (1986), P-sv wave propagation in heterogeneous media: Velocity-stress finite-difference method, *Geophysics*, *51*(4), 889–901.

Wagner, T. (2000), Control of organic carbon accumulation in the late quaternary equatorial atlantic (ocean drilling program sites 664 and 663): Productivity versus terrigenous supply, *Paleoceanography and Paleoclimatology*, *15*(2), 181–199.

Walsh, J. (1988), How much shelf production reaches the deep sea.

Wang, K., J. He, and E. E. Davis (1997), Influence of basement topography on hydrothermal circulation in sediment-buried igneous oceanic crust, *Earth and Planetary Science Letters*, *146*(1-2), 151–164.

WATSON, S., and D. McKenzie (1991), Melt generation by plumes: a study of hawaiian volcanism, *Journal of Petrology*, *32*(3), 501–537.

Watts, A., and E. Burov (2003), Lithospheric strength and its relationship to the elastic and seismogenic layer thickness, *Earth and Planetary Science Letters*, *213*(1), 113 – 131, doi:https://doi.org/10.1016/S0012-821X(03)00289-9.

Watts, A., D. McKenzie, B. Parsons, and M. Roufosse (1985), The relationship between gravity and bathymetry in the pacific ocean, *Geophysical Journal International*, *83*(1), 263–298.

Wegener, A. (1912), Die entstehung der kontinente, *Geologische Rundschau*, *3*(4), 276–292.

White, R. S., D. McKenzie, and R. K. O'Nions (1992), Oceanic crustal thickness from seismic measurements and rare earth element inversions, *Journal of Geophysical Research: Solid Earth*, *97*(B13), 19,683–19,715.

Whitmarsh, R. (1978), Seismic refraction studies of the upper igneous crust in the north atlantic and porosity estimates for layer 2, *Earth and Planetary Science Letters*, *37*(3), 451–464.

Whittaker, J. M., A. Goncharov, S. E. Williams, R. D. Müller, and G. Leitchenkov (2013), Global sediment thickness data set updated for the australian-antarctic southern ocean, *Geochemistry, Geophysics, Geosystems*, *14*(8), 3297–3305.

Wiens, D. A., J. A. Conder, and U. H. Faul (2008), The seismic structure and dynamics of the mantle wedge, *Annu. Rev. Earth Planet. Sci.*, *36*, 421–455.

Wilkens, R. H., G. J. Fryer, and J. Karsten (1991), Evolution of porosity and seismic structure of upper oceanic crust: Importance of aspect ratios, *Journal of Geophysical Research: Solid Earth*, *96*(B11), 17,981–17,995.

Wilson, M. (1992), Magmatism and continental rifting during the opening of the south atlantic ocean: a consequence of lower cretaceous super-plume activity?, *Geological Society, London, Special Publications*, *68*(1), 241–255.

Wirth, E. A., and M. D. Long (2014), A contrast in anisotropy across mid-lithospheric discontinuities beneath the central united statesa relic of craton formation, *Geology*, *42*(10), 851–854.

Zhang, Y.-S., and T. Tanimoto (1991), Global love wave phase velocity variation and its significance to plate tectonics, *Physics of the Earth and Planetary Interiors*, *66*(3-4), 160–202.

Zhang, Y.-S., and T. Tanimoto (1992), Ridges, hotspots and their interaction as observed in seismic velocity maps, *Nature*, *355*(6355), 45.

Zhang, Z., G. Ramstein, M. Schuster, C. Li, C. Contoux, and Q. Yan (2014), Aridification of the sahara desert caused by tethys sea shrinkage during the late miocene, *Nature*, *513*(7518), 401.

Upper Crustal and Lithosphere-Asthenosphere Boundary Seismic Structure of 0-75 Ma old Normal Oceanic Lithosphere in the Equatorial Atlantic Ocean

par **Pranav Audhkhasi**

Résumé

Les études antérieures sur la croûte océanique supérieure se sont limitées à la jeune lithosphère et aux données sismiques à grand angle, qui manquent de résolution dans la croûte supérieure. La limite océanique lithosphèreasthénosphère (LAB) a été largement étudiée par des études sismologiques, mais souffre également d'une faible résolution verticale. L'expérience TransAtlantic ILAB a collecté des données de réflexion sismique multicanaux sur la lithosphère océanique âgée de 0 à 75 Ma formée sur la dorsale médio-atlantique à propagation lente dans l'océan Atlantique équatorial. L'analyse de la croûte supérieure au moyen de l'imagerie sismique et de la tomographie à haute résolution indique que le sommet de la croûte (couche 2A) n'est jamais scellé de 0 à 75 Ma et les systèmes hydrothermaux continuent dans la croûte océanique plus ancienne. La majeure partie de l'évolution se produit dans les 4 premiers Myr, au-delà de laquelle l'intensité de la circulation hydrothermale diminue et la couverture sédimentaire augmente. La limite de la couche 2A / 2B est un contact de lave/digue à l'axe de la crête et un front d'altération hydrothermale éloigné de l'axe de la crête. Les données de flux de chaleur colocalisées de l'expérience LITHOS soutiennent la possibilité de grandes cellules hydrothermales dans une croûte océanique plus ancienne. Le LAB est entièrement imagé sur une lithosphère âgée de 2 à 75 Ma. De 2 à 47 Ma, il existe des preuves d'un canal LAB découplant le manteau lithosphérique du manteau asthénosphérique avec une lithosphère de 25 km d'épaisseur à 2 Myr et de 72 km à 47 Myr. Cependant, à partir de 49-75 Myr, une seule réflexion LAB est imagée, ce qui implique une perturbation possible de la base du canal en raison de la ligne volcanique du Cameroun adjacente. Des preuves solides d'anomalie thermique du manteau proviennent du fait que le LAB est moins profond et d'une lithosphère élevée.

Mots-clés: Lithosphère océanique, couche 2A, limite de la couche 2A/2B, canal LAB, ligne volcanique du Cameroun

Abstract

Previous studies on upper oceanic crust have been limited to young lithosphere and wide-angle seismic data, which lacks resolution in the upper crust. The oceanic lithosphere-asthenosphere boundary (LAB) has been studied extensively by seismological studies, but also suffers from low vertical resolution. The TransAtlantic ILAB experiment collected multi-channel seismic reflection data over oceanic lithosphere aged 0-75 Ma formed at the slow-spreading Mid-Atlantic Ridge in the Equatorial Atlantic Ocean. Analysis of upper crust by means of seismic imaging and high-resolution tomography indicates the top of the crust (Layer 2A) is never sealed from 0-75 Ma and hydrothermal systems continue in older oceanic crust. Most of the evolution happens within the first 4 Myr, beyond which intensity of hydrothermal circulation reduces and sediment cover increases. Layer 2A/2B boundary is a lava/dyke contact at the ridge-axis and a hydrothermal alteration front away from the ridge-axis. Co-located heatflow data from the LITHOS experiment supports the possibility of large hydrothermal cells in older oceanic crust. The LAB is imaged throughout on lithosphere aged 2-75 Ma. From 2-47 Ma, there is evidence of a LAB channel decoupling the lithospheric mantle from the asthenospheric mantle with the lithosphere being 25 km thick at 2 Myr and 72 km thick at 47 Myr. However from 49-75 Myr, a single LAB reflection is imaged implying possible disruption of the base of the channel due to adjacent Cameroon Volcanic Line. Strong evidence of mantle thermal anomaly comes from the LAB being shallower and an uplifted lithosphere.

Keywords: Oceanic Lithosphere, Layer 2A, Layer 2A/2B boundary, LAB channel, Cameroon Volcanic Line